



The 25th International Conference on Plastic Optical Fibres

13th – 15th September 2016, Aston University, Birmingham UK



Conference Proceedings

Sponsored by



Aston Institute of Photonic Technologies

Title POF 2016: 25th International Conference on Plastic Optical Fibres - Proceedings
Editors David .J. Webb, Patricia Scully, Kate Sugden
Publisher Aston University, 1 December 2016
ISBN 978 1 85449 408 5 (this edition has only been published digitally)

This edition is OPEN ACCESS and available from the **Aston Research Explorer** at *publications.aston.ac.uk*

Bibliographic note

© The Author(s) 2017. This article is distributed under the terms of the Creative Commons Attribution 4.0 International License (<http://creativecommons.org/licenses/by/4.0/>), which permits unrestricted use, distribution, and reproduction in any medium, provided you give appropriate credit to the original author(s) and the source, provide a link to the Creative Commons license, and indicate if changes were made.

CONTENT

Sensing I

OP1	Robust Two-Dimensional Pressure Sensing Mattress based on Optical Coupling between Crossing Polymer Optical Fibres <i>Henrie van den Boom, Sebastiaan Overeem, Ton Koonen</i>	1
OP2	POF based distributed SHM sensor based on speckle pattern <i>F. Reis, P. Antunes, P. S André</i>	5
OP3	Strain Dependence of Brillouin Scattering Properties in Plastic Optical Fibers Influenced by High Temperature <i>Kazunari Minakawa, Yosuke Mizuno and Kentaro Nakamura</i>	10
OP4	POF-Based Slope-Assisted Brillouin Optical Correlation-Domain Reflectometry <i>H. Lee, N. Hayashi, Y. Mizuno, and K. Nakamura</i>	14
OP5	2D optical accelerometer using POF array and image detection <i>R. Serrão, P. Antunes, P. S André</i>	18

Data Comms 1

OP6	Stabilized multimode fiber link using graded-index plastic optical fiber with strong mode coupling <i>A. Inoue and Y. Koike</i>	23
OP8	A Fast Fluorescent Light Source for Data Communication over SI-PMMA-POF Flávio <i>André N. Sampaio, Vinicius N. H. Silva, Luiz Anet Neto, Andrés P. L. Barbero, Ricardo M. Ribeiro and Tadeu N. Ferreira</i>	28
OP9	Application of 4-channel LED Module for WDM Transmission over SI-POF <i>R. Kruglov, J. Vinogradov, O. Ziemann, W. Huber</i>	33

Fibre Bragg Gratings 1

OP11	Embedding low loss polymer optical fibre Bragg gratings:Two different approaches <i>A. Lacraz, M. Zubel, G. Demirci, A. Theodosiou, K. Kalli, K. Sugden, B. Gawdzik</i>	36
OP12	Bragg gratings inscription using PMMA polymer optical fibers drawn from preforms with specific thermal pre-treatment <i>Carlos A. F. Marques, Andreas Pospori, Gökhan Demirci, Onur Çetinkaya, Barbara Gawdzik, Paulo Antunes, Pawel Mergo, Paulo André, David J. Webb</i>	40
OP13	Fiber Mach-Zehnder Interferometer system using polymer optical Bragg grating for underwater applications <i>Carlos A. F. Marques, David J. Webb</i>	46
OP14	Improving Temperature Sensing of Polymer Fibre Bragg Grating Sensors with PDMS coating <i>Gökhan Demirci, Amédée Lacraz, Kyriacos Kalli, Barbara Gawdzik</i>	53

Data Comms 2

OP15	Multiband 4G and Gigabit/s Baseband Transmission over Large-Core GI and SI POFs for In-Home Networks <i>F. Forni, Y. Shi, H.P.A. van den Boom, E. Tangdiongga, A.M.J. Koonen</i>	54
OP16	Dynamic Nonlinearities in Directly Modulated Light-Emitting Diodes <i>M. Schüppert and C.-A. Bunge</i>	58

OP17	Simulation of optical module for GI-POF with the Ballpoint-pen connection <i>H. Takizuka, A. Mitsui, H. Suzuki, T. Toma, and Y. Koike</i>	62
Modelling		
OP18	Modelling the bend out-coupling of melt-spun polymer optical fibers <i>Brit M. Quandt, René M. Rossi, Gian-Luca Bona, Birgit Luster mann, Luciano F. Boesel</i>	66
OP19	Analytical model for the angle-dependent power distribution in optical multimode fibers <i>T. Becker, B. Schmauss, M. Gehrke, E. Nkiwane, O. Ziemann</i>	67
Fibre Bragg Gratings 2		
OP20	Characteristics of photo polymerized polymer optical fibres, optical properties and femtosecond laser inscription of Bragg gratings <i>O.Palchik, N. Tal1, E. Shafir, G. Berkovic, S. Zilberman, A. Theodosiou and K. Kalli</i>	78
OP21	Dynamic damage detection of a cantilever carbon beam using a FBG array inscribed in polymer gradient index multimode CYTOP fibre <i>A. Theodosiou, K. Kalli and M. Komodromos</i>	82
OP22	Fiber Bragg grating-based Fabry-Perot interferometer in polymer fiber <i>G. Statkiewicz-Barabach, P. Maniewski, P. Mergo, W. Urbanczyk</i>	86
OP23	Bragg grating photo-inscription in doped microstructured polymer optical fiber by 400 nm femtosecond laser pulses <i>X. Hu, G. Woyessa, D. Kinet, J. Janting, K. Nielsen, O. Bang, P. Mégret, C. Caucheteur</i>	87
POF technology 1 and 2		
OP24	Fabrication and characterization of a lumogen-orange-doped polymer optical fibre <i>Parola, E. Arrospide, M.A Illarramendi, I. Ayesta, J. Zubia, N. Guarrotxena, O. García and C. Vazquez</i>	91
OP25	Joining intransparent components by UV-hardening systems through POF based UV-light initiation <i>Stephanie Bier, Benjamin Mohr, Bernd Marx, Alexander Schiebahn, Markus Beckers, Gunnar Seide, Thomas Gries, Uwe Reisgen, Christian-A. Bunge</i>	95
OP26	Portable polymer optical fibre cleaver <i>D. Sáez-Rodríguez, R.Min, B.Ortega, K.Nielsen, O.Bang, D.J. Webb</i>	100
OP27	Determination of the radial profile of the photoelastic coefficient of plastic optical fiber <i>S. Acheroy, T. Geernaert, H. Ottevaere, H. Thienpont, D.J. Webb, C.A.F Marques, G.-D. Peng, P. Mergo, F. Berghmans</i>	105
OP28	GIPOF-based power delivery systems <i>J.D. López-Cardona, D.S. Montero, P.J. Pinzón, C. Vázquez</i>	110
OP29	Impacts of gamma irradiation on Cytop plastic optical fibres <i>P. Stajanca, L. Mihai, D. Sporea, D. Negut, H. Sturm, M. Schukar, K. Krebber</i>	114
OP30	Textile Integration of POF for lighting applications <i>Benjamin Mohr, Markus Beckers, Pia Münch, Gunnar Seide, Thomas Gries, Christian Bunge</i>	118
OP31	Power over POF activities at the POF-AC Nuremberg <i>J. Fischer, J. Vinogradov, S. Zisler, O. Ziemann</i>	123
OP32	Analysis of Light Emission in Polymer Optical Fibers Doped With Europium <i>Complex J. Arrue, M.A. Illarramendi, B. Garcia-Ramiro, I. Parola, F. Jiménez, J. Zubia, R. Evert, D. Zaremba, H.-H. Johannes</i>	128

OP33	Investigation of Molecular Weight and Optical Behaviour of PMMA with Different Chain Transfer Agents <i>Onur Cetinkaya, Gokhan Demirci, Pawel Mergo</i>	133
------	---	-----

Sensing 2

OP34	Melt-spun polymer optical fibers for decubitus prevention <i>Brit M. Quandt, Damien Ferrario, René M. Rossi, Gian-Luca Bona, Luciano F. Boesel</i>	140
OP35	Strain, temperature and humidity sensing with multimode interference in POF <i>Ricardo Oliveira, Thiago H. R. Marques, Lúcia Bilro, Cristiano M. B. Cordeiro, Rogério N. Nogueira</i>	143
OP36	Analysis of the roughness in a sensing region on D-shaped POFs <i>F. Sequeira, D. Duarte, R. Nogueira, A. Rudnitskaya, N. Cennamo4, L. Zeni, L. Bilro</i>	148
OP37	Refractive Index Sensing Using Ultrasonically Crushed Plastic Optical Fibers <i>S. Shimada, H. Lee, M. Shizuka, H. Tanaka, N. Hayashi, Y. Matsumoto, Y. Tanaka, H. Nakamura, Y. Mizuno, and K. Nakamura</i>	152
OP38	Polymer Optical Fibre Refractive Index Probe for on-line measurement of Alcohol Composition for Distillation Column <i>P.J.Scully, A.Fong, K.Chandran, S. Whyte, X. Chai, M. Emerson, Ralph Stephenson Jones, A. Ahluwalia, M.Spooner, Z Gu, O Qureshi, M.Astaire</i>	156
OP39	POF Sensing Grid: Signal Analysis to extract Human Motion Characteristics <i>P.J.Scully, O. Costilla-Reyes, N.Ahmed, J.Vaughan, E.Stanmore, K.Ozanyan</i>	161
OP40	Radiation induced attenuation in perfluorinated polymer optical fibres for dosimetry applications <i>P. Stajanca, K. Krebber</i>	167

Poster Presentations

PP1	Parallel-multipoint plastic optical fiber sensor based on specklegrams <i>M. Lomer, L. Rodriguez-Cobo, J.M. Lopez-Higuera</i>	171
PP2	POF-based specklegram sensor for continuous patient monitoring <i>L. Rodriguez-Cobo, A. Rodriguez-Cuevas, E. Real, J.M. Lopez-Higuera, M. Lomer</i>	175
PP3	Power consumption analysis of a 3-channel real-time WDM link over SI-POF <i>P.J. Pinzón, C. Vázquez, D. S. Montero, J. Moreno López and Frank A. Dominguez-Chapman</i>	179
PP4	Experimental System for Automatic Alignment of Plastic Optical Fibres <i>F. A. Domínguez-Chapman, J. Mateo, M. A. Losada, A. López, C. Vázquez, J. Zubia</i>	183
PP5	Simplified Optical Correlation-Domain Reflectometry with Proximal Reflection Point Using CYTOP <i>M. Shizuka, H. Lee, N. Hayashi, Y. Mizuno, and K. Nakamura</i>	187
PP6	Capillary Refill Time Monitoring Using Photonic Textiles <i>Chong Liu, Shen Sun, Ricardo Correia, Barrie R Hayes-Gill, Serhiy Korposh, Simon A McMaster, Stephen P Morgan</i>	191
PP7	Transmitted signal quality in Ballpoint-pen interconnect of graded-index plastic optical fibre <i>Y. Kaseda, A. Inoue, A. Mitsui, H. Suzuki and Y. Koike</i>	195
PP8	Laser-Drive-Current Dependence of the Reflection Noise Effect for Graded Index Plastic Optical Fiber <i>T. Omuro, A. Inoue, Y. Koike</i>	199
PP9	Potential of POF sensors for Structural Health Monitoring of fibre composites <i>M. Plümpe, M. Beckers, C.-A. Bunge, T. Gries</i>	203
PP10	Bio Based POF <i>Benjamin Mohr, Daniel Grothe, Markus Beckers, Gunnar Seide, Thomas Gries, Christian-A. Bunge</i>	209

PP13	Multichannel interrogator for FBG sensing <i>D. Ganziy, B. Rose, O. Bang</i>	213
PP14	Design and performance of a cladding mode stripper to simplify the fabrication of mPOFsE <i>Arrospide, G. Durana, G. Aldabaldetrek, I. Bikandi, J. Zubia, Frank A. Dominguez-Chapman, J. Mateo</i>	214
PP15	Mechanical switching with light over POF – the direct approach with smart light-responsive materials <i>P. Dengler, H. Schlachter, M. Lippenberger, O. Ziemann</i>	218
PP16	Photoresponsive materials for intelligent optical devices – a review of the research done in BIOSOL <i>M. Lippenberger, C. Franke, P. Dengler, G. Wehnert, H. Poisel</i>	222
PP17	Demultiplexer for WDM Data Transmission over DSI-POF Based on a Concave Diffraction Grating <i>R. Kruglov, L.V. Bartkiv, J. Vinogradov, O. Ziemann, Ya.V. Bobitski, H. Poisel</i>	229
PP18	Analysis of Light Scattering in Polymer Optical Fibres using Mie Theory: An Analytical Approach <i>E. Nkiwane, T. Becker, M. Gehrke, O. Ziemann, B. Schmauss</i>	233
PP19	Improving OTDR Spatial Resolution using signal processing based on Power Flow Equation simulation data <i>M. Gehrke, B. T. Becker, E. Nkiwane and O. Ziemann</i>	239
PP20	Non-linear relation between modulation frequency and phase response of step-index polymer optical fiber <i>T. Becker, B. Schmauss, M. Gehrke, E. Nkiwane, O. Ziemann</i>	245
PP21	USB to Gigabit Ethernet POF link using KDPOF technology <i>M. Leitmeir, J. Vinogradov, M. Bloos, O. Ziemann</i>	251
PP22	The use of high power LED as photo converters and optical receivers in low speed POF sensor networks <i>T. Schuster, J. Fischer, O. Ziemann</i>	255
PP23	Annealing and etching effects on strain and stress sensitivity of polymer optical fibre Bragg grating sensors <i>A. Pospori, C. A. F. Marques, D. Sáez-Rodríguez, K. Nielsen, O. Bang, D. J. Webb</i>	260
PP24	Study of doping non-PMMA polymer fibre canes with UV photosensitive compounds <i>H. U. Hassan, A. Fasano, J. Janting, G. Demirci, O. Çetinkaya, G. Woyessa, H.K. Rasmussen, O. Bang</i>	264
PP25	Assessing central arterial pressure with a collar POF intensity sensor <i>C. Leitão, P. Antunes, C. Marques, Maria F. Domingues, J. Pinto, J. Mesquita Bastos, P. André</i>	269
PP26	Statistical approach to copolymerization parameter forecast using PM7 calculations <i>D. Zaremba, O. Laudi, R. Evert, W. Kowalsky, R. Caspary, H.-H. Johannes</i>	270
PP27	Polymer Optical Fiber Sensor for Temperature Measurement in Liquids <i>R. Guijarro, A. Tapetado, P. J. Pinzón, P. C. Lallana, D. S. Montero, J. Zubia, C. Vázquez</i>	275
PP28	Polymer Optical Fibre Bragg Grating Humidity Sensor at 100°C <i>G. Woyessa, A. Fasano, C. Markos, H.K. Rasmussen, O. Bang</i>	279
PP29	Intrinsic Pressure Response of a Single-Mode Cyclo Olefin Polymer Microstructured Optical Fibre Bragg Grating <i>J. K. M. Pedersen, G. Woyessa, K. Nielsen, O. Bang</i>	283
PP30	Development and characterization of a low cost sediment concentration optical sensor <i>N. Oliveira, D. Duarte, C. Ferreira, P.A. Silva, R. Nogueira, L. Bilro</i>	287
PP31	Investigation of the in-solution relaxation of polymer optical fibre Bragg gratings <i>A. Fasano, G. Woyessa, J. Janting, H.K. Rasmussen, O. Bang</i>	291
PP32	3D-printed PMMA preform for hollow-core POF drawing <i>M.G. Zubel, A. Fasano, G. Woyessa, K. Sugden, H.K. Rasmussen, O. Bang</i>	295

Robust Two-Dimensional Pressure Sensing Mattress based on Optical Coupling between Crossing Polymer Optical Fibres

Henrie van den Boom^{1*}, Sebastiaan Overeem^{2,3}, Ton Koonen¹

¹ COBRA Institute, Eindhoven University of Technology, Eindhoven, The Netherlands

² Sleep Medicine Centre Kempenhaeghe, Heeze, The Netherlands

³ Dept. of Electrical Engineering, Eindhoven University of Technology, Eindhoven, The Netherlands

*Corresponding author: h.p.a.v.d.boom@tue.nl

Abstract: We present an innovative 2D pressure sensor for application below a mattress. It deploys a matrix of plastic optical fibre crosspoints which is robust, sensitive, scalable, flexible, waterproof, EMI insensitive, and only 3mm thick. Measurements show a nearly linear detection characteristic.

1. Introduction

Currently, people suffering from serious sleep disorders are monitored in special sleep clinics. Monitoring is preferably done without affixing any wires to those persons, in order not to hamper them in their movements. Moreover, when long-term monitoring in the home environment is desired, e.g. for bed-bound patients, a non-contact and non-obtrusive measuring method is paramount [1-3]. Ambulatory sleep registration systems have been developed, but are complex and limited to only 1 or 2 recording nights. There are many potential clinical applications for technology that is easily applicable in the home environment for longer time periods. An important sleep-related parameter pertains to nocturnal body position and its changes. Contactless position sensing can typically be done in various ways, such as monitoring a person by means of a video camera, by which his movements are registered and processed. This requires a clear view of the person at all times, and is in the case of sleeping persons greatly hampered by blankets etc. Moreover, video monitoring in for example the bedroom poses obvious issues with privacy etc.

In this paper, we describe a sensing method for detecting body positions which does not require any physical connections to the objects/persons. It is based on sensing local pressures exerted by them on a surface, in which we propose a 2-dimensional (2D) structure of interwoven plastic optical fibres. Within this structure, light propagation behaviour is changed upon applied pressures, and by measuring these changes in correlation to the position in the structure, the 2D pressure detection is done. E.g., by putting this structure inside or beneath a mattress, the 2D movements of a person during his sleep can be monitored over time, without any influence on the person's sleep behaviour. Note also that the measurements are taken by changes in the optical propagation characteristics of the structure, not by electrical fields. Thus these measurements are not influenced by any disturbing RF electromagnetic fields (coming e.g. from local WiFi systems, or from electrical power supply lines), nor are they generating electromagnetic fields themselves which e.g. could interfere with medical monitoring equipment or with devices inside or near the person (such as heart pace makers, EEG sensors).

As mentioned before, polymer or plastic optical fibre (POF) is used for detecting pressure. POF is typically made from PMMA. POF is commonly used for low-speed, short-distance optical data communication [4] and is robust and flexible, and is insensitive for Electro Magnetic Interference (EMI). Compared with silica glass optical fibres, due to their relatively large core diameters of about 1 mm POFs are robust and easy to handle, and allow the use of low-precision connectors. Because of its bending-sensitive properties, augmented by its ductility, POF can also be used for sensing [5]. Sensor systems based on detecting POF attenuation variations when pressure or bending is applied have been reported [6-7], and commercial products based on this are available [8].

A straightforward 2D position detection system based on only detecting attenuation in a POF is in principle not possible. In a 2-dimensional grid of crossing POFs, with N POFs running in the x-direction and M POFs in the y-direction, we have $N \times M$ crosspoints. If we measure the attenuation variation of each of the POFs in the x and y directions, we have $N + M$ loss measurement values. To calculate the pressure applied on each of the crossing points, we need at least the same number of measurement values as the number of crosspoints. So with

only attenuation detection we require $N + M \geq N \times M$. This holds only for grids smaller than or equal to 2×2 and even the 2×2 grid is unsolvable.

So for 2D position detection we need another approach: we propose to measure the cross-coupling at each crossing of the N x -direction POFs and the M y -direction POFs. This yields $N \times M$ values as a measure of the local pressure at the crossings.

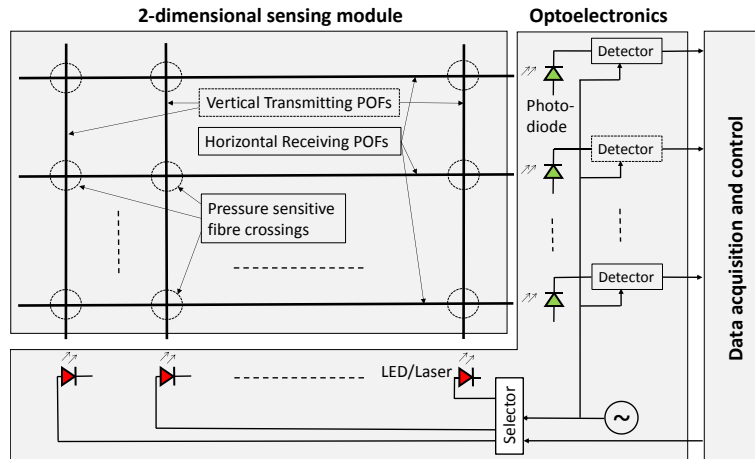


Figure 1. 2D position sensing system deploying a matrix of plastic optical fibre (POF) crosspoints.

2. Description of the 2D pressure sensing system

Figure 1 shows the principle of operation of our system based on monitoring the local pressure exerted per crosspoint on a 2D structure embedded in a 2D surface, such as a mattress. The system consists of a 2D sensing module, an optoelectronics module and a Data Acquisition and Control module. The 2D sensing module is composed of a grid of POFs which form a matrix of crosspoints. The vertical, so-called transmitting fibres of the POF grid are connected to LEDs or lasers and the horizontal receiving fibres to photodiodes of the optoelectronics module. The LEDs or lasers are controlled and the measured data is processed by the Data Acquisition and Control module.

The optical coupling between the POFs at the crosspoints is a function of the local pressure, so by detecting the received optical power, the pressure on a crosspoint can be measured. Because the optical coupling effect between transmitting and receiving fibres is very small, high-sensitivity optical receivers are needed, using transimpedance amplifiers with high gain and a high input impedance. Sensitivity is increased further by modulating each optical source with a low frequency carrier and applying highly-selective synchronous detection, executed by multiplying the received amplified signal with the same carrier signal and low-pass filtering the output.

To achieve a simple and scalable system, a crosspoint scanning method is implemented. The Data Acquisition and Control module in figure 1 controls the Selector, which selects only one LED or laser at a time, and the crossings are scanned column by column. Reading simultaneously the detector outputs line-by-line enables the Data Acquisition and Control module to do the 2D pressure detection.

3. POF crosspoint

The proposed implementation of a single POF crosspoint is shown in figure 2. It is composed by two fibres crossing each other at an angle (e.g. 90 degrees, as sketched in figure 2; other angles are also usable). The core and the cladding are made of a polymer, typically PMMA (poly-methyl metacrylate) which is transparent for light in the visible spectrum (400-700nm). Light is injected in the transmitting fibre. It is guided within the core

of the fibre, and the cladding is surrounded by a soft thin transparent primary coating, and subsequently by a hard protective in-transparent secondary coating. At the crossing, the secondary coating of both fibres is locally removed, which enables the fibres to make physical contact by the primary coating. When some light is forced to leave the core, e.g. by slightly deforming this core, this light can move into the cladding and into the primary coating. By touching the other fibre and the scattering experienced in the soft primary coating, this light may then transition into the primary coating of the other fibre (the receiving fibre), and via the cladding get into the core of that fibre. In order to further enhance the coupling of light which has escaped from the transmission fibre into the receiving fibre, a reflective structure (such as a reflective aluminium foil) was added locally at the crosspoint, as shown in figure 2. Thus in a single crosspoint which is only 3mm thick, some light gets from the transmitting fibre into the receiving fibre, upon the exertion of some force onto the crosspoint.

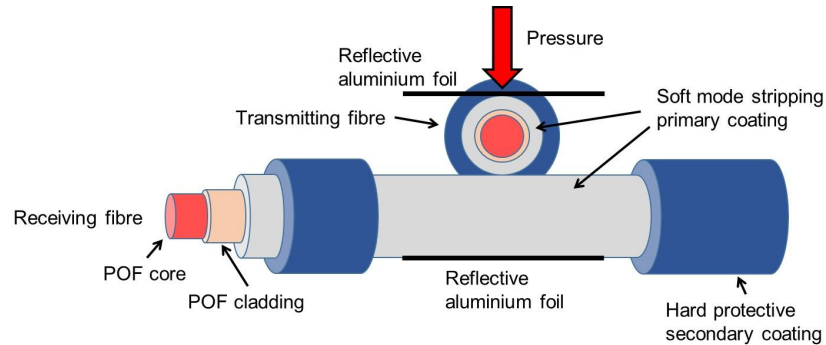


Figure 2. Single POF-based pressure-sensitive crosspoint.

4. Measurement results

The characteristics of a single crosspoint based on graded-index POF (GI-POF) have been measured by loading the crosspoint with some external weight; the measurement setup is shown in figure 3. A 650nm wavelength semiconductor laser with output power of 1.4mW (1.46dBm) is modulated with a square wave signal at 270Hz. At the receiver side, a shielded silicon photodiode is directly connected to an EG&G Brookdeal 5206 Lock-in amplifier with an input impedance of 100MΩ, which performs the amplification and synchronous detection operations. Figure 4 shows the voltage of the lock-in amplifier measured selectively as a function of the applied weight. A weight of 100g can already be detected. This measured signal shows a clear reproducible and nearly linear relation to the weight pressure on the crosspoint. Moreover, the characteristic can be linearised by software.

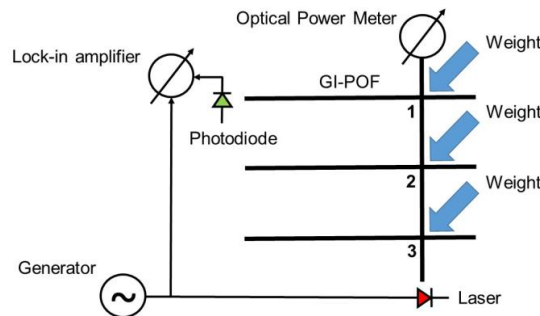


Figure 3. Measuring the pressure sensing characteristics of a single GI-POF crosspoint.

The optical output power of the transmission fibre after the crosspoints is monitored by an optical power meter, see figure 3. Loading all 3 crosspoints with a weight of 1kg introduces an optical power degradation smaller than 1%, so there is no significant influence of weight pressure of crosspoint 2 and 3 (see figure 3) on the measured result of figure 4. This indicates that this method is suitable for large matrices with many crosspoints.

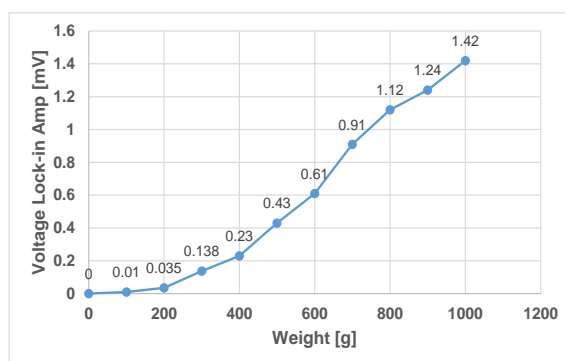


Figure 4. Output voltage at lock-in amplifier, versus exerted pressure on the crosspoint.

As an example we calculate the optical power detected by the photodiode in case of an exerted weight of 100g. The measured voltage of the lock-in amplifier at a weight of 100g is 0.01mV as shown in figure 4. The input impedance of the lock-in amplifier is $100\text{M}\Omega$, so the photodiode current is 10^{-13}A . The responsivity of the silicon photodiode at the wavelength of 650 nm is 0.4A/W , so the received optical power is 40fW or -104dBm and the optical power ratio between photodiode input power and laser output power is -105.46dB .

Conclusions

This paper proposes an optical method to perform 2-dimensional pressure sensing, based on measuring the cross-coupling between POFs arranged in a 2-dimensional structure composed of slightly deformable crosspoints. This sensing method is robust, flexible and waterproof because of the use of POF, is readily scalable because N detectors plus M sources create $N \times M$ sensor points, is not affected by external electrical fields, nor does it generate any electrical fields, and is only 3mm thick. Measurements show a sensitive and nearly linear detection characteristic.

Many application fields can be foreseen. As stated, one particular application is in sleep medicine. Long-term at-home monitoring of sleep-related movements would be an important addition to the arsenal of diagnostic methods. E.g., it may enable the long-term assessment of sleep-related breathing disorders such as sleep apnea which are often body-position dependent. The device would enable confident monitoring of outcome of therapy aiming at changing body position in sleep. It may have diagnostic application for parasomnias such as sleep walking; and for the detection of hampered sleep-related movements in prevalent disorders such as Parkinson's disease. Due to its compact flexible size, it can remain unnoticed by the person/object to be monitored. Moreover, it uses readily available components. First proofs of feasibility showed encouraging results.

References

- [1] G. Guerrero et al., "Detection of sleep disordered breathing with pressure bed sensor", *Proc. 35th IEEE EMBS 2013*, 2013, pp. 1342-1345.
- [2] M. Nishyama et al, "Respiration and body movement analysis during sleep in bed using hetero-core fiber optic pressure sensors without constraint to human activity", *J. of Biomedical Optics* 16(1), pp. 017002-1-6, Jan. 2011.
- [3] J. Abraham et al, "Low-cost and disposable pressure sensor mat for non-invasive sleep and movement monitoring applications", *Proc. 33rd IEEE EMBS 2011*, 2011, pp. 4745-4748.
- [4] Olaf Ziemann et al, *POF Handbook*, Springer, 2008.
- [5] L. Bilro et al, "Optical sensors based on plastic fibers", *Sensors* 2012, 12.
- [6] European Commission 6th Framework project POLYTECT.
- [7] European Commission 6th Framework project OFSETH.
- [8] <http://www.fiberfin.com/index.php/products/security.html>



POF based distributed SHM sensor based on speckle pattern

F. Reis¹, P. Antunes², P. S André^{3,*}

1 Department of Electrical and Computer Engineering and Portuguese Air Force Academy, Instituto Superior Técnico, University of Lisboa, Lisboa, Portugal

2 Instituto de Telecomunicações and Physics Department & I3N, University of Aveiro, Aveiro, Portugal

3 Department of Electrical and Computer Engineering and Instituto de Telecomunicações, Instituto Superior Técnico, University of Lisboa, Lisboa, Portugal

*Corresponding author: paulo.andre@tecnico.ulisboa.pt

Abstract: Structural Health Monitoring (SHM) is a damage detection and control strategy applied to large dimension structures, as dams buildings or bridges, but also to vehicles, as airplanes, where carrying sensors allows the monitoring of the structural health along operation.

In this work we propose and demonstrate, the application of a distributed optical sensor, suitable for SHM, based on polymer optical fibres (POF) and on the speckle pattern to access and evaluate the damage imposed to structures. As the speckle pattern obtained at the fibre output is sensitive to the disturbances along the fibre, the sensing of the measurand is possible with a suitable processing stage of the speckle pattern.

1. Introduction

The structural health is directly related with the performance of the structures and is very important to ensure a safe operation [1]. Structural health monitoring (SHM) of structures has a lot of definitions, however it could intuitively be defined as the diagnosis and prognosis of the structure ability to function properly and maintain their structural integrity throughout its life.

For aircraft structures, it is known that structural degradation caused by aging of materials, due to the environment (fatigue, corrosion, etc.) or even due to unforeseen external events (impacts, earthquakes) is inevitable. So, it is important to take special precautions for aircrafts operating close to or beyond the end of their life cycle when a significant increase of structural defects may occur [2], [3]. For example, in 2000 more than 75 % of the United States Air Force (USAF) aircrafts had more than 25 years [1].

Thus to ensure a safe operation is essential to conduct periodic inspections and, if necessary replace damaged components by unpredictable failures (which cannot be completely eliminated). In the case of a SHM system, the inspections are conducted using non-destructive techniques (visual inspection, radiography, ultrasound, eddy currents, etc.) to provide information of the structure condition, so that an integrity evaluation could be performed and if necessary carrying out repairs in a timely manner [3].

Future tendency will be to complement or replace inspections by continuous structural health monitoring using on-board systems (implemented within the aircraft) increasing security and confidence in the systems and reducing the periodic inspection cycles, eliminating the costs of unplanned maintenance on new aircrafts and ensure greater longevity of the components [2], [4].

Recently different technologies based on sensor networks using optical fibers emerged. These economically attractive technologies have a great potential since they ensure continuous monitoring, don't require extensive maintenance, improve performance and safety of the aircraft and extend the lifetime of structures [1].

A recent study on the requirements of a fighter aircraft inspection (in terms of metallic and composite structures) show that more than 40% of inspection time could be saved if on-board intelligent monitoring systems were used. Such systems may be composed by an assembly of sensors, actuators and signal processors that are able to respond and adapt to changes in their environment [1].

Key Words: POF, SHM, Speckle
Preferred presentation method: Oral



In addition, it is noticed that some researchers assume that more than 20% of the cost of a transport aircraft maintenance/inspection (civil or military) may be saved, when using integrated damage monitoring systems [1].

2. Speckle Pattern

When the beam of a continuous wave laser (laser CW) focuses on a rough surface (with roughness greater than the radiation wavelength) the components of the light scattered by independent areas of the surface get different phases relative to the incident wave phase. The phase shift of these waves (still coherent) results in the interference (constructively or destructively) along space, generating a statistical distribution, the granular speckle pattern. Therefore, this granular pattern observable in an area, consists on a set of bright spots where the interference is constructive and black spots where the interference is destructive [5], [6]. In Figure 1 it is possible to observe a typical speckle pattern experimentally obtained in this work.



Figure 1. Typical speckle pattern

The speckle patterns can also be obtained using multimode (MM) optical fibers like POFs MM. This happens due to interference between the different coherent modes propagating in the guide with different phase velocities [7], [8].

Consequently, if the fiber is disturbed due to external factors, such as temperature, pressure, or vibration, the intensity distribution pattern in the fiber output, which is the aggregation of all individual propagating mode fields, changes immediately.

2.1. Speckle Intensity in POF

The total intensity of the speckle pattern measured at the optical fiber output is approximately constant and when the fiber is exposed to a disturbance is given by:

$$I_i = A_i \{1 + B_i [\cos \delta_i - F(t) \phi_i \sin \delta_i]\} \quad (1)$$

where A_i is the result of mode self-interaction, B_i account for the steady state mode-mode interaction, $F(t)$ is the external disturbance, and ϕ_i is the phase [7].

When the system is disturbed, the mode-mode interaction term is modified by ϕ_i . A_i , B_i and δ_i which are constant values for any given *ith* speckle. The speckle pattern can be seen as an interference matrix under the same perturbation for each *i*. Therefore, when the conditions of the fiber change, either due to temperature, pressure or displacement, the speckle pattern is also changed. Thus, with the analysis of the obtained image

Key Words: POF, SHM, Speckle
Preferred presentation method: Oral



and its evolution is possible to find the disturbance which affect the fiber and its characteristics. Therefore, the implementation of this method as a vibration sensor may be possible by placing a small length of multimode fiber at the desired location [7].

2.2 Correlation Processing Method

When a fiber suffers stress, the induced deformation changes the optical paths lengths of each propagating mode differently and therefore the speckle patterns are changed accordingly. These changes can be detected by comparing the reference pattern with the resulting pattern after deformation [7].

Thus, the correlation parameter is obtained between the reference speckle pattern and the different images speckle representatives of disturbance variations. So, the correlation values represent the values of the perturbation. A good comparison between the patterns can be accomplished using a spatial correlation between them. The intensity distribution of the speckle patterns before the perturbation $I_1(x, y)$ and after the perturbation $I_2(x, y)$ are compared by measuring the coefficient of correlation between these signals:

$$C = \frac{\langle I_1(x, y) I_2(x, y) \rangle - \langle I_1(x, y) \rangle \langle I_2(x, y) \rangle}{\sqrt{(\langle I_1(x, y) \rangle^2 - \langle I_1(x, y) \rangle^2) \times (\langle I_2(x, y) \rangle^2 - \langle I_2(x, y) \rangle^2)}} \quad (2)$$

where the angle brackets mean averaging over the spatial coordinates x and y . The correlation coefficient takes the value one if the intensity distribution of speckle pattern $I_2(x, y)$ is equal to $I_1(x, y)$ and it gradually decreases with the changes in the speckle pattern [7].

3. Optical Sensor Application

The implemented sensor comprises a semiconductor laser (Roithner - LDM650/3LJ), peaking at 650 nm with an optical power of 3 mW. The optical signal is injected in a POF (*Avago Technologies* – HFBR-RUS100Z) with a length of 2.25 m. After propagation the output optical signal is projected in a semi opacity film and the speckle image acquired by the video camera.

The speckle detection is achieved with a Raspberry Pi camera (Raspicam) with 5 megapixel resolution and a frame rate of 30 Hz. The Raspicam is attached to a Raspberry Pi 1 Model B (RPI) responsible for signal processing. However, since the RPI has low processing capacity, we choose to perform all processing on a computer with the use of Matlab software.

To get clearer and perceptible speckle patterns with more contours is necessary to change some image acquisition settings, such as increasing the contrast, brightness and sharpness and decrease the saturation. Increasing the shutter speed and ISO sensitivity, decreases saturation and also increases the detection of contours and the sensitivity to mechanical vibration. Furthermore all automatic effects need to be disabled [9].

To ensure continuous monitoring of structural health is necessary to continuously record the speckle patterns transmitted by the POF output. These videos will then be separated and analyzed frame by frame using three different methods to identify the disturbances in the POF.

Therefore, the first method performs the correlation of the current frame with the previous one, the second method performs a correlation of the current frame with a reference one (usually the first) and the third method calculates the average intensity of each of the video frames.

4. Results

Despite the fact that is necessary to continuously record the speckle patterns to ensure continuous structural health monitoring, for experimental purposes there are recorded short videos of 20 seconds to assure faster signal processing.

Key Words: POF, SHM, Speckle
Preferred presentation method: Oral



For illustrative purposes we presented the test with a negative movement of 3.75 cm occurring at 7 seconds. It is noticed that at the beginning of every test the POF is static. For the speckle analyses several methods were applied: *i*) correlation between each frame and the previously one; *ii*) correlation between each frame and the initial one and *iii*) total frame intensity. It was also considered the local derivative for the described methods.

In Figure 2 we can observe the perturbation results using the described methods. We can see that correlation value is constant (almost 1 when the frames are most correlated) when the POF is static. Then, we observe a correlation value decrease at the instant of perturbation (approximately at 7 seconds). After that instant the correlation value tends to re-stabilize around 1. The occurrence of perturbations is easily observed in the derivative graph, but the values tend to 0 when the POF is static.

Using the second method we also get excellent results, however challenging to analyze. This difficulty can be overcome using the derivative as shown in Figure 2 (middle).

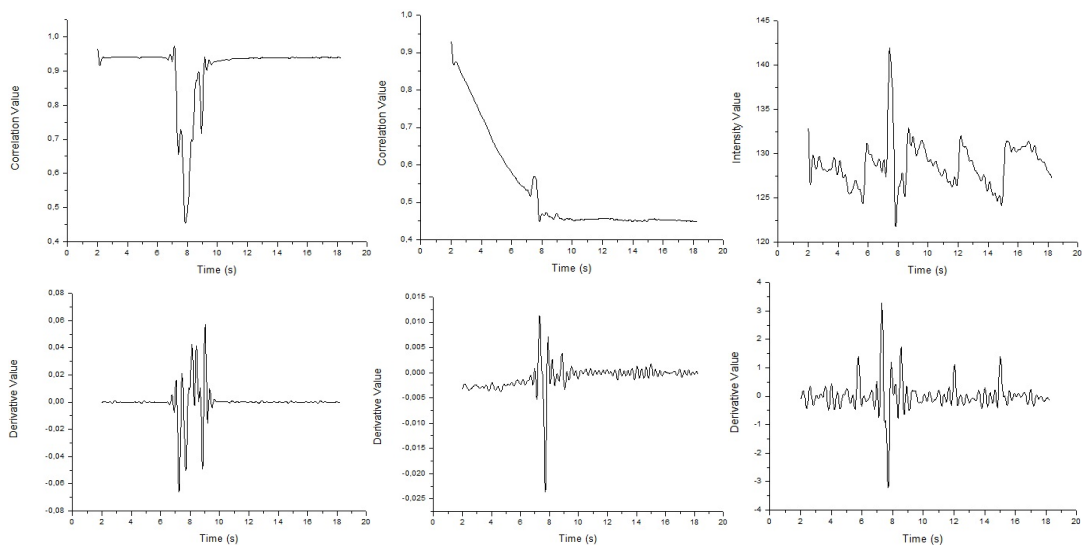


Figure 21 – Results with a negative perturbation of 3.75 cm using the correlation between the current frame and the previous one(left), the correlation of the current frame with the reference one (middle) and the average intensity of frames (right).

Through any of the different testing analysis performed, an easy identification of the occurrence of perturbations was possible, however only the third method (which calculates the intensity of each frame) allowed the estimation of the perturbation amplitude, that is the value of the average intensity of the frame, which gets higher if the amplitude perturbation increases.

5. Conclusion

From the results described in the previous section it was possible to conclude that the optical sensor implemented in this work is low-cost, relatively simple and feasible, with great potential applicability, demonstrating a great ease of identifying isolated or periodic perturbations caused by movement of the fiber or impacts in adjacent areas.

It is estimated that the method that calculates the average intensity of frames is the best method to identify perturbations, allowing an easily identification of disturbances and to estimate the perturbation amplitude. It is

Key Words: POF, SHM, Speckle
Preferred presentation method: Oral



worth noting that, although a frame rate of 30 Hz was used, it has the advantage of significantly higher image processing speeds.

Correlation tests are also excellent methods for detecting perturbations, however in case of the correlation of the current frame with the initial one, only the results obtained by the derivative are easily interpretable. Nonetheless, this method has the advantage presenting low noise signals even without filtering.

These results demonstrated the possibility to use the speckle patterns to monitor the deformation along an infrastructure or an aircraft using a low cost solution.

7. Acknowledgement

This work was financed in the scope of UID/EEA/50008/2013, by the National Funds through the Fundação para a Ciência e a Tecnologia / Ministério da Educação e Ciência, and by the European Regional Development Fund under the PT2020 Partnership Agreement. The support from the Brazilian Ciência sem Fronteiras (PVE) program is also appreciated. P. Antunes acknowledge FCT support through the postdoctoral research fellowship SFRH/BPD/76735/2011.

8. References

- [1] W. J. Staszewski, C. Boller, and G. R. Tomlinson, *Health Monitoring of Aerospace Structures*. Sheffield, UK: John Wiley & Sons, Ltd, 2003.
- [2] C. E. Katsikeros and G. N. Labeas, "Development and validation of a strain-based Structural Health Monitoring system," *Mech. Syst. Signal Process.*, vol. 23, no. 2, pp. 372–383, 2009.
- [3] J. D. Achenbach, "Structural health monitoring - What is the prescription?," *Mech. Res. Commun.*, vol. 36, no. 2, pp. 137–142, 2009.
- [4] N. Meyendorf, B. Frankenstein, and L. Schubert, "Structural health monitoring for aircraft, ground transportation vehicles, wind turbines and pipes-prognosis," in *Emerging Technologies in Non-Destructive Testing V*, 2012, no. April, pp. 15–22.
- [5] Y. Gan and W. Steinchen, "Speckle Methods," in *Springer Handbook of Experimental Solid Mechanics*, 2008, pp. 655–674.
- [6] J. W. Goodman, "Some fundamental properties of speckle," *J. Opt. Soc. Am.*, vol. 66, no. 11, pp. 1145–1150, 1976.
- [7] L. Rodriguez-Cobo, M. Lomer, C. Galindez, and J. M. Lopez-Higuera, "POF vibration sensor based on speckle pattern changes," *Proc. SPIE*, vol. 8421, p. 84212Y–84212Y–4, 2012.
- [8] V. Varyshchuk, Y. Bobitski, and H. Poisel, "Multimode Polymer Optical Fiber Strain Gauge Based on Speckle Correlation," *Int. J. Microelectron. Comput. Sci.*, vol. 5, pp. 5–9, 2014.
- [9] J. C. Haegele, "Polymer Optical Fiber Curvature Measuring Technique based on Speckle Pattern Image Processing," Master's Thesis in Electrical Engineering, Universidade Federal do Espírito Santo (UFES), Vitória, Brazil, 2015.

Key Words: POF, SHM, Speckle
Preferred presentation method: Oral



Strain Dependence of Brillouin Scattering Properties in Plastic Optical Fibers Influenced by High Temperature

Kazunari Minakawa*, Yosuke Mizuno, and Kentaro Nakamura

Institute of Innovative Research, Tokyo Institute of Technology,
4259, Nagatsuta-cho, Midori-ku, Yokohama 226-8503, Japan

*Corresponding author: kminakawa@sonic.pi.titech.ac.jp

Abstract: The strain-temperature cross effect on the Brillouin scattering properties in plastic optical fibers (POFs) is investigated. By measuring the Brillouin gain spectrum (BGS) dependence on strain at different temperatures, first, we show that the strain-dependence coefficient of the Brillouin frequency shift (BFS) is dependent on temperature; in the strain ranges of approximately 0–1.2% and 2–9%, the temperature dependence is linear with a coefficient of 1.5 MHz/%/°C and –0.4 MHz/%/°C, respectively. This result indicates that the strain sensitivity is degraded at higher temperature, and that temperature compensation is required to correctly detect the strain magnitude in POF-based Brillouin sensing. In addition, we show that temperature sensing with no sensitivity to strain can be potentially implemented by using POFs pre-strained for >13%. The height of the BGS is also evaluated.

1. Introduction

Fiber-optic strain and temperature sensing techniques have been extensively studied and used in many application fields including structural health monitoring. Among various types of fiber-optic sensors, those exploiting Brillouin scattering have attracted a great deal of attention owing to their capability of completely distributed measurement based on frequency information [1–9]. Their sensor heads were conventionally composed of glass optical fibers, which are easily broken when a strain of only ~3% is applied. To extend the measurable maximal strain, recently, plastic optical fibers (POFs) have been vigorously studied as alternatives for the glass fibers because POFs are generally so flexible that they can withstand strains of > 50% [10–19].

Brillouin scattering in POFs was first observed in 2010 [10], and since then its properties have been evaluated from a variety of aspects. For instance, the Brillouin frequency shift (BFS) dependences on strain (relatively small strain [11] and large strain [12]) and temperature (relatively narrow range [11] and wide range [13]) have been clarified to be much different from those in silica glass fibers. Other unique features of Brillouin scattering in POFs, such as the BFS hopping phenomenon [14] and the strain and thermal memory functions [20–22], have also been investigated, and distributed strain and temperature measurements have been recently demonstrated [15–17]. However, no reports have been provided regarding the cross effect of strain and temperature on Brillouin scattering properties in POFs. As these two parameters generally change simultaneously in practical applications, clarification of this effect is of crucial importance. Although in the case of standard silica single-mode fibers (SMFs), the cross effect has been shown to be negligibly small in the temperature range from 35 to 83 °C [23], it does not necessarily hold true for the POFs with a much lower glass-transition temperature.

In this work, we investigate the strain-temperature cross effect on the Brillouin scattering properties (BFS and the height of the Brillouin gain spectrum (BGS)) in POFs. Specifically, we measure the BGS dependence on strain at different temperatures. First, we prove that the strain-dependence coefficient of the BFS is linearly dependent on temperature with a coefficient of 1.5 MHz/%/°C for strains of <1.2% and –0.4 MHz/%/°C for strains ranging from ~2 to ~9%, indicating that the strain sensitivity is deteriorated at higher temperature. We then show that by using POFs pre-strained for >13%, temperature sensors with no strain sensitivity can be potentially implemented. In addition, the height of the BGS is found to slightly decrease with increasing strain at lower temperatures, while it is almost constant at higher temperatures.

2. Principle

Incident light into an optical fiber interacts with acoustic phonons and generates backscattered light accompanying a frequency downshift of several gigahertz (called BFS). This phenomenon is Brillouin scattering [24], and the spectrum of the backscattered light is known as BGS. The BFS is expressed by [1,24,25]



$$BFS = \frac{2nv_a}{\lambda_p} = \frac{2n}{\lambda_p} \sqrt{\frac{1-\sigma}{(1-2\sigma)(1+\sigma)}} \frac{E}{\rho}, \quad (1)$$

where n is the refractive index, v_a is the acoustic velocity, σ is the Poisson's ratio, E is the Young's modulus, and ρ is the density of the core material; λ_p is the wavelength of the incident light. As all of these parameters excluding λ_p are dependent on strain and temperature [26–34], the BFS also shows strain and temperature dependence, which serves as the fundamental principle of Brillouin-based sensing. In perfluorinated graded-index (PFGI-) POFs (only POFs in which Brillouin scattering has been experimentally observed) [10, 35], the BFS dependence on strain at room temperature is reported to be non-monotonic; i.e., its coefficient varies including the sign, depending on strain (for the strain of smaller than 1.0%, the coefficient is constantly -121 MHz/%) [11]. In the meantime, the BFS dependence on temperature in PFGI-POFs is reported to be monotonic but not completely linear (in the limited temperature range from -160 to 80 °C at 0% strain, the coefficient is constantly -3.2 MHz/°C) [13].

3. Experimental setup

We used ~ 440 -mm-long PFGI-POF samples with a core diameter of 50 μm , a cladding diameter of 70 μm , an overcladding diameter of 490 μm , a core refractive index of ~ 1.35 , and a propagation loss of ~ 250 dB/km at 1.55 μm . The experimental setup for measuring the BFS dependence on strain at different temperatures is depicted in Fig. 1. A Fresnel-assisted self-heterodyne technique was exploited to acquire the BFS with a high signal-to-noise ratio (SNR) [36]. First, continuous-wave output from a laser diode (LD) with a central wavelength of 1.55 μm and a bandwidth of ~ 1 MHz was guided to a polarization scrambler (PSCR) to randomize its polarization state and thus to suppress the polarization-dependent fluctuations of the signal. The light was then boosted to 30 dBm using an erbium-doped fiber amplifier (EDFA), and via an optical circulator, injected into a POF sample fixed on an automatic translation stage in a thermo-static chamber. Both ends of the POF were polished with an angle (8°), and one of the ends was connected to a silica SMF (pigtail of the circulator) using butt coupling [10]; thus, the Fresnel reflection at the open end of the POF was suppressed. The Brillouin-scattered light from the POF, along with the Fresnel-reflected light from the SMF-to-POF boundary, was amplified again to a total power of approximately -4.5 dBm using another EDFA, the amplified spontaneous emission noise of which was suppressed by an optical band-pass filter (BPF). The light was then guided to a photo detector (PD), which generated an electrical Brillouin signal because of the beating between the Brillouin-scattered light and the Fresnel-reflected light. The Brillouin signal was amplified by 20 dB, observed as a BGS using an electrical spectrum analyser (ESA), and sent to a computer for data processing. The BGS was fitted with a Lorentzian curve [10,13] and the relevant parameters (BFS, peak power, and noise floor) were extracted. By changing the strain from 0 to 16%, the strain dependences of each parameter were measured. Furthermore, this procedure was repeated at different temperatures of 32, 40, 51, and 60 °C, and the temperature dependences of the strain-dependent coefficients of each parameter were derived.

4. Experimental results

Figure 2 shows the BFS dependence on strain measured at 32, 40, 51, and 60 °C. Irrespective of the temperature, with increasing strain, the BFS first decreased (for 0 to $\sim 2\%$ strains), then increased (for ~ 2 to $\sim 13\%$ strains), and finally became constant (for $>13\%$ strains). This behaviour has already been reported at room temperature [12].

For the strains of smaller than $\sim 1.2\%$, the strain dependence was almost linear, and its dependence coefficients was plotted as a function of temperature (Fig. 3(a)). The strain-dependence coefficient was shown to

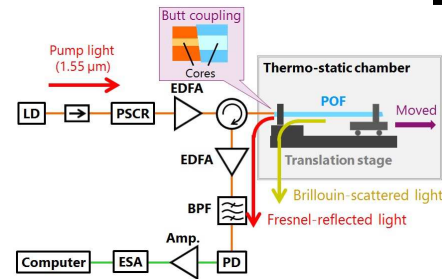


Fig. 1. Experimental setup for measuring the BGS dependence on strain at different temperatures. BPF, band-pass filter; EDFA, erbium-doped fiber amplifier; ESA, electrical spectrum analyser; LD, laser diode; PD, photo detector; PSCR, polarization scrambler. The orange and green lines indicate silica SMFs and electrical cables, respectively.

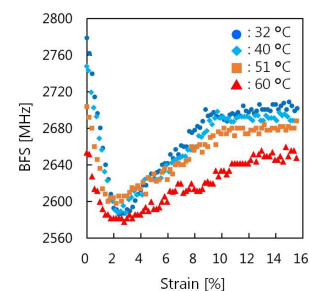


Fig. 2. BFS dependence on strain measured at four different temperatures.

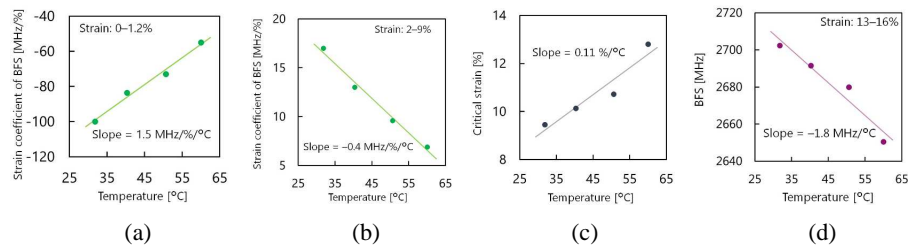


Fig. 3. Strain-dependence coefficients of the BFS plotted as functions of temperature in the strain ranges of (a) 0 to ~1.2% and (b) ~2 to ~9%. (c) Critical strain (at which the BFS became almost constant) plotted as a function of temperature. (d) Temperature dependence of the BFS (averaged in the strain range from 13 to 16%).

be linearly dependent on temperature with a coefficient of 1.5 MHz/%/°C. This indicates that the absolute value of the strain-dependence coefficient (negative value) becomes smaller with increasing temperature, resulting in the deterioration of the strain sensitivity at higher temperature. Therefore, we newly clarified that temperature compensation is necessary to correctly detect the strain magnitude using POF-based Brillouin sensors, especially at higher temperature. Note that the temperature compensation is not required when standard silica SMFs are used at lower than 83 °C [23].

In Fig. 2, by exploiting the BFS dependence on strain in the range from ~2 to ~9%, strain sensing with a wider strain dynamic range appears feasible. In that case, we need to apply ~2% strain beforehand. The strain-dependence coefficient in this range was then plotted as a function of temperature (Fig. 3(b)). The coefficient (or the strain sensitivity) decreased with the slope of -0.4 MHz/%/°C as increasing temperature, indicating that the temperature compensation of the coefficient is also required in BFS-based strain sensing in this strain range. The absolute values of the coefficients in this range was, regardless of the temperature, $<1/5$ of those for 0–1.2% strains, resulting in a lower strain sensitivity.

Subsequently, the critical strain at which the BFS became almost constant was plotted as a function of temperature (Fig. 3(c)). Such critical strains were calculated as the intersection of 1) the regression line of the strain dependence of the BFS in the range from ~2 to ~9% and 2) the horizontal line indicating the BFS value averaged for $>13\%$ strains. The dependence on temperature exhibited a monotonic increase with a roughly linear coefficient of 0.11 %/°C. This result indicates that the strain dynamic range of strain sensing (which exploits the BFS dependence in the range from ~2 to ~9%) is widened at higher temperatures, which is in a trade-off relation with the strain sensitivity (refer to the preceding paragraph). Besides, as the critical strain corresponds to the strain at which the POF partially starts to slim down [14], this temperature dependence may explain the reason why this slim-down phenomenon does not occur in the case of POF tapering performed at high temperature [37, 38].

As mentioned above, the BFS became almost constant for strains of $>13\%$. The temperature dependence of the BFS (averaged in the range from 13 to 16%) is shown in Fig. 3(d). The BFS monotonically decreased with increasing temperature, and the rough linear approximation led to a coefficient of -1.8 MHz/°C. By using POFs pre-strained for $>13\%$, temperature sensors with no sensitivity to strain appears to be implementable.

Finally, Fig. 4 shows the strain dependence of the change in the BGS height measured at 32, 40, 51, and 60 °C. Here the BGS height was defined as the difference between the peak power and the noise floor. At 32 and 40 °C, the BGS height slightly decreased with increasing strain, and its change reached approximately -1 dB at ~16% strain. The slopes of the strain dependences for $>8\%$ strains measured at 32 °C and 40 °C were approximately -0.14 dB/% and -0.12 dB/%, respectively. In contrast, when the temperature was higher than 51 °C, the BGS height was almost constant. Thus, strain sensing using the BGS height, which can be potentially used to implement simultaneous strain and temperature sensing [39], appears difficult at >51 °C (although the SNR is insufficient even at <40 °C at present).

5. Conclusion

We fully investigated the BGS dependence on strain at different temperatures in POFs. First, the strain-dependence coefficient of the BFS was shown to be linearly dependent on temperature with a coefficient of 1.5 MHz/%/°C for

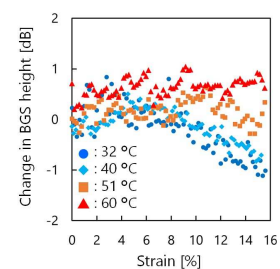


Fig. 4. Strain dependence of the BGS height measured at four different temperatures.



strains of $<1.2\%$ and $-0.4 \text{ MHz}/\%/\text{°C}$ for strains ranging from ~ 2 to $\sim 9\%$, which indicated the degradation of the strain sensitivity at higher temperature. The absolute value of the strain coefficient in the strain range from ~ 2 to $\sim 9\%$ was then found to be smaller than $1/5$ of that for $<1.2\%$ strains at the same temperature, which was in a trade-off relation with the strain dynamic range. In addition, temperature sensing insusceptible to strain was shown to be potentially feasible by using POFs pre-strained for $>13\%$. We also found that the BGS height slightly decreased with increasing strain at lower temperatures, while it was almost constant at higher temperatures. The most important finding is that temperature compensation needs to be performed to correctly detect the strain magnitude in POF-based Brillouin sensing, especially at higher temperature. We hope that this paper will be an important archive in developing distributed strain and temperature sensors based on Brillouin scattering in POFs.

Acknowledgements

The authors are indebted to Neisei Hayashi, the University of Tokyo, Japan, for his experimental assistance. They also acknowledge the staff of the Technical Department, Tokyo Institute of Technology, Japan, for fabricating the chamber used in the experiments. This work was supported by JSPS KAKENHI Grant Numbers 25709032, 26630180, 25007652, and 15J11445, and by research grants from the Iwatani Naoji Foundation, the SCAT Foundation, and the Konica Minolta Science and Technology Foundation.

References

- [1] T. Horiguchi, T. Kurashima, and M. Tateda, *IEEE Photon. Technol. Lett.* **1**, 107 (1989).
- [2] T. Kurashima, T. Horiguchi, and M. Tateda, *Appl. Opt.* **29**, 2219 (1990).
- [3] T. Horiguchi and M. Tateda, *J. Lightwave Technol.* **7**, 1170 (1989).
- [4] Y. Dong, D. Ba, T. Jiang, D. Zhou, H. Zhang, C. Zhu, Z. Lu, *et al*, *IEEE Photon. J.* **5**, 2600407 (2013).
- [5] K. Hotate and T. Hasegawa, *IEICE Trans. Electron.* **E83-C**, 405 (2000).
- [6] Y. Mizuno, W. Zou, Z. He, and K. Hotate, *Opt. Express* **16**, 12148 (2008).
- [7] T. Kurashima, T. Horiguchi, H. Izumita, S. Furukawa, *et al*, *IEICE Trans. Commun.* **E76-B**, 382 (1993).
- [8] D. Garus, K. Krebber, F. Schliep, and T. Gogolla, *Opt. Lett.* **21**, 1402 (1996).
- [9] Y. Mizuno, N. Hayashi, H. Fukuda, K. Y. Song and K. Nakamura, *Light: Sci. Appl.* **5**, e16184 (2016).
- [10] Y. Mizuno and K. Nakamura, *Appl. Phys. Lett.* **97**, 021103 (2010).
- [11] Y. Mizuno and K. Nakamura, *Opt. Lett.* **35**, 3985 (2010).
- [12] N. Hayashi, Y. Mizuno, and K. Nakamura, *Opt. Express* **20**, 21101 (2012).
- [13] K. Minakawa, N. Hayashi, Y. Shinohara, M. Tahara, *et al*, *Jpn. J. Appl. Phys.* **53**, 042502 (2014).
- [14] N. Hayashi, K. Minakawa, Y. Mizuno, and K. Nakamura, *Appl. Phys. Lett.* **105**, 091113 (2014).
- [15] A. Minardo, R. Bernini, and L. Zeni, *IEEE Photon. Technol. Lett.* **26**, 387 (2014).
- [16] Y. Dong, P. Xu, H. Zhang, Z. Lu, L. Chen, and X. Bao, *Opt. Express* **22**, 26510 (2014).
- [17] N. Hayashi, Y. Mizuno, and K. Nakamura, *J. Lightwave Technol.* **32**, 3397 (2014).
- [18] M. G. Kuzyk, *Polymer Fiber Optics: Materials, Physics, and Applications* (CRC Press, 2006).
- [19] H. Ujihara, N. Hayashi, *et al*, *IEICE Electron. Express* **11**, 20140707 (2014).
- [20] I. R. Husdi, K. Nakamura, and S. Ueha, *Meas. Sci. Technol.* **15**, 1553 (2004).
- [21] K. Nakamura, I. R. Husdi, and S. Ueha, in *Proc. SPIE*, **5855**, 807 (2005).
- [22] K. Minakawa, N. Hayashi, Y. Mizuno, and K. Nakamura, *IEEE Photon. Technol. Lett.* **27**, 1394 (2015).
- [23] X. Bao, D. J. Webb, and D. A. Jackson, *Opt. Lett.* **19**, 141 (1994).
- [24] G. P. Agrawal, *Nonlinear Fiber Optics* (Academic Press, San Diego, 1995).
- [25] K. F. Graff, *Wave Motion in Elastic Solids* (Dover Publications, New York, 1975).
- [26] G. B. Hocker, *Appl. Opt.* **18**, 1445 (1979).
- [27] R. M. Waxler, D. Horowitz, and A. Feldman, *Appl. Opt.* **18**, 101 (1979).
- [28] K. Suito, M. Miyoshi, T. Sasakura, *et al*, *High-Pressure Research: Application to Earth and Planetary Sciences* (Terra Sci. Publ. Co. & Am. Geophys. Uni., Tokyo & Washington DC, 1992), pp. 219–225.
- [29] C. Z. Tan and J. Arndt, *J. Phys. Chem. Solids* **61**, 1315 (2000).
- [30] J. M. Cariou, J. Dugas, L. Martin, and P. Michel, *Appl. Opt.* **25**, 334 (1986).
- [31] R. Kono, *J. Phys. Soc. Jpn.* **15**, 718 (1960).
- [32] J. W. Marx and J. M. Sivertsen, *J. Appl. Phys.* **24**, 81 (1953).
- [33] M. Fukuhara and A. Sampei, *J. Polym. Sci. Part B: Polym. Phys.* **33**, 1847 (1995).
- [34] J. J. Curro and R. J. Roe, *Polymer* **25**, 1424 (1984).
- [35] Y. Koike and M. Asai, *NPG Asia Mater.* **1**, 22 (2009).
- [36] Y. Mizuno, N. Hayashi and K. Nakamura, *Electron. Lett.* **50**, 1153 (2014).
- [37] N. Hayashi, H. Fukuda, Y. Mizuno, and K. Nakamura, *J. Appl. Phys.* **115**, 173108 (2014).
- [38] H. Ujihara, N. Hayashi, K. Minakawa, *et al*, *Appl. Phys. Express* **8**, 072501 (2015).
- [39] H. H. Kee, G. P. Lees, and T. P. Newson, *Opt. Lett.* **25**, 695 (2000).

POF-Based Slope-Assisted Brillouin Optical Correlation-Domain Reflectometry

H. Lee^{1*}, N. Hayashi², Y. Mizuno¹, and K. Nakamura¹

¹Institute of Innovative Research, Tokyo Institute of Technology,
4259, Nagatsuta-cho, Midori-ku, Yokohama 226-8503, Japan

²Research Center for Advanced Science and Technology, The University of Tokyo,
4-6-1, Komaba, Meguro-ku, Tokyo 153-8904, Japan

*Corresponding author: hylee@sonic.pi.titech.ac.jp

Abstract: Although the proof of concept of slope-assisted (SA-) Brillouin optical correlation-domain reflectometry (BOCDR) has been demonstrated using silica single-mode optical fibers (SMFs), no reports have been provided on how the performance is affected by use of plastic optical fibers (POFs). In this work, we demonstrate distributed strain and temperature measurements based on SA-BOCDR using POFs. Unlike SMF-based SA-BOCDR, due to the high propagation loss of the POFs, the measurement sensitivity is found to be a function of the sensing location in the POF. We investigate this effect both theoretically and experimentally and present a compensation method for correct distributed measurements along POFs.

1. Introduction

Distributed fiber-optic strain and temperature sensing based on Brillouin scattering [1] has attracted considerable attention for the past several decades as a promising technique for health monitoring of civil structures and materials. A variety of measurement schemes have been developed to acquire the distributed information of Brillouin gain spectrum (BGS), including Brillouin optical time-domain reflectometry (BOTDR) [2,3], Brillouin optical time-domain analysis (BOTDA) [4–6], Brillouin optical frequency-domain analysis (BOFDA) [7], Brillouin optical correlation-domain analysis (BOCDA) [8–10], and Brillouin optical correlation-domain reflectometry (BOCDR) [11–19]. Among them, BOCDR is the only technique with single-end accessibility and high spatial resolution.

Since the basic system of BOCDR was first proposed in 2008 [11], numerous configurations have been implemented to improve the performance [12–15]. For instance, the measurement range was elongated by temporal gating [12] and double modulation [13]; millimeter-order spatial resolutions were achieved by employing a tellurite glass fiber [14] and by apodization [15]; the strain dynamic range was extended by using polymer optical fibers [16–18]. In addition, one of the latest breakthroughs is phase-detection-based BOCDR [19], which enables a high sampling rate of >100 kHz per point. As another high-speed configuration, motivated by the previous implementations in time domain [20,21], we have recently developed slope-assisted (SA-) BOCDR [22], in which the spectral power of the BGS is exploited to deduce the Brillouin frequency shift (BFS). This configuration potentially enables higher-speed operation than the phase-detection-based method, and besides not only strain and temperature change but also optical loss can be detected if necessary. The proof of concept of SA-BOCDR has already been demonstrated [22, 23].

To date, only silica single-mode fibers (SMFs) have been used for the sensor heads of SA-BOCDR, but they are quite fragile and cannot withstand strains of over ~3%. One attractive solution to this problem is to make use of plastic optical fibers (POFs), which have such a high flexibility that they can withstand large strains of several tens of percent. Previous experimental studies on Brillouin scattering in POFs [16–18] have revealed its potential applicability to large-strain sensing [16] and to high-precision temperature sensing with less sensitivity to strain [17]. We have also demonstrated POF-based BOCDR operation, and a 10-cm-long heated section of a 1.3-m-long POF was successfully detected with a theoretical spatial resolution of 7.4 cm and a sampling rate of 3.3 Hz per measured point (corresponding to a measurement time of ~1 minute, if the number of measured points is 200) [18]. However, the use of POFs in power-based SA-BOCDR cannot be regarded as a simple extension of that in standard BFS-based BOCDR, because the high propagation loss of the POFs will greatly influence the performance.

In this work, first, we characterize the performance of SA-BOCDR using a POF and show both theoretically and experimentally that the measurement sensitivity is dependent on the sensing location in the POF. We then demonstrate a basic distributed measurement of strain and temperature along a POF with a spatial resolution of 96 cm and a sampling rate of 100 Hz.

2. Principle and experimental setup

In general, fiber-optic distributed Brillouin sensors operate based on the BFS dependences on strain and temperature [1]. As mentioned above, BOCDR is the only technique with intrinsic single-end accessibility and relatively high spatial resolution, and it resolves the sensing locations by a so-called correlation peak [11], which can be generated in the fiber under test (FUT) by sinusoidal frequency modulation of the laser output. The location of the correlation peak can be scanned along the FUT by sweeping the modulation frequency f_m , and thus distributed BFS measurement becomes feasible. As sinusoidal frequency modulation results in the periodical generation of multiple correlation peaks along the FUT, their interval determines the measurement range d_m as [24]

$$d_m = \frac{c}{2n f_m}, \quad (1)$$

where c is the velocity of light in vacuum, and n is the core refractive index. When f_m is lower than the Brillouin bandwidth $\Delta\nu_B$, the spatial resolution Δz is given by [24]

$$\Delta z = \frac{c \Delta\nu_B}{2\pi n f_m \Delta f}, \quad (2)$$

where Δf is the modulation amplitude of the optical frequency.

In conventional BOCDR, the BFS at one sensing position is derived as a peak frequency after the acquisition of the whole BGS [11, 24]; while in SA-BOCDR, it is obtained using the spectral power change at a fixed frequency by exploiting its one-to-one correspondence to the BFS (Fig. 1) [22]. Consequently, the BFS distribution along the FUT is obtained as power-change distribution in SA-BOCDR. The measurement range and the spatial resolution are given by the same equations as those for standard BOCDR (Eqs. (1) and (2)). Note that with this scheme, loss points can also be detected in a distributed manner and that the sampling rate can potentially be drastically enhanced (refer to Ref. 18 for the detailed operating principle of SA-BOCDR).

The experimental setup of the POF-based SA-BOCDR, depicted in Fig. 2, is basically the same as that of the silica-based SA-BOCDR. The output of a laser at $1.55 \mu\text{m}$ was divided into two light beams, pump and reference. The pump light was injected into the FUT after amplification to ~ 25 dB using erbium-doped fiber amplifier (EDFA), and the reference light was amplified to ~ 2 dB after passing through the ~ 1 -km-long delay fiber. The backscattered Stokes light was amplified with the reference light. As an FUT, we employed a 15.0-m-long PFGI-POF with a core diameter of $50 \mu\text{m}$, a core refractive index of ~ 1.35 , and a propagation loss of 250 dB/km at $1.55 \mu\text{m}$. The modulation frequency f_m and amplitude Δf were set to 6.15 – 6.33 MHz and 0.6 GHz , respectively, corresponding to the measurement range of 18.1 m and the theoretical spatial resolution of 0.96 m according to Eqs. (1) and (2). The repetition

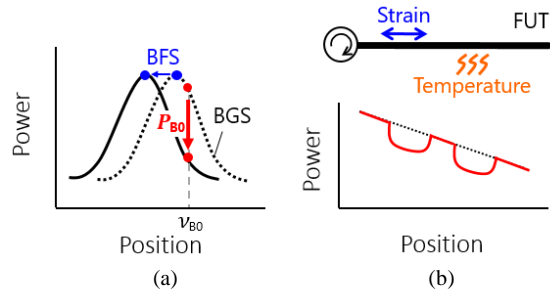


Fig. 1 (a) Schematics of the operating principle of the slope-assisted Brillouin optical correlation-domain reflectometry (SA-BOCDR). (b) Power-change distributions along the fiber under test (FUT); with (solid curve) and without (dotted line) partial strain and heat.

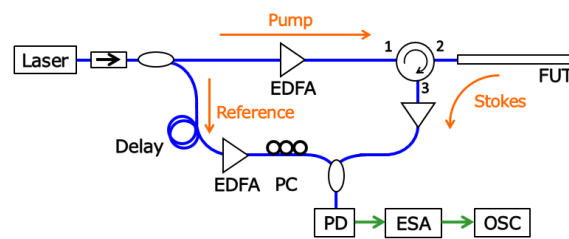


Fig. 2 Experimental setup for POF-based SA-BOCDR. EDFA, erbium-doped fiber amplifier; ESA, electrical spectrum analyser; OSC, oscilloscope; PC, polarization controller; PD, photo diode.

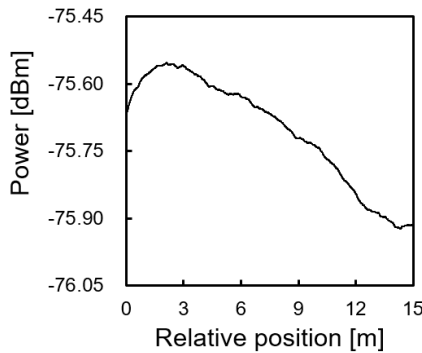


Fig. 3 Power distributions along the POF.

rate was set to 100 Hz, and 128 times averaging was performed on the oscilloscope to improve a signal-to-noise ratio. The room temperature was 25 °C.

3. Experimental results

Figure 3 shows the measured power distributions (without noise floor compensation [22]) along the 15.0-m-long POF using SA-BOCDR. Unlike silica-based SA-BOCDR, where this trend shows almost constant regardless of the position, the power first increased, and then gradually decreased. The initial increase is caused by the correlation peak starting to enter the FUT. The subsequent decrease is because of the high propagation loss in the POF.

Next, the BGS distribution along the POF was measured using a standard BOCDR (Fig. 4). The peak power of the BGS gradually decreased with light propagation, which also induces the reduction of its spectral slope. By analysing the spectral slope precisely, we can derive the theoretical strain/temperature sensitivity as a function of the sensing position (this will be used as theoretical trends in the next paragraph).

Figure 5 shows the measured spectral powers plotted as functions of temperature, when 1-m-long sections (four sections; 2–3, 5–6, 8–9, 11–12 m distant from the proximal POF end) were heated. The measured data were in good agreement with the theoretical trends (indicated by dotted lines). The spectral powers were almost linearly dependent on temperature, and their coefficients were found to decrease with increasing relative position. The temperature sensitivity plotted as a function of the position (Fig. 6) gives the slope of $-0.0005 \text{ dB/}^\circ\text{C/m}$ ($= -0.0202 \text{ dB}/\%/\text{m}$ for strain). By using this value for compensation, the measured power distributions along a POF can be converted into correct strain/temperature distributions.

Finally, we demonstrated a distributed strain and temperature measurement along a POF using SA-BOCDR.

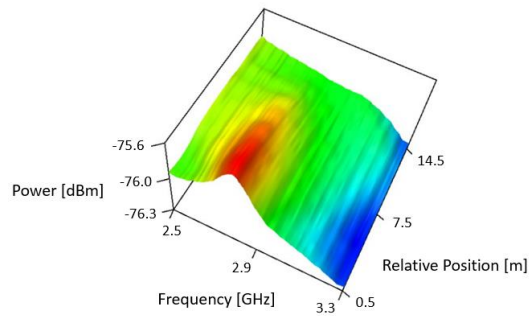


Fig. 4 BGS distribution along the POF.

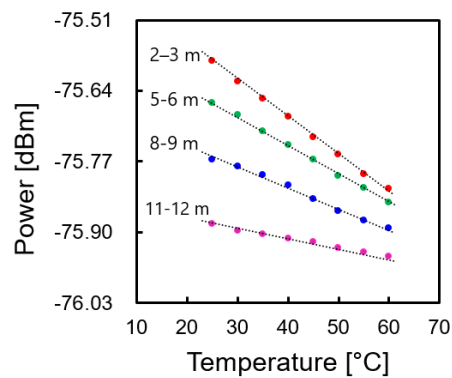


Fig. 5 Spectral powers plotted as functions of temperature; measured at four sections in the POF.

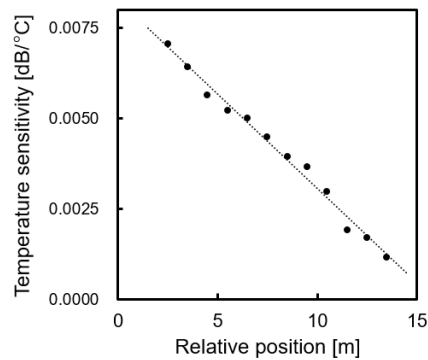


Fig. 6 Temperature sensitivity plotted as a function of position.

The structure of the POF is depicted in Fig. 7(a). Two 1-m-long sections were strained by 1 % and heated to 60 °C. The measured power-change distribution, shown in Fig. 7(b), agrees adequately well with the theoretical trend considering the sensitivity dependence on position and the trapezoidal effect [23]. Thus, the applied strain and temperature change were correctly detected. More detailed discussion on the measurement accuracy etc. will be provided at the conference.

4. Conclusion

We investigated the performance of SA-BOCDR using POFs. The measurement sensitivity was shown to be dependent on the sensing location in the POF. The dependence coefficients were -0.0005 dB/%/m for strain and -0.0202 dB/°C/m for temperature. By compensating this influence, we successfully demonstrated a distributed strain and temperature measurement along a POF. We believe that POF-based SA-BOCDR will provide conventional silica-SMF-based SA-BOCDR systems with various advantages, such as high flexibility, high temperature sensitivity, and the strain and thermal memory effects.

Acknowledgements

This work was supported by JSPS KAKENHI Grant Numbers 25709032, 26630180, and 25007652, and by research grants from the Iwatani Naoji Foundation, the SCAT Foundation, and the Konica Minolta Science and Technology Foundation.

References

- [1] G. P. Agrawal, *Nonlinear Fiber Optics* (Academic Press, Boston, 1995).
- [2] T. Kurashima, T. Horiguchi, H. Izumita, S. Furukawa, and Y. Koyamada, *IEICE Trans. Commun.* **E76-B**, 382 (1993).
- [3] D. Iida and F. Ito, *J. Lightwave Technol.* **26**, 417 (2008).
- [4] T. Horiguchi and M. Tateda, *J. Lightwave Technol.* **7**, 1170 (1989).
- [5] W. Li, X. Bao, Y. Li, and L. Chen, *Opt. Express* **16**, 21616 (2008).
- [6] Y. Dong, L. Chen, and X. Bao, *Opt. Lett.* **36**, 277 (2011).
- [7] D. Garus, K. Krebber, and F. Schliep, *Opt. Lett.* **21**, 1402 (1996).
- [8] K. Hotate and T. Hasegawa, *IEICE Trans. Electron.* **E83-C**, 405 (2000).
- [9] W. Zou, C. Jin, and J. Chen, *Appl. Phys. Express* **5**, 082503 (2012).
- [10] C. Zhang, M. Kishi, and K. Hotate, *Appl. Phys. Express* **8**, 042501 (2015).
- [11] Y. Mizuno, W. Zou, Z. He, and K. Hotate, *Opt. Express* **16**, 12148 (2008).
- [12] Y. Mizuno, Z. He, and K. Hotate, *Opt. Express* **17**, 9040 (2009).
- [13] Y. Mizuno, Z. He, and K. Hotate, *Opt. Express* **18**, 59263 (2010).
- [14] Y. Mizuno, Z. He, and K. Hotate, *Opt. Commun.* **283** 2438 (2010).
- [15] S. Manotham, M. Kishi, Z. He, and K. Hotate, *Proc. SPIE* **8351**, 835136 (2012).
- [16] N. Hayashi, Y. Mizuno, and K. Nakamura, *J. Lightwave Technol.* **32**, 3397 (2014).
- [17] Y. Mizuno and K. Nakamura, *Appl. Phys. Lett.* **97**, 021103 (2010).
- [18] N. Hayashi, Y. Mizuno, and K. Nakamura, *Opt. Express* **20**, 21101 (2012).
- [19] Y. Mizuno, N. Hayashi, H. Fukuda, K. Y. Song, and K. Nakamura, *Light: Sci. Appl.* **5**, e16184 (2016).
- [20] Y. Peled, A. Motil, L. Yaron, and M. Tur, *Opt. Express* **19**, 19845 (2011).
- [21] A. Minardo, A. Coscetta, R. Bernini, and L. Zeni, *J. Opt.* **18**, 025606 (2016).
- [22] H. Lee, N. Hayashi, Y. Mizuno, and K. Nakamura, *IEEE Photonics J.* **8**, 6802807 (2016).
- [23] H. Lee, N. Hayashi, Y. Mizuno, and K. Nakamura, 6th Asia-Pacific Optical Sensors Conference (APOS 2016), W4A.16 (2016).
- [24] Y. Mizuno, W. Zou, Z. He, and K. Hotate, *J. Lightwave Technol.* **25**, 1238 (2010).

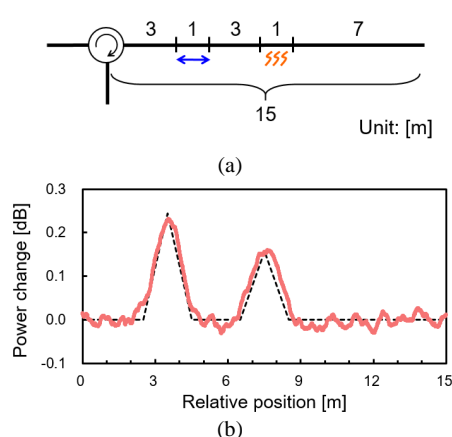


Fig. 7 (a) Structure of the sensing fiber for the final demonstration. (b) Power-change distributions along the sensing fiber.



2D optical accelerometer using POF array and image detection

R. Serrão¹, P. Antunes², P. S André^{3,*}

1 Department of Electrical and Computer Engineering, Instituto Superior Técnico, University of Lisboa, Lisboa, Portugal

2 Instituto de Telecomunicações and Physics Department & I3N, University of Aveiro, Aveiro, Portugal

3 Department of Electrical and Computer Engineering and Instituto de Telecomunicações, Instituto Superior Técnico, University of Lisboa, Lisboa, Portugal.

*Corresponding author: paulo.andre@tecnico.ulisboa.pt

Abstract: In this work we propose and demonstrate the development of an optical 2D accelerometer based on plastic optical fiber array using image detection for data analysis. The design is based in a light emitting diode coupled to a single POF working as a cantilever with an attached inertial mass. The output optical signal at the cantilever fiber is projected into a fiber array and acquired using a webcam. The use of image processing analysis allows the integration of the signal intensity in each fiber core and the estimation of the applied acceleration.

Key Words: Plastic Optical Fibers, Structural Health Monitoring, Low-Cost Optical Accelerometers, Image Processing Analysis.

1. Introduction

Optical accelerometers have proven to be key elements in several applications, such as Structural Health Monitoring (SHM), physiological monitoring, health related research and Cyber Physical Systems (CFS). The massive use of optical accelerometers for these applications requires the incessant development of low cost solutions. This particular type of accelerometers were significantly researched on the latest decades, presenting several advantages compared to other kind of sensors like the insensitivity to electromagnetic interference, electric isolation, reduced dimensions, minimal ambient impact, resistance to corrosion and high values of signal-to-noise ratio [1].

In the last 20 years, many research teams have reported a great variety of solutions and alternative approaches for the implementation of optical accelerometers. This specific type of accelerometers can be implemented using various methods such as intensimetric and polarimetric sensors, fiber Bragg gratings (FBG), and Fabry-Perot an interferometric principle based sensor. Each one of these sub-types has its own specific advantages over one another and are used according to their own area of applications [2].

Although FBG sensors seem to be one of the best options for nowadays applications, there are also some drawbacks using this technology, like the high costs of its implementation and the limitations in size reduction of its physical proportions [1].

Intensimetric accelerometers were one of the earliest developed types of optical fiber sensors and one of the most basic and direct kinds as well [2]. Its sensing principle is based on the measured levels of intensity of the optical signal at the fibers output, as its measured quantity is modulated given the respective variations along time [2]. As inexpensive light sources became increasingly popular and commercially available (as LED's for example), allied to the appearance of low bend-sensitivity fibers, this type of accelerometers offer great commercial prospect for large scale applications and has already proven itself as a very cost-effective solution [2]. This intensity-based type of accelerometer has also been revealed as a great tool for frequency analysis in the field of vibration measurements, as its sensor possesses enough sensitivity for the detection of the oscillatory origins of a given vibration impulse [2].

For the optical accelerometer presented in this article, POF's were selected for the implementation of its sensing principle. As previously referred, POF's are a particular type of optical fibers that have low bend-



sensitivity properties. These plastic optical fibers possess high Numerical Aperture (NA) values which allow a greater radius for its acceptance cone tolerating the emission and capture of optical signals that aren't perfectly aligned at its extremities. This given fact proves that this kind of fiber is ideal for the implementation of intensity-based sensors [2].

This recently developed kind of fibers also comes in large core sizes and are much cheaper to produce when compared to its typical silica counterparts. Being the high attenuation value its major fault, POF's compensate this drawback by offering great robustness and good flexibility making them a very appropriate low-cost solution for large SHM applications [2].

2. Accelerometer Description

The 2D optical accelerometer is based on a single POF (*Avago Technologies* – HFBR-RUS100Z) acting as a cantilever fixed to a U-shaped plastic structure which was constructed in PLA (Polylactic acid) using a polymer 3D Printer from 3D Systems, model Cube 3rd generation, with a 70 microns resolution for higher robustness. Coupled to the single fiber is a red LED (*Industrial Fiber Optics* – IF-E96) emitting at 660 nm with an optical power of 0.2 mW, powered with 1.8V and 20 mA. On the opposite side of the same structure, a bundle of 7 fibers were joined and secured using plastic clamps. These fibers are identical to the one used as the cantilever and are united in a hexagonal configuration for minimizing the available spacing between fibers. At the bundle extremity, the optical signal intensity in each array fiber was accessed using a webcam (*Growing 300K Turtle*), with a 320x240 pixel resolution and frame rate of 25 Hz.

To further test this optical accelerometer and align its array of 7 fibers with the webcam lens. In its static position, the single emitting fiber is aligned with the center fiber in the POF bundle when the accelerometer isn't subject to any external acceleration.

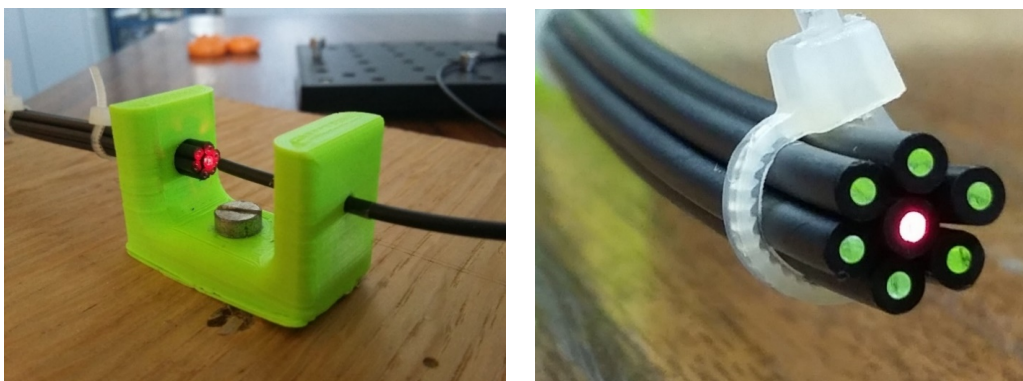


Figure 1. Basic plastic structure used for the assembly of the optical accelerometer printed with the 3D printer (left) bundle of 7 plastic optical fibers with the emitting POF aligned with the central fiber when in static position (right).

After the complete assembly of the sensor described above, a dynamic test was performed by connecting the mounted webcam to a Personal Computer (PC). Making use of the dedicated recording software for the specific camera and with predefined values for ambient lighting and color contrast parameters. The test consisted in recording a 15 seconds video while moving the cantilever fiber, in the direction of each fiber along the bundle's vertical plane. With this experiment, it was intended to simulate a natural vibration to evaluate the accelerometers behaviour. After this procedure, a video file was generated by the computer and saved in Audio Video Interleave (AVI) file format for complete compatibility with the usage of image processing software.



3. Image Processing Analysis

After obtaining the generated test video from the previous experiment, a script file was created in Matlab to perform the image processing analysis required for attaining proper acceleration values to measure the movement previously captured by the webcam.

Starting by opening the video file and observing the position of each one of the 7 fiber cores, a mask for each fiber core was carefully positioned along a given frame. As the bundle position remains continuously static, this mask is suitable for analysing the intensity at each fiber core for all the successive frames in the video. The RGB color image was also converted to a greyscale figure for better readings of the intensity values of each pixel in the frame.

By enumerating each fibers of the bundle from 1 to 7 and compensating the presence of ambient light in the fiber cores, the achieved results for a dynamic test are shown in Figure 2. The left image displays the fiber array output image acquired by the camera for a given position of the cantilever and the right shows the evolution of the intensity on each array fiber core along time.

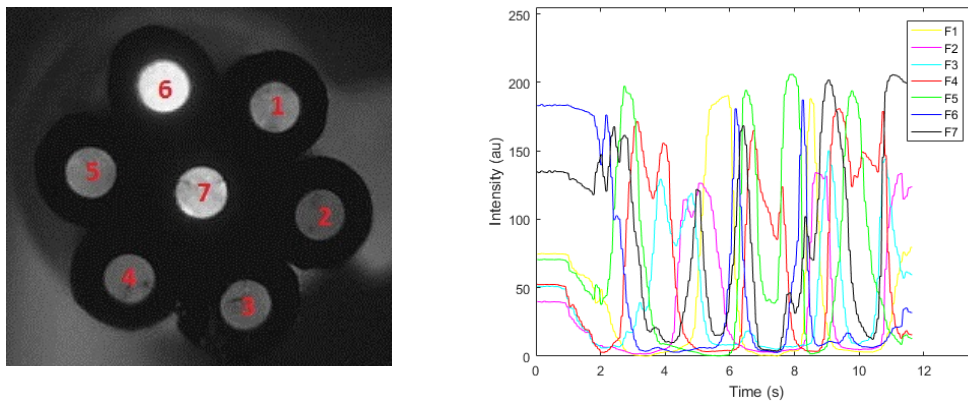


Figure 2. Image of the fiber array output (left) optical signal intensity evolution on each fiber core along time (right). F# refers to the identification of the fiber core, as illustrated in the left image.

The mode field diameter (MFD) parameter, w_0 , was calculated based on the POF's NA value and the distance between the luminous extremity of the cantilever fiber and the vertical plane containing the edge of the fiber array. The loss of the transmitted optical signal between fibers is given by [3]:

$$Loss = 1 - e^{-\left(\frac{x}{w_0}\right)^2} \tag{1}$$

Another important parameter is the distance of each fiber core center to the middle of the array, given by the variable x . Transforming this variable into an equivalent parameter best described as the radial offset given by the relation $R \rightarrow (x, y)$ and rearranging expression (1) in order to this new variable, expression (2) was obtained.

$$R_i = \sqrt{-\ln\left(\frac{P_i}{A_i}\right)} \times w_0 \tag{2}$$

where R_i represents the radius generated for the fiber i of the array, P_i the value of intensity at a given frame of fiber i , and A_i the maximum value of intensity registered by any fiber along the video.



Based on the values achieved for R_i and given the coordinates (x, y) of each fiber array center, MATLAB generates a corresponding circle for each fiber for each frame of the video. An example of the output of one random frame is shown in Figure 3.

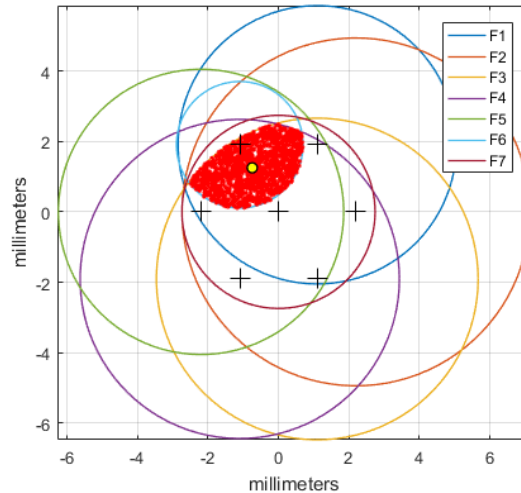


Figure 3. Plot of the generated circles based on the values of R_i calculated by MATLAB for a random frame (frame #12). The yellow dot represents the centroid point of the area in red.

After a geometric analysis, it is possible to achieve the position of the cantilever at a given frame of the video, which corresponds to the centroid of the area where all the circumferences overlap (red area in Figure 3). As the given position of the cantilever is already determined for each frame of the dynamic test video, it is easy to obtain the distance covered by the emitting fiber along the full duration of the sample movie. Lastly, applying the corresponding first and second differential calculations to the values of the accumulated distance according to the video's sample rate, the velocity and acceleration data can be obtained.

4. Results

Given the basic technique of registering movement/acceleration with this particular 2D optical accelerometer, one can easily understand that the proposed sensor belongs to the intensimetric family previously mentioned in this article. After all the procedures of the image processing analysis were complete, the data output generated by the script created on MATLAB can be observed in Figure 4.

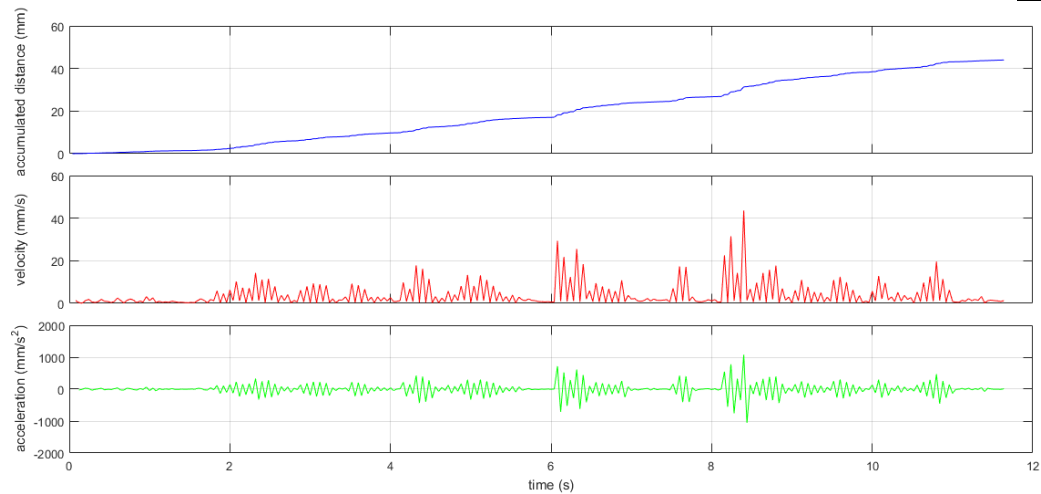


Figure 4. Results obtained for a dynamic test using the proposed 2D optical accelerometer. The data presented, from top to bottom, are the accumulated distance (top), the velocity (middle) and the acceleration (baixo).

5. Conclusions

In addition to the advantages that an optical accelerometer has over the other types of sensors, the suggested work delivers respectable results given the simplicity and the low costs of its implementation. Further improvements can be made to enhance the accuracy of the presented accelerometer by increasing the number of fibers in the arranged bundle, maintaining its hexagonal format for best area coverage purposes. Another aspect that can be easily improved is the usage of double AA alkaline batteries connected to a small value resistor to power up the LED attached to the single optical fiber acting as the cantilever. Although the precision of the results delivered by this accelerometer are yet to be confirmed, subjecting this sensor to a known acceleration will present valuable data so that both results can be easily compared and possible adjustments and improvements can be done to the final product. Lastly, the results that were demonstrated above show the feasibility of a cost effective 2D accelerometer based on POF's.

Acknowledgements

This work was financed in the scope of UID/EEA/50008/2013, by the National Funds through the Fundação para a Ciência e a Tecnologia / Ministério da Educação e Ciência, and by the European Regional Development Fund under the PT2020 Partnership Agreement. The support from the Brazilian Ciência sem Fronteiras (PVE) program is also appreciated. P. Antunes acknowledge FCT support through the postdoctoral research fellowship SFRH/BPD/76735/2011.

6. References

- [1] P. F. C. Antunes, H. Varum, and P. S. André, "Intensity-Encoded Polymer Optical Fiber Accelerometer," *IEEE Sens. J.*, vol. 13, no. 5, pp. 1716–1720, 2013.
- [2] K. S. C. Kuang, S. T. Quek, C. G. Koh, W. J. Cantwell, and P. J. Scully, "Plastic Optical Fibre Sensors for Structural Health Monitoring: A Review of Recent Progress," *J. Sensors*, vol. 2009, 2009.
- [3] L. Moore, "Single Mode Fiber Coupling" *Opti521 Tutorial*, 2006. [Online]. Available: [http://fp.optics.arizona.edu/optomech/student reports/tutorials/LMooreTutorial1.doc](http://fp.optics.arizona.edu/optomech/student%20reports/tutorials/LMooreTutorial1.doc).



Stabilized multimode fiber link using graded-index plastic optical fiber with strong mode coupling

A. Inoue* and Y. Koike

Keio Photonics Research Institute (KPRI), Keio University, Kanagawa, Japan

*Corresponding author: inoue@kpri.keio.ac.jp

Abstract: We demonstrate that a multimode fiber (MMF) link based on a vertical surface emitting laser (VCSEL) can be stabilized using a graded-index plastic optical fiber (GI POF) with strong mode coupling. In the MMF link with strong optical feedbacks to the VCSEL, the GI POF allows for higher quality data transmission with less noises and instabilities than silica GI MMFs. By directly observing beams backreflected to the VCSEL, we show that the transmission quality improvement is closely related to random mode coupling because of light scattering by microscopic heterogeneities in the GI POF core. These results suggest that the low-noise GI POF allows for the low-cost optical interconnects without optical isolators, angled fiber end-faces, and precise alignments for consumer applications.

1. Introduction

Recently, ultra-high definition (UHD) displays have been rapidly developed for video formats with 4K (3840x2160) and 8K (7680x4320) resolutions. In Japan, 4K/8K broadcastings through satellites are scheduled toward the 2020 Tokyo Olympics and Paralympics [1]. This is accelerating research and development of technologies for consumers to watch 4K/8K TV at home. Current UHD displays require uncompressed video data transfer from set-top boxes and smartphones. For 8K video transmission, the data rates can be increased up to ~240 Gb/s [2], suggesting that the interface cables for consumers require extremely high transmission speeds in the upcoming 4K/8K era. Conventional metal interfaces such as serial digital interfaces are not suitable for the in-home applications because they require so many thick cables and electromagnetic interference preventions.

A graded-index plastic optical fiber (GI POF) has been a promising consumer-friendly interface cable because of its flexibility, low installation cost, and high bandwidth, which allows for bit rates up to 40 Gb/s for a length of 100 m [3,4]. In the consumer applications, optical fibers are inserted and removed in very short link below several meters. Moreover, for optical modules and connectors, low-cost optical interconnects without optical isolators, angled fiber end-faces, and precise alignments are desirable. In such a condition, transmitted signal qualities are significantly degraded through optical feedback from some discontinuities in the link [5,6]. Recently, we demonstrated that GI POFs have reflection noise reduction effects because of strong mode couplings in GI POF cores with microscopic heterogeneous structures [7–10]. Here, we demonstrate that the low-noise GI POFs can significantly improve baseband transmission quality in multimode fiber (MMF) link with a multimode vertical cavity surface emitting laser (VCSEL).

2. Experimental

Figure 1 shows the experimental setup. The laser was a multimode VCSEL with an oscillation wavelength of ~850 nm with light-current-voltage (LIV) characteristics shown in Fig. 2. The VCSEL bandwidth was ~8.7 GHz at an injection current of 5 mA. The photodetector was a GaAs PIN PD with a -3 dB bandwidth of 12 GHz. The output beam from the VCSEL was appropriately collimated and focused on a fiber end-face using an antireflection-coated (AR-coated) lens, monitored with a CCD camera to confirm normal light incidence along the fiber axis. The output beam from a fiber was collimated and focused on the PD. These allow for underfilled launching condition with little coupling losses or little modal noises.

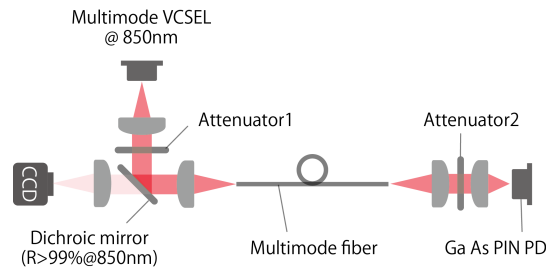


Figure 1. Experimental setup.

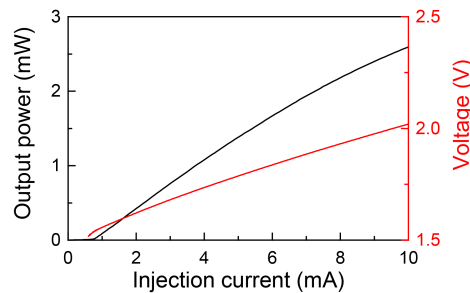


Figure 2. LIV characteristics of the VCSEL.

For evaluation of the MMF link, the VCSEL was directly modulated at a bit rate of 10 Gb/s with an NRZ data ($2^{31}-1$ PRBS pattern length). We measured bit error rates (BERs) and eye diagrams of transmitted data through a 1-m GI POF and a 1-m silica GI MMF, which is a bend-insensitive OM4 fiber. Both the fibers have almost same core diameter of $\sim 50 \mu\text{m}$ and numerical aperture (NA) of ~ 0.2 . In this MMF link for the consumer applications, transmission qualities can be limited by noise and modulation instability rather than fiber bandwidth and attenuation, which are sufficiently high and low for a length of 1 m, respectively. The dominant noise mechanism may be optical feedback from the fiber end-faces and the PD surface because feedback parameters of the backreflected lights can have sufficiently high values to destabilize the VCSEL [6].

3. Results and discussion

Figure 3 shows BER for the GI MMF and the GI POF as a function of peak-to-peak modulation voltage. Measured BERs were increased with a decrease in modulation voltage. This suggests that ever overlooked noises and instabilities significantly affect transmitted data qualities for lower modulation voltages. However, we could significantly decrease the noises and instabilities just by replacing the GI MMF with the low-noise GI POF for all the modulation voltages, as shown in Fig. 3.

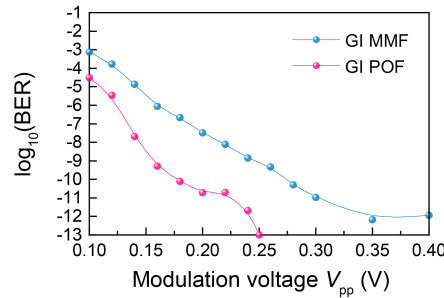


Figure 3. BER for GI MMF and GI POF as a function of peak-to-peak modulation voltage.

To investigate the noise mechanism, an AR-coated neutral density filter was inserted as an attenuator 1 or 2 to control detected average power without changing the light path, as shown in Fig. 1. We measured dependence of BER on insertion loss of the attenuator 1 between the VCSEL and the fiber for a modulation voltage of 0.1 V, as shown in Fig. 4 (a). BERs were lowered by inserting attenuator 1 for insertion losses below ~ 10 dB despite the attenuator decreased average detected power. For higher insertion losses, BER was increased owing to PD noise effects. This indicates that the data transmission qualities are predominantly degraded by optical feedbacks from the fiber end-faces and the PD surface. Although the reflectivity on the GI MMF end face was higher than the GI POF, BER for the GI POF was still lower with the corresponding insertion loss to the backreflected power difference. This indicates that the observed stabilization for the GI POF is not mainly attributed to its low reflectivity compared to the GI MMF.

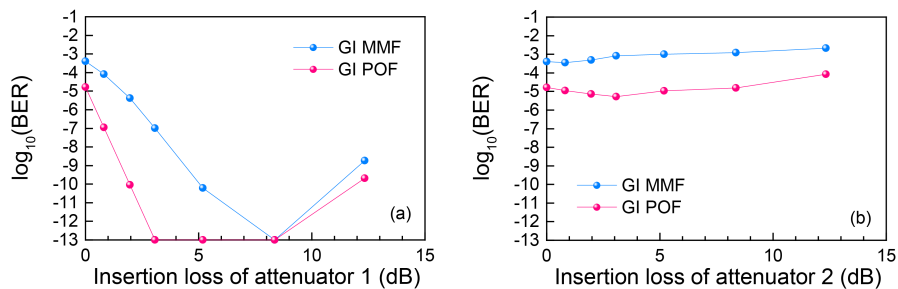


Figure 4. BER for GI MMF (OM4) and GI POF as a function of insertion loss of (a) attenuator 1 and (b) attenuator 2. The modulation voltages were 0.1 V.

Figure 4 (b) shows BER as a function of insertion loss of the attenuator 2 between the fiber and the PD for a modulation voltage of 0.1 V. For insertion losses around 1–3 dB, BERs were slightly decreased by insertion of attenuator 2 whereas the BER was increased with an increase in insertion loss from ~ 3 dB. This also suggests that optical feedback even from PD has influence on BER degradations as shown in Fig. 3.

Figure 5 shows the corresponding eye diagrams to the BER measurement (Fig. 3). For evaluation the eye diagrams with actual jitter in the link, we used constant clock as a clock recovery method. Note that all the eye diagrams were measured for negative logic NRZ data while the VCSEL was modulated with positive logic NRZ data. The results show that the GI POF allow for better eye openings than the GI MMF for all the modulation voltages. For both the GI MMF and GI POF, we observed increased turn-on delay jitters with a decrease in modulation voltage or an increase in zero-level voltage, being likely due to optical feedback [10].



The GI POF had much lower turn-on delay jitter than the GI MMF. This suggests that the reflection noise due to optical feedback effect was significantly reduced in the GI POF.

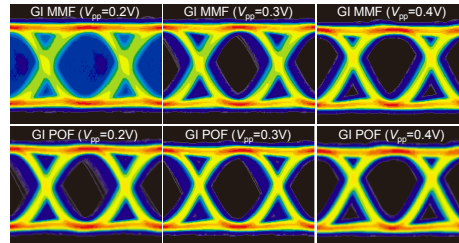


Figure 5. Eye diagrams for GI MMF and GI POF as a function of different modulation voltages with a bias current of 5 mA.

Figures 6 (a) and (b) show the CCD-captured images of backreflected beam patterns on input end faces of the GI MMF and the GI POF, respectively. These correspond to interference patterns of all the backreflected lights. The reflected light from the far-end face and the PD are backward-guided light through fibers. In the GI MMF, the mode power distribution of the backward-guided light is similar to that for the initially launched modes. Therefore VCSEL output strongly interferes with the backward-guided light, as shown in Fig. 6 (a). This suggests that optical feedback from the GI MMF can significantly affect VCSEL through efficient self-coupling of the backreflected light into the VCSEL cavity.

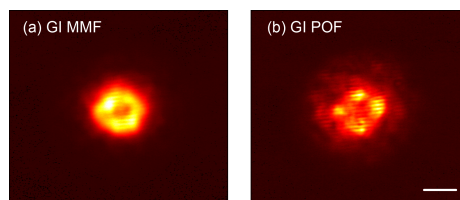


Figure 4. Temporally-averaged intensity patterns of backreflected beams on the input end-faces of (a) GI MMF (OM4) and (b) GI POF for the center launching using modulated VCSEL with modulation voltage of 0.1 V. The scale bar is 10 μm .

On the other hand, the GI POF had significantly different interference pattern from the GI MMF, as shown in Fig. 6 (b). This is attributed to strong mode coupling in the GI POF core where propagated lights are inherently forward-scattered because of microscopic heterogeneities [7,8]. The strong mode coupling resulted in pronounced power transitions from the launched modes to higher-order modes for the round-trip propagation in the GI POF. This can decrease the optical feedback effect through decrease of self-coupling efficiencies into the VCSEL cavity because of its different reflected beam properties from the VCSEL cavity modes, resulting in the significant improvement of BER and eye opening from the GI MMF.

2. Conclusion

We propose the low-noise MMF link that can be intrinsically stabilized using the GI POF with strong mode coupling owing to microscopic heterogeneities in the GI POF core. In the MMF link with strong optical feedbacks to the VCSEL, the GI POF allows for lower BER and better eye opening of the transmitted signal than silica GI MMFs. These results suggest that the low-noise GI POF allows for the low-cost optical



interconnects without optical isolators, angled fiber end-faces, and precise alignments for consumer applications.

3. Acknowledgements

This paper is based on results obtained from a project commissioned by the New Energy and Industrial Technology Development Organization (NEDO).

4. References

- [1] Motohashi, "Media, Culture and Industry in the 4K/8K Smart TV Era," *New Breeze*, Vol. **26**, no. 2, p. 5 (2014).
- [2] INTERFACE FOR UHDTV PRODUCTION SYSTEMS, ARIB ISTD-B58 Version 1.0, 2014.
- [3] Y. Koike, *Fundamentals of plastic optical fibers*, Wiley (2015).
- [4] Y. Koike et. al., "High-speed graded-index plastic optical fibers and their simple interconnects for 4K/8K video transmission," *J. Lightwave Technol.*, Vol. **34**, no. 6, p. 1551 (2016).
- [5] K. Petermann, *Laser diode modulation and noise*, Kluwer (1991).
- [6] J. Ohtsubo, *Semiconductor lasers: stability, instability and chaos*, Springer (2012).
- [7] A. Inoue et. al., "Intrinsic Transmission Bandwidths of Graded-Index Plastic Optical Fiber," *Opt. Lett.*, Vol. **37**, No.13, pp.2583 (2012).
- [8] A. Inoue et. al., "Efficient group delay averaging in graded-index plastic optical fiber with microscopic heterogeneous core," *Opt. Express*, Vol. **21**, No.14, p.17379 (2013).
- [9] A. Inoue et. al., "Reflection noise reduction effect of graded-index plastic optical fiber in multimode fiber link," *Opt. Lett.*, Vol. **39**, No. 12, p. 3662 (2014).
- [10] Y. Matsumoto et. al., "Intrinsic Robustness of Fiber Misaligned Connections and Reflection Noise in Plastic Optical Fiber Links for Cost-Effective Radio-Over-Fiber Systems," *Proc. OFC*, Th4A.5, Los Angeles (2016).
- [11] L. N. Langley, "The effect of external optical feedback on the turn-on delay statistics of laser diodes under pseudorandom modulation," *IEEE Photon. Technol. Lett.* Vol. **4**, No. 11, p. 1207 (1992).



A Fast Fluorescent Light Source for Data Communication over SI-PMMA-POF

Flávio André N. Sampaio¹, Vinicius N. H. Silva^{1*}, Luiz Anet Neto², Andrés P. L. Barbero¹, Ricardo M. Ribeiro¹ and Tadeu N. Ferreira¹

¹ Laboratório de Comunicações Ópticas, Departamento de Engenharia de Telecomunicações, Universidade Federal Fluminense, Niterói, RJ-Brasil, 24210-240

² Orange Labs Networks, 2 Avenue Pierre Marzin 22307, Lannion

*Corresponding author: vnhsilva@telecom.uff.br

Abstract: In 2015, we developed a 560 nm light source composed by a fluorescent optical fibre pumped by a co-propagating source at 520 nm, generated by a green light-emitting diode. This simple and compact light source was designed to operate where the PMMA plastic optical fibre has a minimum attenuation. In this paper, we experimentally assess the use of our wavelength-converted optical carrier at 560 nm for 120 Mb/s with discrete multitone (DMT) data communication. We have achieved 6 bits/s/Hz spectral efficiency over 20 m of step index plastic optical fibre (SI-POF) with a pre-FEC target bit error rate (BER) of 10^{-3} .

1. Introduction

It is well known that plastic optical fibre (POF) is a promising communication medium for short-range telecommunication networks [1]. Besides its relatively high bandwidth, low cost, immunity to electromagnetic interference (EMI) and ease of installation, SI-POF is in particular very attractive since they provide easier light coupling from the light source compared to graded-index POF (GI-POF). Those characteristics aroused the interest of companies from different areas. For example, automotive companies have been developing devices and applications to provide high data rate inside cars [2]. Also, it has been reported that POF are very efficient for In-home networks [3-4].

Those applications promote the research in the field and many projects and articles have demonstrated data rate transmission in the order of Gb/s over 20 – 50 m of POF [5] using top-notch transmitters such as vertical cavity surface emitting laser diodes. Besides, the availability of different types of laser diodes (LD) and LEDs allowed the implementation of wavelength division multiplexing (WDM) technology in transmission links based on SI-POF. The idea is to increase the capacity by using several optical carriers to surpass the inherent limiting factors of the SI-POF such as high attenuation and modal dispersion. Many WDM techniques operating at several wavelength and employing different modulation formats can be found in the literature. However, the yellow/orange transmission window (560-600 nm) is yet unexplored since semiconductor compounds such as GaAsP, AlGaInP and GaP:N are not suitable to develop fast, efficient and fiber-integrable source at this wavelength range [6].

In this paper, we report, for the first time, the experimental demonstration of a single channel transmission on SI-POF at 560 nm. The light source is a commercial fluorescent plastic optical fibre pumped by a green LED at 520 nm. This device is lightweight, eye-safe, compact and it could be very promising for increasing the capacity of WDM communication systems [6-7]. Thanks to the use of DMT modulation, we have shown a data rate up to 120 Mb/s for a target pre-FEC BER of 10^{-3} over 20 m of SI-POF by means of simple direct intensity modulation with direct detection. Transmission spectral efficiencies as high as 6 bits/s/Hz are demonstrated.

2. Experimental Setup

Figure 1 shows the transmission experimental setup. First, a pseudorandom binary sequence (PRBS) is generated and then parallelized into lower bit-rate sequences which are mapped into M-ary quadrature amplitude modulation (QAM) symbols ($M=1, 4, 8, \dots, 64$). Each symbol modulates one of the subcarriers of the transmitted signal. Since the DMT signal has to real to be suitable for optical transmission with direct intensity modulation and direct detection, the subcarriers matrix should satisfy the Hermitian symmetry [8]. Then, those subcarriers are multiplexed by applying the inverse fast Fourier transform (IFFT). Finally, a cyclic prefix (CP) is added to allow extra robustness to intersymbol interference (ISI). The signal is serialized (P/S) before being converted by a digital-to-analog converter (DAC). The electrical signal modulates the fluorescent



light source after being biased to allow linear operation of the LED. After propagation through SI-POF, an analog-to-digital converter (ADC) first digitizes the received signal and then the subcarriers are demultiplexed by means of a fast Fourier transform (FFT). The received symbols are time and frequency synchronized, equalized and finally demapped to allow retrieving some important transmission performance parameters.

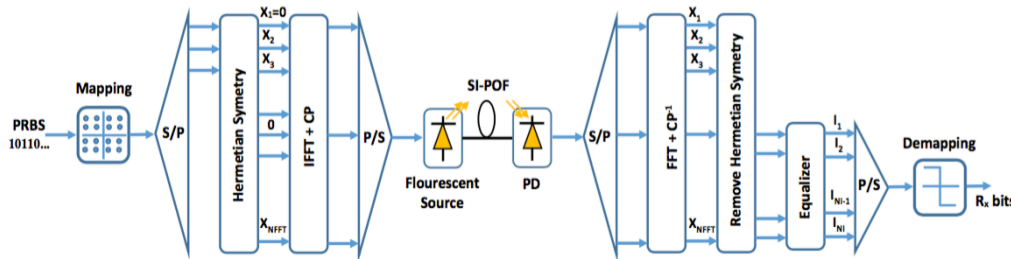


Figure 1 – DMT modulation and demodulation scheme.

The experimental setup (Figure 2) is composed by a personal computer (PC) acting as DMT modulator/demodulator, a DAC from an arbitrary function generator (Tektronik AFG3251), a bias-T (Mini-Circuits ZG85-12G+), a DC source, the fluorescent optical source [6], 20 m of SI-POF, a photodetector (Thorlabs PDA10A) and an oscilloscope (Rohde&Schwarz RTO 1002) responsible for digitizing the received signals. The fluorescent optical fibre has a 3 dB bandwidth of 52.5 MHz. However, since it is pumped by a DieMount green led, the analog bandwidth of the whole, wavelength-converted source is limited to 20 MHz with approximately 120 μ W output power.

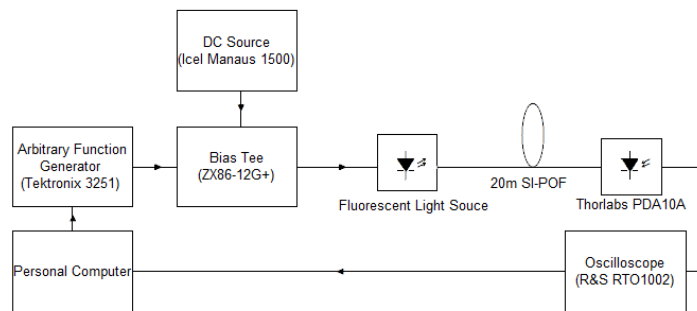


Figure 2 - Block diagram of the experimental setup.

Transmission is performed as follows. Our 20 MHz baseband real-valued DMT signal is composed by 491 useful subcarriers (IFFT size = 984 considering DC and Nyquist null subcarriers). 16 samples per symbol are used as cyclic prefix. The total DMT symbol duration is 25 μ s, of each 24.6 μ s are the useful data and 0.4 μ s represent the guard interval. The DAC and ADC operate at 100 MSa/s and 400 MSa/s respectively. The first step of the transmission consists on using a probe signal to allow measuring the signal-to-noise ratio (SNR) of the channel. In such signal, all subcarriers are QPSK modulated and have the same relative power coefficient. The SNR per subcarrier is then used as an input for the rate-adaptive version of the Levin-Campello bit and power loading algorithm. The principle of this algorithm consists on maximizing the overall bit-rate of the transmission subjected to a global signal power constraint and a target mean BER over all subcarriers chosen by the operator. Basically, it consists on a greedy algorithm which will allocate more information (higher QAM modulation levels) on the subcarriers with better SNR. It then compensates the SNR fluctuations on subcarriers with the same modulation levels by changing the relative power coefficient of each subcarrier individually. SNR, root-mean square error vector magnitude (EVM_{RMS}) and BER per subcarrier are finally assessed over 1000 symbols.



3. Results

Figure 3 shows the received time (80 DMT symbols) and frequency domain signal after propagation. From the received spectrum, we can observe that the transmitting channel acts mostly as a low-pass filter. Some degradation is however observed for frequencies below 1.4 MHz. Figure 4 shows the result of the first step of our transmission with the probing signal. From top to bottom, we observe, for all subcarriers, the relative power coefficient ρ , the number of bits per QAM symbol ($\log_2(M) = 2$ for QPSK), the measured EVM and the SNR and BER estimated from the EVM.

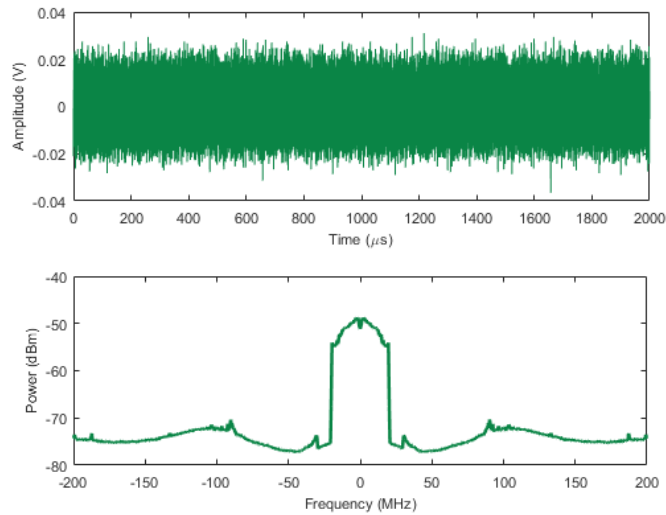


Figure 3 – Received time and frequency domain signal after 20 m SI-POF (560 nm).

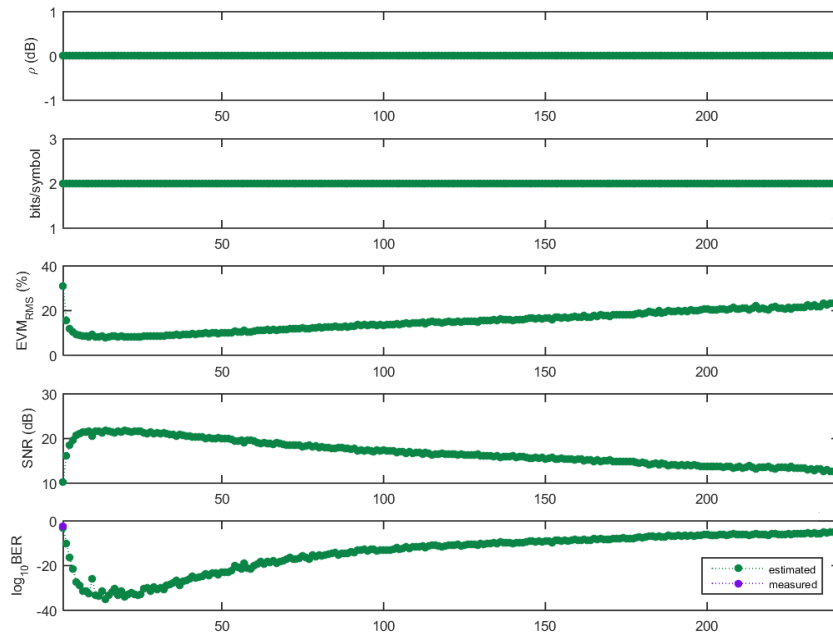


Figure 4 – Single channel transmission results over 20 m of SI-POF at 560 nm with a probing signal.



Figure 5 shows the modulation, power, EVM, SNR and BER per subcarrier after bit and power-loading for a target BER = 10^{-3} . A spectral efficiency of 6.0 bits/Hz is achieved leading to a bit-rate of 120 Mb/s. We can also observe that the estimated BER from the SNR is in very good agreement with the measured BER (purple curve), after demapping of the received symbols. Also, modulation levels as high as 64QAM (6 bits/symbol) are reached in more than 50% of the subcarriers. Figure 5 also shows the received constellations of some subcarriers.

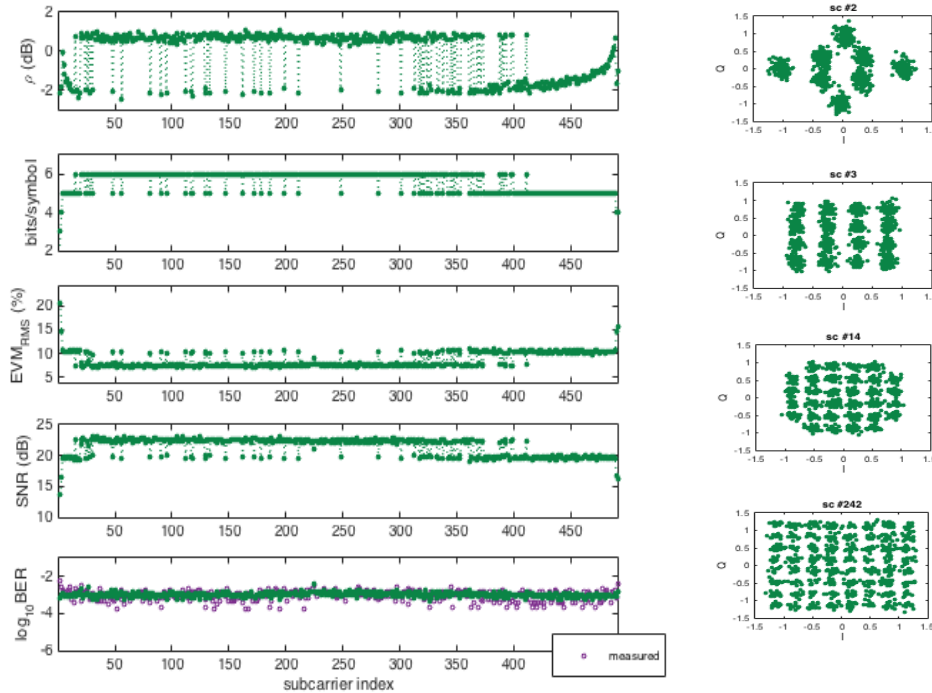


Figure 5 – Single channel transmission over 20 m of SI-POF at 560 nm after bit and power loading with a target BER of 10^{-3} .

Figure 6, shows the spectral efficiency variation for different target BER values. It is interesting to notice that higher than 2 bits/s/Hz could still be attained for a target BER of 10^{-12} . At such BER, the use of forward error correction schemes could be avoided allowing thus the simplification of a real-time transmission system.

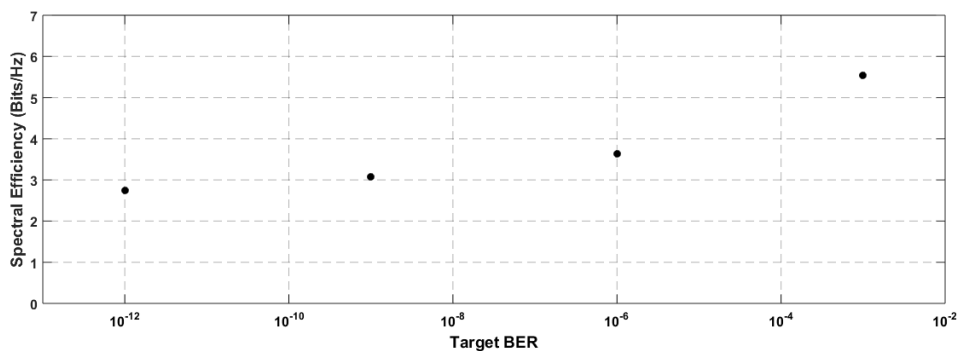


Figure 6 – Spectral efficiency of single channel transmission over 20 m of SI-POF at 560 nm versus BER.



4. Conclusion

We carried out, for the first time, a single channel transmission over 20 m of standard plastic optical using a fluorescent light source at 560 nm developed in our lab. The results show that the source is efficient to delivery up to 120 Mb/s with a target BER of 10^{-3} using QAM modulation and DMT multiplexing. Near 3 bits/s/Hz could still be achieved for a target BER of 10^{-12} and thus without the need of any error correction scheme. Further research will focus on the investigation of the use of different pump sources in order to improve the source bandwidth and increase the transmission spectral efficiency above 6.0 bits/s/Hz.

3. Acknowledgements

The authors would like to thank the Conselho Nacional de Desenvolvimento Científico e Tecnológico (CNPq) and Fundação de Amparo a Pesquisa do Estado do Rio de Janeiro (FAPERJ) for the financial support. The authors gratefully acknowledge the technical support of the under graduated student Vinicius Tremmel.

4. References

- [1] R. Gaudino, "High speed transmission over plastic optical fibres (in- vited paper)," in Proc. ECOC, Sep. 2009, pp. 1–4.
- [2] M. Yonemura, A. Kawasaki, M. Kagami: "250 Mbit/s Bi-directional Single Plastic Optical Fiber Communication System", R&D Review of Toyota CRDL, Vol. 40 (2005)2, P. 18-23
- [3] A. Acakpovi and P. L. M. V. Matoumona, "Comparative analysis of plastic optical fiber and glass optical fiber for home networks," 2012 IEEE 4th International Conference on Adaptive Science & Technology (ICAST), Kumasi, 2012, pp. 154-157.
- [4] J.Lambkin, "In-home plastic optical fibre (POF) networks: Redefining the X in FTTX," in Proc. ICTON, Jun. 2008, p. 202.
- [5] M. Jončić, R. Kruglov, M. Haupt, R. Caspary, J. Vinogradov, and U. H. P. Fischer: Four-channel WDM transmission over 50-m SI-POF at 14.77 Gb/s using DMT modulation, IEEE Photon. Technol. Lett. 26(13), 1328–1331, 2014.
- [6] C. M. Alves, V. N. H. Silva, A. P. L. Barbero, R. M. Ribeiro, "An Improved 560nm Fast Light Source Using Wavelength Conversion by Fluorescence, " in 24th International Conference on Plastic Optical Fibers (ICPOF2015), 2015, Nuremberg.
- [7] [3] O. Ziemann, L. Bartkiv, "POF-WDM, The Truth," in 20th International POF Conference 2011, 2011 Bilbao.
- [8] J. Armstrong, "OFDM for Optical Communications," in Journal of Lightwave Technology, vol. 27, no. 3, pp. 189-204, Feb.1, 2009.

Application of 4-channel LED Module for WDM Transmission over SI-POF

R. Kruglov^{1*}, J. Vinogradov¹, O. Ziemann¹, W. Huber²

1 POF-AC, Technische Hochschule Nürnberg Georg Simon Ohm, Wassertorstrasse 10, 90489 Nuremberg, Germany

2 Chips 4 Light GmbH, Nürnberger Straße 13a, 93152 Etterzhausen, Germany

*Corresponding author: roman.kruglov@pofac.th-nuernberg.de

Abstract: We introduce a 4-channel LED module for WDM POF-based applications operating at 410 nm, 440 nm, 520 nm and 660 nm. Radiation and spectral parameters, as well as transmission characteristics of the LED module were measured and proved for POF applications. The maximal aggregate bit rate of 3700 Mb/s at a BER of 10^{-3} was achieved in WDM transmission link with a demultiplexer based on a planar diffraction grating.

1. Introduction

Many of the polymer optical fiber (POF) transmission systems with a wavelength division multiplexing (WDM) suffer from high insertion losses of the optical components [1-3]. It can be especially critical for the systems with light-emitting diodes (LED) that provide usually poorer transmission characteristics in comparison to the laser diodes (LD).

As a multiplexer for WDM POF links a fiber coupler [4] is often used which might provide a low light coupling efficiency by LED applications. However, high NA and large core diameter of POF allow to arrange several LD/LED chips in a single butt-coupled transmission module. It brings an opportunity to eliminate a coupler from the transmission system and achieve a higher power margin.

In this paper we introduce a 4-channel LED module for WDM POF-based applications operating at 410 nm, 440 nm, 520 nm and 660 nm. Radiation and spectral parameters, as well as transmission characteristics of the LED module were measured and proved for POF applications. Using the LED module a WDM data transmission link was implemented with a demultiplexer (DEMUX) based on a planar diffraction grating.

2. LED module characterization

The top view of the butt-coupled LED module is shown in figure 1. The contour of SI-POF is marked with a black dashed circle. The module includes 4 LEDs operating at 410 nm, 440 nm, 520 nm and 660 nm, which are mounted on the customer-specific ceramic substrate. A protection glass is fixed with a silicon compound.

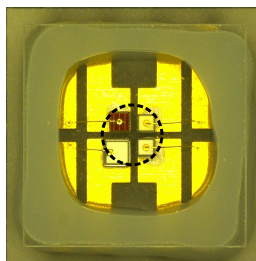


Figure 1. Top view of the LED module.

The fiber-coupled optical power shown in figure 2a was measured at room temperature and different operating currents after 1-m SI-POF aligned towards every single LED. By simultaneous use of 4 LEDs the fiber position was adjusted in a way to provide an equal power reduction for all chips which results in approx. 1 dB loss. Figure 2b shows the electrical-to-optical (E-O) frequency responses of LEDs measured at operating current of 30 mA with a Graviton SPD-2 optical receiver and an Agilent E5071C network analyzer. The 3-dB bandwidths of 8.5 MHz, 17.5 MHz, 20 MHz and 16 MHz correspond to LEDs operating at 410 nm, 440 nm, 520 nm and 660 nm respectively. The spectral characteristics of LEDs are shown in Section 3.

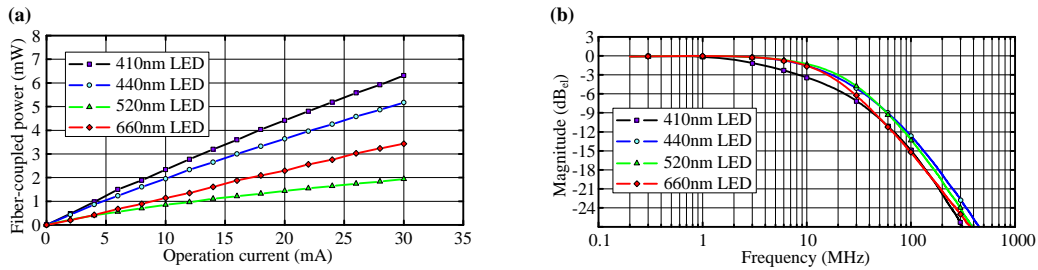


Figure 2. Fiber-coupled optical power after 1-m SI-POF aligned towards every single LED (a) and normalized frequency response of LEDs (b).

3. WDM data transmission test

To show a potential of the LED module it was tested as a part of the WDM transmission link. The measurement setup shown in figure 3 consists of the 4-channel LED module, SI-POF Mitsubishi GH-4001 with 1-mm core diameter (POF class A4a.2, according IEC 60793-2-40), an optical wavelength demultiplexer, and optical receivers with \varnothing 800- μ m silicon pin photodiodes (Hamamatsu S5052) connected to trans-impedance amplifiers [5]. To provide a proper level of the modulation signal additional preamplifiers MERA-556+ (Mini Circuits) were used.

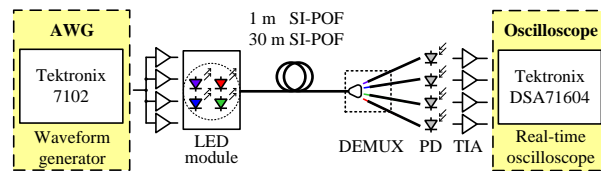


Figure 3. WDM transmission link with 4-channel LED module.

The arbitrary waveform generator Tektronix 7102 and the real-time oscilloscope Tektronix DSA 71604 were used as digital-to-analog and analog-to-digital converters respectively.

The demultiplexer includes an aspheric glass condenser lens 01 LAG 023 (Melles Griot) with a diameter of 75 mm and planar holographic diffraction grating (Carl Zeiss) with groove density of 1800 mm^{-1} and blaze wavelength of 500 nm [4]. Figure 4 shows spectral characteristics of the demultiplexer and LEDs. FWHM spectral widths of 24 nm, 20 nm, 40 nm and 18 nm correspond to LEDs operating at 410 nm, 440 nm, 520 nm and 660 nm respectively. The demultiplexer losses measured at the central wavelengths of LEDs are within the range of 7 to 10 dB. The actual insertion losses of demultiplexer are within the range of 15 to 17 dB which is connected with a wide spectral width of LEDs.

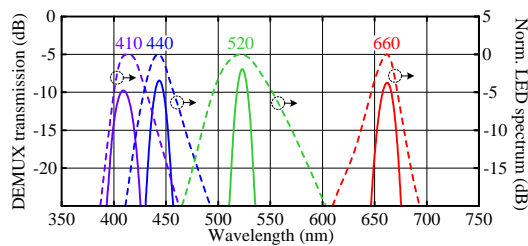


Figure 4. Transmission characteristics of the demultiplexer and LED spectra.

To test the performance of the WDM transmission link the LEDs were modulated over Bias-T by NRZ signals based on pseudo-random binary sequence (PRBS 2^7-1). T/2 fractionally spaced decision feedback equalizer (DFE) with 16 feedforward and 4 feedback taps was employed for the post-processing of the received signals. The maximum throughput in the spectral channels (see figure 5a) was measured for the system with 1-m length and 30-m length SI-POF at a bit-error ratio (BER) of 10^{-3} which is sufficient for implementation of the forward error correction [6].

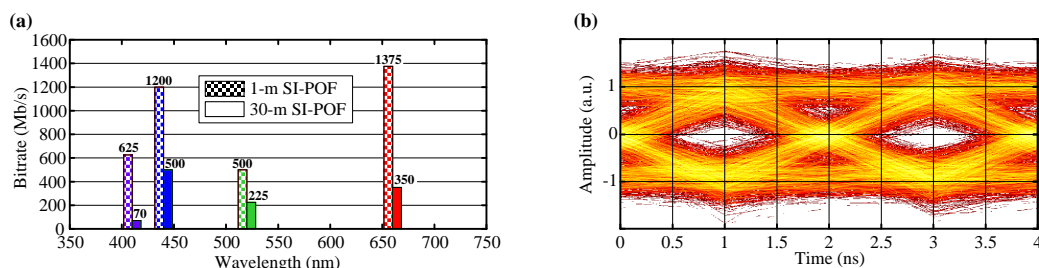


Figure 5. Maximal bit rates at BER of 10^{-3} achieved over 1-m and 30-m WDM transmission links (a) and computed eye-diagram of 500 Mb/s data stream after DFE for 440-nm channel in the 30-m link at BER= 10^{-3} (b).

The aggregate bit rates at BER of 10^{-3} achieved over 1-m and 30-m SI-POF were 3700 Mb/s and 1145 Mb/s respectively. As an example, the NRZ eye-diagram after DFE for 440-nm spectral channel in the 30-m transmission link is shown in figure 5b.

4. Conclusion

Development and implementation of new optical components brings an opportunity to design WDM POF-based systems which characteristics will be acceptable for commercial applications. In the given paper we introduced a 4-channel LED module which provides high fiber coupling efficiency. Data transmission of 3700 Mb/s at a BER of 10^{-3} was demonstrated in WDM transmission link with a demultiplexer based on a planar diffraction grating. The further improvement might be achieved by optimization of the demultiplexer for WDM channels with a wide spectral width.

5. Acknowledgements

The POF-AC Nürnberg is a project of the Hightech Offensive Bavaria. The work was supported by the Bavarian Ministry of Education, Culture, Science and Art and the European Regional Development Fund inside the Project "OHM-Netze" (No. EU-1607-0017).

6. References

- [1] Appelt V, et al. Simple FEXT Compensation in LED Based POF-WDM Systems. In: *Proc. of 11th Int. Conf. on Plastic Optical Fibers, 18-20 September 2002, Tokyo, Japan.* 2002:127-129.
- [2] Pinzon P, et al. Efficient Multiplexer/Demultiplexer for Visible WDM Transmission over SI-POF Technology. *J. of Lightw. Technol.* 2015,33(17): 3711-3718.
- [3] Friedrich K, et al. Application of concave diffraction gratings for WDM transmission over polymer optical fibers. In: *Proc. of 24th Int. Conf. on Plastic Optical Fibers, 22-24 September 2015, Nuremberg, Germany.* 2015:104-109.
- [4] Kruglov R, et al. 21.4 Gb/s Discrete multitone transmission over 50-m SI-POF employing 6-channel WDM. In: *Proc. OFC 2014, 9-13 March 2014, San Francisco, CA.* 2014:Th2A.2.
- [5] Vinogradov J, et al. -22 dBm receiver sensitivity for Gbit/s data communication on SI-POF and glass fiber. In: *Proc. of 14th Int. Conf. on Plastic Optical Fibers, 19-22 September 2005, HongKong, China.* 2005:255 259.
- [6] International Telecommunication Union. ITU-T Recommendation G.975.1. *Forward error correction for high-bit rate DWDM submarine systems.* Geneva; 2004.

Embedding low loss polymer optical fibre Bragg gratings: Two different approaches

A. Lacraz^{1*}, M. Zubeł², G. Demirci³, A. Theodosiou¹, K. Kalli¹, K. Sugden², B. Gawdzik³

1 Cyprus University of Technology, Limassol, Cyprus

2 Aston University, Birmingham, United Kingdom

3 Maria Curie-Skłodowska University, Lublin, Poland

*Corresponding author: amedee.lacraz@cut.ac.cy

Abstract: In this paper, we present two different ways to embed polymer fibre Bragg gratings (FBGs) into polymer matrices. In the first experiment, we embedded the FBG into a 3D printed polymer structure, whereas in the second experiment, the coating was polymerized around the fibre. In both cases, the response of the grating was unchanged, without any loss or distortion of the FBG signal compared with the bare fibre response. The design of the polymer coating was optimised for the measurement of a single measurand. We highlighted two possible applications: surface bend deformation monitoring and improved-sensitivity temperature sensing.

1. Introduction

Low loss polymer optical fibres, drawn from materials such as CYTOP, are good candidates for the realization of polymer fibre sensors. The usable fibre length can reach tens of metres, without a significant attenuation, even in the telecommunication wavelength band. Compared to other polymer optical fibres (POFs), the optical properties are significantly better, with theoretical losses as low as a few tens of decibels per kilometre. However, precisely because of its high transparency, the photosensitivity of a low-loss polymer is dramatically reduced, and this creates difficulties for the inscription of fibre Bragg gratings (FBGs) made of such material with the usual UV irradiation methods. Fortunately, other methods can be used to overcome this difficulty, for example with very short wavelengths, where CYTOP displays greater optical absorption [1]. Here we use a femtosecond laser setup for Bragg grating inscription, where the index change occurs only in the focus point of the laser and relies on nonlinear electronic effects, which allow for a controlled index change and grating properties [2]. The Bragg response of CYTOP gratings under strain and temperature has also been investigated and showed promising results for sensing applications [2].

Polymers are of great interest as they offer considerable mechanical advantages over glass, especially because they are viscoelastic materials that allow for a greater elasticity and potentially improved strain properties. Nevertheless, embedding POF has attracted serious attention because embedding materials offers the capability of sensing and responding to the surrounding environmental stimulus in a different way compared with the bare fibre [3]. When placed in strategic places, the FBGs can yield crucial information about the material in areas not accessible by other sensors; they are also more robust. All-polymer optical devices, consisting of a polymer fibre embedded in a polymer matrix, are particularly sought after for their mechanical and biocompatible advantages [4]. In the recent past, fibres have been embedded in metal [5,6], between the plies of a glass fibre-reinforced plastic [4,7,6] in epoxy [8], in polydimethylsiloxane (PDMS) [9], however, all polymer devices have not been really considered until recently [10].

2. 3D printed embedment of FBGs

The first embedding method that we highlighted consisted of placing the FBG in a 3D printed structure. The material is deposited layer by layer until the chosen height is reached. The process is then stopped and the fibre placed within the structure and glued to the material. The process is resumed and the material is deposited above the fibre. Depending where the fibre placed in the structure, the FBG will respond differently to bend or temperature. If the fibre is on the neutral axis of a longitudinal beam for example, the FBG can be made bend insensitive [10]. The structure had dimensions of about 1mm x 1mm x 10mm in a shape of a rectangular beam along the fibre length.

First, we characterised the strain response of the embedded structure in strain (Figure 1). Unlike with standard strain tests, where the FBG is strained from two fixed points, here the whole structure is strained, which results

in a homogenous strain along the fibre length. This allowed for a much wider strain excursion – more than six millistrain – compared with our previous experiments with this kind of FBG [2], where we couldn't strain more than two millistrains before the fibre showed signs of deterioration. We measured a typical FBG strain response between 0.71 and 0.76 nm/mε, depending on whether the fibre was strained or unstrained, with a relatively good accuracy (low standard deviation) for strain levels, up to 5 mε.

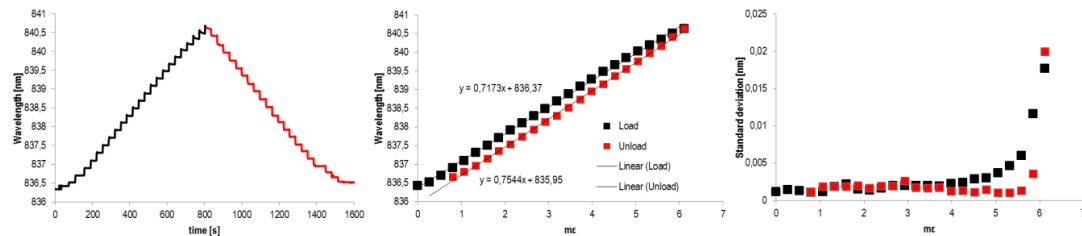


Figure 1. Left. Strain cycle applied to the 3D printing embedded structure. In black the fibre is strained, in red, unstrained
 Middle. Position of the resonance wavelength
 Right. Standard deviation showing a good response up to strain levels of ~5mε



Figure 2. Bend test on the 3D printing embedded structure. The fibre is embedded near the neutral axis of the fibre

In a second experiment, we placed the fibre at the neutral axis of the beam (exactly in the centre, where the fibre should sense no strain or compression when bent. (Figure 2). Figure 3 shows results where we recorded the position of the FBG peak while the structure was bent. We can see that the fibre was not exactly aligned with the neutral axis, but at a point marginally above the centre; this is apparent because the FBG sensed strain when the structure was bent. Nevertheless, the relatively low wavelength shift indicates that the embedded FBG shows an almost bend-insensitive behaviour, or can be tailored to record selected levels of strain on exposure to bending forces.

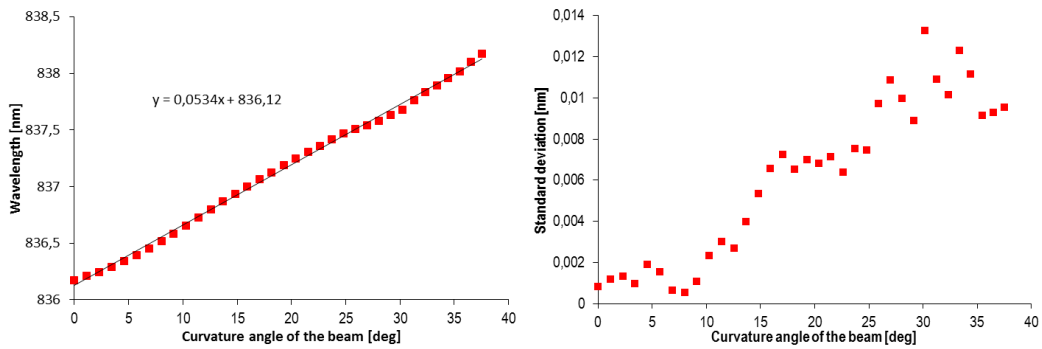


Figure 3. Bend test on the embedded structure
 Right. Position of the FBG resonance
 Left. Standard deviation

3. Embedding FBGs into polymers

The second embedding method relies on the polymerisation or curing of the coating material around the fibre. To illustrate this method, we coated the FBG with commercial gelatine, a derivative of collagen protein, Figure 4. The polymer in its liquid form at $\sim 60^{\circ}\text{C}$ was poured into a circular glass mould where the fibre was placed beforehand. The collagen cured at ambient temperature until a solid form was reached. Such simple embedded sensors could find applications for collagen gel contraction assay, a standardized test for the monitoring of the contraction of skin layers during wound healing [11]. We are investigating this application.



Figure 4. Example of a circular collagen coating around a POF

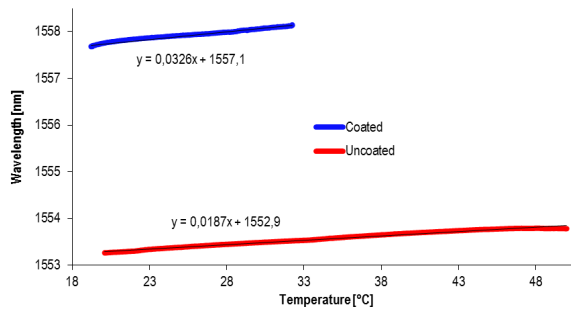


Figure 5. Behaviour of the embedded FBG sensor when PDMS coated and when uncoated

Figure 5 shows the behaviour of the embedded FBG sensor when PDMS coated and its comparison with an uncoated polymer fibre. We observe that there is an increase in the centre FBG wavelength of $\sim 4\text{nm}$, as the grating undergoes compressive strain that results from the embedding process. The coated and uncoated sensors are then exposed to a steady increase in external temperature, from which we observe that both sensors respond

in a linear manner and that the wavelength response to temperature of the coated sensor is almost double that of the uncoated sensor; an increase in response by a factor of 1.7.

4. Conclusion

We have shown that embedding polymer FBGs can be readily realised and offers a means to modify, in a tailored manner, the sensor response to external measurands; this approach can be used to improve the already excellent versatility of FBG sensors. We have used two methods to embed FBG sensors, firstly by embedding via a 3D printing process and secondly by coating the sensor with a polymer gel. The former method enabled the accurate recovery of large strain levels using a robust sensing monolith, whereas the latter showed the advantages of using selective coatings for improved sensor temperature response and the potential for novel applications, e.g. for the process of the PDMS gel contraction assay.

5. Acknowledgements

The work of A. Lacraz, G. Demirci and M. Zubel was supported by the European Union through Marie-Curie Actions under FP7 Program ITN grant “TRIPOD” – Training and Research in Polymer Optical Devices

6. References

- [1] M. Koerdts, S. Kibben, J. Hesselbach, C. Brauner, A. S. Herrmann, F. Vollertsen, L. Kroll: “Fabrication and characterization of Bragg gratings in a graded-index perfluorinated polymer optical fiber”, *Procedia Technology* 15, 2014, 138 -146
- [2] A. Lacraz, M. Polis, A. Theodosiou, K. Kalli: “Femtosecond laser inscribed Bragg gratings in low loss CYTOP polymer optical fiber”, *IEEE Photonics Technology Letters* 27(7), 2015
- [3] X. Li, F. Prinz: “Embedded fiber Bragg grating sensors in polymer structures fabricated by layered manufacturing”, *Journal of Manufacturing Processes* 5(1), 2003
- [4] G. Rajan, M. Ramakrishnan, Y. Semenova, E. Ambikairajah, G. Farrell, G. D. Peng: “Experimental study and analysis of a polymer fiber Bragg grating embedded in a composite material”, *Journal of lightwave technology*, 32 (9), 2014, 1726-1733
- [5] C. E. Lee, J. J. Alcoz, W. Gibler, R. A. Atkins, H. F. Taylor: “Method for embedding optical fibers and optical fiber sensors in metal parts and structures”, *Fiber Optic Smart Structures and Skins IV*, 1991, 110-116
- [6] X. C. Li, F. Prinz, J. Seim: “ Thermal behavior of a metal embedded fiber Bragg grating sensor”, *Smart Materials and Structures* 10, 2001, 575–579
- [7] Y.C. Chena, C.C. Hsieh, C.C. Lin: “Strain measurement for composite tubes using embedded, fiber Bragg grating sensor”, *Sensors and Actuators A* 167, 2011, 63–69
- [8] J. Botsis, L. Humbert, F. Colpo, P. Giaccari: “Embedded fiber Bragg grating sensor for internal strain measurements in polymeric materials”, *Optics and Lasers in Engineering* 43, 2005, 491–510
- [9] G. T. Kanellos, G. Papaioannou, D. Tsiokos, C. Mitrogiannis, G. Nianios, N. Pleros: “Two dimensional polymer-embedded quasidistributed FBG pressure sensor for biomedical applications”, *Optics Express* 18 (1), 2010, 179-186
- [10] M. G. Zubel, K. Sugden, D. J. Webb, D. Saez-Rodriguez, K. Nielsen, O. Bang: “Embedding silica and polymer fibre Bragg gratings (FBG) in plastic 3D-printed sensing patches”, *Proceedings of SPIE* 9886, 2016, doi: 10.1117/12.2228753
- [11] S. Su, J. Chen: “Collagen gel contraction assay”, *Protocol Exchange* (2015), doi: 10.1038/protex.2015.082



Bragg gratings inscription using PMMA polymer optical fibers drawn from preforms with specific thermal pre-treatment

Carlos A. F. Marques^{1,2}, Andreas Pospori², Gökhan Demirci³, Onur Çetinkaya⁴, Barbara Gawdzik³, Paulo Antunes¹, Pawel Mergo⁴, Paulo André⁵, David J. Webb²

¹Instituto de Telecomunicações and Physics Department & I3N, Universidade de Aveiro, Campus Universitário de Santiago, 3810-193 Aveiro, Portugal

²Aston Institute of Photonic Technologies, Aston University, Aston Triangle, B4 7ET Birmingham, UK

³Department of Polymer Chemistry, Maria Curie-Skłodowska University, 20-031 Lublin, Poland

⁴Laboratory of Optical Fibre Technology, Maria Curie-Skłodowska University, 20-031 Lublin, Poland

⁵Instituto de Telecomunicações and Department of Electrical and Computer Engineering, Instituto Superior Técnico, Technical University of Lisbon, 1049-001 Lisbon, Portugal

*Corresponding author: cmarques@av.it.pt

Abstract: In this work, fiber Bragg gratings (FBGs) are inscribed in various undoped poly(methyl methacrylate) (PMMA) polymer optical fibres (POFs) using different types of UV lasers and inscription time and their temperature and strain sensitivities are investigated. The polymer optical fiber Bragg gratings (POFBGs) were inscribed using two UV lasers: a continuous UV HeCd @325 nm laser and a pulsed UV KrF @248 nm laser. The PMMA POFs drawn from a preform without specific thermal pre-treatment need more inscription time than the fibers drawn from a preform that has been pre-annealed at 80°C for 2 weeks. Using both UV lasers, for the latter fiber less than half the inscription time is needed compared with a commercial undoped PMMA POF and other homemade POFs, where the preforms have not had a well-defined thermal pre-treatment. The effect on a POF from a preform that has been annealed prior to drawing is different as previously shown in the literature, where these POFs are much less sensitive to thermal treatment. Also, a proper polymerization process plays a key role as will be discussed. These results indicate the impact of preform thermal pre-treatment as well as polymerization process before the PMMA POFs drawing, which can be an essential characteristic in view of developing POF sensors technology.

1. Introduction

POFs can be considered as a strong alternative to silica fibers in applications such as short distance transmissions, Terahertz waveguides and filters, and mainly in sensing applications [1-4], due to their flexibility, high failure strain, large cores and great elasticity. The mechanical properties provide enhanced sensitivity or longer operational range to intrinsic polymer fibre sensors when they are used for strain, stress, pressure, temperature and humidity monitoring, as well as for transverse force sensing [5-12]. Many POF sensors are based on fibre FBGs, which have been written in different spectral windows in doped and undoped step-index POFs [13], microstructured fibers (including PMMA and TOPAS materials) [13-15], as well as low loss cyclic transparent optical polymer (CYTOP)-perfluorinated POFs [16], and graded-index POFs [17]. Polymer optical fiber Bragg gratings (POFBGs) are inscribed with different laser systems including continuous-wave (CW) HeCd laser (@325 nm) [13-15], pulsed KrF laser (@248 nm) [18], and also femtosecond laser systems [16].

Fabrication of Bragg gratings in mPOF and step-index fibers, with the phase mask technique is a time consuming process. Using a 325 nm UV laser, in undoped mPOFs exposure times from 60 to 270 minutes have been reported [19,20], for up to 10 mm long gratings, with the lowest inscription time reported being approximately 7 minutes [21]. For the step-index fibers times are shorter and typically amount to 45 to 100 minutes [19,22] with the lowest inscription time reported being approximately 20 minutes [13]. The writing time can be reduced by doping the fiber [14] but doped fibers are more difficult and expensive to fabricate, the transmission loss increases and they are less suitable for in-vivo biosensing. Recently, as a way to help manage without the fiber doping, a 248 nm UV laser was used to inscribe Bragg gratings in undoped mPOF, at low fluence and low repetition rate ($I = 33 \text{ mJ/cm}^2$; $R = 1 \text{ Hz}$) in a record time of around 30 s [18], showing that Bragg grating systems designed for silica fibers can be used to inscribe POFBGs, potentially increasing their take-up in more research laboratories.



In order to understand the fabrication process needed to achieve undoped POFs with good performance as well as reduced FBG inscription time, we compare different undoped PMMA POFs using two different UV lasers: a continuous UV HeCd @325 nm laser and a pulsed UV KrF @248 nm laser.

In this paper, we provide evidence that preform thermal pre-treatment as well as control of the polymerization process can be responsible for a better photosensitivity mechanism of undoped PMMA POF based sensors irradiated with UV light. In the experiments we observed that there is an increase of material photosensitivity in samples subjected to a well-defined preform thermal pre-treatment before the PMMA POFs drawing.

2. mPOFs under investigation and FBG inscription systems

Three different undoped PMMA mPOFs, labeled Fiber 1 to Fiber 3, were drawn in different facilities with different drawing conditions, where Fiber 1 is an mPOF from *Kiriama Pty Ltd* [23,24], Fiber 2 [25] and Fiber 3 (fabricated in *Maria Curie-Skłodowska University, Poland*) are homemade mPOFs. The core and cladding dimensions of the fibers are respectively 9/130 μm (Fiber 1), 8/135 μm (Fiber 2) and 9/270 μm (Fiber 3). The core of the fibers is composed of poly-methyl methacrylate (PMMA) with no additional dopants, whilst the cladding is also made of PMMA. All fibers have a three-ring hexagonal cladding structure. For Fiber 1, the air-hole diameter is on average 2.76 μm and the inter-hole pitch is on average 6 μm . For Fiber 2, the average pitch and hole diameter are 4.3 and 1.9 μm , and for Fiber 3 the air-hole diameter is on average 2 μm and the inter-hole pitch is on average 4.6 μm . The draw ratios for fibers 1, 2 and 3 are 20/0.130, 20/0.135 and 11/0.270, respectively. Fiber 1 has been drawn at 30 m/min with a set-temperature of 290 °C and a tension of about 24 g (0.25 N). Fiber 2 was drawn at a rate of 40 m/min with a temperature of 290°C and a tension of 0.2 N. The preform of Fiber 3 was pre-annealed for 2 weeks at 80°C before the fiber was drawn at 290°C with a draw tension between 0.5 N and 1 N and a rate of 30 m/min. For Fiber 1 and 2 the preforms were not annealed. So, the polymerization process for each fiber is different. The parameters of the fibers used are summarized in Table 1.

Table 1. Fiber parameters.

Fiber name	Core/cladding size (μm)	Cladding structure	Hole diameter/pitch (μm)	Draw ratio (mm)	Pulling speed (m/min)	Drawing Temperature (°C)/Tension (N)	Preform with well-defined annealing?
Fiber 1	9/130	All with	2.76/6	20/0.130	30	290/0.25	No
Fiber 2	8/135	three-ring	1.9/4.3	20/0.135	40	290/0.20	No
Fiber 3	9/270	hexagonal	2/4.6	11/0.270	30	290/0.5-1.0	Yes

Two different inscription systems were used to inscribe FBGs in order to compare their performance in each fiber. The first system is based on a 325 nm UV light from a CW HeCd laser with a power output of 30 mW and a beam diameter of 1.2 mm [8]. The HeCd laser beam was focused vertically downward using a 10 cm focal length cylindrical lens, through the phase mask designed for 325 nm operation, and onto the fiber. 10 cm long POF sections were laid in a v-groove and taped down using polyimide tape to prevent them moving during inscription. With this system, the inscription process was monitored using a broadband light source (provided by Thorlabs ASE-FL7002-C4), and an optical spectrum analyzer connected to an optical coupler. The second system is based on a pulsed KrF Bragg Star™ Industrial-LN excimer laser operating at 248 nm [18]. The laser has a beam spot of 6 mm in width and 1.5 mm in height, with pulse duration of 15 ns. A cylindrical lens, followed by a slit with 4.5 mm width, shapes the beam before it arrives to the phase mask, designed for 248 nm operation. 18 cm long POF sections were placed within two magnetic clamps and kept in strain to avoid undesired curvatures. Here, an interrogation system (provided by Micron Optics sm125) was used to monitor the grating growth.

In all cases, POF sections were cleaved with a hot blade on a hot plate and then a butt-coupled connection was made between one arm of a single-mode silica coupler and the POF using an FC/APC connector on the silica fiber. A small amount of index matching gel was used in order to reduce Fresnel reflections, lowering the background noise. In order to compare the FBG reflected amplitude, all the FBGs used in this work were inscribed at the same distance from the FBG monitoring input. The butt-connection loss was minimized by optimizing the alignment between the two fiber types using a 3D micrometric translation stage. This was



controlled from a power measurement in transmission as well as from the noise level in the measured reflected spectrum.

3. Results and discussion

Several FBGs in each fiber type were produced using both FBG inscription systems. Fig. 1 shows the reflected spectra for the three POFs using the 325 nm UV HeCd laser. The inscription times (the time that grating growth stops) for fiber 1, 2 and 3 are on average 90 min, 87 min, and 37 min, respectively. We can notice that for the latter fiber less than half the inscription time is needed compared with Fiber 1 and 2. Although core diameter and three-ring hexagonal cladding structure are very similar for all fibers, the particular grade of PMMA used for each facility must be different (e.g., in terms of molecular weight) and the drawing conditions most probably were different for the three fibers. Besides, we shall recall that the preform of Fiber 3 has been annealed for 2 weeks at 80°C, giving a well-defined thermal pre-treatment when compared with others. The effect of annealing on a POF of which the preform has been annealed prior to drawing is different as reported and discussed recently in [26], where this fiber type is much less sensitive to thermal treatment.

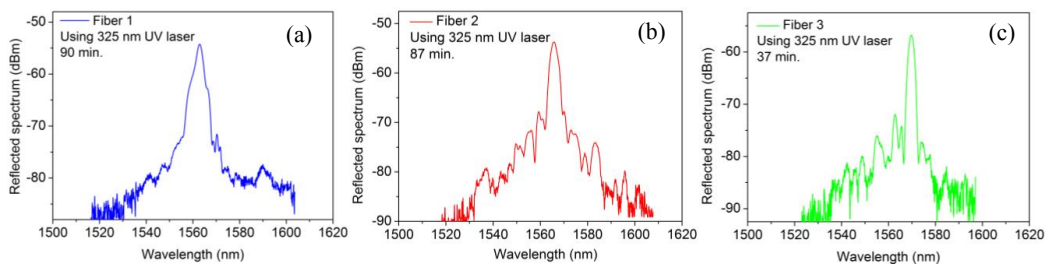


Figure 1. Reflected spectra for POFBGs in (a) Fiber 1, (b) Fiber 2, and (c) Fiber 3 using the CW 325 nm UV HeCd laser.

To substantiate our findings, we repeated the same measurements on the three fiber samples but now using the 248 nm UV KrF laser. The laser parameters were set to a frequency of 1 Hz and a pulse energy of 3 mJ. Fig. 2 shows the reflected spectra and for this case the inscription times for Fiber 1, 2 and 3 are on average 45 s, 40 s and 7 s, respectively. For Fiber 3, the optimum irradiation time was estimated to be 7 seconds meaning that only 7 pulses were needed to produce a saturated refractive index change. In Fiber 3, for which the preform has been annealed prior to drawing, the inscription time is also lower than the inscription time needed for other fibers (indeed we need 5 times less of the total inscription time using Fiber 3), as was the case with inscription using the 325 nm UV HeCd laser.

As is well known, angular orientation of the fiber microstructure has a significant impact on the intensity distribution of the UV beam in the core region, which directly affects the growth dynamics [24]. However, in our case, the success rate of the photo-inscription is quite high – more than 90%.

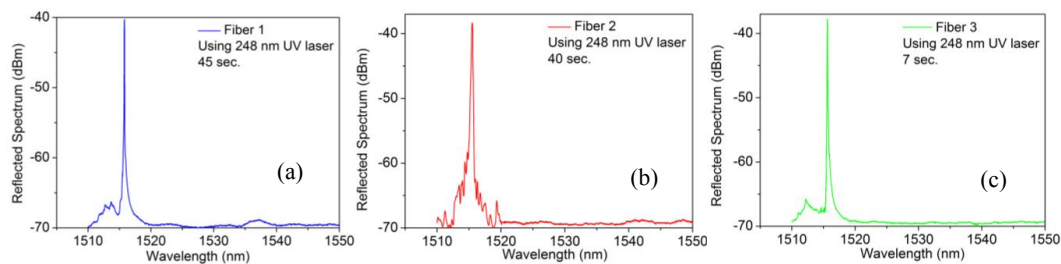


Figure 2. Reflected spectra for POFBGs in (a) Fiber 1, (b) Fiber 2, and (c) Fiber 3 using the pulsed 248 nm UV KrF laser.

The performance in terms of strain and temperature sensitivities was analyzed. A strain characterization was performed in order to show the spectral dependence of the Bragg reflection peak with strain for each fiber using



FBGs inscribed by both laser systems. The results are shown in Fig. 3 and as it can be seen the Bragg wavelength shift was linearly red shifted with 1% deformation. The obtained strain sensitivities for FBGs inscribed were 1.49 pm/ $\mu\epsilon$ (Fiber 1), 1.33 pm/ $\mu\epsilon$ (Fiber 2) and 1.24 pm/ $\mu\epsilon$ (Fiber 3) after using a linear regression model, where the results are similar to the typical values already reported in literature for POFBGs (~ 1.3 pm/ $\mu\epsilon$ in the 1550 nm window) using both UV laser systems [17,18]. Additionally, experiments were carried out to explore the temperature response of each fiber containing FBGs. The fibers were placed in an environmental chamber under varying temperatures to study their response. The temperature was increased from 22°C up to 47°C with steps of 5°C. In each step, the temperature was kept constant over 35 min to ensure thermal equilibrium was achieved. There was no control of the humidity level in the chamber. The temperature sensitivities obtained were similar to the values already reported for POFBGs inscribed in Fibers 1 and 2 with 325 nm laser system [17,27], -159 pm/ $^{\circ}\text{C}$ and -64 pm/ $^{\circ}\text{C}$, respectively. For Fiber 3, we achieved a temperature sensitivity of -53 pm/ $^{\circ}\text{C}$, which is less than achieved for Fiber 1 and 2, as discussed in [26], suggesting that these POFs are much less sensitive to thermal treatment due to the impact of preform thermal pre-treatment before the PMMA POFs drawing.

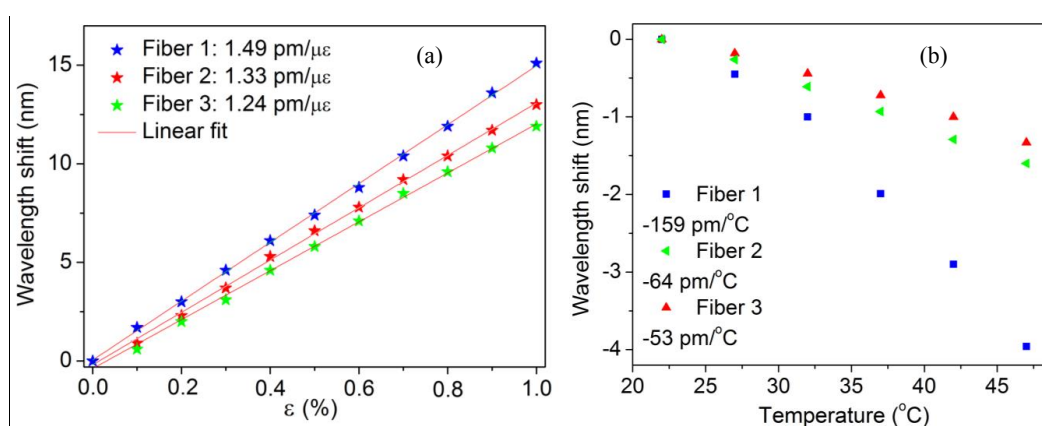


Figure 3. Bragg wavelength shifts obtained from the inscribed FBGs in each fiber under different (a) strains and (b) temperatures.

As well reported in [17], although the temperature sensitivity is lower for annealed fibers than observed in non-annealed fiber, the stability of POFBGs based on annealed fibers is improved, making possible the pre-annealing of fiber prior to FBG inscription in order to extend the quasi-linear operating temperature range. At the same view, the results presented here indicate the impact of preform thermal pre-treatment before the PMMA POFs drawing on the fast inscription of POFBGs, which is an essential characteristic in view of developing stable POFBG based thermo-mechanical sensors. Also, the difference in sensitivity of gratings as well as inscription time in these fibers could be explained by the different polymerization processes, where the thermal pre-treatment of preforms plays a key role to achieve good-quality gratings in less time. The different drawing parameters including drawing tension from which we calculate the draw stress, and the atmosphere surrounding the preform, can also give us a plausible explanation. A more extensive study is required in order to confirm the mechanism(s) behind the observations, and some fibers fabricated in different drawing tensions will be considered in future work.

4. Conclusions

In this work, improvements in the photosensitivity of undoped POFs where there was a well-defined pre-annealing of the preform was reported. We have noticed that with non-annealed preforms, the fiber photosensitivity is lower. The fibers from preforms with specific thermal pre-treatment allow us to achieve less FBG inscription times than fibers with no well-defined annealing, obtaining at the same time FBG sensors with high quality. There are other variables we can further consider in future such as the atmosphere in which the preform is placed during annealing (water content, etc...) and different drawing tensions.



5. Acknowledgments

This work was supported by Marie Curie Intra European Fellowship included in the 7th Framework Program of the European Union (project PIEF-GA-2013-628604). The research leading to these results has also received funding from the People Programme (Marie Curie Actions) of the European Union's Seventh Framework Programme FP7/2007-2013/ under REA grant agreement No. 608382. Also, this work is funded by Fundação para a Ciência e Tecnologia (FCT)/MEC through national funds and when applicable co-funded by FEDER – PT2020 partnership agreement under the projects UID/EEA/50008/2013, and UID/CTM/50025/2013. C. Marques and P. Antunes also acknowledge the financial support from FCT through the fellowships SFRH/BPD/109458/2015 and SFRH/BPD/76735/2011, respectively. We acknowledge and thank David Sáez-Rodríguez, who fabricated the Fiber 2 which was tested in this paper.

6. References

- [1] Y. Shao, R. Cao, Y. K. Huang, P. N. Ji, S. Zhang, "112-Gb/s transmission over 100 m of graded-index POF for optical data center applications," Proc. Optical Fiber Communication Conference (OFC), OW3J.5 (2012).
- [2] S. Zhou, L. Reekie, H. P. Chan, Y. T. Chow, P. S. Chung, K. M. Luk, "Characterization and modeling of Bragg gratings written in polymer fiber for use as filters in the THz region," Opt. Express 20, 9564 (2012).
- [3] D. J. Webb, "Fiber Bragg grating sensors in polymer optical fibers," Meas. Sci. Technol. 26, 092004 (2015).
- [4] K. Peters, "Polymer optical fiber sensors - A review," Smart Mater. Struct. 20, 013002 (2011).
- [5] S. Kiesel, P. Van Vickle, K. Peters, T. Hassan, M. Kowalsky, "Intrinsic polymer optical fiber sensors for high-strain applications," Proc. SPIE 6167, Smart Structures and Materials, 616713-11 (2006).
- [6] C. A. F. Marques, L. Bilro, L. Kahn, R. A. Oliveira, D. J. Webb, R. N. Nogueira, "Acousto-Optic effect in microstructured polymer fiber Bragg gratings: simulation and experimental overview," IEEE/OSA J. Lightw. Technol. 31, 1551 (2013).
- [7] T. X. Wang, Y. H. Luo, G. D. Peng, Q. Zhang, "High-sensitivity stress sensor based on Bragg grating in BDK-doped photosensitive polymer optical fiber", Proc. 3rd Asia Pacific Optical Sensors Conference, 83510M (2012).
- [8] C. A. F. Marques, G. D. Peng, David J. Webb, "Highly sensitive liquid level monitoring system utilizing polymer fiber Bragg gratings," Opt. Express 23, 6058 (2015).
- [9] H. B. Liu, H. Y. Liu, G. D. Peng, P. L. Chu, "Strain and temperature sensor using a combination of polymer and silica fibre Bragg gratings," Opt. Commun. 219, 139 (2003).
- [10] X. S. Cheng, W. W. Qiu, W. X. Wu, Y. Luo, X. Tian, Q. Zhang, B. Zhu "High-sensitivity temperature sensor based on Bragg grating in BDK-doped photosensitive polymer optical fiber," Chinese Opt. Letters 9, 020602 (2011).
- [11] W. Zhang, D. J. Webb, G. D. Peng, "Investigation into time response of polymer fiber Bragg grating based humidity sensors," IEEE/OSA J. Lightw. Technol. 30, 1090 (2012).
- [12] X. Hu, D. Sáez-Rodríguez, C. A. F. Marques, O. Bang, D. J. Webb, P. Mégret, C. Caucheteur, "Polarization effects in polymer FBGs: study and use for transverse force sensing," Opt. Express 23, 4581 (2015).
- [13] C. A. F. Marques, L. Bilro, N. J. Alberto, D. J. Webb, R. N. Nogueira, "Narrow bandwidth Bragg gratings imprinted in polymer optical fibers for different spectral windows," Opt. Commun. 307, 57 (2013).
- [14] D. Sáez-Rodríguez, K. Nielsen, H. K. Rasmussen, O. Bang, D. J. Webb, "Highly photosensitive polymethyl methacrylate microstructured polymer optical fiber with doped core," Opt. Letters 38, 3769 (2013).
- [15] W. Yuan, L. Khan, D. J. Webb, K. Kalli, H. K. Rasmussen, A. Stefani, O. Bang, "Humidity insensitive TOPAS polymer fiber Bragg grating sensor," Opt. Express 19, 19731 (2011).
- [16] A. Lacraz, M. Polis, A. Theodosiou, C. Koutsides, K. Kalli, "Femtosecond laser inscribed Bragg gratings in low loss CYTOP polymer optical fibre" IEEE Phot. Techn. Letters 27, 693 (2015).
- [17] R. Oliveira, C. A. F. Marques, L. Bilro, R. N. Nogueira, "Production and characterization of Bragg gratings in polymer optical fibers for sensors and optical communications," Proc. 23rd International Conference on Optical Fibre Sensors – OFS 23, 915794 (2014).
- [18] R. Oliveira, L. Bilro, R. N. Nogueira, "Bragg gratings in a few mode microstructured polymer optical fiber in less than 30 seconds," Opt. Express 23, 10181 (2015).
- [19] Stefani, W. Yuan, C. Markos, O. Bang, "Narrow bandwidth 850-nm fiber Bragg gratings in few-mode polymer optical fibers IEEE Photonics Technology Letters 23, 660 (2011).
- [20] W. Yuan, A. Stefani, O. Bang, "Direct writing of fiber Bragg grating in microstructured polymer optical fiber", IEEE Photonics Technology Letters 24, 401 (2012).
- [21] I.-L. Bundalo, K. Nielsen, C. Markos, O. Bang, "Bragg grating writing in PMMA microstructured polymer optical fibers in less than 7 minutes," Opt. Express 22, 5270 (2014).



- [22] Y. Luo, B. Yan, M. Li, X. Zhang, W. Wu, Q. Zhang, G.D. Peng, "Analysis of multimode POF gratings in stress and strain sensing applications", *Opt. Fiber Technol.* 17, 201 (2011).
- [23] G. Barton, M. A. van Eijkelenborg, G. Henry, M.C.J. Large, J. Zagari, "Fabrication of microstructured polymer optical fibers," *Opt. Fiber Technol.* 10, 325 (2004).
- [24] H. Dobb, D. J. Webb, K. Kalli, A. Argyros, M. C. J. Large, M. A. van Eijkelenborg, "Continuous wave ultraviolet light-induced fiber Bragg gratings in few- and single-mode microstructured polymer optical fibers," *Opt. Lett.* 30, 3296 (2005).
- [25] D. Sáez-Rodríguez, K. Nielsen, O. Bang, D. J. Webb, "Photosensitivity mechanism of undoped poly(methyl methacrylate) under UV radiation at 325 nm and its spatial resolution limit," *Opt. Lett.* 39, 3421 (2014).
- [26] S. Acheroy, P. Merken, H. Ottevaere, T. Geernaert, H. Thienpont, C. A. F. Marques, D. J. Webb, G.-D. Peng, P. Mergo, and F. Berghmans, "Thermal effects on the photoelastic coefficient of polymer optical fibers," *Opt. Lett.* 41, 2517 (2016).
- [27] C. A. F. Marques, A. Pospori, D. Sáez-Rodríguez, K. Nielsen, O. Bang, D. J. Webb, "Fiber optic liquid level monitoring system using microstructured polymer fiber Bragg grating array sensors: performance analysis", *Proc. SPIE* 9634, 24th International Conference on Optical Fibre Sensors, 96345V (2015).

Fiber Mach-Zehnder Interferometer system using polymer optical Bragg grating for underwater applications

Carlos A. F. Marques^{1,2}, David J. Webb²

¹Instituto de Telecomunicações and Physics Department & I3N, Universidade de Aveiro, Campus de Santiago, 3810-193 Aveiro, Portugal

²Aston Institute of Photonic Technologies, Aston University, Aston Triangle, B4 7ET Birmingham, UK

*Corresponding author: cmarques@av.it.pt

Abstract: In the subsea environment, the monitoring of acoustic signals and vibration is crucial for different applications such as in geophysical surveying and security, e.g. the detection of unwanted craft or personnel. Current technology is predominantly based on piezoelectric (PZT) strain sensors but they suffer from some limitations. To solve these problems, fiber Bragg grating (FBG) sensors are considered as potential alternatives for conventional PZT hydrophones. In this paper, we present our recent experimental studies on FBG based acoustic sensing using polymer optical fiber (POF) in a comparison with the response of silica fiber. Fiber Mach-Zehnder interferometers (MZI) are widely used for FBG sensor interrogation purpose due to their advantages in terms of high resolution, wide bandwidth, and tunable sensitivity. They are appropriate for dynamic strain measurement applications in the areas of vibration analysis, hydrophones, and acoustic emission studies. The interferometer converts the Bragg wavelength shift of an FBG sensor into a corresponding phase shift in an electrical carrier, which can be demodulated using conventional techniques.

In this paper, an interferometric scheme for monitoring low-frequency (few kHz) waves using silica and polymer FBGs is investigated. A heterodyne technique based on an unbalanced interferometric wavelength discriminator is described and the performance of both types of fiber containing FBGs is compared. A considerable sensitivity improvement is achieved using polymer FBG (around 6 times better), and we could explain that considering the lower Young's modulus of POF. Essentially, and despite the strain sensitivity of silica and POFBGs being very similar, this renders the POF much more sensitive to the applied stress resulting from acoustic signals. Results give noise-limited pressure resolutions of 3.68×10^{-6} and 1.33×10^{-4} Pa for silica and POF, respectively, each within a 100 Hz bandwidth.

1. Introduction

Optical fibre based sensors are transforming industry by permitting monitoring in hitherto inaccessible environments or measurement approaches that cannot be reproduced using conventional electronic sensors. A multitude of techniques have been developed to render the fibres sensitive to a wide range of parameters including: temperature, strain, pressure (static and dynamic), acceleration, rotation, gas type, and specific biochemical species [1-3]. Constructed entirely of glass or polymer material [1-4], optical fibre devices like fibre gratings offer a number of attractive features: low loss (especially for silica fiber), dielectric construction, small size, multiplexing capability, and so on [1-3]. In recent years, fiber Bragg grating (FBG) sensors have generated great interests because of their versatile applications in in-situ strain, temperature and pressure monitoring, among others [1-9]. Besides the general advantages of fiber optic sensors, FBG sensors provide many additional attractive features over competing technologies and hence are enjoying widespread acceptance.

The monitoring of acoustic signals and vibration in the subsea environment is crucial for different applications such as in geophysical surveying and security (detection of unwanted craft or personnel). Current technology is predominantly based on piezoelectric strain sensors. They have satisfactory performance but suffer from other limitations: physical size; limited deployment range without local power and amplification (contributing further to physical size); lack of multiplexing capabilities. To solve these problems, there has been a steady move to introduce optical fibre based systems, firstly for surveillance [10] and for geophysical surveying [11]. The first such systems were interferometric in nature, involving coils of fibre wound on a compliant mandrel. Such systems still have the disadvantage of requiring a large diameter cable to contain the coil. Efforts have been made to use Bragg grating sensors along a single straight fibre, but for the most demanding applications standard Bragg gratings do not possess sufficient sensitivity and it has proven necessary to use fibre laser sensors [12], which although keeping the sensor diameter down, add to complexity and cost. Recently, optical hydrophones [13] offer a means of overcoming these difficulties. Previous fibre sensor research has focussed on silica fibres

and only now, with the increasing maturity of the polymer FBG technology have the first relevant but preliminary studies been carried out, looking at an accelerometer, assessing strain response up to a few kHz [14] and demonstrating a fibre grating based acoustic modulator [7]. Very recently, a fiber Mach-Zehnder interferometer (MZI) based silica FBG sensor was reported for underwater low-frequency sensing [15,16]. In this paper, an interferometric scheme for monitoring low-frequency (few kHz) waves using silica and polymer FBGs is investigated. A heterodyne technique based on an unbalanced interferometric wavelength discriminator is described and the performance of both types of fiber containing FBGs is compared. A considerable sensitivity improvement is achieved using polymer FBG (around 6 times better), which arises as a result of the much more compliant nature of POF compared to silica fiber (3 GPa vs 72 GPa, respectively). Essentially, and despite the strain sensitivity of silica and POFBGs being very similar, this renders the POF much more sensitive to the applied stress resulting from acoustic signals or vibration. Preliminary results give noise-limited pressure resolutions of 3.68×10^{-6} and 1.33×10^{-4} Pa for silica and polymer optical fiber (POF), respectively, each within a 1 Hz bandwidth.

2. Experiment

The arrangement used to interrogate the grating is shown in Fig. 1. This utilized a ramped lithium niobate phase modulator (accurately set to produce a 2π peak-to-peak phase excursion) to frequency shift the light in one arm of an unbalanced MZI and thus allowed the use of heterodyne signal processing [17,18]. Light from a broadband light source (provided by Thorlabs ASE-FL7002-C4), giving an output power of 20 mW centered at 1560 nm with a bandwidth of 80 nm, was launched into the unbalanced MZI; hence a channelled spectrum was created at the interferometer's outputs that was incident on the grating. Incorporated in one arm of the MZI was the phase modulator. The other arm contained a variable air gap that allowed the optical path difference (OPD) between the two arms to be adjusted. Provided that the OPD between the MZI's arms is longer than the source coherence length and shorter than the effective coherence length of the back-reflected light from the grating, interference signals are observed at the detector, which can be expressed as

$$I(\lambda_B) = A \left\{ 1 + V \cos \left[\omega_r t + \Phi + \delta\Phi \sin \omega t + \phi(t) \right] \right\}, \quad (1)$$

where λ_B is the wavelength of the reflected light from the modulated grating, ω_r is the angular frequency of the ramp modulation, ω is the angular strain frequency experienced by the grating, A is proportional to the grating reflectivity, V is the visibility of the signals, $\Phi = 2\pi OPD / \lambda_B$, where $OPD = n_{eff} \delta L$, and $\phi(t)$ is a random phase-drift term. A sinusoidal strain-induced change in λ_B from the FBG, ($\delta\lambda_B$), induces a change in phase shift in Eq. (1), given by

$$\delta\Phi \sin \omega t = (2\pi OPD / \lambda_B) (\delta\lambda_B) \sin \omega t \quad (2)$$

Hence from Eq. (1) strain-induced changes in λ_B induce a corresponding phase modulation of the electrical carrier produced at the detector by the phase modulator, which we measured by determining the amplitudes of the upper and lower sideband frequency components observed on an FFT spectrum analyser.

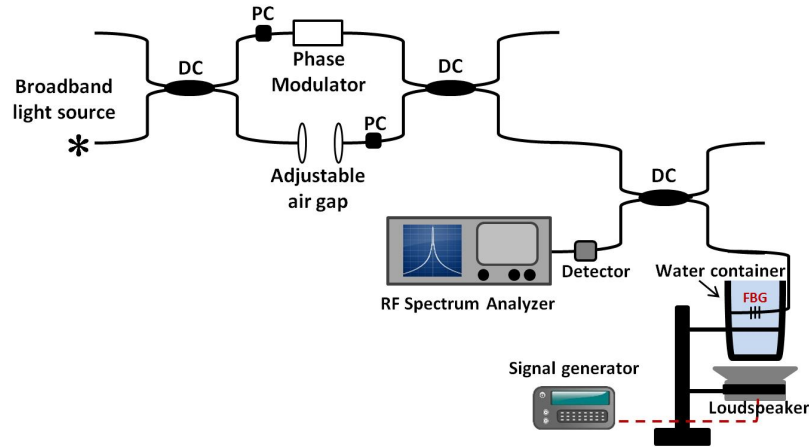


Figure 1. Experimental arrangement. DC: directional coupler, PC: polarization controller.

Two effects affect the sensitivity of the system. First, from Eq. (2), an increase in OPD results in a proportional increase in the amplitude of the phase modulation. Second, increasing the OPD beyond the coherence length of the light reflected by the FBG results in a reduction in the visibility and consequently the height of the carrier and sidebands. Therefore, the sensitivity was optimized by adjusting the OPD to achieve the maximum sideband amplitude. Initially, we calculated the OPD between the two arms of the designed MZI by recording the interference pattern on an OSA using the broadband source. Then, the length difference δL between the two arms of the MZI can be calculated by

$$\delta L = \frac{\lambda_B^2}{2\pi n_{eff} \delta \lambda_B} \delta \phi, \quad (3)$$

where $\delta \phi$ is the phase difference, and $\delta \phi = 2\pi$ for two adjacent peaks separated by the free spectral range.

3. Sensitivity and Results

When the fibre is compressed, the fractional change $\delta \lambda_B / \lambda_B$, induced in the Bragg wavelength λ_B , in response to a pressure change δP , is given by [19]

$$\frac{\delta \lambda_B}{\lambda_B} = \frac{\Delta(n_{eff} \Lambda)}{n_{eff} \Lambda} = \left[\frac{1}{\Lambda} \frac{\partial \Lambda}{\partial P} + \frac{1}{n_{eff}} \frac{\partial n_{eff}}{\partial P} \right] \delta P, \quad (4)$$

where Λ is the spatial period of the grating. The fractional change in physical length of the fiber and refractive index of the fiber core, respectively, are given by

$$\frac{\delta L}{L} = -\frac{(1-2\nu)P}{E} \quad (5)$$

$$\frac{\delta n_{eff}}{n_{eff}} = \frac{n_{eff}^2 P}{2E} (1-2\nu)(2p_{12} + p_{11}) \quad (6)$$

where E and ν are the Young modulus and Poisson ratio of the fiber, respectively, and p_{11} and p_{12} are the components of the strain-optic tensor. As the fractional change in the spatial period of the grating equals the fractional change in the physical length of the sensing section, the pressure sensitivity is then expected to be [19]

$$\frac{1}{\lambda_B} \frac{\delta \lambda_B}{\delta P} = -\frac{1}{E} \left((1-2\nu) - \frac{n_{eff}^2}{2} (1-2\nu)(2p_{12} + p_{11}) \right) \quad (7)$$

With reference to equation (7), the first part in the parenthesis relates to the change in the period of the fabricated grating planes within the fibre core, whereas the second part relates to the refractive index change as a result of the strain optic effect. However, equation (7) is relevant for an isotropic solid, which is acceptable for silica optical fibre; conversely POF is not an isotropic material and so equation (7) may lack validity for POF. During the drawing process of POF manufacture the molecular polymer chains tend to align along the fibre axis, and are therefore an example of a transverse isotropic material where the properties perpendicular to the fibre axis are not the same as the properties that are along the fibre axis.

Using the values presented in Table 1 for the parameters E , ν , n_{eff} , p_{11} and p_{12} for silica and polymer fibers, the predicted fractional wavelength shift is -2.8×10^{-6} /MPa using silica fiber and -1.8×10^{-6} /MPa using polymer fiber, an improvement around 1.5 times for homogenous PMMA fiber. In fact, from [20] the measured fractional changes were -2.5×10^{-6} /MPa (for silica fiber) and 83×10^{-6} /MPa (for POF), where these experimental results refer to some initial static pressure tests, and they showed that the wavelength shift with POF is opposite to that with silica (and much higher in magnitude). We could only explain that by allowing the fibre to be anisotropic as mentioned above.

From our experimental results and using the Bessel Function, the $V_{sideband}/V_{carrier}$ for POF and silica were 0.35 and 0.06, respectively, which means $V_{sideband}/V_{carrier} = J_1(phase)/J_0(phase)$ where $J_0(phase)$ is approximately 1 for small phase modulations [21,22]. So, after calculating the $J_1(phase)$ for both cases, we achieved $J_1(phase)$ 0.17 for POF case, and 0.025 for silica fiber. With this signal processing scheme, the phase modulation we measured is directly proportional to the wavelength modulation experienced by the FBG. In fact, the amplitude of the wavelength modulation is given by $\lambda_B^2 \Phi / 2\pi OPD$. So, the wavelength modulation for the POF is about 6 times greater than that for the silica. The significant difference between our results when compared with work in [20] can be explained by our fiber perhaps being less anisotropic; typically, the case if the fiber is drawn under lower stress.

Table 1: Material properties of PMMA and fused silica.

	PMMA	Fused silica
Parameter		
p_{11}	0.300	0.126
p_{12}	0.297	0.26
E (GPa)	2.95	72.45
n_{eff}	1.481	1.465
ν	0.37	0.165

The phase modulator was ramped, and hence generated a carrier signal, at 10 kHz. The silica and polymer FBGs had nominal Bragg wavelengths of 1550.21 nm and 1573.42 nm, with reflectivities of 90% and 80%, respectively, and both FBGs had a bandwidth around 0.5 nm. Hence, in this scheme, acoustically induced changes in the wavelength reflected from FBG induce a phase modulation of the electrical carrier produced by the phase modulator, which we measured by determining the amplitudes of the side bands observed on the spectrum analyser. As shown in Fig. 1, a standard 8 Ω loudspeaker was driven in continuous mode by a signal generator tuned at the frequency 420 Hz to excite the FBG in water (and in air for comparison). Acoustic signals coming from the loudspeaker excites vibrations in the container, where the FBG is attached, which in turn, induces strain in the FBG sensor.

Fig. 2 (a) shows the 10 kHz carrier signal and sidebands observed on the spectrum analyzer for 0.0625 and 25 W of acoustical power from the loudspeaker when the silica FBG is in air. Fig. 2 (b) shows the detected power of the sidebands (normalized with respect to the carrier signal power) as a function of the acoustical power. From Fig. 2 (b), the results demonstrate a highly linear response over the entire measurement region. The same analysis, but using the container with water, is shown in Figs. 3 (a) and (b). In this case, the difference between carrier amplitude and sidebands amplitude is reduced (25 dB) when compared with the case in air (29 dB). The signal-to-noise ratio measured by the spectrum analyser was 52 dB. Therefore, if the noise-limited resolution is

defined as the RMS pressure amplitude that would lead to a signal-to-noise ratio of unity, the resolution may be calculated to be 3.68×10^{-5} Pa within a 100 Hz bandwidth, corresponding to 3.68×10^{-6} Pa/Hz^{1/2}.

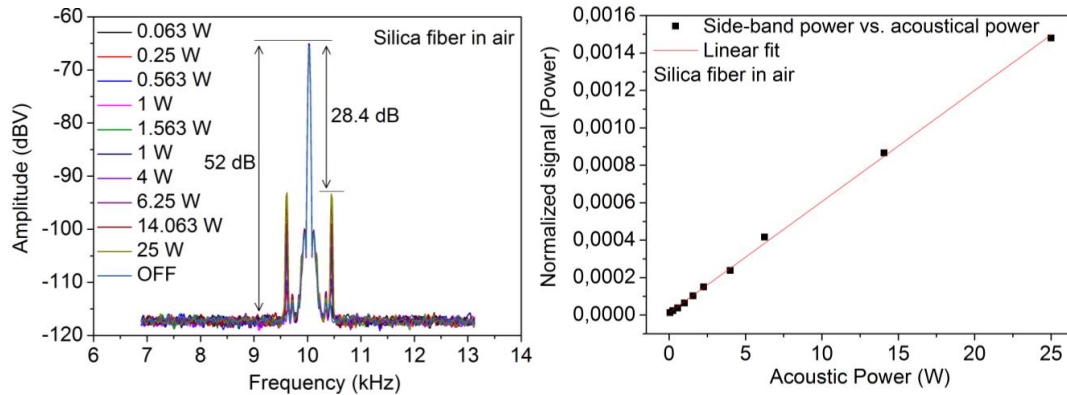


Fig. 2: (a) The carrier signal at 10 kHz and sidebands for different acoustical powers when the silica FBG sensor is in air. (b) The side-band power (normalized with respect to the carrier power) as a function of the acoustical power.

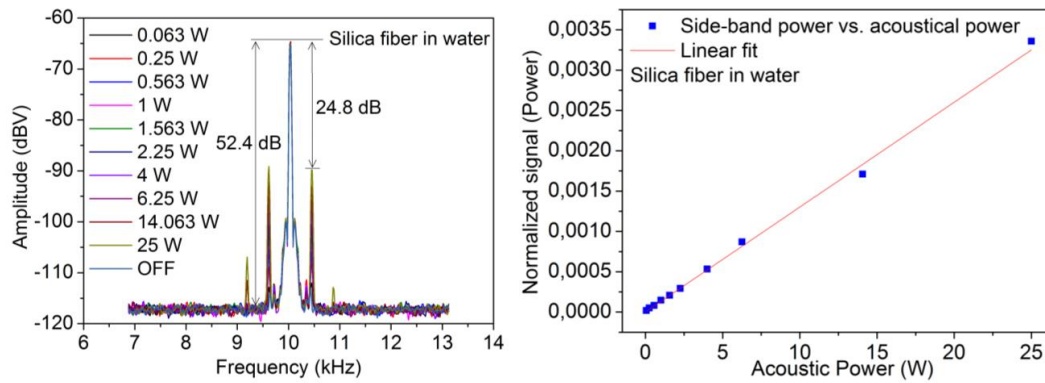


Fig. 3: (a) The carrier signal at 10 kHz and sidebands for different acoustical powers when the silica FBG sensor is in water. (b) The side-band power (normalized with respect to the carrier power) as a function of the acoustical power.

Tests were conducted when a POFBG is used instead of silica FBG. The previous conditions presented for silica FBG are kept to compare the performance. Fig. 4 shows the 10 kHz carrier signal and sidebands observed on the spectrum analyzer for no power from loudspeaker and for 25 W of acoustical when the POFBG is in air. In air, we can observe that the sidebands amplitude is weak at 25 W of acoustical power when compared with silica FBG sensor case. Fig. 5 (a) presents the carrier signal at 10 kHz and sidebands for acoustical power from 0.0625 to 25 W, when the container has the POFBG in water. Fig. 5 (b) illustrates the detected power of the sidebands (normalized with respect to the carrier signal power) as a function of the acoustical power. Here, the sidebands are strong compared with the air case, showing a high linear response. The difference between carrier and sidebands amplitude is reduced when compared with the case of a silica FBG sensor, achieving 9 dB of difference, almost 3 times less than the silica FBG sensor in water. The signal-to-noise ratio measured by the spectrum analyser was 17 dB. To determine the noise-limited resolution of the system, the same procedure was used as above and it was 1.33×10^{-4} Pa/Hz^{1/2}.

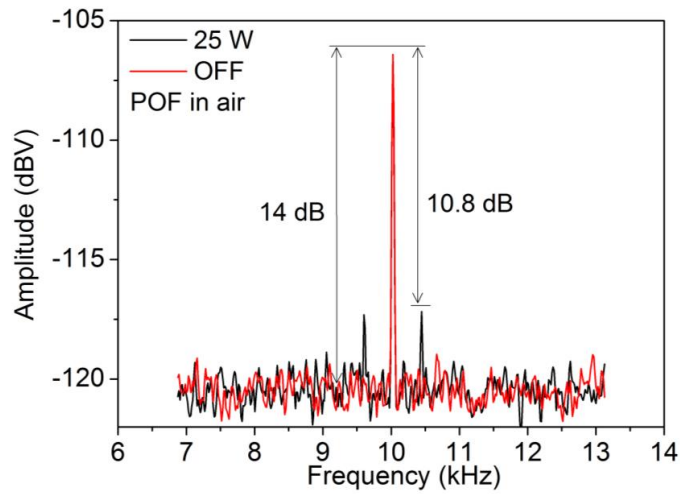


Fig. 4: The carrier signal at 10 kHz and side bands for acoustical powers at 0 W (OFF) and 25 W when the POFBG sensor is in air.

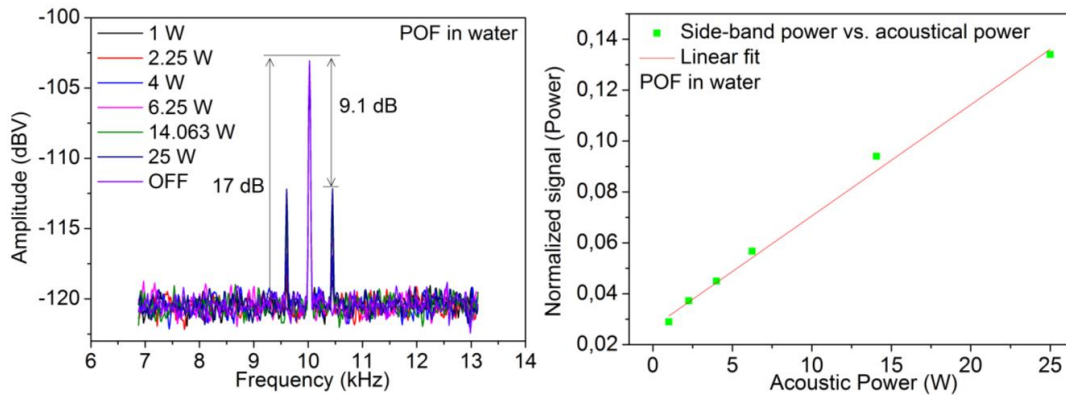


Fig. 5: (a) The carrier signal at 10 kHz and side bands for different acoustical powers when the POFBG sensor is in water. (b) The side-band power (normalized with respect to the carrier power) as a function of the acoustical power.

4. Conclusions

In conclusion, we have presented our recent experimental results towards the development of a polymer FBG based sensor for underwater acoustic sensing. A FBG based sensor head and a fiber MZI interferometer has been fabricated for this purpose for monitoring low-frequency (few kHz) waves. A heterodyne technique based on an unbalanced interferometric wavelength discriminator is described and the performance of both types of fiber containing FBGs is compared. A considerable sensitivity improvement is achieved using polymer FBG (around 6 times better), which arises as a result of the much more compliant nature of POF compared to silica fiber. These results give us noise-limited pressure resolutions of 3.68×10^{-6} and 1.33×10^{-4} Pa for silica and POF, respectively.

5. Acknowledgments

This work was supported by Marie Curie Intra European Fellowship included in the 7th Framework Program of the European Union (project PIEF-GA-2013-628604). Also, C. Marques is grateful for the FCT Fellowship SFRH/BPD/109458/2015.

6. References

- [1] T. G. Giallorenzi, J. Bucaro, A. Dandridge, G. Sigel, J. Cole, S. Rashleigh, R. Priest, "Optical fiber sensor technology," *IEEE Trans. Microw. Theory Techn.* 30, 472 (1982).
- [2] S. Yin, P. B. Ruffin, F. T. S. Yu, *Fiber Optic Sensors*, 2nd ed. Boca Raton, FL, USA: CRC Press, 2008.
- [3] A. Othonos, K. Kalli, *Fiber Bragg Gratings: Fundamentals and Applications in Telecommunications and Sensing*. Norwood, MA, USA: Artech House, (1999).
- [4] D. J. Webb, "Fiber Bragg grating sensors in polymer optical fibers," *Meas. Sci. Technol.* 26, 092004 (2015).
- [5] H. B. Liu, H. Y. Liu, G. D. Peng, P. L. Chu, "Strain and temperature sensor using a combination of polymer and silica fibre Bragg gratings," *Opt. Commun.* 219, 139 (2003).
- [6] K. Peters, "Polymer optical fiber sensors - A review," *Smart Mater. Struct.* 20, 013002 (2011).
- [7] C. A. F. Marques, L. Bilro, L. Kahn, R. A. Oliveira, D. J. Webb, R. N. Nogueira, "Acousto-Optic effect in microstructured polymer fiber Bragg gratings: simulation and experimental overview", *IEEE/OSA J. Lightw. Technol.* 31, 1551 (2013).
- [8] C. A. F. Marques, G. D. Peng, D. J. Webb, "Highly sensitive liquid level monitoring system utilizing polymer fiber Bragg gratings," *Opt. Express* 23, 6058 (2015).
- [9] N. J. Alberto, C. A. F. Marques, J. L. Pinto, R. N. Nogueira, "Three-parameter optical fiber sensor based on a tilted fiber Bragg grating," *Appl. Opt.* 49, 6085 (2010).
- [10] G. A. Cranch, R. Crickmore, C. K. Kirkendall, A. Bautista, K. Daley, S. Motley, J. Salzano, J. Latchem, P. J. Nash, "Acoustic performance of a large-aperture, seabed, fiber-optic hydrophone array", *Journal of the Acoustical Society of America* 115, 2848 (2004).
- [11] P. J. Nash, G. A. Cranch, D. J. Hill, "Large scale multiplexed fibre-optic arrays for geophysical applications", *Proceedings of the Society of Photo-Optical Instrumentation Engineers (SPIE)* 42022000, 55 (2000).
- [12] G. A. Cranch, G. A. Miller, C. K. Kirkendall, "Fiber laser sensors: Enabling the next generation of miniaturized, wideband marine sensors", *Proceedings of Fiber Optic Sensors and Applications VIII (SPIE)* 8028 (2011).
- [13] M. Moccia, M. Consales, A. Iadicicco, M. Pisco, A. Cutolo, V. Galdi, A. Cusano, "Resonant Hydrophones Based on Coated Fiber Bragg Gratings," *IEEE/OSA J. Lightwave Technol.* 30, 2472 (2012).
- [14] A. Stefani, S. Andresen, W. Yuan, O. Bang, "Dynamic Characterization of Polymer Optical Fibers", *IEEE J. Sensors* 12, 3047 (2012).
- [15] B. Das, A. P. Narayan, U. Tiwari, "Fiber Bragg Grating based Acoustic Sensing with Interferometric Interrogation," in 12th International Conference on Fiber Optics and Photonics, M4A.17 (2014).
- [16] V. Chandra, U. Tiwari, B. Das, "Elimination of Light Intensity Noise Using Dual-Channel Scheme for Fiber MZI-Based FBG Sensor Interrogation," *IEEE Sensors Journal* 16, 2431 (2016).
- [17] D. A. Jackson, A. D. Kersey, M. Corke, J. D. C. Jones, "Pseudo-heterodyne detection scheme for optical interferometer", *Electron. Lett.* 18, 1081 (1982).
- [18] N. E. Fisher, D. J. Webb, C. N. Pannell, D. A. Jackson, L. R. Gavrilov, J. W. Hand, L. Zhang, I. Bennion, "Ultrasonic hydrophone based on short in-fiber Bragg gratings," *Appl. Opt.* 37, 8120 (1998).
- [19] M. G. Xu, L. Reekie, Y. T. Chow, J. P. Dakin, "Optical in-fibre grating high pressure sensor," *Electronics Letters* 29, 398 (1993).
- [20] Ian P. Johnson, David J. Webb, Kyriacos Kalli, "Hydrostatic pressure sensing using a polymer optical fibre Bragg gratings", *Proc. of SPIE Vol. 8351 - 3rd Asia Pacific Optical Sensors Conference*, 835106 (2012).
- [21] https://www.st-andrews.ac.uk/~www_pa/Scots_Guide/RadCom/part12/page1.html
- [22] http://uspas.fnal.gov/materials/08UCSC/mml16_modulation_and_detection.pdf



Improving Temperature Sensing of Polymer Fibre Bragg Grating Sensors with PDMS coating

Gökhan Demirci^{1*}, Amédée Lacraz², Kyriacos Kalli², Barbara Gawdzik¹

¹ Department of Polymer Chemistry, Maria Curie-Skłodowska University

² Nanophotonics Group, Cyprus University of Technology

*Corresponding author: luapy2004@gmail.com

In the past, fibre Bragg grating (FBG) sensors have been studied for sensing physical parameters such as temperature, strain, bending, and pressure [1] with optical methods. In the case of temperature sensitivity, bare FBG sensors are not quite responsive due to the low thermal expansion coefficient of the fiber material.

Some polymers were used such as polyimide or polyacrylate for improving the temperature sensing abilities [2]. However, there is need to find new polymers which have higher thermal expansion coefficient and suitable for coating.

In this study, we propose a poly-dimethylsiloxane (PDMS)- coated FBG temperature sensor, where the PDMS is used for enhancing temperature sensitivity as shown in Fig. 1. The thermal expansion coefficient of the PDMS is much higher than those of materials previously used for FBG sensors or coated-FBG sensors as shown in Table 1. Thus, the temperature sensitivity can be effectively enhanced by the tensile force induced by the thermally expanded PDMS. Because PDMS is a chemically stable elastomeric polymer and we can make the PDMS jacket or flat layer on the FBG very easily due to its good adhesion on the polymer surface by using a simple moulding process, this material can be a good candidate for temperature polymer optical fibre sensor.

TABLE 1. The thermal expansion coefficients of materials used for enhancing temperature sensitivity of optical FBG sensors.

Materials	Thermal expansion coefficient (m/m ⁰ C)
PMMA (polymethyl methacrylate)	70-77 x 10 ⁻⁶
PS (Polystyrene)	70 x 10 ⁻⁶
PI (Polyimide)	30-60 x 10 ⁻⁶
PC (Polycarbonate)	70.2 x 10 ⁻⁶
CYTOP (Cyclic transparent optical polymer)	74 x 10 ⁻⁶
PDMS (poly-dimethylsiloxane)	300 x 10 ⁻⁶

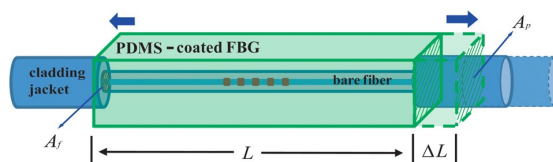


Figure 1. The schematic illustration of the PDMS-coated FBG sensor designed for enhancing temperature sensitivity by using thermal expansion effect of the PDMS jacket. [3]

References:

- 1) A. Othonos and K. Kalli, *Fiber Bragg Gratings Fundamentals and Applications in Telecommunications and Sensing* (Artech House, Boston, USA, 1999).
- 2) Ping Lu, Liqiu Men, and Qiying Chen, *Polymer-Coated Fiber Bragg Grating Sensors for Simultaneous Monitoring of Soluble Analytes and Temperature*, *Ieee Sensors Journal*, (2009)9:4, 340-345
- 3) Chang-sub Park, Kyung-Il Joo, Shin-Won Kang and Hak-Rin Kim, *A PDMS-Coated Optical Fiber Bragg Grating Sensor for Enhancing Temperature Sensitivity*, *Journal of the Optical Society of Korea*, (2010)15:4, 329-334

Key Words: Fiber Bragg Grating, Fiber Coating, Temperature Sensing, Polymer Optical Fiber, Polymer-coated FBG sensors

Preferred presentation method: [Oral]

Multiband 4G and Gigabit/s Baseband Transmission over Large-Core GI and SI POFs for In-Home Networks

F. Forni^{1,2*}, Y. Shi², H.P.A. van den Boom¹, E. Tangdiongga¹, A.M.J. Koonen¹

¹ Institute for Photonic Integration, Eindhoven University of Technology, P.O. Box 513, 5600MB Eindhoven, The Netherlands.

² Genexis, Lodewijkstraat 1A, 5652AC Eindhoven, The Netherlands.

*Corresponding author: f.forni@tue.nl

Abstract: We demonstrated the simultaneous transmission of a multiband 4G (i.e. LTE-A) and gigabit/s baseband signals over 35m of 1mm core diameter PMMA GI and SI POFs. The transceiver consists of a Fabry-Perot 650nm laser diode and p-i-n photodiode. The LTE-A was transmitted with Analog-RoF technique, using a simple equalisation method. 12 LTE-A bands and a 1.9Gb/s 4-PAM baseband signal were co-transmitted over the GI-POF. 7 LTE-A bands and a 1.7Gb/s 4-PAM signal were co-transmitted over the SI-POF. The equalisation technique showed to be an effective method to increase the link throughput, hence enabling POF to be an excellent candidate for an in-home network infrastructure.

1. Introduction

Already in 2014, 70% of the mobile data traffic has been generated indoor (e.g. in in-home networks) and is expected to grow further in the next years [1]. Improvements of the indoor capacity of the current 4G (i.e. LTE-A, Long Term Evolution-Advanced) and future 5G mobile networks are feasible by the femtocell architecture and multiband carrier aggregation [2]. The femtocell approach requires that each antenna is connected to the fronthaul by the residential gateway. Different wired and wireless solutions have been proposed but none of them are completely satisfactory. Plastic optical fibers (POFs) with their do-it-yourself installation capability are an attractive medium to transport 4G/5G signals. Furthermore, a cost-effective in-home wired backbone can be achieved if it is shared among the wireless and wired signals, as shown in Fig. 1. Therefore, a multi-standard, multiband in-home network over POF is highly desired.

Our previous work has shown that 8 LTE-A bands between 465 and 960MHz (aggregated bitrate of 480Mb/s) can be transmitted over up to 50m of graded index (GI) POF [3]. This was realized by a simple equalisation technique using a set of digital amplifiers, each of them amplifying a single LTE-A band and therefore flattening the power spectrum of the combined multiband LTE-A signal. Simultaneously, a 4-level pulse amplitude modulation (4-PAM) baseband signal was transmitted with a minimum spectrum separation from the LTE bands.

In this work, firstly, we further exploit the equalisation for the GI-POF link by adding the LTE-A bands between 1.5 and 2 GHz, exceeding the optical link's -3dB bandwidth. The equalisation technique is optimised to balance also the extra optical link losses incurred by the new bands. Secondly, we applied the equalisation method to a LTE-A multiband transmission over step index (SI) POF based link. Here, the system bandwidth is limited by the SI-POF and the frequency response is sharper than in the GI-POF link. In this case, the same equalisation makes feasible the transmission of a multiband LTE-A 64-QAM and a gigabit/s 4-PAM baseband signal over 35m of standard PMMA SI-POF, which can be considered as reference distance for most of the in-home networks (i.e. single-detached dwellings and apartments).

2. Experimental Setup

The general setup is shown in Fig. 2 and the differences between the SI and GI POF links are highlighted during the analysis. We intended to maximize the LTE-A throughput by choosing the highest standard-compliant modulation order, which is 64-QAM. Furthermore, the largest number of bands is transmitted

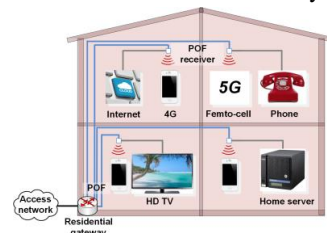


Fig. 1 POF network for multistandard wired and wireless fibre in the home applications

with the Analog-RoF technique. Fig. 3(a) shows the GI and SI POF link frequency response, with a -3dB bandwidth of 1.1GHz and 365MHz, respectively. The equalisation technique already implemented to flatten the in-band LTE-A band power spectrum [3] is here further exploited to increase the transmitted power of the LTE-A bands exceeding the link bandwidth. The equalisation is carried out by digital signal processing through the tailored amplification of band B_i by gain G_i . The gain G_i is chosen in order to have the same received power spectrum. The equalisation balances the low-pass frequency response of the link, which typically does not change over time once installed, hence the G_i tuning is performed only once. Following these choices, 12 LTE-A bands are transmitted over the GI-POF link, as listed in Table 1. Regarding the SI-POF link, the subset of 7 LTE-A bands (B_1, \dots, B_7) is chosen. The LTE-A bands are generated offline in accordance with [4] and equalised. Therefore, the LTE-A signals are combined in the digital domain and then sent to an arbitrary waveform generator (AWG-T122B) working as a digital-to-analogue converter.

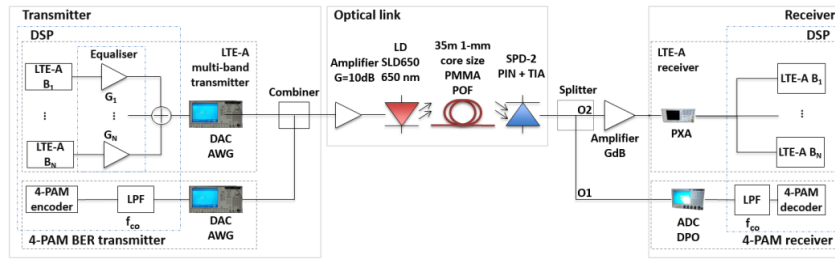


Fig. 2 Block diagram of the transmission setup with $N=7$ for SI-POF link and $N=12$ for the GI-POF link.

Table 1. LTE bands used in the experiments and their most significant parameters.

Parameter	Value											
Band index B_i	1	2	3	4	5	6	7	8	9	10	11	12
Carrier frequency f_{c_i} (MHz)	738	751	763	806	868	883	944	1474	1542	1843	1862	1963
E-UTRA operating band	12	13	14	20	18	19	8	32	24	3	9	25
Bandwidth (MHz)	10		20		15		10		20		10	
Modulation format	64-QAM											
Gain of the digital transmitter amplifier G_i (dB)	0		3		4		2		6		5	

According to the LTE-A bands allocation, the frequency range up to band B_1 (i.e. 733MHz) is unused. In this interval a PRBS 2^7-1 data sequence is offline encoded by 4-PAM modulation and further processed. The symbol sequence is filtered by a digital low pass filter (LPF) with a cut-off frequency (f_{co}) of 700MHz. Subsequently, the baseband signal is generated by a second arbitrary waveform generator (AWG-T122B). The two signals are combined by an electrical power combiner and amplified by a MMIC 10dB amplifier integrated in the laser driver. The resulting signal drives a low-cost Fabry-Perot edge-emitting laser diode (LD). The optical link is an intensity-modulated direct-detection (IM-DD) system. The emitted optical output power of the LD is 5.7dBm at a wavelength of $\lambda=650$ nm and is coupled into the GI and SI POFs by using a ball lens mounted on the LD case. The POFs used are 35m long with 1mm core diameter PMMA Optimedia GI-POF and ESKA GH-4001 standard SI-POF, with fibre loss at 650nm of 0.2dB/m and 0.17dB/m at $\lambda=650$ nm, respectively. The optical receiver is a Graviton SPD-2 module with a FC connector, consisting of a p-i-n photodiode followed by a transimpedance amplifier. The bare fibre is plugged into the Graviton FC connector without any connector. The SPD-2 maximum allowed input power is -4dBm, hence the received optical power is limited to -5.9dBm. As shown in Fig. 2, the electrical output of the optical receiver is fed into an amplifier with a gain G . G is optimized on both links and is equal to 29dB and 26dB for the SI and GI POF links, respectively. The

signal is then acquired by either the baseband 4-PAM or the LTE-A receiver. The baseband receiver is composed by an analogue-to-digital converter (DPO-72304DX), a digital LPF with cut-off frequency f_{co} , and the 4-PAM receiver. Both the LPF and the 4-PAM receiver are implemented offline by MATLAB. For simplicity, no equalisation or precoding is used. The LTE-A bands are received and processed by a vector signal analyser (PXA-N9030A) running the LTE-A analyser software by Keysight.

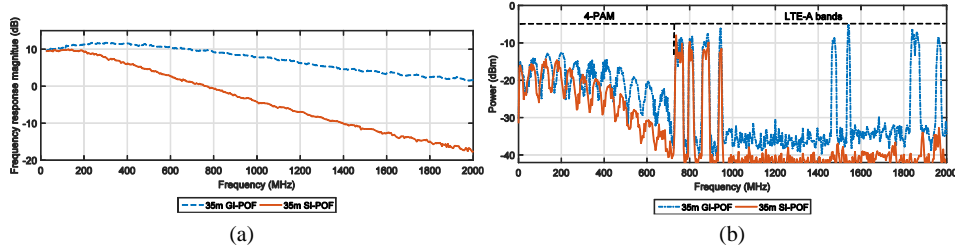


Fig. 3 GI and SI POF frequency responses (a), simultaneous transmission spectra at the LTE-A receiver input after the GI-POF (dashed blue line) and SI-POF (solid orange line).

3. Experimental Results and Discussion

The 4-PAM signal is required to have a pre-FEC bit error rate (BER) lower than 1×10^{-3} . The LTE-A performance is evaluated in accordance with [5], which sets the error vector magnitude (EVM) threshold at 8%. As a reference, the individual transmission of the 4-PAM and LTE-A signals is evaluated for both the links.

Firstly, the received spectrum is analysed. As shown in Fig. 3(b), over the GI-POF the 4-PAM signal is limited by the transmitter LPF, while over the SI-POF it is distorted due to the lower POF bandwidth. Looking to the LTE-A, in both the cases all the bands have similar power, on account of the equalisation, which balances the higher losses for the higher frequencies.

Let us consider the GI-POF link first. The 4-PAM maximum bitrate is 1.9Gb/s and 2Gb/s with and without LTE-A co-transmission, respectively. Therefore, the difference is minimal, which suggests the LTE-A crosstalk is negligibly affecting the 4-PAM throughput. Next, the solitary LTE-A is considered, as shown in Fig. 4(a). Over the electrical back-to-back (eB2B) link the EVM is lower than 3%, the higher frequency bands have a better performance because the equalisation is enabled. Moving to the 35m link, the maximum EVM is 5% (B_{12}). Moreover, the bands from B_8 to B_{12} have slightly higher EVM increment, up to 2% (B_{12}), than the first 7 bands. This higher increase is related with the low-pass behaviour of the link, which is not fully balanced by the equalisation. When the 4-PAM signal is co-transmitted, the EVM increases up to 6.5% (B_{12}). Furthermore, the EVM performance slightly depends on the band, the first 9 LTE-A signals have a smaller EVM increase than the last 3. B_9 has lower EVM than the neighbour bands due to the higher received power, although this is not linked with the equalisation tap G_9 or the link frequency response. The lower EVM of B_9 can be related with the narrower band (i.e. 10MHz) than the adjacent 20MHz bands, which therefore sets higher transmitted power as defined by the standard. Nevertheless, the EVM growth related with the 4-PAM transmission is relatively small. Summarily, all the 12 LTE-A bands have the EVM value smaller than the threshold.

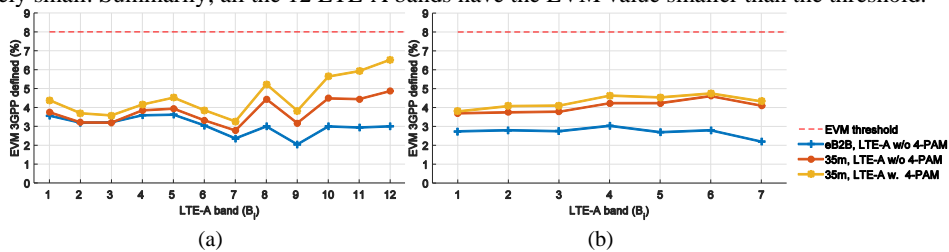


Fig. 4 LTE-A EVM results for the GI-POF (a) and SI-POF (b) link for the eB2B and 35m, with and without 4-PAM transmission, the bands B_i are according to Table 1.

Next, the SI-POF link performance is analysed. The 4-PAM bitrate is equal to 1.7 Gb/s with and without the LTE-A co-transmission. Also in this case the baseband throughput is bandwidth-limited.

However, here it is the POF link which limits the bandwidth and introduces the distortion. Considering the LTE-A transmission, as shown in Fig. 4(b), the EVM over the eB2B is lower than 3%, as the previous eB2B test, the EVM is lower for the highest bands due to the enabled equalisation. Moving to the 35m link, the maximum EVM is 4.6% (B_6), here the increase is mainly caused by two factors. Firstly, for the lower frequency bands, the noise added by the optical link degrades the performance. Secondly, for the high frequency signals, together with the added noise, the equalisation only partially balances the low-pass behaviour of the link in comparison to the GI-POF. When the 4-PAM signal is co-transmitted, the LTE-A EVM slightly increases up to 4.8% (B_6) and, for all the bands, grows less than 1% as compared to the solitary transmission. In summary, all the 7 LTE-A bands have an EVM lower than the threshold.

Both the setups used the frequency division multiplexing of the baseband and radio signals in order to perform the multi-standard transmission over a single POF. At the same time the analogue and digital signal processing is kept as simple as possible using only Analog -RoF technique and FIR filtering. This made possible to achieve LTE-A bands up to 2GHz, covering most of the frequency range used by LTE-A standard.

The simultaneous transmission over the SI-POF showed lower interference of the 4-PAM signal over the LTE-A than over the GI-POF link, which can be related with the lower 4-PAM bitrate over the SI-POF link. Improvement of the LTE-A performance over the GI-POF link can be achieved by a finer tuning of the equalisation taps, in particular for the higher frequency bands, by iterative optimization based on the received signal-to-noise ratio.

Longer link length up to 50m can be achieved for both GI and SI POF links by means of higher link budget and more powerful equalisation. In particular, the GI-POF link length extension is feasible by just increasing the link budget. Longer link length would not severely affect the link bandwidth, which is limited by the transceivers. For the SI-POF, longer link lengths will further decrease the link bandwidth, already smaller than the transceiver bandwidth. Therefore, transmission using SI-POF needs in general more powerful equalisation techniques to extend the link bandwidth a bit further.

4. Conclusion

In this paper we provided experimental results of the co-transmission of a multiband LTE-A standard-compliant signal with a 4-PAM baseband signal over 35m of 1mm core diameter GI-POF and SI-POF links. 12 LTE-A band signals (total throughput 910Mb/s) and a 1.9Gb/s 4-PAM signal are jointly transmitted over the GI-POF link and 7 LTE-A bands (total throughput 450Mb/s) and 1.7Gb/s are successfully transmitted over the SI-POF link. This study showed that the multiband and multi-standard transmission can be achieved over such a bandwidth- and power-limited POF link. Hence, a simple IM-DD system has been shown experimentally which employs low-cost optical and electrical components, low-complexity signal processing, and amplifier gain optimization of the equalizer.

We believe this work has demonstrated the feasibility of using large-core GI and SI POFs as the communication backbone for both wired and LTE-A-based future 5G wireless technologies for in-home networks.

Acknowledgements

This research is conducted in the MEMPHIS (Merging Electronics and Micro and nano-Photonics in Integrated Systems) project A2, Flexible Broadband Communication (FlexCom), supported by the Dutch Technology Foundation STW through the grant no. 13530.

References

- [1] W. Group, "Heterogeneous Networks," *Wirel. Commun. Signal Process.*, September, 2015.
- [2] N. Bhushan, et al., "Network densification: The dominant theme for wireless evolution into 5G," *IEEE Commun. Mag.*, vol. 52, no. 2, pp. 82–89, 2014.
- [3] F. Forni, et al., "LTE-A compliant multi-band radio and gigabit / s baseband transmission over 50m of 1mm core diameter GI-POF for in-home networks," *Electron. Lett.*, vol. 52, no. 9, pp. 738–740, 2016.
- [4] 3-GPP, "LTE - Evolved Universal Terrestrial Radio Access (E-UTRA) Base Station (BS) conformance testing 136.141," 2012.
- [5] 3-GPP, "LTE Evolved Universal Terrestrial Radio Access (E-UTRA); Base Station (BS) radio transmission and reception (3GPP TS 36.104 version 9.13.0 Release 9)," 2011.



Dynamic Nonlinearities in Directly Modulated Light-Emitting Diodes

M. Schüppert^{1*} and C.-A. Bunge¹

¹ Hochschule für Telekommunikation Leipzig, Gustav-Freytag-Str. 43-45, D-04277 Leipzig, Germany

*Corresponding author: schueppert@hft-leipzig.de

Abstract: We present a detailed analysis of nonlinear signal impairments in the electro-optical (E/O) conversion of commercially available LEDs which are specifically designed for POF communication. Nonlinearities are assessed by measuring the generation of 2nd-order intermodulation products in the LED for different modulation frequencies, modulation indices, and bias points. It is shown that the nonlinear modulation behavior of the LEDs is strongly dependent on both modulation frequency and bias. The results further allow a derivation of a general system-theoretic model of the underlying physical processes, as well as conclusions on suitable equalization strategies.

Key words: Light-emitting diodes, communication, modulation, nonlinearities, Volterra series

1. Introduction

Light-emitting diodes (LEDs) are an attractive low-cost alternative to lasers for the use as directly modulated optical transmitters. LEDs offer several advantages over lasers, such as cost effectiveness, better reliability, or lower temperature sensitivity [1]. Further, due to their non-collimated radiation characteristics, eye-safety requirements are inherently easier met with LEDs.

To maximize possible transmission lengths and the LED's power efficiency, LEDs are typically driven with a large-signal modulation. Further, the principle of intensity modulation, employed in LEDs, requires the LED driving current to be always positive. That is, the electrical current $i_{\text{LED}}(t)$ modulating the LED contains a modulation current, $A \cdot i_{\text{mod}}(t)$, carrying the information and a positive bias, i_{bias} , which carries no information; i.e. $i_{\text{LED}}(t) = A \cdot i_{\text{mod}}(t) + i_{\text{bias}}$, with a modulation amplitude A ; for large-signal modulation $A \approx i_{\text{bias}}$. As a result, the LED driving current exhibits a large swing, ranging from low current densities $i_{\text{min}} \approx 0\text{mA}$ up to large current densities of $i_{\text{max}} \approx 2 \cdot i_{\text{bias}}$. Under such driving conditions LEDs are known to introduce nonlinear signal impairments in the electro-optical (E/O) conversion [2] which might severely degrade the performance of the transmission system. In [3] we investigated such nonlinearities occurring in resonant-cavity LEDs (RC-LEDs), showing that under large-signal modulation low modulation frequencies induce the strongest nonlinearities. It was also shown in [3] that the power budget of a typical POF-based short-range transmission system using a RC-LED can be significantly increased by proper equalization of these transmitter nonlinearities. The physical origins of these nonlinearities, however, are not well understood yet. In this contribution we therefore extend the investigations of the aforementioned papers by incorporating the impact of the bias point and the LED's linear frequency response.

2. The Volterra Series Representation of a Dynamic Nonlinear System

A general mathematical description of a dynamic nonlinear system with an input signal $x(t)$ and an output signal $y(t)$ is given by the Volterra series according to [4]

$$\begin{aligned}
 y(t) = & h^{(0)} + \int_{\mathbb{R}} h^{(1)}(\tau_1) x(t - \tau_1) d\tau_1 + \iint_{\mathbb{R}^2} h^{(2)}(\tau_1, \tau_2) x(t - \tau_1) x(t - \tau_2) d\tau_1 d\tau_2 \dots \\
 & + \iiint_{\mathbb{R}^3} h^{(3)}(\tau_1, \tau_2, \tau_3) x(t - \tau_1) x(t - \tau_2) x(t - \tau_3) d\tau_1 d\tau_2 d\tau_3 + \dots
 \end{aligned}
 \tag{1}$$

Where $h^{(n)}$ are the so-called Volterra kernels of order n ; $h^{(0)}$ is a constant and $h^{(1)}(\tau_1)$ is the small-signal impulse response of the system. The Fourier transform of $h^{(1)}(\tau_1)$ is the small-signal frequency response $H(\pm f)$ of the dynamic nonlinear system. Likewise, a frequency response $H_2(\pm f_1, \pm f_2)$ of the 2nd-order intermodulation products (IM2) at $f_{\text{IM}} = \pm f_1 \pm f_2$ of input frequencies f_1 and f_2 may be determined by calculation of the 2D



Fourier transform of $h^{(2)}(\tau_1, \tau_2)$ [2]. $H_2(\pm f_1, \pm f_2)$ is denoted the 2nd-order Volterra kernel transform which then represents a frequency response of the nonlinearities.

In the subsequent investigations we measure the magnitude response $|H_2(\pm f_1, \pm f_2)|$ at the optical output of different commercially available LEDs, which are designed for high-speed POF communication, to characterize their frequency dependent nonlinearities. We investigate $|H_2(\pm f_1, \pm f_2)|$ for different driving conditions to get a closer insight into the underlying physical characteristics. According to the description of $H_2(\pm f_1, \pm f_2)$ above, the measurement results are therefore directly connected to the mathematical theory of the Volterra series of Eq. (1).

3. Measuring the LED's 2nd-order Volterra Kernel Transform

The experimental setup for the measurements of $|H_2(\pm f_1, \pm f_2)|$ is shown in Figure 1(left). A two-tone signal $u(t) = A_1 \cdot \cos(2\pi f_1 t) + A_2 \cdot \cos(2\pi f_2 t)$ is generated in Matlab and loaded to an arbitrary waveform generator (AWG7122C). The AWG drives the LED under test with a simple driver (using a Bias-T Picosecond 5542, an RF amplifier ZHL-6A, and about 100Ω in series with the LED). Flatness of the driver's transfer function is achieved by a precompensation, which adapts A_1 and A_2 to give equal amplitudes at the LED input.

The nonlinearities in the LED's optical output signal are measured after opto-electrical back conversion. For that, the LED's optical output is coupled to an optical receiver (Rx; Graviton SPA-2) through a free space optical (FSO) link. To avoid saturation of the Rx, optical attenuation with a neutral filter is applied in the FSO link. The received signal is captured with a digital sampling oscilloscope (DSO, WaveRunner 640 Zi). The intermodulation products are evaluated in the frequency domain using digital signal processing in Matlab.

Previous works on this topic basically showed that different types of LEDs exhibit very different characteristics in the frequency dependence of 2nd-order nonlinearities [2]. This implied that for the different LED types different physical processes are dominant leading to the observed nonlinearities. And that, in turn, suggests that a unified and generalized modelling of dynamic nonlinearities in the E/O conversion of directly modulated LEDs is not easy. Based on these results, we follow the empirical approach of [2] in this contribution, but with a restriction to one particular LED type, namely resonant cavity LEDs (RC-LEDs), in order to be able to identify similarities between different models of the same LED type. That is, if similarities in $H_2(\pm f_1, \pm f_2)$ are found, common physical phenomena are likely to be present, and hence a very first generalized modelling may be applied.

In the following we investigate two commercially available RC-LEDs, emitting at 650nm; model FB00AKAR by FireComms Ltd. and model L10881 by Hamamatsu Photonics. RC-LEDs are particularly interesting for high-speed POF communication, as they offer advantages over regular LEDs such as a more directed far-field pattern and a higher spectral purity [1]. The small-signal frequency response of the investigated RC-LEDs is shown in Figure 1 (right). A -3dB cut off frequency of about 90MHz (FB00AKAR) and 80MHz (L10881) is observed. We investigate $|H_2(\pm f_1, \pm f_2)|$ for large-signal modulation, as this is demanded in communication.

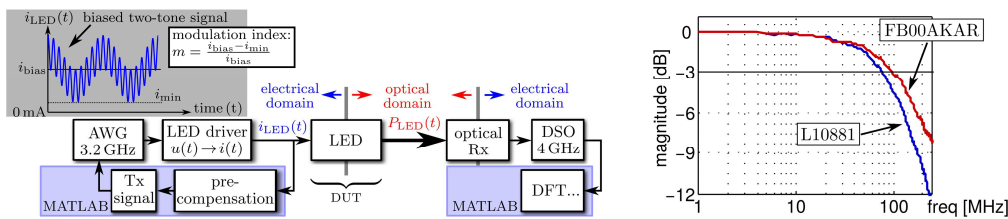


Figure 1: Experimental setup (left) and frequency responses $H(f)$ of the investigated RC-LEDs (right).

4. Results and Discussion

4.1 IM2 at the output of the RC-LED

The measured $|H_2(\pm f_1, \pm f_2)|$ of the two RC-LEDs are shown in Figure 2 for a large-signal modulation with a bias of 30mA and a modulation amplitude of 55mA (peak-to-peak). The investigated input frequency range is [0, 100MHz]. The results are normalized to their maximum and shown in a dB scale as false color images with



the two input variables f_1, f_2 . $|H_2(\pm f_1, \pm f_2)|$ is the magnitude of the 2nd-order intermodulation at frequency $f_{IM} = \pm f_1 \pm f_2$; values at $f_{IM} = 0\text{MHz}$ are not measured.

Both RC-LEDs show a similar behaviour with a maximum of nonlinearities at low input frequencies. For increasing f_1, f_2 the impact of nonlinearities tend to decrease for both devices. We further observe for a given pair of f_1, f_2 different intermodulation magnitudes at $f_1 + f_2$ and $f_1 - f_2$, i.e. $|H_2(f_1, +f_2)| \neq |H_2(f_1, -f_2)|$. As the generation of the nonlinearities mathematically always gives $|H_2(f_1, +f_2)| = |H_2(f_1, -f_2)|$, this implies that a strong frequency selective process is existent *after* the IM2 generation. This linear process will be addressed in Section 4.3. So, to characterize the LED's nonlinear behaviour properly, one must assess the IM2 generation *within* the device (prior to the linear process). This is achieved by choosing pairs of f_1 and f_2 which produce a constant $f_{IM} = \pm f_1 \pm f_2$; that corresponds to measuring a diagonal of $|H_2(\pm f_1, \pm f_2)|$, as exemplarily marked in Figure 2 (right).

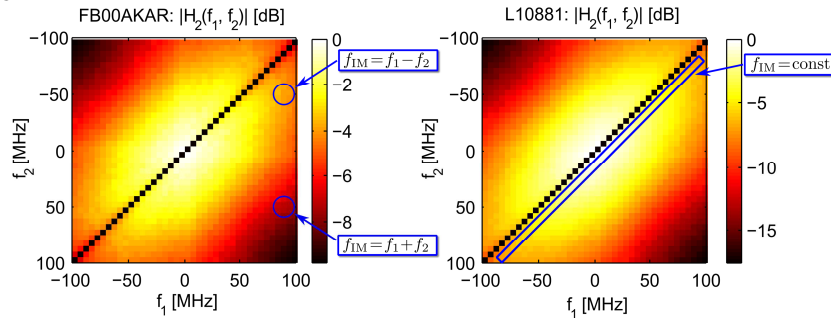


Figure 2: Measured 2nd-order Volterra kernel transforms $|H_2(\pm f_1, \pm f_2)|$ of the two RC-LEDs.

4.2 IM2 Generation within the RC-LED

Large-signal modulation, as used so far, implies that the LED driving signal ranges from low current densities near 0mA up to very large current densities near $2 \cdot i_{bias}$. The modulation characteristics of LEDs are usually expected to vary between low and high injection current densities [1]. Therefore, to get a more accurate insight into the physical characteristics of the IM2 generation in the devices, we evaluate the diagonals of $|H_2(\pm f_1, \pm f_2)|$ (which result in $f_{IM} = \text{const.}$) for a smaller modulation amplitude of 30mA (pk-pk) and now at the two bias points of 20mA and 40mA.

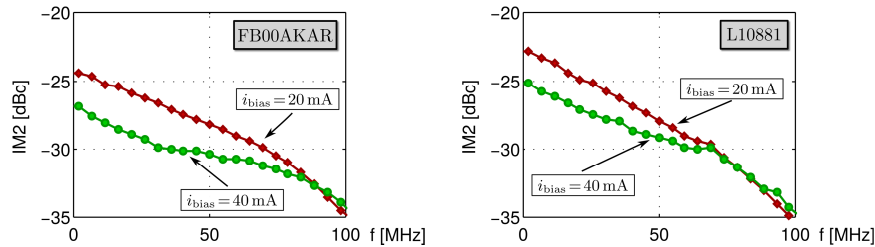


Figure 3: Measured IM2 generation.

The results are shown in Figure 3 in a dBc scale. The dBc scale is a commonly used measure to relate the output intermodulation power at f_{IM} to the output power of the corresponding carrier at f_1, f_2 . However since $f_{IM} \neq f_1, \neq f_2$, the frequency selective process, observed in Figure 2 would affect the dBc calculation. Therefore, we use a second measurement to determine the carrier output power at f_{IM} , where we use the same input level as is used in the IM2 measurement at f_1, f_2 . Then carrier and intermodulation signal undergo the same E/O conversion factor. This eliminates any unwanted effects of the subsequent frequency selective process.

Further, one can easily show that the input frequencies giving a diagonal as marked in Figure 2 are a pair of increasing frequencies f_1, f_2 which are spaced by a constant $\Delta f = f_2 - f_1 = f_{IM}$. We set $f_{IM} = 1.8\text{MHz} \ll f_1, f_2$, and hence we simplify $f_1 \approx f_2 \approx f$ in Figure 3. The IM2 generation in Figure 3 of both devices show a clear low-pass behaviour, that is low electrical modulation frequencies indeed produce the strongest nonlinearities. A



comparison of the two bias points reveals that the low-pass behaviour is more pronounced at low bias points. The observed IM2 drop within 100MHz at $i_{\text{bias}} = 20\text{mA}$ is about 10dB (FB00AKAR) and 12dB (L10881), whereas for $i_{\text{bias}} = 40\text{mA}$ it is about 6dB (FB00AKAR) and 10dB (L10881). It is further obvious that stronger nonlinearities are present at a low bias point. This is an interesting observation, as usually saturation effects at high injection current densities are considered in the context of LED nonlinearities.

The results of Sections 4.1 and 4.2 may be summarized in a system-theoretic model of the RC-LED as depicted in Figure 4: The electrical input signal undergoes a dynamic nonlinear process (which shows a bias dependent low-pass behaviour) followed by a linear frequency selective process.

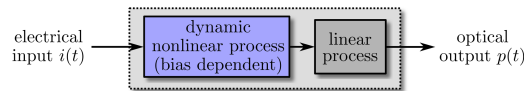


Figure 4: Derived system-theoretic model of the RC-LED's nonlinear modulation behavior.

4.3 The Linear Process after IM Generation

We conclude the investigations by analysing the frequency response of the linear process of Figure 4. The frequency response $H(f)$ of an LED, as shown in Figure 1 (right), is usually approximated to be given by the radiative lifetime [1]. Therefore, if the linear process of Figure 4 resembles $H(f)$, it would give a strong indication that the RC-LED's nonlinearities actually occur prior to the photon generation. We analyse the characteristics of the linear process by re-normalizing the Volterra kernel transforms $|H_2(\pm f_1, \pm f_2)|$ of Figure 2 to the LED's linear frequency response $H(f = f_{\text{IM}})$ of Figure 1 (right). We denote the re-normalized Volterra kernel transform $|\hat{H}_2(\pm f_1, \pm f_2)|$. If the observed linear process resembles $H(f)$, $|\hat{H}_2(f_1, +f_2)| = |\hat{H}_2(f_1, -f_2)|$ must be observed. The results are shown in Figure 5. Therein sketched are the symmetry conditions. As can be seen, good symmetry is achieved. This suggests that the linear process of Figure 4 is indeed $H(f)$. That, in turn indicates that the nonlinearities are originated in the electrical domain. Possible are thermally induced effects such as carrier leakage in the active region [1].

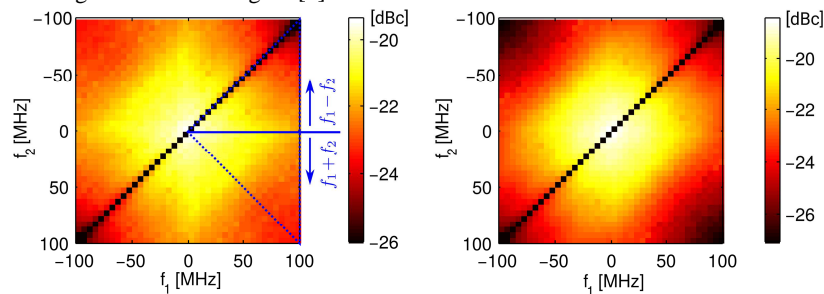


Figure 5: Re-normalized Volterra kernel transforms $|\hat{H}_2(\pm f_1, \pm f_2)|$: FB00AKAR (left), L10881 (right).

5. Conclusion

Dynamic nonlinearities in the E/O conversion of RC-LEDs were studied. It was shown that low modulation frequencies induce the strongest IM2 and smaller bias points result in a stronger IM2 frequency dependence. A system-theoretic model was derived suggesting that the physical origin of the nonlinearities is in the electrical domain. Investigations on these physical origins will be the subject of upcoming work.

6. References

- [1] E. Schubert, *Light-Emitting Diodes*, Cambridge University Press, 2006.
- [2] T. Kamalakis et al., *Empirical Volterra-Series Modeling of Commercial Light-Emitting Diodes*, in *Journal of Lightwave Technology*, vol. 29, no. 14, pp. 2146-2155, July 15, 2011.
- [3] M. Schüppert, C.-A. Bunge, *Characterization and Equalization of Nonlinearities in Directly Modulated Resonant Cavity Light-Emitting Diodes*, in *Proc. ICTON, Trento, 2016*, pp. 1-4.
- [4] M. Schetzen, *The Volterra and Wiener theories of nonlinear systems*, Wiley, 1980.

Simulation of optical module for GI-POF with the Ballpoint-pen connection

H. Takizuka ⁽¹⁾, A. Mitsui ⁽²⁾, H. Suzuki ⁽²⁾, T. Toma ⁽¹⁾, and Y. Koike ⁽¹⁾

1: Keio Photonics Research Institute, Keio University, 7-1 Shin-Kawasaki, Saiwai-ku, Kawasaki, Kanaga-wa 212-0032, Japan

2: Mitsubishi Pencil, 2-5-12 Irie, Kanagawa-ku, Yokohama, Kanagawa 221-8550, Japan

Corresponding author: takizuka@kpri.keio.ac.jp

Abstract: The purpose of this paper is to realize an inexpensive optical module which reduces connection precision using the GI-POF with Ballpoint-pen connection ^[1]. Specifically, an optical simulation using Zemax OpticStudioTM ^[2] is conducted to understand the influence of axial and angle misalignment of the optical module with the Ballpoint-pen connection.

1. Introduction

In order to obtain a more realistic image, the display industry has been expanding substantial improvement on video format; such as color gamut, color depth, frame rate, and resolution ^[3]. In Japan, 8K Ultra High Definition TV (8K-UHDTV) satellite broadcasting is planned to start towards the Olympic Games in 2020. When transmitting un-compressed 8K-UHDTV video data, transmission speed exceeds 100Gbps. GI-POF has been receiving a lot of attention, as it enables high-speed transmission of 8K-UHDTV video, safe and easy handling for consumer apparatus. But there is no optical module which directly connects POF with transmission band beyond 10GHz yet. Therefore, when composing a transmission system with POF, GOF has to be used for a part of the system and it requires expensive connection and joint-loss which reduces performance of the system.

We are developing GI-POF with the Ballpoint-pen connection which protects the end face from dust and scratches. It also reduces connection precision by its collimating beam, and gives a possibility for consumer applications which can be achieved inexpensively. The purpose of this paper is to realize an inexpensive optical module which reduces connection precision using the GI-POF with Ballpoint-pen connection.

2. Validity inspection of a simulation model

Before simulating the optical module, I compare the simulation result with the experimental result, regarding the axis and the angle misalignment in the Ballpoint-pen connection for the purpose of inspecting the validity of the model and the parameter.

The specification of GI - POF and Ballpoint-pen connection are as following,

GI-POF FONTEX (Asahi Glass Co.):

Core diameter: $80 \pm 5 \mu\text{m}$, outer diameter: $490 \pm 5 \mu\text{m}$, Numerical Aperture (NA): 0.245 ± 0.015

Ballpoint-pen connection (Mitsubishi Pencil Co.) (See figure 1):

Ball lens material: N-BK7 (Refractive Index: 1.51@850nm)

Diameter of Ball lens: $550 \pm 5 \mu\text{m}$, Length of Sleeve: $6600 + 0 / - 20 \mu\text{m}$,

Outer Diameter of Sleeve: $720 \pm 10 \mu\text{m}$, Inner Diameter of Sleeve: $50 + 20 / - 0 \mu\text{m}$

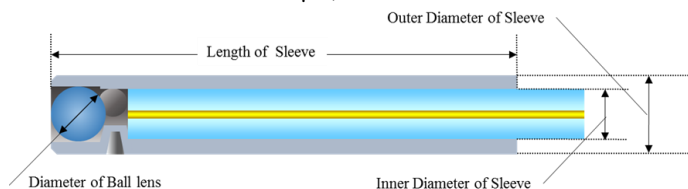
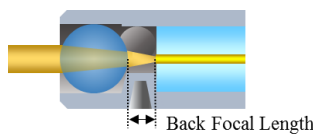


Figure 1. Specification of Ballpoint-pen connection

The distance between the ball lens and the fiber end face is 132 μm of Back Focal Length based on equation (1).



$$BF = \frac{nD}{4(n-1)} - \frac{D}{2} \tag{1}$$

n : Refractive Index of Ball lens,

D : Diameter of Ball lens

Figure 2. Distance between the ball and the fiber end face

Ballpoint-lens connection is expressed by *Non-Sequential-Component* in *Zemax* to determine the loss of axis and angle misalignments. (The terminology in *Zemax* is italicized.)

Transmitting beam from GI-POF used *Source Ellipse* as a light sources. *X Half width* and *Y Half width* of the parameters are the radius of the core. *Gauss Gx* and *Gauss Gy* of the parameters are set at 30 respectively to fit the actual shape. The ball lens used *Sphere*. To measure incident beam quantity to GI-POF, the circular mask pattern of 80 μm of core diameter size, which is defined by *User Defined Aperture*, was set in *Standard Surface*. *Detector Rectangle*, which sets maximum incidence angle θ_{max} at $\sin^{-1}(NA) = 14.18181$ degrees, is located behind the *Standard Surface*.

Y axis (vertical to optic axis) and Z axis (parallel to optic axis) misalignment and angle misalignment were simulated by these components. The comparisons between the simulation result and experimental result are shown in figure 3-5.

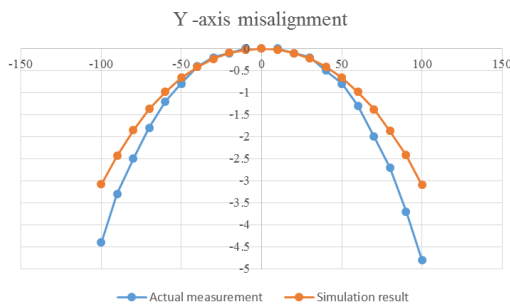


Figure 3. Y-axis misalignment

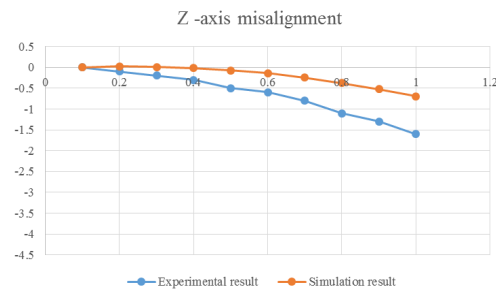


Figure 4. Z-axis misalignment

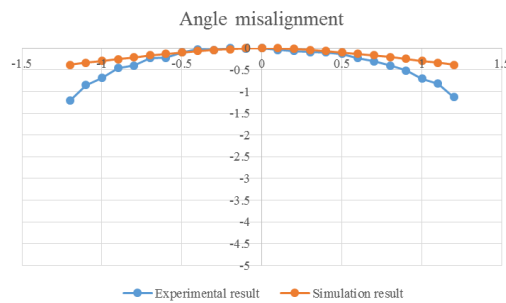


Figure 5. Angle misalignment

The loss in the simulation results are slightly smaller than that in experimental results. I suspect the reasons for the loss are influenced by: eccentricity of the ball lens, GI-POF and the sleeve, change in the maximum incidence angle in the core position of GI-POF and loss of higher-order mode. This model is simple, but I consider the model is good enough to understand the specific characteristic of the optical module.

3. Optical design of optical module

The Optical module for VCSEL (LD) that converts radiation beam to collimated beam and the optical module for Photo Detector (PD) that converts collimated beam to collected beam were designed.

Concerning optical module, in VCSEL beam radiates horizontally from the location where VCSEL is mounted on the circuit board. So structures that bend the beam by 90 degrees using a mirror or a prism are adopted. Lately VCSEL is mounted on a flexible circuit board. Therefore, some optical modules construct straight optical systems. In this paper two types of optical modules are examined.

The loss of optical modules is aimed at approximately 1.0dB.

3.1. Concerning parameters of LD and PD

Emitted beam from LD used *Source Ellipse* as a light source. *X Half width* and *Y Half width* of the parameters are the size of LD. *Gauss Gx* and *Gauss Gy* of the parameters are set at 30 respectively to fit the actual shape. To measure incident beam quantity to PD, the circular mask pattern with 50 μm PD diameter size, which is defined by *User Defined Aperture*, was set in *Standard Surface*. *Detector Rectangle*, which sets maximum incidence angle θ_{\max} at 90 degrees, is located behind the *Standard Surface*. A prism used *Prism45.pob* in *Polygon Object*.

3.2. In case of the Ball Lens

The loss of the optical module when the lens for a Ballpoint-pen connection are used is evaluated. The distance between the lens and PD, and the distance between the lens and LD is Back Focal Length 132μm respectively. The loss of optical module for LD in straight type is 1.29dB, and the loss in prism type is 1.48dB. The loss of the optical module for PD in straight type is 4.9dB, and the loss in prism type is 4.6dB.

3.3. In case of the Spherical Lens

Optical module for PD generate large loss. It is because 50 μm receiving area of high-speed PD is unable to collect beam sufficiently due to spherical aberration of the ball lens. Therefore, spherical lens is used instead of ball lens for the purpose of reducing the loss. The spherical lens is produced using the conic coefficient of *Standard Lens*.

A profile of spherical shaped (sag) is given by the following equation (2).

$$Z(s) = \frac{Cs^2}{1 + \sqrt{1 - (1+k)C^2s^2}} \quad (2)$$

Z: sag, s: the distance from the optical axis, C: curvature, k: conic coefficient

A plano-convex spherical lens which is molded with a prism in the case of the prism type and a convex spherical lens in the case of the straight type are selected.

Sequential-Component is used to design a spherical lens.

In a parameter for LD *Aperture Type* is chosen for *Object Cone Angle*, and *Aperture Value* is set at 20. In a parameter for PD *Aperture Type* is chosen for *Object Space NA*, and *Aperture Value* is set at 0.245.

Type=RMS, *Criteria=Spot Radius*, *Reference=Centroid* are chosen, and also the maximum value of *Boundary Value* is set at 300 μm. These values are in *Optimization Function* in *Merit Function*. The face that becomes spherical surface is converted to a variable. Then optimization executes, and appropriate spherical lens is formed. Formed data is shown in Figure 6 and Table 1.

The loss is evaluated when the spherical lens is used for the optical module. The loss of optical module for LD in straight type is 0.85dB, and the loss in prism type is 1.13dB. The loss of the optical module for PD in straight type is 1.04dB, and the loss in prism type is 1.19dB. The layout of each module is shown in Figure 7.

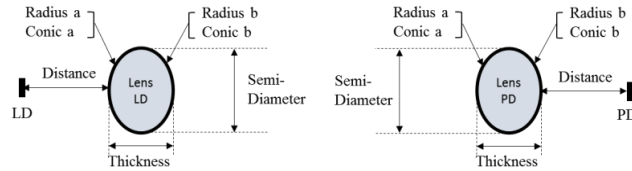


Figure 6. The meaning of the parameters

Table 1. The data of spherical lens

LD/PD	Distance (μm)	Se mi-Diameter (μm)	Radius a (μm)	Conic a	Thikness (μm)	Radius b (μm)	Conic b
Convex (LD)	118	99	771	-94.186	276	-159	-0.663
Plano-Convex (LD)	299	131	151	-2.659	257	Infinity	0
Convex (PD)	100	116	109	-0.757	150	-456	-9.695
Plano-Convex (PD)	200	119	115	-1.823	198	Infinity	0

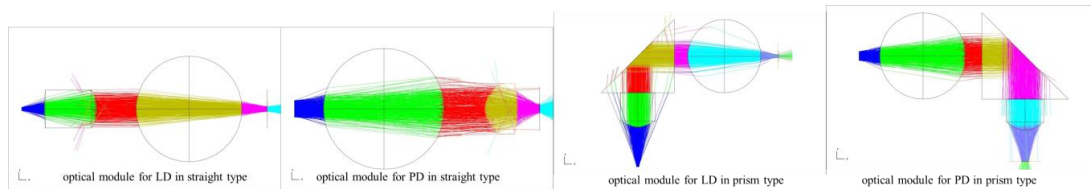


Figure 7. The layout of each module

3.4. Optical module using the different material

To reduce the cost for materials, N-BK7 of glass is replaced with ZEONEX F52R of Cyclo-olefin Polymer (COP) (ZEON Co.). Loss of the prism type PD optical module with F52R is measured. The result is 1.09dB and this means loss has not increased.

3.5. For tolerance

Loss that is generated by tolerance of the prism type PD optical module is checked. The loss that is generated is 0.58 dB because location of PD and spherical lens shift by $\pm 5 \mu\text{m}$ and angle rotates by 1.0 degree. When PD and spherical lens are installed, the device should be handled with utmost care.

4. Conclusion

Optical module is simulated using Zemax™, and it is founds that optical module, which is suitable for Ballpoint-pen connection can be formed with the loss of about 1.0dB. The optical module with molded lens and prism will be developed. This detachable GI-POF cable enables separate soldering of optical module in a manufacturing process of a printed circuit board, which results in reliability improvement and number of parts reduction.

5. References

[1]H. Takizuka , T. Torikai , A. Mitsui , H. Suzuki , Y. Watanabe , T. Toma , and Y. Koike, “A Study on 120Gbps GI-POF Interface for 8K-UHD Video Transmission”, The 22nd International Conference on Plastic Optical Fibers, September 2013
 [2]Zemax OpticStudio 14.2 OpticStuddio User Guide (2015)
 [3]ITU-R BT.2020, “Parameter values for ultra-high definition television systems for production and international programme exchange”, (2013).



Modelling the bend out-coupling of melt-spun polymer optical fibers

Brit M. Quandt^{1,2}, René M. Rossi¹, Gian-Luca Bona^{1,2}, Birgit Luster³, Luciano F. Boesel^{1*}

¹ Empa, Swiss Federal Laboratories for Materials Science and Technology, Lerchenfeldstrasse 5, 9014 St. Gallen, Switzerland

² ETH Zurich, Swiss Federal Institute of Technology, Department of Information Technology and Electrical Engineering, Gloriastrasse 35, 8092 Zurich, Switzerland

³ Hochschule Nordhausen, University of Applied Sciences, Weinberghof 4, 99734 Nordhausen, Germany

*Corresponding author: Luciano.boesel@empa.ch

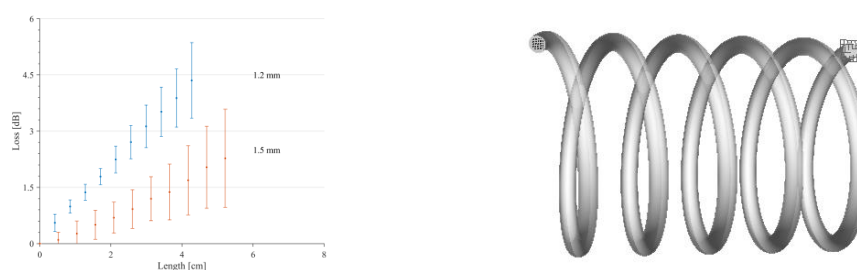


Figure 1: Out-coupling losses of one of our polymer optical fibers being wound around a 1.2 and 1.5 mm diameter wire (left) and the ray tracing model of the bent fiber as a tight spiral (right).

For many applications, bending losses are a critical factor in using optical fibers irrespective of utilisation. For this, information on the extent of light loss is sought both experimentally and through simulation, such as ray tracing with Monte Carlo methods. However, multimode fibers with large cores pose difficulties with their large computational effort. This effort is largely determined by the number of light rays traveling within the fiber. Additionally, the modelling of interfacial scattering between the core and cladding layer leads to an even higher number of ray paths.

The metrological examination of the interface roughness with roughness measurements is usually impossible. Therefore, the parameterization of the used scatter model is based on typical values of a POF interface roughness (in the range of some 10 nm). The principle is described by Luster^[1]

In an in-house melt-spinning plant, we have developed extremely flexible bi-component polymer optical fibers made from a cyclo-olefin core and a fluorinated cladding as published by Reifler et al.^[2] They can be wound around small diameter wires without breaking failure. We finally tested two different fibers at various bending diameters (from 3.2 mm down to 0.12 mm). The losses were logged by used fiber length as well as number of full rotations.

The experimental results of the POF bending investigations were compared with the ray-tracing simulation results for validation of the fiber model.

[1] B. Luster: Modellierung tubulärer optischer Fasern am Beispiel eines optisch-elektrischen Kombinationsleiters, Dissertation, Nordhäuser Hochschultexte, Bd. 4, 2015

[2] F. A. Reifler, R. Hufenus, M. Krehel, E. Zraggen, R. M. Rossi, L. J. Scherer, *Polymer* **2014**, *55*, 5695.

Key Words: melt-spinning, bending radii, simulation, light loss, ray-tracing
Preferred presentation method: oral



Analytical model for the angle-dependent power distribution in optical multimode fibers

T. Becker^{1*}, B. Schmauss², M. Gehrke¹, E. Nkiwane¹, O. Ziemann¹

¹ Polymer Optical Fiber Application Center, Technische Hochschule Nürnberg, 90489 Nürnberg, Germany

² Institute of Microwaves and Photonics (LHFT), Friedrich-Alexander-Universität Erlangen-Nürnberg, 91054 Erlangen, Germany

*Corresponding author: thomas.becker@pofac.th-nuernberg.de

Abstract: We present an analytical model for optical multimode fibers which calculates the angle-dependent power distribution inside the fiber. The model considers the power distribution over the angle to be continuous instead of dealing with discrete modes, which is justifiable for multimode fibers like step-index polymer optical fibers (SI-POF). Based on the power distribution we derive a fully analytical term for the impulse response for different launching conditions. Since the whole approach is analytical, all considered influences can be found in the resulting term. Therefore the model can easily be adjusted to new conditions. Finally, we compare the results with corresponding ray tracing simulations.

1. Introduction

Since optical multimode fibers and especially SI-POF can guide several million modes, their behavior is often modeled using ray tracing simulations instead of solving the wave equation for each mode individually. Ray tracing itself is a discrete approach which, given the number of simulated rays is large enough, can be used to approximate almost continuous power distributions. However, depending on the length of the fiber and the number of rays, ray tracing can consume a tremendous amount of time and memory.

The proposed model can be used to describe an optical transmission system including light source, fiber and receiver. Neglecting the process of scattering, the impulse response of the transmission system can be derived from its power distribution at the receiver. By transferring the impulse response to the frequency domain, we can predict the behavior of the fiber for both, data transmission and analogue sensing applications by its phase and amplitude response. The gained information can for example be used to improve the precision of analogue sensors that are based on phase measurements [1].

2. Theoretical background

This paper presents an analytical approach to calculate the power distribution inside a SI-POF based on the position and the intensity distribution of the light source and the physical parameters of the fiber. As depicted in Figure 1, we define a ray's propagation direction by the angles θ_z , θ_ϕ and α as it was proposed by Snyder and Love [2]. θ_z is the angle of the ray relative to the fiber's axis. θ_ϕ defines the ray's skewness and α is the angle between the ray and the normal to the surface at the point of reflection. Since the three angles depend on each other according to

$$\cos(\alpha) = \sin(\theta_z) \sin(\theta_\phi) \quad , \quad (1)$$

it is sufficient to consider just two of them. Based on these angles every ray can be assigned to a group of modes (Figure 2) which differ from each other by scattering, attenuation and transit time. If α is smaller than the minimum angle for the total internal reflection α_{min} , a part of the ray's power is refracted into the cladding with every reflection and these modes are therefore called refractive modes. The reflected part of the power is so small that its contribution to the impulse response of a fiber is negligible even for relatively short fiber lengths. If α however is larger than α_{min} , the possible group assignment also depends on θ_z . If θ_z is smaller than θ_c , the mode is guided, otherwise it is called a tunneling mode. Even though tunneling modes fulfill the critical angle for the total internal reflection, they face a higher attenuation due to an effect called frustrated total internal reflection which is caused by the curvature of the core cladding interface. The consideration of both angles in the model enables us to distinguish between these three groups and treat attenuation and scattering appropriately, which strongly depends on the skewness.

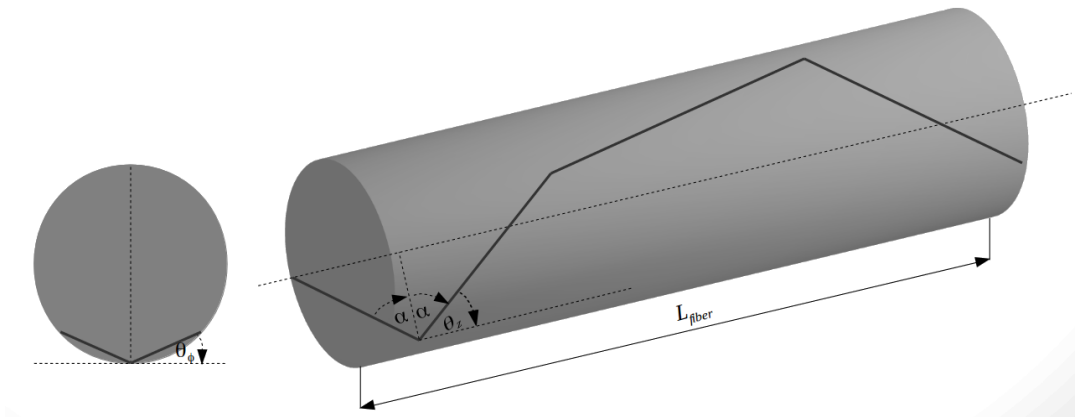


Figure 1. Propagation angles inside the fiber

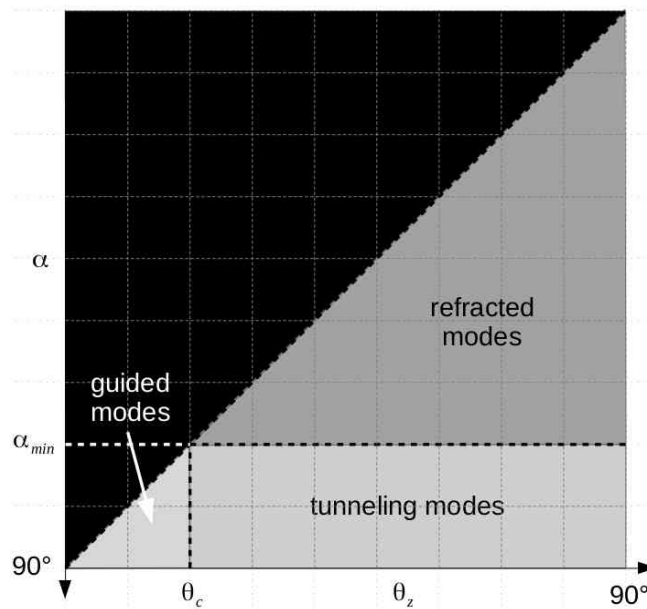


Figure 2. Different kinds of modes

3. Light source

In this chapter we derive the power distribution over the angle relative to the fiber's axis. Since the light source is outside the fiber and therefore usually surrounded by a medium with a refractive index different from the fiber's core, we call this angle θ_{z0} . We start with a point source which has a constant power distribution over the solid angle Ω . If we assume that the total power P_T is emitted into the half-space 2π , the power P , which corresponds to a solid angle Ω , can be expressed as



$$P = \frac{\Omega}{2\pi} P_T \quad (2)$$

For our model we need to express the power distribution with a dependence on θ_{z0} . Therefore we have to express Ω as a function of θ_{z0} . Ω is equal to the area A of the cap of a unit sphere that is spanned by Ω (see Figure 3). In any sphere Ω can be expressed as

$$\Omega = \frac{A}{r^2} \quad (3)$$

where r is the radius of the sphere. The area of the cap is

$$A = 2\pi r h \quad (4)$$

where h is the height of the spherical cap. From Figure 3 it is also clear that

$$h = r - z \quad (5)$$

z is the distance from the bottom of the cap to the center of the sphere. Further we see that

$$\cos(\theta_{z0}) = \frac{z}{r} \quad (6)$$

With equations (2-6) we can finally express the power that corresponds to the angle θ_{z0} :

$$P = \frac{\Omega}{2\pi} P_T = \frac{A}{2\pi r^2} P_T = \frac{2\pi r h}{2\pi r^2} P_T = \frac{r-z}{r} P_T = \frac{r-r\cos(\theta_{z0})}{r} P_T = 1 - \cos(\theta_{z0}) P_T \quad (7)$$

Equation (7) gives us the total power for a point source with a maximum angle of θ_{z0} . Since we are interested in the power distribution over θ_{z0} we have to derive equation (7) with respect to θ_{z0} :

$$\frac{dP}{d\theta_{z0}} = \frac{d(1 - \cos(\theta_{z0}) P_T)}{d\theta_{z0}} = \sin(\theta_{z0}) P_T \quad (8)$$

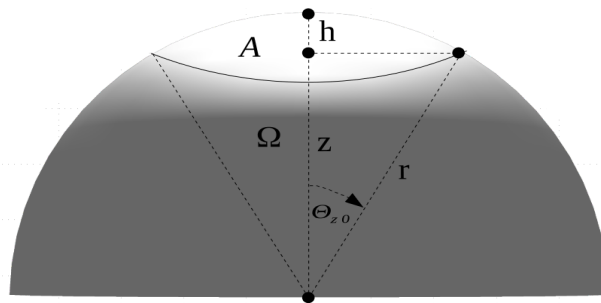


Figure 3. Dependency of Ω on θ_{z0}

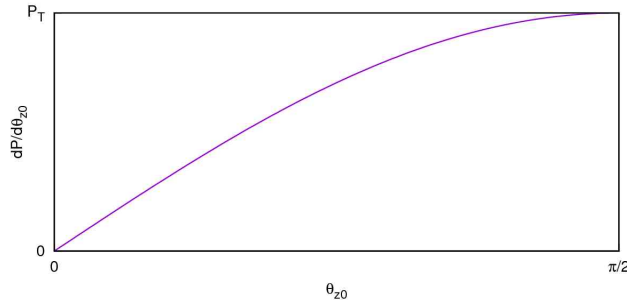


Figure 4. Power distribution of a point source

As we can see (Figure 4), the resulting power distribution of the light source has a sinusoidal dependency on the angle θ_{z0} . Therefore higher order modes carry more power than lower order modes. Of course the power distribution is limited by the maximum θ_{z0} of the light source which we consider to be $\frac{\pi}{2}$ in this paper.

4. Fiber

When the light enters the fiber, we have to consider three different influences. First of all the power distribution over θ_{z0} is transferred to a power distribution over θ_z since the refractive index of the core of the fiber n_{core} is different from the refractive index of the surrounding medium n_0 . The second step is to determine, what kind of modes (see Figure 2) are excited by the light source. Finally we have to consider Fresnel losses at the end surface of the fiber.

4.1. Angular transformation

We need to transfer the power distribution outside the fiber $\frac{dP}{d\theta_{z0}}$ to the one inside the fiber $\frac{dP}{d\theta_z}$, which can be expressed as

$$\frac{dP}{d\theta_z} = \frac{dP}{d\theta_{z0}} \frac{d\theta_{z0}}{d\theta_z} \tag{9}$$

The two angles are connected via Snell's law:

$$n_0 \sin(\theta_{z0}) = n_{core} \sin(\theta_z) \tag{10}$$

Therefore we can derive

$$\frac{d\theta_{z0}}{d\theta_z} = \frac{d\left(\arcsin\left(\frac{n_{core}}{n_0} \sin(\theta_z)\right)\right)}{d\theta_z} = \frac{n_{core} \cos(\theta_z)}{\sqrt{(n_0^2 - n_{core}^2 \sin^2(\theta_z))}} \tag{11}$$

which we can insert into (9) together with (10) and obtain

$$\frac{dP}{d\theta_z} = \frac{dP}{d\theta_{z0}} \frac{d\theta_{z0}}{d\theta_z} = \frac{n_{core} \cos(\theta_z) \sin(\theta_{z0}) P_T}{\sqrt{(n_0^2 - n_{core}^2 \sin^2(\theta_z))}} = \frac{n_{core}^2 \cos(\theta_z) \sin(\theta_z) P_T}{n_0 \sqrt{(n_0^2 - n_{core}^2 \sin^2(\theta_z))}} \tag{12}$$



The resulting power distribution is shown in Figure 5. As we can see, the angular transformation has changed the sinusoidal shape to an almost linear one in the beginning but with a sharp rise towards the end¹. A large part of the total power is shifted to higher order modes. Further the maximum occurring angle has been reduced from $\pi/2$ to $\arcsin(n_0/n_{core})$.

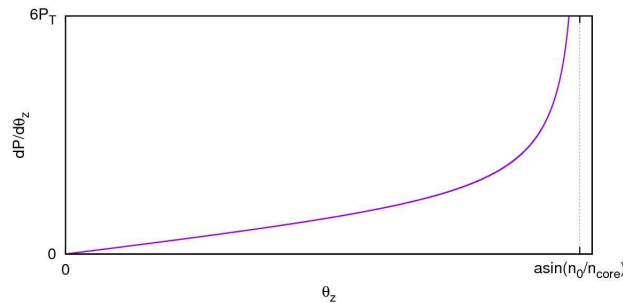


Figure 5. Power distribution of a point source inside the fiber

4.2. Mode groups

So far our obtained terms only depend on θ_{z0} but not on θ_ϕ , which is simply due to the fact that θ_ϕ describes the skewness of a ray which doesn't exist outside the fiber. However if we have a look at Figure 6, we see that we can define an angle β which together with θ_{z0} describes the direction of a ray inside an axially symmetric light source. With the new dependency on β we can rewrite equation (9) as

$$\frac{\partial^2 P}{\partial \theta_z \partial \beta} = \frac{\partial^2 P}{\partial \theta_{z0} \partial \beta} \frac{d\theta_{z0}}{d\theta_z} \tag{13}$$

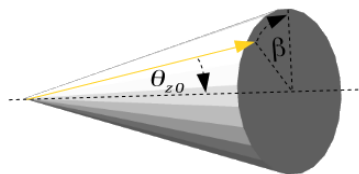


Figure 6. Definition of a ray depending on θ_{z0} and β

Since our light source is axially symmetric, the power doesn't vary with β but we need the dependency to determine the excited mode groups. Figure 7 shows a point source on the front surface of a fiber with the radius r . The distance of the point source from the core of the fiber is a . The source is emitting a ray under the angle β . With the help of the sine rule, we can determine the dependency of β on θ_ϕ :

$$\frac{a}{\sin\left(\frac{\pi}{2} - \theta_\phi\right)} = \frac{r}{\sin\left(\frac{\pi}{2} - \beta\right)} \tag{14}$$

$$\beta = \frac{\pi}{2} - \arcsin\left(\frac{r}{a} \sin\left(\frac{\pi}{2} - \theta_\phi\right)\right)$$

¹ Since the term shows a singularity for $\theta_z = \arcsin\left(\frac{n_0}{n_{core}}\right)$, the plot is limited to a maximum value of $6P_T$



If we analyze the obtained formula for β , we see that it is only defined for a certain range of θ_ϕ . From Figure 7 it is clear that the maximum possible value for θ_ϕ is $\theta_{\phi,max} = \frac{\pi}{2}$. However there is also a minimum value for θ_ϕ that depends on a . The closer the light source is to the boundary of the fiber, the lower the possible values for θ_ϕ . The absolute minimum for a specific a can be obtained by investigating the argument of the $\arcsin(\cdot)$ function in formula (14). The minimum θ_ϕ occurs when the argument crosses the value 1 which leads to:

$$\theta_{\phi,min} = \frac{\pi}{2} - \arcsin\left(\frac{a}{r}\right) = \arccos\left(\frac{a}{r}\right) \tag{15}$$

If we want to express the power distribution inside the fiber dependent on θ_z and θ_ϕ , we can expand equation (13):

$$\frac{\partial^2 P}{\partial \theta_z \partial \theta_\phi} = \frac{\partial^2 P}{\partial \theta_{z0} \partial \beta} \frac{d \theta_{z0}}{d \theta_z} \frac{d \beta}{d \theta_\phi} \tag{16}$$

The only term that we have not obtained yet is the last one which we can derive from equation (14):

$$\frac{d \beta}{d \theta_\phi} = \frac{d \left(\frac{\pi}{2} - \arcsin \left(\frac{r}{a} \sin \left(\frac{\pi}{2} - \theta_{phi} \right) \right) \right)}{d \theta_\phi} = \frac{\sin(\theta_\phi) r}{a \sqrt{1 - \frac{\cos(\theta_\phi)^2 r^2}{a^2}}} \tag{17}$$

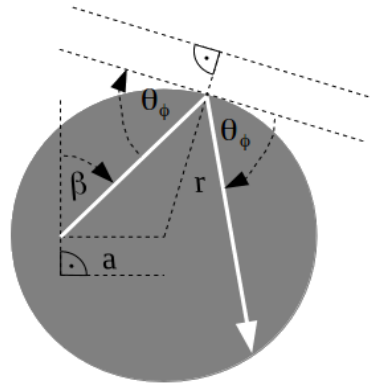


Figure 7. Dependency θ_ϕ of on β

Now we have all necessary terms to describe the full power distribution:

2 Technically speaking the maximum value would be $\theta_{\phi,max} = \pi$, however the range between $\frac{\pi}{2}$ and π describes the same situation as the range between 0 and $\frac{\pi}{2}$ just with a reversed direction of the ray which is not relevant here.



$$\frac{\partial^2 P}{\partial \theta_z \partial \theta_\phi} = \frac{2}{\pi} \frac{n_{core}^2 \cos(\theta_z) \sin(\theta_z) P_T}{n_0 \sqrt{(n_0^2 - n_{core}^2 \sin^2(\theta_z))}} \frac{\sin(\theta_\phi) r}{a \sqrt{1 - \frac{\cos(\theta_\phi)^2 r^2}{a^2}}} \quad (18)$$

It is important to know that the derived power distribution covers all possible group of modes shown in Figure 2. In this paper we want to consider guided and tunneling modes but neglect refracted modes due to their high attenuation. As shown in Figure 2, for refracted modes the condition $\alpha < \alpha_{min}$ holds. Since our model relies on θ_z and θ_ϕ that condition can be expressed as:

$$\theta_{\phi,max} = \arcsin\left(\frac{\cos(\alpha_{min})}{\sin(\theta_z)}\right) \quad (19)$$

All unguided modes with an θ_ϕ larger than $\theta_{\phi,max}$ are refracted modes and can be neglected.

4.3. Fresnel losses

Fresnel losses are relatively easy to consider since they only show a dependency on θ_z but not on θ_ϕ . The necessary equations are well known and can be looked up in [3] for example. The reflectance for perpendicular polarized light is³

$$ers(\theta_{z0}) = \frac{n_0 \cos(\theta_{z0}) - n_{core} \sqrt{1 - \left(\frac{n_0}{n_{core}} \sin(\theta_{z0})\right)^2}}{n_0 \cos(\theta_{z0}) + n_{core} \sqrt{1 - \left(\frac{n_0}{n_{core}} \sin(\theta_{z0})\right)^2}} \quad (20)$$

and the reflectance for parallel polarized light is

$$erp(\theta_{z0}) = \frac{n_{core} \cos(\theta_{z0}) - n_{core} \sqrt{1 - \left(\frac{n_0}{n_{core}} \sin(\theta_{z0})\right)^2}}{n_{core} \cos(\theta_{z0}) + n_{core} \sqrt{1 - \left(\frac{n_0}{n_{core}} \sin(\theta_{z0})\right)^2}} \quad (21)$$

Since we consider the source to emit unpolarized light, the transmittance can be expressed as

$$T(\theta_z) = \frac{(1 - ers(\arcsin(n_{core} \sin(\theta_z)))^2) + (1 - erp(\arcsin(n_{core} \sin(\theta_z)))^2)}{2} \quad (22)$$

The full equation for the modal distribution inside the fiber including the Fresnel reflections is therefore

³ In this paper we only consider the Fresnel reflections at the entry of the fiber since we want to calculate the power distribution inside the fiber. However Fresnel reflections at the end of the fiber can be considered in a similar way.



$$\frac{\partial^2 P}{\partial \theta_z \partial \theta_\phi} = T(\theta_z) \frac{2}{\pi} \frac{n_{core}^2 \cos(\theta_z) \sin(\theta_z) P_T}{n_0 \sqrt{(n_o^2 - n_{core}^2 \sin^2(\theta_z))}} \frac{\sin(\theta_\phi) r}{a \sqrt{1 - \frac{\cos(\theta_\phi)^2 r^2}{a^2}}} . \quad (23)$$

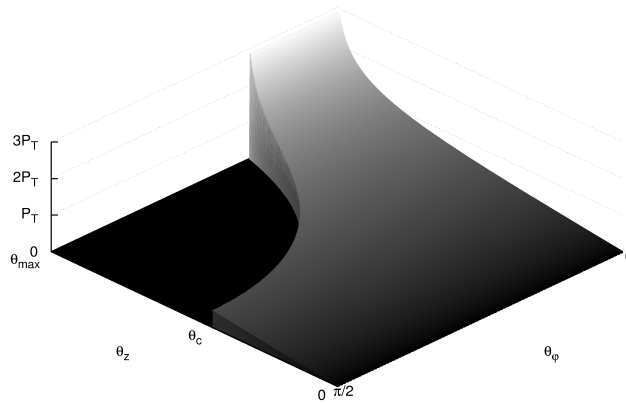


Figure 8. Modal distribution for $a = r$

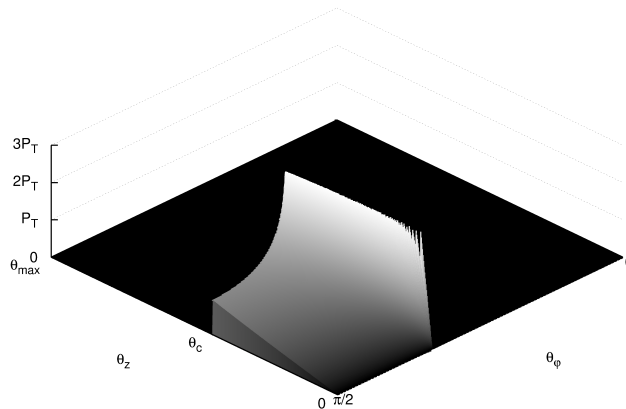


Figure 9. Modal distribution for $a = 0.5 r$

Figures 8 and 9 show the calculated modal distributions for two point sources for the distances from the axis $a=r$ and $a=0.5r$. In the first case all possible modes are excited. The black area is cut out because it represents the refracted modes. We notice that the power of the guided modes as well as the power of the tunneling modes is equally distributed over θ_ϕ . It ranges up to $\theta_{z,max}$ and the power density increases steadily with θ_z along a constant θ_ϕ . In the second case the shift of the light source towards the axis of the fiber has pushed the minimum possible value for θ_ϕ which has several consequences. First of all, the guided modes still carry the same amount of power but the distribution has been compressed and rises towards the



minimum value for θ_ϕ ⁴. Second the average skewness has decreased and finally the maximum value for θ_z has also decreased. That means that a part of the power which contributed to tunneling modes in the first example now belongs to refracted modes.

5. Impulse response

The transmission characteristics of an optical fiber can be fully described as a transmission function in the frequency domain, which can be obtained from the impulse response of the system. To derive the impulse response from our model, two steps are necessary. First we need to integrate equation (23) over θ_ϕ since the transit time for a ray only depends on θ_z :

$$\begin{aligned}
 \frac{dP}{d\theta_z} &= \int_{\theta_{\phi, \min}}^{\theta_{\phi, \max}} \frac{\partial^2 P}{\partial \theta_z \partial \theta_\phi} d\theta_\phi \\
 &= T(\theta_z) \frac{\partial^2 P}{\partial \theta_{z0} \partial \beta} \frac{d\theta_{z0}}{d\theta_z} \int_{\theta_{\phi, \min}}^{\theta_{\phi, \max}} \frac{\sin(\theta_\phi) r}{a \sqrt{1 - \frac{\cos(\theta_\phi)^2 r^2}{a^2}}} d\theta_\phi \\
 &= T(\theta_z) \frac{\partial^2 P}{\partial \theta_{z0} \partial \beta} \frac{d\theta_{z0}}{d\theta_z} \left[-\operatorname{asin} \left(\frac{r \cos(\theta_\phi)}{a} \right) \right]_{\arccos\left(\frac{a}{r}\right)}^{\arcsin\left(\frac{\cos(\alpha_{\min})}{\sin(\theta_z)}\right)} \\
 &= T(\theta_z) \frac{\partial^2 P}{\partial \theta_{z0} \partial \beta} \frac{d\theta_{z0}}{d\theta_z} \left(-\operatorname{asin} \left(\sqrt{1 - \frac{\left(\frac{\cos(\alpha_{\min})}{\sin(\theta_z)}\right)^2}{\left(\frac{a}{r}\right)^2}} + \frac{\pi}{2} \right) \right)
 \end{aligned} \tag{24}$$

The second step is to transform the modal power distribution into a time-dependent power-distribution. We start with the relation between the angle θ_z of a ray and the corresponding transit time which the ray needs to pass the fiber:

$$t = \frac{L_{\text{fiber}} n_{\text{core}}}{c_0 \cos(\theta_z)} \tag{25}$$

c_0 is the speed of light in vacuum and L_{fiber} is the length of the fiber. With equations (24) and (25) we can derive the impulse response:

$$\frac{dP}{dt} = \frac{dP}{d\theta_z} \frac{d\theta_z}{dt} = \frac{dP}{d\theta_z} \frac{L_{\text{fiber}} n_{\text{core}}}{c_0 \sqrt{1 - \frac{L_{\text{fiber}}^2 n_{\text{core}}^2}{c_0^2 t^2}}} \tag{26}$$

6. Comparison between model and ray tracing simulations

We use equation (26) to obtain the impulse responses for a SI-POF with a length of $L_{\text{fiber}} = 10\text{m}$ under the same launching conditions that we used for Figure 8 and Figure 9. In the first case, we place the light source at the edge of the fiber ($a=r$). In the second case, the light source is positioned in the middle between the core

⁴ This is true for the sum of all guided modes as well as for a specific θ_z .



of the fiber and its edge ($a=0.5r$). For the verification of the results we simulate both setups with the ray tracing software *Synopsys LightTools*⁵. Since we need real values for the refractive indexes in the simulations we define $n_0=1$, $n_{core}=1.495$ and $n_{clad}=1.42$. The impulse responses are shown in Figure 10.

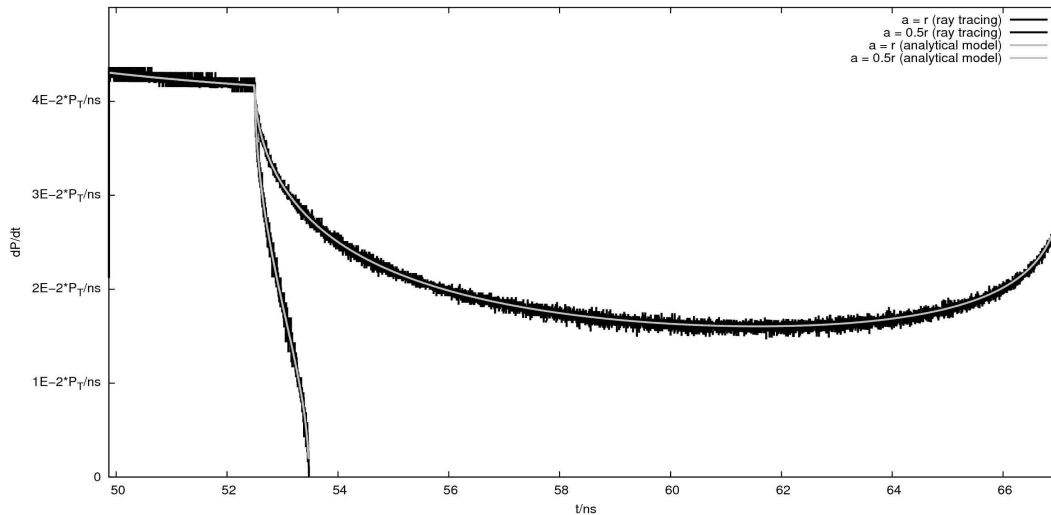


Figure 10. Comparison of the simulated and analytical impulse responses

The gray curves show the impulse responses derived from the analytical model. Both are identical in the beginning which is the area in which the guided modes arrive. Then the impulse response for ($a=0.5r$) decreases rapidly since only little power is carried by tunneling modes. The impulse response for ($a=r$) on the other hand has most of its power in the area of the tunneling modes and is therefore broader. The black curves show the impulse responses derived from the ray tracing simulations⁶. Apart from the noise which is caused by the discrete nature of the simulations, the obtained impulse responses perfectly match the predicted ones from the analytical model. Therefore we consider the presented model to be validated under the given conditions.

7. Conclusion and outlook

We have presented an analytical model for the calculation of the modal power distribution in multimode fibers based on the power distribution of the light source and the physical parameters of the fiber. Further we have derived and evaluated the impulse response of the fiber which can be used to gain the transmission function of the fiber. The transmission function can then be used to consider its influence on a specific application or tweak the application to the behavior of the fiber.

The proposed model shows some similarities to ray tracing simulations when it comes to the definition of the light source or the obtained results. However there are two major differences. Ray tracing simulations are relatively easy to set up but can consume a lot of time or even become unmanageable due to a lack of memory once a certain fiber length is reached. On the other hand the correct consideration of all the influences for the analytical model takes some care. But once it's set up, the modal power distribution or the impulse response can be obtained in practically no time.

Another advantage of the model is its expandability and adjustability. Since the model is analytical, every influence can clearly be identified and modified. Furthermore the consequences can directly be seen without having to run a simulation again which makes it suitable for experimental tasks. Regarding the expandability it should be mentioned that additional influences can be considered by simply expanding the given equations.

⁵ <http://optics.synopsys.com/lighttools/>

⁶ We have shown how to obtain an impulse response from a ray tracing simulation in [4].



Examples for additional influences would be the angular dependency of an optical receiver or a Gaussian power distribution of a light source.

It should not be concealed that the model does not take scattering and attenuation into account yet. The consideration of the angular-dependent attenuation is a relatively simple task since it only affects the modal distribution at the end of the fiber. Scattering however is more complex to integrate since it spoils the fixed relation between the angle θ_z of a mode and its transit time. Nevertheless we are currently working on a series of angular-dependent scattering- and attenuation-measurements whose results will be integrated in the presented model.

8. Acknowledgments

The POF-AC Nürnberg is a project of the Hightech Offensive Bavaria.

The work was supported by the Bavarian Ministry of Education, Culture, Science and Art and the European Regional Development Fund inside the Projects “Optika” (No. F1116.NÜ/13) and “OHM-Netze” (No. EU-1607-0017).

9. References

- [1] T. Becker, S. Loquai, H. Poisel, O. Ziemann, M. Lubert, and B. Schmauss, “Influence of modal dispersion on impulse and frequency response of step-index polymer optical fiber,” in POF Simulation beyond Data Transmission - Summary of the 3rd International POF Modelling Workshop 2015, C. A. Bunge and R. Kruglov, Eds. Norderstedt: Books on Demand, September 2015, p. 23ff.
- [2] A. W. Snyder, J. D. Love. Optical Waveguide Theory. Kluwer Academic Publishers Massachusetts; 2000.
- [3] G. A. Reider, Photonik – eine Einführung in die Grundlagen. 2nd ed. Wien: SpringerWienNewYork; 2005. German.
- [4] T. Becker, B. Schmauss, M. Gehrke, E. Nkiwane and O. Ziemann, “Non-linear relation between modulation frequency and phase response of step-index polymer optical fiber” in in Proceedings of 25th International Conference on POFs and Applications, POF’16, Birmingham (England), Sep. 2016.



Characteristics of photo polymerized polymer optical fibres, optical properties and femtosecond laser inscription of Bragg gratings

O.Palchik^{1,a}, N. Tal¹, E. Shafir^{2,b}, G. Berkovic², S. Zilberman², A. Theodosiou³ and K. Kalli^{3,c}

1 Intellisiv Ltd, Gedera, Israel

2 Soreq NRC, Yavne, Israel

3 Nanophotonics Research Laboratory, Cyprus University of Technology, Limassol, Cyprus

Corresponding authors: ^a olegp@intellisiv.co.il, ^b shafir@soreq.gov.il, ^c kyriacos.kalli@cut.ac.cy

1. Introduction

Polymer optical fibres (POFs) are of interest for a number of applications, from illumination, light harvesting and sensing, to short-range data transmission in automobiles, buildings and industrial automation. A key requirement for the successful development of POF is precisely controlled fibre production. Current POF production is inflexible requiring a number of techniques and manufacturing steps to arrive at the final fibre product, which impacts the fibre's optical and mechanical properties. The fibre supply chain typically consists of separate processes for chemical formulation and polymer manufacture, compound addition and fibre production. Unsurprisingly, the production process is long and complex and it is rarely possible to produce identical properties for two separate batch production runs, particularly when the fibre is produced with the heat-drawing process from a preform.

2. A new type of polymer fibre

In this paper, we present a new type of polymer optical fibre that has been developed by Intellisiv based on an advanced, single-step and highly scalable UV curing (photo-polymerization) process, a readily customizable production process that optimizes resources [1]. The key advantages may be summarised as follows, there is no polymer or master-batch at the production starting point, instead formulations of commercially available monomers & other additives are used as required; a liquid formula injection process is followed by very fast fibre UV polymerization; thus fibre formation and polymerization occurs simultaneously. This approach is highly customisable and flexible, whilst offering environmental advantages, such as a process that is essentially solvent/VOC-free, water-free, with very low emission (<1%).

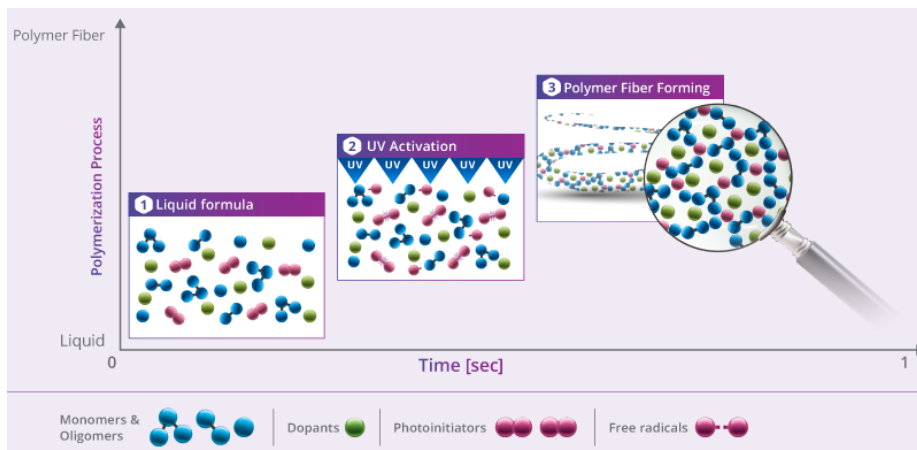


Figure 1. Intellisiv fibre polymerisation process



3. Optical transmission of the fibres

We have measured the optical transmission properties of two representative POFs manufactured by Intellisiv. Measurements were performed by the cut-back method [2] in which light is coupled into a given length of fibre and the transmitted power is measured as the fibre is shortened. Due to the uncertainty regarding the coupling efficiency into the fibre, the measurement of the power output will not yield unequivocally the value of the transmission loss per unit length of the fibre. This uncertainty can be eliminated by successively shortening the fibre at its output end (cut-back), without changing the input coupling conditions, measuring the transmitted power and calculating the loss from the changes in power transmission with fibre length.

Cut-back measurements were performed in two ways: using discrete wavelength light, and also with a broadband visible source and a spectrometer, producing continuous spectral information. The latter approach appears more attractive since it can supply more information, but, as will be detailed below, is more prone to experimental errors. Thus our approach was to first accurately measure the cut-back loss at 532nm using a laser source and then perform the spectroscopic cut-back measurements. When the spectroscopic measurement yielded a result consistent with the laser measurement at 532nm, then the entire spectroscopic measurement was considered verified.

For the discrete measurement, our source was a 5mW 532nm laser (Global Laser Tech) coupled into a 600 μm core NA=0.39 silica fibre patch-cord, with SMA connectors (Thor Labs M21L05). The POF under test was cleaved with a razor blade, inserted into an appropriate SMA connector and butt-coupled to the silica fibre with an SMA fibre adapter. The output end of the POF was also cleaved and the power output was measured with an integrating power meter detector (Newport 818-IS-1). The fibre was cut-back three times to determine the attenuation.

The basis of the spectroscopic cut back measurement was to use as input broadband 300-1000 nm light coupled into the above mentioned 600 μm core NA=0.39 silica fibre patch-cord and similarly butt-coupled to the POF. The transmitted light was detected with a spectrometer. This approach has an inherent problem: the positional and angular coupling to the spectrometer – which quite likely will vary for each fibre cut - influences the resultant spectrum. These issues have very little effect on the previously mentioned monochromatic cut-back measurement, since the detector (power meter) has a large collecting area.

Accordingly, we decided to permanently attach a second silica NA=0.39 fibre patch-cord (with core diameter larger than that of the POF) to the spectrometer SMA fibre input and butt-couple the POF between the two silica fibre patch-cords for the spectroscopic cut-back measurements (see Figure 2). The POF was successively cut back 3 times and each time butt-coupled to the "spectrometer" silica fibre, touching neither the input to the POF nor the coupling between the silica "spectrometer" fibre and the spectrometer. In this way we eliminated the uncertainties (and variations between measurements) also at the input to the spectrometer. We also expect that in this set-up, insertion losses will be essentially wavelength independent. This set-up leaves as the only uncertainty the quality of the POF cleaves and the butt-coupling to the silica "spectrometer" fibre. As stated above, our validation is the compatibility of the spectroscopic 532nm result with that previously obtained with the 532nm laser.

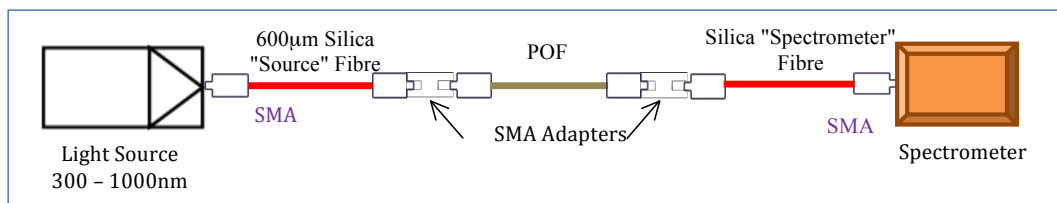


Figure 2: Set-up for spectroscopic cut-back measurements

In Figure 3 (blue curve) we present our results for an acrylate based Intellisiv fibre designated CR002CL0013 (750 μm core diameter, NA=0.47). Having learned these results, the fibre composition and the manufacturing process were refined, with the aim of decreasing losses. Consequently a new fibre was produced, designated



NTO34NTRC (580 μm core, NA=0.47). The losses in the latter (brown curve of Figure 3) are indeed significantly lower, as designed. Both fibres show relatively flat spectral transmission over most of the visible range (which for the second fibre is 3-5 dB/m), with a steep increase in attenuation from 850nm.

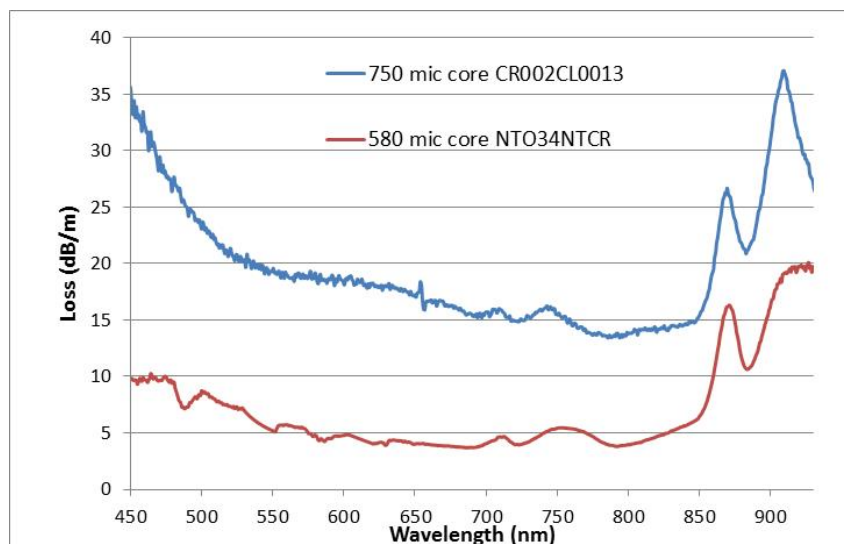


Figure 3: Optical characterization of 2 POFs

4. FBG inscriptions and results

The inscriptions of fibre Bragg gratings (FBGs) were performed using a femtosecond laser system (HighQ laser femtoREGEN) operating at 517-nm, with a 220-fs pulse duration. The fibre sample was mounted on an air bearing, two-dimensional translation stage system (Aerotech) for accurate computer controlled two-axis motion during the inscription. The laser beam was focused from above using a long-working-distance x50 objective (Mitutoyo) mounted on a third stage in order to control the laser focal spot into the optical fibre. The fibre that was tested was the multimode Acrylate fibre CR002CL0013 with a core diameter of a 750- μm . All the grating inscriptions were undertaken with the outer cladding in place to ensure a robust sensing fibre. We used the plane-by-plane femtosecond laser inscription method [3]; this offers sufficient control of the inscription parameters, as the depth, width and the height of the inscription planes can be fully controlled by the user. A pulse picker was used to operate the laser at 2-kHz repetition rate and the laser emitted pulses with energies of $\sim 50\text{nJ/pulse}$. We undertook two inscription processes on two different fibre samples, both of the higher loss fibres described in the preceding paragraph.

First we inscribed a single grating with 200 periods across the centre of the fibre core in a sample having a total fibre length of $\sim 10\text{-cm}$. For the second inscription we used a longer sample $\sim 75\text{-cm}$ and we inscribed two gratings, each consisting of 1000 planes, with a physical distance between them of $\sim 500\text{-}\mu\text{m}$. The period of the gratings was approximately $\Lambda = 2.2\text{-}\mu\text{m}$, with a small difference in the period of the second grating in order to form a two distinct sensor FBG array.

Following the inscription, the gratings were characterized using a broadband source (Thorlabs ASE730) centred at 1560nm coupled to the fibre via a (silica) fibre circulator, and a I-MON spectrometer from Ibsen Photonics. A small amount of index gel was used to reduce the Fresnel reflections from the end of the silica fibre. The reflection spectra of the two fibre samples are shown in Fig. 4; Fig. 4a shows the reflection spectrum of the first grating (inscribed on the short fibre) and Fig. 4b shows the reflection spectrum of the 2-FBG array, when measured from the long side, around $\sim 75\text{cm}$ away from the FBG. The exposure time of the spectrometer was set to 3ms.

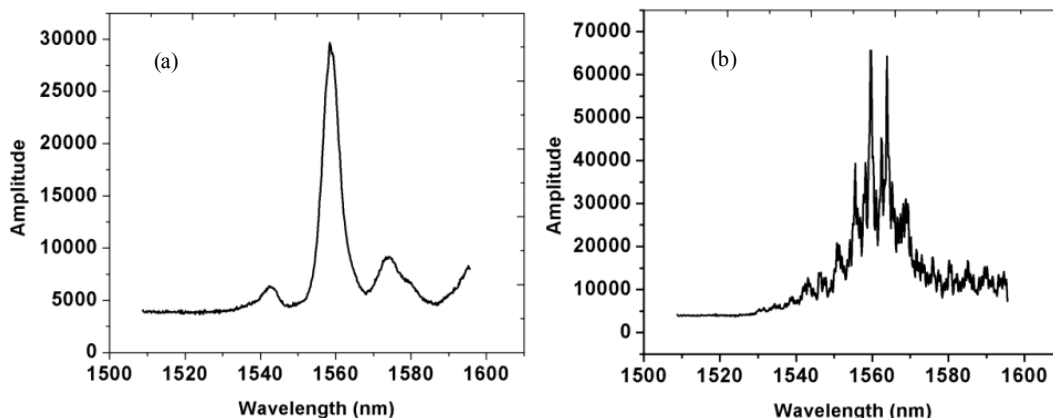


Figure 4: The reflection spectra of the inscribed FBGs in the two fibre samples

As may be seen, all 3 inscriptions were successful, yielding significant reflection spectral profiles, with the 2-FBG array exhibiting much lower signal-to-noise ratio due to the relatively long fibre length (75cm) that has to be traversed twice. We remind the readers also that at these wavelength regions the fibre loss is extremely high. As for the reflection widths, as could be expected the shorter FBG of 200 periods (Figure 4a) shows a broader reflection spectrum of about 3nm, whereas the FBGs in the array, having 1,000 periods each, show a much narrower response.

5. Summary

To summarise, we have shown that fibre Bragg gratings may be inscribed onto the new type of polymer optical fibres that has been developed based on an advanced, single-step and highly scalable UV curing (photo-polymerization) process. The fibres show, at the moment, relatively high transmission losses but further improvements are under way. The FBGs were straight-forward to inscribe, with the fibres showing good mechanical properties. The FBG responses were measured and presented showing expected characteristics. These are just initial results that will be studied more deeply and improved in the near future.

6. References

- [1] <http://www.intellisiv.co.il/>
- [2] see, for example: M.G. Kuzyk, *Polymer Fiber Optics: Materials, Physics, and Applications* (CRC Press Boca Raton, Fla.) 2007, p 146.
- [3] A. Lacraz, M. Polis, A. Theodosiou, C. Koutsides, and K. Kalli "Femtosecond laser inscribed Bragg gratings in low loss CYTOP polymer optical fiber", *IEEE Photonics Technology Letters*, 27(7), 693–696, 2015.



Dynamic damage detection of a cantilever carbon beam using a FBG array inscribed in polymer gradient index multimode CYTOP fibre

A. Theodosiou^{1,2*}, K. Kalli^{1*} and M. Komodromos²

1. Nanophotonics Research Laboratory, Department of Electrical Engineering, Cyprus University of Technology, Limassol, Cyprus.

2. Department of Electrical Engineering, Frederick University, Nicosia, Cyprus.

*Corresponding authors: theodosiou.antreas@gmail.com, kyriacos.kalli@cut.ac.cy

Abstract: In this paper we report on the use of a multiple-FBG array inscribed in gradient index multimode CYTOP POF using an efficient femtosecond laser inscription method. The FBG array was mounted across the cantilever as a quasi-distributed sensor and the time-dependent wavelength information of each particular FBG-point sensor was recovered using a commercial spectrometer, designed to operate at 1550nm. We adjusted the degree of damage detection by using different weights suspended in the middle of the flexible beam.

1. Introduction

Fibre Bragg grating (FBG) sensors in polymer optical fibres (POFs) are typically inscribed in polymethyl methacrylate (PMMA) or cyclic olefin copolymer (TOPAS) materials [1-4]. The key advantage is the very high strain response offering a large wavelength tuning range that can exceed 75 nm, because of the low Young's modulus [5-6]. However, the material losses in both cases are exceptionally high in the near infrared, a wavelength range that is desirable as it offers a compatibility with the majority of optical fibre components, and commercial sensor demodulators. The high optical losses adversely affect FBG sensor applications in PMMA and TOPAS to short distances of a few tens of centimetres. As a result their use for advanced applications, such as multiple FBG sensor arrays, is limited. Bearing this in mind we have focused on other polymer optical fibres based on the polymer CYTOP that is available as a gradient index multimode fibre. CYTOP has excellent transparency at 1550nm allowing for the development of FBG sensing arrays in POF that are tens of metres in length [7]. All the CYTOP POFs that are commercially available are multimode fibres, and FBG inscription in multimode fibres introduces a multi-peak spectrum because of grating-core mode coupling [8-9]. This effect causes difficulties with respect to the interrogation of the FBGs. To overcome this potential hurdle we have used a femtosecond laser inscription method to record FBGs in CYTOP multimode optical fibre by carefully controlling the grating depth, width and length we are able to avoid many of the multiple modes that are typically measured for FBGs in multimode optical fibres [10-11]. We apply this inscription method for the development of a simple interrogation scheme that is used for dynamic health monitoring of a cantilever carbon helicopter air-blade beam. We use a multiple-FBG array inscribed in gradient index multimode CYTOP POF using the aforementioned, efficient femtosecond laser inscription method. The FBG array was mounted across the cantilever as quasi-distributed sensor and the time-dependent wavelength information of each particular FBG-point sensor was recovered using a commercial spectrometer, designed to operate at 1550nm. We adjusted the level of the detected "damage" by using different weights suspended in the middle and at the end of the beam.

2. Experimental details and Results

A femtosecond laser system (HighQ laser femtoREGEN) was used for the inscription of the FBG array. The fibre sample was mounted to an air bearing stage system (Aerotech) for accurate computer controlled translation on two axes during the inscription process. Six FBGs were inscribed in a multimode gradient index CYTOP polymer fibre and the reflection spectrum of the FBG array is shown in Fig. 1. The FBGs were inscribed using the plane-by-plane femtosecond laser inscription method [10]. Each grating consisted of 300 planes with the pitch between two consecutively planes $\sim 2.2\text{-}\mu\text{m}$. Small variations of the grating period were used for the inscription of the rest of the gratings in the FBG array. The fibre had a $62.5\text{-}\mu\text{m}$ core diameter, a cladding layer of $20\text{-}\mu\text{m}$ and an additional polyester and polycarbonate outer cladding to protect the fibre. The total length of the fibre strand was $\sim 1\text{m}$ and the physical distance between the FBGs was 3-cm.

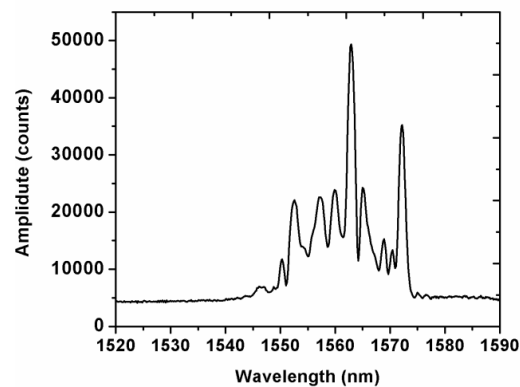


Figure 1: Multiple-FBG array reflection spectrum inscribed in multimode gradient index CYTOP polymer fibre using the plane-by-plane femtosecond laser inscription method.

The multiple FBG array was mounted on a carbon cantilever beam with total length 320-mm, as shown in Fig. 2. A broadband light source (Thorlabs ASE730) was used to illuminate the polymer array and the reflection spectrum was measured through a circulator with a commercial spectrometer (IBSEN I-MON 512 High speed). Note that the coupling between the multimode polymer fibre and the single mode silica was realized using a 3-D manual translation stage and index matching gel was used between the fibres to reduce Fresnel reflections.

The cantilever beam was fixed at one end and the other end was left free to perform a free-vibration motion. We interrogated the response of the FBG array and we recovered the time-dependent wavelength information of each FBG separately for the period of the fluctuation; examples of the raw time-dependent data are shown in Fig. 3. The results for each particular FBG were normalized and the shape of the beam during the vibration was recovered. Note that the FBG array was placed on the beam and covered only part of the beam, as shown in Fig. 2 (red line).

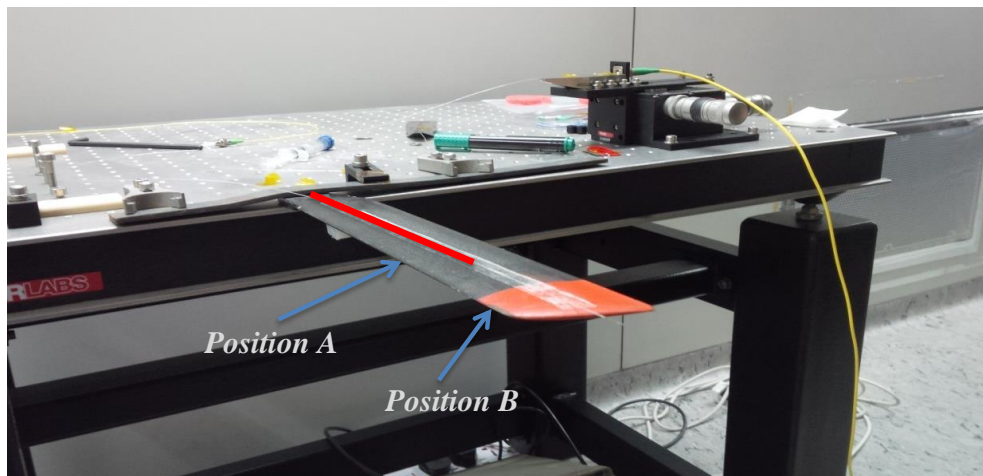


Fig. 2: Experimental setup for damage detection of a cantilever beam using a multiple FBG array inscribed in a multimode gradient index multimode CYTOP fibre.

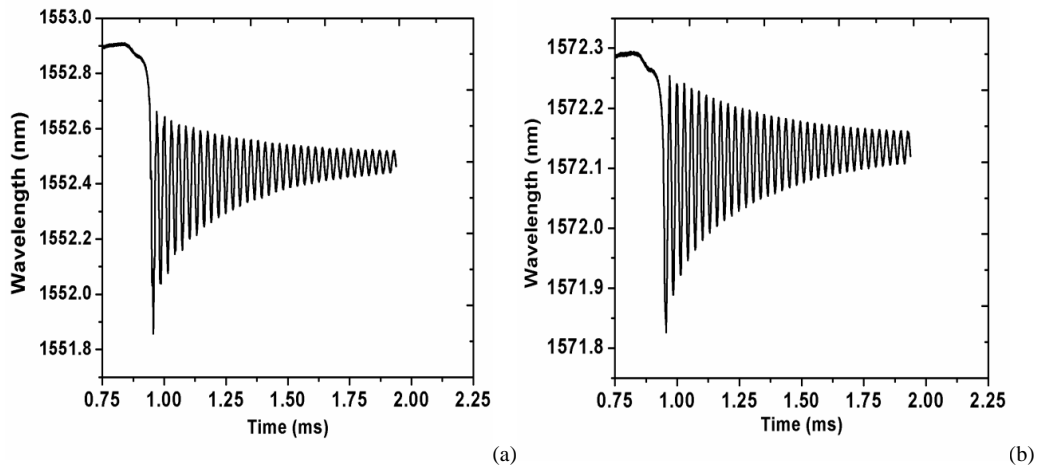


Fig. 3: Time-dependent wavelength information data for two FBGs as recovered using a commercial spectrometer (IBSEN I-MON 512 High speed).

We attempted to mimic the introduction of some degree of “damage” on the beam by adding weights to various positions on the beam. We adjust the position of the “damage” to the beam by changing the position of the weights, for example position A and position B, as shown in Fig. 2. The results for each case were normalized and the shape of the beam was extracted and compared with and without weights. In Fig. 4 we observe the fluctuation of the beam with no load (black line), with the load at position A (red line), and with the load at the position B (blue line). From the results it is clear that when the weights are placed close to a FBG point sensor the wavelength shift indicates a change at that location; conversely far from the FBG point sensors there is poor recovery of information by the FBG point sensors.

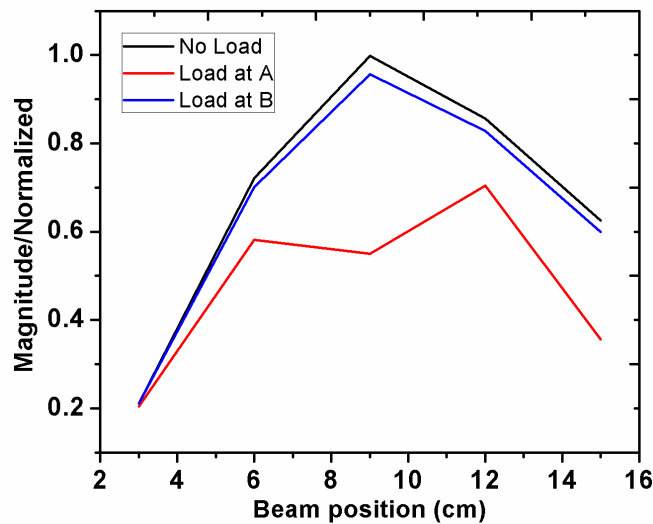


Fig. 4: Comparison between the beam shapes of the cantilever when weights are placed at different positions on the beam.



3. Conclusion

We report on the inscription of a multiple FBG array in gradient index multimode CYTOP fibre using a femtosecond laser inscription method. The FBG array was mounted on a cantilever beam and used as quasi-distributed sensor for the monitoring of the vibration response of the beam. The time-dependend wavelength information was recovered for each particular FBG point sensor and the shape of the beam during the vibration was recovered. Finally, we introduced some degree of “damage” on the beam by using different weights suspended in middle of the beam and we compared the results with and without load to identify the position of the damage.

4. Acknowledgements

The authors want to thank Ultra 555T LAE Ltd. for their support.

6. References

- [1] David J. Webb, Kyriacos Kalli, Karren Carroll, Chi Zhang, Michael Komodromos, Alex Argyros, Maryanne Large, Grigoriy Emiliyanov, Ole Bang, Erik Kjaer, “Recent developments of Bragg gratings in PMMA and TOPAS polymer optical fibers”, Proc. of SPIE, Advanced Sensor Systems and Applications III, Vol. 6830, 2007.
- [2] Y. Wu et al., “Humidity insensitive TOPAS polymer fiber Bragg grating sensor”, Optics Express, Vol. 19, No. 20, pp. 19731-19739, 2011.
- [3] Nielsen, K., Rasmussen, H. K., Adam, A. J. L., Planken, P. C. M., Bang, O., and Jepsen, P. U. “Bendable, low-loss Topas fibers for the terahertz frequency range,” Optics Express 17(10), 8592-8601 (2009).
- [4] C. Zhang, W. Zhang, D.J. Webb, G.D. Peng, “Optical fibre temperature and humidity sensor”, IET Electronics Letters, April 2010.
- [5] Z. Xiong, G. D. Peng, B. Wu, P. L. Chu, “Highly tunable Bragg gratings in single-mode polymer optical fibers”, IEEE Photonics Technology Letters, Vol. 11, No. 3, March 1999.
- [6] P. L. Chu, G. D. Peng, and Z. Xiong, “Highly-tunable polymer optical fiber gratings,” in Proc. 8th Int. POF Conf. '99, July 1999, pp. 242–245.
- [7] Amedee Lacraz, Antreas Theodosiou, Kyriacos Kalli, “Femtosecond laser inscribed Bragg gratin arrays in long lengths of polymer optical fibres; a route to practical sensing with POF”, IET Electronics Letters, August 2016.
- [8] Toru Mizunami, Tzvetanka V. Djambova, Tsutomu Niiho, Sanjay Gupta, “Bragg grating in multimode and few-mode optical fibers”, Journal of Lightwave Technology, Vol. 18, No. 2, February 2000.
- [9] Changgui Lu, Yiping Cui, “Fiber Bragg grating spectra in multimode optical fibers”, Journal of Lightwave Technology, Vol. 24, No. 1, January 2006.
- [10] A. Lacraz, M. Polis, A. Theodosiou, C. Koutsides, and K. Kalli, “Femtosecond laser inscribed Bragg gratings in low loss CYTOP polymer optical fiber”, IEEE Photon. Technol. Lett., vol. 27, no. 7, pp. 693–696, 2015.
- [11] A. Theodosiou, A. Lacraz, M. Polis, K. Kalli, M. Tsangari, A. Stassis, and M. Komodromos, “Modified fs-laser inscribed FBG array for rapid mode shape capture of free-free vibrating beams”, to be published IEEE Phot. Technol. Lett., April 2016.

Fiber Bragg grating-based Fabry-Perot interferometer in polymer fiber

G. Statkiewicz-Barabach^{1*}, P. Maniewski¹, P. Mergo², W. Urbanczyk¹

¹ Department of Optics and Photonics, Faculty of Fundamental Problems of Technology, Wrocław University of Science and Technology, Wybrzeże Wyspiańskiego 27, 50-370 Wrocław, Poland

² Laboratory of Optical Fiber Technology, Maria Curie-Skłodowska University, Pl. M. Curie-Skłodowskiej 3, 20-031 Lublin, Poland

*Corresponding author: gabriela.statkiewicz@pwr.edu.pl

In this work, we demonstrate for the first time Fabry-Perot interferometer (FPI) based on a pair of Bragg gratings fabricated in a step-index PMMA fiber with a core made of PMMA/PS copolymer (SI-PMMA/PS). To ensure better quality of the reflection spectra of Bragg gratings, and thus the FPI spectrum, the polymer fiber was annealed at 85°C for 5 hours, prior to the inscription of the gratings. To inscribe the gratings, we used a CW He-Cd laser with a power of 30 mW. The UV beam was directed through the phase mask and onto the fiber by a plano-convex cylindrical lens with a focal length of 75 mm, located at a distance of 75 mm from the fiber. The inscription process involved the use of the phase mask from Ibsen Photonics with a period of $\Lambda=885$ nm customized for 325 nm writing wavelength. It allowed for the inscription of the gratings with the primary Bragg peak at $\lambda_B=1312$ nm in the SI-PMMA/PS. By choosing an appropriate length of FP cavity between the gratings and fabrication time we can fabricate an interferometer with different number of fringes with very good visibility. Moreover, good long-term stability and very sharp, 3dB width ranging between 50 to 100 pm, fringes are obtained due to the fabrication of FPI with FBGs of type II. The proposed interferometer was tested for measurements of temperature and strain, in the range of 20-70°C and 0-20 mstrain respectively. We showed that the resolution of sensitivity measurements in this case is a few times better comparing to the measurement resolution of reflection spectrum of FBG. The sensitivity coefficients corresponding to fringe displacement are equal 1.09 nm/mstrain and -25.1 pm/°C, for strain and temperature respectively.

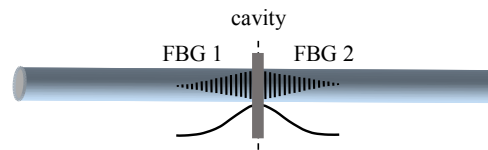


Fig. 1. The schematic configuration of the proposed FPI: Bragg gratings inscribed using a needle with a diameter of 0.1 or 0.3 mm positioned in the middle of the grating.

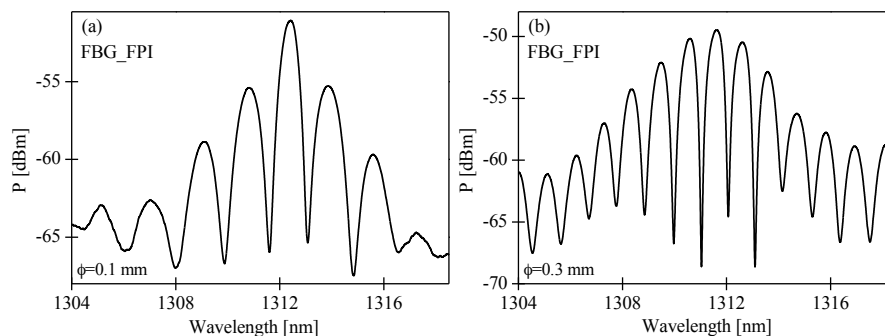


Fig. 2. Reflection spectrum of FPI composed of two Bragg gratings inscribed using a needle with a diameter of 0.1 mm (a) and 0.3 mm (b).

Key Words: Fabry-Perot interferometer, Bragg grating, polymer fiber

Full paper not available



Bragg grating photo-inscription in doped microstructured polymer optical fiber by 400 nm femtosecond laser pulses

X. Hu^{1*}, G. Woyessa², D. Kinet¹, J. Janting², K. Nielsen², O. Bang², P. Mégret¹, C. Caucheteur¹

¹ Electromagnetism and Telecommunication Department, University of Mons (UMONS), Boulevard Dolez, 31, 7000 Mons, Belgium

² DTU Fotonik, Department of Photonics Engineering, Technical University of Denmark, DK-2800 Kgs. Lyngby, Denmark

*Corresponding author: xuehao.hu@umons.ac.be

Abstract: In this paper, we report the manufacturing of high-quality endlessly single-mode doped microstructured poly(methyl methacrylate) (PMMA) optical fibers. Bragg gratings are photo-inscribed in such fibers by means of 400 nm femtosecond laser pulses through a 1060-nm-period uniform phase mask. Preliminary results show a rapid growing process of the reflection band. To preserve a good spectral shape, the photo-inscription process was limited to ~20 seconds, yielding an FBG reflectivity close to 40 %.

1. Introduction

Fiber Bragg gratings (FBGs) were first inscribed in step-index polymer optical fibers (POFs) in 1999 [1]. Since these first achievements and because POFs show different characteristics compared to silica fibers, many investigations have been conducted on FBG inscriptions [2,3] and on their sensing applications [4,5]. Although different polymer materials can be used to manufacture POFs, the most often encountered one is poly(methyl methacrylate) (PMMA). As a result of the low photosensitivity of pure PMMA [6], a photosensitizer is usually added in the fiber core to improve the performance [1-3,6-8]. Taking benzyl dimethyl ketal (BDK) [6,7] for example, the photopolymerization process starts in the core under UV light radiation at 325 nm and induces a positive index change. Another photosensitizer is trans-4-stilbenemethanol [2,3,8], whose isomer structure changes from trans to cis, resulting in a negative index change. However, additional dopants have to be added in the core and (or) the cladding to meet the single-mode fiber criterion [9], which limits the quantity of photosensitizers in the core. In order to achieve POFs more competitive for Bragg grating inscription, Sáez-Rodríguez et al. fabricated microstructured POFs (mPOFs) with only BDK doped in the core without any other dopants [6]. However, not only the doping process was time-consuming but also some bubbles appeared in the fiber core. Here, we report an improved fabrication process for BDK-doped mPOFs. Thanks to a higher temperature (~50 °C) environment, it took less time (35 minutes) to dope the core presenting a better cross-section uniformity after drawing. Finally, FBGs were inscribed by a femtosecond laser using the phase mask technique. The reflectivity reached 40% after ~20 seconds, confirming the good efficiency of the process.

2. MPOF fabrication

2.1 Selected hole doping

The doped mPOF drawn at DTU Fotonik was produced following several steps. During the first one, a commercial PMMA preform with a diameter of 60 mm was drilled allowing us to obtain a hollow three-ring hexagonal cladding structure with a hole diameter of 3 mm and a hole-hole pitch of 5 mm. Afterwards, the preform was drawn to the cane with a diameter of 5.5 mm with reduced hole diameter of 300 μm. In the second step, all the holes except the center one were blocked by UV-glue at one end of the cane (Figure 1a), and then the other end of the cane was immersed in the solution of methanol and BDK with a ratio of 3.3:1 in weight contained in a glassware. Because of capillary force, the solution was sucked into the center hole but not absorbed into other holes as a result of the higher air pressure in the blocked holes. When the cane was vertical in the solution, the distance between the solution level in the glassware and that in the center hole is only 4 cm. Thus, for drawing convenience the doping length was increased by tilting the cane by a large angle (Figure 1b). Then the only unblocked hole at the end was UV-glued as well (Figure 1c). Finally, the cane was moved back to be vertical in order to be easily controlled for the following step. The solution length in the center hole almost remained because of the negative air pressure in the hole (Figure 1d). As a result, more than 10 cm of



doping length was achieved, and meanwhile there was no solution diffusing into other holes or the cane surface. Thereafter, the setup was covered by a film to prevent the methanol evaporation and then it was put into the oven at 51.5 °C for 35 minutes. Compared to the room temperature, the higher temperature in our case greatly improves the diffusion speed [10].

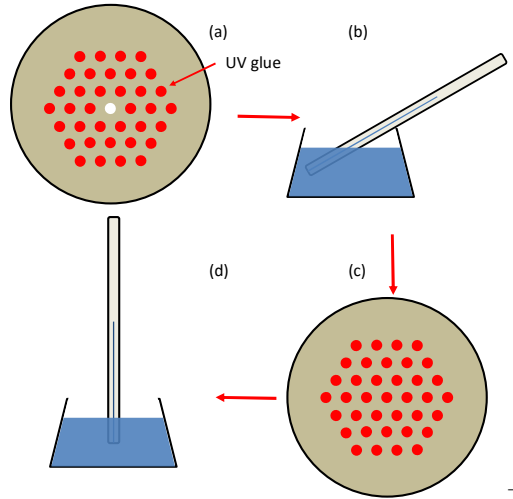


Figure 1. Scheme of BDK-doping preparation (all the holes blocked except the center hole at one end of the cane (a), the cane in the solution with a large angle (b), the center hole blocked at the same end of the cane (c) and the cane moved to vertical position (d)).

2.2 Preform annealing

In a following step, the cane was kept at 22 °C for 2 days and then annealed in the oven at 75 °C for two more days in order to make the methanol evaporate gradually to avoid the cracks generated on the hole surfaces. Figure 2 shows a cross-section image of the cane after these 4 days. The black area around the center hole is the BDK-doped PMMA.

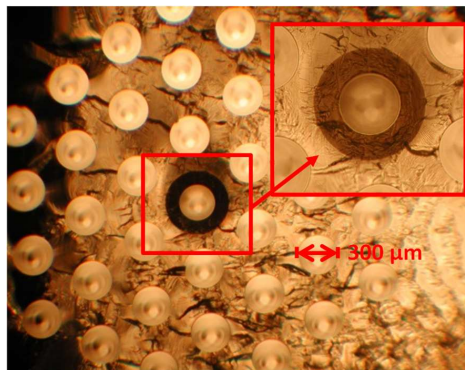


Figure 2. Cross-section image of the doped cane (4 days after doping).

2.3 Fiber drawing

In the last step, the cane was sleeved with several PMMA tubes to form a new preform, which was finally drawn to a mPOF. During the drawing process, the center hole was blocked by the BDK-doped PMMA by gravity, since the melting point of BDK (64 °C) is much lower than that of PMMA (160 °C). Figure 3 presents a perfect cross-section image of the fiber. The average hole diameter and pitch in the fiber are 1.5 μm and 3.79



μm , respectively. So, the ratio of the hole diameter to the pitch was calculated to be 0.4, confirming that the mPOF was endlessly single-mode. Since the diameters of the core and the cladding are $6 \mu\text{m}$ and $150 \mu\text{m}$, respectively, this fiber can be easily connectorized with a standard single mode silica optical fiber.

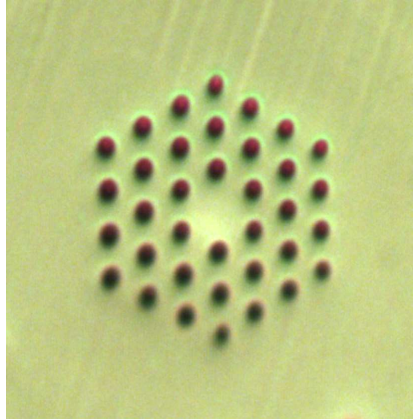


Figure 3. Cross-section image of the doped fiber.

3. FBG fabrication

After manufacturing the doped mPOF, the grating was inscribed at the University of Mons thanks to a femtosecond laser and a phase mask, both optimized to operate at 400 nm . The beam diameter was 6 mm with a power of 8 mW , which was tightly focused on the fiber core by a 5-cm -focal-length cylindrical lens. The experimental set-up is similar to the one used to inscribe grating in step-index POFs, as done in our previous work [11]. During inscription, the grating evolutions were recorded in both reflection and transmission modes, as shown in Figures 4 and 5, respectively. FBG reflection peaks appeared and grew gradually with a blue wavelength shift because of the accumulated heat from the laser. Although the grating spectra present a good shape in both reflection and transmission modes, the noise level in reflection started to increase dramatically after 16 seconds and the transmission losses grew at a rate of 0.1 dB/s . Hence, to keep a grating shape of sufficiently good quality, the photo-inscription process was limited to $\sim 20 \text{ s}$. The corresponding FBG reflectivity has been computed equal to 40% , which is by far enough for sensing applications. The aforementioned phenomena might be attributed to the BDK-doped core that, compared to pure PMMA, has a lower glass transition temperature (T_g) and a lower melting point. Thus, to produce gratings with a higher reflectivity, both laser power and inscription time should be optimised.

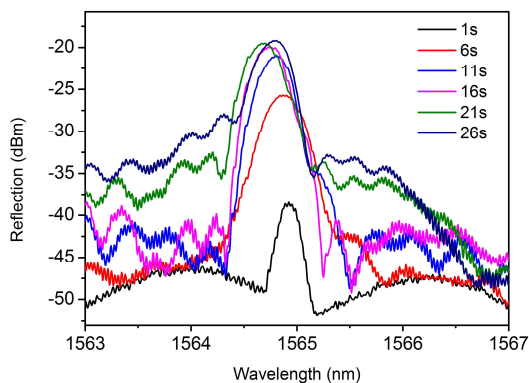


Figure 4. Evolution of the reflected amplitude spectrum during the photo-inscription process.

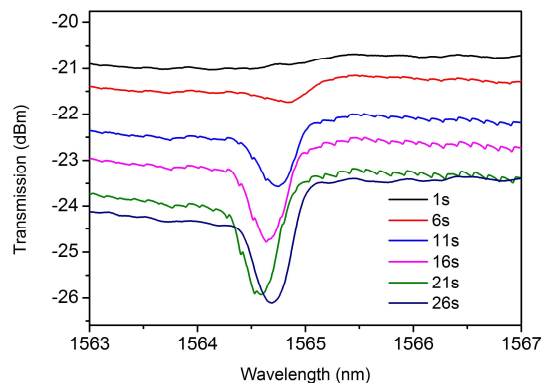


Figure 5. Evolution of the transmitted amplitude spectrum during the photo-inscription process.



4. Conclusion

In the first part of this paper, we reported the manufacturing of BDK-doped mPOF. Thanks to the selected center hole doping technique in the cane phase, the fiber was drawn with perfect cross-section image. In the second part, uniformed FBGs were photo-inscribed in the mPOF using 400 nm femtosecond laser pulses with the phase mask technique reaching saturation after 21 seconds with a reflectivity of 40 %.

5. Acknowledgements

The research leading to these results has received funding from the People Programme (Marie Curie Actions) of the European Union's Seventh Framework Programme FP7/2007-2013/ under REA grant agreement n° 608382. This research has also been conducted in the frame of the *ERC (European Research Council) Starting Independent Researcher Grant PROSPER* (grant agreement N° 280161 – <http://www.umons.ac.be/erc-prosper>) and the *Actions de la Recherche Concertées* research programme (PREDICTION project) supported by the *Ministère de la Communauté française de Belgique—Direction générale de l'Enseignement non obligatoire et de la Recherche scientifique*. C. Caucheteur is supported by the F.R.S.-FNRS.

6. References

- [1] Z. Xiong, G. D. Peng, B. Wu, and P. L. Chu, "Highly tunable Bragg gratings in single-mode polymer optical fibers," *IEEE Photon. Technol. Lett.* 11(3), 352-354 (1999).
- [2] X. Hu, C.-F. J. Pun, H. Y. Tam, P. Mégret, and C. Caucheteur, "Highly reflective Bragg gratings in slightly etched step-index polymer optical fiber," *Opt. Express* 22(15), 18807-18817 (2014).
- [3] X. Hu, D. Kinet, P. Mégret, and C. Caucheteur, "Control over photo-inscription and thermal annealing to obtain high-quality Bragg gratings in doped PMMA optical fibers," *Opt. Lett.* 41(13), 2930-2933 (2016).
- [4] D. J. Webb, "Fibre Bragg grating sensors in polymer optical fibres," *Meas. Sci. Technol.* 26(9), 092004 (2015).
- [5] X. Hu, D. Saez-Rodriguez, C. Marques, O. Bang, D. J. Webb, P. Mégret, and C. Caucheteur, "Polarization effects in polymer FBGs: study and use for transverse force sensing," *Opt. Express* 23(4), 4581-4590 (2015).
- [6] D. Sáez-Rodríguez, K. Nielsen, H. K. Rasmussen, O. Bang, and D. J. Webb, "Highly photosensitive polymethyl methacrylate microstructured polymer optical fiber with doped core," *Opt. Lett.* 38(19), 3769-3772 (2013).
- [7] Y. Luo, Q. Zhang, H. Liu, and G. D. Peng, "Gratings fabrication in benzildimethylketal doped photosensitive polymer optical fibers using 355 nm nanosecond pulsed laser," *Opt. Lett.* 35(5), 751-753 (2010).
- [8] J. M. Yu, X. M. Tao, and H. Y. Tam, "Trans-4-stilbenemethanol-doped Photosensitive Polymer Fibers and Gratings," *Opt. Lett.* 29(2), 156-158 (2004).
- [9] D. Gloge, "Weakly guiding fibers," *Appl. Opt.* 10(10) 2252-2258 (1971).
- [10] N. L. Thomas, and A. H. Windle, "Transport of Methanol in Poly(methyl methacrylate)," *Polymer* 19(3), 255-265 (1978).
- [11] X. Hu, D. Kinet, K. Chah, P. Mégret, and C. Caucheteur, "Bragg gratings inscription in step-index PMMA optical fiber by femtosecond laser pulses at 400 nm," *Proc. SPIE* 9916, 99161X (2016).



Fabrication and characterization of a lumogen-orange-doped polymer optical fibre

I. Parola^{1*}, E. Arrospide², M.A Illarramendi¹, I. Ayesta² J. Zubia³, N. Guarrotxena⁴, O. García⁴ and C. Vazquez⁵

1: Dept. Applied Physics I, University of the Basque Country UPV/EHU, Faculty of Engineering of Bilbao, Alda. Urquijo s/n, E-48013 Bilbao, Spain.

2: Dept. Applied Mathematics, UPV/EHU, Faculty of Engineering of Bilbao.

3: Dept. Communication Engineering, UPV/EHU, Faculty of Engineering of Bilbao.

4: Instituto de Ciencia y Tecnología de Polímeros (ICTP), Consejo Superior de Investigaciones Científicas (CSIC), Juan de la Cierva 3, Madrid 28006, Spain.

5: Electronics Technology Department, Universidad Carlos III de Madrid, Madrid, Spain.

*Corresponding author: itxaso.parola@ehu.eu

Abstract: In this work the steps followed for the fabrication of lumogen-orange-doped polymer optical fibres, are presented together with a spectral and temporal characterization of the emission properties of these doped POFs. This characterization includes a detailed study of the effects of the propagation distance and of the fluorescence life-times.

Key Words: doped polymer optical fibres; organic dyes; polymer optical fibre fabrication; fluorescent materials; fibre drawing.

1. Introduction

Over the last few years, polymer optical fibres (POFs) have raised a great interest in applications such as short-haul communication links and a wide variety of sensing applications. Due to their low manufacturing temperatures, it is possible to embed a large range of active materials into them, ranging from conjugated polymers, to rare-earth ions and organic dyes with large absorption and emission cross sections. Therefore, the potential of these fibres is widely improved, and they become suitable for achieving efficient applications in the field of lasers, amplifiers, illuminators, switches and sensors in the visible region [1,2]. One of the major drawbacks of these devices is their operational life-time, limited by thermal and/or chemical degradation processes. Dyes derived from perylene, as it is lumogen-orange, have particularly attractive optical properties due to an exceptional chemical, thermal and photochemical stability [3]. Moreover, recent studies on UV/blue-to-visible light converter luminescent solar concentrators have been reported using fibre geometry and these types of dyes [4].

The aim of this work is to present the steps followed for the fabrication of lumogen-orange-doped polymer optical fibres, and to report a spectral and temporal characterization of the emission properties of these doped POFs.

2. Experimental

2.1. Materials and characterization of the polymer PMMA sample

Commercial poly-(methyl methacrylate) (PMMA), obtained from Atochem, was used for the fabrication of the preforms. PMMA is an appropriate material for the fabrication of polymer preforms since it has very low oxygen permeability, and thus, it is suitable for avoiding photochemical degradation. PMMA sample was purified using tetrahydrofuran (THF, Scharlau) as solvent and water as precipitating agent. After that, it was washed in methanol and dried under vacuum at 40 °C for 48 h. THF was distilled under nitrogen, with aluminium lithium hydride (Aldrich) to remove peroxides immediately before use.

The molecular weight distribution of the PMMA sample was calculated by SEC using a chromatographic system (515 Waters Division Milipore). For measuring the glass transition



temperature (T_g), a differential scanning calorimeter (DSC) on a Mettler TA 300 instrument was employed. The molecular weight and the T_g values were found equal to 44,900 g/mol and 93.5 °C, respectively.

2.2. Preparation of the fibre and set-up

An active dye derived from perylene (Lumogen F Orange 240, 0.003 wt%, BASF) was physically incorporated into a previously prepared fully polymerized PMMA matrix. The preform was produced by an extrusion process, where the doped material is fed into a reaction chamber. There, it is, first, melted at 165 °C, and then, directed to the screw extruder. The material is pushed through a small nozzle (9 mm), and finally the preform is generated with a diameter value of 11 mm. The preform was annealed during two weeks in a climate chamber before drawing to a 1 mm fibre using our POF-drawing-tower at a maximum furnace-temperature of 185 °C (Figure 1.). The fibre-preform is continuously fed into the furnace, yielding homogeneous fibre at the other end.

The samples analyzed are only-core PMMA polymer optical fibres doped with lumogen-orange (LO), the dopant concentration being 0.003 wt%. The diameters of the samples are 1 mm with a tolerance less than 2 %. The fibre samples were cut into lengths of about 25 cm, and their ends were carefully hand-polished using polishing papers.

The prepared samples were transversally pumped in a spot of 1.2 mm of diameter using a tunable ultrafast femtosecond laser (Spectra Physics Mai Tai HP) with a wavelength range of 690 nm to 1040 nm and 80 MHz of repetition rate. This source emits Gaussian pulses with a temporal width of about 100 fs. The output signal of a frequency-doubler (Radiantis Inspire Blue) was used, enabling optical pumping at the desired wavelengths in the visible region. The pulse energy was controlled by adjusting a beam splitter, located between the laser and the frequency-doubler.

For the acquisition of the emission spectra, an ultrafast Streak Camera detector with a resolution of 10 ps was used (Hamamatsu C5680-21). This detector can operate in a spectral range covering from 200 to 800 nm. The device comprises a delay unit for the proper synchronization of the measurement. To measure the effects of the propagation distance, a linear stage driven by a motor controlled was employed in order to change the position of the excitation point.

The absorption spectra were obtained at room temperature on a Cary 50 UV-Vis spectrophotometer equipped with a fibre optic coupler accessory. The sample length was about 1 cm so that the absorption band of the dopant could be correctly detected.



Figure 1. Photograph of the preform settled in the drawing tower.

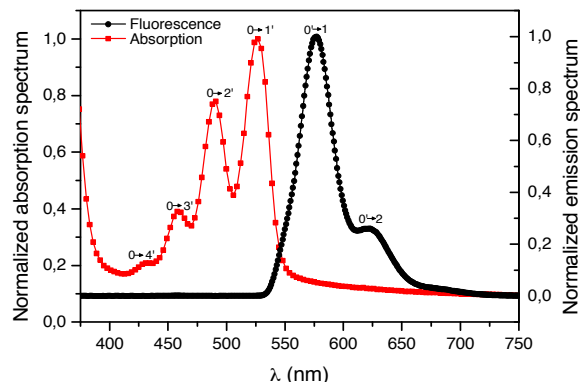


Figure 2. Absorption and emission spectra of our fibre at room temperature.



3. Results and discussion

3.1. Absorption and emission bands

The absorption and emission bands of the LO doped fibres are shown in Figure 2. The absorption peaks corresponding to transitions from the ground state, S_0 , to several vibrational levels of the excited state, S_1 , were observed at 430, 457, 490 and 526 nm in that order, this latter being the strongest absorption peak. The fluorescence was acquired by exciting the sample at 457 nm, with a non-excited distance, z_{ne} , of 3.3 cm. The integration time of the emission was 100 ms, and the entrance slit was $0.25 \mu\text{m}$ (spectral resolution of 1 nm). The emission band presents only a two-peak structure, which are called, from now on, main and secondary peaks respectively. Note that there exists an overlap between the absorption and the emission spectra. This fact will cause shifts in the emission when the distance travelled by the light is changed, due to reabsorption and reemission effects.

3.2. Effects of the propagation distance

In this subsection the effects of varying the total propagation distance of the fibre will be analyzed. The sample was excited at 457 nm with a pumping irradiance of 0.22 W/cm^2 , which was high enough for detecting the emission. When the excitation point is moved further from the detector, there is a decrease on the measured intensity, and the emission peak is shifted towards higher wavelengths, due to the aforementioned reabsorption and reemission effects. The evolution of the emission spectra for different propagation distances is represented in Figure 3(left). As can be seen, the emission spectrum undergoes a red-shift while the non-excited length of the fibre increases. It is also shown that there is a growth on the intensity of the secondary emission peak. This may be due to the importance this peak acquires as the emission endures the aforementioned red-shift. On the right side of Figure 3, the evolution of the peaks of the main and secondary emission bands is shown. By performing a linear fit to both experimental data, it is demonstrated that both peaks endure similar red-shifts, namely $0.54 \pm 0.04 \text{ nm/cm}$ and $0.67 \pm 0.09 \text{ nm/cm}$ for the main peak and the secondary peak respectively. This kind of results are of great interests for the design of displacement sensor applications based on doped POFs.

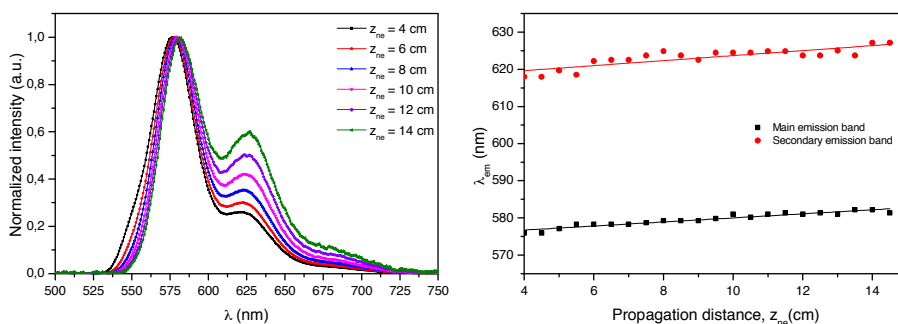


Figure 3. Evolution of the emission spectra for different propagation distances (left). Evolution of the emission peaks as a function of the propagation distance (right).

3.3. Calculation of the life-time

For the temporal characterization of the fibre, the sample was excited at 457 nm with an irradiance of 0.042 W/cm^2 . Figure 4(left) shows the evolution of the detected intensity, both in wavelength and in time. On a temporal swept, no changes on the spectral characteristics of the emission have been detected. At the same time the decay of the fluorescence has been analyzed for different wavelengths. In Figure 4(right), the fluorescence decay for the main emission peak ($\lambda_{em} = 580 \text{ nm}$) is represented for an integration time of 50 ns. As can be seen, the electrons are relaxed to the



ground-state in a process that can be well reproduced to a single exponential equation. By fitting the experimental curves, the obtained life-time value is 4.75 ± 0.02 ns. This result is in agreement with previously reported values obtained for LO doped acrylic plastic plates [5]. In this case too, no variations on the life-times have been detected for different emission wavelengths.

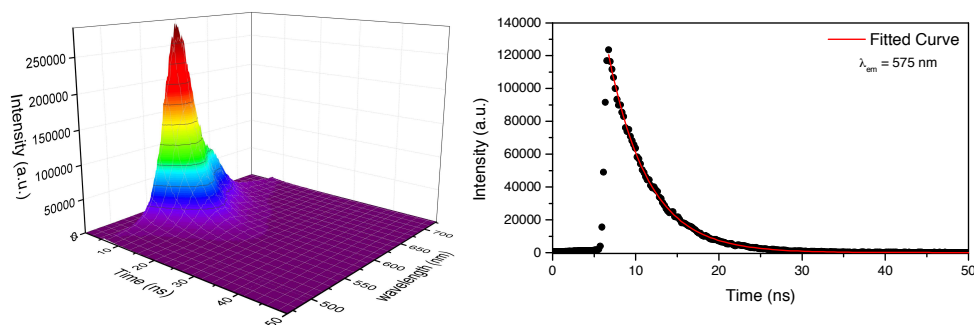


Figure 4. Evolution of the intensity detected on the streak camera (left). Fluorescence decay curve for the main emission peak (right). In both cases $\lambda_{ex} = 457$ nm, and a z_{ne} of 3.3 cm.

4. Conclusions

We have presented the steps followed for a complete fabrication process of a lumogen-orange-doped polymer optical fibre, from the characterization of the polymer, to the two-step method of extrusion and drawing. Besides, these home-made fibres have been characterized both spectrally and temporally. The effects of the propagation distance have been studied, and it has been demonstrated that the two emission peaks corresponding to the main and secondary emission bands undergo red-shifts with slopes of 0.54 ± 0.04 nm/cm and 0.67 ± 0.09 nm/cm respectively. Regarding the temporal characterization, the fluorescence life-time of the dopant has also been measured, obtaining a value of 4.75 ns in the emission peak, and detecting no variations when the analyzed emission wavelength is changed.

5. Acknowledgments

This work has been funded in part by the Fondo Europeo de Desarrollo Regional (FEDER); by the Ministerio de Economía y Competitividad under project TEC2015-638263-C03-1-R; by the Gobierno Vasco/Eusko Jaurlaritza under projects IT933-16 and ELKARTEK; by the University of the Basque Country UPV/EHU under programmes UFI11/16 and Euskampus; and by Ministerio de Economía y Competitividad under project MAT2014-57429-R. The work carried out by I. Parola has been funded by a research grant given by the Departamento de Educación, Política Lingüística y Cultura del Gobierno Vasco/Eusko Jaurlaritza for her PhD thesis.

6. References

- [1] Illarramendi, M.A. et al., "Amplified spontaneous emission in graded-index polymer optical fibers: theory and experiment," *Optics Express*, 21, no. 20, pp. 24254-24266. (2013).
- [2] Parola, I. et al., "Characterization of the optical gain in doped polymer optical fibres," *J. Lumin.* 177, pp 1-8. (2016).
- [3] Cerdán, L. et al., "New perylene-doped polymeric thin films for efficient and long-lasting lasers," *J. Mater. Chem.*, 22, pp. 8938-8947. (2012).
- [4] Y Edelenbosch, O. et al., "Luminescent solar concentrators with fiber geometry," *Opt. Express*. 21, pp. A503-A514 (2013).
- [5] Fukuda, M. et al., "Perylene Orange Doped Acrylic Polymer for Solid-State Dye Laser," *J. Appl. Phys.*, 40, pp. L440-L442. (2001).



Joining intransparent components by UV-hardening systems through POF based UV-light initiation

Stephanie Bier^{1*}, Benjamin Mohr^{2*}, Bernd Marx¹, Alexander Schiebahn¹, Markus Beckers², Gunnar Seide², Thomas Gries², Uwe Reisgen¹, Christian-A. Bunge³

1. Welding and Joining Institute (ISF) at RWTH Aachen University
Pontstraße 49
52062 Aachen, Germany
2. Institut für Textiltechnik (ITA) at RWTH Aachen University
Otto-Blumenthal-Str. 1
52074 Aachen, Germany
3. Institut für Kommunikationstechnik at Hochschule für Telekommunikation Leipzig,
Gustav-Freytag-Straße 43 - 45
04277 Leipzig, Germany

*Corresponding authors: bier@isf.rwth-aachen.de
 Benjamin.Mohr@ita.rwth-aachen.de

Abstract: UV-light hardening adhesives provide many advantages as fast curing and good handling compared to PUR-based adhesives. But currently their use is limited as they may only be used if at least one adherent is transparent. The authors proved that the use of UV-light hardening adhesive systems on non-transparent adherents is possible using POF for UV-light initiation in the adhesive gap. Therefore the POF is integrated to the adhesive gap and remains there after curing is completed. The UV light is guided through the POF and initiates the joining process, which may reduce the processing time to below 3 minutes.

1. Introduction

Adhesives provide more than 13 million tons in annual sales worldwide and a projected growth of 3.1% p. a.. By 2022 a rapidly growing and economically much-promising mass market is predicted [1]. The Tech Strategy 2020, of the German federal government schedules a development towards more resource efficient, environmentally friendly and socially acceptable production processes. This is also reflected in a trend towards the use of environmentally friendly, solvent-free adhesives such as UV-curing adhesives in the production of Automotive.

At the present state of the art UV curing adhesives (reaction by radical polymerization) may be applied only, if there is at least one transparent adherent, since conventional UV adhesives cure in principle only where UV-light exposure takes place. Thus, there is no cure in shadow areas. A particularly striking example is the bonding of sensor holders on the windshield. Here 1K polyurethane adhesives are usually used, while long curing times are one of the main deficits. Furthermore, the adhesive bond has to be stored more than 24 hours after the joining operation, before the adhesive has reached its ultimate strength and the windshield can be further processed.

In the presented research it shall be proven, that UV-light initiation based on POF integrated to the adhesive layer allows joining intransparent adherents by UV-curing adhesives. Therefor the three step approach shown in Figure 1 was followed.

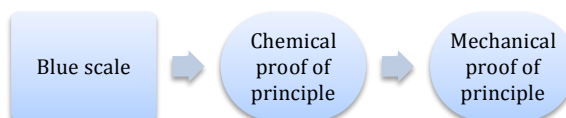


Figure 1: Three step approach of proof of principle



2. Experimental tests

At first the UV light guidance of the POF should be proven by blue scale experiments. The second step was to prove, that the initiated UV-light is sufficient to start a curing reaction of the adhesive. Therefore Raman spectroscopy analysis had to prove the chemical reaction on a molecular level. At least a mechanical analysis by tensile shear tests shall prove the feasibility for use in a sensor holder system.

2.1 Materials

The POF investigated in this study is made of PMMA, supplied by Evonik Industries AG, Essen, Germany and produced by a special method of melt spinning process developed and patented by the ITA [2]. The UV-curing adhesive Dymax Multi-Cure 6-621-Series was supplied by Dymax Europe GmbH, Wiesbaden, Germany. Adherents made of aluminum (size: 25.00 mm x 100.00 mm) are used as samples for the tensile shear tests. ISO Blue scale No.1 based on DIN EN ISO 105 B-Serie was purchased from Carl von Gehlen Spezialmaschinen und Zubehör GmbH & Co. KG, Mönchengladbach, Germany.

2.2 UV-curing

The UV-curing adhesive is UV-irradiated with a new strategy of curing (see Figure 2, D). Therefore the UV-spot lamp Dymax PC-3 Ultra (Dymax Europe GmbH, Wiesbaden, Germany) and a self-made UV-light coupling element is used to guarantee a lossless coupling of UV-light from spot lamp to POF. Furthermore, the POF is used as UV-light guidance into the adhesive layer. POF with a length of about 50-100 mm are used.

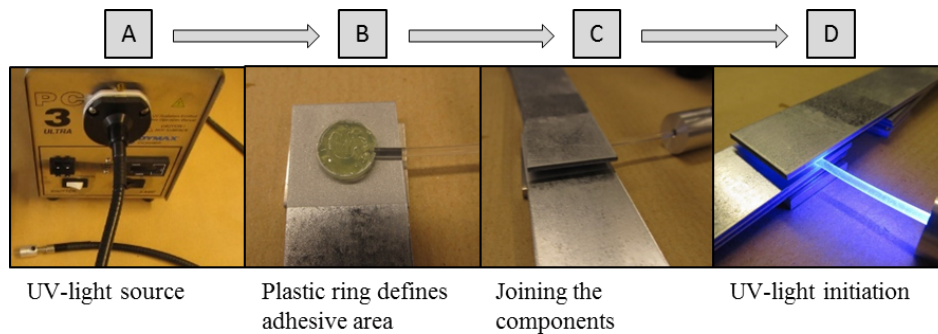


Figure 2: New developed UV-curing strategy

2.3 Measurements

Proof of UV-light guidance by blue scale experiments: First of all, experiments are carried out which investigate in the ability of fibers, especially POF, to guide UV-light. Blue scale No.1 based on DIN EN ISO 105 B-Serie is fixed on the POF in a radial and orthogonal way to the fiber (see Figure 3).

The sample is sealed up with aluminum foil to prevent that the UV-light of the sunlight simulator Sol2 (Dr. Hönle AG, Gräfeling, Germany) get into the sample by another way than through the fiber. The sample is exposed with UV-light for 4 weeks and evaluated concerning the bleaching of the blue scale.

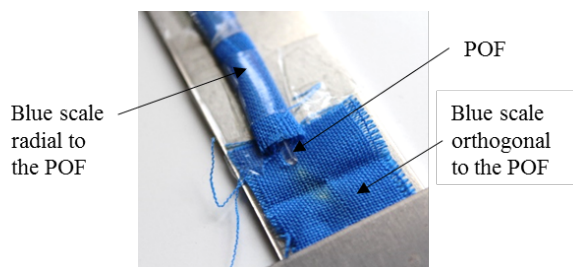


Figure 3: Sample for UV-irradiation in Sol2 before sealing with aluminum foil

Chemical proof of principle by Raman spectroscopy: To bring proof of feasibility on a molecular level the chemical conversion of C=C bonds is determined with a RFS 100/S Raman spectrometer with following parameters: Nd:YAG laser, $\lambda=1064$ nm, spectral resolution of the recorded spectra 4 cm^{-1} , laser power 250 mW (Bruker Corporation, Massachusetts, United states). The curing behavior of the UV-curing adhesive is analyzed by observing the changes in the Raman spectra concerning the peak at 3103cm^{-1} (CH stretching, unsaturated [3]). As reference the carbonyl peak at 1720cm^{-1} (C=O stretching [3]) is observed to consider variations, e.g. different sample thicknesses and instrumental recording. The C=C content of the uncured adhesive is defined as 100%. The adhesive samples are cured for 30 sec, 60 sec and 90 sec using the mentioned UV-curing strategy.

Mechanical proof of principle by tensile shear tests: Tensile shear tests based on DIN EN ISO 1465 are carried out to bring proof of feasibility on a mechanical level. Aluminum samples (25.00 mm x 100.00 mm) are joined by the use of UV-curing adhesives and the UV-curing strategy shown in figure 2. The bonding area is limited by a plastic ring with a diameter of 10.00 mm and a thickness of 1.00 mm. Furthermore, the bonding area of the aluminum sample is blasted with corundum and additionally cleaned with 2-propanol. The UV-light curing is performed for 60 sec. Five samples are manufactured.

3. Results and discussion

3.1 Proof of UV-light guidance by blue scale experiments

After UV-exposition the blue scale shows significant bleaching at the orthogonal positioned blue scale. At the radial positioned blue scale and the blank no bleaching effect could be recognized. In contrast, some further experiments were carried out with conventional glass fibers. In this study no light guidance could be proved in any case. In principle, the ability of PMMA-POF to guide and emit UV-light at the end of the POF is proved.

3.2 Chemical proof of principle by Raman spectroscopy

In principle, the Raman spectroscopy shows that the UV-curing strategy induces the decrease of C=C bonds, because of the decreasing peak at 3103 cm^{-1} (see Figure 4). The reason for this is the conversion of C=C bonds as a result of the light-induced radical polymerization.

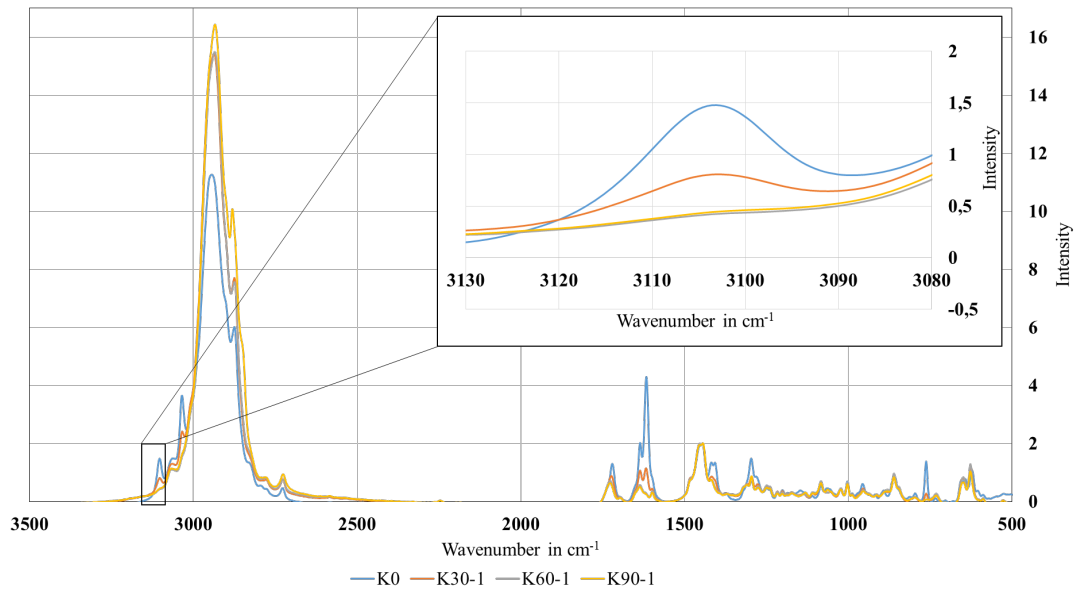


Figure 4: Raman spectra of UV-cured adhesives for different curing times (K0: uncured adhesive, K30-1:30 sec-cured adhesive, K60-1: 60 sec-cured adhesive, K90-1: 90 sec-cured adhesive)

As a consequence, the Raman spectroscopy shows that with increasing curing time (30-90 seconds) a homogenous curing profile can be generated within an adhesive layer of 1mm thickness. Furthermore, at curing times of 30 sec there can be recognized an increasing conversion of C=C bonds with decreasing distance to the POF (remaining C=C bonds in average 31-2%). At curing times of at least 60 sec the curing-profile disappears (remaining C=C bonds in average 2-3%). Combined, curing-profiles caused by increasing distance to the POF can be reduced by adequate curing times of at least 60 sec. As result the proof of principle for the UV-curing strategy is given on chemical basis.

3.3 Mechanical proof of principle by tensile shear tests

In general, cohesion strength can only be generated if there is a cross-linking respectively a curing induced by the UV-curing strategy and the initiating of a radical polymerization. As a consequence the tensile strength can be seen as indirect indicator of the curing-progress. The experiments show that an average tensile strength of 8.1 +/- 0.7 MPa can be realized. All samples showed an adhesive failure mode. 90 % of the adhesive area is cured, but there remains a non-cured adhesive area of 10 % in the periphery areas (see Figure 5).

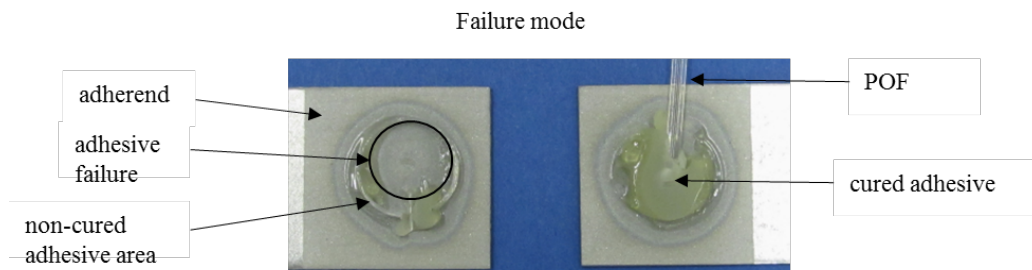


Figure 5: Failure mode analysis of tensile shear test

To sum it up, the experiment gives a proof of principle for the new developed UV-curing strategy on mechanical basic.



5. Conclusion

The presented research proves, that PMMA based POF are suitable for UV-light guidance. Furthermore, it shows that the guided UV-light is sufficient to trigger the curing reaction of the UV-curing adhesive. The mechanical analysis showed that the resulting adhesive bond provides potentially sufficient mechanical stability to be used for a sensor-holder system on windshields. Thus it has been verified, that it is possible to use POF based UV-light initiation to join intransparent adherents by UV-curing adhesives.

4. References

- [1] Ceresana eK, editor, Marktstudie Klebstoffe-Welt, 2nd Edition (2013), <http://www.ceresana.com/de/marktstudien/industrie/klebstoffe-welt/ceresana-markt-studie-klebstoffe-welt.html>, state: 01.06.2016
- [2] Becker, M., inventor: Freundes- und Förderkreis des Institutes für Textiltechnik der RWTH Aachen e.V., assignee; A process for melt spinning a varying over its cross section fiber and their use. German patent DE102013009169 B4.2016 May 12.
- [3] Socrates, G.: Infrared and Raman characteristic group frequencies: Tables and charts. Chichester: John Wiley and Sons Ltd.; Third Edition, 2004

PORTABLE POLYMER OPTICAL FIBRE CLEAVER

D. Sáez-Rodríguez^{1*}, R.Min¹, B.Ortega¹, K.Nielsen², O.Bang², D.J. Webb³

1: ITEAM, Universidad Politécnica de Valencia, Valencia, Spain,

2: DTU Fotonik, Dept. of Photonics Engineering, Technical University of Denmark, DK-2800 Kgs. Lyngby, Denmark.

3: Aston Institute of Photonic Technologies, Aston University, Birmingham, UK.

*Corresponding author: dasaerod@upv.es

Abstract: Polymer optical fibre (POF) is a growing technology in short distance telecommunication due to its flexibility, easy connectorization, and lower cost than the mostly deployed silica optical fibre (SOF) technology. Microstructured POFs (mPOFs) have particular promising potential applications in the sensors and telecommunications field, they could specially help to reduce losses in polymer fibres by using hollow-core fibres. However, mPOFs are intrinsically more difficult to cut due to the cladding hole structure and it becomes necessary to have a high quality polymer optical cleaver. In the well-known hot-blade cutting process, fibre and blade are heated, which requires electrical components and increases cost. A new method has recently been published to cut POF without the need for heating the blade/fibre, therefore electronically devices are not required if it is used a proper mechanical system. In this paper, we present a passive and portable polymer optical cleaver implemented with a mechanical system formed by a constant force spring and a damper.

Key words: POF, Polymer optical fiber, Polymer optical cleaver, cleaver, mPOF

1. Introduction

Photonic crystal fibers (PCF) are single material fibers with a specific holes pattern in the cladding to allow guidance of light; the first example was made by knight et. al. in 1996 [1]

The flexibility in design allowed by the microstructured geometry allows the manufacture of fibers with properties unachievable with step-index fibers, such as air guidance [2], endlessly single mode operation [3], larger or smaller modal area [4,5], etc... This has suggested a variety of applications including fiber lasers, nonlinear active fibers or biological sensing [6].

Polymer optical fiber (POF) technology has advanced rapidly in recent years and it is expected that it will form an integral part of datacom networks. They offer a broader bandwidth, easier installment replacement for copper cables [7]. In contrast to a glass optical fiber a thick POF will remain mechanically flexible, which, in combination with a large core, offers easy and inexpensive connectivity of fibers during installation. Despite these achievements, POF has not yet achieved widespread deployment; some of the technical reasons behind this are large modal dispersion, as a consequence of multimode operation, and the higher losses than silica fiber.

Polymer PCFs, commonly known as microstructured polymer optical fibers (mPOFs), were firstly made by M.A. Van Eijkelenborg et. al. in 2001 [8]. The variety of possibilities of mPOF can help to overcome the aforementioned problems. On the one hand, polymer hollow-core fiber can be implemented to reduce losses significantly; the first example of this kind of fiber was reported by Argyros et. al. [9] and according to their theoretical calculations [10] losses can be as small as 50 dB/km in PMMA based fibers, comparable to the CYTOP fibers [11].

Furthermore, fabricating an mPOF with proper control of the pitch and hole size in the hole array allows fibers with a large modal area working in single mode operation to be fabricated[4].

However, mPOF are intrinsically difficult to cleave due to the hole array, therefore present and future commercial applications will require the development of a portable high-quality polymer optical cleaver. So far, several methods have been implemented to cleave mPOF [12-14], but none of them is well suited to the creation of a portable device. In the most commonly used and effective approach, fiber and blade are heated close to the glass transition temperature of the polymer, and then, the blade cleaves the fiber with a controlled speed [13,14]; this method requires the assembly of a POF cleaver

with several electronic components (temperature and motor controller, heater, stepper motor, power supply) which make it expensive not electrically passive and hence hardly portable for outdoor applications. Recently, we have published a new method to cleave POF [15] at room temperature. The method is based on the time-temperature equivalence principle of polymers [16] which allows the heating of the blade and fiber to be replaced by a slow cleave. In this method, an end-face free of crazing is achieved by increasing the process of cleaving longer than a certain time, which is characteristic of each polymer. Allowing sufficient time for the cut enables the stress in the cutting tip to relax, preventing crazing.

Figure 1 shows the cleaver used in our previous work [15], where the fiber was sawed rather than chopped (we use the word chop to describe the case when the blade cuts the fiber by being moved in a direction at 90° to the blade edge). For the purposes of a detailed study, a translation stage was used to move the blade at different controlled constant velocities. The smaller the blade angle the higher the sawing time for a constant speed of the blade. An illustrative scheme is shown in fig. 2, which defines the blade angle α . According to [15], high quality PMMA cleaving was accomplished with relatively high blade velocities (0.1-1 mm/s) using blade angles from 1 to 5 degrees.

In this work, we present an electrical passive and portable POF cleaver, where the correct range of velocities can be achieved by using a simple mechanical system composed of a constant force spring and a damper.

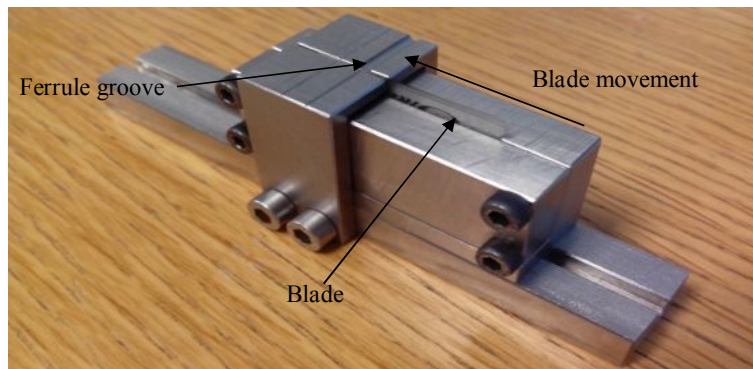


Figure 1: Fibre and blade positioning in the polymer optical cleaver

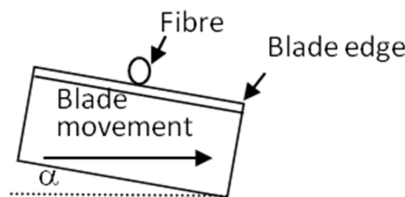


Figure 2: Transversal section of the cleave process

2. Cleaver fabrication

In order to make the cleaver portable, it was mounted onto a mechanical system composed of a constant force spring and a damper as showed figure 3.

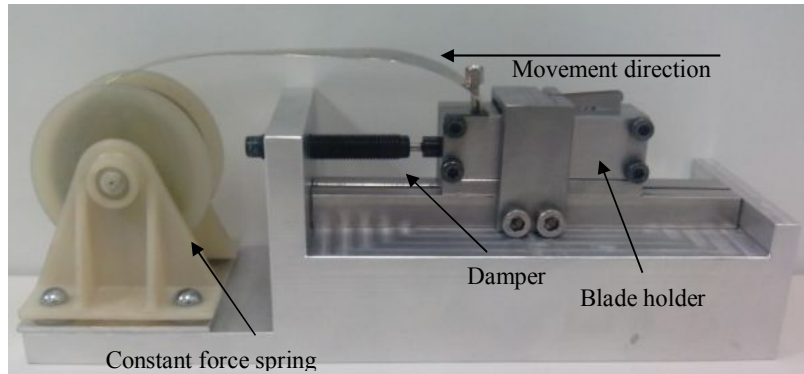


Figure 3: Full Polymer optical cleaver

In figure 3, the constant force spring pulls the blade holder and the damper dampens this movement. The constantly damped mechanical system is driven by the following differential equation:

$$\frac{d^2x}{dt^2} + \frac{b}{m} \cdot \frac{dx}{dt} - \frac{F_{SF}}{m} = 0 \quad (1)$$

where x is the position of the blade, F_{SF} is the difference between F_S (spring force) and F_F (friction force of the blade holder), b is the damping coefficient of the spring, t is the time and m is the mass of the blade holder. The solution of this equation gives the velocity of the blade as:

$$v(t) = \frac{F_{SF}}{b} \cdot \left(1 - e^{-\frac{b \cdot t}{m}} \right) \quad (2)$$

where v is the blade velocity. Using our system parameters, for times over a few milliseconds, $t \gg \frac{m}{b}$, the velocity is approximately constant and is given by the following expression:

$$v = \frac{F_{MR}}{b} \quad (3)$$

The spring was provided by Spiroflex and pulls with a constant force of 7,8 N. The damper was provided by Ace Controls Inc (model HB-12-10) and according to our experiments the b coefficient can be modified from 300 to 25000 N/m/s. For the minimum value, the damper can travel a distance 7.5 mm while a length of 5 mm is covered when set to its maximum value.

Three minor additional modifications were done to improve the cleaving process. Firstly, the fiber being cleaved was only held from one side unlike in [15] where it was clamped either side of the cutting point. Figure 4 shows both situations and typical results. In Figure 4(a) the fiber is held from two sides and the fiber is sawed in the middle. This creates axial stress in the fiber and consequently produces an end-facet with an end-crack, as can be seen in figure 4(c). This crack is observed in all the cuts in [15] and represents a region where part of the fiber has been torn away by the cleaving process. In contrast, in Figure 4(b) the fiber is only held from one side avoiding the stress and therefore it is free of such cracks, as shown in figure 4(d). Secondly, a new groove was included in the blade holder to allow cutting the fiber when it has been mounted inside a connector ferrule, as shown in figure 1.

Finally, a modified blade with one almost flat-side, as shown in figure 5, is employed in the cleaver. The flat-side of the blade is placed as close as possible to the clamping point of the fiber in figure 4 (b) in order to increase the stiffness of the fiber section between the blade and the clamping point, as is discussed in [15].

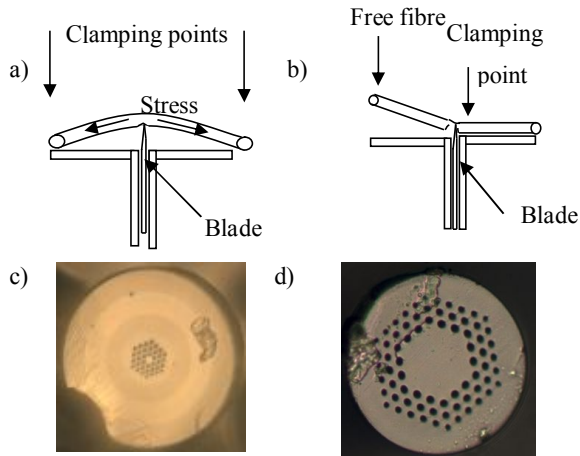


Figure 4: (a) Schematic with two sides fibre holding. (b) Schematic with one side fibre holding. (c) End-face cleave using scheme (a). (d) End-face cleave using scheme (b).

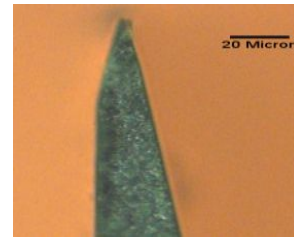


Figure 5: Photograph of the blade tip

3. Cleaving demonstration

A multimode microstructure polymer optical fibre (mPOF) based on PMMA was manufactured at Denmark Technical University (DTU), by using a fabrication procedure analogous to [15]. These fibre was used to perform a full characterization of the portable POF cleaver under different cutting times and angles.

The multimode fibre is depicted in figure 6. As it was demonstrated in [15], the end-face is free of crazes for enough long cutting times.

t (s)	2 degree	t (s)	3 degree	t (s)	4 degree	t (s)	5 degree
10.9		6.8		5.6		4.5	
8.8		7.5		3.8		1.3	
2.6		2.0		1.2		0.4	

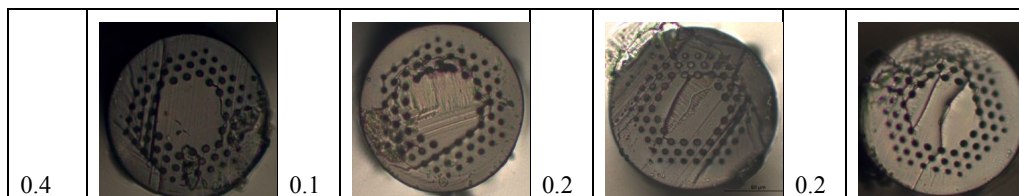


Table 1 Cleaving demonstration with multimode fiber.

3. Conclusions

In conclusion, we have described the construction and testing of the first high quality passive and portable polymer optical fiber cleaver. The device has been satisfactorily characterized by using a multimode microstructured polymer optical fiber which, in general, are difficult to cut.

Acknowledgements

This work was supported by a Juan de la cierva Program of the Spanish Government and by Generalitat Valenciana under Grant PROMETEO 2013/012. We also acknowledge the support of the China Scholarship Council.

References

- [1] J.C. Knight, T.A. Birks, P.St. Russell, D.M. Atkin "All-silica single-mode optical fiber with photonic crystal cladding" *Opt. Lett.*, **21**, 1547, 1996.
- [2] R.F. Cregan, B. J. Mangan, J. C. Knight, T. A. Birks, P. St.J. Russell, P. J. Roberts and D. C. Allan, "Single-mode photonic band gap guidance of light in air," *Science* **285**, 1537, 1999.
- [3] N.A.Mortense, J.R. Folkenberg, M.D. Nielsen, K.P. Hansen, "Modal cutoff and the V parameter in photonic crystal fibers" *Opt. Lett.*, **28**, 1879, 2003.
- [4] J.C. Knight, T.A. Birks, R.F. Cregan, P.St.J. Russell, J.P.Sandro "Large mode area photonic crystal fiber", *Electron. Lett.*, **34**, 1347, 1998.
- [5] L. Yan-feng, HU. Ming-lie, C. Lu, W. Ching-yue, "Enhanced nonlinear effects in photonics crystal fibers" *Front. Phys. China*, **2**, 170, 2006.
- [6] A. Cerqueira S Jr, "Recent progress and novel applications of photonic crystal fibers" *Rep. Prog. Phys.*, **73**, 024401, 2010.
- [7] I.T. Monroy, H.P.A. Boom, A.M.J. Koonen, G.D. Khoe, Y. Watanabe, Y. Koike, T. Ishigure, "Data transmission over polymer optical fibers" *Opt. Fib. Tech.*, **9**, 159, 2003.
- [8] M.A van Eijkelenborg, M. Large, A. Argyros, J. Zagari, S. Manos, N. Issa, I. Bassett, S. Fleming, R. McPhedran, C. M. de Sterke,, N. A. P. Nicorovici, "Microstructured polymer optical fiber," *Opt. Express*, **9**, 319, 2001.
- [9] A. Argyros, M.A. van Eijkelenborg, M.C.J. Large, I.M. Bassett, "Hollow-core microstructured polymer optical fiber" *Opt. Lett.*, **31**, 172, 2006.
- [10] M.C.J. Large, L. Poladian, G. Barton, M.A. van Eijkelenborg, "Microstructured polymer optical fibers" chapter 8, Springer, 2008.
- [11] G. Giraretta, W. White, M. Wegmuller, T. Onishi, "High-speed (11 Gbit/s) data transmission using perfluorinated graded-index polymer optical fibers for short interconnects (<100)" *Phot. Tech. Lett.*, **12**, 347, 2000.
- [12] J. Canning, E. Buckley, N. Grothoff, B. Luther-Davies, J. Zagari, "UV laser cleaving of air-polymer structured fiber," *Opt. Commun.*, **202**, 139, 2002.
- [13] S. H. Law, M. A. Van Eijkelenborg, G. W. Barton, C. Yan, R. Lwin, and J. Gan, "Cleaved end-face quality of microstructured polymer optical fibers," *Opt. Commun.*, **265**, 513, 2006.
- [14] A. Stefani, K. Nielsen, H.K. Rasmussen, O. Bang, "Cleaving of TOPAS and PMMA microstructured polymer optical fibers: core-shift and statistical quality optimization," *Opt. Commun.*, **285**, 1825, 2012.
- [15] D. Sáez-Rodríguez, K. Nielsen, O. Bang, D.J. Webb, "Simple room temperature method for polymer optical fiber cleaving" *Journal of lighthwave technology*, **33**, 4712, 2016.
- [16] I. M. Ward, *Mechanical Properties of Solid Polymers*. New York, NY, USA: Wiley, 1983.



Determination of the radial profile of the photoelastic coefficient of plastic optical fibers

S. Acheroy^{1*}, T. Geernaert², H. Ottevaere², H. Thienpont², D.J. Webb³, C.A.F Marques⁴, P. Gang-ding⁵, M. Pawel⁶, F. Berghmans²

- 1 Royal Military Academy, Dept of Communication, Information, Systems and Sensors (CISS), Ave Renaissance 30, 1000 Brussels, Belgium
- 2 Vrije Universiteit Brussel, Dept. of Applied Physics and Photonics, Brussels Photonics Team (B-PHOT), Pleinlaan 2, B-1050 Brussels, Belgium
- 3 Aston Institute of Photonic Technologies, Aston University, Aston Triangle, B4 7ET Birmingham, UK
- 4 Instituto de Telecomunicações and University of Aveiro Physics Department & I3N, Campus de Santiago, 3810-193 Aveiro, Portugal
- 5 Photonics & Optical Communications, School of Electrical Engineering & Telecommunications, University of New South Wales, Sydney 2052, NSW, Australia
- 6 Laboratory of Optical Fibers Technology, Maria Curie Skłodowska University Skłodowska Sq 3, 20-031 Lublin, Poland

*Corresponding author: sophie.acheroy@rma.ac.be

Abstract: We developed a measurement method to determine the radial distribution of the photoelastic coefficient $C(r)$ in step-index polymer optical fibers (POFs). The method is based on the measurement of the retardance profile of a transversally illuminated fiber for increasing tensile load. The radial profile $C(r)$ is obtained from the inverse Abel transform of this retardance profile. We measured polymer fibers from different manufacturers. The radial profile of the photoelastic constant can considerably vary depending on the type and treatment of POFs, even when made from similar materials, which leads to the conclusion that the photoelastic constant should be characterized for each different type of POF. The impact of annealing the fiber samples on $C(r)$ is also addressed.

1. Introduction

In the field of optical sensors, polymer optical fibers (POFs) provide an interesting alternative for their glass counterparts, owing to their specific characteristics compared to glass fibers. For example, they feature higher elastic limits and can be made from biocompatible materials [1–3]. Simulating and predicting the response of physical or dynamometric optical fiber sensors to externally applied mechanical load requires good knowledge of the fiber material parameters. In this respect it is well known that the photoelastic effect plays a crucial role in glass and polymer fibers, when these are used as transducers for mechanical quantities such as stress, strain and pressure. More particularly, it is important to use correct values of the stress-optic coefficients C_1 and C_2 [Pa^{-1}] and of the photoelastic coefficient $C = C_1 - C_2$ when calculating the response of optical fibers to mechanical load, since these parameters link the applied stress to the change of the refractive index in the fiber. In this paper we describe a method to determine the photoelastic coefficient in POFs. More specifically, we experimented with fibers drawn from polymethylmethacrylate (PMMA) as that material is most commonly used to manufacture polymer fibers. The value of C for PMMA reported in the literature varies significantly from $-1.08 \times 10^{-10} \text{ Pa}^{-1}$ to $5.3 \times 10^{-12} \text{ Pa}^{-1}$ [4–8]. In the particular case POFs, the drawing conditions and presence of dopants in the polymer could influence the value of the photoelastic constant and lead to the necessity to measure the value of C for each type of POF. The measurement methods to determine C in glass and polymer proposed in the literature rely on the hypothesis that C is constant throughout the fiber section but making such assumption is not straightforward [9, 10]. Therefore we also attempted to determine the radial distribution of the photoelastic constant $C(r)$ in PMMA fibers before and after a specific annealing process. In section 2 we describe the measurement method. The measurement results on the POFs before and after annealing are presented and discussed in the third section. Section 4 closes our article with a summary of our findings.

2. Presentation of the measurement method

2.1 Retardance measurement

The determination of $C(r)$ requires the measurement of the retardance profile of a transversally illuminated fiber as a function of the tensile load applied to the fiber. The inverse Abel transform of the retardance allows



obtaining $C(r)$. In previous publications we have detailed the measurement method to obtain the retardance profile of the fiber [11, 12]. We recall the main steps below for the sake of completeness.

We subject the fiber to a known axial load σ_z . We assume that the load is constant across the fiber section. We measure the retardance for tensile stress values varying from 10 MPa to 50 MPa. To do so the fiber is illuminated with monochromatic light at 633 nm, linearly polarized light at 45°C with respect to the fiber axis. As illustrated in Figure 1 the wave vector of the light is perpendicular to the fiber axis and parallel with the x-axis. The fiber is immersed in index matching liquid to avoid refraction at the boundaries of the optical fiber.

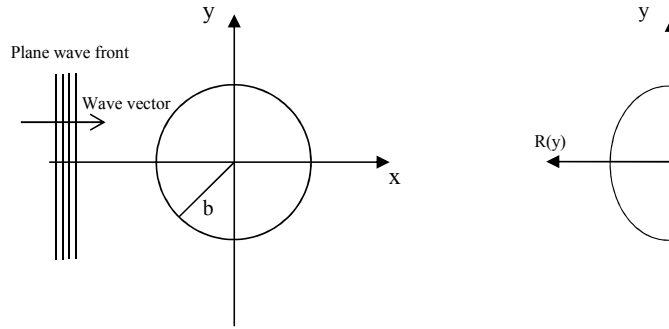


Figure 1: Illustration of an optical fiber transversely illuminated with a plane wave (left) and resulting retardance profile $R(y)$ (right). b is the radius of the fiber. The z-axis is taken along the fiber length with a direction exiting the page.

The axial load applied to the fiber induces birefringence in the fiber material. The two linearly polarized components along the y and z directions will experience a different phase shift that can be observed as the projected retardance $R(y)$ between these two orthogonal components. The projected retardance $R(y)$ is related to the axial stress by an inverse Abel transform [13–15], as given by equation (1):

$$\sigma_z \times C(r) = -\frac{1}{\pi} \int_r^b \frac{dR(y) / dy}{\sqrt{y^2 - r^2}} dy \quad (1)$$

The photo-elastic constant $C(r)$ is the regression coefficient linking the inverse Abel transform of the projected retardance $R(y)$ and the applied known axial stress σ_z . r is the radial distance taken from the fiber’s center and b is the radius of the fiber. To obtain the radial profile of the photoelastic constant $C(r)$, we use a polarizing microscope and apply the Sénarmont compensation method to measure the full-field view of $R(y)$.

2.1 Inverse Abel transform

In a previous publication [16] we have introduced two algorithms to compute the inverse Abel transform. Both algorithms are based on Fourier theory but the approach is somehow different. In the first algorithm we expand the measured retardance $R(y)$, corresponding to a specific value of the axial load, in Fourier series. We compute the inverse Abel transform of the expansion of $R(y)$ and we obtain equation (2).

$$\sigma_z \times C(r) = -\frac{\pi}{2b} \sum_{k=1}^{k_{\max}} a_k k \frac{2}{\pi} \int_0^{\sqrt{1-\rho^2}} (t^2 + \rho^2)^{-1/2} \times \sin(k\pi\sqrt{t^2 + \rho^2}) dt \quad (2)$$

where $\rho = r / b$ is the normalized radius, $t = \sqrt{1 - \rho^2}$ and a_k is the k^{th} Fourier coefficient of the Fourier series of the retardance.

In the second algorithm we expand the result $C(r) \cdot \sigma_z$ of the inverse Abel transform in Fourier series. The expression of the expansion is given in equation (3).



$$[\sigma_z \times C(r)]_F = a_0 + \sum_{k=1}^{\infty} a_k \cos(k\pi \frac{r}{b}) \tag{3}$$

The forward Abel transform of the expansion yields the measured retardance. The expression of the retardance becomes (4).

$$R_F(y) = b.a_0 \int_0^{\sqrt{1-\rho^2}} dt + b \sum_{k=1}^{\infty} a_k \int_0^{\sqrt{1-\rho^2}} \cos(k\pi \sqrt{t^2 + \rho^2}) dt \tag{4}$$

where $\rho = x/b$ is the normalized radius and $t = \frac{\sqrt{r^2 - y^2}}{b}$. To determine the amplitude of the Fourier

coefficients a_k in equation (4), $R_F(y)$ is compared to the measured retardance by applying the least square criterion. The main difference between the two algorithms is the presence of a constant term in the expansion of $\sigma_z \times C(r)$ in the second algorithm. It allows the algorithm to converge with a lower amount of Fourier coefficients. Moreover, the first algorithm requires the integration of a derivative, which is very sensitive to measurement noise. To establish the radial distribution of the photoelastic constant, we have demonstrated in [16] that both algorithms are fully equivalent, but that the first algorithm requires a larger amount of Fourier coefficients. If we consider increased measurement noise, the influence of the noise on the inverse Abel transform becomes predominant and a large number of Fourier coefficients leads to very noisy shapes. In that case the amount of considered coefficients has to be reduced and $C(r)$ should then be calculated with the second algorithm.

3. Measurement results and discussion

We have measured $C(r)$ of five singlemode polymer fibers. The description of the composition and specific fabrication process of each fiber has already been detailed in a previous publication [17]. We summarize the main characteristics of the fibers in Table 1.

Table 1: Main characteristics and of the polymer optical fibers used to measure the retardance and determine the radial profile of the photoelastic coefficient [18–20]. The mean measured value of C on the unannealed and annealed fibers are also mentioned

Fiber	Type	d_{core}	$d_{cladding}$	Thermal treatment of the preform	Drawing Temperature	C unannealed [$\times 10^{-12}$ Pa $^{-1}$]	C annealed at 80°C [$\times 10^{-12}$ Pa $^{-1}$]
1	PMMA	10 μ m	110 μ m	45°C to 75°C within 4 days	220°C	0,047	1,23
2	PMMA	10 μ m	133 μ m	45°C to 75°C within 4 days	220°C	-0,93	1,50
3	PMMA	12 μ m	260 μ m	36°C to 88°C within 4,5 days	225°C	0,504	1,57
4	PMMA	9 μ m	110 μ m	*	*	-0,15	1,54
5	PMMA	4 μ m	210 μ m	80°C during 2 weeks	290°C	3,85	3,94

*The thermal treatment of the preform and the drawing temperature have not been communicated by the manufacturer.

We have determined $C(r)$ for the pristine samples. We then annealed the samples for 8 hours at 80°C and we have determined the mean value of C and $C(r)$ following each annealing step. The influence of annealing the fibers at 80°C for 8 hours is clearly visible. The results are shown in Figure 2 and the mean values of the measured C are also summarized in Table 1. There is no specific annealing treatment of the preform for Fibers 1, 2 and 3. We can assume that there was no specific temperature treatment for the commercially available Fiber 4. Our findings evidence the impact of annealing at a higher temperature. The variance decreases in all fibers that did not benefit from a specific temperature treatment of the preform, which explains a smoother shape of $C(r)$. The annealing process increases significantly the value of $C(r)$ towards a comparable mean value. Note that the overshoot at $r = 0$, i.e. in the center of the fiber, correspond to a numerical artefact of the inverse Abel transform. The height of the overshoot depends on the amount of Fourier coefficients considered in the expansion of the inverse Abel transform, as we explained in details in [12], and cannot be related to an actual property of the optical fiber. The radial profile of $C(r)$ for fiber 5 is not affected by the annealing process. The preform of that fiber has been annealed for 2 weeks at 80°C prior to drawing. We find a mean value for C of 4×10^{-12} Pa $^{-1}$, which is larger than the values we measured for Fibers 1 to 4.

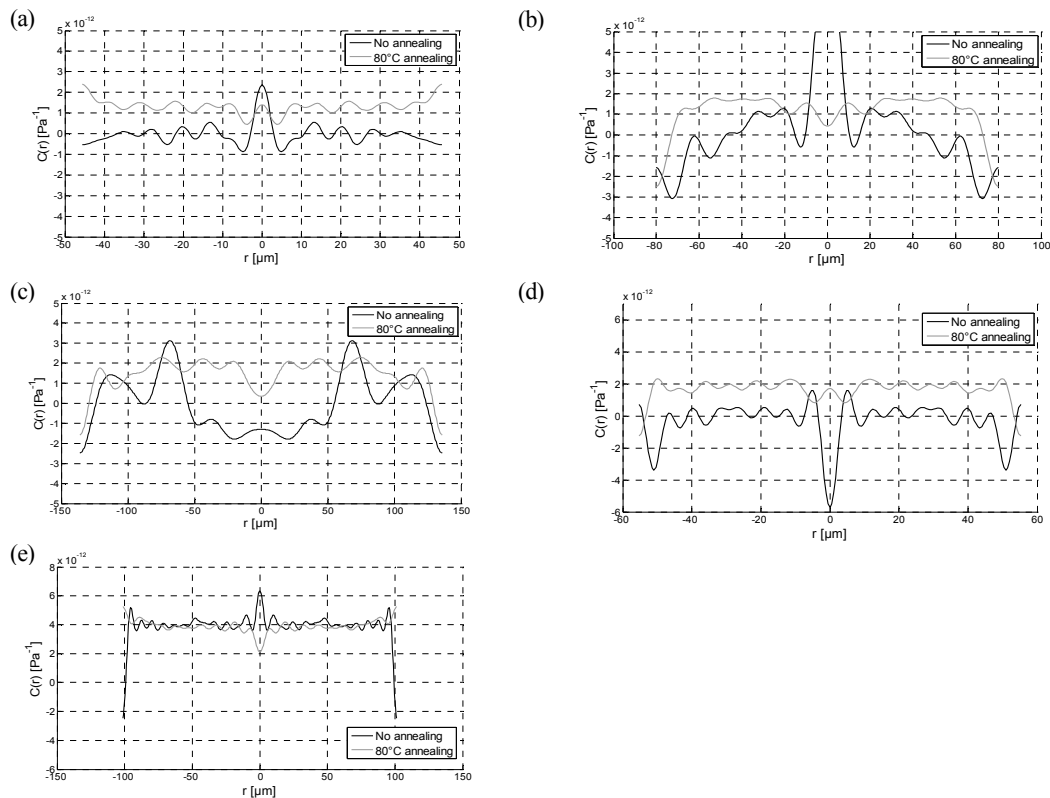


Figure 2 Comparison of the radial distribution of the photoelastic coefficient $C(r)$ of the POFs under test without annealing and with 8 hours annealing at 80°C in (a) Fiber 1, (b) Fiber 2, (c) Fiber 3, (d) Fiber 4 and (e) Fiber 5 .

4. Conclusion

We have measured the radial distribution of the photoelastic constant $C(r)$ in five types of PMMA optical fibers. The same distribution has been measured again after an annealing treatment of 8 hours at 80°C .

To do so we determined the retardance of the laterally illuminated fibers. We obtained a full field view of the retardance with the use of a polarizing microscope. We applied two algorithms based on Fourier theory to calculate the inverse Abel transform of the measured retardance. The first algorithm decomposes the measured retardance in Fourier series before to performing the inverse Abel transform, whilst the second algorithm expands the desired radial profile and then computes the forward Abel transform. The result of that operation is then compared to the measured retardance profile. The main conclusion is that the second algorithm is more robust when one has to deal with noisy data.

We found the measured photoelastic constants C of the five samples of PMMA fibers to be very different. This indicates that C cannot be approximated by any standard value. Moreover, the annealing treatment of fibers 1 to 4 significantly increases C and yields a more regular and smooth profile $C(r)$. This may indicate a reduced variation of the material parameter C across the fiber section and an increased homogeneity in the cross-section of the POF. The effect of annealing on Fiber 5, of which the preform has been annealed prior to drawing, is different. This fiber is much less sensitive to thermal treatment and the mean value of C is much higher.



5. Acknowledgements

This work was partially supported by the IWT-SBO Project with Contract 120024 ‘Self Sensing Composites - SSC’. T. Geernaert is post-doctoral research fellow with the Research Foundation Flanders (FWO). The authors would also like to acknowledge financial support from the Methusalem and Hercules Foundations. The Belgian Science Policy Interuniversity Attraction Pole P7/35 is acknowledged as well. Carlos A.F. Marques was supported by Marie Curie Intra European Fellowship included in the 7th Framework Program of the European Union (project PIEF-GA-2013-628604) and FCT Fellowship (SFRH/BPD/109458/2015).

6. References

- [1] N. G. Harbach, “Fiber bragg gratings in Polymer Optical Fibers,” EPFL, 2008.
- [2] K. Peeters, “Polymer optical fibre sensors - A review,” *Smart Mater. Struct.*, vol. 20, no. 013002, 2011.
- [3] F. Berghmans and H. Thienpont, “Plastic Optical Fibers for Sensing Applications,” *OFC*, pp. 3–5, 2014.
- [4] W. Xu, X. F. Yao, H. Y. Yeh, and G. C. Jin, “Fracture investigation of PMMA specimen using coherent gradient sensing (CGS) technology,” *Polym. Test.*, vol. 24, pp. 900–908, 2005.
- [5] R. M. Waxler, D. Horowitz, and A. Feldman, “Optical and physical parameters of Plexiglas 55 and Lexan,” *Appl. Opt.*, vol. 18, no. 1, pp. 101–104, 1979.
- [6] A. Tagaya, L. Lou, Y. Ide, Y. Koike, and Y. Okamoto, “Improvement of the physical properties of poly(methyl methacrylate) by copolymerization with N-pentafluorophenyl maleimide; zero-orientational and photoelastic birefringence polymers with high glass transition temperatures,” *Sci. China Chem.*, vol. 55, no. 5, pp. 850–853, 2012.
- [7] A. Tagaya, H. Ohkita, T. Harada, K. Ishibashi, and Y. Koike, “Zero-birefringence optical polymers,” *Macromolecules*, vol. 39, pp. 3019–3023, 2006.
- [8] F. Ay, A. Kocabas, C. Kocabas, A. Aydinli, and S. Agan, “Prism coupling technique investigation of elasto-optical properties of thin polymer films,” *J. Appl. Phys.*, vol. 96, no. 12, pp. 7147–7153, 2004.
- [9] A. Bertholds and B. Dändliker, “Determination of the individual strain-optic coefficients in single-mode optical fibers,” *J. Light. Technol.*, vol. 6, no. n°1, pp. 17–20, 1988.
- [10] N. Lagakos and R. Mohr, “Stress optic coefficient and stress profile in optical fibers,” *Appl. Opt.*, vol. 20, no. 13, pp. 2309–2313, 1981.
- [11] S. Acheroy, M. Patrick, G. Thomas, H. Ottevaere, H. Thienpont, and F. Berghmans, “On a possible method to measure the radial profile of the photoelastic constant in step-index optical fiber,” in *Optical Sensing and Detection III*, 2014.
- [12] S. Acheroy, P. Merken, H. Ottevaere, T. Geernaert, H. Thienpont, and F. Berghmans, “Influence of measurement noise on the determination of the radial profile of the photoelastic coefficient in step-index optical fibers,” *Appl. Opt.*, vol. 52, no. 35, pp. 8451–9, 2013.
- [13] Chu and Whitbread, “Measurement of stresses in optical fiber and preform,” *Appl. Opt.*, vol. 21, no. 23, pp. 4241 – 4245, 1982.
- [14] K. Tatekura, “Determination of the index profile of optical fibers from transverse interferograms using Fourier theory,” *Appl. Opt.*, vol. 22, no. 3, pp. 460 – 463, 1983.
- [15] H. Poritsky, “Analysis of thermal stresses in sealed cylinders and the effect of viscous flow during anneal,” *Physics (College. Park. Md.)*, vol. 5, pp. 406 – 411, 1934.
- [16] S. Acheroy, P. Merken, T. Geernaert, H. Ottevaere, H. Thienpont, and F. Berghmans, “Algorithms for determining the radial profile of the photoelastic coefficient in glass and polymer optical fibers,” *Opt. Express*, vol. 23, no. 15, p. 18943, 2015.
- [17] S. Acheroy, P. Merken, H. Ottevaere, T. Geernaert, H. Thienpont, C. A. F. Marques, D. J. Webb, P. Gang-Ding, M. Pawel, and F. Berghmans, “Thermal effects on the photoelastic coefficient of polymer optical fibers,” *Opt. Lett.*, vol. 41, no. 11, pp. 2517–2520, 2016.
- [18] “<http://i-fiberoptics.com/fiber-detail.php?id=120>.”
- [19] “<http://www.paradigmoptics.com/>.”
- [20] W. Wu, Y. Luo, X. Cheng, X. Tian, W. Qiu, B. Zhu, G. Peng, and Q. Zhang, “Design and fabrication of single mode polymer optical fiber gratings,” vol. 12, no. 8, pp. 1652–1659, 2010.

GIPOF-BASED POWER DELIVERY SYSTEMS

J.D. López-Cardona¹, D.S. Montero^{1*}, P.J. Pinzón¹, C. Vázquez¹

¹: Electronics Technology Dpt., Universidad Carlos III de Madrid, Avda. de la Universidad 30, 28911, Leganés (Madrid), Spain

*Corresponding author: dsmontero@ing.uc3m.es

Abstract: In this work the feasibility for remote power delivery through GIPOF is investigated. Experimental measurements of the system are presented for different 120 μ m core diameter GIPOF fiber lengths. We discuss the system requirements and technical issues of the system components. An electrical power of 45.9mW after 50m (6.28V, 7.3mA) of GIPOF can be obtained, yielding 12.8% of system efficiency. With the proposed approach, optically powered remote units are envisaged in the fields of avionics, automotive and domotics.

Key words: PF-GIPOF, power-over-fiber (PWoF), system efficiency.

1. Introduction

Optical-fiber-linked power-by-light systems usually consist of a high-power laser diode (monochromatic source), a transmission line (optical fiber), and a converter (i.e. a photovoltaic, PV, cell). Both the optical fiber and the PV converter are placed inside an exclusion region, where the electric energy provisioning becomes difficult or inaccessible, whereas the light source is located within a problem-free area. The converter stage remotely transforms the received optical power into electricity thus driving an electronic circuit directly or by means of an intermediate signal conditioning stage. PV converters are the most suitable devices for this optical power conversion process due to their efficiency performance and no requirement for any kind of biasing. Limitations of overall system performance mostly depend on the efficiencies of the high-power optical source, the transmission medium and the PV converters [1].

The main advantages of using such optical-fiber based systems include galvanic insulation between two ends of the fiber, lack of electromagnetic noise, savings in copper cable weight, and no need for external batteries or public power lines. POFs with their large numerical aperture have acceptable flexibility, relaxed connector tolerance, easy and efficient coupling to high numerical aperture light sources, as well as quick and easy termination procedures. These properties boost the use of these systems in applications such as aircraft engine control, i.e. fly-by-light systems, firing sets, mining, or harsh environments with a risk of explosion, that have been well documented. They can also be WDM expanded in a feasible and efficient way, as recently proposed in [2]. In this scenario, the low attenuation coefficient of standard silica multimode fiber has opened up more recent large network area coverage applications, such as optically powered remote sensor networks [3] and remote powering of transponders (antennas) in picocellular network architectures for radio-over-fiber systems [4-6]. In contrast, Graded-Index Polymer Optical Fiber (GIPOF) shows several advantages over conventional silica multimode optical fiber in short distances thus being more flexible and ductile, making it easier to handle as well as offering potential lower cost associated with its easiness of installation, splicing and connecting while maintaining the potential transmission capacity [7]. The main limitation for power transmission via POF is the maximum operating temperature of the POF material which is closely related to its quite low glass transition temperature [8]. Additionally, the power loss figure of GIPOF is not comparable to its silica counterpart thus reducing the system efficiency. However, recent advances in power-efficient innovative hardware, low-energy medium access control protocol and power consumption savings in electronics [9] boost the market niche of optically powered systems through GIPOF. Short-range distance applications within the automotive, aircraft, home networking fields are envisioned to be excellent candidates to boost GIPOF-based power-delivery systems.

In this work, we evaluate the feasibility and the limitations for remote power delivery through GIPOFs in short-range and harsh-environment applications that require low- and mid-power operation of remote units. In order to design a reliable power-over-fiber (PWoF) system it is necessary to understand the impacts of the different optical and optoelectronic devices throughout the link. In Section 2 we describe the experimental setup. Section 3 reports the experimental tests that have been performed over different PF-GIPOF lengths and the overall system efficiency is evaluated. Finally, the main conclusions are addressed in Section 4.

2. Experimental setup

The schematic of the proposed power-by-light system is illustrated in Fig. 1. A 805-nm Fabry-Perot type high-power laser diode (HPLD) with FC-connector, see Fig. 2a, and with maximum power of 2W@3.3A is employed to launch optical power into the system. At reception, a PV power converter is located. A picture of the system is shown in Fig. 2b, where the HPLD and the PV are connected via a 120 μ m core diameter PF GIPOF from Chromis Fiber with typical numerical aperture (NA) value of 0.185. Different m-long GIPOF links were con-

nected between the HPLD and the PV converter by means of FC connectors. Lower coupling losses would be expected as larger fiber diameters were tested if similar numerical apertures were assumed. We define the optical feed power P_{in} as the total effective power launched from the HPLD into the optical fiber. We note P_{out} as the received effective optical power impinging the PV after all transmission losses arising the link, including all connector losses. A 0.04dB/m (i.e. 40dB/km) fiber loss between the transmitter output and receiver input was assumed for the PF GIPOF at the operating wavelength. We define P_{elec}^{DR} as the electrical power consumed by the HPLD driver that includes mainly both the laser diode and a Peltier-based temperature control loop. P_{elec}^{LD} defines the power consumption of the HPLD itself. Finally, the converted effective electrical power obtained from the PV is expressed by both the open circuit voltage V_{oc} and the open short circuit current I_{sc} , respectively.

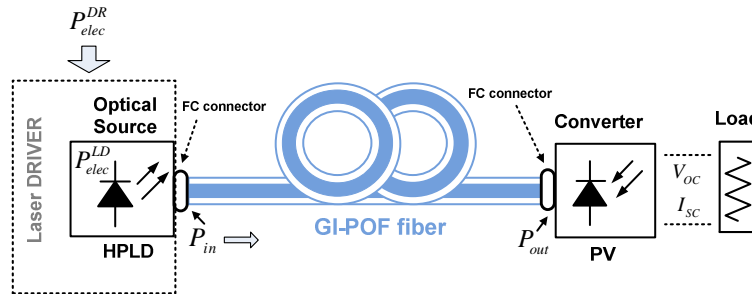


Fig. 1. Schematic of the GIPOF-based power-by-light system.

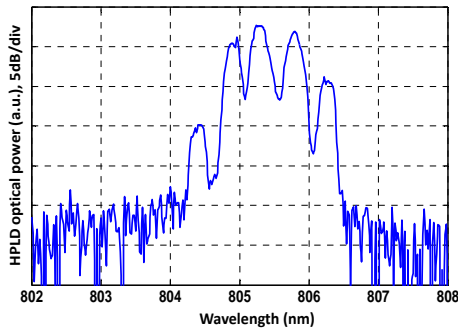


Fig. 2. (a) HPLD optical spectrum; (b) Photograph of the GIPOF based power delivery system.

3. Power over GIPOF fiber results

To characterize the performance of the system several measurements over a 120 μ m core diameter PF GIPOF were carried out. Link lengths of 25m, 50m and 100m were evaluated thus covering typical short-range applications that can be optically powered such as picocellular indoor systems [4, 10] and automotive or aircraft areas [11]. The optical power emitted by the HPLD versus bias current was characterized thus obtaining the dashed line depicted within Fig. 3 fixing the control temperature at 25 $^{\circ}$ C. It is important to use a large-core fiber to increase the fiber coupling efficiency as well as to reduce the power density inside the fiber to avoid POF melting [8]. The HPLD coupling efficiency is optimized (vendor specs) for a 200 μ m core diameter 0.22 NA fiber, i.e. \sim 100% of the optical power emitted is injected into the fiber. However, we estimate an effective coupling efficiency around 0.66 (1.8dB loss) due to the mismatch between the vendor recommendation and the PF GIPOF characteristics, see solid blue line within Fig. 3. We experimentally tested a 50 μ m core diameter PF GIPOF system and observed that it started melting at around 1.2A of bias current that corresponds to an effective optical power injected into the fiber (estimated) of 128mW. For the 120 μ m case, we obtained a maximum bias current around 1.5A leading to a maximum optical power of 528mW. These values are in agreement with those experimentally evaluated and predicted by Mizuno et al. [12] in their work related to the fiber fuse phenomenon in GIPOF fibers. Experiments were carried out biasing the HPLD at 0.8A, 0.9A and 1.0A thus injecting into the fiber 139mW, 197mW, and 254mW, respectively. The latter are symbolized within Fig. 3 by means of solid square markers.

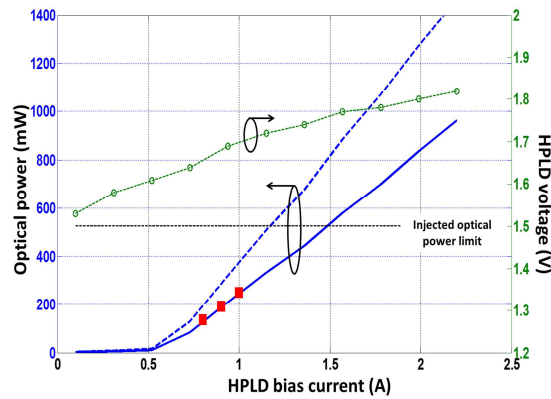


Fig. 3. (Left axis) HPLD optical power versus bias current I_F (dashed line ---); HPLD effective optical power injected into the $120\mu\text{m}$ PF GIPOF versus bias current I_F (solid line —). (Right axis) HPLD forward voltage versus bias current. Red solid squares correspond to the operating conditions fixed during the trials.

For the longest distance tested (100m) and biasing the HPLD at 1.0A an optical power of 97.2mW impinging the PV was obtained, which means that losses due to the transmission through the fiber and the couplings are around 4.2dB and only 38% of power reached the PV. Because the attenuation for a 100-m GIPOF link is around 4dB@805nm, the coupling losses are ~0.18 dB. The PV converter efficiency was measured in the system. The load resistance was varied from short circuit to open circuit, thus experimentally obtaining I_{SC} (short-circuit current) and V_{OC} (open-circuit voltage). The maximum PV efficiency achieved, defined as $V_{OC} \cdot I_{SC} / P_{out}$ (see Fig. 1), was 39.2% for testing conditions $L=50\text{m}$ and $I_F=0.8\text{A}$, thus delivering 33mW of electrical power ($V_{OC}=6.22\text{V}$, $I_{SC}=5.3\text{mA}$). Fig. 4a shows the open-circuit voltage V_{OC} and short-circuit current I_{SC} obtained during the trials, respectively. Their corresponding PV conversion ($V_{OC} \cdot I_{SC} / P_{out}$) and system efficiencies ($V_{OC} \cdot I_{SC} / P_{in}$) are depicted in Fig. 4b, respectively. It is worth mentioning that the HPLD power consumption ranges from 1.36W to 1.7W depending on the selected bias current thus leading to a maximum overall electrical power efficiency, given in terms of $V_{OC} \cdot I_{SC} / P_{elec}^{LD}$, of around 4% obtained for a testing condition $L=25\text{m}$ and $I_F=1.0\text{A}$. Nevertheless if the total amount of electrical power consumed by the laser driver is considered it yields to an overall system efficiency, given by $V_{OC} \cdot I_{SC} / P_{elec}^{DR}$, of ~1%.

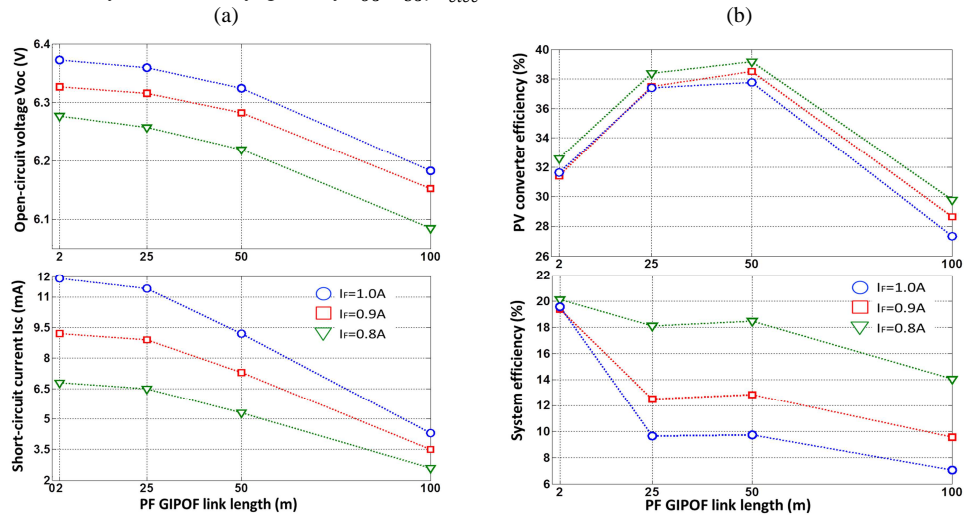


Fig. 4. (a) Measured V_{OC} and I_{SC} versus GIPOF link distance. (b) PV conversion and system efficiency versus GIPOF link distance.

4. Conclusions

A 120 μ m core diameter GIPOF-based power delivery system was manufactured and analyzed. An electrical power of 45.9mW after 50m (6.28V, 7.3mA) of GIPOF has been obtained yielding 12.8% of system efficiency. Additionally, the approach can deliver an electrical power up to 27mW at 100m with an efficiency of 7% ($V_{OC} \cdot I_{SC}/P_{in}$) although this value can be improved. Best-case scenarios obtained for GIPOF lengths up to around 50m can achieve a system efficiency around 19%, which is quite satisfactory compared to previously reported silica-based power-over-fiber delivery systems, but at the cost of reducing the HPLD biasing operation thus limiting the electrical power delivered. There is available power margin to improve the system performance in terms of the overall efficiencies shown within this work. Computing $V_{OC} \cdot I_{SC}/P_{elec}^{DR}$, which determines the ratio between the electrical power delivered by the PV converter and the feeding electrical power of the whole system, the GIPOF based power-over-fiber approach performs an efficiency near 1% as competitive as commercially available PwOF systems.

Acknowledgements

This work was partially supported by the Spanish Ministry of Economy and the European Regional Development Fund under grant TEC2015-63826-C3-2-R (MINECO/FEDER) and from Comunidad de Madrid under grant S2013/MIT-2790.

References

- [1] M. Dumke, G. Heiserich, S. Franke, L. Schulz, and L. Overmeyer, "Power transmission by Optical Fibers for Component Inherent Communciation," *Systemics, Cybernetics and Informatics*, vol. 8, no. 1, pp. 55–60, 2010.
- [2] P. J. Pinzón, I. Pérez, and C. Vázquez, "Visible WDM System for Real-Time Multi-Gb/s Bidirectional Transmission over 50-m SI-POF," *IEEE Photon. Technol. Lett.*, vol. 28, no. 15, pp. 1696–1699, 2016.
- [3] R. Peña, C. Algora, I.R. Matías, and M. López-Amo, "Fiber-based 205-mW (27% efficiency) power-delivery system for an all-fiber network with optoelectronic sensor units," *Applied Optics*, vol. 38, no. 12, pp. 2463–2466, 1999.
- [4] M. Matura, and J. Sato, "Bidirectional Radio Over Fiber Systems using Double-Clad Fibers for Optically Powered Remote Antenna Units," *IEEE Photon. J.*, vol. 7, no. 1, paper 7900609, Feb. 2015.
- [5] D. Wake, A. Nkansah, J. Gomes, C. Lethien, C. Sion, and J. Vilcot, "Optically Powered Remote Units for Radio-over-Fiber Systems," *J. Light. Technol.*, vol. 26, no. 15, pp. 2484–2491, Aug. 2008.
- [6] C. Vázquez, D.S. Montero, W. Ponce, P.C. Lallana, D. Larrabeiti, J. Montalvo, A. Tapetado, and P.J. Pinzón, "Multimode fiber in millimeter-wave evolution for 5G cellular networks" *Proc. of SPIE Broadband Access Communication Technologies*, vol. 9772, paper 97720F, San Francisco 2016.
- [7] D.S. Montero and C. Vázquez, "Analysis of the electric propagation method: theoretical model applied to perfluorinated graded-index polymer optical fiber links," *Opt. Lett.*, vol. 36, no. 30, pp. 4116–4118, 2011.
- [8] E. Dolvonov and H. Poisel, "Optical power transmission via POF," 15th *International Conference on Plastic Optical Fibers (POF)*, pp. 491–497, Seoul (Korea), Sep. 2006.
- [9] M. Röger et al., "Optically powered fiber networks," *Opt. Express*, vol. 16, no. 26, pp. 21821–21834, Dec. 2008.
- [10] C. Lethien, C. Loyez, J. Vilcot and P. A. Rolland, "Potentialities of multimode fibres as transmission support for multiservice applications, from the wired small office/home office network to the hybrid radio over fibre concept" *Book chapter: Optical Fiber New Developments*, Intech, 2009.
- [11] U.H.P. Fisher, M. Haupt and M. Joncic, "Optical transmission systems using polymeric fiber," *Book chapter: Optoelectronics - Devices and Applications*, Intech, 2011.
- [12] Y. Mizuno, N. Hayashi, H. Tanaka, K. Nakamura and S. Todoroki, "Observation of polymer optical fiber fuse," *Appl. Phys. Lett.*, vol. 104, pp. 043302, 2014.

Impacts of gamma irradiation on Cytop plastic optical fibres

P. Stajanca^{1*}, L. Mihai², D. Sporea², D. Negut³, H. Sturm¹, M. Schukar¹, K. Krebber¹

¹ Bundesanstalt für Materialforschung und –prüfung (BAM), Unter den Eichen 87, 12205 Berlin, Germany

² National Institute for Laser Plasma and Radiation Physics, Atomistilor St. 409, 077125 Magurele, Romania

³ National Institute of Physics and Nuclear Engineering, Reactorului St. 30, 077125 Magurele, Romania

*Corresponding author: pavol.stajanca@bam.de

Abstract: Impact of gamma radiation on transmission of a commercial Cytop polymer optical fibre (Lucina, Asahi Glass Company) is investigated. Spectral dependence of radiation-induced attenuation in the investigated fibre is measured in the VIS-NIR spectral region. Besides attenuation increase, radiation is found to increase fibre susceptibility to water as well. While pristine Cytop fibre is rather humidity insensitive, strong humidity-related absorption in the NIR region is observed after fibre irradiation. Selective irradiation of separate fibre sections is proposed as a way of fibre humidity sensitization and quasi-distributed water detection is demonstrated using optical time domain reflectometry at 1310 nm.

1. Introduction

Optical fibres offer several advantages for operation in harsh environments both for data transmission and sensing applications. These include electromagnetic immunity, low-weight, small dimensions, low loss and high bandwidth. However, before any fibre-based system can be employed in radiation environment, impact of the high-energy radiation on the fibre and system performance need to be evaluated. Effects of gamma radiation on silica-based fibres have been subject of numerous studies for more than three decades [1]. In contrast, investigations on plastic optical fibres (POFs) are rather scarce. Nevertheless, considerable attention has been devoted to development of POFs which proved their potential for short-range data transmission [2] and numerous sensing applications [3]. Among variety of available POFs, graded-index (GI) Cytop-based fibres are one of the most promising candidates exhibiting low attenuation and dispersion [4]. In general, two different types of multi-mode (MM) Cytop fibres are commercially available; co-extruded POFs manufactured by Chromis Fiberoptics, and fibres drawn from a preform produced by Asahi Glass Company. Compared to co-extruded type, Cytop fibres drawn from a preform are known to have higher degree of purity. Thanks to that, they typically exhibit lower attenuation and smoother back-reflection traces [4]. In previous works, we have studied effects of gamma radiation on performance of co-extruded Cytop POFs [5, 6]. However, radiation effects on fibre transmission properties can be strongly dependent not only on fibre material but also manufacturing procedure [1]. Therefore, here we investigate impacts of gamma irradiation on a commercial Cytop POF drawn from a preform. Radiation damages molecular structure of the fibre, which leads to attenuation increase. Fibre's radiation-induced attenuation in the VIS-NIR spectral region is measured and discussed. Moreover, we show that in addition to attenuation increase, irradiation makes fibre more susceptible to moisture. We show that fibre irradiation can be used to sensitize the fibre for humidity monitoring applications.

2. Radiation-induced attenuation

2.1 Fibre irradiation

Commercial Cytop-based MM POF Lucina from Asahi Glass Company was used in this study. The fibre has 120 µm graded-index Cytop core with 500 µm over-cladding and is drawn from a preform. Radiation-induced attenuation (RIA) of the fibre was measured on-line in 400-1000 nm region. A 2.3 m long piece of the fibre was homogeneously irradiated with ⁶⁰Co irradiator up to maximal dose of 36.7 kGy at a dose rate of 267 Gy/h. Halogen lamp (AQ4305, Yokogawa) was used as a broadband light source, while CCD-based spectrometer (HR4000, Ocean Optics) was used to monitor fibre transmission during the irradiation. All auxiliary interconnecting fibres and connectors were shielded from radiation by lead bricks. Fibre's RIA was evaluated from spectral transmission data as

$$RIA(\lambda, t) = -\frac{10}{L_0} \log \left(\frac{I(\lambda, t)}{I(\lambda, 0)} \right) \quad (1)$$

where $I(\lambda, t)$ is the recorded transmitted spectral intensity at time t from the start of irradiation and L_0 is the length of irradiated fibre section (2.3 m). Time dependence of RIA evolution was later transform to dependence on radiation dose D accounting for utilized dose rate and irradiation time.

On-line investigation of RIA deeper in the NIR region (> 1000 nm) was not possible with the employed setup. After the irradiation session was finished, spectral attenuation of the irradiated fibre was measured by the cutback method in the NIR spectral region (1000-1700 nm). Halogen lamp light source (AQ4305, Yokogawa) and an interferometric optical spectrum analyser (Q8347, Advantest) were used for off-line spectral attenuation measurements. RIA of the fibre was then evaluated relative to the spectral attenuation of pristine Lucina fibre that was measured by the same method.

2.2 Results and discussion

Figure 1 depicts the spectral dependence of fibre's RIA measured on-line for 400-1000 nm spectral region (a) and off-line for 1000-1700 nm region (b). Measured RIA of the investigated fibre has similar spectral character as in case of co-extruded Cytop POF [6]. Fibre transmission is very radiation sensitive for the visible wavelengths (Figure 1a), where RIA reaches fairly large values of several dB/m already for dose levels under 100 Gy. Magnitude of induced attenuation shows strong spectral dependence and generally increases towards UV wavelengths with a local minima and maxima in the VIS region at around 540 nm and 650 nm, respectively. RIA drops rapidly from the visible region towards the IR wavelengths. Results in the NIR (Figure 1b) indicate much lower magnitude of RIA in this spectral region, considering rather high irradiation dose of 36.7 kGy. RIA spectral profile has a minimum at around 1250 nm, from where RIA starts to grow again towards longer wavelengths. Strong attenuation feature with three distinct peaks is present in the RIA profile around 1400 nm.

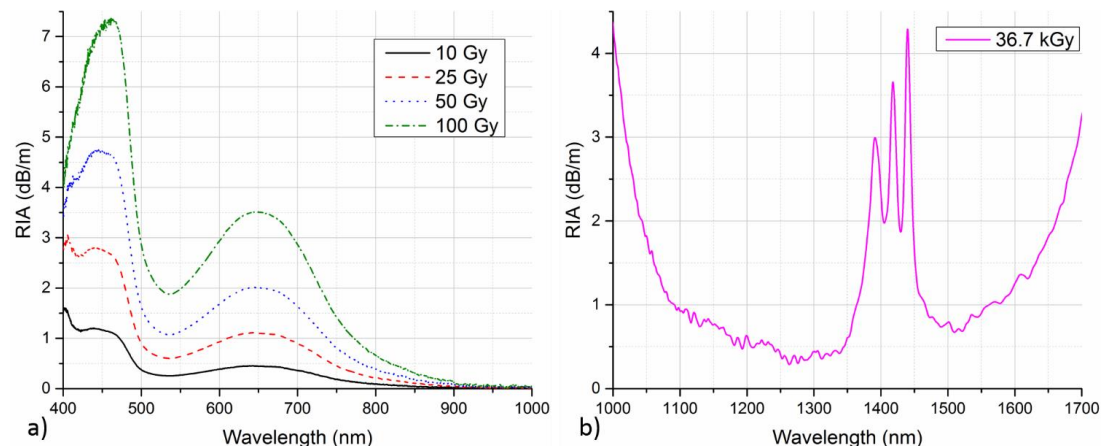


Figure 1. Spectral dependence of fibre's RIA in 400-1000 nm region (a) measured on-line and in 1000-1700 nm region (b) calculated from off-line measurement.

In the case of glass optical fibres, RIA typically comes from an absorption on colour centres generated in the fibre material during irradiation [1]. Presence of paramagnetic centres upon gamma irradiation has been demonstrated previously also for perfluorinated POFs [7]. In addition to colour centre formation, irradiation of polymer materials may lead to more profound alteration of material molecular structure. In particular, formation of systems with increased conjugation is typically associated with attenuation increase and discoloration in polymers. More than one mechanism are involved in RIA increase for POFs in the visible range. With regard to strong RIA feature around 1400 nm, OH group is known to have vibrational absorption overtone in this spectral region [8] and corresponding moisture-related absorption peak has been observed in various optical fibres. Growth of this attenuation feature upon irradiation of Cytop POF indicates increased amount of water absorbed into the fibre. Fibre transmission properties will be therefore more sensitive to environmental conditions around the fibre, namely relative humidity (RH) of the fibre's surroundings.

3 Humidity-induced attenuation

Even though increased humidity susceptibility of the fibre may be undesirable for most of the practical applications, it can be exploited for fibre optic humidity sensing. While pristine Cytop POF is relatively humidity insensitive, attenuation of irradiated fibre at suitable wavelength can exhibit rather large dependence on RH level. Monitoring of fibre attenuation can be then used for humidity sensing. In this section we show, that irradiation can be used to locally sensitize the fibre for RH monitoring applications.

3.1 Methodology

To demonstrate possibility of selective fibre sensitization to humidity, two different segments of 30 m Lucina fibre were irradiated simultaneously to 36.7 kGy while the rest of the fibre was shielded. The same irradiation facility and dose rate as in previous section was used. Approximate position and length of the first irradiated section was 10 m from the beginning of the fibre and 1 m, respectively. The second irradiation section started roughly at 21 m and was approximately 1.6 m long. After irradiation, the fibre was coiled and placed in a cylindrical container. The container with the fibre was kept inside a climate chamber (VCL 4006, Vötsch Industrietechnik) except of connectorised input end of the fibre which was left outside of the chamber. Optical time domain reflectometer (ν -OTDR, Luciol Instruments) operating at 1310 nm was used to monitor fibre attenuation profile. Distributed attenuation measurement enables verification of localized fibre sensitization only in the irradiated regions. RIA as well as humidity-induced attenuation (HIA) in the irradiated fibre are strongly wavelength dependent. Strong inherent attenuation in the fibre would limit the length of the fibre that can be monitored with OTDR technique. On the other hand, monitoring at wavelength where there is no HIA would lead to no RH sensitivity. Selected wavelength of 1310 nm is a compromise between the two criteria. It lies, both, close to the RIA minimum around 1250 nm and on the rising edge of a 1400 nm moisture-related absorption peak. The fibre in the climate chamber was firstly kept at 20 °C and 10 % RH for 24 hours to allow for desorption of excessive water from the fibre. After this time, the container with fibre was filled with water and left in the climate chamber at 20 °C for another 28 hours. Fibre's OTDR trace was measured continuously during this period with 2 minute averaging.

3.2 Results and discussion

Figure 2a compares OTDR traces of the investigated fibre in the climate chamber before (10 % RH) and 28 hours after immersion in water (100 % RH). Two irradiated sections are indicated by red bars on graph X axis.

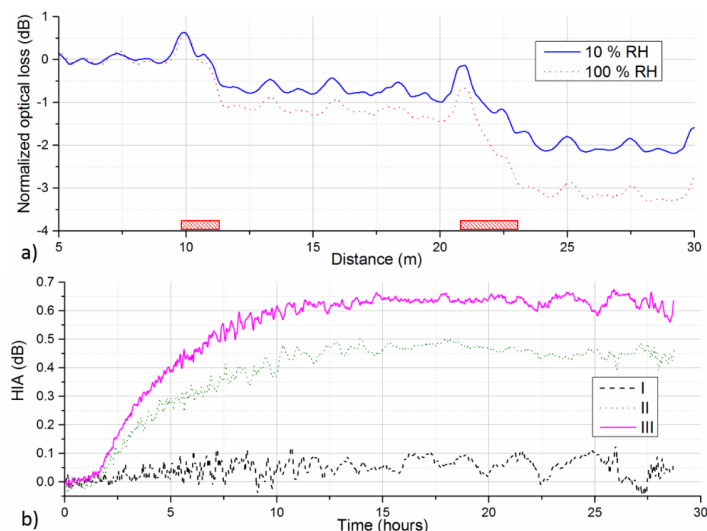


Figure 2. a) Comparison of 1310 nm OTDR traces of 30 m Lucina fibre with two irradiated sections at 10 % and 100 % relative humidity (RH). Position and length of irradiated sections are roughly indicated by red striped bars at the X axis.

b) Relative temporal evolution of HIA in: I – the non-irradiated fibre section (12-20 m); II - the first irradiated fibre section (10-12 m); III - the second irradiated fibre section (21-23 m)

It is obvious that irradiated sections exhibit larger loss than the rest of the fibre. However, induced RIA is small enough so it does not limit OTDR's sensing range in this case. Upon change in RH level, attenuation in the irradiated section rises while the rest of the fibre remains unaffected. This demonstrates that the irradiated sections have been selectively humidity sensitized while the rest of the fibre remains rather humidity insensitive. To evaluate magnitude and temporal response of the humidity-induced attenuation in the irradiated sections, evolution of mean loss values from OTDR traces between different fibre regions are calculated (Figure 2b). Attenuation in the first irradiated section is calculated as difference of mean OTDR loss level of region before the irradiated section (5-9 m) to section after the irradiated section (12-20 m). Relative increase of this difference after fibre immersion in water then expresses HIA evolution in the first irradiated section (Figure 2b – curve II). Analogically, HIA in the second irradiated section (Figure 2b – curve III) is evaluated from the data from 12-20 m versus 24-29 m regions of the fibre. For comparison, also HIA evolution between 12-15 m and 17-20 m regions in the non-irradiated section of the fibre (Figure 2b – curve I) was evaluated.

While there is virtually no HIA increase in the non-irradiated section of the fibre after fibre immersion into water, growth of HIA in the two irradiated sections is obvious. Water absorption into the fibre core is a rather slow, diffusion-based process. Therefore, response time of the fibre is rather long and steady conditions are reached after roughly 15 hours. Magnitude of HIA reaches approximately 0.45 dB and 0.65 dB in the first and second irradiated section, respectively. The difference in HIA levels between the two sections reflect the different lengths of the sections. Higher HIA in the second section, that is roughly 1.6 times longer than the first one, is expected. Presented results demonstrated that irradiation of PF-POF can be used to locally sensitize the fibre for humidity monitoring applications.

4. Conclusion

In the presented work, RIA of a commercial low-loss Cytop POF (Lucina, Asahi Glass Company) was measured in the VIS-NIR spectral region. Fibre exhibits rather high radiation sensitivity in the VIS region with RIA increasing strongly towards the UV wavelengths. On the other hand, sensitivity drops rapidly in the NIR region and has minimum around 1250 nm. Strong moisture-related absorption around 1400 nm was found for the irradiated fibre, showing that irradiation increases fibre's affinity for water. Potential of fibre irradiation as a mean of fibre sensitization for humidity monitoring applications was proposed. Local sensitization and quasi-distributed water detection was demonstrated with partly irradiated Cytop fibre utilizing OTDR measurement at 1310 nm.

5. Acknowledgements

Research funded by FP7-PEOPLE/2007-2013/ (608382) and by the Romanian Executive Agency for Higher Education, Research, Development and Innovation Funding (8/2012). Authors would like to thank Dr. A. Denker of Helmholtz-Zentrum Berlin for facilitating the fibre irradiation.

6. References

- [1] S. Girard, J. Kuhnenn, A. Gusarov *et al.*, "Radiation Effects on Silica-Based Optical Fibers: Recent Advances and Future Challenges," IEEE. Trans. Nucl. Sci., 60(3), 2015-2036 (2013).
- [2] O. Ziemann, J. Krauser, P. E. Zamzow *et al.*, [POF Handbook: Optical Short Range Transmission Systems (2nd edition)] Springer, Berlin (2008).
- [3] K. Peters, "Polymer optical fiber sensors - a review," Smart Mater. Struct., 20(1), 013002 (2011).
- [4] C. Lethien, C. Loyez, J.-P. Vilcot *et al.*, "Exploit the Bandwidth Capacities of the Perfluorinated Graded Index Polymer Optical Fiber for Multi-Services Distribution," Polymers, 3, 1006-1028 (2011).
- [5] P. Stajanca, D. Sporea, L. Mihai *et al.*, "Gamma Radiation Induced Effects in Perfluorinated Polymer Optical Fibers For Sensing Applications," in [POF Simulation beyond Data Transmission; Summary of the 3rd International POF Modelling Workshop 2015] Books on Demand, Norderstedt, 95-103 (2015).
- [6] P. Stajanca, L. Mihai, D. Sporea *et al.*, "Effects of gamma radiation on perfluorinated polymer optical fibers," Opt. Mater., 58, 226-233 (2016).
- [7] A. Sporea, L. Mihai, D. Negut *et al.*, "On-line monitoring of gamma irradiated perfluorinated polymer optical fiber," Proc. of SPIE, 9886, 98861Q (2016).
- [8] J. J. Workman, and L. Weyer, [Practical Guide to Interpretive Near-Infrared Spectroscopy] CRC Press, Boca Raton, FL (2008).



Textile Integration of POF for lighting applications

Benjamin Mohr^{1*}, Markus Beckers¹, Pia Münch¹, Gunnar Seide¹, Thomas Gries¹, Christian Bunge²

1 Institut für Textiltechnik at RWTH Aachen University
Otto-Blumenthal-Str. 1
52074 Aachen, Germany

2 Institut für Kommunikationstechnik at Hochschule für Telekommunikation Leipzig,
Gustav-Freytag-Straße 43 - 45
04277 Leipzig, Germany

*Corresponding author: Benjamin.Mohr@ita.rwth-aachen.de

Abstract: Side-emitting optical polymer fibers provide properties as low cost and weight compared with robustness, which make them perfect candidates for lighting applications. Due to their textile processibility they can be formed in many shapes. They keep their textile flexibility, which makes them suitable for shape-changing applications. They open up a lot of design possibilities, which will lead to new ways of applications, in particular in the context of illumination.

1. Introduction

New energy-harvesting systems in form of kites, solar balloons or wind turbines are just a few examples for innovative approaches that can be enhanced by illumination. They have two things in common: On the one hand they have to be illuminated due to flight safety issues. But also they have to fight with low acceptance by the local population due to their optical influences on landscapes and views. Thus the perfect balance can be combining artistic expression with the necessary characteristics of lighting. The hesitation will fade away with artistic exhibitions. Those may help to overcome skepticism against wind turbines and similar projects. Recently, the ITA succeeded in braiding and weaving illuminated POF structures in a rope for kind kites. This lead to the proof of principle that POF is suitable for that textile-based lighting applications. This paper will give an introduction to the possibilities in textile processing of POF and the resulting lighting applications.

Charles Kao predicted lasers and fibres for communication purposes exactly 50 years ago [1]. A lot has changed since then with usage, production and materials. But, the principle of transmitting light has stayed the same. Polymer optical fibres have some significant advantages over glass fibres: They show robust qualities when faced with bending/stretching forces and other occurring environmental effects, which are of particular interest in textile structures. In the right configuration and placement POF can save substantial weight compared to conventional light sources.

Today, POF finds application in lighting mainly in two different ways: The first application is to guide the light from a source at a central location to another place and illuminate it. In this way one needs only a single power supply or the light source can be put in a safe environment. The second approach is to use the POF itself as a distributed light source to illuminate contours and outlines for example [3]. This paper concentrates on the latter.

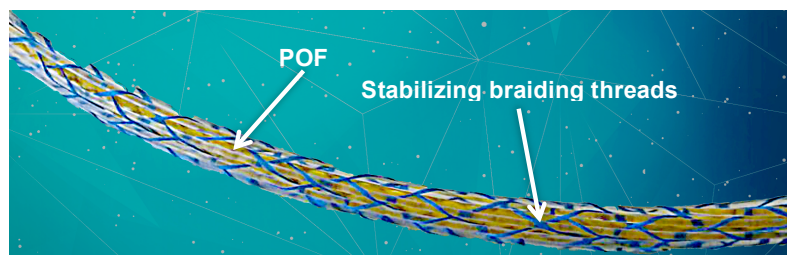


Figure 1: Braided POF structure



2. Assortment of selected textiles

The main reason of POF material to be inserted in textile material is to guide electromagnetic waves, mostly in the form of light. The placement of POF in the fabric is versatile and depends on the type of fabric and its production. Long, straight lines or bent forms can be manufactured.

The aim is for a constant illumination over the fibre length with as little loss or decrease of brightness as possible over a long distance. One main factor that determines the light output is the undulation or the difference from a straight line to a loop. Having loops in the fabric can lead to an increased brightness at the bends thus leading to shorter maximum distances. But bent sections can also be used to intentionally create bright spots or increase the brightness level locally.

How to place the POF in different fabrics with positive results will be discussed in the next paragraphs. The following section also highlights the different fabrics and what should be known when working with POF.

2.1 Woven fabrics

The production of woven fabrics is known as weaving. It describes the interlacement of warp (0°) and weft (90°). The weft yarn can be placed under or above the warp depending on the weaving pattern. The most popular patterns are plain, twill, satin, basket, leno and mock leno. The pattern plain is shown in a layout underneath.

POF can be integrated as either weft or warp. The chosen pattern determines the resulting undulation of the fibres and the lighting effect of the fabric. The use of POF in the position of weft is considered to be more flexible [4]. The production of a woven fabric with integrated POF may not be possible with every available weaving machine. This is due to the insertion mechanism of the machine and the thickness of the POF yarn. Furthermore, the stability and coherence of the fabric depends on the interaction of the chosen pattern and the properties of the POF yarn. The leno weaving pattern has shown to result in promising fabrics [5].

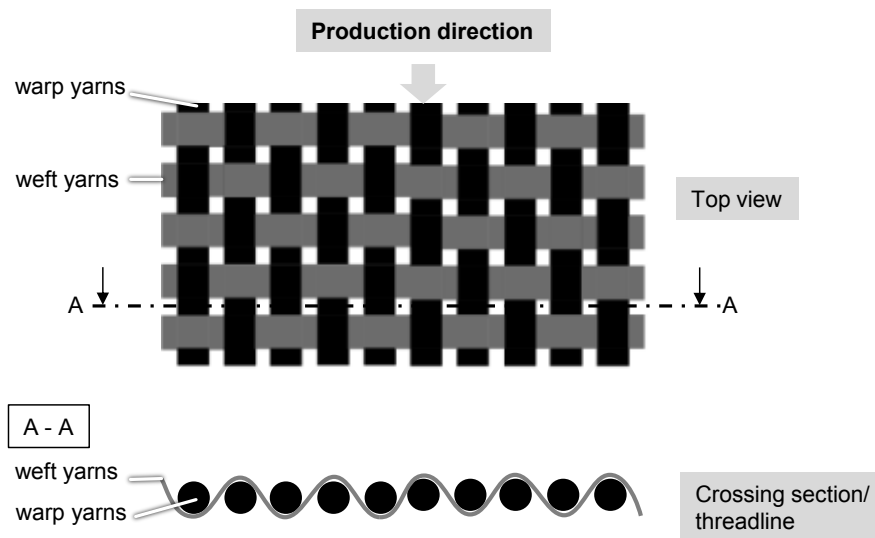


Figure 2: Structure of a woven fabric in top view and cross section [4]



2.2 Knitted fabric

The production of a knitted fabric can be categorised in two varieties: The weft-knit and the warp-knit. The formation of the symmetrical loops for the warp-knit is done in direction of the production. The weft-knit is distinguished by the loop formation 90° turned to the former. Because of the structure, knitted fabrics are flexible and can be better distorted in comparison to woven products.

The high undulation of the yarn for this fabric poses a problem for the work with POF. The transmission of light is not possible. Therefore are knitted fabric with POF as a primary yarn not possible to fabricate [4]. The integration of POF between the loops as a weft or warp yarn but has potential. The POF is integrated in straight lines in the production of the fabric. This process is possible with most available production equipment on the market today. The possible configurations are shown in Fig. 3.

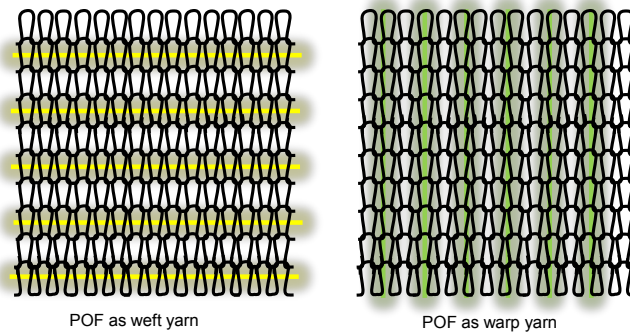


Figure 2: POF integration in knitted fabrics [4]

2.3 Braided fabrics

Braiding is the technic of placing three or more yarns in-between of one another to form a flat or tubular structure. The process is flexible and the form of the fabric can be changed to a variety of appearances. Three dimensional structures with changing diameter on the main axis are possible to be produced. The manufacturing of braided fabrics is a continuous process. The integration of additional threads in the structure is possible. This is important because POF cannot be used as primary yarn. The undulation and turning in the process hinders the manufacturing of POF integrated fabrics. This does not allow the transition of light in the completed fabric [4]. The concept of braiding is illustrated in Fig. 4.

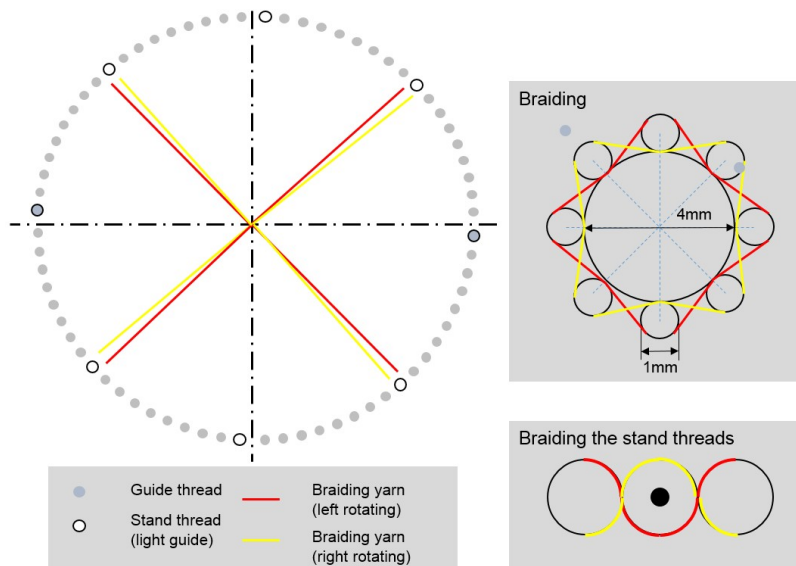


Figure 3: Concept of braiding process



Two possible ways of including POF in braided fabrics will be further discussed. One possibility is to place the POF yarn in longitudinal direction between the braided yarns. This creates a straight orientation of the POF in the production axis. This enables a transmission of light through it. The second way of integrating POF is in the radial braiding process. The POF is used as a core material and the braided fabric is formed around it. The use of a core is an essential method of braiding and can be used with various shapes [4]. A sketch of this overbraiding of the POF is shown in Fig. 5.

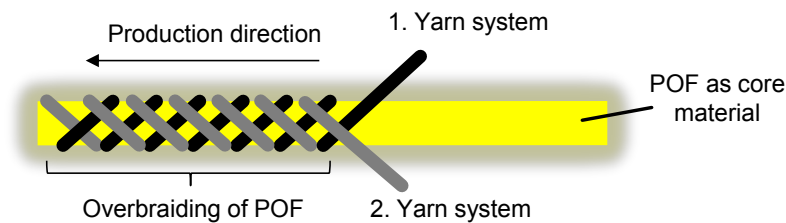


Figure 5: Process of braiding with POF core [4]

2.4 Multiaxial Non-Crimp Fabric

The structure of multiaxial non-crimp fabric (NCF) consists of two or more layers of fibres which are oriented in the same direction. The build-up can be adapted and tailored to the specific use of the fabric. The plies of fabric are held together by a stitched yarn. It is integrated in the fabric with needles after the layers of fibres are orientated and laid on one another. This stitching prevents the movement or crimping of the laminate. A possible combination of layers in different directions is pictured on the right.

NCF is used in composite applications because of the adaptable design. It has good impregnation behaviour due to the space created by the the stitches. POF can be positioned in every ply of fabric and the lighting result can thus be changed. The higher in the stack they are positioned, the brighter the light will be on the surface.

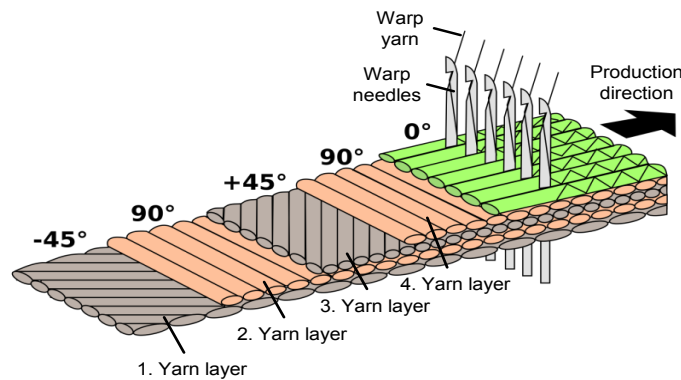


Figure 6: NFC layout with warp yarn and needles [4]

3 Examples of use cases

Medicine: Bringing light to hard-to-reach places is a way to make none-invasive surgeries and procedures possible in the field of medicine [6]. The market of medical fibre optics will increase by 7.6% from 2013 to 2019 [6] Other applications of POF in the medical sector include lighting in dental procedures. The limited space demands a fitting solution to bring illumination to almost inaccessible places and an optimal experience



for the patient. Surgical and diagnostic instrumentation will see new innovations with the advancement of POF.

Safety: High-stress applications demand a durable and reliable product. Safety lighting on wind turbines are exposed to temperatures from -20°C to 60°C , corrosive elements in the air and rain. Offshore wind parks have to withstand the sodium chloride saturated environment by the sea and heavy winds. With an application on balloons, the POF has to be flexible and resistant to tensile and compressive forces.

Art/Design/Fashion: The art world has already taken a liking to the POF technology. The free form of application has inspired many artists to create light installations all around the world. One example is a 49,000 square metres project in the Australian desert near the Uluru rock by the artist Bruce Munro [7]. POF were placed all over the ground of the desert in different colours, interconnections and forms. For the fashion sector is POF an obvious material to work with. New design from Haute Couture to designs for young and flashy collections are becoming more and more popular in the future.



Figure 4: Illustration of a hot-air balloon with safety lights.

4. Conclusion

There are a lot of possibilities for the use of POF in textiles for lighting applications. POF might be integrated to almost all textile structures, but due to their high stiffness, tight bends have to be avoided. If integrated to textile structures in a linear form, e. g. as warp or weft yarn in weaving or knitting or as filler yarn in braiding, POF are most suitable to illuminate textile structures.

4. References

- [1] Chirgwin, R. (2016, 07 18). *theregister.co.uk*. Retrieved from http://www.theregister.co.uk/2016/07/18/happy_birthday_the_optical_fibre_revolution_is_50_years_old/
- [2] Harmon, J. e. (13. September 2001). *Optical Polymers*. Washington, DC: ACS Symposium Series; American Chemical Society.
- [3] Daum, W. (2002). *POF - Polymer Optical Fibers for Data Communication*. Berlin: Springer-Verlag Berlin Heidelberg GmbH.
- [4] V. Schrank und M. Beer (2016). POF in textile fabric structures, 2015. In Bunge, A.; Gries, T.; Beckers, M. *Polymer Optical Fibres*, Woodhead Publishing
- [5] De Clercq, G. (2010). Leno-weaving : the past, present and future of a promising weaving technology. *Conference: Seminar on Leno Technologies*. Gent.
- [6] Research, P. M. (2016, July 8th). *medgadget.com*. (Persistence Market Research) Retrieved from <http://www.medgadget.com/2016/07/medical-fiber-optics-market-growing-at-the-rate-of-7-6-from-2013-to-2019-according-to-pmr-report.html>
- [7] Ruiz, C. (23. February 2016). *theartsnewspaper.com*. from: <http://theartsnewspaper.com/news/bruce-munros-light-installation-to-illuminate-ayers-rock/>
- [8] Relations, M. (19. July 2016). *Osa.org*. (The Optical Society) from http://www.osa.org/en-us/about_osa/newsroom/news_releases/2016/new_detector_from_facebook_s_connectivity_lab_over_abgerufen



Power over POF activities at the POF-AC Nuremberg

J. Fischer*, J. Vinogradov, S. Zisler, O. Ziemann

POF-AC, Technische Hochschule Nürnberg Georg Simon Ohm, Wassertorstrasse 10, 90489 Nuremberg, Germany

*Corresponding author: Jakob.Fischer@pofac.th-nuernberg.de

Abstract: The transmission of power over optical fibers is a well-established technology. Many commercial systems make use of the combination of low loss silica glass fibers and high power infrared laser diodes. Up to typically 1 W power can be transported over 1 kilometer at least. The application of Polymer Optical Fibers offers new possibilities for low cost solutions in mass productions at lower power levels and for shorter distances. This paper will give a short overview on the latest POF-AC activities in this technology.

1. Introduction

The use of fiber optic based powering (called power over fiber) is applied in several applications with high voltages and/or strong electromagnetic fields. These applications make use of the fact that glass or polymer optical fibers are not conducting cables. On the other hand Power over Fiber requires additional components, namely the light source and the optical power converter. The transmission efficiency is lower than an electrical transmission and the optical fiber needs a special handling. Nevertheless, in many applications an electrical solution is to expensive, not sufficiently save and sometimes not possible. The former company JDSU (split into Viavi Solutions and Lumentum Holdings Inc. in 2015) lists the following possible applications for optical powering on glass fibers:

- Medical
- Wireless communication
- Industrial sensors
- Energy
- Aerospace
- Defense

It is obvious, that mass or private customer based applications do not occur in this list. The reasons are the relatively high price, the difficult handling of the fiber and eye safety issues. We believe that polymer fibers may expand the application area onto the low cost segment. Several sensor applications require very small electrical power values. In combination with intermediate energy storage and pulse mode operation a few microwatts may be sufficient for a sensor application. Taking into account, that most of the applications in private environment bridge distances below 50 m, the POF can fulfill all requirements on the fiber. The following table compares typical parameters of POF and glass fiber based solutions.

Table 1: Comparison of POF and GOF for power transmission

	Glass fiber	Polymer fiber
source	Infrared laser diode	LED or 650 nm LD
fiber-Ø	50 .. 200 µm	1 mm
typ. power	100 mW	1 mW
detector	silicon	silicon (and others?)
distance	some 100 m	up to 50 m
advantages	<ul style="list-style-type: none"> • very efficient laser • high overall efficiency 	<ul style="list-style-type: none"> • very low costs and simple mounting • flexible cable with low bend radius • visible light
disadvantages	<ul style="list-style-type: none"> • not eye save • infrared light • expensive parts/complex connectors 	<ul style="list-style-type: none"> • low power • short distances • use only up to +85°C



2. Projects

The work on “Power over POF” subjects was supported by several projects over the last years, as listed below (see [1..6] for published project results).

- BeSEL: Operating and Switching of Electrical Systems with Light, Semikron Foundation
- ST-POF: Switching of Transistors with Light, Bavarian Science Foundation
- POF-Control: POF based Measuring, Control and Switching, Bavarian Ministry for Science and Education
- OHM-Netze: Optical Home- and Mikro Networks, European Regional Development Fund

In the subchapters below a few of the results of these projects are shown.

2.1 “BeSEL”

The aim of the project “BeSEL” was mainly to build up basics in the POF-AC regarding power over POF. Parts of the results were the investigation of high-power LEDs for energy transmission and initial approaches of optimized coupling of LED into POF. Additionally a first demonstrator using a commercial alarm clock with a thermometer as electrical consumer was developed during this project (see fig. 1).



Figure 1: POF powered sensor application

For this first demonstrator a POF-coupled LED with a wavelength of 460 nm and a fiber coupled power of 7 mW was used. The coupling was realized using a commercial module based on a micro structured parabolic reflector setup. The maximum output power produced by the system was 1.625 mW for a load of roughly 1 k Ω . This made it possible to power the electrical device over 50 m POF

The special feature of this demonstrator is the use of an InGaP converter (developed at the “Fraunhofer Institut für Solare Energietechnik Freiburg”). The output voltage is about 1.4 V, compared with typically 0.45 V to 0.7 V for silica converters. The advantage is that no additional voltage conversion is required. Other possibilities to achieve such a high voltage are the used of cascaded converters or passive transformers ([3]).

2.2 “ST-POF”

The ST-POF project pursued the approach of using polymer fibers as a transmission medium to switch thyristors with light. The main goal was to investigate if a combination of LED and POF supplies enough energy to switch an existing light triggered thyristor. Some results of this project were already released previously at the international POF-Conference 2015 [5].



There are two central questions which should be clarified for this project. The first one is the question of the minimum light power for short wavelength (450 nm to 850 nm), which is necessary to switch the thyristor. The second one is, what fiber coupled pulse output is needed using LEDs with different wavelengths.

The minimum light power which is necessary to switch the thyristor is highly wavelength dependent. While for switching the thyristor at 908 nm only a power of about 6 mW is necessary, for 650 nm already a power of 20 mW is needed. For the shortest measured wavelength of 450 nm a power of almost 70 mW is needed. Figure 2 shows an approximation of the needed power depending on the wavelength. As it can be seen the dependency follows the exponential function $P = 1400 \text{ mW} \cdot e^{\frac{-\lambda}{147.4 \text{ nm}}} + 3.02 \text{ mW}$ with:

P: Power which is necessary to switch the thyristor

λ : Wavelength of the incident light

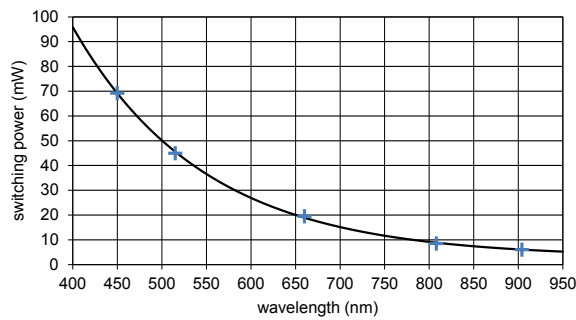


Fig. 2: Needed switching power for the thyristor over wavelength [5]

The maximum fiber coupled pulse output using LEDs was measured for LEDs which are already equipped with a fiber clamping. Three different LEDs with a wavelength of 650 nm, 850 nm and 940 nm were used. The fiber coupled power was measured after one meter POF. In figure 3 the optical power for 500 mA LED current and a pulse width of 100 μ s can be seen.

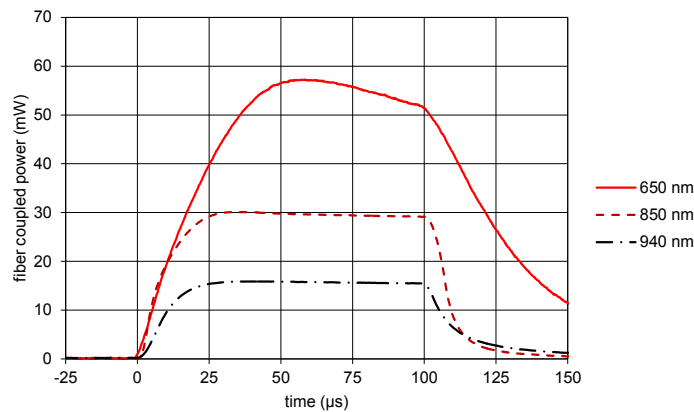


Fig. 3: Fiber coupled power for different wavelengths [5]

For all three wavelengths the fiber coupled power after 1 m POF is sufficient to switch the thyristor, even if the coupling losses using POF compared to the PCS fiber which the light triggered thyristor was designed for are taken into account.



2.3 “POF-Control”

The project “POF-Control” is still running and part of it is the development of remote powered sensor systems as well as optical switched power electronics.

A part of this project was the realization of a demonstrator by Klüher, Englert and Urbanek in 2015 (see [6] for details). A liquid level sensor is powered over a piece of POF using a high power blue LED with 460 nm wavelength. The reverse data transmission is realized over a second POF. The data transmission works in burst mode operation. In order to supply sufficient power, the continuously transmitted light is converted by the previously described InGaP converter into electrical energy, voltage-up-converted and stored in a double layer capacitor which requires only a few minutes for complete loading. A possible application is the measurement of filling levels in tanks with flammable or explosive liquids or the measurement of the electrolytic conductivity (conductometry) of liquids. Figure 4 shows the final setup for the measurement of filling levels.

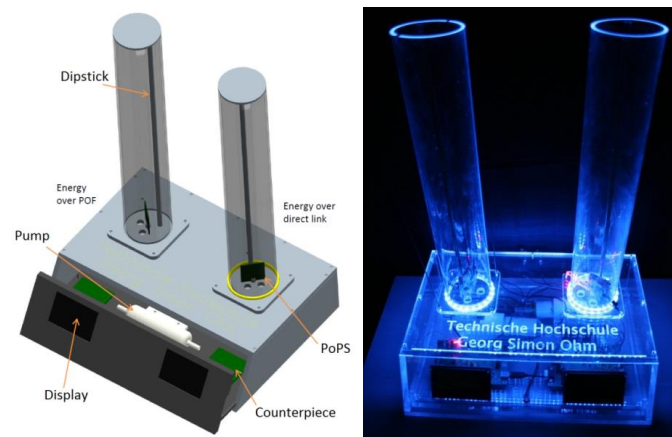


Fig. 4: Level measurement demonstration setup

2.4 “OHM-Netze”

The latest project “OHM-Netze” started in June 2016. It includes the cooperation with 9 local small and medium enterprises and is funded by the European Regional Development Fund (EFRE). Power over POF solutions will be developed as one fundamental parts of this four years cooperation.

As one of the first tasks of this project, a further development of the demonstrator from the “BeSEL” project was realized (see fig. 5). Therefore a high power LED with an active area of 1 mm² was coupled into a 2 mm POF using a reflective taper. Thus it is possible to couple about 45 % of the power into the fiber and achieve up to 60 mW electrical power on the consumption side. Compared to a setup without a taper an increase of about 50 % is attained. The electrical consumer of this demonstrator is a bell-type armature motor which is running directly with the 1.4 V of the InGaP converter.

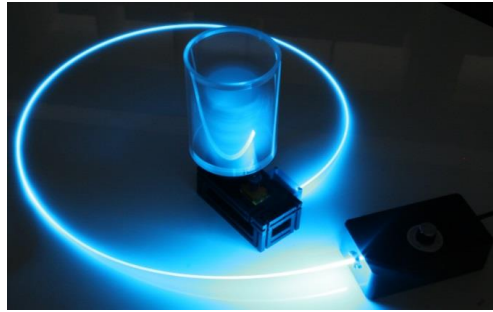


Fig. 5: First demonstrator out of the project “OHM-Netze” using Power over POF to drive a motor

3. Conclusion

We have introduced some first applications of powering over POF. In some running projects we will investigate possible improvements of the concept. The main focus is set on the reduction of required components in order to make the solutions robust, low cost and highly reliable.

The POF AC Nürnberg is a project of the Hightech Offensive Bavaria. The work was supported by the Bavarian Ministry of Education, Culture, Science and Art inside the Project “Optika²” (No. F1116.NÜ/13) and the European Regional Development Fund inside the Project “OHM-Netze” (No. EU-1607-0017).

4. References

- [1] O. Ziemann, M. Lubert, H. Poisel, J. Fischer, M. Bloos: “POF-ferngespeiste Sensoren - ein Ausblick”, Workshop “Sensoren mit POF, Wernigerode, 06.11.2012
- [2] H. Poisel, O. Ziemann, J. Fischer, M. Lubert: „Power over POF - Overview“, Intern. POF Conference POF’2013, 11.-13.09.2013, Rio de Janeiro, pp. 317 - 321
- [3] J. Fischer, M. Lubert, S. Vryonis, O. Ziemann, H. Poisel: „Power over POF using passive Transformers“, Intern. POF Conference POF’2013, 11.-13.09.2013, Rio de Janeiro, pp. 182 - 188
- [4] K. Smirnow, S. Loquai, J. Fischer, O. Ziemann, T. Becker: „Switching Electrical Power with Polymer Optical Fibers“, Intern. POF Conference POF’2014, 08.-10.10.2014, Yokohama, pp. 118 - 120
- [5] S. Loquai, M. Bölting, U. Kellner, J. Fischer, H. Poisel: „Switching Direct Light Triggert Thyristors with Polymer Optical Fibers“, Intern. POF Conference POF’2015, 22.-24.09.2015, Nürnberg, pp. 193 - 199
- [6] J. Klüher, P. Englert, P. Urbanek, O. Ziemann: „Powered over POF Sensors: Level Measurement“, Intern. POF Conference POF’2015, 22.-24.09.2015, Nürnberg, pp. 115 - 120



Analysis of Light Emission in Polymer Optical Fibers Doped With Europium Complex

J. Arrue^{1*}, M.A. Illarramendi¹, B. Garcia-Ramiro¹, I. Parola¹, F. Jiménez¹, J. Zubia¹,
R. Evert², D. Zaremba², H.-H. Johannes²

1 University of the Basque Country (Spain)

2 Technische Universität Braunschweig (Germany)

*Corresponding author: jon.arrue@ehu.es

Abstract: Polymer optical fibers doped with Eu^{3+} can be employed as light sources or amplifiers in the visible region, or as fluorescent collectors for solar energy conversion. In this paper, their main optical properties and the dependence of their emission on the pump power are analyzed theoretically and experimentally. The numerical simulations are carried out by solving a set of four rate equations in stationary state as a function of fiber length for several pump powers and pump wavelengths. The experimental results provide additional information about changes in the spectral emission when the pump power is varied.

1. Introduction

Light generation and transmission at visible wavelengths can be achieved by employing poly(methyl methacrylate) polymer optical fibers (PMMA POFs) doped with active materials that emit visible light when pumped at a shorter wavelengths, as is the case of Eu^{3+} or organic dyes [1,2]. Such active POFs are especially suitable for remote illumination, owing to their typically large diameter (≈ 1 mm), to their high flexibility, and to the fact that their attenuation is lowest in the visible region. Alternatively, doped POFs could also be used as solar light collectors, on the basis that dopant molecules might strongly absorb the ultraviolet (UV) light of the sun when this illuminates the fiber laterally [3]. In such a case, UV light enters the fiber in directions that are not guided, but it serves to pump dopant molecules to an excited energy state. These molecules are employed to generate visible light in all directions, including guided directions. Another possible field of application of doped POFs is as amplifiers of telecommunications signals in the visible range of the spectrum, which may be useful to compensate for the large attenuation of such signals in POFs longer than 100 metres [4].

This paper is focused on Eu^{3+} -doped POFs. The main advantage of Eu^{3+} over organic dopants is the absence of photodegradation of the dopant [2]. Although europium is not directly soluble in PMMA, each europium ion may be surrounded by a ligand that makes it soluble, thus enabling the manufacture of POFs [1,2]. In this paper, we present results of POFs doped with the europium complex called Eu(AC46). The ligand dramatically increases the absorption cross section of bare rare earth ions, which serves to employ shorter fiber lengths. Specifically, the values of the absorption cross sections of the europium complex are comparable to those of typical organic dyes. As a consequence, when the fiber is pumped longitudinally, the active volume along which a positive local gain is achieved is typically shorter than a few centimeters, although its length depends on the pump power and on the pump wavelength. This fact will be analyzed in detail the theoretical section of this paper. The paper also includes an experimental section, in which we present the evolution of the spectral emission as the pump power is increased.

2. Details about the europium complex and fiber analyzed

2.1 Energy levels of the europium complex

As shown in Fig. 1, the Eu^{3+} ions are excited indirectly via energy transfer from the ligands. In a first step, the ultraviolet pump light at wavelength λ_p excites the ligand from the ground state S_0 to the singlet state S_1 , from which it rapidly decays to the triplet state T in a non-radiative way. In a second step, a radiationless energy transfer to the state 5D_1 of the Eu^{3+} ion takes place, with a probability that is proportional to the inverse of the lifetime $\tau_{T \rightarrow D}$. This is the transition that occurs in most cases, although a transition to S_0 may occur instead, but with a much lower probability, which is proportional to the inverse of the lifetime $\tau_{T \rightarrow S_0}$. Once excited to the state 5D_1 , the Eu^{3+} ion immediately relaxes non-radiatively to the state 5D_0 , from which it eventually relaxes to one of the low-energy states of europium, yielding fluorescence emission with a probability that is inversely proportional to $\tau_{D \rightarrow F}$. The preferred relaxation path is ${}^5D_0 \rightarrow {}^7F_2$, which has a lifetime of 0.9 milliseconds. This



transition occurs by emission of a red photon at a wavelength of about 614 nm. It can also be stimulated by other photons of the same wavelength.

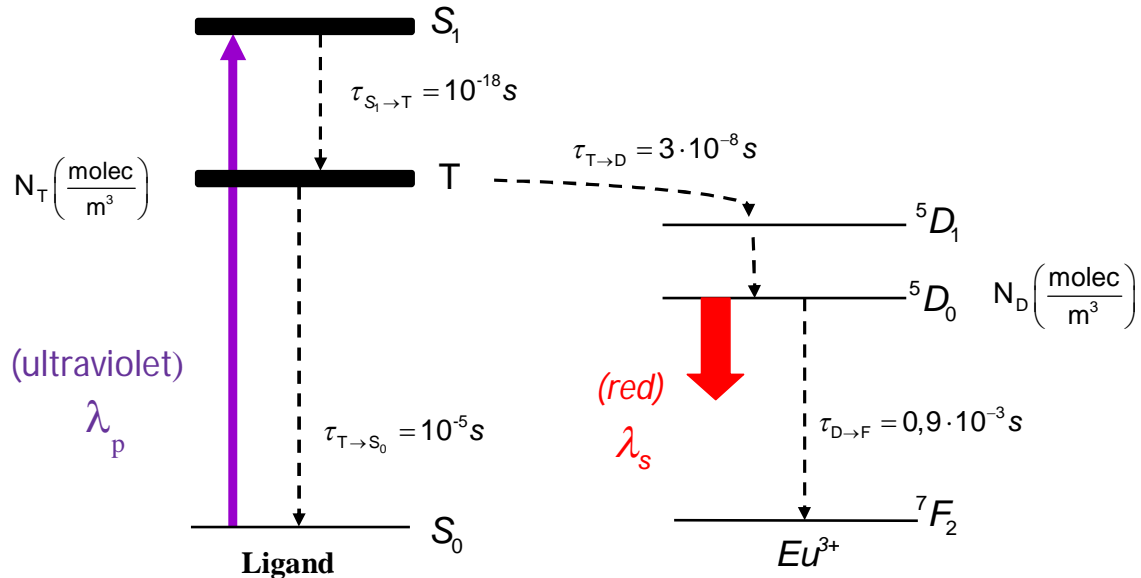


Figure 1. Energy levels and transitions in the europium complex.

1.2 Numerical simulation of the europium complex

For a given pump power P_p , the unknown variables are the power P generated at wavelength λ_s , the number N_T of excited ligands per m^3 at state T, and the number N_D of excited Eu^{3+} ions per m^3 at state 5D_0 . In stationary state, the derivatives of N_T and N_D with respect to time become 0, so two of the rate equations become $N_T = N_T(P, P_p)$ and $N_D = N_D(P, P_p)$. By substituting these expressions for N_T and N_D in the rate equations that govern the derivatives with distance z of P and P_p we obtain $P_p' = f_1(P, P_p)$ and $P' = f_2(P, P_p)$. These differential equations are solved by means of the Runge-Kutta method of order 4 using a sufficient number of steps in the desired interval of distances, e.g. 10000 steps from 0 to 3 cm.

1.3 Fiber analyzed

In both the theoretical and the experimental sections, the fiber analyzed is a $Eu(AC46)$ -doped PMMA POF, with a UV-curing acrylate cladding. The fiber numerical aperture is 0.5. The fiber diameter is 1 mm and the core diameter is 980 μm . Only the core is doped. The dopant concentration is $N = 5 \cdot 10^{19}$ molecules/ cm^3 . The spectral attenuation of this fiber is shown in Fig. 2. It was manufactured in the way reported in [1].

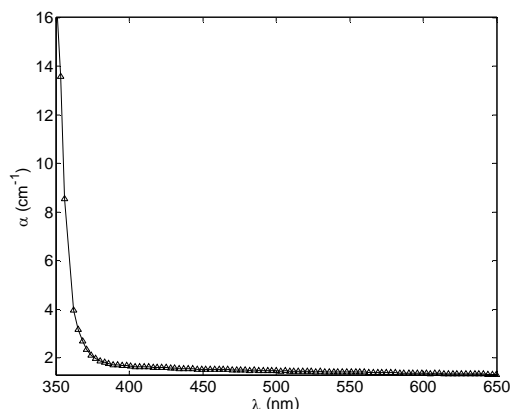


Figure 2. Attenuation coefficient of our europium-doped POF.

2. Simulation results

From Fig. 2, it is straightforward to calculate that there are certain pump wavelengths (e.g. 350 nm) at which our fiber would absorb the majority of the pump power in distances as short as 1 mm. This fact is advantageous in the case of side pumping, in which the length available for absorption is limited to the core diameter. However, the question then arises as to what wavelengths should be employed in the case of longitudinal pumping from the fiber end, i.e. when the length available for absorption is not limited. To clarify this issue, Fig. 3 shows the evolution of the density of excited Eu^{3+} ions with distance for two different wavelengths: 355 nm, which corresponds to the third harmonic of an Nd-YAG laser, and 377 nm, which is a wavelength of much lower attenuation (see Fig. 2). As expected, the pump wavelength of lower attenuation yields the largest active volume containing excited Eu^{3+} ions that emit light. This is so for any incident pump power $P_p(z=0)$, although the active volume increases when the incident P_p is augmented. For the shortest distances, the pump power is high enough for N_D to saturate to its maximum value $N_D \approx N$. After a certain distance, N_D decreases to approximately zero, which can be explained because P_p becomes negligible due to its attenuation along z . The behaviour of N_T is similar, but N_T decreases to approximately zero in a shorter distance than N_D (see Fig. 4). This difference between N_D and N_T is a consequence of the rapid depopulation of the excited state T of the ligand and the corresponding population growth of the excited state of the Eu^{3+} ion, due to the already commented low lifetime $\tau_{T \rightarrow D}$ as compared to $\tau_{T \rightarrow S_0}$ (see Fig. 1). Despite these differences, both N_D and N_T tend to penetrate to larger values of z when the pump attenuation is lower, which explains the results obtained in Fig. 5, in which the generated power is considerably higher at 377 nm than at 355 nm, in spite of the higher value of $N_T(z=0)$ at 355 nm shown in Fig. 4.

3. Experimental results

From the previous discussion, we can expect that the third harmonic (355 nm) of a pulsed Nd-YAG laser will yield an active volume that only extends about 1 cm or less into the fiber, as predicted in Fig. 3. This result was observed experimentally by our group. Our laser produced pulses of 20 ns (full width at half maximum), and the corresponding spectral emission at the other end of a 20 cm fiber is shown in Fig. 6 (left). It was measured with a fiber spectrometer containing a CCD camera. We can observe that the areas of the two highest spectral peaks, which represent the energies of the peaks, seem to increase more rapidly with the pump energy E_p from a value of E_p of approximately 2 mJ (see Fig. 6 (right)). This could be indicative of the onset of Amplified Spontaneous Emission (ASE). Since the fluorescence lifetime $\tau_{D \rightarrow F}$ is long (0.9 ms), long exposure times are needed to detect the four peaks with the fiber spectrometer. Otherwise, the lowest fluorescence peaks would not appear in the measurement, as we have checked experimentally, while the highest peaks could be detected with shorter exposure times, due to the fact that the presence of ASE reduces the average transition time. Preliminary results have also confirmed that a very intense emission can be obtained by pumping the fiber with a continuous (CW) laser diode of 377 nm.

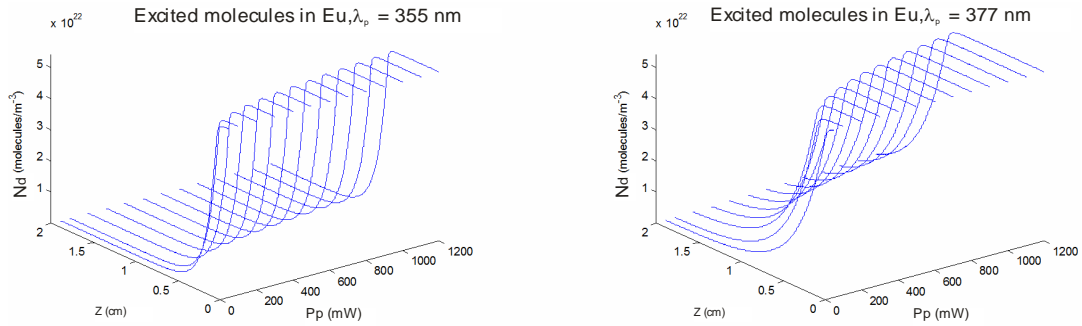


Figure 3. Theoretical evolution of the density of excited Eu^{3+} ions for two different pump wavelengths.

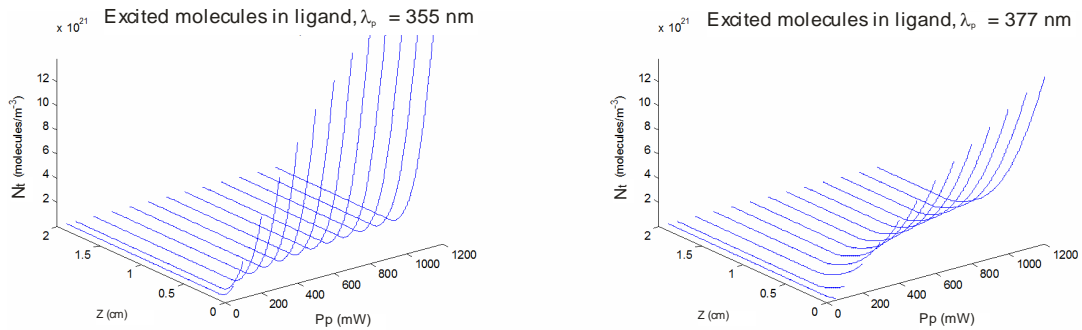


Figure 4. Theoretical evolution of the density of excited ligands for two different pump wavelengths.

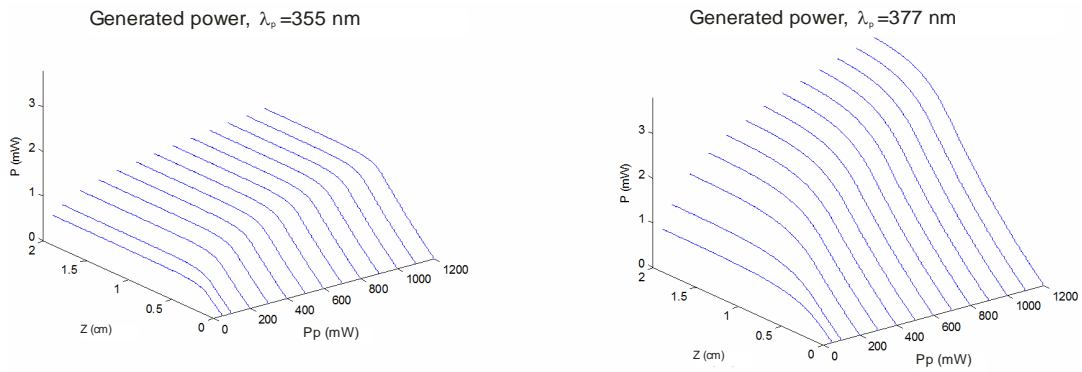


Figure 5. Theoretical evolution of the generated power at about 614 nm for two different pump wavelengths.

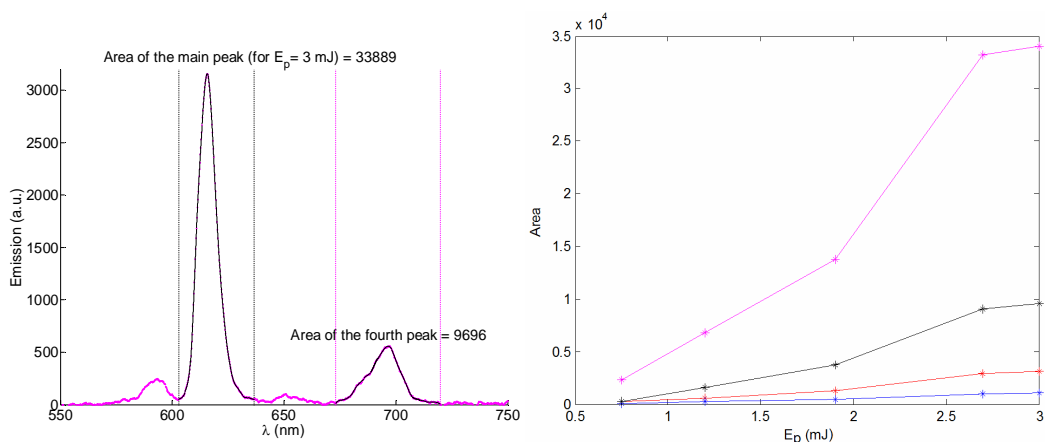


Figure 6. Experimental spectral emission for $E_p = 3$ mJ (left), and evolution of the area of each spectral peak with E_p (right), the four curves being in descending order of areas, i.e. the uppermost curve corresponding to the main peak.

4. Conclusions

Compact light sources of a few centimetres in length emitting in the red can be achieved by longitudinally pumping Eu(AC46)-doped PMMA POFs at ultraviolet wavelengths. A fiber as short as 1 cm has proved to be feasible for this purpose if a sufficiently short pump wavelength is employed. However, longer fibers serve to obtain higher gains, as long as the pump wavelength is also increased. The main optical properties of these active POFs and the dependence of their emission on the pump power have been analyzed theoretically and experimentally.

5. Acknowledgements

This work has been funded in part by the Fondo Europeo de Desarrollo Regional (FEDER); by the Ministerio de Economía y Competitividad under project TEC2015-638263-C03-1-R; by the Gobierno Vasco/Eusko Jaurlaritza under projects IT933-16 and ELKARTEK; and by the University of the Basque Country UPV/EHU under programmes UFI11/16 and Euskampus; The work carried out by I. Parola has been funded by a research grant given by the Departamento de Educación, Política Lingüística y Cultura del Gobierno Vasco/Eusko Jaurlaritza for her PhD thesis.

6. References

- [1] R. Caspary, S. Möhl, A. Cichosch, R. Evert, S. Schütz, H.-H. Johannes, W. Kowalsky, "Eu-Doped Polymer Fibers," *Proceedings of ICTON*, 2013.
- [2] D. Oh, N. Song, and J.-J. Kim, "Plastic optical amplifier using europium complex," *Proceedings of SPIE*, **4282**, 2001.
- [3] A. Goetzberger, and W. Greubel, "Solar Energy Conversion with Fluorescent Collectors," *Appl. Phys.* **14**, pp. 123-139, 1977.
- [4] L. H. Slooff, A. van Blaaderen, and A. Polman, "Rare-earth doped polymers for planar optical amplifiers," *Journal of Appl. Phys.*, **91**, no. 7, 2002.



Investigation of Molecular Weight and Optical Behaviour of PMMA with Different Chain Transfer Agents

Onur Cetinkaya¹, Gokhan Demirci², Pawel Mergo^{1*}

1) Laboratory Optical Fiber Technology, Faculty of Chemistry, Maria Curie-Skłodowska University, Lublin, Poland

2) Department of Polymer Chemistry, Faculty of Chemistry, Maria Curie-Skłodowska University, Lublin, Poland

*Corresponding author: onurc@umcs.pl

Abstract: In bulk thermal polymerization of MMA, pentamethyl disilane (PMDS), isopropyl alcohol (IPA) and n-butyl mercaptan (nBMC) were used as chain transfer agent (CTA) for the purpose of control the molecular weight of PMMA. As it was expected, molecular weights were inversely correlated with amount of chain transfer agents. In comparison of different CTAs, it was observed that molecular weight of samples which were prepared with same amount of CTA were not same due to reactivity of compounds. According to scattering studies the highest amount of CTA showed more scattering. No relationship between amount of CTAs and transmission was found. Amount of CTA also has no effect on refractive index of samples. But there is very small difference for different type of CTA.

1. Introduction

Producing polymer which has good transparency and proper molecular weight is quite important in optical fibre technology to have fine optical fibre. Polymer optical fibres have a lot of applications and some better properties according to silica fibres for short haul communications such as lower cost, higher ductility, larger core-diameter, relative immunity to dust and electromagnetic interference, easy handling low weight, multiplexing capabilities [1,2].

Poly(methyl methacrylate) is one of the polymers widely used in obtaining polymeric optical fibres [3-8]. It has better elastic limit (10%) according to silica (1-3%) and can show no break 30% strains [9]. But loss of PMMA optical fibre is higher than silica fibres almost 100 to 200 times, because of impurities and intrinsic absorption [10] mainly caused by C-H bonds and impurities [11].

Radical chain transfer reactions are useful technique for producing polymers by controlling molecular weight and molecular distribution and also for degree of functionalization studies [12]. Detailed studies about mechanism and kinetic of chain transfer agents were done by many researchers [13-19]. Polymerization with chain transfer agents also change structure of the polymer which cause to effect on heating resistance [20].

Gennadii et al. and Zaremskii et al. studied about controlled pseudo-living radical polymerization [21,22] which were used for preparing monodisperse polymers, nevertheless even at high temperature (100 -120 °C) the polymerization rate is low due to reversible inhibition. It is important to produce polymer with narrow molecular weight distribution with high polymerization rate. Therefore, Semchikov et al. studied about the molecular-weight characteristics of polymers prepared with polyfunctional silicon hydrides for overcoming this problem [23]. Bulgakova et al. showed that organohydrodisilanes are more effective according to mercaptans which are widely used as chain transfer agent [24,25]. In their another study, silicon hydrides were used as chain transfer agents and the reactivity of silicon hydrides for styrene and methyl methacrylate and effect on the molecular weight were compared [26]. The activity of monomer, the chemical structure of chain transfer agents (silicon atom sequences) effect its reactivity.

Since weakness of the S-H bond, thiols are favourably used as efficient chain transfer agent [27,28]. This chain transfer agent is effective for well-known vinyl monomers such as methyl methacrylate and styrene [29].

The significance of this work is comparison of different types of chain transfer agents to observe effects on optical properties of PMMA polymer samples which were fabricated in our laboratory for uses in optical technology. Molecular weights, transmission, refractive index and attenuation of polymers were measured.

2. Materials and Methods



Methyl methacrylate (MMA, 99%, Aldrich) was purified before using as a monomer via vacuum distillation method. The initiator benzoyl peroxide (BPO, 75%, Aldrich) was used in all polymerizations after purification. Isopropyl alcohol (IPA, 99.9%, Fluka) and n-butyl mercaptan (nBMC, 99% Sigma-Aldrich) were employed as chain transfer agents (CTA) without further purification. Pentamethyldisilane (PMDS, 97%) was also used as a CTA after purified by silica column (Silica gel 60, 70-230 mesh, Merck). The purity of PMDS after purification was calculated 98.3% by gas chromatography (GC). For measurement of molecular weight, chloroform (98.5, POCH Basic) was used.

3. Experimental

3.1. Polymerization

Thermal bulk polymerization was carried out in glass test tubes. The monomer (MMA), initiator (BPO, 0.4%) and CTA (IPA, nBMC or PMDS) which is in different ratio (Figure 1) were mixed. After polymerization samples were annealed at 80 °C for thermal stability. PMMA samples with purified PMDS and unpurified PMDS were prepared to see the effect of purification.

3.2. Characterization

3.2.1. Molecular weights

Molecular weights of PMMA samples with different chain transfer agents were determined by Ostwald viscometer in chloroform at 30 °C. The molecular weights of PMMA samples were calculated by following formula [30],

$$[\eta] = 4.9 \cdot 10^{-5} \times M^{0.8} \quad (1)$$

where η is viscosity of solution of PMMA sample in chloroform and M is molecular weight of PMMA sample.

3.2.1. Optical Properties

The samples were prepared as cylindrical with 1 cm radius and 1.6 cm length. Green laser (534nm wave length) was used to observe scattering during propagating inside of the samples. In transmission studies, we used 20mm length samples which both front faces were optically polished. Refractive indexes were measured by the Abby refractometer.

4. Results

4.1. Effect of chain transfer agent on molecular weight

As it is known molecular weight can adjust by chain transfer agents which arrange polymer chains during polymerization. Molecular weight of polymer is increased by decreasing amount of chain transfer agents [31]. It can be seen clearly in Figure 1.

Same amount of different CTA led to have different molecular weight (Figure 1). The reason for this is reactivity of CTAs are different due to having different chemical structure [17, 32].

According to commercial available PMMA which is used for fabricating optical fibre, molecular weight is between 100,000-150,000 g/mol. Therefore, in our studies, it was aimed to keep molecular weight in this range with using as low amount as chain transfer agents due to avoid from impurities.

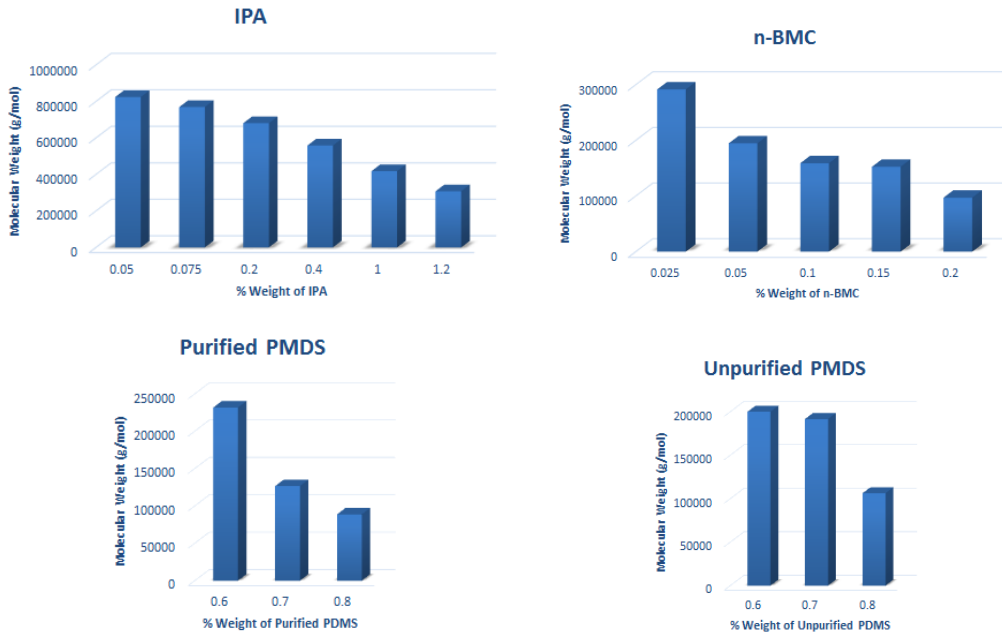


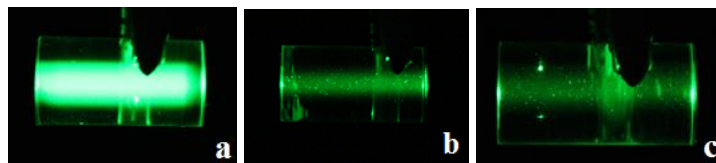
Figure 1. Molecular weights of sample with different amount of CTAs

Purity of compounds is one of the most important parameter to obtain homogeneous bulk preforms. Purification effect of PMDS was investigated. As seen in Figure 1, it can be considered that purified PMDS caused to increase molecular weight more regularly than unpurified PMDS.

According to results, optimum CTA which is suitable for the purpose is n-BMC. It was reached with lower amount of CTA to the desired molecular weight range (Figure 1). Thus, it was thought that optical loss due to compound in polymer structure was decreased. In case of IPA, for hindering to increase impurity, higher amount of IPA was not studied. In Figure 1 minimum molecular weight was reached to above of commercial PMMA.

4.2. Optical Results

Scattering properties of samples were investigated by green laser. As seen in Figure 2-5, the highest amount of CTAs showed scattering visibly. Only purified PMDS samples has lower scattering and it means that PMDS is useful among CTAs used in study for producing optical fibres. Impurities in unpurified PMDS might affect the polymerization process therefore bubbles and high polymer chain distribution could be occurred.



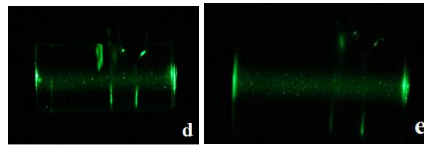


Figure 2. Laser scattering of PMMA bulk samples produced by n-BMC (a:0.2%, b: 0.15%, c:0.1%, d: 0.05%, e:0.025%)

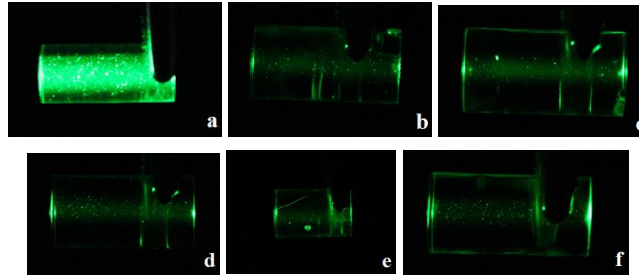


Figure 3. Laser scattering of PMMA bulk samples produced by IPA (a:1.2%, b:1%, c:0.4%, d:0.2%, e:0.075%, f:0.05%)

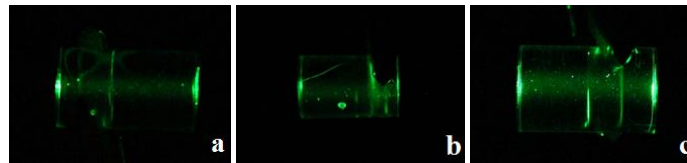


Figure 4. Laser scattering of PMMA bulk samples produced by purified PMDS (a:0.8%, 0.7%, 0.6%)

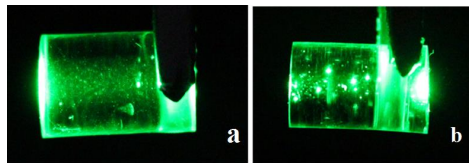
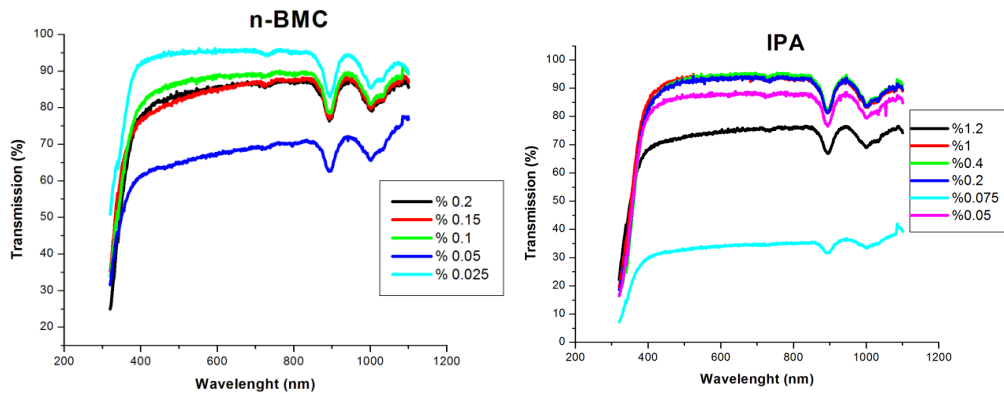


Figure 5. Laser scattering of PMMA bulk samples produced by unpurified PMDS (a:0.8%, 0.7%, 0.6%)

It can be said that there is no regular effect of CTAs on transmission. It can be seen that transmission is effected by amount of CTA randomly in Figure 6. This results may be occurred by polymerization. But averagely transmission values of samples are around 90%. It can be accepted for using in optical technology.



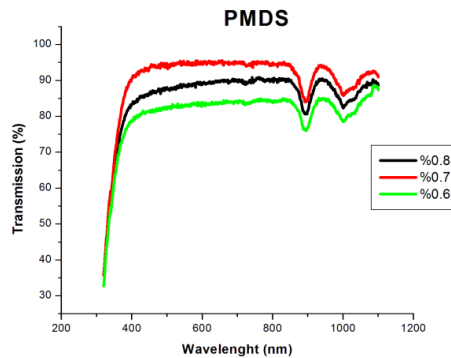


Figure 6. Transmission of samples with different type and amount of CTAs

Table 1 shows the refractive index values of all samples. Although the amount of CTA was increased for each CTA, there was no variation of refractive index values. Small changes for a CTA may be caused by errors during measurement.

Table 1. Refractive index values of all samples

CTA (%)	Refractive Index			
	IPA	n-BMC	PMDS	Unpurified PMDS
1.2	1.4911	-	-	-
0.8	-	-	1,4915	1,4916
0.7	-	-	1,4914	1,4916
0.6	-	-	1,4914	1,4916
0.4	1.4910	-	-	-
0.2	1.4909	1,4912	-	-
0.15	-	1,4912	-	-
0.1	-	1,4913	-	-
0.075	1.4911	-	-	-
0.05	1.4910	1,4914	-	-
0.025	-	1,4913	-	-

Conclusion

Different types of CTA were used for producing bulk samples and molecular weight, transmission, and refractive index of samples were measured scattering of samples were studied. Because of reactivity of CTA, molecular weight of samples was varied although it was used same amount of CTA. Only highest amount of CTA which was used in this study was observed higher scattering than other samples and almost no scattering was seen for purified PMDS. Since polymerization with unpurified was not proper, in both all samples scattering was occurred. Transmission studies showed that there is no regular change for samples which were produced with same but different amount of CTA. Refractive index is also not effected by changing the amount of CTA but very small changes were seen between different types of CTA. Polymers

Acknowledgment



The research leading to these results has received funding from the People Programme (Marie Curie Actions) of the European Union's Seventh Framework Programme FP7/2007-2013/ under REA grant agreement n° 608382.

References

- [1] A.D. Alobaidani, D. Furniss, M.S. Johnson, A. Endruweit, A.B. Seddon, Optical transmission of PMMA optical fibres exposed to high intensity UVA and visible blue light, *Opt Laser Eng* 48 (2010) 575–582.
- [2] K. Peters, Polymer optical fiber sensors—a review, *Smart Mater. Struct.* 20 (2011) 1 3002.
- [3] Z. Xiong, G.D. Peng, B. Wu, P.L. Chu, Highly tunable bragg gratings in single-mode polymer optical fibers, *IEEE Photonic Tech. L.* 11 (1999) 3.
- [4] M.A. van Eijkelenborg, M.C.J. Large, A. Argyros, J. Zagari, S. Manos, N.A. Issa, I. Bassett, S. Fleming, R.C. McPhedran, C. Martijn de Sterke and N.A.P. Nicorovici, Microstructured polymer optical fibre, *Opt. Express* 9 (7) (2001) 319-327.
- [5] D.X Yang, J. Yu, X. Tao, H. Tam, Structural and mechanical properties of polymeric optical fiber, *Mat. Sci. Eng. A* 364 (2004) 256–259.
- [6] M. Rajesh, K. Geetha, M. Sheeba, C.P.G Vallabhan, P. Radhakrishnan, V.P.N. Nampoore, Characterization of rhodamine 6G doped polymer optical fiber by side illumination fluorescence, *Opt. Eng.* 45 (7) (2006) 075003 (1-4).
- [7] A. Stefani, K. Nielsen, H.K. Rasmussen, O. Bang, Cleaving of TOPAS and PMMA microstructured polymer optical fibers: Core-shift and statistical quality optimization, *Opt. Commun.* 285 (2012) 1825–1833.
- [8] Latino, R. Montanini, N. Donatoc, G. Neri, Ethanol sensing properties of PMMA-coated fiber Bragg grating, *Procedia Eng.* 47 (2012) 1263 – 1266.
- [9] M.C.J. Large, J. Moran, L. Ye, The role of viscoelastic properties in strain testing using microstructured polymer optical fibres (mPOF), *Meas. Sci. Technol.* 20 (2009) 034014 (1-6).
- [10] A.N.Z. Rashed, Submarine fiber cable network systems cost planning considerations with achieved high transmission capacity and signal quality enhancement, *Opt. Commun.* 311 (2013) 44–54.
- [11] P. Mergo, M. Gil, K. Skorupski, J. Klimek, G. Wójcik, J. Pędzisz, J. Kopec, K. Poruraj, L. Czyzewska, A. Walewski, A. Gorgol, Low loss poly(methyl methacrylate) useful in polymer optical fibers technology, *Photonics Letters of Poland* 5 (4) (2013) 170-172.
- [12] M.O. Zink, D. Colombani, P. Chaumont, Chain transfer by addition-fragmentation mechanism-9. Access to diene-functional macromonomers using 5-(substituted)- 1,3-pentadiene-type addition-fragmentation chain-transfer agents in radical polymerization, *Eur. Polym. J.* 33 (9) (1997) 1433-1440.
- [13] F.R. Mayo, Chain Transfer in the Polymerization of Styrene: The Reaction of Solvents with Free Radicals, *J. Am. Chem. Soc.* 65 (12) (1943) 2324–2329.
- [14] F.R. Mayo, R.A. Gregg, M.S. Matheson, Chain transfer in the polymerization of styrene. VI. chain transfer with styrene and benzoyl peroxide; the efficiency of initiation and the mechanism of chain termination, *J. Am. Chem. Soc.* 73 (1951) 4 1691–1700.
- [15] F.R. Mayo, Chain transfer in the polymerization of styrene. VIII. chain transfer with bromobenzene and mechanism of thermal initiation, *J. Am. Chem. Soc.*, 75 (24) (1953) 6133–6141.
- [16] R.A. Gregg, D.M. Alderman, F.R. Mayo, Chain transfer in the polymerization of styrene. V. polymerization of styrene in the presence of mercaptans, *J. Am. Chem. Soc.*, 70 (11) (1948) 3740–3743.
- [17] C. Henriquez, C. Bueno, E.A. Lissi, M.V. Encinas, Thiols as chain transfer agents in free radical polymerization in aqueous solution, *Polymer* 44 (2003) 5559–5561M.
- [18] T. Furuncuoglu, I. Ugur, I. Degirmenci, V. Aviyente, Role of chain transfer agents in free radical polymerization kinetics, *Macromolecules* 43 (2010) 1823–1835.
- [19] J. Mendoza, J.C. De la Cal, J.M. Asua, Kinetics of the styrene emulsion polymerization using n-dodecyl mercaptan as chain-transfer agent, *J. Polym. Sci. A1* 38 (2000) 4490–4505.
- [20] S.A. Zhiltsov, S.A. Bulgakova, Y.D. Semchikov, Effect of organosilicon chain transfer agents on heat resistance of vinyl polymers, *Russ J Appl Chem+* 81 (7) (2008) 1262-1266.
- [21] G.V. Korolev, A.P. Marchenko, 'Living'-chain radical polymerisation, *Russ. Chem. Rev.* 69 (2000) 409-434.



- [22] M.Y. Zaremskii, V.B.Golubev, Reversible inhibition of radical polymerization. *Soedin.*, Ser. C. 43 (9) (2001) 1689-1728.
- [23] Y.D. Semchikov, S.A. Bulgakova, L.M. Mazanova Use of organohydridodisilanes for controlling the molecular-weight distribution of high-conversion polymers, *Russ. J. Appl. Chem+* 78 (7) (2005) 11661-169.
- [24] S.A. Bulgakova, Y.D. Semchikov, L.M. Mazanova, V.V.Semenov, Organodisilane hydrides: a promising new class of chain-transfer agents in free-radical polymerization. *Polym. Sci. B* 40 (1-2) (1998) 5-7.
- [25] C. Walling, *Free Radicals in Solution*, New York: Wiley, 1957.
- [26] S.A. Bulgakova, L.M. Mazanova, V.V. Semenov, Y.D. Semchikov, Organosilicon hydrides in macromolecular design: Reactions of chain-transfer and hydrosilylation, *Eur. Polym. J.* 43 (2007) 644-651.
- [27] F.G. Bordwell, X.M. Zhang, A.V. Satish, J.P. Cheng, Assessment of the importance of changes in ground-state energies on the bond dissociation enthalpies of the O-H Bonds in phenols and the S-H bonds in thiophenols, *J. Am. Chem. Soc.* 116 (1994) 6605-6610.
- [28] P. Wardman, C. Von Sonntag, Kinetic factors that control the fate of thiyl radicals in cells, *Methods Enzymol*, 251 (1995) 31-45.
- [29] G. Moad, D.H. Solomon, *The chemistry of free radical polymerization*, Oxford: Pergamon Press, (1995).
- [30] Houwink , 1940," *J. Prakt. Chem.* " , 157, 15.
- [31] S.Y. Yang, Y.H. Chang, B.H. Ho, W.C. Chen, T.W.Tseng, Studies on the Preparation of Gradient-Index Polymeric Rods by Interfacial-Gel Copolymerization *J Appl Polym Sci*, 56, (1995) 1179-1182.
- [32] S.G. Gaynor, J.S. Wang, K. Matyjaszewski, Controlled radical polymerization by degenerative transfer: effect of the structure of the transfer agent, *Macromolecules* 28 (1995) 8051-8056.

Melt-spun polymer optical fibers for decubitus prevention

Brit M. Quandt^{1,2}, Damien Ferrario³, René M. Rossi¹, Gian-Luca Bona^{1,2}, Luciano F. Boesel^{1*}

¹ Empa, Swiss Federal Laboratories for Materials Science and Technology, Lerchenfeldstrasse 5, 9014 St. Gallen, Switzerland

² ETH Zurich, Swiss Federal Institute of Technology, Department of Information Technology and Electrical Engineering, Gloriastrasse 35, 8092 Zurich, Switzerland

³ CSEM, Swiss Center for Electronics and Microtechnology, Rue Jaquet-Droz 1, 2002 Neuchâtel, Switzerland

*Corresponding author: Luciano.boesel@empa.ch

Decubitus ulcers, deep wounds at pressure spots, are prevalent in paraplegics and drastically decrease quality of life with high threat of infection. Bulky options create further pressure spots and thus ulcers. However, oxygen saturation in the tissue and mechanical load on tissue are thought to be the primary causes. In this work we report our recent developments on textiles incorporating flexible POFs developed at our institute. The different types both show high flexibility to allow for textile integration while transferring the signal. We report on the calibration of the pressure-sensitive fibers as well as the low-friction behaviour of the heart rate sensor. Both combined could give make personalized prevention programs possible.

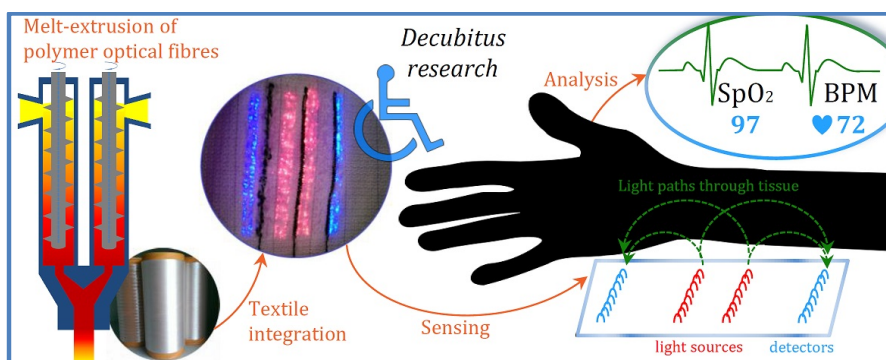


Figure 1: The project includes the development of polymer optical fibers including their optical and mechanical characterization. From there, they are integrated into textiles to form flexible sensors. We aim to complete a prototype showing the relationship between pressure on tissue and perfusion.

INTRODUCTION

In the area of textile-integrated sensors, polymer optical fibers (POF) have been used for measuring various vital parameters, such as heart rate, oxygen saturation, and respiratory rate.[1] We have developed a flexible and durable textile with incorporated polymer optical fibers engineered in our laboratory. With these, we can log heartbeat (with a core/cladding-step index structure) and pressure on tissue (core-only fibres). Previous studies also logged the blood oxygenation and strain due to respiration.[2] We would like to combine the two fibres within one sensing set-up to understand tissue changes under load. The data from the two sensors then allows for personalized care and greater understanding of e.g. tissue changes under load.

These changes are not understood yet due to a lack of flexible, non-chafing sensing solutions which then create additional pressure points on the tissue.

MATERIALS and METHODS

We present the melt-spinning of POFs from commercial urethane/siloxane block copolymers. Additionally, a bi-component optical fibre is produced at high speed (up to 400 m/min) similar to Reifler et al.[3] Both fibre

types were developed without preparation of a preform. The fibres are extruded with one respectively two single-screw extruders. They were analysed regarding their homogeneity and optical properties including light attenuation for the spectrum of visible and near-infrared light.

Photoplethysmograph: The bi-component fibres were intended for the monitoring of the oxygen saturation in tissue using photoplethysmography. This is achieved by light bend out-coupling from the optical fibres. Demonstrator tests allowed monitoring blood pulsations.

The optical fibers were produced by melt-spinning process with a cyclo-olefin polymer (Zeonor 1020R, Zeon, Düsseldorf, Germany) as the core and a fluorinated polymer (THVP 2030GX, Dyneon, Burgkirchen, Germany) as cladding material. To create the sensing textile, the optical fiber was embroidered using an embroidery machine ERA TM 0625 (Saurer AG, Switzerland). The used substrate textile was chosen due to its own low-friction behaviour and development for decubitus ulcer prevention.

Pressure and strain sensor: The pressure-sensitive POFs were melt-spun with a single-screw extruder similarly to the other fibre though omitting use of a cladding polymer. Hence, air acts as the cladding and the fibre becomes very sensitive to macro-bending. The fibres have a critical angle of total reflection of 44.8° with the materials' refractive index being 1.42. Production parameters were the temperature at both extruder and heating collar as well as the pull-off speed. Deflection of light by pressure on the pressure-sensitive siloxane/urethane block copolymer fibres was analysed during load cycles. There, a perpendicularly-oriented pressure stamp applied load on the fibre which consequently deformed. From these results, a simple calibration of our sensor is possible with the well-known linearity of response of POFs. Additionally, long-term signal output was investigated.

RESULTS AND DISCUSSION

Photoplethysmograph: The embroidered PPG-setup featured an emitter-line and a detector-line, both optimized for their respective use. For each line, 64 bundled fibres were used. The emitting line was used to send light into the tissue where it is then scattered. The detecting fibres then re-coupled the reflected light back into the fibre. The heart rate was logged.

For verification of comfort, a textile friction analyser was used against synthetic skin models (PUR). As shown in **Figure 2**, the coefficient of friction (also in dry conditions) is well below those of typical hospital bedsheets, either cotton or cotton/polyester. Our new POF demonstrates good compatibility also for sensitive skin.

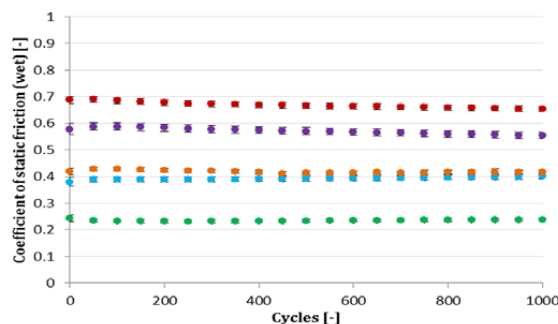


Figure 2: Friction of PPG-setup (orange and blue for two different bi-component fibres) versus a skin model compared to hospital bedsheets (red/purple) and a low-friction textile (green).

Pressure and strain sensor: The pressure-sensitive fibres were calibrated in a controlled test environment (Zwick tensile tester) and showed good reproducibility as can be seen in **Figure 3** with the error bars just visible at the base line after the first loading cycle. Responses vary with production parameters (such as extruder temperature and pull-down speed) and material grades, which vary in siloxane chain length. Such, fibres can be chosen depending on the application's needed sensitivity. Linearity of the response has been

shown for different fibres and conversion from load to pressure was possible due to the controlled loading mechanism.

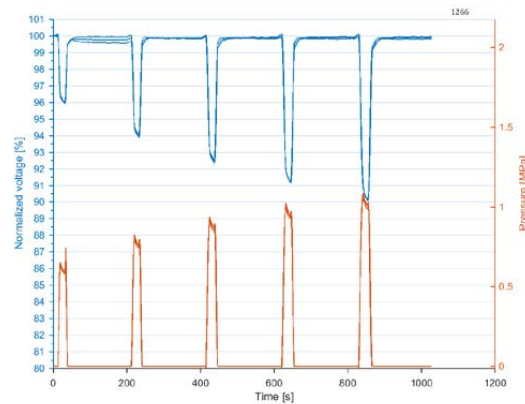


Figure 3: Pressure cycles on a block copolymer fiber, as the pressure is increased, the normalized voltage decreases as a response. Standard deviations are indicated in both load application and response.

CONCLUSION and OUTLOOK

The use of the new-developed polymer optical fibers for the development of textile sensors leads to flexible, wearable sensors. These photonic textiles show versatility with sensor placement. The polymer optical fiber fabrics (POFFs) have shown to be low-friction. They can hence be used for long-term measurements, also on sensitive skin. These comfortable monitoring devices will allow for an improvement in the quality of life. From here, we will work on improving the signal/noise ratio to also monitor oxygenation with the all-LED based system.

ACKNOWLEDGMENTS

We would like to thank Benno Wüst for his help during fiber spinning. This work was funded by Nano-Tera.ch via the projects ParaTex and ParaTex-Gateway.

REFERENCES

- [1] B. M. Quandt, L. J. Scherer, L. F. Boesel, M. Wolf, G. L. Bona, R. M. Rossi, *Adv. Healthc. Mater.* **2015**, *4*, 330.
- [2] a) M. Krehel, M. Wolf, L. F. Boesel, R. M. Rossi, G.-L. Bona, L. J. Scherer, *Biomedical Optics Express* **2014**, *5*, 2537; b) M. Krehel, M. Schmid, R. Rossi, L. Boesel, G.-L. Bona, L. Scherer, *Sensors* **2014**, *14*, 13088.
- [3] F. A. Reifler, R. Hufenus, M. Krehel, E. Zraggen, R. M. Rossi, L. J. Scherer, *Polymer (United Kingdom)* **2014**, *55*, 5695.

STRAIN, TEMPERATURE AND HUMIDITY SENSING WITH MULTIMODE INTERFERENCE IN POF

Ricardo Oliveira^{1*}, Thiago H. R. Marques², Lúcia Bilro^{1,3}, Cristiano M. B. Cordeiro², Rogério N. Nogueira¹

1: Instituto de Telecomunicações, Campus Santiago, 3810-193 Aveiro, Portugal

2: Instituto de Física "Gleb Watagin", Universidade Estadual de Campinas, UNICAMP, Brazil

3: I3N/FSCOSD - Institute of Nanostructures, Nanomodelling and Nanofabrication - Physics Department of University of Aveiro, Aveiro, Portugal

*Corresponding author: oliveiraricas@av.it.pt

Abstract: In this work, we have used a multimode polymer optical fiber (MM-POF) sandwiched between two silica single-mode fibers, to create a multimode interferometer (MMI) based on a POF. A beam propagation method was used to calculate the MM-POF length needed to produce a peak centered in the near-infrared region. Therefore, a peak centered in the 1550 nm region was created by using the 18th self-image. The sensor was characterized to three parameters and the sensitivities obtained were -2.8 pm/ $\mu\epsilon$, 212 pm/ $^{\circ}\text{C}$ and 67 pm/%RH, for the strain, temperature and humidity tests, respectively.

Key words: Multimode interference (MMI), polymer optical fiber (POF), optical fiber sensor.

1. Introduction

Nowadays, silica optical fibers have been the preferred choice for the production of fiber optic sensors. However, polymer optical fibers (POFs) offer new opportunities when compared with their silica counterparts. In fact, some advantages that polymers may offer are: the negative and much larger thermo-optic coefficient [1]; the smaller Young modulus [2], allowing to withstand at high elongation regimes [3,4]; flexibility in bending; non-brittle nature and biological compatibility [5]. Among the different polymer materials available, polymethylmethacrylate (PMMA) is the most commonly used for the production of POFs [1]. Nevertheless, other polymers, such as polycarbonate (PC) [6], polystyrene (PS) [7], CYTOP (amorphous fluoropolymer) [8], TOPAS a cycloolefin copolymer (COC) [5] and ZEONEX® a cycloolefin polymer (COP) [9], have also been employed as the core and cladding materials of multicore, step-index (SI) and also in microstructured POFs (mPOFs). Some of these polymer materials present specific properties that may benefit some applications. Thus, if high glass transition temperature is needed, PC, COC and COP can be used (145 $^{\circ}\text{C}$ for the PC and 138 $^{\circ}\text{C}$ for COC and COP [1]). On other hand, it is known that most of polymer materials absorb water and some authors have reported the capability to measure the environment humidity [10,11]. On the other hand, if the application requires no water absorption, COP and COC based materials can be employed (absorption is less than 0.01 % per day [1]). Thus, POF sensors based on these materials have also been reported to withstand at high temperatures [12,13] and also to be humidity insensitive [14,15].

One interesting fiber optic technology that is receiving attention in recent years is the fiber modal interferometry, commonly known as MMI (multimode interference). This device is composed of a single-mode-multimode-single-mode (SMS) fiber structure and the inherent low cost of production, the high sensitivity and compactness, allows the detection of a variety of parameters, such as strain [16,17], temperature [16–18], refractive index [18], and humidity [19,20], where for the later, it is necessary to incorporate thin layers hygroscopic polymer materials.

The special characteristics offered by polymers when compared with silica have already lead the scientific community to produce and characterize SMS structures containing POFs [4,21,22]. Consequently, the capability to measure large strain with a PMMA based multimode polymer optical fiber (MM-POF) sandwiched between two single-mode (SMF) silica fibers has already been reported [4]. Additionally, the measurement of strain and temperature for the low loss region of perfluorinated [21] and also partially chlorinated [22] graded index POFs was also subject of study, achieving the best sensitivities for sensors based on SMS structures.

In this work a step-index (SI) MM-POF, composed of a ZEONEX® 480R core and PMMA cladding was used between two silica single-mode fibers to produce an SMS structure based on POF. The length of the MM-POF was estimated through a beam propagation method, allowing the creation of an SMS structure with peak centered at 1550 nm region. The structure was characterized in transmission to strain and temperature, showing sensitivities similar to the ones reported in literature for SMS structures based on POFs. Additionally, the absorption capabilities offered by the PMMA cladding layer of the MM-POF, was used to measure for the first time, the relative humidity.

2. Principle of operation and sensor fabrication

2.1. Design of the MMI-POF sensor

When the input light field of a single-mode fiber enters in a multimode fiber (MMF), several modes of the MMF will be excited. Thus, differential phases between the modes will accumulate generating constructive and destructive interference along the MMF. Therefore, the self-imaging distance is the length of MMF where the maximum input light field is replicated in both amplitude and phase. If the MMF fiber is cleaved where one of those images is being formed, a well-defined wavelength peak will occur, which will be sensitive to the external conditions.

In order to know the distance from the SMF where the light field is replicated inside the MM-POF, a two-dimensional beam propagation method (BPM) was employed. The simulation was carried at 1550 nm region taking into account the high losses of POFs at this region. This has been done due the availability of devices and components needed for the experiment. The silica-SMF fiber employed in the simulation has refractive index of 1.44615 and 1.43950 and diameters of 8.2 μm and 125 μm , respectively for the core and cladding. Regarding the MM-POF (see Fig. 1a)), the diameters were 73.5 μm and 446 μm and the refractive index at 1550 nm were 1.51 (extrapolated from the data taken in reference [1]) and 1.479 (from the Sellmeier equation [23]), for the core (ZEONEX® 480R) and cladding (PMMA), respectively. The simulation results concerning the light field along the MM-POF can be seen in Fig. 1b) and c).

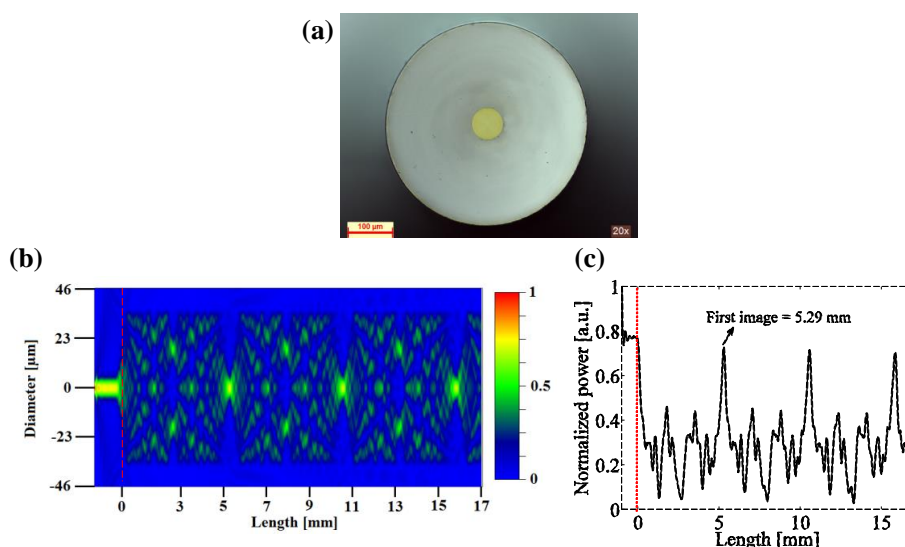


Fig. 1. a) Microscope image of the MM-POF cross section. b) Light field propagation inside a MM-POF. c) Power, normalized to the input power along the optical axis of the MM-POF, against the length of the MM-POF.

From the simulation results, one can find that the condensation of the light field occurs in multiples of 5.29 mm. In order to have enough length for the manipulation of the MM-POF during the splicing as well as in the strain characterization process, we decide to use the 18th image, which corresponds to 9.52 cm of MM-POF.

2.2. Fabrication of the SMS structure based on MM-POF

In order to fabricate the SMS structure, we have annealed the MM-POF at 65°C during 24 hours. This helps to remove any residual stresses present during the fabrication process. The MM-POF was then measured with a digital caliper and cleaved at 90° angle with a hot blade at the 18th image, corresponding to 9.52 cm. The next step was to treat the fiber end face with a proper polishing procedure [24], which gave a smooth end face needed to avoid coupling losses between the fibers. Two silica-SMF pigtailed were cleaved at 90° angle and spliced to each terminal of the prepared MM-POF. The alignment between the silica-SMF with the MM-POF was visualized using two cameras placed at each orthogonal axis, and the fibers were moved with 3D mechanical positioners. Between the silica and the MM-POF, it was added a drop of an UV curing optical adhesive (Loctite 3525), which offers enough strength for manipulation. The splicing process was then repeated for the other MM-POF terminal. The splicing steps used during the fabrication of the SMS structure can be seen on Fig. 2 a) and b).

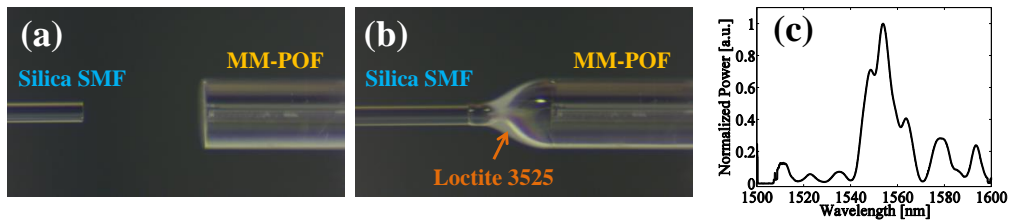


Fig. 2. a), b) Splicing process between silica-SMF and the MM-POF. c) Normalized power after the SMS structure.

After the splicing process the SMS structure was kept straight and the output transmission spectrum was acquired (see Fig. 2c). The transmission loss for the maximum peak achieved 25 dB. This value is mainly due to the attenuation of the ZEONEX 480R core material at 1550 nm region and also due to the coupling loss between the fibers, even so, the transmission losses are well acceptable for sensing purposes.

2.3. Strain, temperature and humidity characterization

To characterize the fiber sensor a C+L ASE light source was injected in one end of the silica-pigtail fiber and at the other end it was used an optical spectrum analyzer (Yokogawa AQ6375).

For the strain tests, the central part of the MM-POF was fixed with glue to a stationary and to a mechanical linear stage. The distance between the fixation points was 7.6 cm. The strain steps of 263.2 $\mu\epsilon$ were made in a total range of 2631.6 $\mu\epsilon$. The tests were performed in controlled environmental conditions, keeping the temperature at 25 °C and the relative humidity at 85 %RH.

The temperature characterization was done placing the strain characterization setup inside a climatic chamber (Angelantoni CH340), with resolutions of 0.25 °C and 3 %RH in temperature and humidity, respectively. The fiber was kept straight in order to avoid curvature effects on the SMS structure. The temperature was swept from 25 to 40 °C in steps of 5 °C, where the humidity was maintained at 85 %. For each temperature step it was given 1 hour of stabilization before collecting the data.

For the humidity tests the temperature was maintained at 25 °C and the fiber was kept straight. The humidity was swept from 30 % to 80 % in steps of 10 %, giving 1 hour for each step, allowing enough time for the uptake of water by the PMMA polymer.

3. Results and discussion

From the strain results, it can be seen that spectra was linearly blue shifted with increasing strain (see Fig. 3a). The evolution of the wavelength peak power with increasing strain can be seen on Fig. 3b). When the axial strain is applied to the MM-POF, there will be a change in the length, diameter and in the refractive index of both core and cladding layers. The combination of both effects leads to a shift in wavelength.

A linear regression model was adjusted to the data presented in Fig. 3a), obtaining an R-square value of 0.998 and a sensitivity of -2.77 pm/ $\mu\epsilon$. This value is similar to the one reported in literature for an SMS structure containing a PMMA based MM-POF core [4].

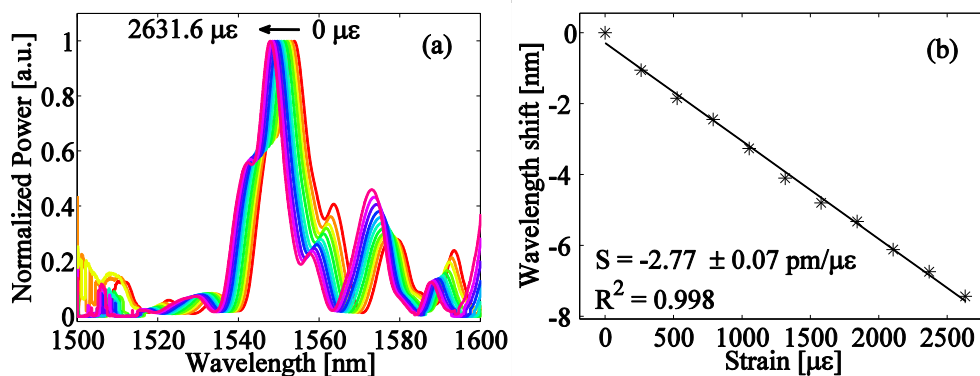


Fig. 3. a) Normalized spectra collected for different strain values. b) Correspondent peak power wavelength shift (@1550 nm), for different strain values.

In what concerns the temperature tests, the spectra collected for each temperature were linearly red shifted. (see Fig. 4a). The sensitivity obtained from the linear regression model on Fig. 4b) was 212 pm/°C with an R-square value of 0.999. This value was lower than the ones found in literature for perfluorinated (48.8 nm/°C [21]) and partially chlorinated (6.76 nm/°C [22]) graded index POFs. The reason is due to the net contribution of the thermal expansion and thermo-optic coefficient of PMMA and ZEONEX® 480R materials that compose the MM-POF. Additionally, the core diameter and the dopants present in the MM fiber play also an important role on the sign and sensitivity of the structure [16].

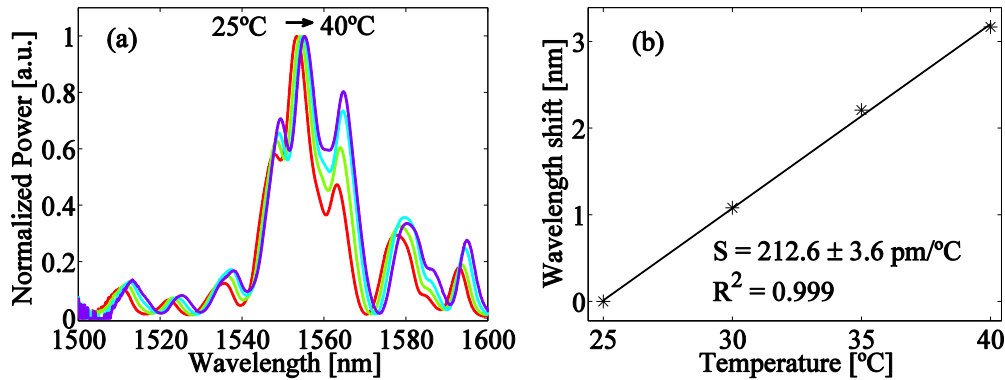


Fig. 4. a) Normalized spectra collected for different temperatures. b) Correspondent peak power wavelength shift (@1550 nm).

For the humidity tests, the spectra was red shifted with increasing humidity (see Fig. 5a). However, in this test due to unknown reasons, the wavelength peak power (@1550 nm) did not changed with the humidity conditions. For that reason we decide to use the wavelength shift that appears at 1570 nm. The data collected is shown in Fig. 5b), and as can be seen the wavelength shift is linearly red shifted with increasing humidity. In this test, since the PMMA and ZEONEX® 480R materials are humidity sensitive and insensitive respectively, the wavelength shift observed is due to the absorption of water by the PMMA cladding layer. This absorption leads to the swelling of the PMMA material, which imposes stresses in different directions in the core MM-POF. Additionally, the uptake of water leads inherently to a refractive index change of the PMMA. The combination of both effects around the polymer core, will affect directly the modes that are being propagated leading to a change in wavelength. A linear regression model was applied to the data shown in Fig. 5b) and a sensitivity of 67 pm/%RH (R-square = 0.991) was obtained. This sensitivity value is close to the ones found for fiber Bragg gratings (FBGs) written in PMMA based POFs [10,11] and for silica SMS structure coated with hygroscopic polymers [19].

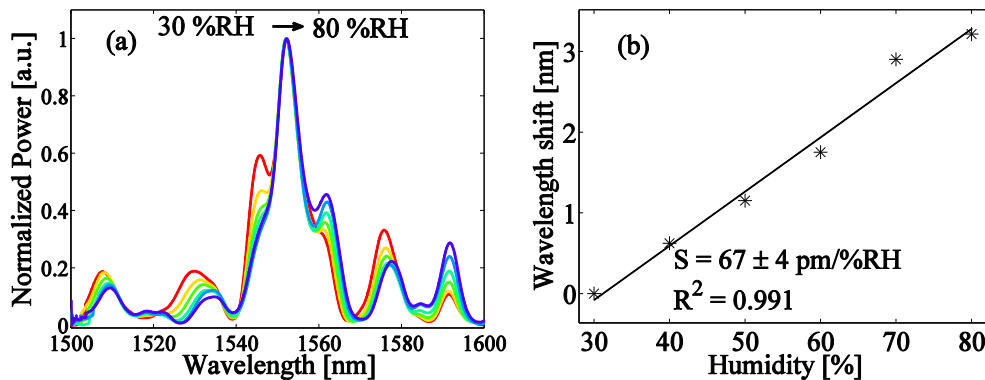


Fig. 5. a) Normalized spectra collected for different humidity conditions. b) Correspondent dip wavelength shift (@1570 nm), for each humidity value taken after 1 hour.

3. Conclusions

In this work we have created an SMS structure based on a MM-POF, composed of PMMA cladding and ZEONEX® 480R core materials. A BPM simulation was employed to determine the length of MM-POF needed to have a peak centered at the 1550 nm region. The structure assembly was done in a special arrangement in order to allow axial alignment between the silica fibers and the MM-POF. Additionally, the sensor was characterized to temperature and strain, revealing sensitivities similar to the ones found in literature. Furthermore, the absorption capabilities offered by the PMMA cladding material of the MM-POF, lead us to characterize for the first time this structure to humidity. Results revealed sensitivities close to the ones found for FBGs written in PMMA based POFs and silica SMS structures with hygroscopic polymer coatings. In conclusion, the easy fabrication procedure, the low cost of production and the high sensitivity offered by this fiber sensor makes it appealing for the sensing area.

Acknowledgements

This work was funded by FCT-Fundação para a Ciência e Tecnologia through portuguese national funds by UID/EEA/50008/2013 (project SWAT) and hiPOF (PTDC/EEI-TEL/7134/2014), PhD Scholarship SFRH/BD/88472/2012, investigator grant IF/01664/2014 and project INITIATE. This study also received financial support of FINEP (under the project 0112039300).

References

- [1] Bäumer S 2011 *Handbook of Plastic Optics* (John Wiley & Sons)
- [2] Cusano A, Cutolo A and Albert J 2011 *Fiber Bragg grating sensors: Recent advancements, industrial applications and market exploitation* (Sharjah : Bentham Science Publishers)
- [3] Xiong Z, Peng G D, Wu B and Chu P L 1999 Highly tunable Bragg gratings in single-mode polymer optical fibers *IEEE Photonics Technol. Lett.* **11** 352–4
- [4] Huang J, Lan X, Wang H, Yuan L, Wei T, Gao Z and Xiao H 2012 Polymer optical fiber for large strain measurement based on multimode interference *Opt. Lett.* **37** 4308
- [5] Emiliyanov G, Jensen J B and Bang O 2007 Localized biosensing with Topas microstructured polymer optical fiber *Opt. Lett.* **32** 460–2
- [6] Tanaka A, Sawada H, Takoshima T and Wakatsuki N 1988 New plastic optical fiber using polycarbonate core and fluorescence-doped fiber for high temperature use *Fiber Integr. Opt.* **7** 139–58
- [7] Makino K, Akimoto Y, Koike K, Kondo A, Inoue A and Koike Y 2013 Low Loss and High Bandwidth Polystyrene-Based Graded Index Polymer Optical Fiber *J. Light. Technol.* **31** 2407–12
- [8] Koike Y and Koike K 2011 Progress in low-loss and high-bandwidth plastic optical fibers *J. Polym. Sci. Part B Polym. Phys.* **49** 2–17
- [9] Leon-saval S G, Lwin R and Argyros A 2012 Multicore composite single-mode polymer fibre *Opt. Express* **20** 141–8
- [10] Zhang W and Webb D J 2014 Humidity responsivity of poly (methyl methacrylate) - based optical fiber Bragg grating sensors *Opt. Lett.* **39** 3026–9
- [11] Oliveira R, Bilro L, Heidarialamdarloo J and Nogueira R 2015 Fabrication and characterization of polymer fiber Bragg gratings inscribed with KrF UV laser *24th International Conference on Plastic Optical Fibers* (Nuremberg) pp 371–5
- [12] Fasano A, Woyessa G, Stajanca P, Markos C, Nielsen K, Rasmussen H K, Krebber K and Bang O 2016 Fabrication and characterization of polycarbonate microstructured polymer optical fibers for high-temperature-resistant fiber Bragg grating strain sensors *Opt. Mater. Express* **6** 693–6
- [13] Woyessa G, Fasano A, Stefani A, Markos C, Rasmussen H K and Bang O 2016 Single mode step-index polymer optical fiber for humidity insensitive high temperature fiber Bragg grating sensors *Opt. Express* **24** 3296–8
- [14] Yuan W, Khan L, Webb D J, Kalli K, Rasmussen H K, Stefani A and Bang O 2011 Humidity insensitive TOPAS polymer fiber Bragg grating sensor. *Opt. Express* **19** 19731–9
- [15] Woyessa G, Fasano A, Stefani A, Markos C, Nielsen K, Rasmussen H K and Bang O 2015 Humidity insensitive step-index polymer optical fibre Bragg grating sensors *24th International Conference on Optical Fiber Sensors* vol 9634 pp 96342L – 1–4
- [16] Tripathi S M, Kumar A, Varshney R K, Kumar Y B P, Marin E and Meunier J-P 2009 Strain and Temperature Sensing Characteristics of Single-Mode–Multimode–Single-Mode Structures *J. Light. Technol.* **27** 2348–56
- [17] Andre R M, Biazoli C R, Silva S O, Marques M B, Cordeiro C M B and Frazao O 2013 Strain-Temperature Discrimination Using Multimode Interference in Tapered Fiber *IEEE Photonics Technol. Lett.* **25** 155–8
- [18] Li L, Xia L, Wuang Y, Ran Y, Yang C and Liu D 2012 Novel NCF-FBG Interferometer for Simultaneous Measurement of Refractive Index and Temperature *IEEE Photonics Technol. Lett.* **24** 2268–71
- [19] Gu B, Yin M, Zhang A P, Qian J and He S 2011 Optical fiber relative humidity sensor based on FBG incorporated thin-core fiber modal interferometer *Opt. Express* **19** 15–20
- [20] Xia L, Li L, Li W, Kou T and Liu D 2013 Sensors and Actuators A : Physical Novel optical fiber humidity sensor based on a no-core fiber structure *Sensors Actuators A. Phys.* **190** 1–5
- [21] Numata G, Hayashi N, Tabaru M, Mizuno Y and Nakamura K 2014 Ultra-sensitive strain and temperature sensing based on modal interference in perfluorinated polymer optical fibers *IEEE Photonics J.* **6** 1–7
- [22] Goki N, Neisei H, Marie T, Yosuke M and Kentaro N 2015 Strain and temperature sensing based on multimode interference in partially chlorinated polymer optical fiber *IEICE Electron. Express* **12** 20141173–2014117
- [23] Ishigure T, Nihei E and Koike Y 1996 Optimum refractive-index profile of the graded-index polymer optical fiber, toward gigabit data links. *Appl. Opt.* **35** 2048–53
- [24] Oliveira R, Bilro L and Nogueira R 2015 Smooth end face termination of microstructured , graded-index , and step-index polymer optical fibers *Appl. Opt.* **54** 5629–33



Analysis of the roughness in a sensing region on D-shaped POFs

F. Sequeira^{1,2*}, D. Duarte¹, R. Nogueira¹, A. Rudnitskaya^{2,3}, N. Cennamo⁴, L. Zeni⁴, L. Bilro^{1,5}

1 Instituto de Telecomunicações, Aveiro, Portugal

2 CESAM, University of Aveiro, Aveiro, Portugal

3 Department of Chemistry, University of Aveiro, Aveiro, Portugal

4 Department of Industrial and Information Engineering, Second University of Naples, Aversa, Italy

5 I3N/FSCOSD, Department of Physics, University of Aveiro, Aveiro, Portugal

*Corresponding author: fsequeira@av.it.pt

Abstract: The preliminary studies about the dependence of the sensitivity and resolution of a D-shaped POF sensor with the roughness of the sensing region are presented. The sensing principle is based in the variation of the transmitted optical signal with the variation of the external refractive index, from 1.332 to 1.471. The obtained results show that the sensitivity is strongly dependent on the roughness of the sensing surface and are in accordance with the simulations performed using the transfer matrix formalism. The obtained resolution (10^{-3} RIU) allows the further development of these sensors for chemical and/or biochemical sensing, by means of surface modification with chemical selective layers.

1. Introduction

Numerous studies related to refractive index (RI) plastic optical fiber (POF) sensors can be found in the literature. Bilro *et al.* reported theoretical modelling of D-shaped POF at different macrobending conditions and external RI, which was validated by experimental results [1]. Feng *et al.* reported that the best performance of a POF based RI sensor with a tapered structure was achieved at 633 nm, for RI ranging from 1.33 to 1.41 [2]. An optimization of depth and curvature radius of a D-shaped POF sensor, aiming to increase linearity range and sensitivity to RI, was reported by Feng *et al.* with the best results being obtained for a depth of 500 μm and a curvature radius of 5 cm [3]. Cennamo *et al.* have reported several sensors for chemical sensing based on a D-shaped POF – SPR (surface plasmon resonance) platform with 1 cm length of sensing region, with typical resolution of about 10^{-4} RIU [4].

A previous work based in the optimization of the length of D-shaped POF sensors was presented by this group [5]. Aiming the improvement of the performance of the sensor, targeting chemical and biochemical sensing applications, here are presented the preliminary studies related with the dependence of the sensitivity and resolution of a D-shaped polymeric optical fiber sensor with the roughness of the sensing region.

2. Materials and methods

2.1 D-shaped sensors

POF's with 1 mm diameter and 0.5 numerical aperture (NA) were selected. The core, 980 μm , is made of polymethyl methacrylate (PMMA) with 1.49 refractive index and the cladding consists in a fluorinated polymer. The fibers were cut to 20 cm with a fiber optic cutter and were embedded in grooves engraved on planar supports with 6 cm length. The planar platforms used in this study were made with ABS plus™ production-grade thermoplastic, produced with Mojo® 3D Printer, provided by Stratasys® FDM®. The dimensions of the groove inscribed were 1 mm width and 700 μm depth, with an instrumental error of 100 μm .

The surface of the fibers embedded in the planar surface was polished with sandpaper of 5 μm (LFG5P), with a “Figure 8” pattern, in order to remove the cladding and part of the core, obtaining the desired D-shape. Sandpaper of 3 μm (LFG3P) and 1 μm (LFG1P) were also used for the final polishing procedure of the Sensor 1, in order to obtain a smoother surface. The D-shaped POF region was evaluated by Scanning Electron Microscopy (SEM), model Zeiss SUPRA 35, Figure 1.

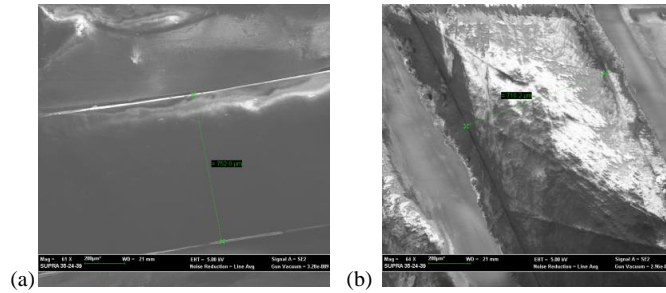


Figure 1. SEM image of the D-shaped sensors polished with (a) 5, 3 and 1 μm sandpaper (b) 5 μm sandpaper.

2.2 Optical sensing setup

The intensity-based detection scheme allowed the measurement of the transmitted light that passed through the fiber with the D-shaped region. The experimental setup, Figure 2, comprised a stabilized power supply, LED (wavelength centered at 650 nm), optical coupler (50:50), two photodetectors and a Picoscope. Output data, time and voltage of the reference and sensor signals, in mV ($V_{reference}$ and V_{sensor} , respectively), were logged into a PC by means of Picoscope’s software. The self-referenced transmitted signal, k , was used to correct source fluctuations and variations due to external conditions, equation (1).

$$k = \frac{V_{sensor}}{V_{reference}} \quad (1)$$

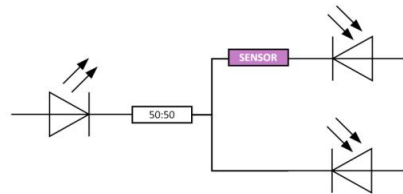


Figure 2. Outline of optical sensing setup.

2.3 Refractive index sensing

The D-shaped POF sensors were tested using glycerin solutions with increasing refractive index varying from 1.332 to 1.471. In each test performed, the refractive index of the tested solutions was measured with an Abbe Refractometer, Model RMI, from Exacta and Optech Labcenter.

Each test was starting by adding water Milli-Q to the D-shaped sensor area, corresponding to the lowest refractive index. All the signals were normalized to this value. After adding the tested solution to the D-shaped sensor, the signals were recorded for 5 minutes, and the average and standard deviation of the referenced signal were calculated with MATLAB software. Between measurements the sensors surface was washed repeatedly with the next test solution in order to clean the surface and eliminate any residues of the previous solution.

The sensor response to refractive index variation was measured three times in order to validate the obtained results. For each sensor the average value and standard deviation of the three tests were calculated, for simplicity $I = \tilde{k}_{norm}$ and δI , respectively. The obtained normalized transmitted signal, I , is a function of the external refractive index, n_{ext} ; if the external refractive index is altered by Δn_{ext} , there is a change in the obtained transmitted signal of ΔI . The sensitivity, S , of the D-shaped sensors is defined by:

$$S = \frac{\partial I}{\partial n_{ext}} \left[\frac{a.u.}{RIU} \right] \quad (2)$$

The resolution, Δn , is defined as the minimum change in refractive index that can be detected:

$$\Delta n = \frac{1}{S} \cdot \delta I_{max} [RIU] \quad (3)$$



where δI_{max} is the maximum value of standard deviation obtained in the refractive index range of interest.

2.4 Sensor modeling

A simulation model of the sensor was implemented to compare with the obtained experimental results. This model was based on the transfer matrix formalism using a geometric approach and its considerations for a D-shaped fiber with a bended surface morphology as reported by Bilro *et al.* [1]. A power loss roughness coefficient (s) with a linear decrease profile in respect to the external refractive index (until cladding RI is reached) was considered to simulate the roughness of the sensing region.

3. Results and discussion

Figure 3a shows the response of the D-shaped sensors with external refractive index. The normalized transmitted signal, I , increases with the increase of the D-shaped sensors roughness, in the considered RI range, which is in accordance with the simulations based on a transfer matrix formalism.

This work aims the optimization of sensitivity and resolution of D-shaped POF sensors for chemical and biochemical sensing in aqueous solutions, where the RI range of interest will depend in the RI of the selected selective layer, but should be between 1.33 – 1.39. In this range a linear fitting was applied to the obtained experimental results for Sensor 1 (with $R^2=0.99173$) and polynomial fitting for Sensor 2 (with $R^2=0.99946$), Figure 3b.

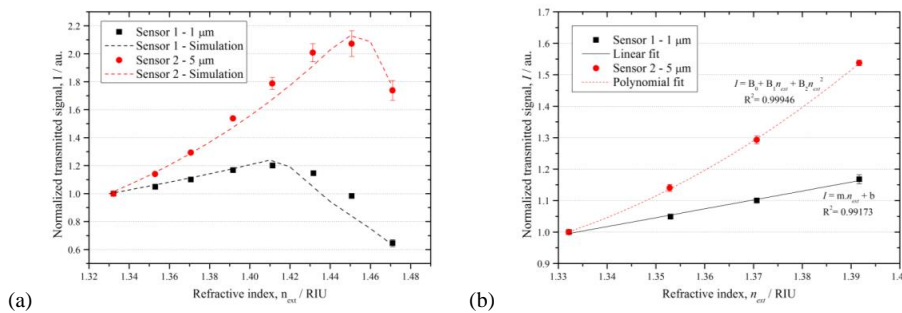


Figure 3. Response of the D-shaped POF sensors with external refractive index (a) RI: 1.33 – 1.47 - simulation and experimental results; (b) RI: 1.33 – 1.39 - Linear and polynomial fitting for Sensor 1 and 2, respectively.

The obtained results show that the sensitivity of the D-shaped POF sensors to RI is strongly dependent on the roughness of the sensing surface. The sensitivity and resolution were calculated by equations (2) and (3), for the range of interest of 1.33 – 1.39 RIU, and are depicted in Figure 4a and 4b.

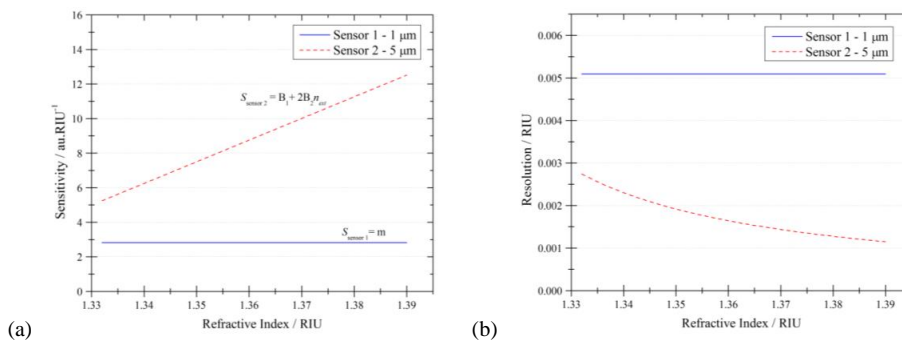


Figure 4. Sensitivity (a) and resolution (b) of the D-shaped POF sensors in the RI range 1.33 – 1.39 RIU.



Although there is an improvement in the resolution with the increase of the roughness of the D-shaped sensor, the obtained resolution for both sensors is around 10^{-3} RIU. These results allow the further development of these sensors for chemical and/or biochemical sensing.

4. Conclusions

The preliminary studies related with the performance of a D-shaped POF sensor vs roughness of the sensing region were presented. These sensors are easy to produce, allow a fast and low-cost sensing of RI and are suitable for chemical and biochemical sensing.

The sensitivity is strongly dependent with the roughness of the sensing surface. Experimental results are in accordance with the simulations performed using the transfer matrix formalism. The sensitivity of Sensor 2, is twice to four times bigger than the sensitivity obtained for sensor 1 (dependent on RI value), with increased roughness and smoother surface, respectively. The resolution of Sensor 2 is also slightly better than Sensor 1, although is still around 10^{-3} RIU. The obtained resolution allows the further development of these sensors for chemical and/or biochemical sensing, by means of surface modification with chemical selective layers.

5. Acknowledgements

This work is funded by FCT/MEC through national funds and when applicable co-funded by FEDER – PT2020 partnership agreement under the project UID/EEA/50008/2013 (project sWAT and Daniel Duarte research grant in the framework of PROLAB 2015), hiPOF (PTDC/EEI-TEL/7134/2014), PhD fellowship (Filipa Sequeira: SFRH/BD/88899/2012), and investigator grant (Lúcia Bilro: IF/01664/2014; project INITIATE). Alisa Rudnitskaya wish to acknowledge financial support from CESAM (UID/AMB/50017), FCT/MEC through national funds and the co-funding by the FEDER, within the PT2020 Partnership Agreement and Compete 2020 and through fellowship SFRH/BPD/104265/2014. The work was partly supported by Italian Ministry of University and Research (MIUR) PON 03PE_00155_1 OPTOFER. Authors wish to thank Pasquale Cirillo and Andrea Cirillo, from the Department of Industrial and Information Engineering, Second University of Naples, Aversa, Italy, for the production of the planar supports with grooves by Mojo® 3D Printer.

4. References

- [1] L. Bilro, N. J. Alberto, L. M. Sá, J. de L. Pinto, and R. Nogueira, “Analytical Analysis of Side-Polished Plastic Optical Fiber as Curvature and Refractive Index Sensor,” *J. Light. Technol.*, vol. 29, no. 6, pp. 864–870, 2011.
- [2] D. Feng, G. Liu, X.-L. Liu, M.-S. Jiang, and Q.-M. Sui, “Refractive index sensor based on plastic optical fiber with tapered structure,” *Appl. Opt.*, vol. 53, no. 10, pp. 2007–2011, 2014.
- [3] D. Feng, M. Zhang, G. Liu, X.-L. Liu, and J. Dong-Fang, “D-Shaped Plastic Optical Fiber Sensor for Testing Refractive Index,” *IEEE Sensors*, vol. 14, no. 5, pp. 1673–1676, 2014.
- [4] N. Cennamo, D. Massarotti, L. Conte, and L. Zeni, “Low cost sensors based on SPR in a plastic optical fiber for biosensor implementation,” *Sensors (Basel)*, vol. 11, no. 12, pp. 11752–60, 2011.
- [5] F. Sequeira, L. Bilro, A. Rudnitskaya, M. Pesavento, L. Zeni, and N. Cennamo, “Optimization of an evanescent field sensor based on D-shaped plastic optical fiber for chemical and biochemical sensing,” in *EuroSensors*, 2016. (Submitted)

Refractive Index Sensing Using Ultrasonically Crushed Plastic Optical Fibers

S. Shimada¹, H. Lee¹, M. Shizuka¹, H. Tanaka¹, N. Hayashi², Y. Matsumoto³,
Y. Tanaka⁴, H. Nakamura⁵, Y. Mizuno^{1*}, and K. Nakamura¹

1 Institute of Innovative Research, Tokyo Institute of Technology, 4259, Nagatsuta-cho, Midori-ku, Yokohama 226-8503, Japan

2 Research Center for Advanced Science and Technology, The University of Tokyo, 4-6-1, Komaba, Meguro-ku, Tokyo 153-8904, Japan

3 Toyohashi University of Technology, 1-1, Hibarigaoka, Tempaku, Toyohashi, Aichi 441-8580, Japan

4 Tokyo University of Agriculture and Technology, 2-24-16, Naka-cho, Koganei, Tokyo 184-8588, Japan

5 Tokyo Metropolitan University, 1-1, Minami-osawa Hachioji-shi, Tokyo 192-0397, Japan

*Corresponding author: ymizuno@sonic.pi.titech.ac.jp

Abstract: We demonstrate power-based refractive index (RI) sensing using an ultrasonically crushed polymer optical fiber (POF). This structure can be fabricated easily and cost-efficiently for a short time (of ~1 s) with no need to employ external heat sources or chemicals. What is required is an ultrasonic transducer, the horn of which is pressed against part of the POF. The RI dependence of the transmitted power is investigated, and almost linear trends are obtained in the RI ranges of from ~1.32 to ~1.36 (coefficient: -62 dB/RIU (RI unit)) and from ~1.40 to ~1.44 (coefficient: -257 dB/RIU). When the RI is fixed at 1.33, the temperature dependence of the transmitted power is also investigated (coefficient: -0.094 dB/°C), which shows the temperature-dependent error in RI sensing can be compensated.

1. Introduction

Optical fiber sensors have been vigorously studied because of their measurement capability of various physical parameters, such as strain [1,2], temperature [1,2], pressure [3], acoustic impedance [4,5], humidity [6], reflectivity [7,8], nuclear radiation [9], etc. Among them, refractive index (RI) sensing using optical fibers has been attracting considerable attention in biological and chemical research, and numerous techniques have been developed for the past several decades [10-13]. RI sensing based on evanescent waves generated at the tapered region of glass optical fibers [12,13] is one of the most cost-efficient techniques with high sensitivity. However, glass optical fiber tapers are fragile and need to be fabricated and handled with care. One promising solution is to exploit polymer optical fiber (POF) tapers [14-20], which exhibit much higher flexibility.

To date, various POF tapering methods have been developed. Two widely used methods are based on a heat-and-pull technique with an external heat source [14-17] and a chemical etching technique [18]. However, employment of external heat sources (e.g., flame [14], a compact furnace [15,16], and a solder gun [17]) and chemicals is not convenient and lacks safety. Though a POF tapering technique of converting propagating light energy into heat without the use of an external heat source has been developed [19], requirement of high-power light injection may cause burning at the POF ends [21] or a so-called fuse effect [22,23]. RI sensing using V-shaped POFs has also been reported [20], but because of the structural instability, their measurement accuracy was not sufficiently high.

In this work, RI sensing using an ultrasonically crushed POF is demonstrated for the first time to the best of our knowledge. This structure can be fabricated easily with no need to employ external heat sources or chemicals; the horn of an ultrasonic transducer is pressed against part of the POF for a short period. First, we clarify that the RI dependence of the transmitted power shows a non-monotonic behavior, which indicates that this RI sensor can be directly used only in the limited RI ranges. For instance, the dependence coefficients are -62 dB/RIU (RI unit) and -257 dB/RIU in the RI ranges of from ~1.32 to ~1.36 and from ~1.40 to ~1.44, respectively. Then we find that, when the RI is fixed at 1.33, the transmitted power shows a negative dependence on temperature with a coefficient of -0.094 dB/°C, leading to the feasibility of temperature compensation in RI sensing.

2. Materials and methods

The POF used in the experiment was a perfluorinated graded-index (PFGI-) POF [24,25] with a core diameter of 50 μm , a cladding diameter of 70 μm , an overcladding diameter of 490 μm , and a propagation loss of ~ 250 dB/km at 1550 nm. The RIs of the core center, cladding, and overcladding at 1550 nm were 1.356, 1.348, and 1.590, respectively. The core and cladding layers consisted of the identical material (i.e., polyperfluorobutenylvinyl ether; with different dopant concentrations), and their boundary was not visible. In contrast, the overcladding layer was composed of polycarbonate, and its boundary with the cladding layer was observable with a microscope. PFGI-POFs are known to absorb much less water than standard poly(methyl methacrylate)-based POFs [14,16], which is desirable for RI sensing of liquids [26].

Figure 1 illustrates the POF processing procedure. The horn (diameter: 6 mm) of a Langevin-type ultrasonic transducer with a resonance frequency of ~ 18.7 kHz was pressed against the midpoint of the 40-cm-long POF on an anvil with 10-N preload for 1 s [27]. Then the 6-mm-long region of the POF was crushed. With this ultrasonic method, the POF was first partially melt and then solidified after distortion, resulting in stable fabrication (as simple press without ultrasonic oscillations was susceptible to incomplete plastic deformation, stable fabrication of the crushed structure was difficult). For ease of handling, the crushed region was bent around its midpoint, and was used as a sensing head.

An experimental setup for RI sensing using the crushed POF is depicted in Fig. 2. The output light from a laser at 1550 nm (power: 10 dBm, bandwidth: ~ 1 MHz) was guided through a 1-m-long silica single-mode fiber (SMF) and injected into the POF. The transmitted light was then guided to an optical spectrum analyzer (OSA) via a 3-m-long silica multimode fiber (MMF) with a core diameter of 50 μm (to suppress the optical coupling loss at the boundary between the POF and the silica fiber), and its spectral peak power was precisely measured with 100-times averaging. Both ends of the POF were connected to the silica fibers by butt-coupling via “FC/SC” adaptors [25].

First, we investigated the RI dependence of the transmitted power when the crushed region was immersed into sucrose solution at 25°C, the RI of which was varied from 1.318 to 1.437 by controlling the concentration in the range from 0% to 65% [28]. Subsequently, when the ambient RI of the crushed region was fixed at 1.333 (concentration: 10%), the temperature dependence of the transmitted power was investigated in the range from 10°C to 35°C.

3. Experimental results

Figures 3(a)–(d) are the micrographs of the crushed POF. The side views are shown in Fig. 3(a) (around the boundary between crushed and uncrushed regions) and Fig. 3(b) (around the middle of the crushed region). The crushed region had a height of ~ 270 μm , which was ~ 1.8 times smaller than the outer diameter (490 μm) of the

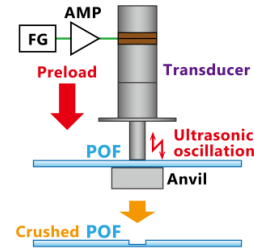


Figure 1. Processing procedure of partially crushed polymer optical fiber. FG: function generator.

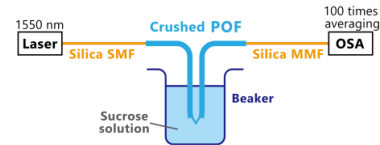


Figure 2. Experimental setup for refractive index sensing using crushed polymer optical fiber (POF). MMF, multimode fiber; OSA, optical spectrum analyzer; SMF, single-mode fiber.

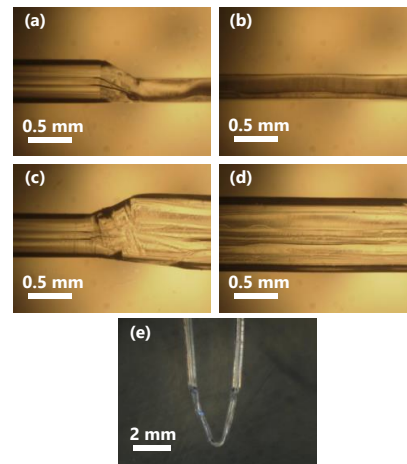


Figure 3. Micrographs of the crushed polymer optical fiber; (a,b) side views and (c,d) top views; (a,c) around the boundary between crushed and uncrushed regions, (b,d) around the middle of the crushed region. (e) Photograph of the crushed region bent around its midpoint.

uncrushed region. The top views are also shown in Fig. 3(c) (around the boundary) and Fig. 3(d) (around the midpoint). The width of the crushed region was $\sim 850 \mu\text{m}$, which was ~ 1.7 times larger than the initial outer diameter ($490 \mu\text{m}$). The photograph of the crushed POF after bending is shown in Fig. 3(e). The bending angle around the midpoint of the crushed region was $\sim 35^\circ$.

The measured RI dependence of the transmitted power at 25°C is shown in Fig. 4(a). The vertical axis was normalized so that the power at $\text{RI} = 1.318$ (sucrose concentration = 0%) became 0 dB (note that the propagation loss at the crushed region of the POF was ~ 35 dB). With increasing RI to ~ 1.36 , the transmitted power decreased (the loss increased); but it increased by ~ 1 dB when the RI increased to ~ 1.37 . After that, with increasing RI, the power monotonically decreased; the dependence abruptly became large when the RI was higher than ~ 1.40 .

This non-monotonic behavior, which was probably caused by the multimodal effect, has also been observed in other POF-taper-based RI measurement [18]. We performed the same measurement three times, and confirmed the high repeatability. As the transmitted power and the RI are not in one-to-

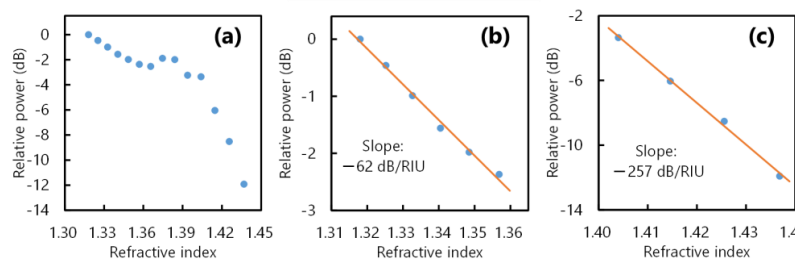


Figure 4. Measured relative transmitted power dependences on refractive index (RI). The magnified views of (a) are (b) and (c). The RI ranges are (a) 1.318–1.437, (b) 1.318–1.357, and (c) 1.404–1.437.

one correspondence with each other, the RI range needs to be limited for practical application of this sensor. If the RI range is limited to from ~ 1.32 to ~ 1.36 , the transmitted power directly gives the RI value with a dependence coefficient of -62 dB/RIU (see Fig. 4(b) for the magnified view in this RI range). In the same way, if the RI range is limited to from ~ 1.40 to ~ 1.44 , the transmitted power corresponds to the RI with a dependence coefficient of -257 dB/RIU (see Fig. 4(c)). Although it is difficult to fairly compare these absolute values with those in previous reports measured under different conditions and POF structures, the negative coefficient of the transmitted power (or the positive coefficient of the loss) against RI agrees with some of the previous POF-taper-based results [14,19]. When the uncrushed regions of the POF were immersed into the sucrose solutions, no quantifiable influence was observed on the transmitted power.

Finally, we set the ambient RI of the crushed region to 1.333 (sucrose concentration: 10%), which is nearly located at the midpoint of the linear region shown in Fig. 4(b). We then investigated the temperature dependence of the transmitted power in the range from 10°C to 35°C . The vertical axis was normalized so that the power measured at 25°C became 0 dB. The influence of the temperature dependence of the sucrose solution was compensated [29]. As shown in Fig. 5, with increasing temperature, the transmitted power monotonically decreased; this behavior is the same as that of bent-POF-based sensors [30]. When we roughly applied linear fit to the data in this range, the temperature dependence coefficient of the transmitted power was calculated to be -0.094 dB/ $^\circ\text{C}$. Once this one-to-one correspondence between RI and temperature is known, the temperature-dependent error in RI sensing can be compensated in principle.

4. Conclusion

We demonstrated RI sensing by exploiting an ultrasonically crushed POF, the structure of which can be easily fabricated with no need to employ external heat sources or chemicals. What we need is to simply press the horn of an ultrasonic transducer against part of a POF for a short time (of ~ 1 s). First, the transmitted power was experimentally shown to have a non-monotonic dependence on RI with a high repeatability; this indicated

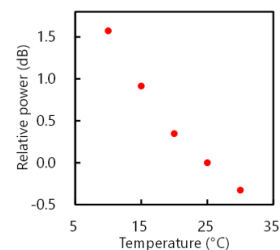


Figure 5. Relative transmitted power dependence on temperature when the refractive index was fixed at 1.333.

that it is difficult to directly use this sensor in the whole RI range. However, in the limited RI ranges, the transmitted power and the RI were in a one-to-one correspondence with dependence coefficients of -62 dB/RIU (RI from ~ 1.32 to ~ 1.36) and -257 dB/RIU (RI from ~ 1.40 to ~ 1.44). When the RI was fixed at 1.33, a negative dependence of the transmitted power on temperature (coefficient: -0.094 dB/ $^{\circ}$ C) was also clarified, which leads to the possibility of temperature compensation in RI sensing. Thus, we anticipate that this unique RI sensing based on ultrasonically crushed POF will be of great use in implementing stable and cost-effective fiber-optic RI sensors for biological and chemical application in future.

5. Acknowledgements

This work was supported by MLIT Construction Technology Research and Development Subsidy Program, by JSPS KAKENHI Grant Numbers 25709032, 26630180, and 25007652, and by research grants from the Iwatani Naoji Foundation, the SCAT Foundation, and the Konica Minolta Science and Technology Foundation.

6. References

- [1] Y. Mizuno, N. Hayashi, H. Fukuda, K. Y. Song, and K. Nakamura, *Light: Sci. Appl.* **5**, e16184 (2016).
- [2] Y. Dong, H. Zhang, L. Chen, and X. Bao, *Appl. Opt.* **51**, 1229 (2012).
- [3] J. Ma, W. Jin, H. L. Ho, and J. Y. Dai, *Opt. Lett.* **37**, 2493 (2012).
- [4] Y. Antman, A. Clain, Y. London, and A. Zadok, *Optica* **3**, 510 (2016).
- [5] N. Hayashi, H. Lee, Y. Mizuno, and K. Nakamura, *IEEE Photonics J.* **8**, 7100707 (2016).
- [6] G. Woyessa, K. Nielsen, A. Stefani, C. Markos, and O. Bang, *Opt. Express* **24**, 1206 (2016).
- [7] M. Shizuka, N. Hayashi, Y. Mizuno, and K. Nakamura, *Appl. Opt.* **55**, 3925 (2016).
- [8] T. Okamoto, D. Iida, K. Toge, and T. Manabe, *J. Lightwave Technol.*, in press (DOI: 10.1109/JLT.2016.2590507; to be updated at the revision/proof stage).
- [9] P. Stajanca, L. Mihai, D. Sporea, D. Negut, H. Sturm, M. Schukar, and K. Krebber, *Opt. Mater.* **58**, 226 (2016).
- [10] H. J. Patrick, A. D. Kersey, and F. Bucholtz, *J. Lightwave Technol.* **16**, 1606 (1998).
- [11] T. Takao and H. Hattori, *Jpn. J. Appl. Phys.* **21**, 1509 (1982).
- [12] Z. Tian, S. S. H. Yam, J. Barnes, W. Bock, P. Greig, J. M. Fraser, H. Loock, and R. D. Oleschuk, *IEEE Photonics Technol. Lett.* **20**, 626 (2008).
- [13] A. Leung, K. Rijal, P. M. Shankar, and R. Mutharasan, *Biosens. Bioelectron.* **21**, 2202 (2006).
- [14] D. J. Feng, G. X. Liu, X. L. Liu, M. S. Jiang, and Q. M. Sui, *Appl. Opt.* **53**, 2007 (2014).
- [15] N. Hayashi, H. Fukuda, Y. Mizuno, and K. Nakamura, *J. Appl. Phys.* **115**, 173108 (2014).
- [16] Y. Jeong, S. Bae, and K. Oh, *Curr. Appl. Phys.* **9**, e273 (2009).
- [17] A. A. Jasim, N. Hayashi, S. W. Harun, H. Ahmad, R. Penny, Y. Mizuno, and K. Nakamura, *Sens. Actuators A* **219**, 94 (2014).
- [18] Y. M. Wong, P. J. Scully, H. J. Kadim, V. Alexiou, and R. J. Bartlett, *J. Opt. A* **5**, S51 (2003).
- [19] H. Ujihara, N. Hayashi, K. Minakawa, M. Tabaru, Y. Mizuno, and K. Nakamura, *Appl. Phys. Express* **8**, 072501 (2015).
- [20] H. Lee, N. Hayashi, Y. Mizuno, and K. Nakamura, *Jpn. J. Appl. Phys.* **54**, 118001 (2015).
- [21] Y. Mizuno, N. Hayashi, and K. Nakamura, *Opt. Lett.* **38**, 1467 (2013).
- [22] Y. Mizuno, N. Hayashi, H. Tanaka, K. Nakamura, and S. Todoroki, *Appl. Phys. Lett.* **104**, 043302 (2014).
- [23] Y. Mizuno, N. Hayashi, H. Tanaka, and K. Nakamura, *IEEE Photonics J.* **6**, 6600307 (2014).
- [24] Y. Koike and M. Asai, *NPG Asia Mater.* **1**, 22 (2009).
- [25] Y. Mizuno and K. Nakamura, *Appl. Phys. Lett.* **97**, 021103 (2010).
- [26] S. Ando, T. Matsuura, and S. Sasaki, *Chemtech* **24**, 20 (1994).
- [27] S. Shimada, H. Tanaka, K. Hasebe, N. Hayashi, Y. Ochi, T. Matsui, I. Nishizaki, Y. Matsumoto, Y. Tanaka, H. Nakamura, Y. Mizuno, and K. Nakamura, *Electron. Lett.* **52**, 1472 (2016).
- [28] D. R. Lide, *Handbook of Chemistry and Physics* (CRC Press, Boca Raton, FL, 2004).
- [29] P. Schiebener, J. Straub, J. M. H. Levelt Sengers, and J. S. Gallagher, *J. Phys. Chem. Ref. Data* **19**, 677 (1990).
- [30] N. Jing, C. X. Teng, X. W. Zhao, and J. Zheng, *Appl. Opt.* **54**, 1890 (2015).



Polymer Optical Fibre Refractive Index Probe for on-line measurement of Alcohol Composition for Distillation Column

P.J.Scully^{1,2*}, A.Fong², K.Chandran², S. Whyte, X. Chai, M. Emerson², Ralph Stephenson Jones^{1,2}, A. Ahluwalia², M.Spooner², Z Gu², O Qureshi², M.Astaire².

¹ The Photon Science Institute.

² School of Chemical Engineering and Analytical Science (CEAS).

The University of Manchester, Oxford Road, Manchester, M13 9PL, UK

*Corresponding author: patricia.scully@manchester.ac.uk

Abstract: We present a polymer optical fibre (POF) refractive index (RI) probe for on-line measurement of alcohol composition for optimisation of a distillation column, producing methanol at 97% purity. The refractive index of methanol-water binary solutions varies with composition, and so the methanol composition of the distillate is routinely measured using time consuming and expensive off line methods. We have developed an on-line POF sensor probe using a bundled arrangement of emitting and receiving 1mm diameter fibres with a reflecting mirror channel through which the distillate flows, to monitor distillate composition on a Methanol-Water binary batch distillation column.

1. Introduction

The overall aim is to convert a batch distillation process to a continuous operation under composition control with the alcohol composition measured using a polymer optical fibre (POF) sensor rather than the normal configuration of indirect regulation of composition using temperature (at constant pressure there is a direct relationship between temperature and composition for a binary mixture). The POF sensor measures refractive index of the distillate, and is designed for on-line measurement of alcohol composition for a distillation column, producing methanol (MeOH) at 97% purity. It is comprised from an optical fibre bundle of emitting and receiving 1mm diameter fibres with a reflecting mirror channel through which the distillate flows, to monitor distillate composition on a Methanol-Water binary batch distillation column.

The refractive index of methanol-water binary solutions varies with composition, and so the methanol composition of the distillate is routinely measured using time consuming and expensive off line methods such as an Abbe refractometer or other analytical methods such as Gas Chromatography with Flame Ionisation Detector (GC-FID). This makes it difficult to develop distillation control strategies using composition control since the installed cost would be up to £100 K per instrument. The objectives are listed below:

1. Optimise a plastic optical fibre (POF) sensor probe; developed previously [1-4], by determining the optimum mirror distance and angle of inclination at which the probe shows highest sensitivity to concentration changes.
2. Trial a simple two-stage amplification circuit for analogue processing of the probe concentration measurements to produce a voltage output in the range of 0 – 10 V, to interface into the Seimens Distributed control system in the University of Manchester pilot plant facility.
3. Characterise the probe sensor sensitivity and resolution, by calibration against the Bellingham Stanley RFM390 refractometer, with resolution of ± 0.0001 refractive index units.
4. Integrate the probe and signal processing circuit onto a methanol-water batch distillation column.
5. Evaluate the potential to use the probe for composition control, in a closed-loop control scheme to maintain the distillate output at 97 v/v % methanol with a Siemens PCS-7 control scheme.

2. Optical Fibre Probe Design and Construction

The sensing probe utilised a 650 nm LED to transmit light through an emitting fibre, to form a cone of emitted light, which reflected off a movable mirror, back into a receiving fibre, parallel to the emitting fibre, as shown in Figure 1(a) [3]. The refractive index of the distillate, flowing between the fibres and the mirror, affected the optical path of the light coupled between the transmitting and receive fibre and thus causing a change in the output from the receiving fibre. A range of fibre arrangements and sizes were evaluated in the optimisation process [1-4] and the arrangement that had 6 emitting fibres and 1 receiving fibre, as shown in Fig. 1(b) and 1(c) [6] had the optimal signal and sensitivity for 1 mm diameter POF.

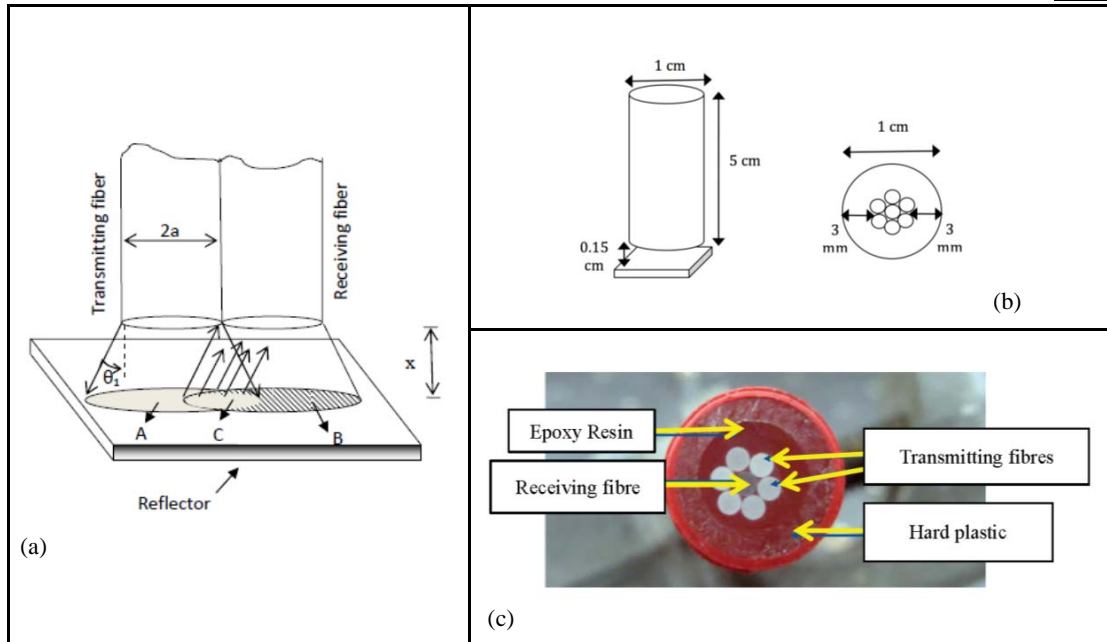


Figure 1. POF probe design and construction [5]: (a) Sensor principle; (b) Sensor design and dimensions [6]; (c) photograph of sensor distal end [6].

3. Instrumentation

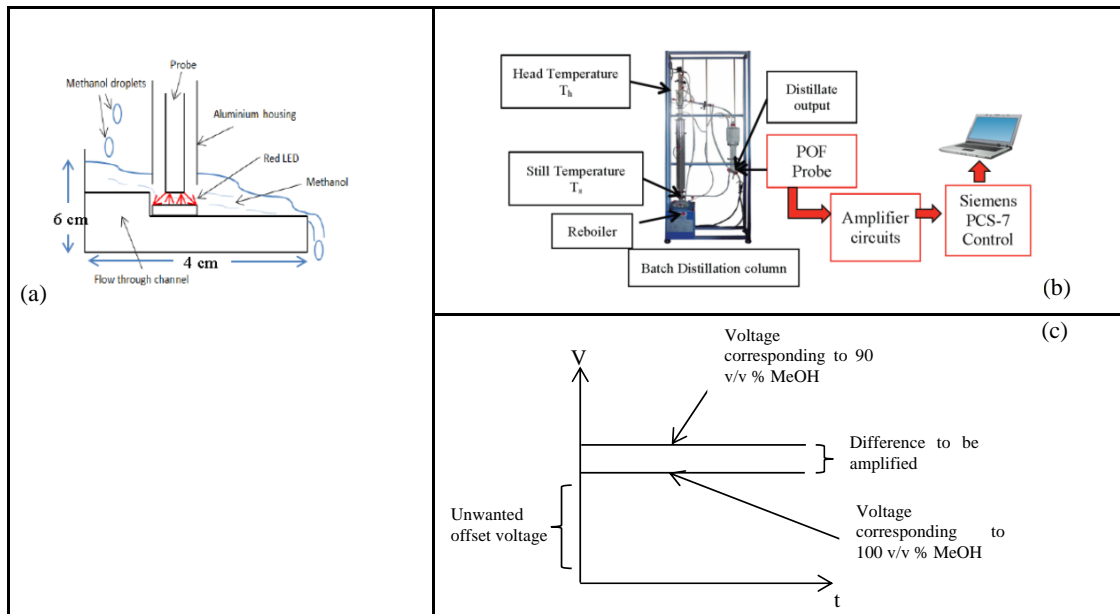


Figure 2: (a) Flow channel to ensure distillate interacts with probe sensing surface [6]; (b) Distillation column setup with the POF probe and amplifier connected to the Siemens PCS-7 control system [6]; (c) Output of first stage transimpedance amplifier; desired voltage range to be amplified [5].



The optical signal to the probe was illuminated using 6 red encapsulated LEDs (Multicomp OVL-3328 625nm), coupled to the 6 illuminating fibres. Light was reflected back from the mirror into the single receiving fibre, which was inputted to a Thorlabs silicon transimpedance amplifier photodiode (PDA100A). The voltage output from the amplifier contained an unwanted voltage offset, as shown in Fig 2(c). The voltage difference between 90 v/v % and 100 v/v % MeOH concentration was very small due to the small difference in refractive index. The second stage differential subtracted the offset and amplified the voltage difference, to produce a output voltage range corresponding to distinguishable MeOH concentrations, in the range of 0-10 V to be compatible with the Siemens PCS-7 I/O DCS.

A 3D-printed flow-through channel was created to facilitate the flow of MeOH past the probe end at an angle at the distillate output, as shown in Fig. 2(a) [6]. A batch distillation column was used to investigate the performance of the POF probe to measure methanol concentration of methanol in the distillate output from the column. The ultimate aim is to investigate whether the POF probe can be used for composition control, to maintain the purity of distillate at 97 v/v % MeOH by using the POF probe as a sensor to continuously monitor the concentration of MeOH in distillate, using closed-loop control. The batch distillation unit used in this project consists of 30 sieve-packed plates, with the batch still charged with 10 v/v % MeOH solution before operation. At column start-up, still heating was provided by a reboiler. The POF probe was placed at the distillate output of the column to measure the distillate concentration, and the voltage output from a two stage amplifier (transimpedance plus differential) was connected to a Siemens PCS-7 Distributed I/O control system.

A minimum volumetric flow rate of $0.125 \text{ cm}^3\text{s}^{-1}$ was required in order for the probe to detect MeOH flowing past its sensing surface. The optimum mirror distance was at 1.5 mm from the end of the probe, as shown in Fig 3(a) [5]. The POF sensor was optimised for the range 90 v/v % to 100 v/v %, which correspond to refractive indices of 1.328 to 1.336 as shown in Fig 3(b). To date the probe demonstrated a resolution of $\pm 0.21 \text{ v/v %}$ and $\pm 0.000174 \text{ RI units}$.

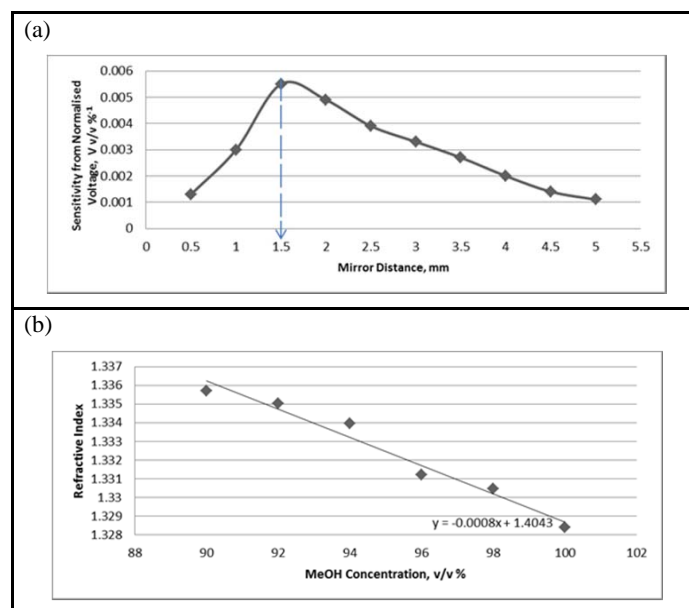


Figure 3.(a) Comparison of the relative probe sensitivities for 90 – 100 v/v % MeOH at different mirror distances [5]; (b) Linear trend of refractive index obtained within the MeOH concentration range of 90 – 100 v/v % [6].

4. POF probe performance for Batch Distillation

To demonstrate the POF probe in operation, the distillation column in Fig. 2(b) was run through a batch process for different reflux ratios. Fig. 4(a) shows the head temperature, still temperature and POF sensor output voltage logged during a typical batch distillation process using a constant reflux ratio of 100%



withdrawal. The pulsed peak voltage outputs represent the POF sensor output reading reaching a peak value each time a drop of distillate flows past the POF probe surface. The graph demonstrates that initially the voltage output and head temperature remain constant, then, as the head temperature increases, the voltage output increases indicating a change in refractive index of the distillate. The POF probe was calibrated before the experiment to relate the peak voltage output to a representative methanol concentration. The calibration model was based on the voltage difference from 99.5 v/v% as this was the smallest voltage output expected to be seen for the methanol concentrations of interest. The calibration equation for the 100% withdrawal trial is shown in Equation 1. The resultant distillate methanol concentrations are shown in Fig 4(b), using the POF probe.

$$\text{Methanol concentration} = \frac{(3.5883 - \text{voltage difference from } 99.5 \frac{v}{v}\%)}{0.0355} \quad (1)$$

Preliminary monitoring and control strategies were explored to control MeOH distillate concentrations at 97 v/v %, found to be at a column head and still temperature of 67.5°C and 94.5 – 100.3°C respectively. The distillation column was run, using a range of reflux ratios, to monitor still and head temperature and distillate output through a batch process.

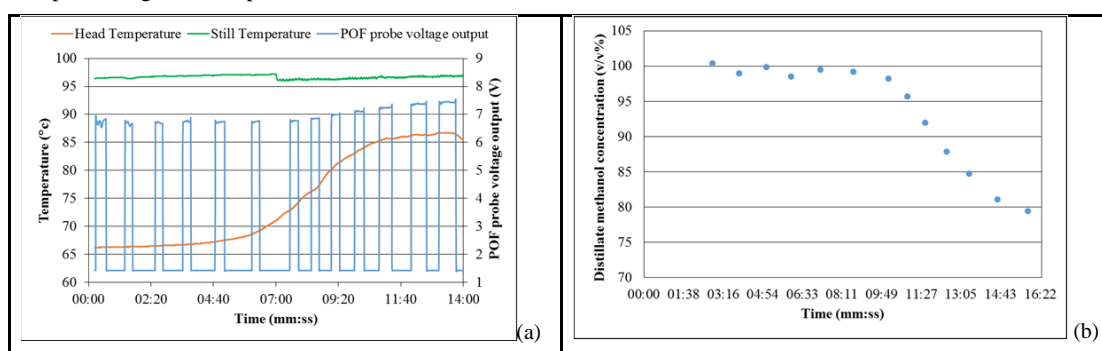


Figure 4: (a) Batch distillation process at a constant reflux ratio of 100% withdrawal; (b) Distillate methanol concentration for batch process at 100% withdrawal.

5. Conclusion

This project demonstrates construction and implementation of a low cost polymer optical fibre probe sensor with simple electronics aimed at on-line measurement and control of a routine chemical engineering process. The POF sensor was constructed from 1mm diameter standard data communications Toray POF using simple cutting and polishing techniques and the project was carried out by Chemical Engineering undergraduate and masters students [1-7] providing experience of building and optimising instrumentation and control procedures and applying new photonic sensors to chemical engineering challenges. The POF probe demonstrated a resolution of 0.21 v/v % and 0.000174 RI, which falls below the target resolution of 0.001 v/v % (industry standard) and 0.0001 RI (Bellingham RFM390 Refractometer) respectively. The probe performance can be improved by applying common mode rejection, and wavelength referencing techniques, and replacing the flow channel with a microfluidic channel to facilitate continuous flow past the POF sensor probe, instead of pulsed flow, and taking steps to protect the POF probe sensing face from methanol degradation using optical windows or a glass optical fibre bundle.

6. Acknowledgements

Thank you to the many dissertation students who have worked in our lab and to Dr John Vaughan and Nabeel Ahmed who taught them how to handle POF. Thanks also to Patricia Turnbull, Ali Arafah and Dr Abdullah Alfutimie for advice in operating the distillation column.

7. References

1. Qureshi, O (2014). MEng Dissertation. Design of an Optical Fibre Refractometer to Continuously Determine Methanol-Water Concentrations, The University of Manchester, Manchester, UK.



2. M. Astaire (2014). MEng Dissertation. Development of a Polymer Optical Fibre Probe Sensor to monitor Methanol content of Distillate in Methanol Purification Process. The University of Manchester, Manchester, UK.
3. A. Ahluwalia (2015). MEng Dissertation. Optical Fibre Sensor for the Continuous Measuring of the Refractive Index of Methanol-Water Solutions within a Distillation Process," School of Chemical Engineering and Analytical Sciences, The University of Manchester, Manchester, UK.
4. Spooner, M. (2015). MEng Dissertation, Development of Extrinsic Optical Fibre Probe For Application to Methanol Distillation, The University of Manchester, Manchester, UK.
5. A. Fong (2016). MEng Dissertation. Application of a Plastic Optical Fibre Sensor Probe to Monitor Methanol Concentrations Within a Batch Distillation Column. The University of Manchester, Manchester, UK.
6. K. Chandran (2016). MEng Dissertation. Plastic Optical Fibre (POF) Sensor for Concentration Measurement and Control of a Distillation Column, The University of Manchester, Manchester, UK.
7. Z. Gu (2014). MSc Dissertation. "Closed loop control of distillation column using optical on line sensor to monitor alcohol content of distillate," School of Chemical Engineering and Analytical Sciences, The University of Manchester, Manchester, UK.



POF Sensing Grid: Signal Analysis to extract Human Motion Characteristics

P.J.Scully^{1,2*}, O. Costilla-Reyes^{1,3}, N.Ahmed^{1,2}, J.Vaughan^{1,2}, E.Stanmore⁴, K.Ozanyan^{1,3}

1:Photon Science Institute.

2:School of Chemical Engineering and Analytical Science (CEAS).

3:School of Electrical and Electronic Engineering (EEE).

4: School of Nursing, Midwifery and Social Work (NMSW).

The University of Manchester, Oxford Road, Manchester, M13 9PL, UK

*Corresponding author: patricia.scully@manchester.ac.uk

Abstract: Low cost standard polymer optical fibre (POF) is incorporated into a standard carpet or rubber mat, enabling unobtrusive collection of longitudinal data from individuals walking or exercising on the mat. We present several data analysis methods applied to distributed sensor mats using POF grids for measuring human motion, including detection of position, locus and motion of a person at any position, using tomographic imaging, and for measuring the balance and changes in centre of mass of a person who is stationary on the mat using analogue null balance methods, and pattern recognition and machine learning classification, to identify different types of walking.

1. Introduction

Low cost standard, 1mm diameter step-index polymer optical fibre (POF), normally used for datacomms and LAN applications, was embedded in a standard carpet or rubber mat, so that it experienced transmission losses due to fibre bending, when pressure was applied to the mat when a person stood or walked on it. Toray POF (multimode, 980 μ m inner diameter, 10 μ m cladding) was arranged in a grid or network to detect fibre deformation over a 2-D area. This paper presents the signal analysis methods and fibre arrangements used to measure gait and mobility of people walking on the mat, enabling unobtrusive collection of longitudinal data on individual users performing everyday routines for healthcare and security applications.

We have developed several data analysis methods applied to distributed sensor mats using POF grids for measuring human motion, and created two categories of fibre arrangement within the mat substrate.

The first type of mat construction (iMagiMat) is designed so that a person can walk or stand anywhere on the mat, as shown in Fig. 1 (a), and their position, locus and motion be detected at any point, and the mats can be tessellated to cover a larger area to create a distributed sensor. This three projection optical fibre grid, was originally designed for tomographic imaging with a periodicity designed to detect the heel to toe parameter [1], but we have investigated other techniques including pattern recognition, machine learning [3] and centre of mass locus [1,4].

The second type of mat (Optical Force Plate) requires the person to stand in a fixed position on a fibre arrangement, as shown in Fig. 1(b), that is spatially arranged to optimize the interaction, with optimal location of the toe and heel [3], using an optical Wheatstone Bridge null balance configuration.

This paper will compare the POF mat signal analysis and performance for the different applications, and their advantages and limitations.

2. Selection of POF as Sensing Element

The POF grids have been created from 1mm diameter data-communication fibre, edge-connected to LEDs, with the transmitted light through the fibres, detected using photodiodes. Stepping on, and walking on the POF grid deformed the POFs by bending, and changed their transmission, affecting the amplitude and frequency characteristics of the transmitted optical signals.

POF is ideal for this application compared to glass optical fibre (GOF), because it is formed from a rugged polymer material (poly methyl methacrylate) with 1mm diameter, so is less sensitive to mode stripping and mode instability at the interface between fibre and LEDs/photodiodes. The large diameter of the POF enables high efficiency coupling with light sources and detectors and thus efficient transmission of light signals through the fibre over short lengths in the orders of metres. The POF is easy to handle, and cut and terminate at low cost, compared with glass fibre. For these mat constructions, 1mm diameter holes were drilled into the transparent polycarbonate domes of encapsulated LED (Multicomp OVL-3328 625nm) and photodiode



(Vishay TEFD4300) housings, and the fibres were glued and index matched to the embedded semiconductor chip, providing a mechanically secure coupling at the periphery of the mat. Our current mats no longer require the fibre to be sensitised by grooving or cladding removal along its length as described in reference [1] because we have investigated a range of step-index POF. POF is intrinsically sensitive to pressure changes and undergoes transmission losses due to macro-bending over the radii of curvature exerted by the human foot contours. The criterion for the fibre selection is that it exhibits a linear loss due to deformation along its length, and that a substrate is selected to allow the fibre to deform sufficiently through its radius of curvature to give sufficient losses, without total compression, in which case the fibre would be squashed flat.

The deformation experienced by the POF is affected by the force applied by the human foot and the mechanical properties and thickness of the carpet underlay that cushions the POF grid from the unyielding ground. The POF sensor elements have been integrated within a standard carpet underlay enabling the POF grid to be hidden from view under the normal carpet surface. The thin and flexible structure formed by the POF layer, enables the mats to be fitted to stepping blocks, stair treads and curved surfaces such as a treadmill, as well as sloped and undulating surfaces.

The bending sensitivity of a range of POF step-index fibre sourced from Toray and Mitsubishi, was assessed by forming them into various radii of circles of radius 10 – 20 mm radius and measuring the transmission losses. FX grade Toray fibre with NA of 0.5, Mitsubishi POF with NA of 0.5 and a low NA Toray PFU FB1000, with NA of 0.46 were compared, and the fibre with the lower NA displayed highest bending sensitivity. This was further evaluated by comparing the PFU 1mm diameter fibre with a 0.75 mm diameter PFU fibre with the same NA under the same bending conditions. From Fig. 1 (c) it can be seen that the larger diameter fibre exhibited higher bending losses (7 times more sensitive at a bending radius of 10 mm in comparison to the smaller diameter fibre) and was thus selected for use in mat construction.

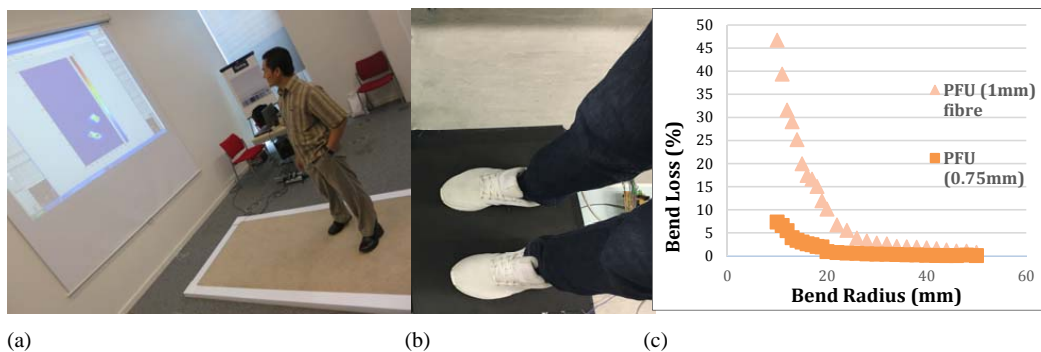


Figure 1. (a) iMagiMat, a 1 by 2 metre mat that allows several steps; (b) Optical Fibre Force Plate to monitor balancing in a fixed position; (c) Comparing Bending Loss of 1mm & 0.75 mm PFU FB Grade Fibre [2,3]

3. Imagimat Construction optimised for Photonic Guided Path Tomography using Radon Transform

iMagiMat is a 1 by 2 metre mat, (photographed in Fig 1(a)), that is large enough to accommodate several steps, formed from a grid of plastic optical fibres (POF). The POF arrangement is as shown in Fig. 2 (a), with 116 POF arranged in three angular directions or projections at 0 (20 fibres), 60 and 120 degrees (with 48 fibres each), with a constant separation of 0.06 m, selected to match the average heel-metatarsal distance of the human foot. The 3 angle projection fibre arrangement has been optimised for imaging fibre deformation using Photonic Guided-Path Tomography (PGPT) [1], in which the optical fibre attenuation for each fibre is measured along its full optical path, forming a line integral, and an image is formed from combining the attenuation all 116 POF fibres using a sparse angle technique to form a 3-angle Radon transform of the surface deformation. The low power optoelectronic transmitters and receivers (LEDs and photodetectors) are connected at the carpet edge, as shown in Fig. 2(b), so the mat is electrically passive and intrinsically safe. The



transmitter and receiver edge connected circuits are controlled/interrogated by a Programmable Logic Device (PLD) and the optical signals are interfaced to an external laptop via a LabVIEW signal processing software using a NI-9205 analog input module with a NI-cDAQ-9172 chassis.

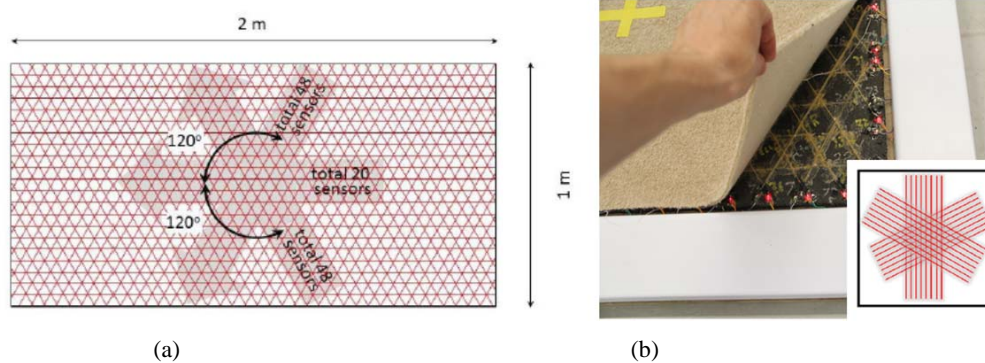


Figure 2. (a) POF lay-out for 2 by 1 metre mat. 116 fibres arranged in 3 directions or projections. (b) Photo of a corner of iMagiMat to show 3 projection POF arrangement, LEDs and photodetectors.

GPT has five advantages:

1. The image is formed from combining the signals measured along the lengths of each of the 116 POF elements, significantly reducing the number of measurements and sensor connections per unit area, compared with competing techniques such as competing technologies such as GAITRite (www.gaitrite.com). PGPT enables a saving of $N \times (N-2)$ measurements and $N \times (2N-4)$ contact wires compared with an $N \times N$ array of singlepoint pressure sensors, each having two contact wires [1].
2. Since the electronics is edge-connected, large areas can be covered, at low cost. The optoelectronic edge-connectors scale linearly with the contiguous edges of the mats, and can be minimised.
3. The forward Radon transform processing excludes signals arising from static deformation of the carpet (such as furniture), limiting image reconstruction to dynamic signals only via data inversion, and also performs zeroing by removal of background deformation and noise.
4. Individual mats can be tessellated to form a large sensing surface; scale up requires additional low-cost sensing tiles with edge connected electronics, costing £100 per square metre and potentially less when manufactured on a large scale.
5. GPT allows imaging in non-planar surfaces determined by the guided paths, which means that a flexible surface formed in this way can be mapped onto a 3D object to form a sensing skin.

4. Speeding up processing using Parallel Centre-of- Mass Algorithm

The disadvantage of GPT is that it is computationally challenging, and speeding up of the process was required to enable real-time processing of footsteps on the National Instruments/Labview platform. A computationally efficient "centre-of-mass" reconstruction, was developed using the sinusoidal Hough transform, combined with sinogram recovery using the inverse Radon transform [5]. This was intended for applications where fast processing of the locus and speed of progression of the footsteps were more important than imaging pressure distribution, such as tracking the positional coordinate of a walking person. The Parallel Center-of- Mass Algorithm (PCoMA) [1,5] reduced processing time to microseconds, and enabled detection of multiple feet on the mat, essential for tracking a living space with traffic from several individuals. The Centre of Mass (CoM) coordinates were generated without needing to reconstruct the foot image, saving computing time. The PCoMA was implemented in a hardware-based system based on a FPGA [5].



5. Identifying Different Walking using Machine Learning and Temporal Pattern Recognition

Another disadvantage of GPT is that locus and pressure information is logged, but the computational complexity does not capture the temporal data in sufficient detail to distinguish conditions where signal frequencies could indicate dynamic motor control processes affecting balance and gait, and relate them to on-set of conditions such as Parkinson's, or Alzheimer's, as well as environmental changes such as different types of walking in the same individual carrying loads or wearing different shoes. To investigate time dependent effects, the raw optical fibre loss signals, outputted from each of the 116 POF fibres in the 1 by 2 m iMagiMat, were summed together to give a cumulative signal that was analysed, to distinguish changes in gait for a single person, performing 10 different styles of walking. So the iMagiMat constructed for tomographic imaging, was used as the basic sensor mat, but the acquisition speed was speeded up, so 1400 full frames were captured at 256 Hz, so that at least 2 gait cycles (4 to 5 consecutive footsteps) were captured. The 10 manners of walking that were sampled, affected the amplitude and frequency characteristics of the temporal signals in different ways. Normal, slow and fast gait and motion affected the frequency content of the optical signals, while barefoot gait and loaded gait (carrying weight) modified the optical signal amplitude.

A total of 855 gait experiments were captured, yielding approximately 111 million unique POF sensor signals. The data processing and analysis of the raw POF signals were developed from the open source software packages such as Python, NumPy/SciPy and scikit-learn machine learning library, after pre-processing with a Savitzky-Golay filter for smoothing. Five temporal features were analysed using 14 different machine learning models, representing linear, non-linear, ensemble and deep learning models, and the optimal classification performance was observed for a Random Forest model with the Adjacent Mean temporal feature, yielding a mean validation score of 90.09 ± 5.24 % [4]. This demonstrated that different types of gait performed by the same individual could be distinguished using pattern recognition techniques applied in the time domain, despite the iMagiMat POF arrangement not actually being optimised for this application. However, only two of the 116 POF sensors in the iMagiMat were required to obtain reliable mean validation scores for the presented type of gait activities, so this an exact subset of POFs can be preselected to create the best classification scores from temporal data; thus influencing the design and the principles of data acquisition in future sensor mats. It also indicates that the spatial periodicity of the mat is less important, and failures of optical fibre sensor links could be compensated for and redundancy built into the mat design.

6. Optical Fibre Force Plate to measure Balance and Posture

The second type of mat (Fig 1(b)), was designed to measure balance and posture, by detecting changes in the centre of pressure (CoP) of a person, standing on the mat in a fixed position as shown in Fig. 3(a). The POF fibre arrangement was spatially arranged to optimize the interaction as shown in Fig. 3(b), using an optical Wheatstone Bridge null balance configuration. The maintenance of balance and body orientation when a person is standing quietly and maintaining a posture, is used for rehabilitation, and to improve physical and sport activities; for example: neurological disorders (eg. Parkinsons), ageing, surgical intervention, strength and conditioning, and training in sports that require a stable base, such as golf putting, shooting, archery. A commercial force plate is expensive, (up to £40K to equip a lab) , but for posturography, a plate consisting of four load cells can be used to measure the vertical component of the ground reaction force and the two Centre of Pressure (CoP) coordinates (which represent the two moments of force in the x and y axis). The CoP locus is displayed on a graph and represents the movement of the CoP in the x-y direction. The x direction represents side to side or mediolateral (ML) movement, and the y direction denotes back to front or anterior-posterior (AP), as shown in Fig. 3(a). Thus a time dependant display of the CoP coordinates is plotted in a standard display known as a stabilogram, and is used to assess balance, posture and swaying, plus performance of exercises such as squatting.

The advantages of using a POF mat instead of a force plate include the ability to customise the spatial POF fibre arrangement on a thin deformable substrate (in this case rubber matting) to measure pressure in each of four quadrants Z_1 , Z_2 , Z_3 and Z_4 , so that the ML and AP movements could be detected according to equations 1 and 2.

CoP calculation:

$$ML = [(Z_4 + Z_2) - (Z_1 + Z_3)] \quad (1)$$



$$AP = [(Z_4 + Z_2) - (Z_1 + Z_3)] \quad (2)$$

Several fibre loops were arranged to detect the pressure in each quadrant as shown in Fig. 3(b) and their optical signal outputs converted to voltage signals and weighted and summed together, to measure fibre deformation due to the heel and toe sections (metatarsal and calcaneus) for each foot. The summed outputs for each of the four quadrants were sampled using a National Instruments hardware; an NI 9219 4 Channel Isolated, 24-bit, ± 60 V, 100 S/s AI Module which fed into the cDAQ-9188, CompactDAQ Universal chassis (8 Slot ENET). This chassis was then connected to a laptop and LabVIEW software was used for data analysis of the voltage signals related to deformation of each POF loop. The signals from each quadrant were summed to form an arm of a Wheatstone Bridge null balance configuration, programmed with Labview to represent a central CoP point, displayed with x (ML) and y(AP) coordinates as shown in Fig.3 (a), on a real-time computer or tablet display for form a stabilogram where the CoP locus motion is tracked in time as shown in Fig. 3(c) and (d). The CoP locus mean, standard deviation and frequency components, and changes in loci with movement and exercise provided information about the subject's postural stability. Fig. 3(c) shows the stabilogram with eyes open for a subject standing quietly, Fig. 3(d) shows that the CoP shifts and the amplitude of movement increases when the subject tries to balance with closed eyes. Detailed calculations and signal processing are described in [3]

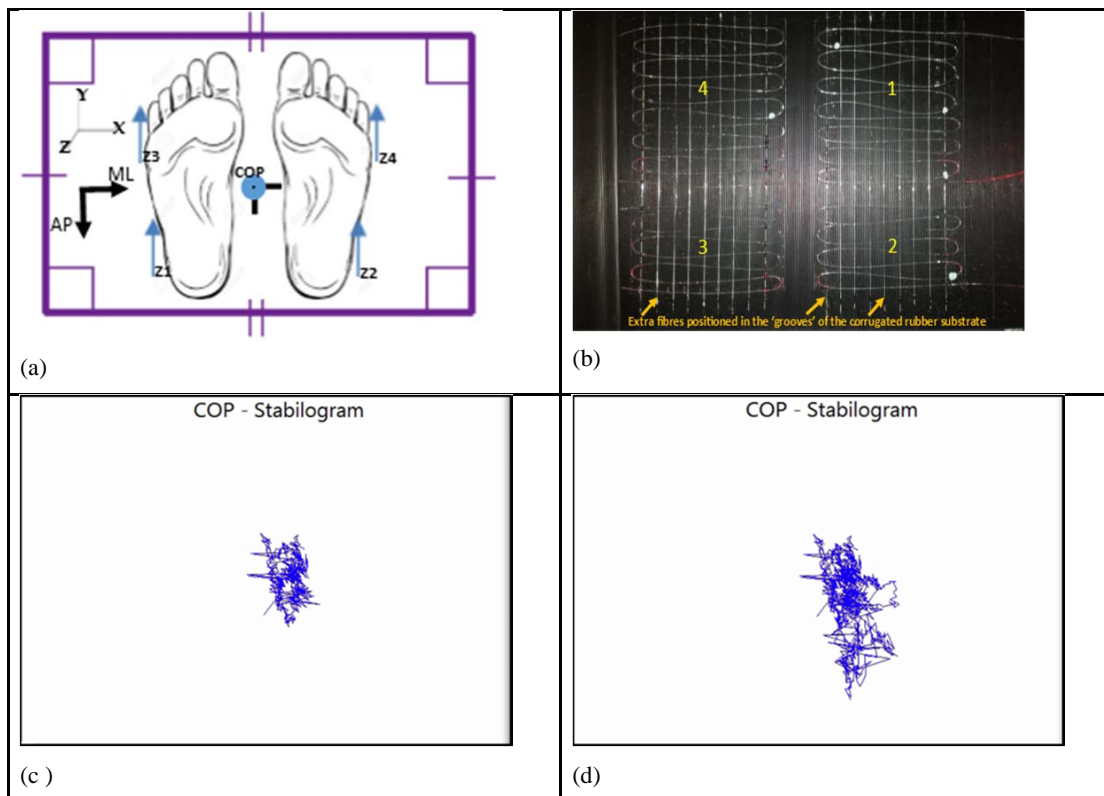


Figure 3: (a) Diagram to show Centre of Pressure (CoP) coordinates, x and y axes and zones Z_1 , Z_2 , Z_3 and Z_4 . [2]; (b) Initial POF arrangement to measure sway and balance; (c) Stabilogram for standing still with eyes open. (c) Stabilogram for standing still with eyes closed.

The thin flexible rubber substrate shown in Fig 3.(b), can adapt to curved or undulating surfaces, and interfaced to USB or wireless interfaces at low cost, for self-assessment on mobile phone. Fig. 3(c) shows the There is scope for applying pattern recognition and machine learning to the sensor outputs, together with sensor fusion to wearable body position and motion sensors.



7. Conclusion

We have developed a range of signal processing methods to extract data from POF sensor elements to measure human motion ranging from balance to walking. Both the fibre spatial arrangements and the signal processing methods have advantages and limitations. Together with tomographic and analogue null balance methods, we have explored pattern recognition and machine learning classification, to identify different types of walking. Applications include gait analysis for detection of early onset of dementia affecting the executive function of the brain and thus mobility, and rehabilitation, sports and security. imaging and recording the geometry, spatial location and time of each footfall, to extract gait measures that define mobility.

8. Acknowledgements

Photon Science Institute (University of Manchester) Pump Prime Fund; Engineering and Physical Sciences Research Council (EPSRC) Bridging the Gap and Translational Research and Pathways to Impact fund; Manchester Institute for Collaborative Research on Ageing (MICRA), Manchester Integrating Medicine and Innovative Technology (MIMIT); Arthritis Research UK, Manchester Academic Health Science Centre (AHSC) Healthcare Challenge; Conacyt for funding Omar Constilla-Reyes, and EPSRC for funding Nabeel Ahmed.

9. References

1. Cantoral-Ceballos, J. A., Nurgiyatna, N., Wright, P., Vaughan, J., Brown-Wilson, C., Scully, P. and Ozanyan, K. B. (2015). "Intelligent Carpet" System, Based on Photonic Guided-Path Tomography, for Gait and Balance Monitoring in Home Environments. *IEEE Sensors Journal*, 15(1), 279-289. [6861424]. DOI:10.1109/JSEN.2014.2341455
2. Ahmed, N., Vaughan, J., Scully, P.J. and Stanmore, E. (2015). POF Optical Force Plate. *International Polymer Optical Fibre Conference 2015*. Nurnberg, Germany, September 2015.
3. Ahmed, N., Scully, P.J., Vaughan, J, Brown Wilson, C. and Ozanyan, K. (2014). Polymer Optical Fibre Sensor for Measuring Breathing Rate of Lying Person. *Proceedings of the 8th International Conference on Sensing Technology (ICST 2014)*. Liverpool, UK, 2-4 September 2014. *International Journal on Smart Sensing and Intelligent Systems*: 435-440.
4. Costilla Reyes, O., Scully, P., & Ozanyan, K. (2016). Temporal Pattern Recognition in Gait Activities Recorded with a Footprint Imaging Sensor System. *IEEE Sensors Journal*, PP(99). 10.1109/JSEN.2016.2583260
5. Cantoral-Ceballos J.A., Wright P., Vaughan J., Scully P and Ozanyan K.B (2015). "Real-time Reconstruction of Footprint Positions using an "Intelligent Carpet". *Proceedings of IEEE SENSORS 2015. Imaging Sensor*. IEEE SENSORS 2015; 02 Nov 2015-04 Nov 2015; Busan, South Korea. New Jersey, USA: IEEE; 2015.

Radiation induced attenuation in perfluorinated polymer optical fibres for dosimetry applications

P. Stajanca*, K. Krebber

Bundesanstalt für Materialforschung und –prüfung (BAM), Unter den Eichen 87, 12205 Berlin, Germany

*Corresponding author: paval.stajanca@bam.de

Abstract: Real-time measurement of radiation-induced attenuation (RIA) in a commercial perfluorinated polymer optical fibre (PF-POF) is performed with regard to on-line radiation monitoring purposes. Spectral character and dose dependence of fibre's RIA is measured in 450-900 nm spectral region. Fibre exhibited high radiation sensitivity in the visible region with strong increase towards the UV wavelengths. Good linearity and high sensitivity reaching up to $130 \text{ dBm}^{-1}/\text{kGy}$ was demonstrated in the VIS region for a low-dose range. This of-the-shelf PF-POF could be therefore interesting for on-line remote dosimetry applications.

1. Introduction

Considerable efforts have been devoted to the development of optical fibre-based dosimeters (OFDs) over the last decades [1, 2]. Compared to other available dosimetry techniques, OFDs offer numerous advantages including possibility of remote and real time monitoring, electromagnetic immunity or small footprint. Various effects taking place in optical fibres upon irradiation can be used for dosimetry purposes; for example radiation-induced attenuation (RIA), radiation-induced luminescence, thermally- or optically-stimulated luminescence. Among these, RIA monitoring represents one of the most straightforward OFD techniques. Ionizing radiation degrades the fibre transmission and corresponding attenuation increase can be correlated to the total dose absorbed by the fibre. Most of the research activities have been focusing on more common glass optical fibres (GOF). However, recent advancements of polymer optical fibres (POF) have made them an attractive alternative for various applications [3, 4]. POFs are typically robust multi-mode (MM) fibres which are easy to handle and their interconnections are not as technically demanding as in case of glass fibres. In addition, POFs don't fail in brittle manner and are generally more acceptable for in-vivo medical applications. Utilization of polymethyl methacrylate (PMMA) POF as a low-cost, real-time OFD has been suggested and demonstrated in the past [5]. Our recent study suggested that radiation sensitivity of perfluorinated (PF) POFs might be considerably higher than in case of PMMA [6]. Perfluorinated fibres based on Cytop polymer offer low-loss operation in a broad spectral region unmatched by any other POF [7]. Therefore, here we investigate RIA sensitivity of PF-POF in a more precise on-line irradiation experiment and explore possibilities of utilizing the fibre as for real-time radiation monitoring.

2. Methodology

A commercially available MM PF-POF GigaPOF-50SR from Chromis Fiberoptics was investigated in this work. The fibre has $50 \mu\text{m}$ graded-index (GI) Cytop core with $490 \mu\text{m}$ polycarbonate over-cladding and is prepared by co-extrusion process [8, 9]. In on-line spectral RIA measurement, 2.3 m long piece of the fibre was homogeneously irradiated with ^{60}Co irradiator at a dose rate of 267 Gy/h . Experimental configuration of fibre irradiation is schematically illustrated in Figure 1.

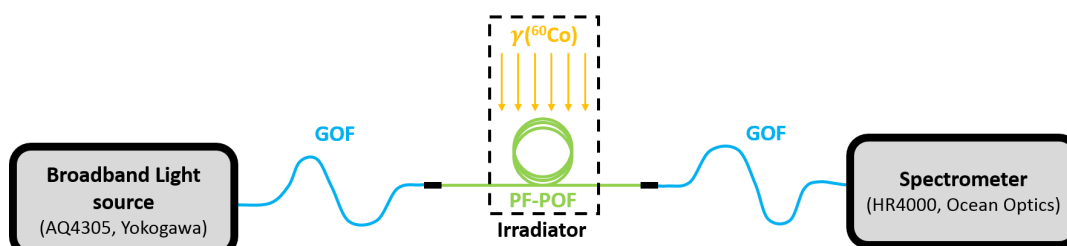


Figure 1. Schematic illustration of experimental configuration utilized for on-line measurement of spectral RIA in the investigated PF-POF.

Broadband light from fibre coupled Halogen lamp (AQ4305, Yokogawa) was send into the irradiated fibre sample with the help of auxiliary GOF. Transmission spectrum from irradiated fibre was monitored with a CCD-based spectrometer (HR4000, Ocean Optics) working in the VIS-NIR spectral range. Auxiliary interconnecting GOFs as well as connectors were shielded by lead bricks. The RIA (in dB/m) evolution with total dose $D(t)$ was evaluated from spectral transmission data as

$$RIA(\lambda, D) = -\frac{10}{L_0} \log \left(\frac{I(\lambda, D)}{I(\lambda, 0)} \right). \quad (1)$$

Here, $I(\lambda, D)$ is the measured transmitted spectral intensity at dose D and L_0 is the length of irradiated fibre (2.3 m). The dose D was calculated according to utilized dose rate and irradiation times.

3 Results and discussion

Radiation degrades the material of optical fibre which manifest itself as an intensity decrease of light transmitted through the fibre. Figure 2a illustrates a drop of transmitted spectral intensity of the investigated fibre upon irradiation. High radiation sensitivity of the fibre in the visible region is evident, when wavelengths below 700 nm are completely depleted already for doses at 500 Gy level. Here we would like to note that monitoring range of interrogating system is limited by depletion of the transmitted signal below detection level of utilized spectrometer. Dose level at which this limit is reach depends on the fibre radiation sensitivity, length of irradiated section and the spectral intensity distribution before irradiation. The actual sensitivity range of the fibre may greatly overcome this practical monitoring range imposed by the experimental apparatus. At the same time, performance of RIA-based OFD can be widely tailored by changing the interrogation wavelength or length of irradiated fibre.

To visualize the spectral dependence of the induced attenuation, Figure 2b depict the dose evolution of fibre's spectral RIA in a low-dose region (< 100 Gy) calculated from transmission data according to eq. (1). Increase of fibre's RIA sensitivity from NIR towards UV wavelengths is apparent. In the VIS region, RIA exhibits a local minima around 540 nm and local maxima at 650 nm. The figure illustrates that a wide range of sensitivities and sensing ranges can be achieved with this type of the fibre.

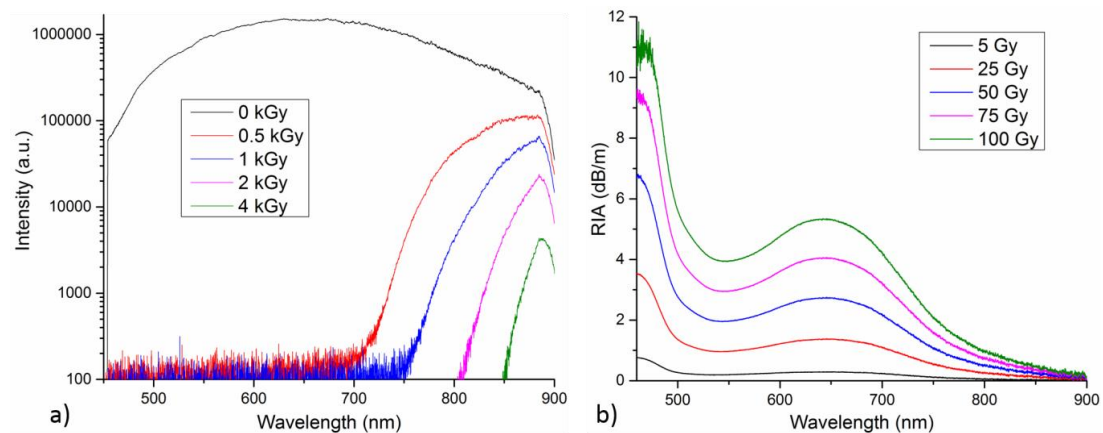


Figure 2. Evolution of fibre's transmission spectrum (a) and spectral RIA (b) with increasing radiation dose.

Due to spectral dependence of RIA, wide range of radiation sensitivities can be achieved through selection of suitable monitoring wavelength. In practice, sensitivity of OFD can be further increased by irradiating longer fibre section, boosting the RIA impact on the system transmission. At the same time, RIA monitoring range is dependent on the fibre radiation sensitivity, length of irradiated section and the spectral intensity distribution before the irradiation. Based on these parameters, upper limit of monitoring range is defined as a point when the measured spectral intensity drops below the spectrometer noise level. RIA-based fibre dosimeters thus offer large space for tailoring of OFD sensing parameters.

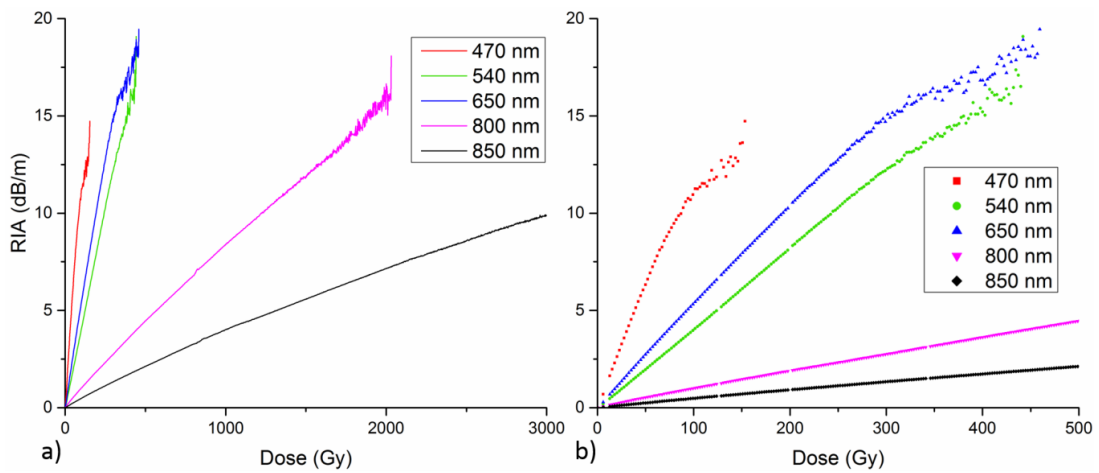


Figure 3. RIA as a function of radiation dose at five selected wavelengths up to total dose of 3 kGy (a) and detail on low-dose region up to 500 Gy (b).

Figure 3 shows the evolution of fibre’s RIA with total radiation dose at five selected wavelengths from the monitored spectral range. Only the data in system monitoring range at respective wavelengths is presented. Fibre RIA sensitivity can be determined from an apparent slope of presented RIA versus dose dependence curves. Red curve of 470 nm wavelength represents highly sensitive region at the blue edge of the monitored spectral interval. Wavelengths of 540 and 650 nm correspond to local spectral RIA minima and maxima in the VIS range, respectively. Near-infrared wavelengths of 800 nm and 850 nm illustrated the rapid sensitivity drop towards the longer wavelengths. Fibre RIA response has slightly sub-linear character that becomes apparent when monitored over kGy dose range (Figure 3a). However, for limited dose range intervals, good linearity between measured RIA and applied dose can be found (Figure 3b). Monitoring of fibre’s RIA within these intervals can be exploited for on-line radiation dosimetry.

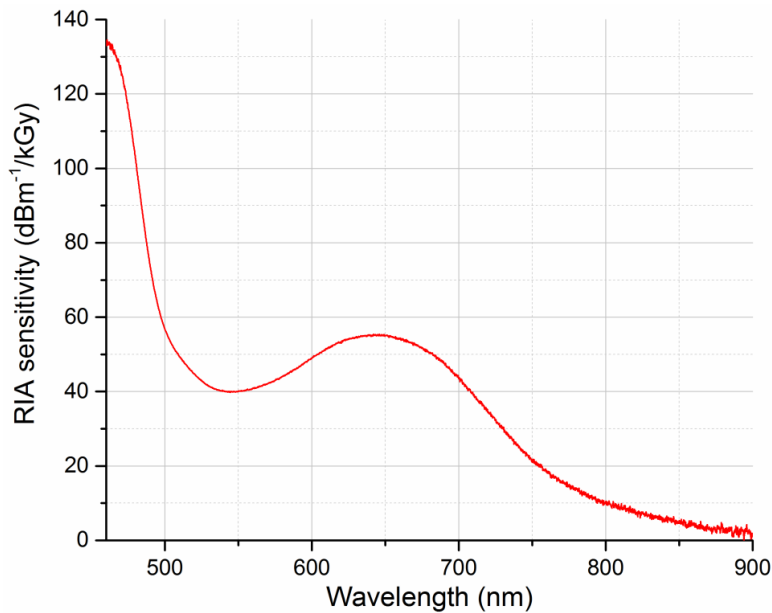


Figure 4. Spectral character of radiation sensitivity of GigaPOF-50SR PF-POF calculated as a linear fit of fibre’s RIA versus dose dependence in the low-dose range (0-60 Gy).

Figure 4 presents the spectral dependence of fibre's RIA sensitivity evaluated from linear regression of RIA response curves at individual wavelengths in the low-dose region of 0-60 Gy, where good linearity is achieved at all monitored wavelengths. The evaluated dose range is more than sufficient for personal dosimetry or radiotherapy monitoring applications, where imparted doses are at the level of single Gy and lower. Broad range of sensitivities spanning from 40 dBm⁻¹/kGy to over 130 dBm⁻¹/kGy can be achieved in the visible range. Spectral character of the RIA sensitivity curve on the blue edge of our monitoring spectral region suggests that even larger sensitivities can be achieved at shorter wavelengths. On the other hand, operation at less sensitive NIR wavelengths can be used for applications involving larger radiation doses. Recorded sensitivity values are more than two orders of magnitude higher than those measured for PMMA POFs [5]. Even though higher sensitivities has been achieved with specialty custom-made P-dope silica fibres [10, 11], PF-POF offers considerably higher sensitivity than the most of the studied silica-based fibres [12]. Therefore, performance of the investigated fibre is highly promising, especially considering that it is readily available of-the-shelf POF.

4. Conclusion

Sensitivity of a low-loss commercial PF-POF (GigaPOF-50SR, Chromis Fiberoptics) to gamma radiation was measured and exploited for on-line dosimetry purposes. Due to strong spectral dependence of fibre's RIA, wide range of OFD sensitivities can be achieved by the choice of suitable interrogation wavelength. For a limited dose range, fibre's RIA response exhibits good linearity with increasing dose and can be therefore used for dosimetry purposes. In the low-dose range up to 60 Gy, RIA sensitivities spanning from 40 dBm⁻¹/kGy to over 130 dBm⁻¹/kGy were measure in the VIS range (450-700 nm). Lower sensitivities down to single dBm⁻¹/kGy can be reached further in the NIR region. Demonstrated sensitivities significantly exceeds performance of PMMA POFs [5] and most of the silica-based fibres [12]. As an of-the-shelf polymer fibre, investigated PF-POF holds a considerable potential for on-line radiation monitoring applications.

5. Acknowledgements

Research leading to these results has received funding from the People Programme (Marie Curie Actions) of the European Union's Seventh Framework Programme FP7/2007 2013/ under REA grant agreement n° 608382. Authors would like to thank Dr. A. Denker of Helmholtz-Zentrum Berlin for facilitating the fibre irradiation.

6. References

- [1] A. L. Huston, B. L. Justus, P. L. Falkstein *et al.*, "Remote optical fiber dosimetry," *Nuclear Instruments and Methods in Physics B*, 184, 55-67 (2001).
- [2] S. O'Keefe, C. Fitzpatrick, E. Lewis *et al.*, "A review of optical fibre radiation dosimeters," *Sensor Review*, 28(2), 136-142 (2008).
- [3] O. Ziemann, J. Krauser, P. E. Zamzow *et al.*, [POF Handbook: Optical Short Range Transmission Systems] Springer, Berlin(2008).
- [4] K. Peters, "Polymer optical fiber sensors - a review," *Smart Mater. Struct.*, 20(1), 013002 (2011).
- [5] S. O'Keefe, and E. Lewis, "Polymer optical fibre for in situ monitoring of gamma radiation processes," *International Journal on Smart Sensing and Intelligent Systems*, 2(3), 490-502 (2009).
- [6] P. Stajanca, L. Mihai, D. Sporea *et al.*, "Effects of gamma radiation on perfluorinated polymer optical fibers," *Opt. Mater.*, 58, 226-233 (2016).
- [7] H. P. A. van den Boom, W. Li, P. K. van Bennekom *et al.*, "High-Capacity Transmission over Polymer Optical Fibre," *IEEE J. Sel. Top. Quantum Electron.*, 7, 461-470 (2001).
- [8] W. White, "New Perspectives on the Advantages of GI-POF," *Proceedings of POF 2005*, (2005).
- [9] C. Lethien, C. Loyez, J.-P. Vilcot *et al.*, "Exploit the Bandwidth Capacities of the Perfluorinated Graded Index Polymer Optical Fiber for Multi-Services Distribution," *Polymers*, 3, 1006-1028 (2011).
- [10] S. Girard, Y. Querdane, C. Marcandella *et al.*, "Feasibility of radiation dosimetry with phosphorus-doped optical fibers in the ultraviolet and visible domain," *J. Non-Cryst. Solids*, 357, 1871-1874 (2011).
- [11] M. C. Paul, D. Bohra, A. Dhar *et al.*, "Radiation response behavior of high phosphorous doped step-index multimode optical fibers under low dose gamma irradiation," *J. Non-Cryst. Solids*, 255, 1496-1507 (2009).
- [12] S. Girard, J. Kuhnenn, A. Gusarov *et al.*, "Radiation Effects on Silica-Based Optical Fibers: Recent Advances and Future Challenges," *IEEE. Trans. Nucl. Sci.*, 60(3), 2015-2036 (2013).

Parallel-multipoint plastic optical fiber sensor based on specklegrams

M. Lomer^{1*}, L. Rodriguez-Cobo¹, J.M. Lopez-Higuera¹

¹ Photonics Engineering Group, University of Cantabria, 39005, Santander (Spain)

*Corresponding author: lomerm@unican.es

Abstract: In this work a new configuration of a plastic optical fiber sensor disposed in parallel to detect at multiple points is presented. The sensor is based on the high sensitivity of changes in the speckle pattern when the fiber is perturbed. Plastic optical fibers used are 980 and 240 μm core diameter. The fibers are connected in parallel to 1mm POF fibers, both at the input and at the output. We proved that perturbation can be detected by one or more fibers arranged in parallel maintaining the properties of speckle fiber. The proposed sensor is highly sensitive and can be used in the protection of works of art.

1. Introduction

Usually, protection, security and intrusion detection systems are sophisticated and expensive. Some of these systems are based on different technologies such as electrical, optical, magnetics or acoustic: they use surveillance cameras, IR detectors, electronic alarms or optical fibers. Optical fiber sensors have several advantages including small size and low cost, they are immune to electromagnetic interferences from the surrounding environment. Optical fiber sensors are very attractive for applications in safety and security of valuable items such as works of art, being able to be also employed as optical communication systems [1]. Optical fiber sensors use different modulation techniques of light, intensity, phase, polarization or wavelength. In recent years, random interference between modes propagated by a multimode fiber are used in various sensing applications [2-4]. Particularly, the high sensitivity exhibited by the speckle pattern achieved when the fiber it is perturbed highlights over other techniques. Although its use has been since the 1980s [5], in recent years their applications have increased because they can be based on cheap diode lasers and CCD cameras with better performance. In addition, the signal processing techniques are much faster, thanks to the advanced calculation methods and computer capacity.

In this paper a new multi-point sensor using changes in the speckle pattern generated in fiber is presented. A set of 12 fibers are arranged in parallel where the ends are joined and coupled to 1 mm fiber sections; input fiber is coupled to laser diode and output fiber is coupled to CCD camera. The sensor uses two types of step-index multimode plastic optical fibers (POF) of the core-cladding diameters of 240/250 μm and 980/1000 μm , respectively. Although the output beam travels through different fibers, the speckle phenomenon is present in the fiber output and recorded by the CCD. The proposed sensor can be used in safety and security systems such as works of art, it is of simple construction and low cost.

2. Sensor Concept and experimental setup.

The generation of speckle patterns when a coherent multimode beam propagates inside have been widely studied. Indeed, the phenomenon speckle fiber is obtained by random interference between modes propagated [6], observable from the output face of the fiber, the speckle pattern is highly sensitive to external perturbations in the fiber, and for this reason it is the basis for numerous applications. When a light beam is injected into the multimode fiber, the beam is decomposed into modes propagating with different phases, they are randomly distributed in the core section. The modes interfere, present at the output face of the fiber form the speckle pattern, whose amount is similar to the number of modes of the fiber. If the coherence of the light source is good enough and the lengths of the fibers are not very large, it is possible to couple the speckle pattern to another fiber, with identical or different characteristics. After this coupling, the speckle phenomenon is maintained and can be used in sensor applications, although reducing slightly its sensitivity. In order to have multiple sensitive points in a sensor system using a single source and a single CCD camera, sensor shown in Figure 1 have been proposed. Each section of the fibers can detect perturbations in parallel independent sub-systems. The advantages POF fiber, large diameter and great flexibility, allowing coupling light easily without special equipment and adapt in different fields of application.

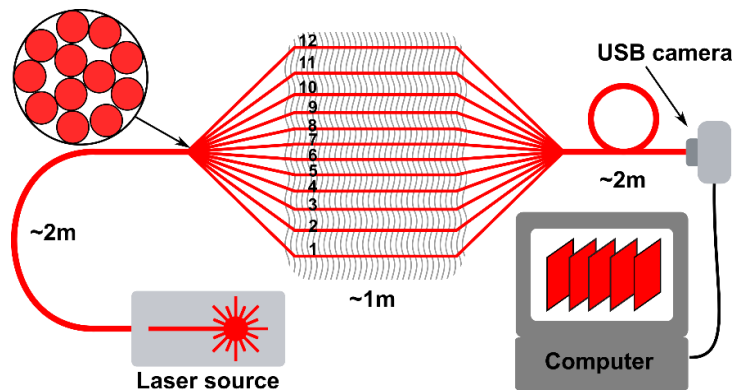


Figure 1. Experimental setup multipoint sensor based on fiber specklegrams.

The sensor shown in Fig. 1 system consists of a laser diode ($\lambda = 653.5 \text{ nm}$ and coherence length 0.42 mm), three sections POF (input and output POFs of $1000/980 \text{ }\mu\text{m}$ diameter, sensing section of 12 POFs of $240/250 \text{ }\mu\text{m}$ diameter), and the output section is connected CCD camera. Sensing fibers have a length of 1 m long. Both types of fiber are PMMA based and has a numerical aperture $\text{NA} = 0.5$. In operation, the CCD camera records sequences speckle patterns at a rate of 30 frames per second, called specklegrams. The specklegrams are processed in the computer to obtain a signal representative of the perturbation. When the light beam is coupled in the POF of 1 mm , over 2 million modes propagate in the fiber core, it is output has a distribution similar to the amount of speckle modes. The fiber of $250/240 \text{ mm}$ diameter supports about 160 thousand modes.

The coupling between the fibers 12×1 and 1×12 ($980/240 \text{ mm}$ diameter ratio) was achieved within a plastic jacket 1.1 mm in diameter and 2 cm long. The separation distance between fibers core is approximately a hundred microns. Although the coupling between fibers can be considered random and complex, speckle patterns observed in each of the 12 fibers after passing a fiber of $980 \text{ }\mu\text{m}$ to other $240 \text{ }\mu\text{m}$ core, can be noticed in Figs. 2 (a) and (b). In Fig. 2 (c) the speckle pattern achieved at the output of a $980 \text{ }\mu\text{m}$ core fiber coupled to the 12 fibers $240 \text{ }\mu\text{m}$ core is depicted. The speckle pattern projected at the output end of the fiber and can be used for sensing applications.

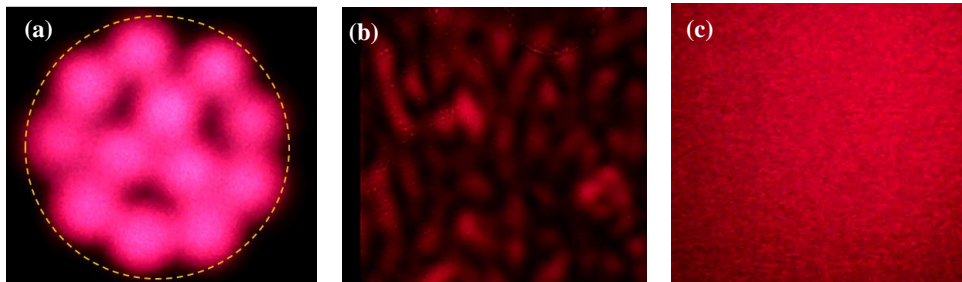


Figure 2. Speckle patterns output fiber. (a) output end 12 core fibers $240 \text{ }\mu\text{m}$ coupled by a fiber of $980 \text{ }\mu\text{m}$, (b) the speckle pattern at the output of a single fiber of $240 \text{ }\mu\text{m}$ core, and (c) speckle pattern output fiber $980 \text{ }\mu\text{m}$ core after being coupled by 12 fibers of $240 \text{ }\mu\text{m}$ core diameter.

3. Results

Using the arrangement of Fig. 1, perturbations in different sections of the arrangement of fibers have been provoked. In order to obtain a signal representative of the event, the specklegram sequence captured by the CCD

images (30 frames per second) is processed by simple difference between frames using MATLAB program, as described in reference [4]. In Fig. 3 the obtained results are depicted. The method of perturbation of the fibers, with random intervals and duration, was performed in the following sequence. First, the common input fiber, of 980/1000 μm diameter, is perturbed and the other fibers are held fixed, the result is represented by the signal A. Second, the fibers in parallel, of 240/250 μm diameter, are perturbed independently according to the sequence shown in Fig. 1. The results are shown in Fig. 3 and numbered from 1 to 12 for these signals. Third, the common output fiber of diameter 980/1000 μm , is perturbed and the remaining fibers remain fixed, the result is represented by the signal B.

Based on the experimental results, each individual perturbation can be easily identified. The higher intensity of signal A can be explained by the fact that all perturbations in the input fiber modes are coupled into the fibers 12 and propagated to the recoupling in the output fiber. A similar result is observed when the output fiber (signal B) is perturbed. The lower intensity of the individual signals in the fibers parallel is due to the smaller diameter core, propagating less modes and with a lower light intensity. Thus, the contribution of each perturbation propagated to the recombined speckle pattern detected by the CCD is lower. This can be verified simultaneously perturbing multiple fibers in parallel, observing the signal increase.

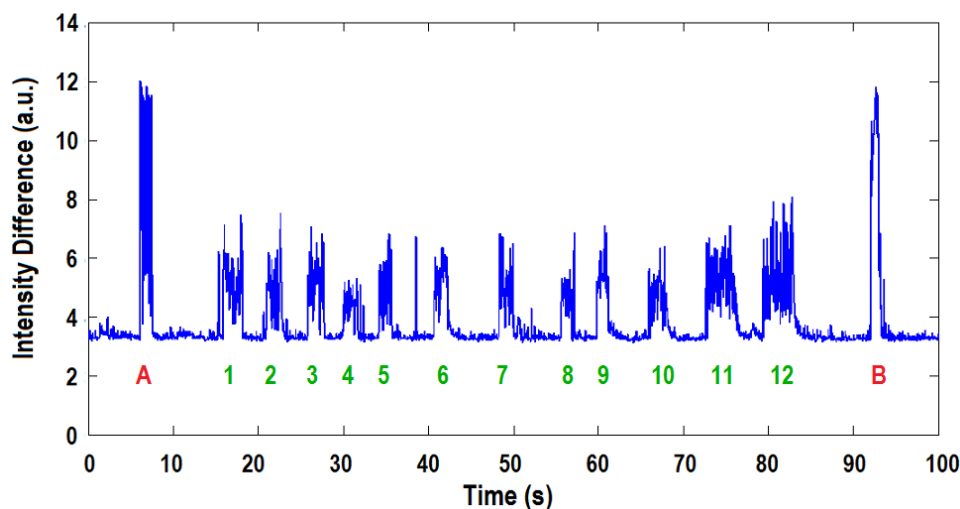


Figure. 3. Experimental results with perturbations in the fibers of the multipoint sensor.

3. Discussion

In our experimental setup, we have used short lengths fibers, where the links between the emitter and receiver fibers are performed with fibers of different diameters. Although coupling losses, the propagated modes are mixed randomly along fiber, at the output end of the fiber (980/1000 μm diameter) the speckle pattern can be observed.

However, when longer fiber must be employed for this configuration, several parameters can limit the performance of this sensor. Among other factors, the sensitivity of the sensor fiber specklegrams depends on the contrast of speckle pattern. The contrast of the speckle pattern, i.e., the difference between light and granules dark background, is mainly driven by the coherence of the laser source, which in turn is related to the spectral bandwidth. By definition, the coherence length of the light source is given by $L_c = \lambda^2/\Delta\lambda$ where λ is the center wavelength of the spectrum and $\Delta\lambda$ the bandwidth. In turn, L_c depends on the operating current of the laser diode. Typically, lasers diodes Fabry-Perot type, as in our case, have understood L_c among the tens of microns and few mm. In our experiment used a laser diode centered $\lambda = 653.5$ nm spectral width and $\Delta\lambda = 1$ nm, which has a coherence length $L_c = 0.42$ mm.

On the other hand, when the laser beam propagates in multimode fiber, the maximum degree of spatial coherence at the output of the optical fiber remains unchanged if the spectral width of the source and the maximum difference in transit time between all guided modes is true that [7], $\partial\nu\cdot\partial\tau \ll 2\pi$. Thus, the length l_c , critical length at which the two rays do not interfere anymore, is [7]

$$l_c \approx \frac{n_2 c}{n_1(n_1 - n_2)\partial\nu} \quad (1)$$

where c is the speed of light in vacuum, $\partial\nu$ it is the spectral width in Hz, and n_1 and n_2 are the refractive indices of the core and fiber cladding, respectively. One can say therefore that from this distance speckle pattern is provided by the sum of the intensities of the separate modes, as has been demonstrated in reference [8]. Using data from the fiber and the characteristic of the laser diode used in this experiment, $n_1 = 1.49$, $n_2 = 1.4$, and $\partial\nu = 467$ GHz, we obtain $l_c \approx 6.7$ mm. According to described, the contrast of speckle pattern generated in fiber remains acceptable up to a few tens of meters of fiber length when a laser diode Fabry-Perot type, enough to be used in sensor applications and using methods used statistical calculation, as presented in this paper. The coupling of fibers of different diameters core in different sections does not have remarkable influence on the final sensor configuration.

4. Conclusion

It has been presented and demonstrated the operation of a multipoint sensor based on changes of specklegrams when fibers are perturbed, either by vibration, pressure or contact. The high sensitivity of the fibers to external shocks are reflected in changes in specklegrams and detect signals. The excellent adaptability and flexibility of POFs can be used to distribute discreetly contacts point in the protection of works of art, such as pictures or busts in art museums or showrooms. The proposed sensor is simple to implement and represents a low-cost sensor systems for safety and security.

5. Acknowledgements

This work has been supported by the project TEC2013-47264-C2-1-R.

6. References

- [1] J.M. Lopez-Higuera Edit., *Handbook of Optical Fibre Sensing Technology*, 2002 (New York: Wiley).
- [2] P. Podbreznik, D. Donlagic, D. Lesnik, B. Cigale, D. Zazula, "Cost efficient speckle interferometry with plastic optical fiber for unobtrusive monitoring of human vital signs", *Journal of Biomedical Optics*, 18(10):107001-1-107001-8, (2013).
- [3] B. Redding, S.M. Popoff, H. Cao, "All-fiber spectrometer based on speckle pattern reconstruction", *Opt. Express* **21**, 6584–6600 (2013).
- [4] L. Rodriguez-Cobo, M. Lomer and J.M. Lopez-Higuera, "Fiber Specklegram Multiplexed Sensor", *IEEE J. Lightwave Technol. IEEE*, **33**(12), 2591–2597 (2015).
- [5] W. Spillman Jr., B. Kline, L. Maurice, P. Fuhr, "Statistical-mode sensor for fiber-optic vibration sensing uses", *Applied Optics* **28** (15), 3166–3176, (1989).
- [6] J. W. Goodman, *Speckle Phenomena in Optics: Theory and Applications*, Englewood, CO, USA: Roberts and Company, 2007.
- [7] B. Crosignani, B. Daino, and P. Di Porto, "Speckle-pattern visibility of light transmitted through a multimode optical fiber", *J. Opt. Soc. Am.*, **66** (11), 1312-1313 (1976).
- [8] E.G. Rawson, J.W. Goodman, R.E. Norton, "Frequency dependence of modal noise in multimode optical fibers", *J. Opt. Soc. Am.*, **70**, (8), 968-976 (1980).

POF-based specklegram sensor for continuous patient monitoring

L. Rodriguez-Cobo^{1*}, A. Rodriguez-Cuevas¹, E. Real¹, J.M. Lopez-Higuera¹, M. Lomer¹

¹ Photonics Engineering Group, University of Cantabria, 39005, Santander (Spain)

*Corresponding author: luis.rodriquez@unican.es

Abstract: In this work, different schemes to detect vital signs of bedding patients are proposed and experimentally verified. Employing speckle in multimode polymer optical fibers as sensing element, the fiber is placed under the bed linen to collect the small movements provoked by the patient. This kind of sensor takes advantage of the remarkably high sensitivity exhibited by fiber specklegram sensors. Based on a proper sizing of the employed multimode fiber, it can be placed in different locations trying to favour the detection of heart beating or movement. When the patient does not exhibit any conscious movement (e.g. while he is sleeping) its heart rate can be measured.

1. Introduction

At the present time, 24h-monitoring only occurs in the ICU (Intensive Care Units) even in the most developed countries. Nonetheless several studies have found strong evidences that continuous monitoring methods, as compared to conventional ones, can be more effective to avoid health deterioration of hospital patients, especially those cases related to heart conditions [1, 2]. Cardiac arrest is, in most cases, preceded by an abnormal breathing and heartbeat frequencies and therefore in many cases can be detected on time before it takes place, therefore patients can be transferred from their regular hospital rooms to the more prepared ICU and proceed to a further health evaluation. Eventually an important reduction in average recovering time of hospital patients can be achieved, reducing long-term economic cost as well.

Optical fiber based techniques have grown in importance for the non-contact monitoring field due to their versatility and the possibility of being used into singular environments such as magnetic resonance imaging scans, where placing metal or common electronic components is not an option since it can cause them to heat up and malfunction [3]. Among these techniques, fiber specklegram sensors have emerged as very promising methods to monitor of heartbeat and motion due to its high sensitivity and relative low cost. In this regard one of the first test was made in the University of Virginia in 2004 and it concludes that these types of sensors have the potential to become into a cost effective way of automating long term monitoring of patients[4]. After this test, similar experiments have been carried out in different institutions[5].

In this work, different speckle-based optical fiber sensors are employed to detect and measure the movement and heart rate of patients lying on a bed. Proposed devices are placed without direct contact to the patients and are able to measure those parameters when lying in different positions. The achieved results proved the applicability of these kind of sensors to be employed in real scenarios.

2. Sensor design

Three Polymer Optical Fibers (POF) with core diameters of 50 μm , 240 μm and 980 μm were tested in combination with several different support materials including thin wooden boards, silicone supports, soft plastics, bare fiber, cotton fabric and other textiles. Later, several fiber geometries were tested as well. Based on sensitivity and noise compromise, two sensors were selected: Band sensor and Ring sensor. Both sensors consisted of a semiconductor laser emitting at 638nm wavelength, a CCD camera which produces data at a rate of 30 frames per second, and a plastic fiber optic 200cm long and 240 μm diameter core.

In the case of the Band sensor, the POF was set inside two lateral seams of cotton fabric of 7 cm wide and 80 cm long. In the Ring sensor, the POF was rolled creating 10 laps of an average diameter of 6cm and was set inside two cotton fabrics of 10cm of side.

2. Processing scheme

There is a model [6] that determines the relation between the speckle pattern variation and the perturbation to be measured. This model is limited to small perturbations and in order to extract this information, a differential processing method can be applied, being able to obtain the desired perturbation as the sum of the absolute value of the changes in all the signals [7]. Thus, consequently, The first step in every processing method was to compute the differential sequence. The value of each pixel of the frame $n-1$ is subtracted from the value of the equivalent pixel of the frame n (the next frame) and add them in absolute value. This sequence is then buffered using a 6 seconds window to analyse both movement and heart rate.

2.1 Motion detection

Next step is devoted to analyze the amount of movement detected by the specklegram sensor, to avoid its misunderstanding with the vital signs of the patient. The buffer size is divided in two sections: the recent time window, comprising the 20% most recent points, and the oldest time window, comprising the previous 80% (Fig. 1a). Both sections are averaged by the number of points in each section, in order to obtain the mean intensity level of the recent and old status. The ratio among recent and old takes values near 1.0 when the signal is similar, but varies strongly when there is an intense motion. If the ratio deviates more than a established threshold, movement detection is triggered.

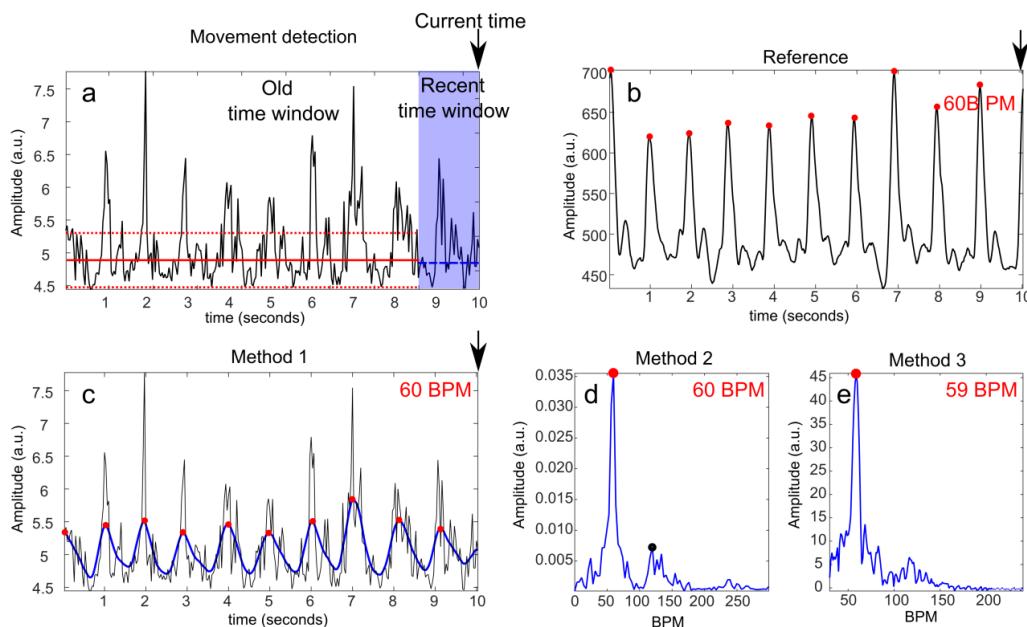


Figure 1 In-line processing of current time (black arrow) applying a 10 seconds window. (a) Original signal and movement detection mean values. Blue line represents the recent time mean value. Red line represents old time mean value. Dashed red is the 10% trigger threshold. (b) Pulse oximeter reference. (c) Method 1: original time signal (black) and smoothed (blue). (d) Method 2: Fourier Transform of the first derivative. (e) Method 3: convolution by sinusoid. For every method (b to e), the obtained instantaneous heart rate is displayed.

2.2 Heart rate measurement

2.2.1 Method 1: Filtered signal and peak detection

This is the most straightforward approach (Fig. 1c). Calculating the time lapse between 2 pulses, T , the frequency in Hertz can be calculated as the inverse: $F=1/T$, and in BPM as $60/T$. The signal obtained with the specklegram

sensor is very sensitive and noisy, so a moving average filter is applied to this signal to reduce noise. After this step, peaks are detected and the median time between pulses, T_m , is obtained.

2.2.2 Method 2: First derivative and Fourier Transform

The first derivative is used to remove the offset of the original signal, not affecting the peaks present in the signal. Then a soft moving average filter is applied and the Fast Fourier Transform (FFT) is obtained. The FFT frequency presenting the maximum component corresponds to the heartbeat, expressed in BPM (Fig. 1d). The previous moving average filter is needed to avoid high frequency noise.

2.2.3 Method 3: Convolution by known frequency signal

Firstly, a moving average filter is applied to this signal to reduce noise. Then, the signal is convoluted with sinusoids of different frequencies. The convolution result will be maximum when the specklegram sensor signal and the sinusoid present the same frequency (Fig. 4e). The frequency sweep, f_c , goes from 0.33Hz (to detect 20 BPM) to 4Hz (240 BPM). The different sinusoids are stored in advance, to reduce in-line computation time.

3. Experiments and results

Both the Band sensor and the Ring sensor were employed to take measurements simultaneously with a pulse oximeter meter which was acting as the reference. Two different 160-seconds-long measurements were taken with each sensor from each of the 20 volunteer (one laying on their back and one laying on their side). Those measurements were differentially processed before applying the movement detector and the three methods to detect the heart rate.

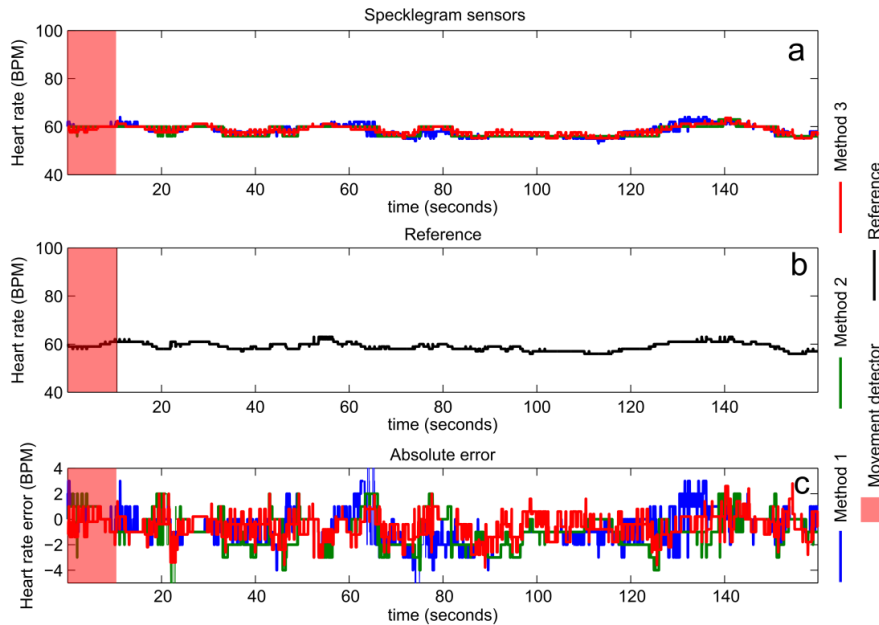


Figure 2 In-line processing result for one of the patients for a measurement of 160 seconds. (a) Heart rate estimated with the tree proposed methods. (b) Pulse oximeter reference. (c) Error for each of the three methods with respect to the reference. The reddish delimited region corresponds to movement detection active window, computed with the original signal. Note that it is active for the sequence beginning.

The performance (in terms of error) is tested for each method and sensor. The recorded 160 seconds measurements are processed frame by frame, mimicking real time acquisition. The mean heart rate obtained instantly can be compared in Fig. 2. The error percentage metric in Table 1 shows that measurements of laying

on the side of the patient have better instant precision, both ring and band sensor and with the processing method 1. Also, method 3 performs good with the band sensor. In those cases, error is committed below 3% of the time.

Processing method	Side		Back	
	Ring	Band	Ring	Band
1	<u>0.0248</u>	<u>0.0209</u>	0.2778	0.2021
2	0.0741	0.0645	0.3102	0.2266
3	0.0415	<u>0.0291</u>	0.2714	0.1858

Table 1. Heart rate percentage error in time normalized for all the combinations.

4. Conclusion

A non-invasive monitoring system has been evaluated in this work and based on the obtained results it is possible to conclude that a fiber optic specklegram sensor exhibits the potential to be employed as a continuous monitoring heart rate and motion detection tool, achieving a high range of accuracy. The best-achieved results have been obtained using the band sensor and the smoothed signal method that also exhibits the best computation time. Eventually the combination of the optimal spatial distribution and the optimal processing method shows accuracies below 3% instantaneous error. As opposed to most of the current monitoring methods, this specklegram system is a low cost and widely applicable tool, hence it has the potential for being used as a basic monitoring system in all the hospital rooms and local environment.

5. Acknowledgements

This work has been supported by the project TEC2013-47264-C2-1-R of the Spanish government and by a Parliament of Cantabria postdoc grant.

6. References

1. Chaboyer, W., et al., *Predictors of adverse events in patients after discharge from the intensive care unit*. American Journal of Critical Care, 2008. **17**(3): p. 255-263.
2. Young, M.P., et al., *Inpatient transfers to the intensive care unit*. Journal of general internal medicine, 2003. **18**(2): p. 77-83.
3. ukasz Dziuda, Ł., *Fiber-optic sensors for monitoring patient physiological parameters: A review of applicable technologies and relevance to use during magnetic resonance imaging procedures*. Journal of biomedical optics, 2015. **20**(1): p. 010901-010901.
4. Spillman Jr, W., et al., *A 'smart' bed for non-intrusive monitoring of patient physiological factors*. Measurement Science and Technology, 2004. **15**(8): p. 1614.
5. Škrabec, J., et al., *Preliminary detection of periodic perturbations using speckle imaging and interframe gradient*. Recent Advances in Applied & Biomedical Informatics and Computational Engineering in Systems Applications. Florence, Italy, 2011: p. 251-256.
6. Spillman Jr, W., et al., *Statistical-mode sensor for fiber optic vibration sensing uses*. Applied optics, 1989. **28**(15): p. 3166-3176.
7. Lomer, M., et al. *Speckle POF sensor for detecting vital signs of patients*. in *OFS2014 23rd International Conference on Optical Fiber Sensors*. 2014. International Society for Optics and Photonics.



Power consumption analysis of a 3-channel real-time WDM link over SI-POF

P.J. Pinzón^{1*}, C. Vázquez¹, D. S. Montero¹, J. Moreno López¹ and Frank A. Dominguez-Chapman²

¹ Electronics Technology Dpt., Universidad Carlos III de Madrid, Avda. de la Universidad 30, 28911 Leganés (Madrid), Spain

² Department of Electronic Engineering, University of Zaragoza, C/ María de Luna 1, E-50018 Zaragoza, Spain

*Corresponding author: ppinzon@ing.uc3m.es

Abstract: This paper presents the power consumption analysis and optimization of a data transmission system based on a visible wavelength division multiplexing (visible WDM) scheme at 3-Gb/s over more than 50-m of step-index plastic optical fiber (SI-POF). The transmission scheme is composed of 3 channels, operating at 405, 515 and 650 nm; each one with a maximum data transmission rate of 1-Gb/s (3-Gb/s of aggregated data rate). The system performance has been tested using a real-time setup (without any post-processing or storage) which operates with bit error rate (BER) values below 1×10^{-6} . We achieved a energy efficiency improvement greater than 75% in comparison with other recent proposals based on visible WDM over SI-POF.

1. Introduction

Primarily due to the ‘do-it-yourself’ installation, easy maintenance and high bending tolerance, large core step-index (SI) plastic optical fibers (POFs) are considered more suitable than 50 μm core diameter multimode glass optical fibers (GOFs), perflourinated POFs or graded index POFs [1] in many short-range applications (< 50 m) [2]. Local Area Networks (LANs), In-Home and Office networks [3], Automotive [4] and Avionic multimedia buses, or Data Center interconnections [5] are envisaged as target applications and scenarios. On the other hand, SI-POF technology has also an important application niche in providing a solution to the exponential growth of infotainment devices within the car, along with the proliferation of ADAS (Advanced Driver Assistance Systems) that have created a demand for a more efficient way to interconnect devices within the automobile. ADAS global market is substantially growing during recent years and requires increasing the available bandwidth, nowadays up to 1-Gb/s [6] and potentially, in the near future, up to 5-Gb/s [7]. However, today it is a matter of fact that the volume of data transmitted by short-range networks is increasing beyond the Gb/s, exceeding the capabilities of current networking technologies (twisted pair, coax cable, Ethernet Cat-5 cable, powerline and wireless) [8], so it is necessary to implement new solutions.

Gigabit/s transmission capacity over SI-POF links has been widely demonstrated [3] using single channel based systems. However nowadays, visible wavelength division multiplexing (visible WDM) is proposed as a solution to expand the transmission capacity of SI-POF based systems and to overcome future traffic demands. Current proposals are based on spectral grids with channels between 400 and 700 nm using laser diodes (LDs) or light emitting diodes (LEDs) based transmitters. Visible WDM systems using offline-processed DMT modulation and data rates up to 21.4-Gb/s over 50 m [5], and 8.26-Gb/s over 75 m [9], with 6 and 4 channels, respectively, achieving a bit error rate (BER) of 1×10^{-3} , have been recently reported.

On the other hand, energy efficiency is gaining increasing interest in our society in recent years. There is growing consensus on the necessity to put this issue at the top of the research agenda, as one of the most compelling and critical issues. The energy consumption of computers and network equipment is becoming a significant part of the global consumption [10]. As the coverage of Information and Communications Technology (ICT) is spreading rapidly worldwide, the energy consumption and carbon footprint of ICTs are also increasing fast [11].

In this paper, the energy consumption analysis and optimization of a more than 50m-long SI-POF data transmission system based on a visible WDM scheme is presented. The proposed WDM system is composed of 3 channels at 405, 515 and 650 nm each one with a data transmission rate of 1-Gb/s (3-Gb/s of aggregated data rate) and a BER below 1×10^{-6} . The energy consumption optimization is done at the transmitter’s level, by adjusting the laser diodes’ modulation parameters to reduce the minimum optical power required at the receiver (sensitivity) to keep the system’s BER lower than 1×10^{-6} . Finally, the energy consumption analysis is



done considering the power consumption per transmitted bit taking into account the bit error rate implication for a TCP/IP networks throughput.

2. Transmission Scheme

Fig. 1 shows the general description of the proposed visible WDM SI-POF transmission system. The personal computers (PC1 and PC2) are equipped with 3 Gigabit Ethernet interfaces in combination with 3 Media Converters (MCs) that are used to generate and to process the transmitted data bits, respectively. The MCs transform the standard Gigabit Ethernet frames into 16-PAM signals (called Tx-signals), and vice versa. In the transmitter side (Tx), the different Tx-signals modulate each Laser Diode (LD) of its respective channel. A fiber bundle based multiplexer (mux) transmits the 3 channels over the SI-POF link, and a diffraction grating based demultiplexer (demux) splits the different channels to their respective receivers (Rx) at the end of the link. The received optical signals are converted back to electrical signals (Rx-signals) by using a pin-photodiode based receiver [12]. Finally the Ethernet frames are recovered by the MCs.

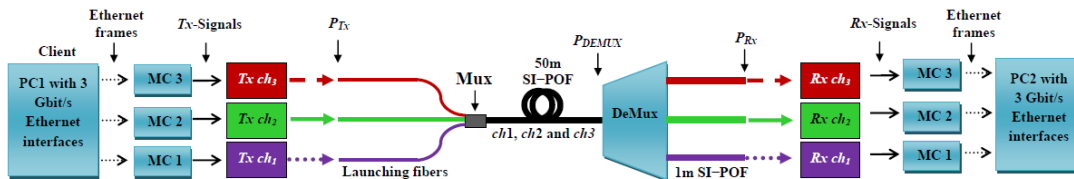


Fig. 1. Transmission scheme of the proposed SI-POF visible WDM system with 3 channels between 400 and 700 nm.

The multiplexing is performed using a fiber bundle based coupler (see Fig. 2). It consists of 3 plastic optical fibers (called launching fibers) acting as inputs which are then joined forming a bundle of less than 1 mm of diameter, which is faced to one of the 50m-long SI-POF ends. The launching fibers are made of 1 m-long graded index plastic optical fibers (GI-POFs) with 120/490µm core/cladding diameter and 0.185 of numerical aperture (NA). They are faced to a standard SI-POF section of 980 µm core diameter, 1 mm cladding diameter and 0.5 NA. The multiplexer insertion loss (IL) ranges from 2.2 to 2.9 dB depending on the selected channel, and includes the coupling losses between the LDs and the GI-POFs.

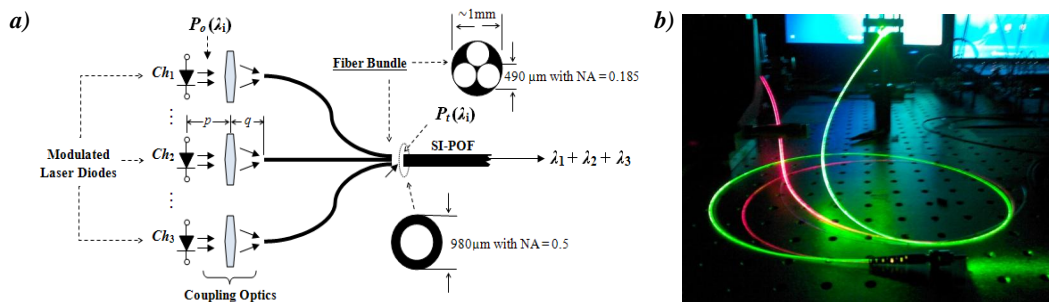


Fig. 2. a) Fiber bundle based multiplexer. b) Picture of the multiplexer within the experimental setup.

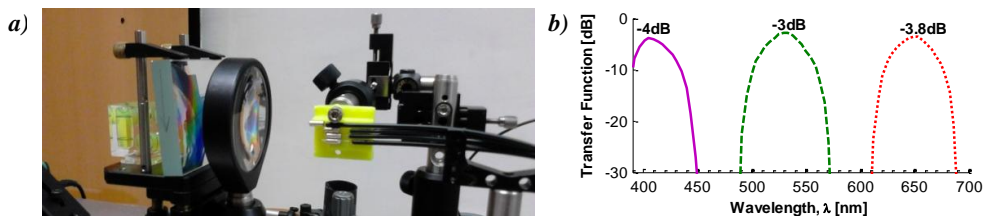


Fig. 3. a) Diffraction grating based demultiplexer for SI-POF: a) experimental setup; b) transfer function.

The demultiplexing is performed using a low insertion loss (IL) 3-channel demux [13]. It is based on a collimator/focusing lens and a reflective diffraction grating. The transfer function (P_{RX} / P_{DEMUX} , see Fig. 1) of



each channel is shown in Fig. 2. The demux IL is lower than 4 dB showing a uniformity of 1.1 dB for all channels. Their -3dB spectral band-pass bandwidth is greater than 30 nm.

3. Optimizing the Transmission Power

The transmission capacity of the proposed system has been demonstrated on previous works [14]. Now, the goal is to reduce the optical transmission power required to keeping the data transmission speed of each channel at 1-Gb/s with a BER $< 10^{-6}$ over a SI-POF link of more than 50 m. This is done by carefully choosing the modulation parameters in terms of the bias and modulation currents (I_{bias} and I_{peak} , respectively) of the different LDs.

A blue-violet, a green and a red laser diode is used for the ch_1 , ch_2 and ch_3 transmission, respectively. These LDs have a threshold current (I_{th}) of ~ 24 , 55 and 32 mA (at the operating temperature, and without thermal stabilization), respectively. Each LD is directly modulated using a V_{MOD} signal (which is obtained by conditioning the MCs' Tx-signals) and a bias-tee that is connected to the LD via a coaxial cable and an impedance matching resistance. The current flowing through the laser diode is then given by:

$$I_{LD} = I_{bias} + I_{peak} = I_{bias} + \frac{V_{MOD}}{100\Omega} \quad (1)$$

We have determined the optimal modulation parameters for each transmitter. These parameters are shown in Table 1. It is important to note that the MCs require a minimum SNR of about 25.5 dB for 1-Gb/s operation with BER $< 10^{-6}$. Figures 4.a, 4.b and 4.c show the electrical SNR of each channel as a function of the optical power at the receiver, P_{RX} , for the modulation parameters reported on Table 1. It can be shown that the sensitivity of ch_1 , ch_2 and ch_3 is about -16.09 , -14.14 and -18.48 dBm, respectively.

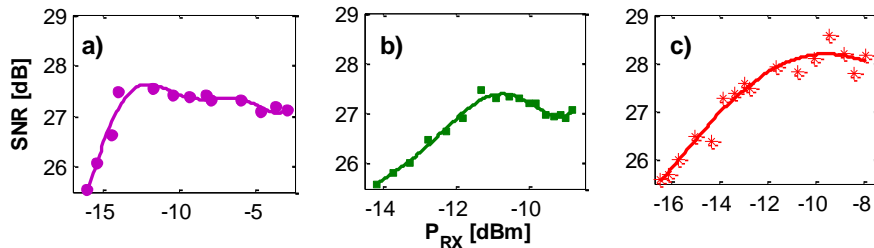


Fig. 4. Results of the electrical SNR versus the received optical power for: a) ch_1 , b) ch_2 and c) ch_3 .

4. Power Consumption

As a first approach to estimate power consumption the power per transmitted bit (P_{Tb}) at the LDs is defined, taking into account the BER implication for TCP/IP networks throughput in terms of Network Throughput (T) as reported in [14]. The mean optical power of the instantaneous transmitted signal is given by $\langle P_{opt}(t) \rangle = \beta I_{peak}$, where the quantum efficiency β and the driving signal with peak amplitude I_{peak} are used. This peak amplitude can be expressed in terms of the LD modulation index m_i as $I_{peak} = m_i \times (I_{bias} - I_{th})$. Then, the P_{Tb} is given by:

$$P_{Tb} = \frac{\beta \times I_{peak}}{T} \quad \text{with} \quad T = R[1 - BER(P_{size} + IPG)] \quad (2)$$

where P_{size} is the Ethernet packets size and IPG is the inter packets gap. T is calculated in the worst case scenario, where each single bit error provokes a packet-error. A minimum of 64 bytes Ethernet packet P_{size} and IPG of 96 bits are considered. However, it is important to note that T is reduced for a larger P_{size} . Therefore, a transmission efficiency of 39.2% is obtained with a BER of 1×10^{-3} . This efficiency is about 99.94% for BERs $< 1 \times 10^{-6}$ [15].

The energy consumption analysis presented on Table I shows that the proposed system uses values of power per transmitted bit below 2.05 pJ/b per channel in order to establish a 3-channel visible WDM system with an aggregated data rate of 3-Gb/s and BERs $< 1 \times 10^{-6}$. This represents an improvement greater than 75% in comparison with other recent proposals based on visible WDM over SI-POF [14].



TABLE I: CHARACTERISTICS OF THE PROPOSED VISIBLE WDM SYSTEM (SI-POF LINK OF 50 M @ 1 GB/S).

Parameter		405 nm	520 nm	650 nm
Budget	LD output Power, P_o (dBm)	3.9	1.47	1.41
	Launching coupling IL (dB)	0.90	1.3	0.80
	Multiplexing IL (dB)	2.0	1.5	1.4
	50 m SI-POF (dB)	10.58	5.24	8.53
	Demultiplexing IL (dB)	4.05	3.05	3.8
	Receiver Sensitivity (dBm) ⁽¹⁾	-16.09	-14.14	-18.48
	Link Margin (dB)	2.46	4.52	5.36
Throughput	Data Rate, R (Gb/s)	1		
	BER	$<1 \times 10^{-6}$		
	Data Throughput, T (Gb/s)	~ 1.00		
Power	Bias current I_{bias} (mA)	35.5	57.1	26.5
	I_{peak} (mA)	3.0	1.71	1.82
	Modulation index m_i	0.86	0.9	0.91
	Quantum efficiency β (W/A)	0.685	0.51	0.667
	Power per bit P_{Tb} (pJ/b) ⁽²⁾	2.05	0.87	1.2

Notes: ⁽¹⁾ The received power is measured at the end face of the SI-POF (see Fig. 1 and 4), so it does not include the focalization losses due to the internal optics at the MC's receiver (typically 2 dB). ⁽²⁾ From Eq. (2), considering Ethernet frames of 64 Bytes and IPG of 96 bits.

5. Conclusion

A SI-POF 50 m link with an aggregated capacity of 3-Gb/s and an average power consumption per transmitted bit below 2.05 pJ/b achieving BERs $< 1 \times 10^{-6}$ is reported. The system is based on a 3-channel visible WDM scheme with real-time transmission of Ethernet frames encoded in PAM-16 signals. Each channel accessible power can be adjusted to be less than 0 dBm in compliance with visible eye safety-limits (ANSI-Z136.1-2000).

Acknowledgements

This work was partially supported by the Spanish Ministry of Economy and the European Regional Development Fund under grant TEC2015-63826-C3-2-R (MINECO/FEDER) and from Comunidad de Madrid under grant S2013/MIT-2790.

References

- [1] D.S. Montero and C. Vázquez, "Analysis of the electric propagation method: theoretical model applied to perfluorinated graded-index polymer optical fiber links," *Opt. Lett.*, vol. 36, no. 30, pp. 4116-4118, 2011.
- [2] M. J. Koonen et al., "Photonic Home Area Networks," *J. Lightwave Technol.*, 32, 4, 591-604, 2014.
- [3] Mollers et al., "Plastic optical fiber technology for reliable home networking: overview and results of the EU project POF-ALL," *IEEE Commun. Mag.*, 47, 8, 58-68, 2009.
- [4] M. Rayon Co., "Plastic Optical Fiber (POF) technology for Automotive, Home network systems," in Proceedings of IEEE 802.3 GEPOF Study Group meeting, May 2014.
- [5] R. Kruglov et al., "21.4 Gb/s discrete multitone transmission over 50-m SI-POF employing 6-channel visible WDM," in Proceedings of OFC, pp. 1-3, 2014.
- [6] Automotive Applications, <http://www.kdpof.com/applications/automotive/>
- [7] MOST in future automotive connectivity, http://automotive-eetimes.com/en/most-in-future-automotive-connectivity.html?cmp_id=71&news_id=222903019
- [8] E. (Yuxin) Dai, "Home Networking bandwidth growth needs and POF," in Proceedings of IEEE 802.3 GEPOF Study Group Meeting, October 2014.
- [9] U. H. P. Fischer, S. Höll, M. Haupt, and M. Joncic, "Polymeric demultiplexer component for wavelength division multiplex communication systems using polymer fibers," *Proc. SPIE* 9368, 93680Q (2015).
- [10] W. Vereecken et al., "Energy efficiency in telecommunication networks," in European Conference on Networks and Optical Communications & Optical Cabling and Infrastructure (NOC), 2008.
- [11] Y. Zhang, P. Chowdhury, M. Tornatore and B. Mukherjee, "Energy Efficiency in Telecom Optical Networks," *IEEE Communications Surveys & Tutorials*, vol. 12, n° 4, pp. 441-458, 2010.
- [12] O. Ciordia et al., "Commercial Silicon for Gigabit Communication over SI-POF," in Proceedings of ICPOF, 109-116, 2013.
- [13] P. J. Pinzón, I. Pérez and C. Vázquez, "Efficient Multiplexer/Demultiplexer for Visible WDM Transmission over SI-POF Technology," in *Journal of Lightwave Technology*, vol. 33, no. 17, pp. 3711-3718, Sept. 1, 2015.
- [14] P. J. Pinzón, I. Pérez and C. Vázquez, "Visible WDM System for Real-Time Multi-Gb/s Bidirectional Transmission Over 50-m SI-POF," in *IEEE Photonics Technology Letters*, vol. 28, no. 15, pp. 1696-1699, Aug. 1, 2016. doi: 10.1109/LPT.2016.2529703
- [15] The Impact of Bit Error Rate on LAN Throughput, http://www.pemosa.com/descargar_documento.php?did=551.

Experimental System for Automatic Alignment of Plastic Optical Fibres

F. A. Domínguez-Chapman¹, J. Mateo^{*1}, M. A. Losada¹, A. López¹, C. Vázquez², J. Zubia³

¹ GTF, Aragón Institute of Engineering Research (i3A), Department of Electronic Engineering, University of Zaragoza, María de Luna 1, E-50018 Zaragoza, Spain.

² Electronics Technology Department, Carlos III University of Madrid, Avda. de la Universidad 30, E 28911 Leganés (Madrid), Spain.

³ Department of Communications Engineering, Faculty of Engineering Bilbao / University of the Basque Country UPV/EHU, Al. Urquijo s/n, E-48013 Bilbao, Spain.

*Corresponding author: jmateo@unizar.es

Abstract: Here, we present a system that permits to change the relative position of two plastic optical fibres along six different coordinates and is controlled by specifically designed software. Our implementation has a flexible design that performs automatic alignment of the two fibres while it also allows manual control. This system constitutes a versatile tool indispensable in a POF characterization laboratory that can be included as a positioning modulus in the design of experimental set-ups or used together with other measurement equipment to obtain fibre parameters. As application example, the program also includes a block to measure coupling losses for combined misalignments.

1. Introduction

The deployment of short-area networks which use plastic optical fibres (POFs) as their transmission medium often require multiple connections that introduce power loss and alter the angular power distribution introducing changes in transmission properties [1-3]. In some POF applications such as avionics networks [4], the high number of connectors seriously compromises the power budget. In these scenarios, the implementation of techniques to join two POF ends with a low coupling loss is decisive for POF success. Nevertheless, to achieve minimum loss when splicing two POFs, the first step is to optimize their alignment along all possible axes.

Here, we present an automatic system that performs the alignment of two fibres by their relative motion using six degrees of freedom given by the three Cartesian coordinates and the angular coordinates relative to each axis. The rotation relative to the fibre longitudinal axis is indispensable to apply this methodology to micro-structured or multi-core fibres. The alignment is made in a two-step approach that is first achieved using geometric parameters extracted from the live images of the fibre ends and then, refined by reducing their coupling loss. Our implementation also provides manual positioning control and a specific feature to measure misalignment losses. In addition, the flexibility and modularity of our system design make it suitable for integration with other measurement equipment to devise different experiments and applications.

The paper is organized as follows: First, the physical design of the experimental set-up and the program interface are shown describing each of their features and then, we show the versatility of our system providing initial results of aligning 1-mm PMMA fibres and 50- μ m Silica fibres and also, measurements of combined misalignment loss scans. Finally, we present our conclusions and comment on future extensions and applications of the implemented tool.

2. System implementation

In this section, the physical components of the positioning, imaging and power measurement subsystems are described as well as the graphical interface that integrates and manages the different capabilities of the system. The system is controlled using a protocol based on an event control sequence written in the commercial measurement and automation software LabViewTM, that integrates all necessary processes including the control matrix connected to all the actuators to change fibres relative position.

2.1 Positioning subsystem

The experimental set-up is shown in Figure 1. The fibres are mounted into motorized precision stages to change their relative position along three linear coordinates (X, Y and Z), and three angular coordinates (Roll,

Pitch, and Yaw) that are defined as rotation relative to the X, Y and Z axes. The fibre on the left moves along the linear coordinates while the fibre on the right rotates over the three angular coordinates.

For motion along the linear axes, three linear stages NSA 12 mounted onto a linear XYZ-LH base from Newport have been used. They have a precision of $0.1 \mu\text{m}$. The angular stages are: NSR1 platform for the Roll, M-GON65-L for the Pitch, and PR50CC for the Yaw. They allow minimum steps of 0.016° , $6 \cdot 10^{-5}^\circ$, and 1° respectively. They are connected to motorized stages that are controlled by the specifically designed computer program.

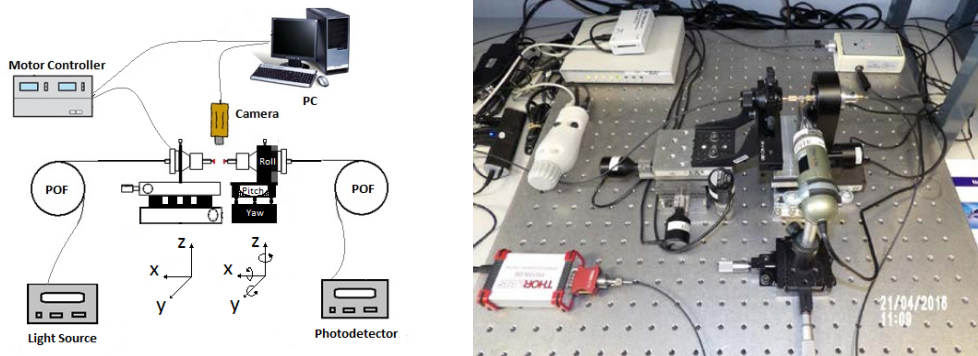


Figure 1. Schematic and picture of the experimental set-up used for POF alignment.

2.2 Image processing subsystem

The image processing subsystem is responsible for image acquisition, processing and border extraction used to aid automatic alignment. It is responsible for the first step of the automatic alignment process. The set-up in Figure 1 incorporates a CCD camera (Dino-Lite digital microscope) with a mirror at 45° to visualize both fibre ends from two different vantage points at a 90° angle. This image is shown on the left of Figure 2. It shows the ends of the two fibres on the plane XY (below) and on the plane XZ (above).

For each fibre, two regions of interest (ROIs) are extracted as shows the schematic on the upper right of Figure 2. The fibre contour edges are located (lines 1, 2 and 3 on the lower left image) to estimate the fibre axis (LE) and the central points of the edges (P). These parameters are fed to the algorithm designed to assess the necessary motions to obtain an initial coarse alignment.

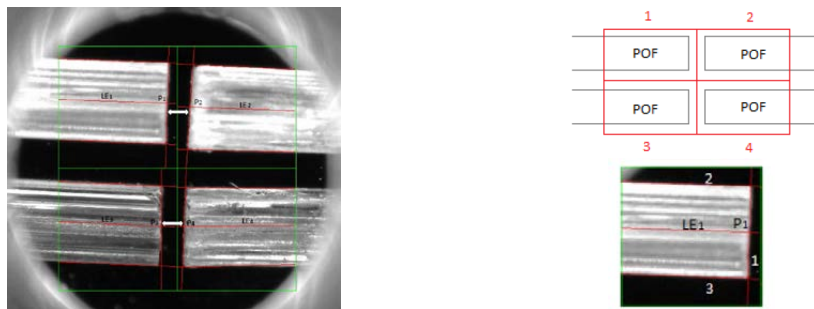


Figure 2. Microscope image and geometric parameters used by the image processing subsystem.

2.3 Optical power subsystem

The fibres are connected to a 635-nm LED source (FOTEC T750) and a photodetector (Thorlabs) whose output feeds the control program and is continuously displayed in the graphical user interface. Automatic alignment is refined and optimized by this subsystem, which also aids the user in case of manual alignment.

2.4 Graphical interface

The user interface and its main features are shown in Figure 3. It offers both automatic and manual control of the actuators in all dimensions.

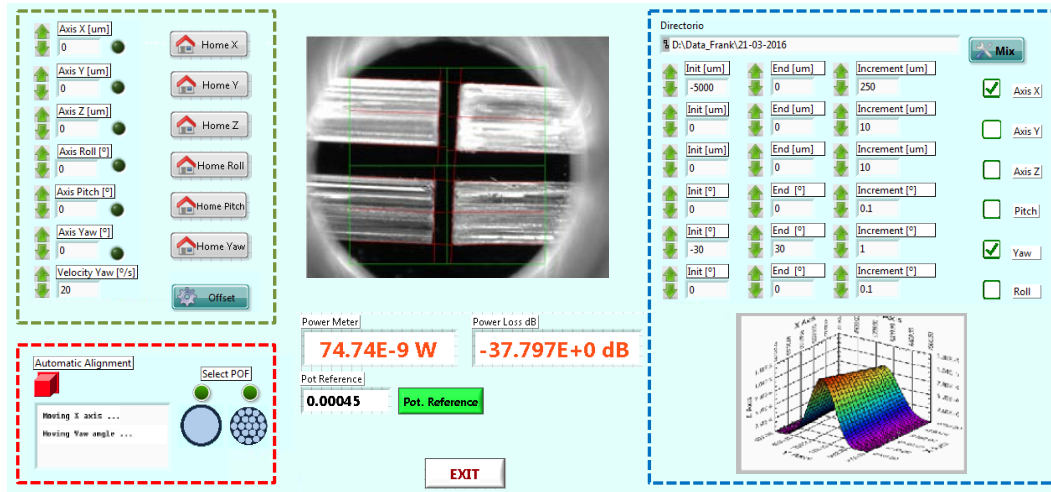


Figure 3. Graphical user interface of the implemented system.

The position of the fibres can be changed manually using the controls in the upper left area framed by a dashed green rectangle. The “Offset” button allows the user to store a given position as the reference, while the “Home” button searches the hardware origin of the positioners.

The automatic alignment area is placed on the lower left of the interface framed by a dashed red rectangle. Automatic alignment starts by switching the red button. The fibre type has to be specified using the Select POF switch to choose between single-core or multi-core fibres as the later has an extra degree of freedom (Roll). The automatic alignment is performed in two steps: the first is based on the parameters extracted from the processed image described before. The optimization tends to achieve the minimum slope differences and to align the Y and Z coordinates of the central points as close as possible. The longitudinal (X) distance is set to put the fibres at the green central line. The second step is based on the iterative search of the maximum power coupled for each of the six coordinates. The text block below the automatic alignment switch button provides information of the axis that is being moved.

The image and the power values are always shown in real-time. Thus, the program interface allows the user to visualize the camera capture as well as the ROIs and the geometric parameters extracted to help the alignment process. The coupled power in real-time obtained directly from the power-meter is also shown in Watts on the left box directly below the image window. The reference power shown below is introduced by the user by pushing the green button and the relative power loss in dB is calculated from both values.

In addition to manual and automatic control, a useful feature has been implemented in this system to obtain misalignment losses, whose controls are framed by a blue rectangle on the right hand side of Figure 3. Relative movement of the fibres along two of the six coordinates can be combined, setting the initial and final values as well as the increment. The power coupled is measured using the power-meter and saved in a file along with the values of the two coordinates. Finally, the results are shown as a surface plot on the lower left corner of the interface.

3. System applications

The system has been designed as a versatile and extensible tool with many potential applications. Here, we show the results obtained for some capabilities that have already been implemented.

3.1 Auto-alignment capability

The automatic alignment mode has been tested using two different types of POFs and also a glass multimode fibre that are shown in Figure 4. The procedure for both POFs was the following: The reference power was measured with a 2-m fibre segment. This segment was then cut, stripped, introduced in the fibre chuck and installed in the system. Notice that the fibres were not polished to evaluate the robustness of our method. After the automatic alignment power loss was below 0.4 dB for the SI-POF and below 0.3 dB for the 19 core MC-POF. The alignment precision was also tested using a glass multimode fibre (MM-GOF) of 50 μm of diameter. In this case, the source was a He-Ne laser emitting light at 635 nm and the reference was the laser coupled power. In this case, the result was below to 0.2 dB.

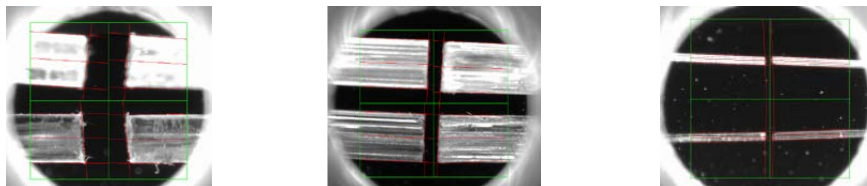


Figure 4. Images of auto-aligned fibre segments: 1-mm SI-POF (left), 1-mm MC-POF (centre), 50- μm MM-GOF (right).

3.2 Misalignment losses

Our implementation permits to set an experiment to measure coupled power scanning two different coordinates. The user is able to assign values to the starting and ending position of the fibres in two of the six coordinates using the controls inside the blue rectangle. When the user presses the “Mix” button, the coupled power is measured and stored for all combined misalignments. The surface graph in Figure 3 shows the results combining misalignment on the X and Y axis. These results have been compared to previous experimental measurements [5] exhibiting similar quantitative values.

4. Conclusion

We have introduced a versatile tool to control the position of two plastic optical fibres along six different coordinates that is capable of aligning POFs of one and several cores with very low coupling loss and has also proven to yield suitable results for glass multimode fibres. The applications of this system range from precise alignment to develop and test splicing techniques specific for POFs to measurement of misalignment losses along different combined axes whose analysis is crucial to know the limits to POF network performance. In addition, the modularity of the system design permits its integration with other experimental systems to obtain fibre measurements such as far or near field patterns. Moreover, it can be adapted with minor modifications to align other fibres to POFs, which will be a very useful tool in the case of multicore POFs for the characterization of the individual cores as well as for the study of space division multiplexing techniques.

5. Acknowledgements

This work has been funded by the Fondo Europeo de Desarrollo Regional (FEDER) and by the Spanish Ministerio de Economía y Competitividad under project TEC2015-63826-C3-3-R (MINECO/FEDER).

6. References

- [1] A. Esteban, M. A. Losada, J. Mateo, N. Antoniades, A. López, J. Zubia, “Effects of Connectors in SI-POFs Transmission Properties Studied in a Matrix Propagation Framework”, in *Proc. 20th Int. Conf. on Plastic Optical Fibers and Applications*, Bilbao, Spain (2011).
- [2] M. A. Losada, F. A. Domínguez-Chapman, J. Mateo, A. López, J. Zubia, “Influence of Termination on Connector Loss for Plastic Optical Fibres”, in *Proc. 16th Int. Conf. on Transparent Optical Networks*, Graz, Austria (2014).
- [3] E. Grivas, D. Syvridis, G. Friedrich, “Influence of connectors on the performance of a VCSEL-Based standard Step-Index POF link”, *IEEE Photon. Technol. Lett.*, 21(24), 1888-1890 (2009).
- [4] D. H. Richards et al., “Modeling Methodology for Engineering SI-POF and Connectors in an Avionics System”, *J. Light. Technol.*, 31(3), 468-475 (2013).
- [5] J. Mateo, M. A. Losada, A. López, “POF misalignment model based on the calculation of the radiation pattern using the Hankel transform”, *Opt. Express*, 23(6), 8061-8072 (2015).

Simplified Optical Correlation-Domain Reflectometry with Proximal Reflection Point Using CYTOP

M. Shizuka^{1*}, H. Lee¹, N. Hayashi², Y. Mizuno¹, and K. Nakamura¹

¹Institute of Innovative Research, Tokyo Institute of Technology,
4259, Nagatsuta-cho, Midori-ku, Yokohama 226-8503, Japan

²Research Center for Advanced Science and Technology, The University of Tokyo,
4-6-1, Komaba, Meguro-ku, Tokyo 153-8904, Japan

*Corresponding author: mshizuka@sonic.pi.titech.ac.jp

Abstract: We develop a new configuration of simplified optical correlation-domain reflectometry using a proximal reflection point. The experimental setup is basically composed of standard silica fibers and includes neither an optical frequency shifter such as an acousto-optic modulator nor an explicit reference path. The light reflected at the proximal reflection point, which is artificially fabricated near an optical circulator, is used as a reference light. Unlike the conventional silica-based setup, this configuration can perform a distributed reflectivity measurement along the distal half of the sensing fiber. After demonstration of the basic operation, the incident optical power dependence of the reflectivity distribution is investigated, and the existence of the optimal incident power is clarified.

1. Introduction

Fiber-optic distributed reflectometers have been vigorously studied as one of the key tools for developing smart materials and structures [1–4]. Among various types, those based on Fresnel reflection enables us to detect bad connections (or splices) and other reflection points along fibers under test (FUTs) in a distributed manner. Two of its successful configurations are optical time-domain reflectometry (OTDR) [5–9] and optical frequency-domain reflectometry (OFDR) [10–14], which nevertheless suffer from the insufficient spatial resolution and the relatively low measurement speed and from the phase fluctuations caused by environmental disturbance, respectively. To mitigate these shortcomings, optical correlation (or coherence)-domain reflectometry (OCDR) [15–25] based on a synthesized optical coherence function (SOCF) [22] has been developed and extensively studied. Among many SOCF-OCDR configurations using directly modulated laser outputs [17–22] and optical frequency combs, [23,24] those based on direct sinusoidal modulation of the laser outputs [17–19] can be most cost-efficiently implemented.

To further reduce the implementation cost and boost the convenience in practical applications, we have been focusing on the simplification of the SOCF-OCDR systems using sinusoidal modulation. First, by exploiting the foot of the Fresnel reflection spectrum, we developed a configuration without using an optical frequency shifter such as an acousto-optic modulator (AOM) [26]. We subsequently implemented this AOM-free SOCF-OCDR without using an explicit reference path [27]; in this configuration, the Fresnel-reflected light generated at the distal open end of an FUT (silica single-mode fiber (SMF)) was exploited as a reference light. This configuration, however, poses two problems: 1) the measurement range is limited to the proximal half of the FUT length, and 2) the measurement cannot be continued when the FUT has even one breakage point. In order to alleviate these problems, a polymer optical fiber (POF) was used as an FUT in the same configuration without a reference path [28], which enables us to exploit the Fresnel reflection at the proximal boundary between the silica SMF and the POF (instead of that at the distal open end of the FUT). The reflectivity measurement along the distal half of the FUT, which is more convenient for practical applications, was successfully demonstrated. Besides, the measurement was not interrupted even when the part of the FUT was broken. However, use of non-silica fibers is not ideal in some cases, because they are not compatible with the fiber-optic telecommunication systems which are mostly composed of silica SMFs.

In this work, we newly develop a silica-SMF-based configuration of AOM-free SOCF-OCDR without an explicit reference path. As a reference light, we use the Fresnel-reflected light at a partial reflection point artificially produced near an optical circulator. A distributed reflectivity measurement along the distal half of

the FUT is demonstrated, and then the incident optical power dependence of the reflectivity distribution is also investigated.

2. Principle and experimental setup

In general, distributed reflectivity measurements by SOCF-OCDR with explicit reference paths (either with or without an AOM) are performed based on the optical correlation control [26]. Specifically speaking, the optical frequency of the laser output is sinusoidally modulated to generate what we call a correlation peak in the FUT [22]. By controlling the modulation frequency, the position of the correlation peak can be scanned along the FUT, and thus the reflected light can be measured in a distributed manner. On account of the periodicity of the correlation peaks, the measurement range D of standard SOCF-OCDR systems is determined by their interval as

$$D = \frac{c}{2nf_m}, \quad (1)$$

where c is the optical velocity in vacuum, n is the core refractive index, and f_m is the modulation frequency of the laser output. The bandwidth of the correlation peak determines the spatial resolution Δz as

$$\Delta z \cong \frac{0.76c}{\pi n \Delta f}, \quad (2)$$

where Δf is the modulation amplitude.

Subsequently, consider the performance of reference-path-free SOCF-OCDR systems. As detailed in Ref. 27, when the Fresnel-reflected light at the open end of the FUT is used as a reference light, the measurement range is limited only to the proximal half of the FUT rather than Eq. (1). Here, we instead produce an artificial reflection point at the proximal end of the FUT (near an optical circulator) and suppress the reflection at the distal end. Then the Fresnel-reflected light at the proximal end of the FUT can be used as a reference light. In this case, the 0th correlation peak (i.e., the zero-optical-path-difference point) is constantly located at the proximal reflection point, and the 1st correlation peak is exploited for distributed measurement. Considering that the 2nd correlation peak starts to enter the FUT at the distal end of the FUT when the 1st correlation peak is scanned from the distal end to the midpoint, the measurement range is limited to the distal half of the FUT. This operating principle has been described in more detail in the case of POF-based system [28]. Note that similar configuration has been reported in Brillouin-based OCDR systems [29,30].

The experimental setup of the reference-path-free SOCF-OCDR is depicted in Fig. 1. All the optical paths were basically composed of silica SMFs. The output of a laser at $1.55 \mu\text{m}$ with a 3-dB bandwidth of ~ 1 MHz was amplified using an erbium-doped fiber amplifier (EDFA) and was injected into the FUT via an optical circulator. The reflected light from the FUT was amplified to ~ 3 dBm using another EDFA. The optical beat signal of this reflected light and the Fresnel-reflected light was converted into an electrical signal using a photo diode and was sent to an electrical spectrum analyser (ESA). The resolution bandwidth and the video bandwidth of the ESA were set to 300 kHz and 1 kHz, respectively. To enable high-speed operation, the spectral power at 2 MHz (with a maximal signal-to-noise ratio (SNR)) [26] was continuously output from the analog terminal of the ESA to an oscilloscope.

The proximal partial reflection point was, in this experiment, composed of a 650- μm -long air gap filled with cyclic transparent optical polymer (CYTOP) liquid, which has been used as the core material for perfluorinated graded-index POFs with relatively low propagation loss (~ 250 dB/km at $1.55 \mu\text{m}$) [31–33]. The

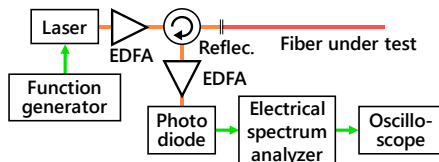


Fig. 1. Experimental setup of the silica-based reference-path-free SOCF-OCDR system. EDFA, erbium-doped fiber amplifier.

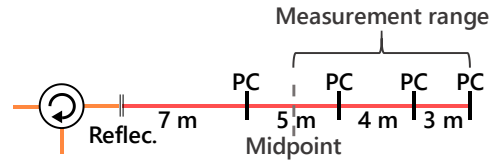


Fig. 2. Structure of the fiber under test.

reflection point was fabricated between the open end of a 1-m-long pigtail (silica SMF; 2nd port) of the optical circulator and the proximal end of the FUT. The structure of the FUT is shown in Fig. 2, where 7-, 5-, 4-, and 3-m-long silica SMFs were sequentially connected using “FC/PC” connectors (loosely connected to imitate weak reflection points). The distal PC end of the FUT was kept open. The modulation amplitude Δf was 3.9 GHz and the modulation frequency was swept from 5.15 MHz to 10.3 MHz, corresponding to the nominal spatial resolution of ~30 mm according to Eq. (2), which is > 40 times larger than the gap of the partial reflection point. The repetition rate was 20 Hz, and 32-times averaging was performed.

3. Experimental results

Figure 3 shows the measured reflection power distribution along the distal half of the FUT when the incident power was 0 dBm. The horizontal axis indicates the distance from the reflection point where the 0th correlation peak was located. The three weak reflection points including the open end were successfully detected at the correct positions. Note that because of the total loss of the proximal reflection points is high, the reflected light at the distal open end of the FUT becomes relatively low in power, and thus does not serve as a reference light.

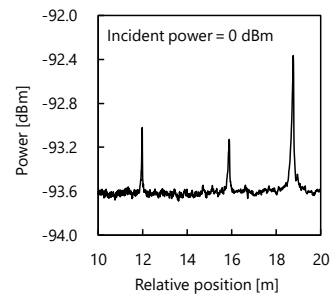


Fig. 3. Reflection power distribution measured along the distal half of the FUT. The incident power was 0 dBm. The horizontal axis indicates the distance from the reflection point where the 0th correlation peak was located.

We then measured the incident optical power dependence of the reflectivity distribution. Figure 4 shows the reflectivity distributions when the incident power was changed from -6 dBm to 3 dBm. Each result is shifted by 0.25 m. The power of each peak increased when the incident power increased from -6 dBm to 0 dBm, but it decreased when the incident power further increased. Here, we define the SNR of each peak detection as the difference between the peak power and the noise floor (the power at the position of 14 m was used). Figure 5 shows the SNRs of the each peak plotted as functions of the incident optical power. Irrespective of the peaks, the SNR was maximal when the incident power was 0 dBm. This behaviour is the same as that reported in Ref. 27. Thus, the optimal incident power was shown to exist from the viewpoint of the SNR.

4. Conclusion

In conclusion, a new configuration of AOM-free SOCF-OCDR without an explicit reference path was implemented using a silica SMF as the FUT. A proximal partial reflection point was artificially fabricated near an optical circulator, and the reflected light at this point was used as a reference light. The measurement capability of a distributed reflectivity measurement along the distal half of the FUT was experimentally proved. In addition, the incident optical power dependence of the reflectivity distribution was investigated, and the

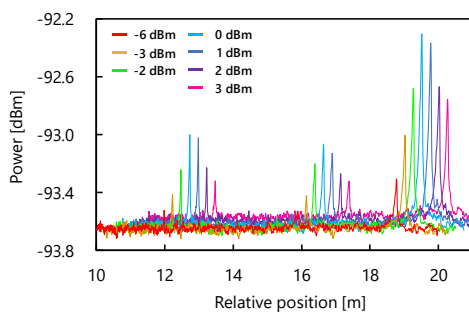


Fig. 4. Reflectivity distributions measured when the incident power was changed from -6 dBm to 3 dBm. Each distribution is shifted by 0.25 m; the horizontal scale is true only for the result at -6 dBm.

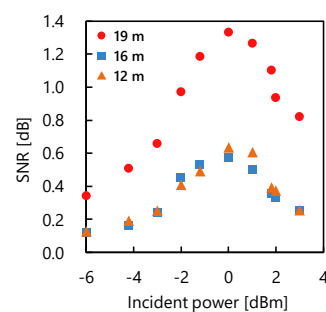


Fig. 5. Incident optical power dependence of the SNR of the three peaks at the relative positions of 12, 16, and 19 m.

existence of the optimal incident power was clarified. We anticipate that our silica-based AOM-free SOCF-OCDR system without an explicit reference path will be of great use in implementing cost-effective distributed reflectivity sensors in the near future.

Acknowledgments

This work was supported by JSPS KAKENHI Grant Numbers 25709032, 26630180, and 25007652, and by research grants from the Iwatani Naoji Foundation, the SCAT Foundation, and the Konica Minolta Science and Technology Foundation.

References

- [1] C. K. Y. Leung, K. T. Wan, D. Inaudi, X. Bao, W. Habel, Z. Zhou, J. Ou, M. Ghandehari, H. C. Wu, and M. Imai, *Mater. Struct.* **48**, 871 (2015).
- [2] A. Barrias, J. R. Casas, and S. Villalba, *Sensors* **16**, 748 (2016).
- [3] W. Zou, S. Yang, X. Long, and J. Chen, *Opt. Express* **23**, 512 (2015).
- [4] Y. Mizuno, N. Hayashi, H. Fukuda, K. Y. Song, and K. Nakamura, *Light: Sci. Appl.* **5**, e16184 (2016).
- [5] M. K. Barnoski and S. M. Jensen, *Appl. Opt.* **15**, 2112 (1976).
- [6] G. P. Lees, H. H. Kee, and T. P. Newson, *Electron. Lett.* **33**, 1080 (1997).
- [7] M. Zoboli and P. Bassi, *Appl. Opt.* **22**, 3680 (1983).
- [8] P. Healey and P. Hensel, *Electron. Lett.* **16**, 631 (1980).
- [9] Q. Zhao, L. Xia, C. Wan, J. Hu, T. Jia, M. Gu, L. Zhang, L. Kang, J. Chen, X. Zhang, and P. Wu, *Sci. Rep.* **5**, 10441 (2015).
- [10] W. Eickhoff and R. Ulrich, *Appl. Phys. Lett.* **39**, 693 (1981).
- [11] D. Uttam and B. Culshaw, *J. Lightwave Technol.* **3**, 971 (1985).
- [12] B. J. Soller, D. K. Gifford, M. S. Wolfe, and M. E. Froggatt, *Opt. Express* **13**, 666 (2005).
- [13] S. Venkatesh and W. V. Sorin, *J. Lightwave Technol.* **11**, 1694 (1993).
- [14] F. Ito, X. Fan, and Y. Koshikiya, *J. Lightwave Technol.* **30**, 1015 (2012).
- [15] R. C. Youngquist, S. Carr, and D. E. N. Davies, *Opt. Lett.* **12**, 158 (1987).
- [16] E. A. Swanson, D. Huang, M. R. Hee, J. G. Fujimoto, C. P. Lin, and C. A. Puliafito, *Opt. Lett.* **17**, 151 (1992).
- [17] K. Hotate, M. Enyama, S. Yamashita, and Y. Nasu, *Meas. Sci. Technol.* **15**, 148 (2004).
- [18] Z. He, T. Tomizawa, and K. Hotate, *IEICE Electron. Express* **3**, 122 (2006).
- [19] Z. He, M. Konishi, and K. Hotate, *Proc. SPIE* **7004**, 70044L (2008).
- [20] K. Hotate and O. Kamatani, *Electron. Lett.* **25**, 1503 (1989).
- [21] Z. He and K. Hotate, *J. Lightwave Technol.* **20**, 1715 (2002).
- [22] K. Hotate, *Meas. Sci. Technol.* **13**, 1746 (2002).
- [23] Z. He, H. Takahashi, and K. Hotate, "Optical coherence-domain reflectometry by use of optical frequency comb," CLEO2010, CFH4.
- [24] H. Takahashi, Z. He, and K. Hotate, "Optical coherence domain reflectometry by use of optical frequency comb with arbitrary-waveform phase modulation," 36th ECOC2010, Tu.3.F.4.
- [25] T. Okamoto, D. Iida, K. Toge, and T. Manabe, *J. Lightwave Technol.*, in press (DOI: 10.1109/JLT.2016.2590507).
- [26] M. Shizuka, S. Shimada, N. Hayashi, Y. Mizuno, and K. Nakamura, *Appl. Phys. Express* **9**, 032702 (2016).
- [27] M. Shizuka, N. Hayashi, Y. Mizuno, and K. Nakamura, *Appl. Opt.* **55**, 3925 (2016).
- [28] N. Hayashi, M. Shizuka, K. Minakawa, Y. Mizuno, and K. Nakamura, *IEICE Electron. Express* **12**, 20150824 (2015).
- [29] N. Hayashi, Y. Mizuno, and K. Nakamura, *IEEE Photon. J.* **7**, 6800407 (2015).
- [30] N. Hayashi, Y. Mizuno, and K. Nakamura, *IEEE Photon. J.* **6**, 6803108 (2014).
- [31] Y. G. Zhao, W. K. Lu, Y. Ma, S. S. Kim, S. T. Ho, and T. J. Marks, *Appl. Phys. Lett.* **77**, 2961 (2000).
- [32] Y. Koike and M. Asai, *NPG Asia Mater.* **1**, 22 (2009).
- [33] Y. Mizuno and K. Nakamura, *Appl. Phys. Lett.* **97**, 021103 (2010).



Capillary Refill Time Monitoring Using Photonic Textiles

Chong Liu^{1*}, Shen Sun¹, Ricardo Correia¹, Barrie R Hayes-Gill¹, Serhiy Korposh¹, Simon A McMaster²,
Stephen P Morgan¹

¹ Optics and Photonics Group, Faculty of Engineering, University of Nottingham, NG7 2RD, UK

² Footfalls & Heartbeats (UK) Limited

*eexcl19@nottingham.ac.uk

Abstract: Plastic optical fibre (POF) sensors have been incorporated into a photonic sensing sock to monitor the reflected light intensity changes at 3 different positions on the sole of the foot. Each POF sensor consists of a pair of 500µm diameter POF to deliver/receive light between an opto-electronic device and the foot. The photonic sensing sock is used to monitor capillary refill time (CRT) on the sole of the foot during walking. Pressure changes are measured at the same positions and simultaneously using an electrically conductive yarn based pressure sensor. Results demonstrate changes in pressure and blood volume under the foot during walking. Since one factor in tissue breakdown is a change in the microcirculation, this wearable device has potential to predict onset of foot ulcers.

Keyword: Plastic optical fibre, Capillary refill time, Wearable devices, Diabetic foot ulcers, Photonic textile

1. Introduction

Foot ulcers are a common complication of diabetes as the cumulative lifetime incidence can reach up to 25% [1]. Diabetic foot ulcers can cause a huge problem both to individual patient and to healthcare providers due to treatment costs. Diabetes mellitus can cause decreased peripheral perfusion which can result in formation of pressure ulcers. There is a need for a long-term monitoring device to identify patients who will develop foot ulcers as a result of diabetes. One property of the microvasculature that can be readily monitored is the capillary refill time (CRT) of patients, which has the potential to predict the tissue breakdown and alert to the onset of foot ulcers of diabetics [2]. This paper introduces a photonic sensing sock which is designed to record key parameters (CRT and pressure) of subjects during free walking. These data are useful in further research to determine the long term properties of blood flow in the diabetic foot that leads to tissue breakdown in comparison with the healthy foot.

CRT is defined as the time taken for a distal capillary bed to regain its colour after blanching caused by pressure exerted on it. It has been used to assess perfusion, dehydration and shock [3]. The first recorded medical use of CRT was as part of a numerical trauma score [4]. A CRT more than 2s was proposed as an indication of abnormality [4]. An alternative proposed application suggested that CRT >3s is an indicator for febrile neutropenia after applying pressure to the index finger for 15s [5].

Currently, CRT is measured through manual assessment of the time taken for the colour to return to an external capillary bed after applying pressure to blanch the tissue [6]. Since every walking step results in a natural blanching pressure under the foot, the sensing sock is capable of monitoring CRT during free walking of subjects. In this case, it is easier to implement long term CRT monitoring. Three sensors each consisting of a pair of angle-cleaved plastic optical fibres (POF) and a pressure sensing patch (based on an electrically conducting yarn) are integrated in the sensing sock to monitor key parameters (CRT and pressure) from three different positions on the sole of the foot. People usually have their constant gait cycle (stance phase and swing phase) when they walk normally. Thus, the duration and the magnitude of the pressure generated by walking steps are relatively constant, which is beneficial for high accuracy CRT monitoring.

2. Method

2.1 Design and implementation of CRT sensing system

The photonic sensing sock shown in Figure 1 integrates three sensors each consisting of a pair of POF into the textile structure at three different positions (shown in Figure 1). Light is delivered/received between the sensor and an opto-electronic unit situated at the ankle via POFs. In this way, the POF sensor can be used to monitor the reflected light intensity during walking. Electrically conducting yarn is situated at the same positions as the



POF sensors (black circled). This consists of an S-shield yarn which is a spun staple fibre yarn consisting of 80% low pill PES (polyester) and 20% Inox steel fibre AISI 316L. The electrical resistance of the knitted structure changes when the textile patch is placed under different pressure. Thus, this sensing sock is capable of monitoring the reflected light intensities and pressure changes at three positions.

Figure 1 Photonic sensing sock. The black circles highlight the positions of the POF sensors. The grey regions are pressure sensors comprised of electrically conducting yarn.

Figure 2a is a cross-sectional diagram of the constructed opto-electronic unit. This opto-electronic unit consists of five PCB boards shown in Figure 2b. One green LED (LXML-PM01-0080, 530nm) was mounted on the left top PCB board (LED board) to deliver light to CRT test positions via three POFs (one for each sensor). A second PCB board (frontend board) consists of three photodiodes (VISHAY-BPW21R, 565nm), three photodiode front-end circuits (trans-impedance amplifier) and three pressure sensor front-end circuits (negative feedback amplifier). On the third PCB board (ADC board), six analogue to digital converters (ADCs) (ADS1252U-IC, 24bit) were applied to convert analogue outputs from the three photodiode front-end circuits and three pressure sensor front-end circuits. The fourth board is a commercial FPGA (field programmable gate array) board (XuLA-200 Board) which is configured to control the system. Two voltage regulators powered by a 9V battery were embedded on the power board to supply constant 5V power to the system and the Bluetooth (HC-06) board. All data is wirelessly transferred from the opto-electronic unit via Bluetooth.

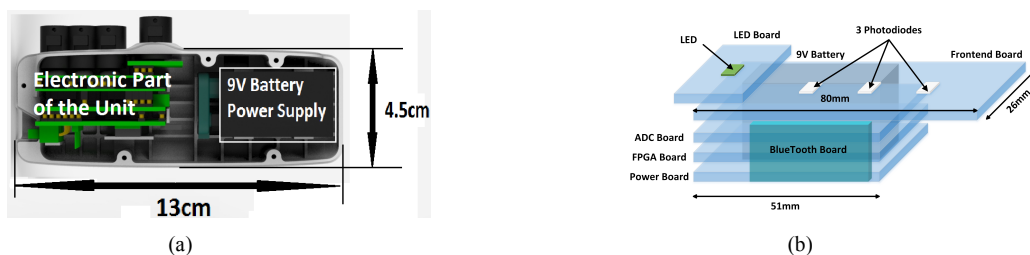


Figure 2 (a) Cross-sectional diagram of the opto-electronic unit (b) schematic of the electronic part of the unit

2.2 CRT Testing

The following describes a few simple laboratory based experiments carried out to test individual parts of the system and to demonstrate performance.

2.2.1 Finger CRT testing

In this test, a photonic textile patch (using the same textile as the sensing sock) was utilised along with an external photodiode (PDA100A-EC, Thor Labs). A subject pressed their index finger (right hand) on the photonic textile to blanch the finger for 5 – 8s, and then released the pressure to allow blood to return to the tissue. This process was repeated 5 times. Before the test, the subject cleaned hands with an antibacterial hand gel.

2.2.2 Walking CRT testing



The photonic sensing sock was utilised to measure the CRT on the sole of the foot with the designed opto-electronic system. Three POF sensors and pressure sensing patches integrated into the sensing sock recorded the CRT (reflected light intensity) and the pressure on the sole of the foot respectively. The test consisted of walking in the lab for 20s. This process was repeated 3 times. The subject cleaned their foot with an antibacterial hand gel.

3. Results

3.1 Finger CRT monitoring using photonic textile

Figure 3a shows light intensity recorded (blue line) and the pressure sensing-patch output (green line) on finger and figure 3b is the zoom-in of one complete test cycle. During the test, when the subject presses the index finger, there is an increase in both pressure output voltage and reflected light intensity recorded. When the subject releases the pressure, the pressure sensor output and the reflected light intensity recorded decrease.

From 28.5s to 32s (Figure 3b), the subject pressed the index finger on the photonic textile which resulted in an intense increase in both light intensity recorded (blue line) and pressure output (green line). From 32s to 38s, the subject held the press. Thus there is no large change in both the reflected light intensity (blue line) and the pressure output (green line) during this period. From 38s to 38.4s, the output of pressure sensor (green line) drops sharply to a low stable level as the subject released the pressure. For the light intensity change recorded (blue line), it decreases to a lower stable level more slowly than the pressure sensor output (green line) due to the time taken for blood to flow back into the tissue.

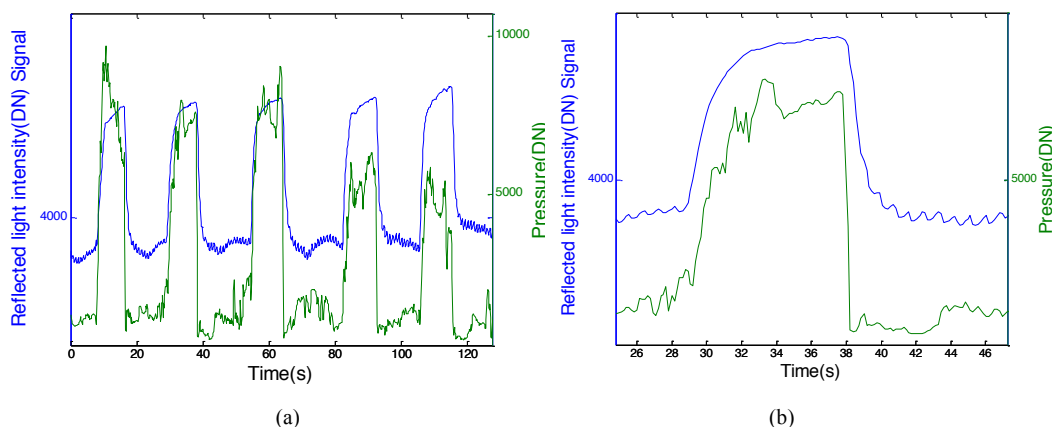


Figure 3 Finger test (a) The blue trace is the reflected light intensity of the index finger (DN-digital number). The green trace is the output of the pressure sensor (DN- digital number). (b) Zoom-in diagram of the first cycle.

3.2 Walking test

Figure 4a shows three positions on the sole of the foot where the sensing sock test. Figure 4b shows an example of the reflected light at three different positions under the foot of one test process (20s) with changes in the output of the pressure sensor recorded at the same time (green line). The upper trace shows a similar response to the finger experiment with the optical signal taking longer to return to a baseline value. This is less obvious at positions 2 and 3 and needs further investigation with a larger number of subjects.

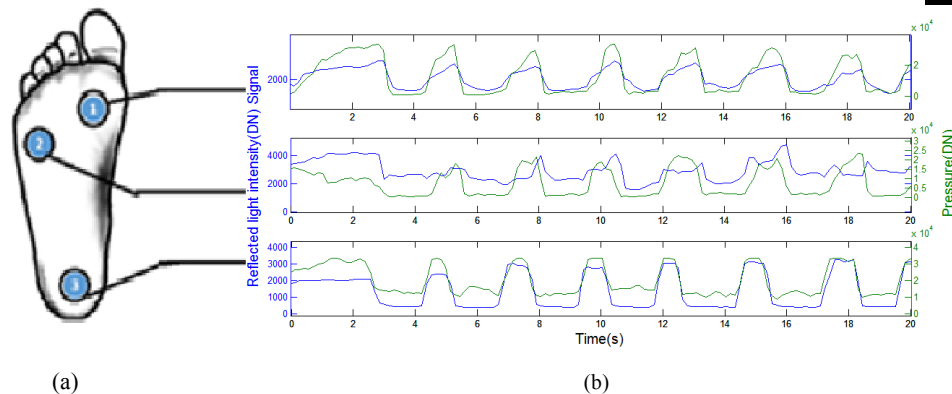


Figure 4 Walking test (a) Foot positions chosen for CRT detection. (b) The blue trace in each diagram is the reflected light intensity of different positions on the sole of the foot (DN-digital number). The green trace in each diagram is the output of the pressure sensor (DN- digital number).

4. Discussion and Conclusion

Preliminary results have demonstrated that the system is capable of monitoring pressure and blood flow changes under the foot. There are several tasks that need to be completed before the device can become a clinically useful tool.

The opto-electronic is practical for laboratory based experiments and field testing over relatively short times (~days). However as a clinical tool the size and form of the unit will need to be reduced. The unit described has not been optimised for space and so there is scope to reduce the size to at least half of the current size. Further work is also needed in order to accurately calibrate the textile based pressure sensor.

Although CRT measurements have the potential to be used to indicate changes in the microvasculature, it is unknown whether long term measurements can be used to predict tissue breakdown as such a monitoring device has not previously existed. Clinical studies will still need to be conducted with a refined device. The photonic textile platform also enables alternative biomarkers to be measured such as oxygen saturation and the photoplethysmogram (PPG). For example, in the finger CRT test (finger 3b), PPG signals can be observed during periods where low pressure is applied to the tissue.

CRT measurements are also affected by temperature and ambient light levels [3]. The sensing sock is unaffected by ambient light as it is usually located in a shoe. For environment temperature, the system would benefit from a temperature sensor, although relative measurements at different foot positions and between different feet may still be indicative of tissue breakdown.

References

- [1]. HM. Rathur, AJM. Boulton, "The diabetic foot", *Clin Dermatol* 2007; 25: 109-20.
- [2]. E. Atlas, Z. Yizhar, S. Khamis, N. Slomka, S. Hayek, A. Gefen, "Utilization of the foot load monitor for evaluating deep plantar tissue stresses in patients with diabetes: Proof-of-concept studies", *Gait Posture*, 2009 Apr; 29(3): 377-82.
- [3]. L. L. Blaxter, D. E. Morris, J. A. Crowe, C. Henry, S. Hill, D. Sharkey, H. Vyas, B. R. Hayes-Gill, "An automated quasi-continuous capillary refill timing device", *Physiol Meas.* 2016 January; 37(1): 83-99. Doi:10.1088/0967-3334/37/1/83.
- [4]. HR. Champion, WJ. Sacco, AJ. Carnazzo, W. Copes, WJ. Fouty, "Trauma score", *Crit. Care Med.* 1981; 9:672-76
- [5]. A. G. Da Ponte, R. H. Jácomo, "Capillary refill time in febrile neutropenia", *Revista Da Associacao Medica Brasileira*, 2016; 62(4):320-323.
- [6]. A. Bordoley, R. Irwin, V. Kalyani, C. McDonald, D. Standish, V. N. MD, Katherine J. Kuchenbecker, Robert L. Jeffcoat, "D1Git: automated temperature-calibrated measurement of capillary refill time", 2012 April 26, MEAM Senior Design Paper.



TRANSMITTED SIGNAL QUALITY IN BALLPOINT-PEN INTERCONNECT OF GRADED-INDEX PLASTIC OPTICAL FIBER

Y. Kaseda^{1*}, A. Inoue¹, A. Mitsui², H. Suzuki² and Y. Koike¹

¹ Graduate School of Science and Technology / Keio University, 3-14-1
Hiyoshi, Kohoku-ku, Yokohama, Kanagawa 223-0061, Japan.

² Mitsubishi Pencil, 2-5-12 Irie, Kanagawa-ku, Yokohama, Kanagawa 221-
8550, Japan

*Corresponding author: yugo.kaseda@gmail.com

Abstract: We demonstrate that ballpoint-pen interconnect enabled better transmission for largely-misaligned connection of graded-index plastic optical fiber (GI POF) than conventional butt-coupling. This may result from the reduction of coupling loss and some noises such as modal noise and reflection noise by using the ballpoint-pen interconnect, where a ball lens is precisely mounted on a fiber end faces for ball-lens coupling of GI POFs. Moreover, we show that power penalties in the ballpoint-pen interconnect are lower for larger lateral offsets in spite of higher coupling loss. This is closely related to the reduction of reflection noise with an increase in lateral misalignment as the ballpoint-pen interconnect were laterally misaligned.

Key words: Graded-index plastic optical fiber (GI POF), Ballpoint-pen interconnect, Transmission signal quality.

1. Introduction

A graded-index plastic optical fiber (GI POF) with a high bandwidth and flexibility is expected to be a transmission medium for in-home networks ^[1]. However, appropriate interconnects of GI POFs for consumer applications have not yet emerged. For connection of GI POFs, we have developed ballpoint-pen interconnects where a ball lens can be precisely mounted on GI POF end face using ballpoint-pen production technologies, enabling easy connection, low-cost production, and fiber end face protection of GI POFs ^[2]. In this paper, misalignment-dependence of data transmission quality for coupled GI POFs with ballpoint-pen connector is investigated. For evaluating data transmission quality, we measured BER curve in ballpoint-pen interconnect for misaligned coupling.

2. Data transmission in the ballpoint-pen interconnect

2.1. Experimental setup

Figure 1 shows the ballpoint-pen interconnect, where a ball lens is precisely mounted on a GI POF end face for ball-lens coupling of GI POFs. The connector production technology is based on the simple and low-cost ballpoint-pen technology. This ballpoint-pen connector significantly increases tolerance for misalignments of the GI POF axes, resulting from the expanded and collimated output beam. The ball lens in the ballpoint-pen connector have a refractive index of 1.51, a diameter of 550 μm , and an effective focal length of 407 μm . The core diameter and the numerical aperture (NA) of the GI POF were 80 μm and 0.25, respectively.

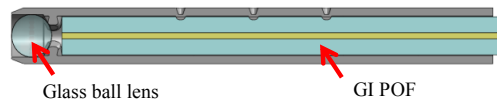


Fig. 1 Schematic structure of ballpoint-pen interconnect.

As shown in Fig. 2 (a), we measured BERs versus received optical powers for coupled 1-m GI POFs with ballpoint-pen interconnect. As a reference, butt coupling of GI POFs were also evaluated. The transmission experiments were performed using a 10 Gbps non-return to zero data pattern with a $2^{31}-1$ pseudorandom binary sequence. A bias current and a modulation voltage were 5 mA and 0.5 V, respectively. An 850-nm vertical cavity surface emitting laser (VCSEL) was directly modulated. The output beam from the GI POF 2 was received by the photo diode (PD). As shown in Fig. 2 (b) and (c), both the ballpoint-pen connector separation and GI POF separation were $\sim 100 \mu\text{m}$. For evaluating back-to-back transmission, we measured the BER curve when there is no transmission medium such as GI POFs, as shown in Fig. 2 (d).

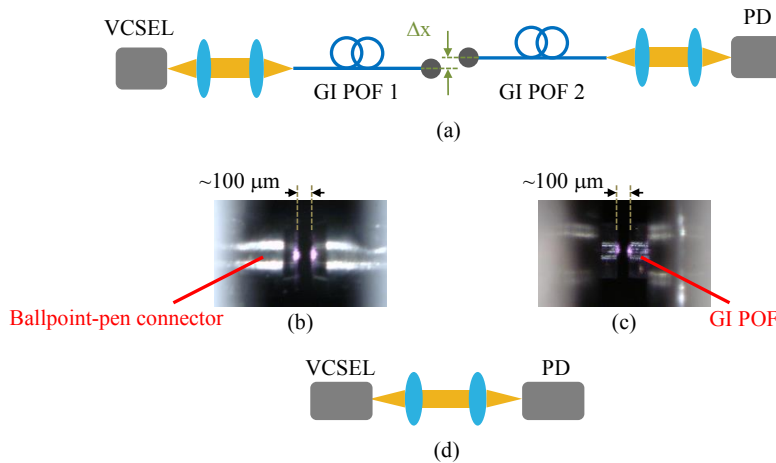


Fig. 2 (a) Experimental setup for measuring BER curve for coupled 1-m GI POFs. Microscopic images of coupled GI POFs with (b) ballpoint-pen interconnect and (c) conventional butt-coupling. (d) Experimental setup for measuring back-to-back transmission.

2.2. BER curve for misaligned coupling with and without ballpoint-pen connector

Figure 3 shows misalignment-dependence of coupling losses for connected GI POFs with and without the ballpoint-pen connector for center launching with an 850-nm VCSEL. The coupling loss could be significantly decreased by using the ballpoint-pen interconnect because the output beam is expanded and collimated.



Figure 4 shows the BER versus received optical power for 1-m coupled GI POFs using ballpoint-pen interconnect for a lateral offset of 40 μm , which results in larger coupling loss or lower transmission quality for the butt coupling. Note that ballpoint-pen coupling enables better transmission than conventional butt-coupling for same received optical powers in Fig. 4. This may result from the reduction of coupling loss and some noises such as modal noise and reflection noise by using the ballpoint-pen interconnect. For instance, modal noise occurs in multimode fibers as fluctuations of the coupling power as a consequence of time variations of the speckle pattern. By using ballpoint-pen connector, the modal noise may decrease compared with butt coupling since coupling power fluctuation was small because of a small ratio of lateral offset to beam width of the output beam from GI POF with ballpoint-pen interconnect.

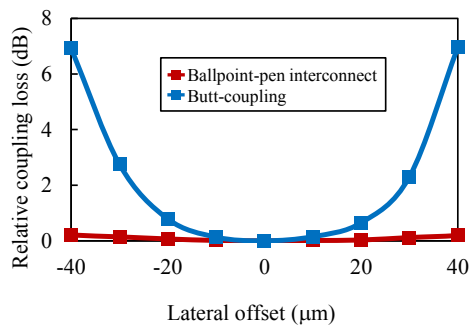


Fig. 3 Relative coupling loss for the butt-coupling and the ballpoint-pen interconnect as a function of lateral offset.

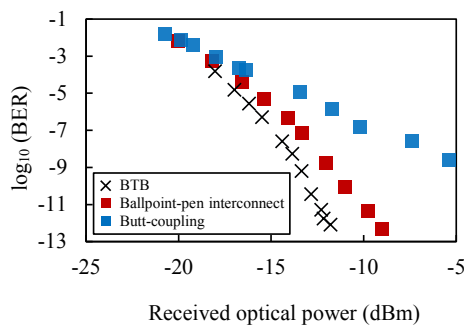


Fig. 4 BER versus received optical power for connected 1-m GI POFs with ballpoint-pen interconnect and butt-coupling for a lateral offset of 40 μm .

2.3. Misalignment-dependence of power penalty in the ballpoint-pen interconnect

Figure 5 shows the misalignment-dependence of BER curves for the transmission experiments with the 850-nm VCSEL with the ballpoint-pen coupling. Lower power penalties were obtained for larger lateral offsets in the ballpoint-pen interconnect in spite of higher coupling loss, as shown in Fig. 6.

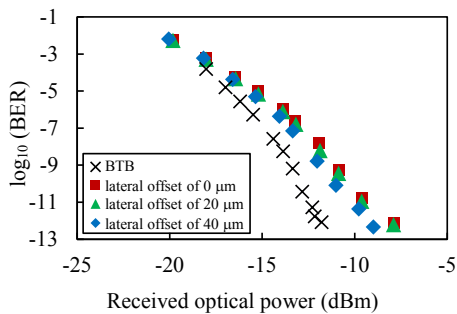


Fig. 5 Misalignment-dependence of BER curves in the ballpoint-pen interconnect for a lateral offset of 0 μm , 20 μm , and 40 μm .

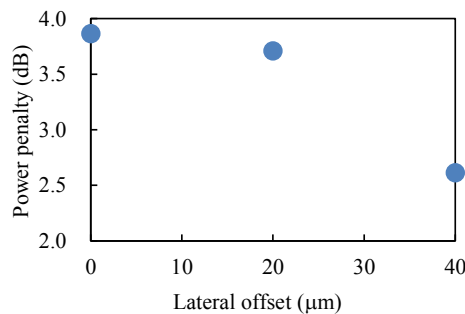


Fig. 6 Power penalties for coupled 1-m GI POFs with ballpoint-pen connector as a function of lateral offset.



To clarify the reason that the power penalty becomes lower with larger lateral offset, we evaluated the misalignment-dependence of relative intensity noise (RIN) spectra of optical links which consist of unmodulated 850-nm VCSEL, PD, and coupled 1-m GI POFs with ballpoint-pen interconnect, as shown in Fig. 7. For different lateral offset conditions, we observed similar spectra of periodic peaks with an equal spacing of ~ 100 MHz, which corresponds to the round-trip frequencies of the external cavities with external mirrors of the fiber end faces and ball lens surfaces in ballpoint-pen connectors. However, the peak powers of reflection noises were decreased as the lateral offset becomes larger. This result suggests that reflection noises may have been reduced by decreasing the reflection from the fiber end face and a ball lens surface in the ballpoint-pen connector of the GI POF 2 for misaligned coupling. As shown in Fig. 6, power penalties in the ballpoint-pen interconnect are lower for larger lateral offsets in spite of higher coupling loss.

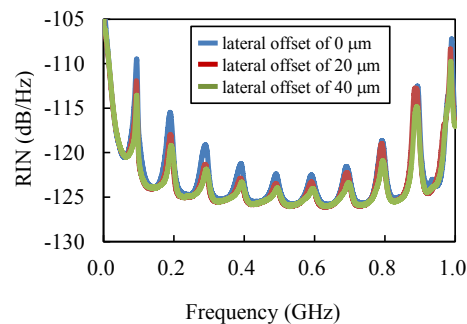


Fig. 7 RIN spectra of optical links for coupled 1-m GI POFs with ballpoint-pen connectors for a lateral offset of 0 μm , 20 μm , and 40 μm .

3. Conclusions

We demonstrate that ballpoint-pen interconnect enabled better transmission for largely-misaligned connection of GI POF than conventional butt-coupling. This may result from the reduction of coupling loss and some noises such as modal noise and reflection noise by using the ballpoint-pen interconnect, where a ball lens is precisely mounted on a fiber end faces for ball-lens coupling of GI POFs. Moreover, we show that power penalties in the ballpoint-pen interconnect are lower for larger lateral offsets in spite of higher coupling loss. This is closely related to the reduction of reflection noise with an increase in lateral misalignment as the ballpoint-pen interconnect were laterally misaligned.

References

- [1] Y. Koike, *Fundamentals of plastic optical fibers*, Wiley, New York, 2015.
- [2] Y. Koike and A. Inoue, "High-speed graded-index plastic optical fibers and their interconnects for 4K/8K video transmission," *J. Lightw. Technol.*, vol. 34, no. 6, pp. 1551-1555, Mar. 2016.



Laser-Drive-Current Dependence of the Reflection Noise Effect for Graded Index Plastic Optical Fiber

T. Omuro*, A. Inoue, Y. Koike

Graduate school of Science and Technology, Keio University, 7-1 Shinkawasaki, saiwai-ku, Kawasaki 212-0032, Japan

*Corresponding author: takaya-omuro@a8.keio.jp

Abstract: We show that a GI POF can significantly reduce reflection noise in a multimode fiber link with a vertical-cavity surface-emitting laser (VCSEL) for drive currents below 10.0 mA. By directly observing the backreflected beam patterns from the fibers to the VCSEL, we showed that the noise reduction effect is closely related to the strong mode coupling because these may lower self-coupling efficiencies into the VCSEL. These results suggest that the GI POF is promising candidate for more level transmission with higher signal-to-noise ratio.

1. Introduction

The growing demand for increased transmission speed in application such as 4K/8K television motivates the development of optical cables for the high-speed data transmission. The proposed optical transmission media for 8K display consists of twenty-four glass multimode fibers (MMFs), which require the high production cost, the large connecting part, and dust elimination. To decrease the number of the fibers for transmission media, multilevel modulation scheme has been studied. The multilevel transmission can increase bitrate over 2-level transmission, but is subject to noise problems because signal-to-noise ratio (SNR) decreases with an increase in number of levels. The flexible and high-bandwidth graded-index plastic optical fiber (GI POF) is expected to be used for the multilevel transmission media [1, 2].

Recently, we experimentally demonstrated that GI POF can intrinsically reduce reflection noise in a MMF link with a vertical-cavity surface-emitting laser (VCSEL) [3]. In multilevel transmission, more VCSEL drive currents corresponding to more levels are required than 2-level modulation scheme, so it is required to investigate the drive-current dependence of the transmission noise for high quality multilevel transmission. In this report, we evaluated the drive-current dependence of the reflection noise for GI POF in MMF links with a VCSEL.

2. Experimental section

Figure 1 shows the experimental setup for evaluation of reflection noise in MMF links. The laser is a multimode VCSEL with an oscillation wavelength of 850 nm. The photodetector is a PIN PD with TIA. The output beam from the VCSEL was collimated and focused on a fiber end-face using an antireflection coated (AR-coated) lens. The input fiber end-face irradiated with the incident beam was monitored using a CCD camera. The output beam from the fiber was collimated and focused on the PIN PD with TIA using an AR-coated lens. Under restricted mode-launching condition, we measured the noise floor spectra of the MMF links with an unmodulated VCSEL. Figure 2 shows the averaged relative intensity noise (RIN_{av}) over the frequency range from 0.01 to 10 GHz versus a drive current with the 1m GI POF and the 1m glass GI MMF. Figure 3 shows the measured RIN spectra of optical links for the GI POF and the glass GI MMF with an unmodulated VCSEL, which was operated with a drive current of 3.0 mA, 5.0 mA, and 8.0 mA.

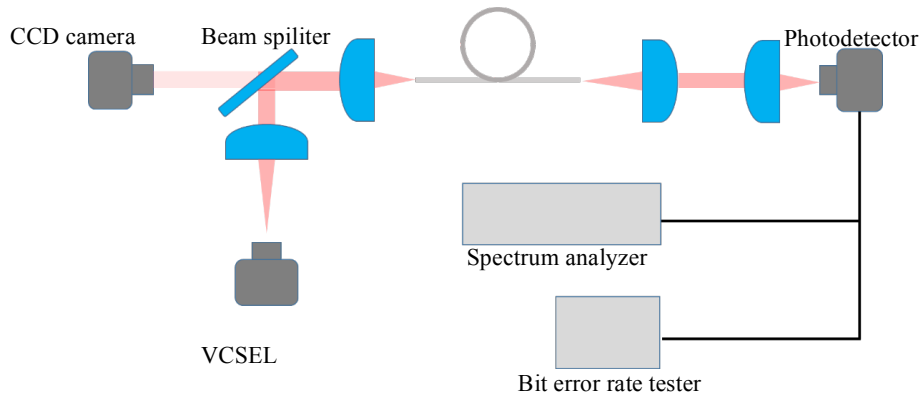


Fig. 1 Schematic diagram of experimental arrangement.

As shown in Fig. 2, the RIN_{av} of the GI POF was lower than that of the glass GI MMF for drive currents below 10.0 mA. The difference between the RIN_{avs} for GI POF and the glass GI MMF was increased with an increase in drive current. Both the spectra of the GI POF and the glass GI MMF have peaks with an equal spacing of 1 GHz, which corresponds to the round-trip frequencies of the external cavities with the reflector of the fiber input face, as shown in Fig. 3. Also, both the spectra have peaks with an equal of 100 MHz, which corresponds to the round-trip frequencies of the external cavities with the reflector of the fiber output face, and the peak levels of the GI POF were decreased with an increase in a drive current. The refractive index of the GI POF is lower than that of the glass GI MMF, so the Fresnel reflectance at the GI POF end faces are lower than those from the glass GI MMF. This can lower reflection noise for the GI POF. However, note that this is not only the mechanism for reflection noise reduction of the GI POF.

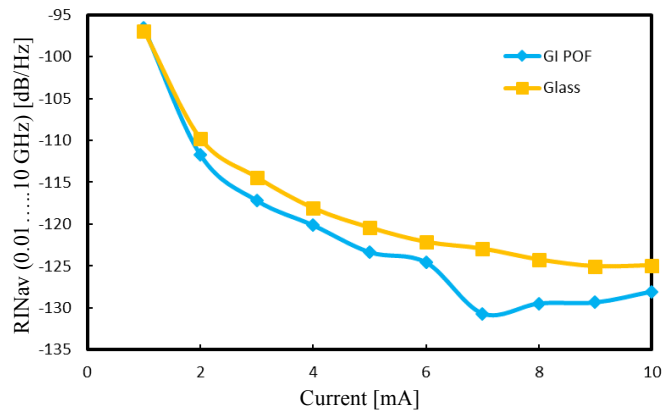


Fig. 2 RIN_{avs} with the GI POF and the glass GI MMF



Figure 4(a)-4(c) show the reflected light from the GI POF and figure 4(d)-4(f) show the reflected light from the glass GI MMF. For GI POF with strong mode coupling, the backreflected beam patterns had significantly different beam patterns from the glass GI MMF. This suggests that the MMF link using the GI POF has lowered self-coupling efficiencies into the VCSEL cavity. Therefore, the RIN_{av} of the GI POF was lower than that of the glass GI MMF.

We also experimentally investigated the bit error rate (BER) of the MMF links with modulated VCSEL with a voltage of 0.1 V (peak to peak) and 10 Gb/s NRZ-coded pseudo random bit sequence pattern. The measurement time is ten minutes. Figure 5 shows the BER versus a drive current. The BERs for the GI POF is lower than those for the glass GI MMF for drive currents between 2.0mA and 8.0 mA. For the GI POF, the BERs tended to increase with an increase in drive current whereas the BER performance degraded with a drive current of 2.0 mA and 3.0 mA This suggests that the GI POF can allow for multilevel transmission with high signal-to-noise ratio.

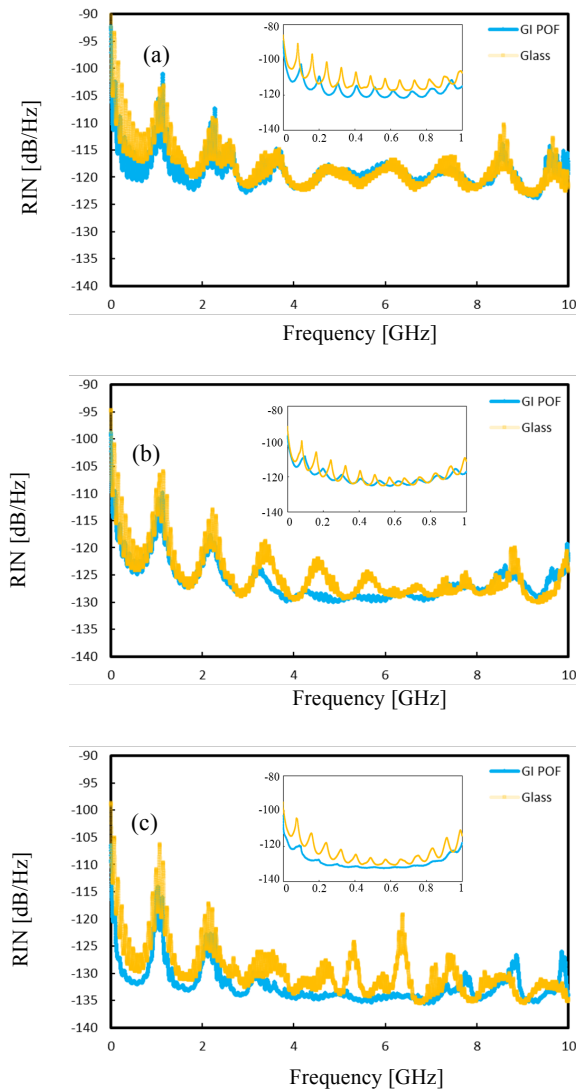


Fig. 3 RINs with the GI POF and the glass GI MMF between 0 GHz and 10 GHz for (a) 3.0 mA, (b) 5.0 mA and (c) 8.0 mA. Insert: enlarged figure between 0 GHz and 1 GHz.

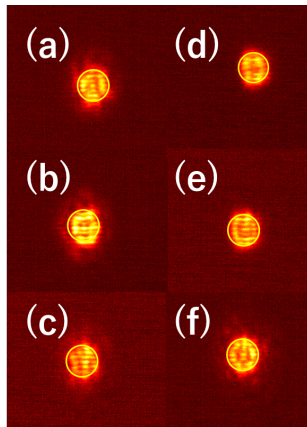


Fig.4 Microscopic images of backreflected beam patterns from the GI POF (left) and the glass GI MMF (right). (a) and (d) 3.0 mA. (b) and (e) 5.0 mA. (c) and (f) 8.0 mA. The yellow circle shows the corresponding oxide aperture of the VCSEL.

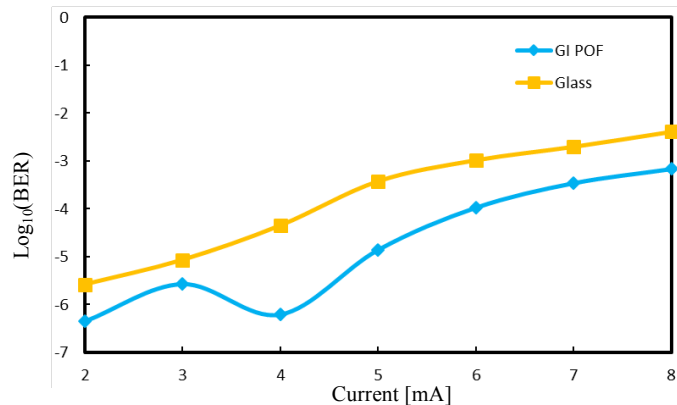


Fig. 5 BERs with the GI POF and the glass GI MMF.

3. Conclusion

We have experimentally demonstrated that a GI POF can significantly reduce the averaged RIN over the frequencies below 10 GHz for drive currents below 10.0 mA. By directly observing the backreflected beam patterns from the fibers to the VCSEL, we showed that the noise reduction effect may be related to the strong mode coupling because this may lower self-coupling efficiencies into the VCSEL. These results can be related to the reduction of the bit error rate for the GI POF for all the drive current between 2.0 mA and 8.0 mA. We are currently investigating the detail relationship between the noise reduction effect in the GI POF and the drive current. These results suggest that the GI POF is promising candidate for more level transmission with higher signal-to-noise ratio.

4. References

- [1] Y. Koike and A. Inoue., "High-speed graded-index plastic optical fibers and their simple interconnects for 4K/8K video transmission," *J. Lightwave Technol.*, 34, 1551-1555(2016).
- [2] Y. Koike., *Fundamentals of plastic optical fibers.*, John Wiley & Sons, (2014).
- [3] A. Inoue et al., "Reflection noise reduction effect of graded-index plastic optical fiber in multimode fiber link," *Opt. Lett.*, vol. 39, no. 12, pp. 3662-3665, June(2014).



Potential of POF sensors for Structural Health Monitoring of fibre composites

M. Plümpe^{1*}, M. Beckers¹, C.-A. Bunge², T. Gries¹

¹RWTH Aachen University, Institut für Textiltechnik, Germany

²Hochschule für Telekommunikation Leipzig

*magdalena.pluempe@ita.rwth-aachen.de

Abstract: Structural Health Monitoring (SHM) refers to the long-term and reliable surveillance of potential damage in structural components during operation by direct implementation of non-destructive testing (NDT) systems on or into the structure. A short summary of the most important SHM techniques will be given and evaluated in regards to their suitability for the application in fibre reinforced plastics (FRP). Special attention will be paid to the use of polymer optical fibres (POF) regarding their good sensorial properties (high failure strain and small bending radius) as well as their easy and direct integration into reinforcement textiles. Three different concepts are evaluated and whereof the most suitable are implemented in specimen to test their processability. The results are compared to commercially available glass optical fibre (GOF) sensors.

1. Introduction

Lifetime calculations of fibre composites are currently evaluated conservatively, as no exact models exist. Since maintenance is offline, this results in high downtime and maintenance costs. The term Structural Health Monitoring (SHM) refers to online-monitoring of the structure while usage [01]. So, real lifetime can be exhausted by recognizing damage before failure of the composite, reducing weight by decreasing safety coefficients and by lowering the maintenance effort by condition-based maintenance instead of time-based.

Varying approaches for SHM exist. Within those different sensor systems are developed. One opportunity is the application of polymer optical fibres (POF). These can be integrated during the manufacturing process and so directly embedded into fibre composites. The principle is shown in Figure 1.

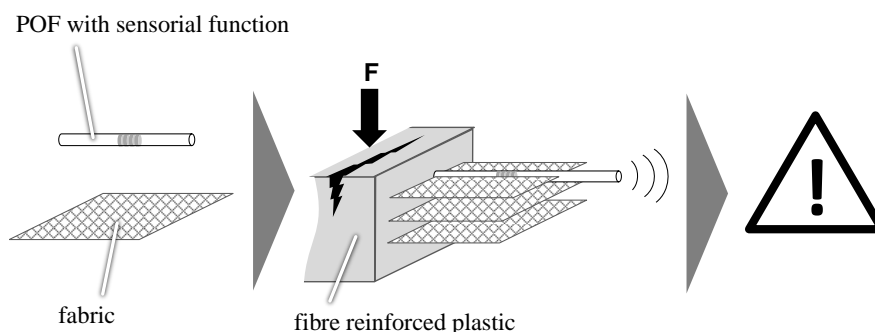


Figure 1: Automatic online-monitoring of fibre reinforced plastics by sensorial, optical polymer fibre integrated into the textile

By now, for this purpose glass optical fibres (GOF) are used mostly. However, these fibres have a low elongation at break, with a maximum of 1 %, and a high bending stiffness which complicates the processing, positioning and measurement of high elongations [02]. Polymer optical fibres show minor attenuation characteristics. Thus, potential transmission distances are shortened to approx. 100 m. On the other side, POF can be stretched over 30% and placed in smaller bending radii [03].

2. Sensors for SHM

The following figure classifies different sensors to the categories electronics, acoustics and optics based on their measuring principles. The section of optical sensors just takes account of Fibre Bragg Gratings (FBG) and Optical Time/Frequency Domain Reflectometry (OTDR/FDR) due to of their superiority.

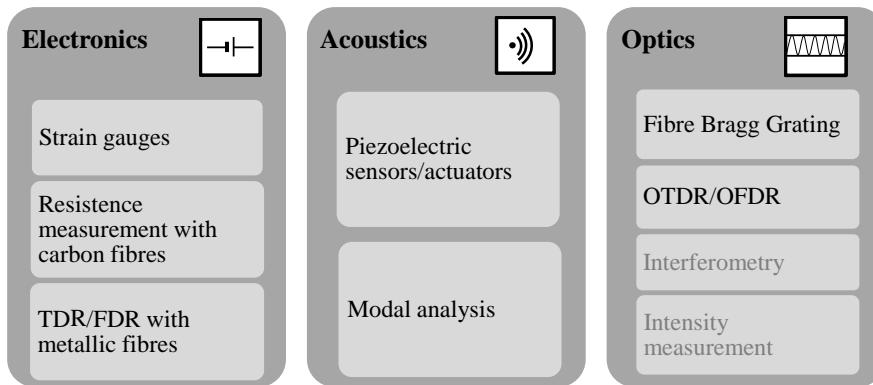


Figure 2: Categorization of sensors in SHM by measuring principle, following [04]

The essential characteristics of every sensor system are summarized in Table 1. This includes a listing of all possible measurands, their expansion, temperature application range [05] and main advantages and disadvantages.

Because the TDR can usually be used up to 12 m [06] and offers a location accuracy of 10 mm, elongation accuracy can approximately calculated at:

$$\frac{10 \text{ mm}}{12000 \text{ mm}} \approx 0,08 \% = 800 \mu\epsilon$$

The minimum detectable default length of 3-10 mm by Piezoelectric-Wafer Active Sensors (PWAS) [07] was compared to 1 m² and is, under the assumption that the defect extends equally in both dimensions, calculated as:

$$\frac{3 \cdot 3 \text{ mm}^2}{1.000.000 \text{ mm}^2} \approx 0,0009 \%, \text{ bzw. } \frac{10 \cdot 10 \text{ mm}^2}{1.000.000 \text{ mm}^2} \approx 0,01 \%$$

To determine accuracy of elongation and temperature of a FBG in a SM-GOF (1,2 pm wavelength shift per $\mu\epsilon$ and 10 pm per °C [08]) it is assumed that 0,1 nm = 100 pm wavelength shift can be reliably identified. Therefore, the sensitivity of a SM-GOF-FBG amounts to:

$$\frac{100 \text{ pm}}{1,2 \frac{\text{pm}}{\mu\epsilon}} \approx 83 \mu\epsilon < 100 \mu\epsilon, \quad \frac{100 \text{ pm}}{10 \frac{\text{pm}}{^\circ\text{C}}} \approx 10 \text{ }^\circ\text{C}$$




The accuracy for temperature of GI-POF-FBG is

$$\frac{100 \text{ pm}}{213 \frac{\text{pm}}{^\circ\text{C}}} \approx 0,47 \text{ }^\circ\text{C},$$

with a temperature sensitivity of 213 pm per °C, measured with a GI-POF manufactured at the Institut für Textiltechnik at RWTH Aachen [04].



Table 1: Summary of characteristics of the presented sensors, following [04]

Sensors	Measurands	Accuracy	Temp. application range	Main advantages	Main disadvantages
Electronics 	DMS	100 - 2000 µε [09] Depending on sensor density	-40-180 °C	Established technique	Discrete measurement
	Resistance measurement with carbon fibres	Min 5 % of filaments broken for longitudinal measurement [10] Only by alignment of measuring section, not more exactly [11]	No data	Few additional components, continuous measuring	Only for electrically conductive structures, no localization
	TDR, FDR	800 µε [12] Min 5 % of monitored surface [12] 10 mm [12]	-20-50 °C	Continuous measuring	Only for electrically conductive structures
Acoustics 	PWAS	Min 0,01 % of monitored surface [07] Depending on sensor density	-20-150 °C	Within one step addable to surface as film	Discrete measurement, complex evaluation
	Modal analysis	Min 10 % of monitored surface [13] Hardly possible	No data	Global measuring	Very complex evaluation
Optics 	FBG	<100 µε [08] SM-GOF: 10 °C, GI-POF: 0,47 °C no data no data depending on sensor density	-40-80 °C	Electromagnetic insensitive, very exact	Discrete measurement
	OTDR, OFDR	POF: 5000 µε, GOF: 10.000 µε [02, 14] 25 °C [02] no data 1 mm - 100 mm [02, 14]	-30-70 °C	Electromagnetic insensitive, continuously in fibre direction	Lower sensitivity than FBG



3. Approaches for integration of POF in textile reinforcement

In a FRP laminate generally three different approaches are possible. These are shown in Table 2. Approach 1 was not implemented, due to its poor protection against environmental influence, its low vicinity to stress and its heavy workload at manual integration. In approach 2 and 3 a single mode glass fibre and a gradient-index polymer fibre were used.

Table 2: Approaches for monitoring of fibre composites with optical fibres

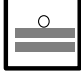
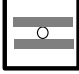
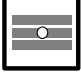
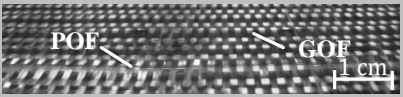
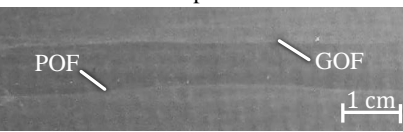
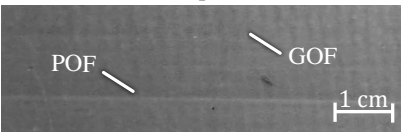
Approach 1 	Approach 2 	Approach 3 
Gluing the sensor fibre to surface	Positioning of sensor fibre between layers	Integration of sensor fibre into textile
-	-	Glass fibre weave with optical fibres 
-	FRP with optical fibres 	FRP with optical fibres 




Table 3 shows the used optical fibres' specifications. The GI-POF was manufactured at the Institut für Textiltechnik at RWTH Aachen with a continuous melt spinning process [04] and then integrated as warp thread into a woven glass fibre fabric.

Table 3: Specifications of applied optical fibres

	GI-POF	SM-GOF
Material	PMMA	Quartz
Cladding diameter [µm]	1000	250
Attenuation [dB/km]	4820 (632,8 nm)	0,22 (1550 nm)
Numerical aperture	k.A.	0,14

Relevant parameters for are listed in Table 4. Regarding to their applicability of monitoring FRP, all approaches are assessed on basis of these indicators.

Table 4. Applicability of approaches for fibre optical sensors for monitoring FRP

Parameter	Appr. 1 	Appr. 2 	Appr. 3 
Protection against environment	-	+	+
Potential for automation	-	-	+
Vicinity to stress within structure	-	+	+
Alignment of sensors	0	-	+
	+ very suitable	0 medium suitable	- not suitable

The flexibility of POF in textile processing was limited due to its large diameter. This appears in form of breakage of fibre by increasing speed of weaving process (>40 wefts/minute), as well as during leading the fibre out of laminate and during demoulding process. The last two breakage types also appeared during handling of GOF. For POF as well as for GOF applies: to manage the contact to measurement electronics, approximately 20-30 cm bare fibre length are necessary. Therefore the fibre must not break at the leading out zone at the edge of the component. The biggest challenge is a robust transitional solution without any kinks.



The alignment of sensory fibres clearly distinguishes approach 2 from approach 3: the optical fibres between layers deviates after resin injection – even though they were fixed with a sealing tape – for several millimetres from their initial position, while sensory fibres, woven into the material, remain in their position.

4. Conclusion

As a summary optical fibre sensors are assessed concerning suitability of different fibre types (see Table 5) and concerning competing technologies (see Figure 3). To meet the high standards needed for SHM systems, the following requirements have to be fulfilled by POF: A small fibre diameter has large impact on good textile processing and on homogenous stress distribution within the laminate. Nevertheless, a compromise has to be found between a small diameter for a good processability and a large diameter for easy manual handling. Additionally, processing characteristics also depend on the material. Beside PMMA-POF, elastomers with good optical properties may be taken into account. This is currently examined at ITA.

Table 5. Advantages and Disadvantages of optical fibre for fibre optical sensors, following [04]

	Advantages	Disadvantages
Single mode fibre	<ul style="list-style-type: none"> • Clear peak in reflection spectrum • Low attenuation (GOF) • Low disturbance of laminate properties due to small diameter 	<ul style="list-style-type: none"> • Uneasy handling due to small diameter • High attenuation (POF)
Multi-mode fibre with graded index profile	<ul style="list-style-type: none"> • Several clear peaks (temperature und elongation parallelly measurable) • Low attenuation • Easy handling due to high diameter 	<ul style="list-style-type: none"> • Risk of breakage due to high diameter (POF) • Disturbance of laminate properties due to high diameter (POF)
Glass fibre	<ul style="list-style-type: none"> • High chemical resistance 	<ul style="list-style-type: none"> • Brittleness and low flexibility of material • Low thermal expansion
Polymer fibre	<ul style="list-style-type: none"> • High flexibility, therefore small bending radii and high elongation at break possible • High poisson's ratio ν • High thermal expansion coefficient α • Low costs 	<ul style="list-style-type: none"> • Low chemical resistance

To compensate current weaknesses of POF and to increase competitiveness with other technologies, especially a practical solution for contacting the sensor fibre has to be developed. Apart from that, fibre-optic sensors in general convince due to automatable, precise integration into FRP, their independence of the reinforcement material, and a low susceptibility to failure (see Figure 3).

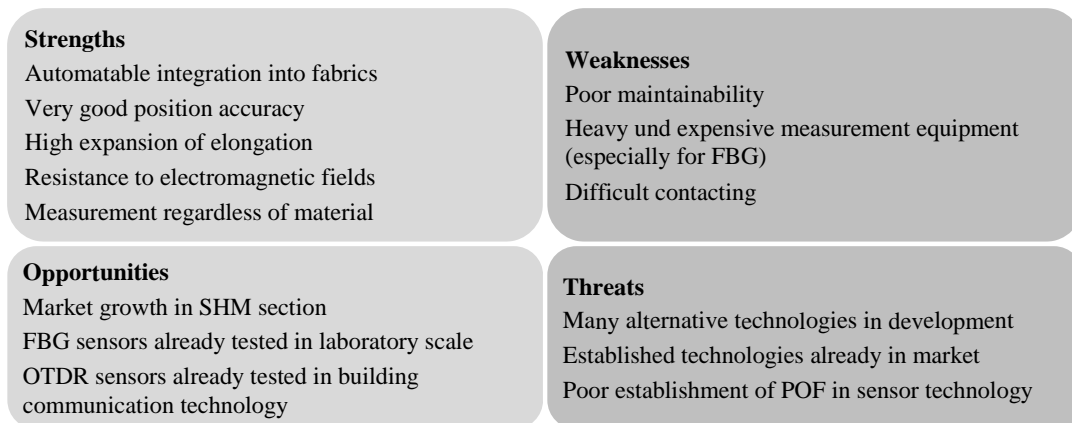


Figure 3. SWOT-analysis of POF for use as fibre optical sensor in SHM of FRP



4. References

- [01] Farrar, C. R.; Worden, K.: Structural Health Monitoring: A Machine Learning Perspective. New York, John Wiley & Sons, 2012
- [02] Liehr, S.; Lenke, P.; Wendt, M.; Krebber, K.; Seeger, M.; Thiele, E.; Metschies, H.; Gebreselassie, B.; Münich, J. H.: Polymer Optical Fiber Sensors for Distributed Strain Measurement and Application in Structural Health Monitoring. IEEE Sensors Journal (2009), Vol. 9, No. 11, pp. 1330-1338
- [03] Peters, K: Polymer optical fiber sensors – a review. Smart Material Structures (2011), Vol. 20, No. 1, pp. 013002
- [04] Beckers, M.: Development and analysis of a new manufacturing process for polymer optical fibers (POF), (in german). RWTH Aachen University, Dissertation, Aachen, Shaker Verlag, 2016
- [05] Walter, S.: Entwicklung piezoelektrisch wirksamer Sensorfasern auf Basis von Polyvinylidenfluorid. RWTH Aachen University, Dissertation, Aachen, Shaker Verlag, 2012
- [06] Sequid GmbH: HF-Geräte – Impedanzkontrolle auf Leiterplatten, Steckverbindungen und Leitungen. Fachvortrag bei der FED Regionalgruppe Berlin, 2014 <http://www.fed.de/Verband/Regionalgruppen/Berlin/Bericht-undVortragsfolien---Contag-AG/456d963/> (16.02.2016)
- [07] Tscharncke, D.: Fehlerdiagnose in der Ultraschallprüfung durch iterative Modellierung. Bundesanstalt für Materialforschung und -prüfung, Dissertation, Berlin, 2002
- [08] Morey, W. W.; Meltz, G.; Glenn, W. H.: Fiber optic Bragg grating Sensor. Proc. SPIE (1992), 1582, pp. 36-4
- [09] Hoffmann, K.: An introduction to stress analysis and transducer design using strain gauges. Darmstadt, HBM Publication, 2012
- [10] Wang, X.; Fu, X.; Chung, D.: Strain sensing using carbon fiber. Journal of Materials Research (1999), Vol. 14, No. 3, pp. 790-802
- [11] Chung, D. D. L.: Structural health monitoring by electrical resistance measurement. Smart Materials and Structures (2001), Vol. 10, pp. 624-636
- [12] Obaid, A.; Yarlagadda, S.; Yoon, M. K.; Hager, N. E.; Domszy, R. C.: A time-domain reflectometry method for automated measurement of crack propagation in composites during mode I DCB testing. Journal of Composite Materials (2006), Vol. 40, No. 22, pp. 20472066
- [13] Staszewski, W. J.; Boller, C.; Tomlinson, G. R.: Health Monitoring of Aerospace Structures: Smart Sensor Technologies and Signal Processing. 1. Edition, New York: John Wiley & Sons, 2004
- [14] Giurgiutiu, V.: Structural Health Monitoring of aerospace composites. 1. Edition, Amsterdam, Elsevier Inc., Academic Press, 2015



Bio Based POF

Benjamin Mohr^{1*}, Daniel Grothe¹, Markus Beckers¹, Gunnar Seide¹, Thomas Gries¹, Christian-A. Bunge²

1. Institut für Textiltechnik (ITA) at RWTH Aachen University
Otto-Blumenthal-Str. 1
52074 Aachen, Germany
2. Institut für Kommunikationstechnik at Hochschule für Telekommunikation Leipzig,
Gustav-Freytag-Straße 43 - 45
04277 Leipzig, Germany

*Corresponding author: Benjamin.Mohr@ita.rwth-aachen.de

Abstract: In times of increasing resource scarcity, global warming and bio economics, bio based materials get more and more important. In this paper we show the possibilities and limitations of POF based on bio polymers. Two different bio-TPU were investigated regarding their optical potential and processed to fibers. Bio based POF are compared to PMMA based POF. It is shown that the reviewed material Estane[®] is not suitable as GI-POF for textile fabric due to missing color neutrality. While it is possible to process the second reviewed material Pearlthane[®], its optical properties are improvable compared to PMMA based POF.

1. Introduction

Polymer optical fibers (POF) are used for data transmission, in sensor systems or in lighting applications. While they are already well-established in the fields of sensor systems and data transmission, POF offer great market- and development potential in lighting applications. Especially Graded-Index POF (GI-POF) have distinct advantages compared to Step-Index POF (SI-POF) or glass optical fibers in specific applications. A main deficit of GI-POF, its high production price, is approached in [1] by a novel continuous manufacturing process.

Today the mainly used material for POF is PMMA. Due to its high stiffness it is of limited suitability for further processing in textiles. Therefore, a material is needed which is spinnable, with high flexibility and good optical properties. Bio based thermoplastic elastomers offer the flexibility of elastomers while maintaining the ability to be used in melt spinning. Furthermore, the use of bio based polymers considers the increased importance of bio economics and conservation of resources.

During a bio economics focused project of the “Bundesministerium für Bildung und Forschung” two different thermoplastic polyurethanes were investigated and tested for their spinnability, their suitability for optical lighting applications and their suitability for further processing in textiles. Figure 1 shows the followed approach in four steps.

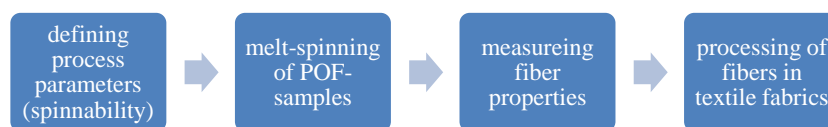


Figure 1: Four steps to evaluate the chosen thermoplastic polyurethanes

2. Experimental tests

The first step is to define process parameters for the chosen materials. The goal is to be able to melt-spin GI-POF with a diameter of 0.5-1 mm. In the next step POF-samples are melt-spun for the next steps. Then the properties of the fibers are measured. In step four different textile fabrics are processed from the fibers. Important properties for the POF are the damping of the light, tensile strength and diameter of the fiber.



2.1 Materials

The materials that are used in this study are two bio based thermoplastic polyurethanes (TPU) Estane[®] ECO 62A NAT 021 TPU and Pearlthane[®] ECO D12T80. The polymers are provided by the companies Lubrizol Advanced Materials BVBA, Westerlo-Oevel, Belgium and Lubrizol Advanced Materials Manufacturing Spain, S.L., Barcelona, Spain. Characteristic for the used TPU is their aromatic structure and the high amount of soft blocks that are responsible for the high flexibility.

2.2 Evaluation steps

Defining process parameters for spinnability: The process parameters for the melt-spinning process are the mass flow rate \dot{m} and the haul-off speed v_w . These parameters are limited by constraints of the machine as well as theoretical considerations regarding their effect on spinnability and fiber properties.

Melt-spinning of POF-samples: Based on the previously determined range of process parameters, GI-POF-samples are spun. The melt-spinning process is based on a novel manufacturing process for GI-POF developed at the Institut für Textiltechnik der RWTH Aachen University [1].

Measuring fiber properties: After melt-spinning monofilament samples of the chosen TPU the samples are investigated regarding their fiber properties. To be applicable in lighting applications the POF need low damping, and good tensile strength. A diameter around 0.5-1 mm is needed to fit the available connectors. The damping of the light is determined by measuring the light intensity of a fiber sample, shortening it and measuring the light intensity again. The difference in power is caused by the damping of the shortened fiber piece.

The tensile strength of the POF is measured with a tensile tester from Zwick-Roell, Ulm, Germany on the basis of DIN EN ISO 2062. The diameter of the fiber is measured using a light microscope.

Processing of fibers to textile fabrics: To bring proof of the suitability for further processing into textile fabrics, knitted and weaved fabrics are created from the spun POF-samples. As small diameters are beneficial for the process, GI-POF with a diameter of 0.5 mm are used.

3. Results and discussion

3.1 Defining process parameters for spinnability

Based on the machine-limited process parameters the range is narrowed down further to keep the diameter within the defined range of 0.5-1 mm. Figure 2 shows the range of the process parameters for Pearlthane[®].

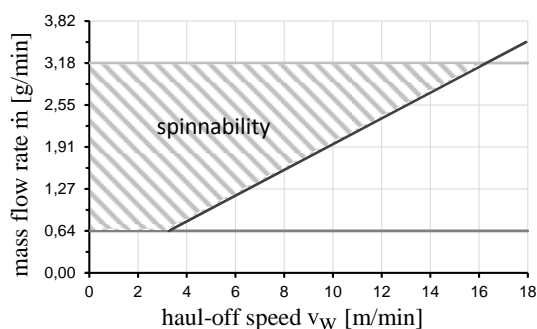


Figure 2: Range of process parameters for Pearlthane[®] ECO D12T80



3.2 Melt-spinning of POF-samples

A general suitability to melt-spin both chosen materials to GI-POF can be shown. The required diameters of 0.5-1 mm can be achieved. Both materials show some stickiness when spun out. This is believed to be caused by the cooling behavior and may be resolved by adjusting the spinning process.

The material Estane[®] ECO 62A NAT 021 TPU shows a yellow tint in the granulate material. The created monofilament still has the yellow tint. Therefore Estane[®] is not suitable for further processing into textile fabrics as a requirement is color neutrality. Pearlthane[®] ECO D12T80 is color neutral. Figure 3 shows a sample made of Estane[®].

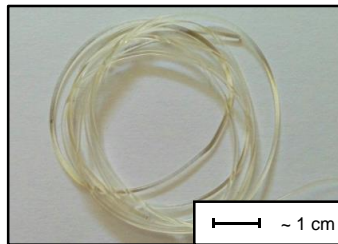


Figure 3: Yellow tinted POF-sample made of Estane[®] ECO 62A NAT 021 TPU

3.3 Measuring fiber properties

As spun fibers made of Estane[®] show a yellow tint they are not investigated any further.

The diameter of the POF-samples made of Pearlthane[®] show partly a significant deviation. This is believed to be caused by the experimental setup. POF-samples with low diameter deviation are suitable for further processing to textile fabrics.

Compared to typical used materials, the tensile strength of Pearlthane[®] is very low. As expected the use of TPU results in low tensile strength and high elongation. Figure 4 shows Pearlthane[®] in comparison to typical textile materials.

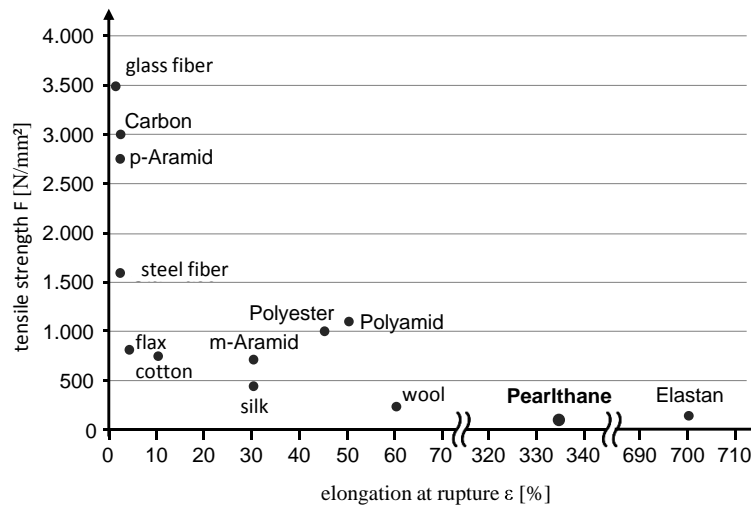


Figure 4: Comparison of tensile strength of Pearlthane[®] ECO D12T80 and other typical textile materials (based of [2])



Compared to GI-POF made from PMMA the light damping of GI-POF made from Pearlthane[®] is very high. The intensity of the injected light drops to 18 % after 10 cm. At the current state the material is only applicable for light transmission of short lengths.

3.4 Processing of fibers to textile fabrics

The general suitability of Pearlthane[®] ECO D12T80 for processing to knitted and weaved fabrics can be shown. The creation of a circular knitted fabric was successful. The in section 3.2 mentioned stickiness of the POF is responsible for very low production speed. Problems appear at the weaving process due to the stickiness of the material. This caused bad weaving results. Because of the high elasticity of the TPU a precise control of the weft tension is needed.

4. Conclusion

As materials for melt-spun GI-POF for lighting applications the two bio based thermoplastic polyurethanes Estane[®] ECO 62A NAT 021 TPU and Pearlthane[®] ECO D12T80 were investigated regarding their spinnability, their optical properties and their suitability for further processing to textile fabrics. While both materials can be melt-spun to GI-POF, only Pearlthane[®] offers the properties to be further processed to textile fabrics. The processing to circular knitted fabric was successful. Also weaving is possible, although problems regarding the fabric appearance occurred during the research.

The damping of the TPU-POF is considerably higher than the damping of typical GI-POF made from PMMA. Therefore, at the current state, GI-POF made from the thermoplastic polyurethanes can only be used at very short distances.

5. References

- [1] Beckers, M., Entwicklung und Analyse eines neuartigen Herstellungsverfahrens für optische Polymerfasern (POF), Dissertation, Shaker Verlag, Aachen, 2016
- [2] Gries, T., Veit, D., Wulfhorst, B., Textile Fertigungsverfahren – Eine Einführung, 2. Aufl., Carl Hanser Verlag, München, 2015



Multichannel interrogator for FBG sensing

D. Ganziy^{1,2*}, B. Rose¹, O. Bang²

1: Ibsen Photonics A/S, Ryttermarken 15-21, 3520 Farum, Denmark;

2: DTU Fotonik, Department of Photonics Engineering, Technical University of Denmark 2800 Kgs. Lyngby, Denmark

*Corresponding author: denis.ganziy@ibsen.com

Abstract: We propose a novel type of multichannel spectrometer based FBG interrogator. In a standard spectrometer different colors are dispersed by the diffraction gratings across the linear detector. Here we replace the linear detector with a Digital Micromirror Device (DMD). The DMD is a 2D mirror array with several hundred thousand microscopic mirrors, that can be set individually in either on or off state to switch selected wavelengths towards a single detector while sending the remaining light to a dump. The DMD is typically cheaper and has better pixel sampling than an InGaAs detector used in the 1550 nm range, which may lead to cost reduction and better performance. More important is that the DMD is a 2D array, which means that multichannel systems can be implemented without any additional optical components in the spectrometer, which makes the proposed interrogator highly cost-effective. The presence of multiple channels also allows to measure simultaneously several parameters, like temperature, strain, humidity, etc. In addition, the digital nature of the DMD makes it very flexible and provides opportunities for advanced programmable spectroscopic analysis, such a Hadamard spectroscopy, which may lead to new ways of interrogating particularly multimode FBGs written in standard commercial multimode POF.

Key Words: fiber Bragg gratings (FBG), DMD, Spectroscopy, Multichannel spectrometer, FBG sensor
Full paper not available due to IP issues



DESIGN AND PERFORMANCE OF A CLADDING MODE STRIPPER TO SIMPLIFY THE FABRICATION OF mPOFs

E. Arrospide^{1*}, G. Durana², G. Aldabaldetrekua², I. Bikandi², J. Zubia², Frank A. Dominguez-Chapman³, J. Mateo³.

- 1: Department of Applied Mathematics, Faculty of Engineering of Bilbao, University of the Basque Country, E-48013, Bilbao.
- 2: Department of Communication Engineering, Faculty of Engineering of Bilbao, University of the Basque Country, E-48013, Bilbao.
- 3: Department of Electronics and Communications Engineering, University of Zaragoza, Zaragoza.

*Corresponding author: eneko.arrospide@ehu.eus

Abstract: In this work, we fabricate a hexagonal-like microstructured fibre with three rings. The fibre consists of a polymethyl methacrylate monopolymer, with the aim of reducing the complexity of the fabrication process. The resultant fibre is few-moded with an appreciable quantity of cladding modes. In order to remove them, we propose a simple concept of mode stripper. The effectiveness of the developed mechanism is validated by means of near-field pattern measurements of the fibre.

1. Introduction

A precise coupling of a free space laser beam into an optical fibre is a key factor in order to maximize the amount of laser light entering the fibre. Most of this optical power may then propagate in the fibre core. Some fraction of the power, however, will propagate through the cladding as leaky modes. While these cladding modes are useful in a great range of sensor applications they can be damaging for others like polarimetric sensors or high power fibre lasers. In the former, cladding modes, in the same way as guided higher order modes in the core depolarize the light. In the latter, cladding modes can over-heat and damage the fibre. There are different alternatives to remove the cladding modes in short length optical fibres. For example, in a bare optical fibre different index-matching gels [1,2] or metals [3] may be applied to eliminate the cladding modes. Alternatively, during the fabrication process a double cladding with a higher refractive index and attenuation coefficient [4] can be added. Also mechanical devices that add a microbending in the fibre have been developed [5].

In the case of microstructured polymer optical fibres (mPOFs), different techniques can be applied during the fabrication process in order to avoid the propagation of cladding modes through the fibre. The most common one is to wrap the polymethyl methacrylate (PMMA) cane in a polycarbonate external tube in the last sleeving process of the fabrication [6]. In this work, we fabricate a hexagonal-like mPOF with three rings. The fibre consists of a PMMA monopolymer, which reduces the complexity of the fabrication process but allows for transmitting high level of light traveling through the cladding. In order to remove these cladding modes, we have designed and implemented a cost effective and precise concept of mode stripper. Near field pattern measurements have been performed in order to validate the proposed technique.

2. Experimental Setup

The analyzed mPOF was designed and fabricated in our drawing tower. A monolithic cylinder made of commercial polymethyl methacrylate (PMMA) with a glass transition temperature of 107 °C and weight average molecular weight of 150,000 g/mol was used as a preform. In order to create the microstructure, three concentric hexagonal arrays of holes (rings) were drilled. The diameter of the holes in the inner two rings was 3.0 mm, while the outer one had 4.5 mm diameter holes. The hole-to-hole spacing (or pitch) was 6.685 mm in all the structure. The preform was annealed for two weeks in a climatic chamber at 90 °C before drilling and before drawing. The preform was drawn to fibre in a two-step process. The cane 4 mm in diameter achieved in the first step was sleeved into a PMMA tube and was drawn to a 250.0 µm fibre with average hole diameter of 2.3 µm and average pitch of 4.52 µm (see Fig. 1).

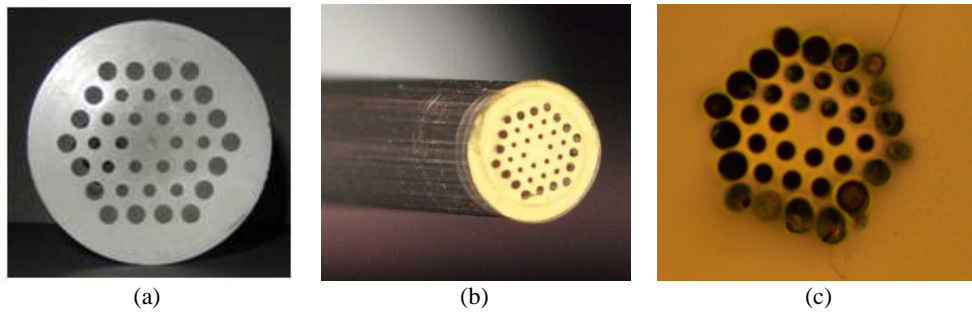


Fig. 1. Cross-sectional view of (a) the preform, (b) the cane, and (c) mPOF fibre.

Figure 2 shows the experimental set-up employed to analyze the effect of the designed mode stripper on the near field pattern of the fabricated mPOF sample. A 594 nm wavelength and 5 mW He-Ne laser was used as the light source. The laser beam was expanded and collimated using lenses L1 and L2. Mirrors M1 and M2 redirected the beam to an objective of numerical aperture (NA) 0.4. We chose this objective in order to match the NA of the light beam to the NA of the fibre, so that we obtained a high coupling efficiency. The fibre, fixed in a chuck holder, was screwed on a xyz-micropositioner, which allowed a very precise positioning of the focal point with respect to the fibre input, in order to minimize the coupling losses. Fibre samples of 80 cm in length were carefully prepared, and microscopic images of the resultant endfaces were acquired in all cases.

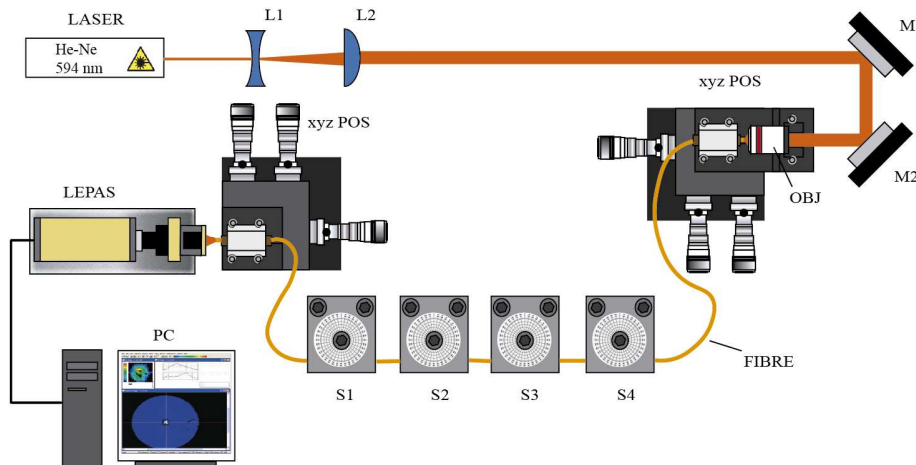


Fig. 2. Experimental set-up employed to measure the effect of a mode stripper on the near field pattern of an mPOF sample. L1: bi-concave lens ($f' = -40$ mm); L2: plano-convex lens ($f' = 200$ mm); M1, M2: mirrors; OBJ: 20X/0.4-NA objective; xyz POS: xyz-micropositioner; S_i : i th stripper.

In order to characterize the effect of the mode stripper on the light emerging from the mPOF, we specifically designed a mode stripper that induces controlled curvatures in the mPOF sample. The drawing in Figure 3 represents a side view of the mode stripper, illustrating the way in which the mPOF is curved. The stripper consists of two steel plates (32 mm x 43 mm x 4 mm), placed one above the other. The hole drilled in the bottom plate is intended to bend the fibre that lays on the bottom plate and runs along the hole diameter. The silicon semi-sphere attached to the upper plate presses the fibre down, and therefore bends it, by means of the tightening screw that joins both plates.

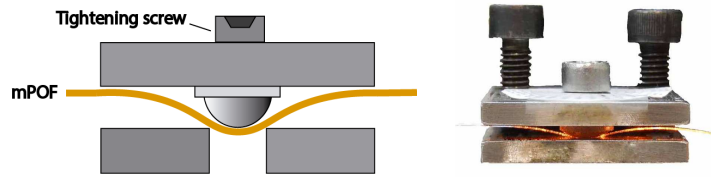


Fig. 3. Drawing (figure on the left) and picture (figure on the right) that represents a side view of the mode stripper, illustrating the way in which the mPOF is curved.

With the aim of measuring the effect of the stripper on the redistribution of power in the fibre cross-section, we have analyzed the near field or spatial distribution of the light at the fibre endface, considering different configurations for the stripper. For that purpose, the LEPAS-12 Precision Laser Beam Profiler from Hamamatsu has been employed. The endface of the mPOF sample is aligned and precisely positioned at the focal point of the LEPAS-12 objective. In order to measure the spatial distribution of light throughout the mPOF surface, that is, in the core region and in the cladding region, an objective with 50X magnifying power and 12 mm focal length has been used. Neutral density filters were inserted in the LEPAS-12 filter holder in order to avoid saturation in the core region.

3. Results

We first show the experimental results obtained considering different number of mode strippers in a series configuration, going from zero to four strippers (see Fig. 4 (a)). We have analyzed four samples and the measurements for each sample have been repeated four times. The mean value has been taken in order to obtain more accurate values (the vertical bars denote the uncertainty associated with each measurement). Regarding the power inside the core, a very slight decrease can be observed as the number of mode strippers increases, remaining above 85% of initial power in all the measured fibres. A very different behaviour can be observed with regard to the power distribution all around the fibre surface, that is, considering the core and cladding. In this case, when the first mode stripper is applied, light power decreases below 60 %, and continues decreasing significantly as the number of mode strippers increases, reaching the power attenuation level of 75% for the four measured fibres.

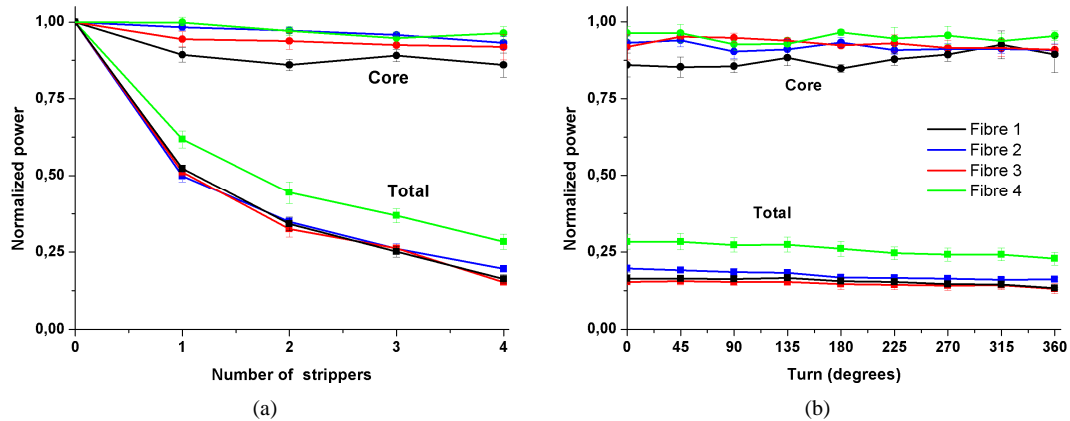


Fig. 4. Normalized total power and normalized guided power along fibre core in the four sample fibres (a) for different number of strippers and (b) for the sum of the turns of the tightening screws for the configuration of four mode strippers.

Regarding the effect of the pressure on the mode strippers, the configuration of four mode strippers was analyzed. Experimental results are shown in Fig. 4 (b). In these measurements, the tightening screws are turned 90 degrees clockwise in each stripper, in steps of 45 degrees, using the degree rule drawn on the upper



plate. In this case, light power inside the core and light power in the whole fibre hardly decreases, showing a very similar behaviour. Specifically, whereas in the whole fibre surface a very slight attenuation can be observed, in the case of the power measured inside the core, it does not decrease for none of the measured fibres.

4. Conclusion

In this work, we have investigated the effect of an ad-hoc designed and implemented mode stripper on the mode distribution of mPOFs. For the mPOFs designed and fabricated in our drawing tower, we can deduce from the experimental results, that the number of mode strippers, and therefore, the number of curvatures induced in the mPOF is the key factor towards the removal of the cladding modes. In particular, power in the cladding region has decreased above 75% when four mode strippers have been applied, whereas power in the core has kept almost constant. On the other hand, the pressure applied in each of the curvatures does not have a significant effect on the spatial power distribution, keeping almost constant in the whole fibre.

5. Acknowledgements

This work has been funded in part by the Fondo Europeo de Desarrollo Regional (FEDER); by the Ministerio de Economía y Competitividad under project TEC2015-638263-C03-1-R; by the Gobierno Vasco/Eusko Jaurlaritza under projects IT933-16 and ELKARTEK; by the University of the Basque Country UPV/EHU under programmes UF11/16 and Euskampus.

6. References

- [1] M. Meleshkevich, V. Ilyashenko and O. Shkurikhin, "High power fiber laser system with cladding light stripper," US Patent 7839901 B2, June 2010.
- [2] W. Guo, Z. Chen, H. Zhou, J. Li and J. Hou, "Cascaded Cladding Light Extracting Strippers for High Power Fiber Lasers and Amplifiers," IEEE Photonics Journal, June 2014.
- [3] A. Babazadeh, R. R. Nasirabad, A. Norouzey, K. Hejaz, R. Poozesh, A. Heidariazar, A. H. Golshan, A. Roohforouz, S. N. Tabatabaei Jafari and M. Lafouti, "Robust cladding light stripper for high-power fiber lasers using soft metals," Appl. Opt. 53, 2611-2615, 2014.
- [4] G. Kar, "Coated optical waveguide fibers," US Patent 4877306 A, October 1989.
- [5] M. Pacheco, M. Finot and J. Gurusamy, "Attenuation of cladding modes in optical fibers," US Patent 6983096, October 2004.
- [6] M. Large, L. Poladian, G. Barton and M.A. van Eijkelenborg, *Microstructured polymer optical fibres* (Springer, 2007).



Mechanical switching with light over POF – the direct approach with smart light-responsive materials

P. Dengler^{1*}, H. Schlachter², M. Lippenberger¹, O. Ziemann¹

1 Polymer Optical Fiber Application Center, Technische Hochschule Nürnberg, Wassertorstrasse 10, 90489 Nürnberg, Germany

2 Department of Macromolecular Chemistry, Technische Hochschule Nürnberg, Prinzregentenufer 47, 90489 Nürnberg, Germany

*Corresponding author: philipp.dengler@pofac.th-nuernberg.de

Abstract: In this paper we present the use of a light-responsive smart material as actuating element in a UV-light driven switch. Especially under environmental conditions where a strong electromagnetic field is present a complete galvanic decoupling is necessary to guarantee secure operation. The elementary feature of this optical relay is the actuator itself transforming UV-light directly to mechanical motion. So the relay can be operated without any additional circuits relying on semiconductor technology.

1. Introduction

Liquid-Crystal Elastomers show an outstanding behavior in many ways. But one of their most astonishing characteristic is their ability to convert thermal energy into motion. When being exposed to thermal excitation energy the material contracts up to 40% showing complete reversibility. This behavior basically leads back to its extraordinary structure. The backbone of the polymer consists of a special silicone partially crosslinked to form an elastomeric network. The functionalization is done by doping the network with rigid rod-like molecules. These mesogens are able to perform a phase transition from crystalline to liquid. During the phase transition triggered by thermal stimuli the mesogens change their ordered anisotropic phase to an isotropic liquid phase. The material reacts to this transformation of the underlying network with a change of shape. Furthermore the material is not limited to thermal excitation. In fact the possible excitation is determined by its molecular structure. In this particular case the molecules are modified with azo-benzenes. The azo-benzene molecules react to UV-irradiation with a change of shape disturbing the order of the mesogen network around them. So the phase transition is initiated by UV-irradiation. The LCE is sensor as well as actuator but has no sensitivity to electromagnetic fields which qualifies it for the use in strong EMF environments. One possible application is in an optical relay for complete galvanic decoupling. In contrast to conventional decoupling devices the actuation of a mechanical switch inherits one outstanding advantage which is the absence of any integrated circuits or semiconductors within the EMF environment. In the following chapter the material as well as the composition of our testing device will be further described.

2. Optical Relay

Obviously the core of the device is the Liquid-Crystal Elastomer.

2.1 Material

The used LCEs provided with azomesogenes were synthesized according to the route proposed by Finkelmann et al. [1, 2]. The basic structure of the LCE is formed by a reactive polyhydromethylsiloxane backbone polymer. The siloxane is slightly linked with the crosslinker 1,4-bis(undec-10-ene-1-yloxy)-benzene to form a flexible elastomer. To obtain a liquid crystalline elastomer the backbone is functionalized in a hydrosilylation reaction with two kinds of liquid crystalline monomers [3, 4].

The mesogen 4-methoxyphenyl-4-(but-3-ene-1-yloxy)-benzoate causes a defect in the liquid crystalline state when exceeding the clearing point. This is the reason for the thermal contraction of the material.

The azomesogen (E)-4-(hex-5-ene-1-yloxy)-4'-methoxyazobenzene induces the contraction by photoisomerisation as a result of UV irradiation [5]. The azomesogenes induce a disorder in the system with changing its molecule dimension from the rod-like shape (*trans*) to the bended shape (*cis*). Figure 1 shows the components and the reaction to obtain the LCEs.

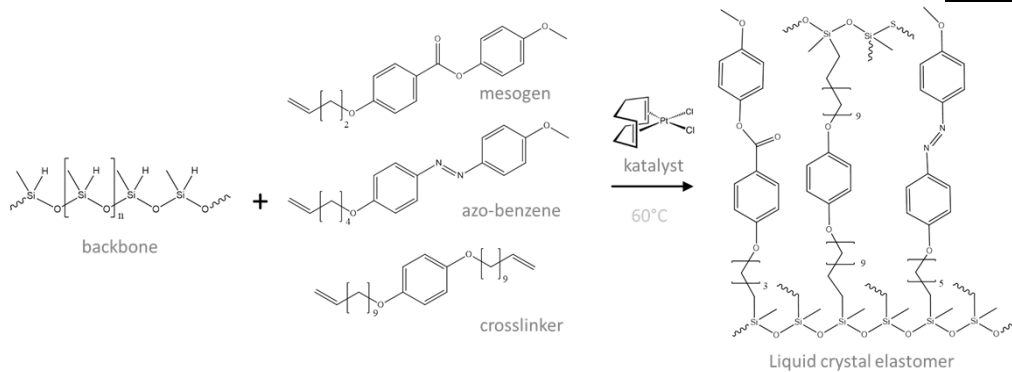


Figure 1. Components and Synthesis of LCEs

2.2 Characterization

Due to the LCE being the most essential part of the optical relay it is crucial to determine its behavior. Especially the contraction of the material that should be functionalized in the device and the cycles till failure are of interest. Furthermore the available tension of the material is releasing during contraction is needed to choose an appropriate switch to match the available force.

Figure 2 shows the reaction of the material to thermal excitation while Figure 3 shows its reaction to UV-irradiation. The diagram has been measured on a highly precise thermal-mechanical analyzer (TMA). The green solid line represents the contraction of the material while the red dashed graph is the temperature. During the thermal excitation the temperature in the oven of the TMA is risen to above 90°C which is clearly above the excitation temperature of the LCE. Therefore the LCE shows a contraction from up to 40%.

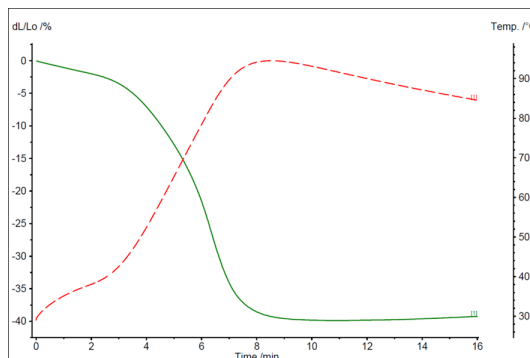


Figure 2. Contraction induced by thermal excitation

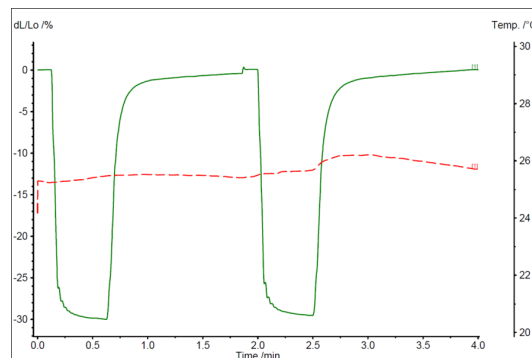


Figure 3. Contraction induced by UV-irradiation

Figure 3 represents the results of an UV-light induced excitation of the material. As can be seen on the red temperature graph the temperature is barely rising during the irradiation of UV-light. Still the material shows a contraction of up to 30%. During the thermal excitation as well as during the UV-irradiation the LCE is preloaded with constant 25 kPa of tension.

Now that the maximal contraction is known the tension and therefore the available force of the material has to be determined. In Figure 4 the developing force over time while irradiation is shown. During the measurement the LCE is fixated between two rigid clamps of which one is connected to a force sensor.

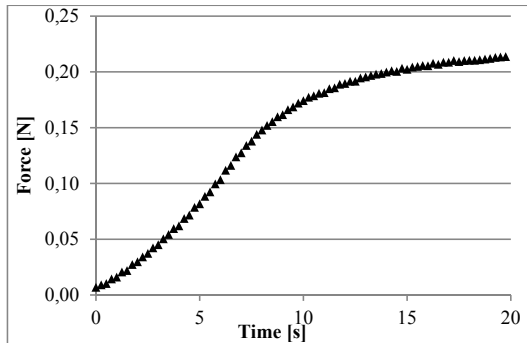


Figure 4. Developing excitation force over time

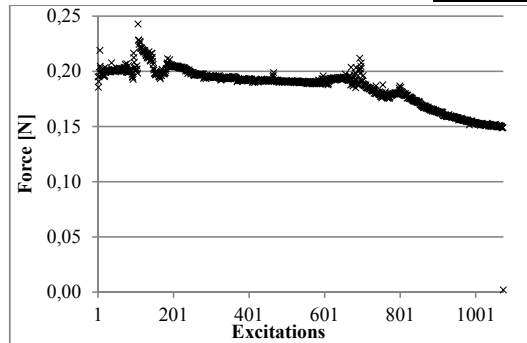


Figure 5. Excitation cycles till failure

While irradiated 20 seconds the LCE develops a maximal force of 213 mN. With its given width of 4 mm and its thickness of 0.25 mm the resulting tension is 213 kPa. With the maximal contraction and the maximal available tension a LCE is able to generate a suitable mechanical switch can be singled out. But yet another characteristic value of the LCE is of great interest: The number of consecutive activation cycles until failure. Figure 5 shows the resulting absolute force of more than 1000 cycles until failure. As before the LCE was fixated between two rigid clamps while the resulting force during excitation is measured. As can be seen the resulting force is slightly decreasing over time but should still be enough to actuate a micro-switch. With the determination of all essential parameters a test device can be built.

2.3 Fiber guide an illumination

In order to decouple both the circuit completely from each other it is crucial to have the light source as well as the whole control-circuit at a distance from the relay itself. Therefore the light is guided by a POF bundle to the Liquid-Crystal Elastomer as can be seen in Figure 7. The black-cleaved bundle with the aluminum bundle end reaches into the housing of the relay. Another advantage is the lower energy density within the bundle compared to a single POF and the possibility to shape each bundle end as demanded. So the bundle intake is circular to match the irradiation pattern of the high-power UV-LED while the bundle outlet is rectangular to match the shape of the LCE film. Due to the high attenuation of the of the POF in the spectral region of 365 nm (approx. 1200 dB/km), the numerical aperture and the losses in the gaps between the fibers the efficiency of the irradiation system is about 50% with 60 cm of POF length. As source a high-power UV-LED is used as a source with a peak-wavelength of 365 nm and a radiant flux of 800 mW which means that approximately 400 mW of irradiation reach the surface of the LCE film. With the chosen dimensions of the LCE 390 mW/cm² of irradiation are achieved.

2.4 Composition of the testing device

The LCE is clamped on top of the linear motion guide as seen in Figure 6. The lower clamp is guided in contraction direction of the material. It is mounted to a lever which is itself mounted to an eccentric to react to differences in contraction or force capabilities of the LCE film. The linear motion guide is slid into the housing.

Figure 7 shows the whole setup of the demonstrator. The fiber bundle reaches from the right side into the housing and illuminates the LCE. On the bottom left there is the hinge lever of the micro-switch. Its actuation force is with about 80 mN and a movement differential of 0.8 to 1.1 mm within the capabilities of the Liquid-Crystal Elastomer. Due to the LCE being cut manually its size and shape might differ slightly from each other. Therefore not only the lever is mounted on the eccentric but there is also a spherical mirror on the opposing side of the fiber bundle inlet.



The UV light passing through or beside the LCE film is being thrown back on the opposing surface so that the overall efficiency of the optical system does not vary with different LCE film dimensions. The assembled optical relay in motion can be found on www.youtube.com [6]

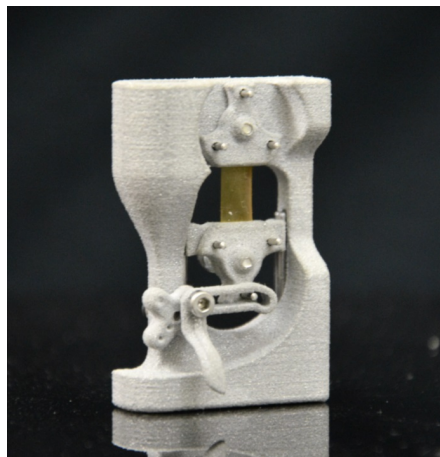


Figure 6. Detachable linear motion guide

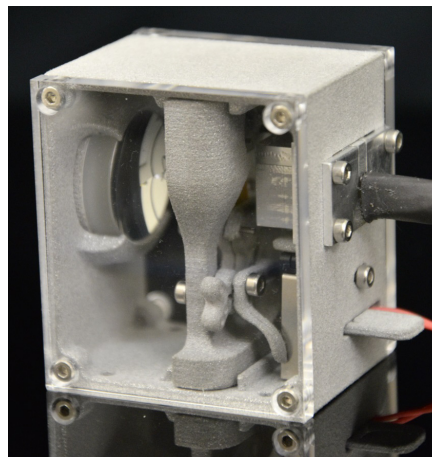


Figure 7. Linear motion guide in casing

3. Conclusion and outlook

Summarized the above described optical relay proves that an actuation with uv-radiation over POF is possible. Under optimal conditions the switch could be operated more than 1000 times before the Liquid-Crystal Elastomer would fail. Working under strongest electromagnetic fields this concept opens up a variety of possible applications. For example the medical processes of MR imaging could show possible applications for a LCE switch. Not only as switching device on the MRI device itself but even as a tool for a surgery, e.g. operating a scalpel, while receiving live feedback via the MRI device. Despite the results already achieved the material needs further examination. 1000 cycles are a solid starting point but in order to push the material from the laboratory to the industrial application there is still room for improvements.

5. Acknowledgements

The POF-AC Nürnberg is a project of the Hightech Offensive Bavaria.

The work was supported by the Bavarian Ministry of Education, Culture, Science and Art inside the Project "POF-Control" (No. F1116.NÜ/16/3).

6. References

- [1] Garcia-Amorós, J., Pinol, A., Finkelmann, H., Velasco, D., *Org. Lett.*, Vol. 13, 9, 2011
- [2] Sánchez-Ferrer, A., Merekalov, A., Finkelmann, H., *Macromol. Rapid Commun.*, Vol. 32, 2011
- [3] Speier Jr., J. L., US Patent 2 527 590, 1950
- [4] Speier Jr., J. L., US Patent 2 527 591, 1950
- [5] Franke, C., *Darstellung und Charakterisierung heliotrope Polymere*, Master Thesis, Technische Hochschule Nürnberg, Germany, 2016
- [6] "Optical Relay - Liquid Crystal Elastomer (LCE)", 13.05.2016, Web, Accessed on: 15.08.2016, https://www.youtube.com/watch?v=531_pXf7UH4

Photoresponsive materials for intelligent optical devices – a review of the research done in BIOSOL

M. Lippenberger^{1*}, C. Franke², P. Dengler¹, G. Wehnert², H. Poisel¹

¹ Polymer Optical Fiber Application Center, Technische Hochschule Nürnberg, Wassertorstraße 10, 90489 Nürnberg, Germany

² Department of Macromolecular Chemistry, Technische Hochschule Nürnberg, Prinzregentenufer 47, 90489 Nürnberg, Germany

*Corresponding author: michael.lippenberger@th-nuernberg.de

Abstract: This paper reviews the results of our project BIOSOL. To achieve a mechanical movement induced by light and to realign and move a polymer optical fiber (POF) we use Liquid Crystal Elastomers (LCE) with photoisomerizable groups. We discuss the route of the chemical synthesis and the resulting material properties. To transfer the material to real applications we present characterisation techniques and discuss the aspects of the final application. In our case this is to adjust a POF endface that is misaligned in relation to the focus area of concentration optics. Here we use the effect of destabilizing the crystal phases due to geometrical changes of photoisomerizable azo-groups. So by irradiating the material with appropriate short-wavelength radiation a photomechanical effect can be triggered. In the experimental part we present photomechanical measurements as well as tests to evaluate the long-time properties including an irradiation experiment with a high dose of ultraviolet radiation to investigate possible degeneration effects due to ultraviolet radiation exposure.

1. Introduction

1.1 Materials

Only liquid crystal elastomers (LCEs) are presently known as Materials which can act as sensors and actuators simultaneously. LCEs exhibit mechanical properties like rubber elasticity and additionally exceptional anisotropic properties like photochromism. These characteristics are determined by chemical bonding of low molar mass anisotropic liquid crystalline moieties – so called mesogens – as side groups formed on an elastomeric network. As a consequence of this coupling, monodomain side-chain LCEs enforce a significant change in shape due to external stimulation by light or heat [1], [2]. The changes of geometry are induced by the chemical isomerization of the LCEs. When the stimulation is turned off the material relaxes completely reversible to its initial state.

To achieve such a significant change in shape activated by UV irradiation and to move and realign a POF, monodomain LCEs containing azoderivatives were synthesized according to the route proposed by Finkelmann et al. [3]. A section of the chemical structure of these LCEs together with the molecular structure of bounded components is shown in figure 1.

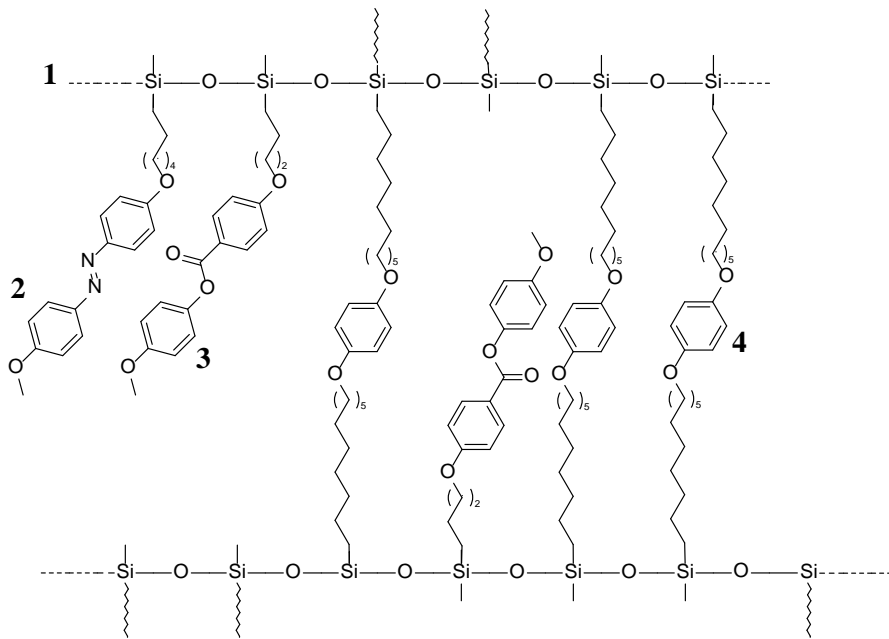


Figure 1. Section of chemical structure of synthesized LCE

The basic structure of the LCE is formed by an ultra-flexible siloxane (polyhydromethylsiloxane **1**). The length of this backbone polymer is determined before synthesis. In contrast to other backbones, e. g. polyacrylates, polymethacrylates and polymalonates where the backbone is formed while polymerization. The siloxane is crosslinked with 1,4-bis(undec-10-ene-1-yloxy)-benzene (**4**) in low crosslinking density to form an elastomer. The elastomer is functionalized with two kinds of liquid crystalline monomers. The mesogenic components are grafted lateral in the subsequent synthesis by hydrosilylation [4]. The mesogen 4-methoxyphenyl-4-(but-3-ene-1-yloxy)-benzoate (**3**) causes a defect in the liquid crystalline state by reaching and exceeding the clearing point. The azomesogen (E)-4-(hex-5-ene-1-yloxy)-4'-methoxyazobenzene (**2**) is being subjected to a photoisomerisation as a result of UV irradiation. As a consequence the molecule dimension is changing from the rod-like shape (*trans*-isomer) to the bended shape (*cis*-isomer). Based on the parallel arrangement of a large number of mesogens in the LCE a chain reaction occurs due to light or heat, which leads to a contraction of the LCE up to 40 % [5]. The mechanism of contraction is illustrated in figure 2 schemetically.

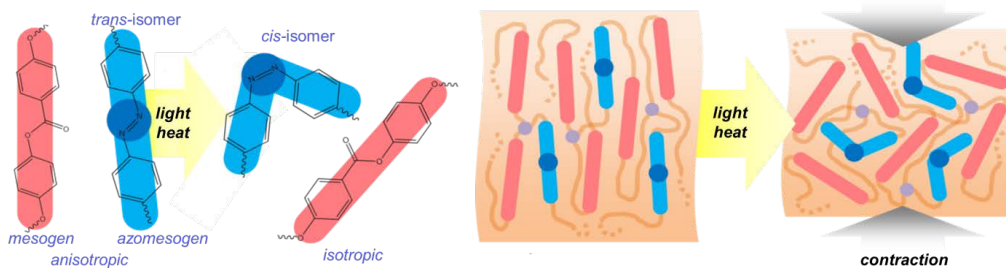


Figure 2. Schematic mechanism of contraction

1.2 Application

The photomechanical effect of LCEs is directly used to move a misaligned POF back to the focus area. This centering mechanism is particularly of interest in cases where the POF is used for daylighting with concentrated sunlight (SOLLEKTOR). In this case the high illumination densities for photoactivation are inherently available and can be used to trigger the photoisomerisation process. The general principle of the SOLLEKTOR is described in [6], [7] but for this paper we only consider the focus of the concentration optics respectively the coupling between the optical fiber and the concentration optics. In fig. 3. the general principle is demonstrated. The optical fiber is driven in reverse modus so we see the illuminated tip. When the LCE is not activated we have the starting position. The starting position is defined by the construction of the centering mechanism itself depending on the material properties and the illumination density. The overall contraction of the LCE is based on the internal material properties, the mechanical fixation after the first crosslinking step and the applied weight / force in the application. Due to the laboratory scale of the synthesis of the material, standardized material properties are not available. Empirical values based on numerous photomechanical measurements show, that materials with a contraction between 25 % - 30 % are technical feasible and useful. When the LCE is irradiated (in this case with a 365 nm LED) we see a remarkable contraction of the LCE coupled with a movement of the fiber of nearly 3 mm. This macroscopic demonstration of the mechanism shows the general approach.

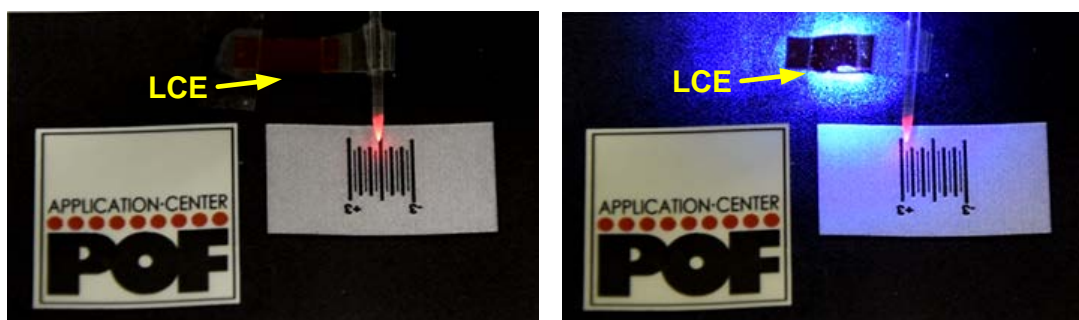


Figure 3. Moving a POF with LCE-film and ultraviolet radiation, shown is the non-activated LCE (left) and the activated LCE (right)

3. Methods

3.1 Mechanical measurements

To achieve a standardized characterisation of the material properties and not only a fingerprint value, we activate through two possible activation channels. The first one is the activation based on the latter application where we apply ultraviolet radiation (365 nm) to trigger the photoisomerisation process that leads to the destabilisation of the liquid crystal phases. The second channel aims to destabilise the liquid crystal phases through thermal excitation. The displacement respectively the contraction is then measured. We use here a modified commercial Thermo-Mechanical Analysator (TMA). An important boundary condition is the initial and constant stress during the activation process (constant force). It should be very small so we measure only the contribution of the contraction that is based on the photo- respectively thermoactivation and not an artificial contraction through an external force. But the applied force should be as high, so that a static defined measurement condition is fulfilled. We calculate the applied force in that way that we reach an initial stress of the LCE of 25 kPa. Fig. 4 shows the general measurement set up for photomechanic and thermomechanic characterization.

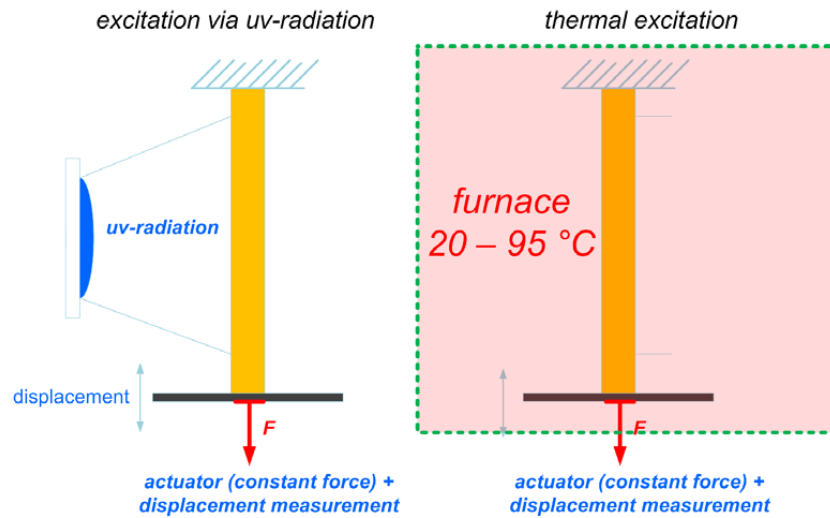


Figure 4. Measurement set-up for thermomechanical and photomechanical measurements

3.2 Weathering with artificial sunlight

For the use of LCEs in solar daylighting the material must not only withstand the interesting ultraviolet radiation in the range of 365 nm but also with the other parts of the ultraviolet radiation of the sun, that approximately begins at 300 nm. The problem now is to simulate this degenerative stress that is caused through the sunlight and especially to accelerate the long-time use of the material. For this case we orientate ourselves on a normative document [8]. The main question now is the time that is needed to simulate for example one year in a sunny region (e.g. Arizona). The starting point is the definition of the interesting wavelength range. Here we concentrate on the ultraviolet range, that causes photodegenerative stress in the region between 300 nm – 400 nm. For the reference-region we must know the dose of radiation in this range of sunlight that is applied to the material and then simulate this solar stress until the one-year dose is reached. Through the fact that the ultraviolet radiation in the range between 300 nm – 400 nm is set in the simulation to 60 W/m² we can calculate the time of artificial weathering for every region's individual dose. The practical aspects of weathering are described in [9]. The acceleration is only based on the fact that we simulate midday sun the whole time and cut off the nights and daytime with low sunlight. In this case we simulate approximately 8 months in a sunny region with an artificial weathering of 2 months. The only change of parameters concerns the effect of water. Here we use no spray due to the fact that the material is not exposed respectively protected against fog or rain in the latter application.

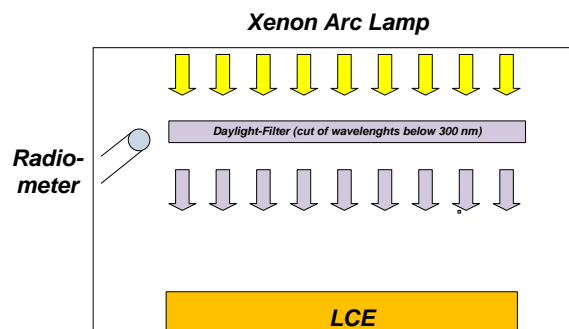


Figure 5. Testing chamber for artificial accelerated weathering

Within the project BIOSOL the POF-Team installed a SOLLEKTOR Monitoring station that logs important climate-data, for example the spectrum and dosage of sunlight respectively radiation. The interested reader will be referenced to [10].

4. Results and Discussion

The photomechanical measurements and the thermomechanical measurements reveal slight degeneration effects of the LCE. But no change of the crucial behaviour can be observed, neither the contraction nor the durability. The material shows a good contraction in the photomechanic as well as in the thermomechanic way before and after the weathering with an acceptable decrease of the contraction. Fig. 6. shows the photomechanic properties after the weathering experiment. The photomechanic properties before weathering were not measured in order to prevent a pre-damage caused by the ultraviolet-excitation process.

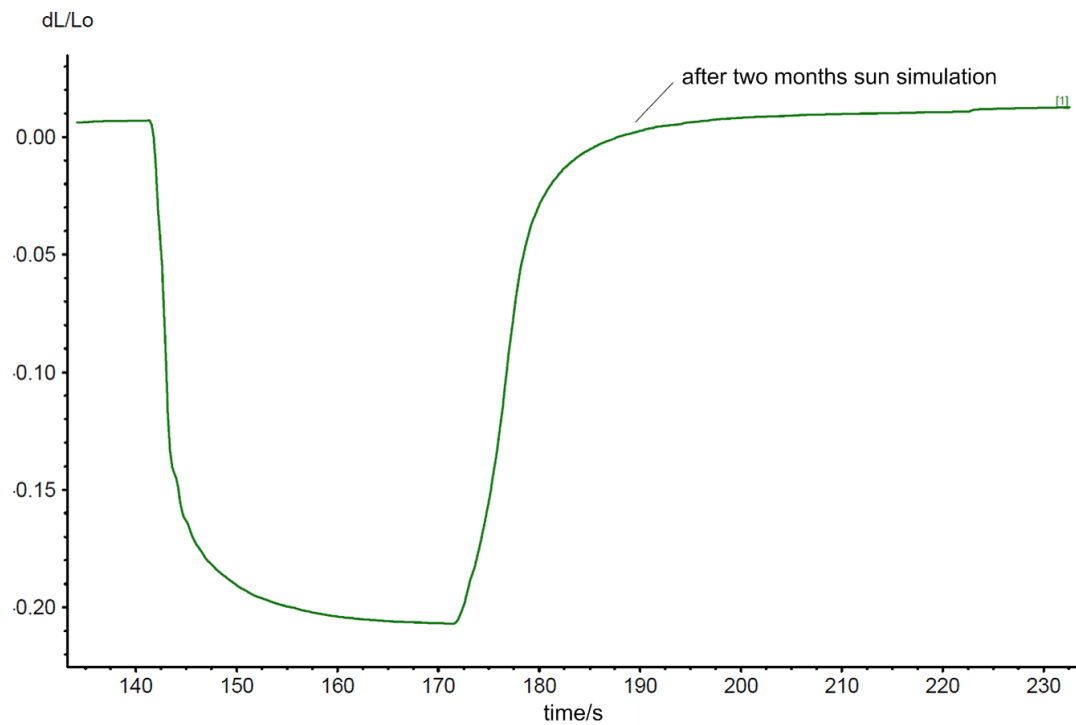


Figure 6. Photomechanical properties of the LCE after 2 months of sun simulation. The triggered photomechanic behaviour is recorded by measuring the time-dependent contraction (dL/L_0)

In fig. 7 the initial thermomechanic properties are displayed as well as after one month and after two months of sun simulation.

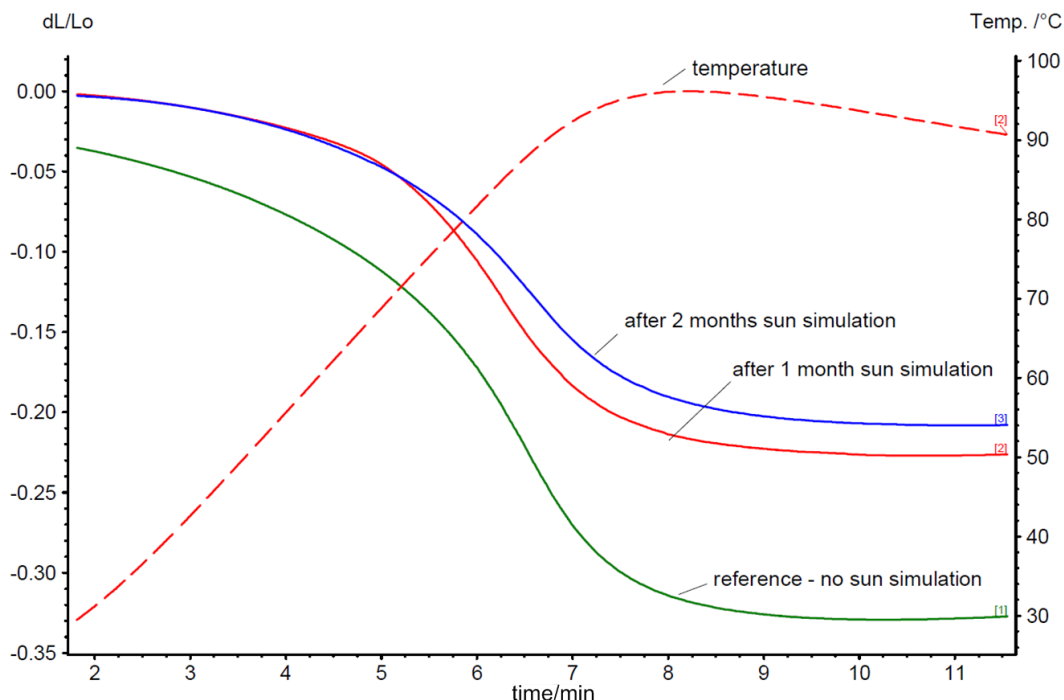


Figure 7. Thermomechanical properties of the LCE. The thermomechanic response is recorded by measuring the-time dependent contraction (dL/L0).

A possible reason for this positive result after the sun simulation may be the high inherent absorption of the material. The main part of the damaging ultraviolet radiation is filtered out in the first layers due to the azomesogens as a result of their high quantum yield, so the bulk-material is not affected.

5. Conclusion

Smart Materials opens up interesting fields of applications. In our case the direct transformation of photonic energy from the ultraviolet range triggers a reversible photocontraction. This photocontraction can basically be used to move or relocate a POF in respect to the focus area to enhance the efficiency of concentration optics, especially for daylighting with sunlight over POF. But this application is accompanied by special requirements, in particular the need for a defined characterization of the photomechanic response and the feature of the material to withstand the damaging parts of radiation of the sunlight. These two requirements were investigated. With the photomechanic characterization the design and dimensioning of a centering mechanism is possible. Furthermore the weathering experiments indicate a slight decrease of the maximum contraction capacity.

5. Acknowledgements

This work has been supported by BIONICUM, a project of Initiative Aufbruch Bayern, financed by Bavarian State Ministry of the Environment and Consumer Protection. The authors are very grateful for this support.

6. References

- [1] Zhao, Y., Ikeda, T., Smart Light Responsive Materials, Wiley-VCH, 2009
- [2] Warner, M., Terentjev, E. M., Liquid Crystal Elastomers, Oxford Clarendon Press, 2006
- [3] (a) Garcia-Amorós, J., Pinol, A., Finkelmann, H., Velasco, D., Org. Lett., Vol. 13, 9, 2011
(b) Sánchez-Ferrer, A., Merkalov, A., Finkelmann, H., Macromol. Rapid Commun., Vol. 32, 2011
- [4] (a) Speier Jr., J. L., US Patent 2 527 590, 1950
(b) Speier Jr., J. L., US Patent 2 527 591, 1950
- [5] Franke, C., Darstellung und Charakterisierung heliotrope Polymere, Master Thesis, Technische Hochschule Nürnberg, Germany, 2016
- [6] H. Poisel et al., "Daylighting with POF", 16th POF conference Turin/Italy, Sept. 10 –12, 2007
- [7] H. Poisel et al., "Energy Savings with daylight usage" , 20th POF conference, Sept. 14-16, 2011, Bibao/Spain
- [8] Deutsches Institut für Normung e. V., DIN EN ISO 4892: Künstliches Bestrahlen oder Bewittern in Geräten, Teil 1 und Teil 2, Beuth Verlag GmbH, 2009
- [9] Atlas Material Testing Technologies, Guidebook, 2010
- [10] Götz, Peter: Entwurf und Aufbau einer Monitoring-Station für das Tageslichtsystem SOLLEKTOR, Masterarbeit Master of Applied Research, TH Nürnberg, 28.05.2014

Demultiplexer for WDM Data Transmission over DSI-POF Based on a Concave Diffraction Grating

R. Kruglov^{1*}, L.V. Bartkiv², J. Vinogradov¹, O. Ziemann¹, Ya.V. Bobitski^{2,3}, H. Poisel¹

1 POF-AC, Technische Hochschule Nürnberg Georg Simon Ohm, Wassertorstrasse 10, 90489 Nuremberg, Germany

2 Department of Photonics, Lviv Polytechnic National University, 12 Stepana Bandery Str., 79013 Lviv, Ukraine

3 Department of Mechatronics and Automation, University of Rzeszów, ul. Stanisława Pignonia 1, 35-310 Rzeszów, Poland

*Corresponding author: roman.kruglov@pofac.th-nuernberg.de

Abstract: We report on a proposal for a WDM demultiplexer based on a commercially available concave aberration-reduced holographic diffraction grating. The demultiplexer has been tested for applications with a 1-mm core diameter step index POF (SI-POF) as well as double step index POF (DSI-POF). Applying offline-processed discrete multitone modulation, bit rates of 13.4 Gb/s and 19.2 Gb/s at a bit-error rate of 10^{-3} were achieved over 50-m SI-POF and DSI-POF, respectively.

1. Introduction

The implementation of wavelength-division multiplexing (WDM) technology in data transmission systems based on plastic optical fibers (POF) might overcome the major disadvantages of POF caused by the high attenuation and bandwidth limitation. Recent publications show that a development of WDM POF-based systems is impeded by the lack of commercial WDM components with corresponding characteristics at a reasonable price. The key element of those systems is an optical wavelength demultiplexer (DEMUX). During the last years several prototypes of demultiplexers based on interference filters and plane diffraction gratings were realized [1-5].

In this paper we offer a proposal for a DEMUX based on a commercially available concave aberration-reduced holographic diffraction grating (Newport's Richardson Gratings). A self-focusing grating allows to reduce the number of optical elements in DEMUX and thus, to decrease the insertion losses in the transmission system. The DEMUX has been tested for applications with step index profile POF (SI-POF) as well as double step index profile POF (DSI-POF). Data transmission over 50-m POF link was realized on the basis of a discrete multitone (DMT) modulation scheme.

2. Transmission setup

The WDM transmission link is shown in figure 1. It includes 5 spectral channels based on butt-coupled edge-emitting laser diodes (LD) operating at wavelengths of 405 nm, 442 nm, 490 nm, 515 nm and 660 nm.

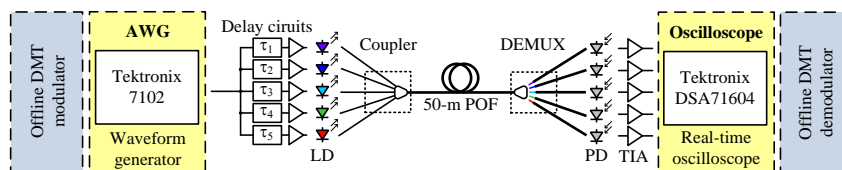


Figure 1. WDM transmission link with 5 spectral channels.

The LDs operating at 405 nm (DL-5146-101S, Sanyo), 442 nm (PL 450B, Osram Opto Semiconductors) and 660 nm (ADL-66505TL, Arima Lasers) are commercially available, whereas 490 nm and 515 nm devices are R&D samples produced by OSRAM Opto Semiconductors. Presently, OSRAM Opto Semiconductors offers these LDs as commercial products (PLT5 488, PLT5 510). The optical sources were directly driven over Bias-T with a modulation index of 0.9. An arbitrary waveform generator Tektronix 7102 with a resolution of 10 bits was used as a digital-to-analog converter.

As an optical multiplexer a fiber coupler was used [6]. It consists of seven 340- μm core-diameter SI-POFs arranged into a hexagon bundle and mounted into FSMA connector which can be connected easily to a 1-mm core diameter POF using FSMA coupling. For the measurements reported below five off-axis channels of the coupler were connected to the optical sources.

The demultiplexer is based on a commercially available concave holographic diffraction grating (Newport's Richardson Gratings) with a diameter of 29 mm and groove density of 664 mm^{-1} . A self-focusing aberration-reduced grating (see figure 2) brings an opportunity to minimize the number of optical elements in DEMUX and thus, to decrease potentially the insertion losses in the transmission system. As can be seen from figure 2, the optical setup with a concave grating provides a numerical aperture (NA) of about 0.18, which is smaller than NA of POF. But to the best of authors' knowledge, it was the most optimal choice among the gratings available on the market. The 1-m length output fibers Mitsubishi GH4001 located at the meridional focal plane of the concave grating were connected directly to optical receivers.

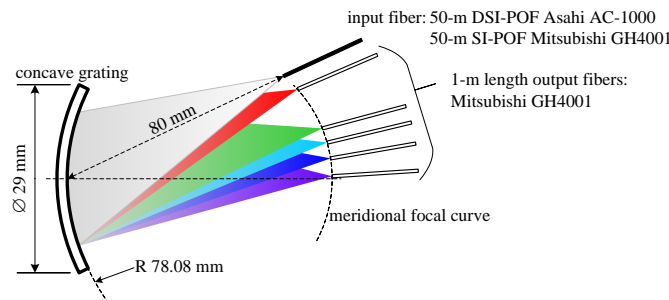


Figure 2. Optical layout of the demultiplexer based on a concave grating.

The receivers consist of $\varnothing 800\text{-}\mu\text{m}$ silicon pin photodiodes (Hamamatsu S5052) and trans-impedance amplifiers based on the commercially available components [7]. An acquisition of the received signal was carried out with a resolution of 8 bits by the real-time oscilloscope Tektronix DSA 71604. The algorithms for DMT signal construction, demodulation and error counting were realized offline, on the basis of MATLAB® software.

The performance of the 50-m length WDM transmission link was tested with two types of POF: SI-POF Mitsubishi GH4001 with NA of 0.5 and DSI-POF Asahi AC-1000 with NA of 0.32. Using the POF with a low NA brings an opportunity to reduce the losses in the transmission system and increase the overall 3-dB bandwidth.

3. Measurement results

The DEMUX was tested first with six LDs operating at the wavelengths of 405 nm, 442 nm, 459 nm, 490 nm, 515 nm and 660 nm [6]. Figure 3a shows the output spot diagram in the image plane with Asahi AC-1000 as an input fiber for DEMUX. The contours of the output fibers are marked with the white dashed circles. As can be seen from Figure 3a, the spots of the 442-nm and 459-nm channels overlap which leads to crosstalk distortions.

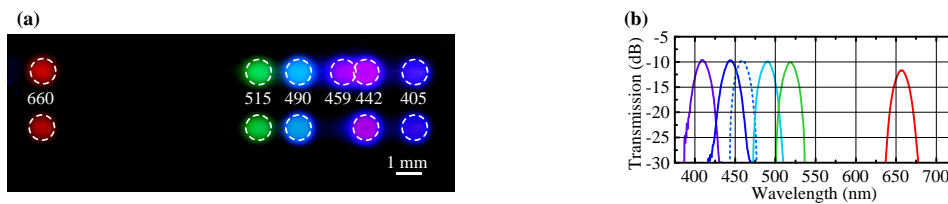


Figure 3. Transmission characteristics of the demultiplexer with DSI-POF Asahi AC-1000 as an input fiber: output spots in the imaging plane for six and five spectral channels (a); measured transmission spectra of the wavelength channels (b).

The measured transmission spectra of DEMUX shown in figure 3b confirm the poor crosstalk suppression between the channels mentioned; therefore 459-nm channel was excluded from the transmission system. The crosstalk suppression between 5 remaining channels exceeds 25 dB. Using the SI-POF Mitsubishi GH4001 as input fiber increases the insertion losses by 1-1.5 dB/channel which is caused by higher NA incompatibility.

Table 1. Operation parameters of the transmission link.

Spectral channel, nm	LD reference	Fiber-coupled power*, dBm		Received power, dBm		Occupied signal bandwidth, MHz		Net bit rate at BER=10 ⁻³ , Gb/s	
		SI-POF	DSI-POF	SI-POF	DSI-POF	SI-POF	DSI-POF	SI-POF	DSI-POF
405	DL-5146-101S	12.8	12	-9.2	-6.8	609.4	882.8	2.55	4.01
442	PL 450B	14	13.2	-6.6	-4	728.1	980.5	3.32	4.66
490	R&D OSRAM	11.5	10.7	-8.1	-6.1	712.5	953.1	3.16	4.36
515	R&D OSRAM	9.3	9	-9.3	-9.2	665.6	839.8	2.66	3.57
660	ADL-66505TL	12	11.4	-15.3	-14	500	756.1	1.71	2.62

* - measured after 1-m length POF connected to the coupler.

The data transmission tests were carried out with a DMT which provides high operation flexibility and bandwidth utilization. A pseudo-random binary sequence (PRBS 2¹⁵-1) was mapped to a DMT signal according to Chow's rate adaptive bit loading algorithm [8]. The maximum number of subcarriers was set to 256 with a subcarrier spacing of 3.125 MHz and 3.9 MHz for SI-POF and DSI-POF optical link, respectively. DMT frames were generated with a cyclic prefix of 3.125% and clipping level of 9.5 dB. Parameters of the DMT signals as well as optical power levels along the transmission link are shown in Table 1.

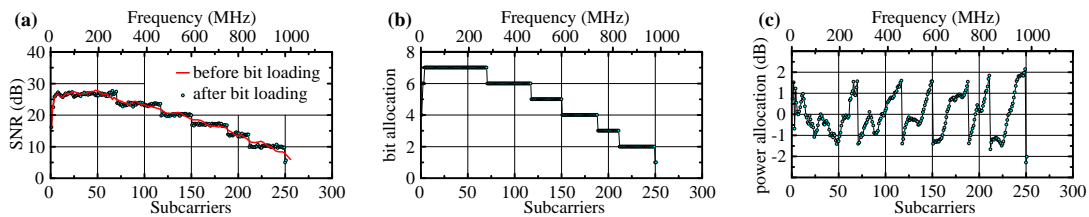


Figure 4. Parameters of the DMT signal transmitted over 442-nm spectral channel of DSI-POF optical link: measured SNR per subcarrier before and after bit loading (a); bit-loading scheme (b); power allocation (c)

The net bit rates shown in Table 1 were obtained after deduction of the DMT transmission overhead. Thus, the aggregate bit rates of 13.4 Gb/s and 19.2 Gb/s were achieved at a bit-error rate of 10⁻³ over 50 m SI-POF and DSI-POF optical link, respectively. If 7% forward error correction (FEC) overhead [9] is applied, the bit rates of 12.5 Gb/s and 17.9 Gb/s can be provided over the corresponding types of POF.

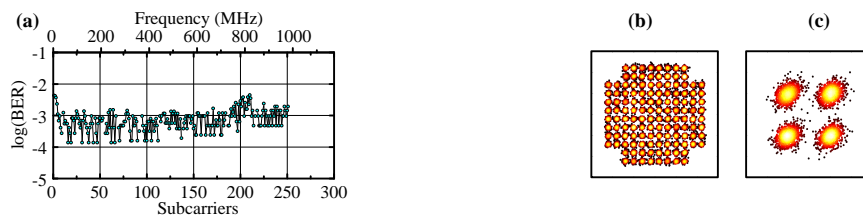


Figure 5. BER per subcarrier (a) and received constellations for subcarrier groups modulated with 128-QAM (c) and 4-QAM (d) for 442-nm channel of DSI-POF optical link

As an example, the basic transmission parameters of the DMT signal transmitted over 442-nm spectral channel of DSI-POF optical link are shown in figure 4: SNR per subcarrier before and after applying the bit loading algorithm, bit-loading scheme and power allocation.

Figure 5 shows the BER per subcarrier and received constellations for the 442-nm channel DSI-POF optical link. A better performance of the DSI-POF optical link is connected with both higher signal levels at the receiver and a wider 3-dB bandwidth of the fiber.

4. Conclusion

We demonstrated a proposal for the WDM demultiplexer based on a commercially available concave aberration-reduced holographic diffraction grating. The DEMUX has been tested as a part of the WDM transmission link with 50-m length SI-POF as well as DSI-POF. The spectral resolution of the diffraction grating was high enough to provide five spectral channels operating at 405 nm, 442 nm, 490 nm, 515 nm and 660 nm with sufficient crosstalk suppression. A bit rate of 13.4 Gb/s was achieved over 50-m SI-POF at BER of 10^{-3} . This result outperforms a previous publication [10] by a factor of 2. The transmission link based on 50-m DSI-POF provides a capacity of 19.2 Gb/s.

5. Acknowledgements

The POF-AC Nürnberg is a project of the Hightech Offensive Bavaria. The work was supported by the Bavarian Ministry of Education, Culture, Science and Art and the European Regional Development Fund inside the Project "OHM-Netze" (No. EU-1607-0017). The authors would like to thank OSRAM Opto Semiconductors, Regensburg, Germany, for providing the R&D samples of the laser diodes.

6. References

- [1] Joncic M, et al. Four-channel WDM transmission over 50 m SI-POF at 14.77 Gb/s using DMT modulation. *IEEE Photon. Technol. Lett.* 2014; 26(13):1328-1331.
- [2] Kruglov R, et al. 21.4 Gb/s Discrete multitone transmission over 50-m SI-POF employing 6-channel WDM. In: *Proc. OFC 2014, 9-13 March 2014, San Francisco, CA.* 2014:Th2A.2.
- [3] Attia R, et al. Wavelength multiplexing and demultiplexing for plastic optical fibres using diffraction grating. In: *Proc. of 5th Int. Conf. on Plastic Optical Fibers, 22-24 October 1996, Paris, France.* 1996:78-82.
- [4] Tschekalinskij W, et. al. Low-cost multiplexer and demultiplexer for POF. In: *Proc. of 11th Int. Conf. on Plastic Optical Fibers, 18-20 September 2002, Tokyo, Japan.* 2002:139-140.
- [5] Junger S, et. al. Video distribution and multimedia transmission systems for home networks. In: *Proc. of 12th Int. Conf. on Plastic Optical Fibers, 14-17 September 2003, Seattle, WA.* 2003:237-239.
- [6] Kruglov R, et al. 10.7 Gb/s WDM Transmission over 100-m SI-POF with Discrete Multitone. In: *Proc. OFC 2016, 20-22 March 2016, Anaheim, CA.* 2016:W4J.5.
- [7] Vinogradov J, et al. -22 dBm receiver sensitivity for Gbit/s data communication on SI-POF and glass fiber. In: *Proc. of 14th Int. Conf. on Plastic Optical Fibers, 19-22 September 2005, HongKong, China.* 2005:255-259.
- [8] Chow PS, Cioffi JM, Bingham JAC. A practical discrete multitone transceiver loading algorithm for data transmission over spectrally shaped channels. *IEEE Trans. Commun.* 1995;43(2/3/4):773-775.
- [9] International Telecommunication Union. ITU-T Recommendation G.975.1. *Forward error correction for high-bit rate DWDM submarine systems.* Geneva; 2004.
- [10] Friedrich K, et al. Application of concave diffraction gratings for WDM transmission over polymer optical fibers. In: *Proc. of 24th Int. Conf. on Plastic Optical Fibers, 22-24 September 2015, Nuremberg, Germany.* 2015:104-109.

Analysis of Light Scattering in Polymer Optical Fibres using Mie Theory: An Analytical Approach

E. Nkiwane^{1*}, T .Becker¹, M .Gehrke¹, O. Ziemann¹, B .Schmauss²

1: Polymer Optical Fiber Application Center, Technische Hochschule Nürnberg, 90489 Nürnberg, Germany

2: Institute of Microwaves and Photonics (LHFT), Friedrich Alexander University Erlangen Nürnberg, 91054, Germany

*Corresponding author: emmanuel.nkiwane@th-nuernberg.de

Abstract: It is important that POF optical characteristics are fully understood. This assists in the design of optimal POF based systems. Experiments carried out at the Polymer Optical Fibre Application Centre in Nuremberg have shown that the far field distribution of POF is wavelength dependant [1]. The far field for lengths up to 200 m was measured for different wavelengths, launch conditions and fibre samples. For all samples a sharp peak can be observed for shorter wavelengths. In this paper we present simulation results including particle scattering with-in POF based on Mie theory. These results give insight into the scattering characteristics at the particle level inside POF. The model will be scaled to simulate volume scattering and the influence of scattering on the far field distribution.

Key words: Mie theory, Rayleigh, scattering, Far Field distribution, Cross section, Phase function.

1. Introduction

The motivation of this paper is based on far field distribution experiments that were recently carried out at the Polymer Optical Fibre Application Centre (POF-AC) in Nuremberg, Germany [1]. The far field distribution for various wavelengths was observed to be different as seen in figure 1.

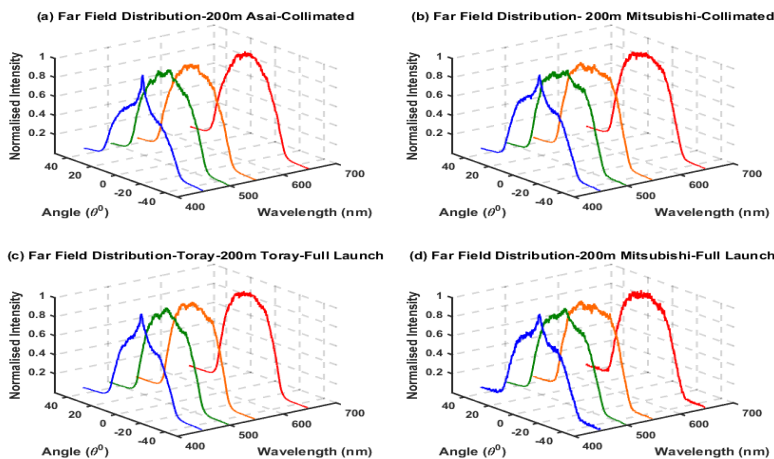


Figure 1. Far field distribution for different wavelengths, launch conditions and POF samples

It can clearly be seen that for shorter wavelengths a sharp peak at low propagation angles is visible for longer fibre lengths. In this paper we present simulation results of particle light scattering in POF based on Mie theory. This particle scattering model will be extended to a volume scattering model which will be used to simulate the scattering dependent far field in POF. In the first section relevant Mie theory concepts will be

discussed. In the second section the simulation results will be presented followed by a discussion, conclusion and outlook in the third section.

2. Theoretical Background

Scattering occurs when electromagnetic radiation interacts with the molecules of an object and energy is reradiated in all directions. Molecules contain charges and when electromagnetic radiation interacts with the object, it causes the charges within its molecules to oscillate at the same frequency as the incident radiation, resulting in charge separation. The charge separation is referred to as an induced dipole moment [2, 3]. The oscillating dipole moment radiates light in all directions which we refer to as scattered light [2, 3] as seen in figure 2

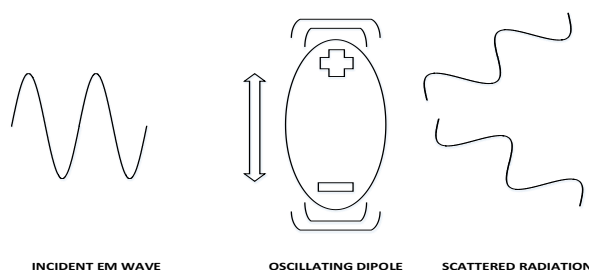


Figure 2. Oscillating dipole moment reradiating electromagnetic radiation

Besides scattering also absorption will take place. Both scattering and absorption result in extinction which is the attenuation of light due to interaction with an object [2]. After propagating a particular distance l , the irradiance of the electromagnetic wave can be represented as

$$I_t = I_i e^{-\alpha_{ext} l} \quad (1)$$

Where I_t is the transmitted irradiance, I_i is the incident irradiance and α_{ext} is the total extinction which is given as

$$\alpha_{ext} = \eta (C_{abs} + C_{sca}) \quad (2)$$

Where η is the number of particles per unit volume, C_{abs} is absorption cross section and C_{sca} is the scattering cross section. The cross section is a value that quantifies the probability of an event (absorption or scattering) occurring. Both scattering and absorption contribute to attenuation of light but in different scenarios one can dominate the other contributing more to reduction of irradiance. Scattering also determines the intensity distribution as it results in the redistribution of light intensity into different directions. Understanding the scattering phenomenon of POF at the particle level allows for the understanding of how it contributes or affects the shape of the intensity distribution.

Scattering can be divided into two distinct categories. Rayleigh scattering which refers to the scattering that occurs when the particle size is smaller than (at least one tenth) the size of the wavelength of the incident radiation [2, 3, 4].

The second category is Mie scattering. Mie scattering refers to scattering that occurs when the particle size is comparable to the wavelength of the incident radiation [2, 3, 4]. Mie theory is the mathematical formulation that gives the solution for the scattering of electromagnetic radiation by a sphere. However, there is no particle size limitation in this theory hence it can be used to describe Rayleigh scattering [2, 3]. In this paper, the particle scattering results presented for Mie and Rayleigh scattering are based on Mie theory which is comprehensive enough to describe the two distinct scattering regimes.

2 Mie Theory

The electric field that is scattered by a particle can be represented as

$$E_{sca} = \frac{\exp(-ixR+ikz)}{ixR} \begin{bmatrix} S_2 & S_3 \\ S_4 & S_1 \end{bmatrix} E_{inc} \quad (3)$$

Where $x = \frac{2\pi n}{\lambda}$ is the size parameter, k the propagation constant and R is the distance to the observation point

To obtain the scattered electric field, the amplitude scattering matrix, $\begin{bmatrix} S_2 & S_3 \\ S_4 & S_1 \end{bmatrix}$, must be computed first [2]. It gives the relationship between the amplitude and phase of the incident and scattered electric fields and it is calculated for each scattering angle. Its elements are calculated from the formulae

$$S_1(\theta) = \sum_n \frac{(2n+1)}{n(n+1)} (a_n \pi_n + b_n \tau_n) \quad (4)$$

$$S_2(\theta) = \sum_n \frac{(2n+1)}{n(n+1)} (a_n \tau_n + b_n \pi_n) \quad (5)$$

$$S_3(\theta) = S_4(\theta) = 0 \quad (6)$$

a_n and b_n are the scattering coefficients [2]. They determine how scattering depends on both size and wavelength. They are calculated from the formulae

$$a_n = \frac{m\psi_n(mx)\psi'_n(x) - \psi_n(x)\psi'_n(mx)}{m\psi_n(mx)\xi'_n(x) - \xi_n(x)\psi'_n(mx)} \quad (7)$$

$$b_n = \frac{\psi_n(mx)\psi'_n(x) - m\psi_n(x)\psi'_n(mx)}{\psi_n(mx)\xi'_n(x) - m\xi_n(x)\psi'_n(mx)} \quad (8)$$

Where m is the relative refractive index of the medium, x is the size parameter, ψ_n and ξ_n are Ricatti –Bessel functions [2] which are calculated as

$$\psi_n(x) = xj_n(x) \quad (9)$$

$$\xi_n(x) = -xy_n(x) \quad (10)$$

Where $j_n(x)$ and $y_n(x)$ are Spherical Bessel functions

The angle dependent functions τ_n and π_n determine the angle dependency of the amplitude scattering matrix elements [2] hence they directly determine the angular dependency of the scattered electric fields. They are calculated from the formulae

$$\pi_n = \frac{2n-1}{n-1} \mu \pi_{n-1} - \frac{n}{n-1} \pi_{n-2} \quad (11)$$

$$\tau_n = n\mu\pi_n - (n+1)\pi_{n-1} \quad (12)$$

Where $\mu = \cos \theta$

Both angular dependent functions are calculated using upward recurrence where the current term is computed using the values of the last two terms. For this computation $\pi_0 = 0$ and $\pi_1 = 1$. To obtain a sufficiently accurate result the number of terms to be computed for the series summation of the amplitude scattering matrix elements is given by $x = 4x^3 + 2$ where x is the size parameter.

The scattering cross section is computed from the scattering coefficients [2] as follows

$$C_{sca} = \frac{2\pi}{x^2} \sum_n (2n + 1) (|a_n|^2 + |b_n|^2) \quad (13)$$

From the formulae it is evident that C_{sca} depends on the particle size and wavelength as a_n and b_n depend on both. The angular dependent scattering (phase function) is obtained by plotting the differential scattering cross section for all the given angles. The differential scattering cross section quantifies the energy scattered per unit time into a solid angle in a particular direction. It is given by

$$\frac{dC_{sca}}{d\Omega} = \frac{|S_1|^2 + |S_2|^2}{x^2} \quad (14)$$

The most important quantities that should be computed to evaluate particle scattering are the angle dependant scattering (phase function) and the scattering cross section.

3 Results

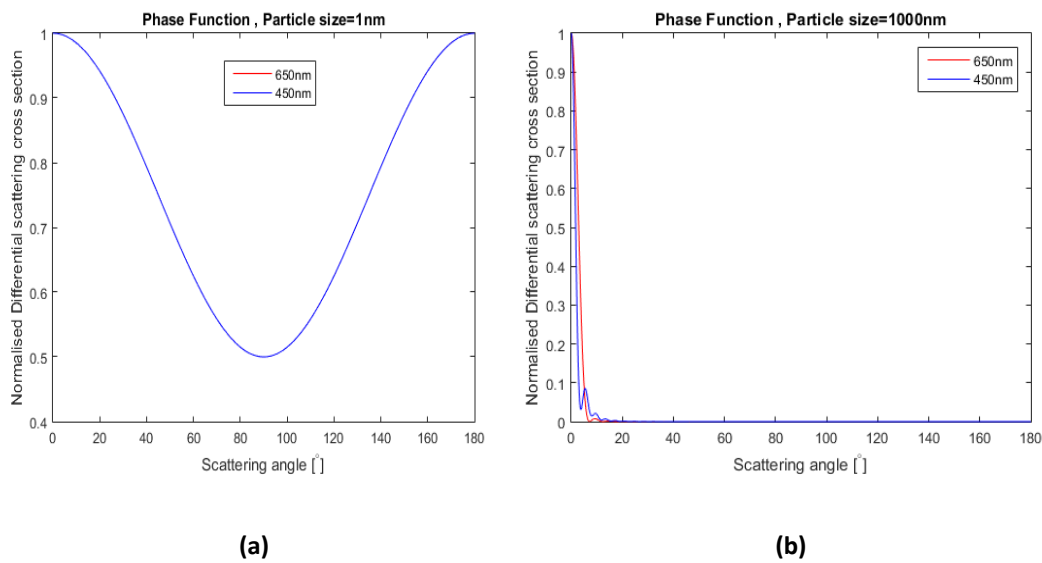


Figure 3. Simulated (Matlab) angular scatter distribution for different wavelengths and particle sizes (1 nm and 1000 nm) for a POF particle

Figure 3 (a) is the simulated scattering distribution for particle sizes with in the Rayleigh regime. As seen the forward and backward scattered intensity is the same, that is, the angular scattering is symmetric. This is because for small particle sizes the angular dependant functions have forward and backward lobes which are weighted equally resulting in a symmetric angular distribution. As the particle size increases (Mie Regime) the scattering distribution becomes asymmetric with more intensity being scattered in the forward direction as seen in Figure 3 (b). This can be attributed to the fact that as the particle size increases the angle dependant functions with a dominant forward lobe are weighted more resulting in a narrower forward scattered peak.

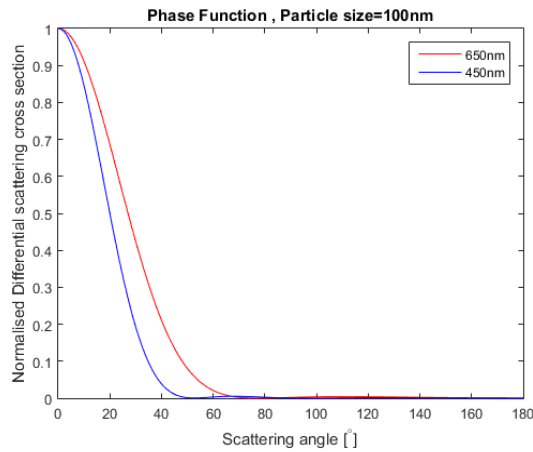


Figure 4. Simulated angular scatter distribution for different wavelengths and particle of 100 nm

It can be seen that as the particle size increases the angular distribution becomes more forward directed as seen in Figure 4 (from the Rayleigh to the Mie scattering regime). The far field distribution of a standard PMMA POF was simulated using a model developed with the optics simulation package Light tools. In this model scattering was taken into account only at the core cladding interface and it was implemented using package functions based on Mie theory. The reason for having scattering only at the core cladding interface was that the core scattering computations were very time consuming and simulating just one step for different wavelengths and particle sizes took a very long time hence the need to have a self-developed model that is much more efficient which would make it easier to simulate the far field distribution with both core and core cladding interface scattering. The preliminary results for far field simulations done with Light tools are displayed below

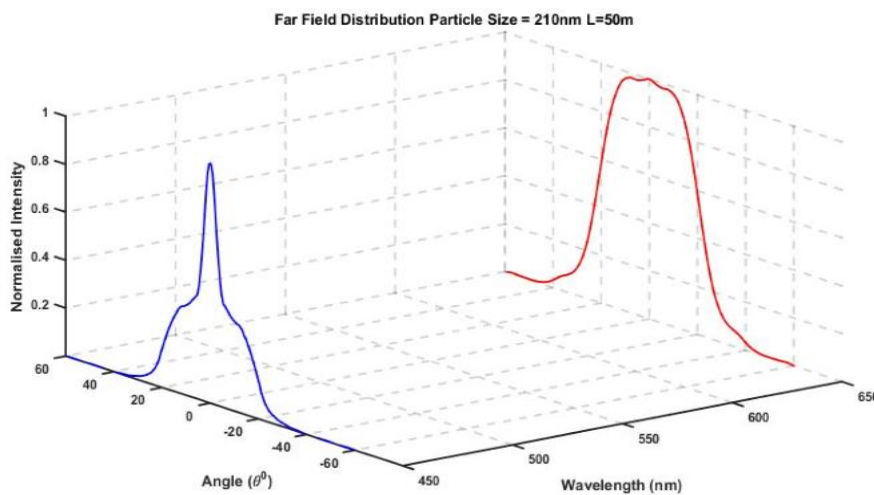


Figure 5. Simulated far field distribution for 50 m, two wavelengths (450 nm, 650 nm) and a particle size of 210 nm [4].

From the diagram it can be seen that there is a peak that develops with distance for shorter wavelengths. This can be attributed to the fact that the forward lobe for shorter wavelengths is narrower as seen in Figure 4 and

also the scattering cross section which is inversely proportional to the scattered intensity is much higher. It can be assumed that at the core cladding interface most of this forward scattered intensity is coupled into the lower order modes which result in this peak for shorter wavelengths.

3. Conclusion and Outlook

Scattering influences the far field distribution in PMMA POF. Mie theory can be used to model scattering and it can be extended to find solutions for volume scattering. The next step is to develop a full volume scattering model based on the particle scattering model to simulate the far field distribution in POF with both core and core cladding interface scattering.

3. Acknowledgements

The POF-AC Nürnberg is a project of the High-tech Offensive Bavaria.

The work was supported by the Bavarian Ministry of Education, Culture, Science and Art and the European Regional Development Fund inside the Projects "Optika" (No. F1116.NÜ/13) and "OHM-Netze" (No. EU-1607-0017).

4. References

1. E. Nkiwane, S Loquai, A. Bachmann, O. Ziemann, B. Schmauss, "Evolution of the Far Field Distribution for Different Wavelengths in Step Index Polymer Optical Fibers" , POF Conference, 2015.
2. C-F. Bohren, D-R. Huffman, "Absorption and Scattering of Light by Small Particles" , Wiley-VCH Verlag GmbH & Co, 2004
3. D-W Hahn, "Light Scattering Theory", University of Florida, 2009
4. C-A Bunge, R .Kruglov, H .Poisel, "Rayleigh and Mie Scattering in Polymer Optical Fibers", Journal of Lightwave Technology Vol24, 2006.



Improving OTDR Spatial Resolution using signal processing based on Power Flow Equation simulation data

M. Gehrke^{1*}, B. Schmauss², T. Becker¹, E. Nkiwane¹ and O. Ziemann¹

1 Polymer Optical Fiber Application Center, Technische Hochschule Nürnberg, 90489 Nürnberg, Germany

2 Institute of Microwaves and Photonics (LHFT), Friedrich-Alexander-Universität Erlangen-Nürnberg, 91054 Erlangen, Germany

*Corresponding author: martin.gehrke@th-nuernberg.de

Abstract: This paper presents a possibility of improving the spatial resolution of Optical Time Domain Reflectometer (OTDR) measurement data of large core step-index polymer optical fibers (POF) using signal processing based on time-dependent simulations. During its propagation along the fiber a Dirac signal, which is used to obtain such measurements, is subjected to influences caused by the fiber like modal dispersion, attenuation and scattering. These propagation effects lead to an impulse broadening along the fiber, which in turn limits the spatial resolution of the measurement itself. In order to improve the precision without influencing other aspects of the measurement device, such as the sensitivity, specific signal processing can be applied to the measurement data in order to negate or at least minimize the fiber influences. The required simulation data used for these operations is obtained using the power flow equation.

1. Introduction

Investigating optical links in order to verify their respective transmission quality has been an area of interest for as long as optical connections have been established. In the beginning, verifying reliable light transmission of the optical medium of long haul telecom data transmission links has been the focus of these measurement devices. Different measurement options to obtain fiber loss have been developed over time. One of these devices is the OTDR, which enables the measurement of fiber or connector losses in addition to the ability to locate physical damage to an optical fiber using only one end of the optical link. [1]

Since POF are primarily used in either sensing applications or for short distance data communication in home or automotive applications the need for affordable measurement equipment designed specifically for the requirements of POF has been of importance as well. Due to the higher attenuation and dispersion of POF the measurement resolution of OTDR devices is inherently limited. In this paper a method to improve those qualities post-measurement is proposed using simulation data as it was previously hinted at in [2].

This work first briefly describes the basic concept of OTDR operation and the required underlying theoretical background since this is the main topic this work applies to. Secondly we describe the simulation model which was used to obtain the required frequency and impulse responses of POF. It is based upon Gloge's power flow equation [3] solved numerically [4] which yields reasonably accurate predictions of the angular and temporal power distributions of POF. This is a continuation of previous research performed by [5] and [6]. Afterwards we explain the deconvolution algorithm which is used to improve the spatial resolution of OTDR. In the fourth chapter we show several OTDR measurements on specific fibers before and after applying our improvement algorithm in order to quantify the gained improvement. In the fourth chapter the obtained results are discussed and the performance of the algorithm is evaluated. In the end a summary is provided and an outlook towards future work is given, especially in regards to possible applications.

2. Basics of OTDR

This chapter gives a brief description of the basic principle of OTDR measurements and the physical cause of the effects which are used to obtain the respective data.

During this measurement procedure a narrow light pulse is coupled into the fiber under test using a Y-coupler. While the pulse is propagating along the fiber it interacts with the molecules inside the transmission medium which in turn leads to the incurrence of different interplay effects. These include, but are not limited to Fresnel reflections, Rayleigh scattering, Mie scattering and Raman scattering.



From a power level perspective the most significant signals are the Fresnel reflections, which occur at places of significant refractive index differences like defects, connectors or the ends of the fiber. Inside the core however the most significant effect is Rayleigh scattering [7]. It is created by interactions between the electromagnetic field of the propagating light pulse and the density fluctuations of the core material. These are caused by the slightly irregular composition of the core itself, which in turn leads to small refractive index differences. Thus the excited chain molecules oscillate with the same frequency as the incident wave, which is by definition a quasi-elastic scattering process. The absorbed energy is subsequently radiated in all directions uniformly. All amorphous materials like polymers show this intrinsic process. [8]

All signals which are captured and thus transmitted backwards by the fiber are guided to a receiver through the Y-coupler and are afterwards logged. This essentially completes the working principle of an OTDR, which is shown in figure 1a. Using the equation

$$z = 0.5 \cdot \frac{c}{n} \cdot t, \tag{2.1}$$

the distance z from the beginning of the fiber of each recorded event can be obtained using the recording delay t and the vacuum speed of light c , if the refractive index n of the fiber is known [9]. A graph depicting power over time can thereupon be given. A theoretical example, in which measurable occurrences (reflections, connectors, damages and Rayleigh scattering) are highlighted, is given in figure 1b.

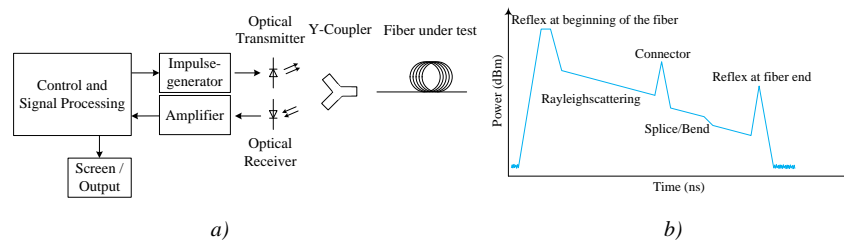


Figure 1. Schematic (a) and exemplary trace (b) of an OTDR

The spatial resolution ΔL is generally given by the duration of the launched pulse τ . In order to achieve the desired resolution the condition

$$\tau \leq \frac{2n\Delta L}{c} \tag{2.2}$$

has to be met. Since the total backscattered power which defines the signal to noise ratio (SNR) of the device is given by the well known formula [10]

$$P_{bs} = \frac{S\alpha_{Rayleigh}P_0\tau v_g}{2} \cdot e^{-2\alpha z}, \tag{2.3}$$

one can instantaneously see the conflict which is automatically incurred. The fiber constants of captured refracted power ratio S , the group velocity v_g and both the Rayleigh attenuation $\alpha_{Rayleigh}$ as well as the total fiber attenuation α cannot be modified. Thus the only possible ways to influence the resolution or the SNR are the launched power and the impulse duration, which are both limited by the constraints of the used light source. Both factors of course inversely influence each other.

3. Simulation Model

In this chapter the mathematical derivation of a numerical solution of the time-dependent power flow equation is provided briefly. It has been shown previously in [4] and different but similar solutions have previously been given by Losada et. al. [11] and Breyer [12].

In order to describe the distribution of the electromagnetic field inside a fiber, which is caused by propagating light, this work uses the term mode. This term commonly references an assumed light ray which travels along



the fiber with a certain propagation angle, which is defined by the ray's direction in relation to a line parallel to the fiber axis. In the following this angle is called θ . A graphical depiction of the concept can be seen in Snyder [13] or Becker et al. [14].

3.1 Fundamental derivation of the power flow equation

In order to accurately model scattering and absorptions processes of multimode fibers Gloge [15] has derived the power flow equation including two functions representing modal attenuation and diffusion to approximate the physical effects which define the angular and temporal behavior of the fiber when regarded as a transmission system. This kind of simulation can be applied as an alternative to the classical solution of the wave equations which proves difficult for million mode fibers or to raytracing which requires significant processing power. The basic form of the power flow equation is given by:

$$dP = -\alpha(\theta)Pdz + \frac{1}{\theta} \cdot \frac{\partial}{\partial \theta} \cdot \left(\theta \cdot D(\theta) \cdot \frac{\partial P}{\partial \theta} \right) dz \quad (3.1)$$

The modal attenuation is given by $\alpha(\theta)$ and the mode coupling between neighboring modes is described by $D(\theta)$. A temporal dependency can be introduced to equation (3.1) by accounting for the different zigzag travel paths different modes are subjected to inside a fiber depending on their propagation angle.

If P is function of time and angle, equation (3.1) can be rewritten using the total differential and furthermore applying a relative path length relation to obtain the classical time-dependent power flow equation

$$\frac{\partial P(\theta, z, t)}{\partial z} = -\alpha(\theta)P(\theta, z, t) - \frac{n}{c \cdot \cos(\theta)} \cdot \frac{\partial P(\theta, z, t)}{\partial t} + \frac{1}{\theta} \cdot \frac{\partial}{\partial \theta} \cdot \left(\theta \cdot D(\theta) \cdot \frac{\partial P(\theta, z, t)}{\partial \theta} \right). \quad (3.2)$$

Equation (3.2) has been solved numerically both in the time [4] as well as the frequency domain by applying the Fourier transform to eliminate the time dependency [7,8]. The result is given in equation (3.3) which shows the possibility to obtain the power distribution $P_n(\theta, z + \Delta z, t)$ of the next distance step including both angular and temporal dependencies by using the propagation matrix T and the previously given power distribution $P(\theta, z, t)$:

$$\underline{P}_n(\theta, z + \Delta z, t) = \underline{T} * \underline{P}(\theta, z, t) \quad (3.3)$$

The end result yields a mathematical model which can be used to simulate the behavior and development of arbitrary power distributions along the course of a fiber. Different lengths can be considered by repeatedly executing the explained process until the desired length has been reached.

3.2 Deconvolution Algorithm

For the purpose of the signal processing explained in this paper a fiber of a specific length can be simplified and thus regarded as a transmission system in the classical sense of a linear time-invariant system, where the input $X(j\omega)$ and output $Y(j\omega)$ of said system can be correlated with the transfer function $G(j\omega)$ using equation (3.4):

$$Y(j\omega) = G(j\omega) \cdot X(j\omega) \quad (3.4)$$

The output signal of a certain length of an ideal, i.e. not damaged, cracked or bent, fiber can be obtained using the solution the power flow equation given in equation (3.3) with respect to the input signal. By matching the simulation input to actual OTDR measurement constraints (pulse shape of the used system) the ideal measurement result can be predicted. However actual measurement will inevitably not match perfectly since real world applications usually are not identical to laboratory conditions and the simulation result is based upon perfect reflection conditions which do not apply to the measurement as well.

This can be used to gain an advantage for an improvement of the measurement data. By removing the basic transmission characteristics of the ideal fiber like modal dispersion from the measurement results one is essentially left with the result of other effects impacting the propagating impulse. This can be done by deconvolving the measurement data with the simulation data. If this process is performed in the frequency



domain the convolution becomes a trivial division of the measured output signal $Y_{measured}(j\omega)$ by the simulated transfer function $G_{sim}(j\omega)$:

$$Y_{decon}(j\omega) = \frac{Y_{measured}(j\omega)}{G_{sim}(j\omega)} \quad (3.5)$$

In an ideal case the resulting deconvoluted signal $Y_{decon}(j\omega)$ would be identical to the launched pulse. However even in real measurements, where the measured pulse is also influenced by imperfections not covered by the simulations, a significant improvement regarding the spatial resolution can still be achieved by minimizing the pulse broadening inherent to multimode fibers.

4. Measurements and results

In this chapter a couple of measurements taken with a commercially available *Luciol LOR* OTDR will be presented. It is based on a 650 nm red laser diode with a fixed pulse width of 1 ns. Afterwards we apply the aforementioned deconvolution algorithm based on simulation data using current coefficients [16] to the measurement data and compare the results.

The first measurement in figure 2a shows the fiber end reflex of a Mitsubishi Eska GH 1 mm step index POF at 100 m. Since the *Luciol* OTDR is a high quality device and features a high sensitivity detector with significant dynamic range the quality of such a measurement is usually very accurate with regards to noise level. In order to show the possibilities of the deconvolution process for less than ideal measurement conditions the measurement has been intentionally negatively influenced by adding a noise floor with ambient light and by removing any averaging processes of the measurement device. However the pulse broadening of the POF can still clearly be seen albeit with a certain degree of underlying noise. The graph is shown in normalized units with an arbitrary baseline. The axis of abscissas shows the one way delay of the reflected light. For a significant improvement in usability the deconvolution process can increase the readability of the measurement output. A corresponding simulation of an input impulse of 1 ns for the same fiber and length has been performed using the power flow equation (equation (3.3)) and can be seen in figure 2b.

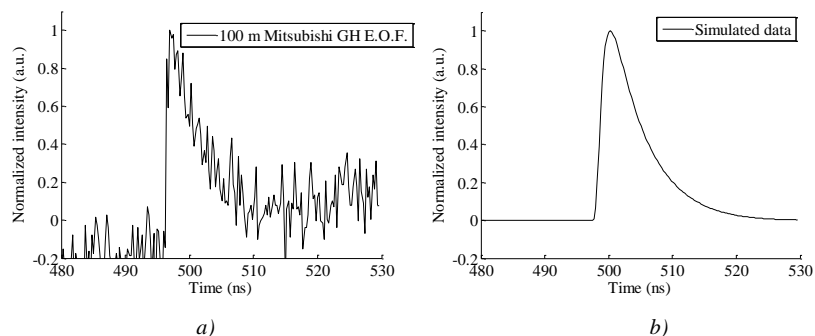


Figure 2. Fiber end reflex measured with *Luciol* OTDR after 100 m Mitsubishi Eska GH fiber (a) and corresponding simulation data (b)

As previously explained this simulation result can be used to deconvolve the measurement using equation (3.5). This minimizes the fiber influence and the result is a much narrower and thus significantly more defined impulse, which clearly shows the end of the fiber as it is depicted in figure 3a. Further improvements could be achieved for example by applying a form of noise reduction to the obtained measurement data. For visualization purposes all three graphs are depicted simultaneously in figure 3b.

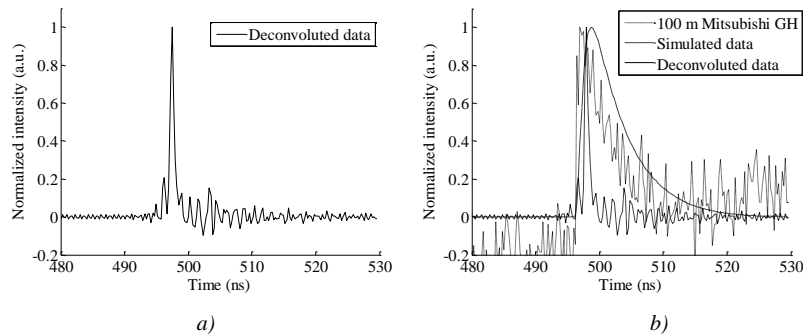


Figure 3. Deconvoluted measurement (a) and superposition of the processed data (b)

In order to visualize the improvement more clearly one can obtain a different measurement with significantly increased complexity. In this measurement we use a 0.5 m fiber connected to 100 m fiber. Both fibers are Mitsubishi Eska GH. Due to the increased pulse width caused by dispersion along the fiber the two end reflexes cannot be recorded separately and thus distort each other up to a degree, where it is very difficult to discern the two even with the knowledge of their existence. This is especially obvious if the usual presentation, in which the power level is plotted in decibel (dB), is used. A double impulse cannot be seen clearly in figure 4a.

After simulating the appropriate impulse response and subsequently applying the described deconvolution the result, which is shown in figure 4b, is significantly improved. Both singular impulses can now be separated and clearly be identified. The result does however show a non negligible noise floor even though the original measurement (figure 4a) was performed with averaging and without ambient light or other interferences, in order to receive the best starting data as possible. In this case the measurement and the simulation data show outstanding correlation which in turn leads to excellent deconvolution results. If the measured data is significantly worse the two point detection method cannot be applied since the noise overshadows the actual measurement data.

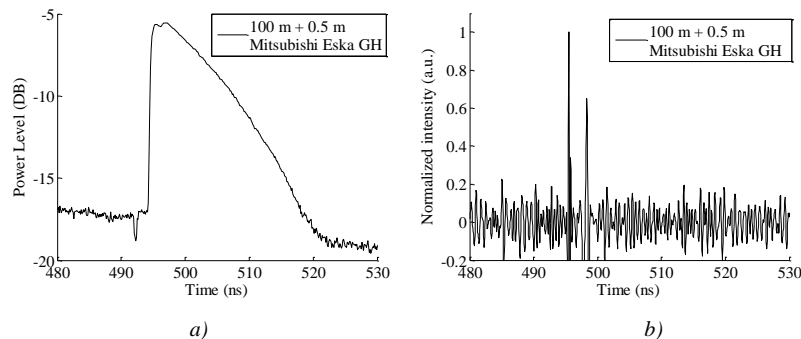


Figure 4. Measurement of a double reflex after 100 m Mitsubishi Eska GH fiber (a) and the deconvoluted result (b)

5. Conclusions

We have proposed an application of simulation results obtained using the power flow equation to increase the spatial resolutions of OTDR. This can either be used to more clearly and precisely identify reflective events or even to generate usable data from measurement near the edge of the capability of the measurement device. The latter possibility is especially useful not for laboratory equipment but for possible low cost applications which might be useful in the grading or monitoring of automotive, industrial or domestic appliances, where high end and thus expensive measurement equipment is not feasible. We have explained the mathematical operations required to perform the algorithm and have additionally provided several different measurements which could



significantly be improved by applying the deconvolution. This process could in the future be implemented in low cost OTDR devices to improve their quality of measurement without increasing the cost significantly.

6. Acknowledgements

The POF-AC Nuremberg is a project of the Hightech Offensive Bavaria. The work described in this paper was supported by the grant “Optika” (No. F1116.NÜ/13) from the Bavarian State Ministry for Education, Science and the Arts and by the grant “OHM-Netze” (No. EU-1607-0017) from the Bavarian State Ministry for Economic Affairs and Media, Energy and Technology and the European Regional Development Fund. The authors gratefully acknowledge the support of the graduate study group Fiber Optic Transmission and Sensing (FiTS).

7. References

- [1] D.R. Anderson, L.M. Johnson, FG Bell, “Troubleshooting Optical Fiber Networks: Understanding and Using Optical Time-Domain Reflectometers”, Academic Press; 2004
- [2] M. Gehrke, O. Ziemann, S. Loquai, and B. Schmauss, “Polymer optical fiber backscatter simulation model using the power flow equation solved in the time domain”, *Proc. 24th Intl. Conf. on Plastic Optical Fibers and Applications*, Nuremberg, September 2015, pp. 277ff.
- [3] D. Gloge, “Optical Power Flow in Multimode Fibers”, *Bell System Technical Journal* 51.8, pp. 1767-1783, 1972
- [4] M. Gehrke, S. Loquai, O. Ziemann, and B. Schmauss, “Time-domain solution to the power-flow equation and possible applications”, *POF Simulation beyond Data Transmission – Summary of the 3rd International POF Modelling Workshop*, pp. 57-68, 2015
- [5] S. Otto, H. Karl, C.-A. Bunge, O. Ziemann, “Deconvolution for OTDR Spatial Resolution Enhancement“, *Proc. 11th Intl. Conf. on Plastic Optical Fibers and Applications*, Tokyo, September 2002, pp. 177-179.
- [6] A. Schloetterer, “Low Cost Zeitbereichsreflektometer”, Diplomarbeit, Georg-Simon-Ohm Fachhochschule Nürnberg, 2003
- [7] C.A. Bunge, R. Kruglov, and H. Poisel, “Rayleigh and Mie scattering in polymer optical fibers”, *Journal of lightwave technology* 24(8), pp. 3137ff, 2006.
- [8] C. Emslie, "Polymer optical fibres", *Journal of materials science* 23.7, pp. 2281-2293, 1988
- [9] S.D. Personick. “Photon Probe—An Optical - Fiber Time - Domain Reflectometer”, *Bell System Technical Journal* 56(3), pp. 355-366, 1977
- [10] O. Ziemann, J. Krauser, P.E. Uamzow, and W. Daum, “ POF-Handbuch: optische Kurzstrecken-Übertragungssysteme“. Springer-Verlag, 2007
- [11] M.A. Losada, J. Mateo, and J.J. Martinez, ”SI-POFs frequency response obtained by solving the power flow equation”, *Proc. 17th Intl. Conf. on Plastic Optical Fibers and Applications*, Santa Clara, 2008
- [12] F. Breyer, “Multilevel Transmission and Equalization for Polymer Optical Fiber Systems”, *Verlag Dr. Hut*, 2010
- [13] A.W. Synder and J. Love, “Optical Waveguide Theory”, *Springer Science & Business Media*, 1983
- [14] T. Becker, S. Loquai, B. Schmauss, O. Ziemann, H. Poisel, and M. Luber, “Temperature dependence of light propagation in Polymer optical fibers”, *Proc. 24th Intl. Conf. on Plastic Optical Fibers and Applications*, Nuremberg, 2015
- [15] D. Gloge, “Impulse Response of Clad Optical Multimode Fibers”, *Bell System Technical Journal* 52.6, pp. 801-816, 1973
- [16] M. Mundus, J. Hohl-Ebinger, and W. Warta. "Estimation of angle-dependent mode coupling and attenuation in step-index plastic optical fibers from impulse responses" *Optics express* 21.14, pp. 17077-17088, 2013



Non-linear relation between modulation frequency and phase response of step-index polymer optical fiber

T. Becker^{1*}, B. Schmauss², M. Gehrke¹, E. Nkiwane¹, O. Ziemann¹

¹ Polymer Optical Fiber Application Center, Technische Hochschule Nürnberg, 90489 Nürnberg, Germany

² Institute of Microwaves and Photonics (LHFT), Friedrich-Alexander-Universität Erlangen-Nürnberg, 91054 Erlangen, Germany

*Corresponding author: thomas.becker@pofac.th-nuernberg.de

Abstract: Considering an optical fiber as a transmission system, its characteristics can be described via its amplitude and phase response. We investigate the phase response of large core (1 mm) step index polymer optical fiber (SI-POF) under different launching conditions. Due to modal dispersion, the shape of the phase response strongly depends on the excited modes of the fiber. We compare the measured phase responses of a 50 m POF with the theoretical ones obtained with an analytical model which considers modal dispersion but neglects scattering and attenuation. It can be seen that the experimental results are in good agreement with the theoretical predictions.

1. Introduction

Optical length or strain measurement techniques using modulated signals often rely on a linear relationship between the length of an optical fiber and the phase shift that is caused by the required transit time [1-4]. This relation can however be spoiled by a variety of effects including, but not limited to, scattering, chromatic and modal dispersion as well as attenuation. Any deviation from a linear phase response results in a length measurement error and therefore limits the accuracy of the respective sensor. The aforementioned effects are intrinsic to the fiber. Although they depend on the physical and geometrical parameters of the fiber, they can never be fully avoided in multimode fibers. Thus the only possibility to increase the precision of this kind of sensor is a good understanding of the real phase response of the utilized fiber.

We have evaluated the theoretical impact of modal dispersion on the phase response of a step-index polymer optical fiber before [5] and recently proposed an analytical model for multimode fibers which allows us to obtain the theoretical phase response of a fiber [6]. This paper investigates the real phase response of a SI-POF recorded with a network analyzer and compares it with the results of the analytical model.

2. Theoretical background

If we treat the fiber as a transmission system, its characteristics can be described by its frequency response $R_F(f_{mod})$ which can be separated into the amplitude response $R_A(f_{mod})$ and the phase response $R_P(f_{mod})$, where f_{mod} is the modulation frequency. The amplitude response describes the influence of the fiber on the amplitude of a modulated signal and the phase response expresses how that signal is delayed. Both amplitude and phase response are functions of the modulation frequency.

If we consider an ideal fiber, which is free from dispersion, scattering and attenuation, its phase response can be expressed as

$$R_{pi}(f_{mod}) = \frac{-L_{fiber} 360^\circ}{\lambda_{mod}} = \frac{-L_{fiber} 360^\circ f_{mod} n_{core}}{c_0}, \quad (1)$$

where L_{fiber} is the length of the fiber, n_{core} is the refractive index of the core and c_0 is the speed of light in vacuum. The expected deviations from the absolute phase response are relatively small. Therefore it is hard to detect deviations directly in the phase response. To overcome this issue we will work with the corresponding group delay instead:

$$\tau_g = \frac{-1}{360^\circ} \frac{\partial R_{pi}(f_{mod})}{\partial f_{mod}} \quad (2)$$



Since τ_g is proportional to the slope of the phase response, any deviation from the ideal phase response can easily be seen.

3. Measurement

The setup for the measurement of the phase response is depicted in Figure 1. The network analyzer is used to modulate an edge-emitting laser diode, which has a wavelength of 660 nm. The divergence of the farfield of the laser is reduced with a lens. It is not possible to fully collimate the farfield with an axially symmetric lens due to its asymmetric shape. Before the light is coupled into the fiber, its angular power distribution is shaped by Light Shaping Diffusers™ (LSD). The purpose of the LSD is the manipulation of the laser's divergence in order to excite different modes in the fiber. In our experiment we use three different LSD Sheets: POC 10, 30 and 80. POC refers to the company Physical Optics Corporation and the subsequent number is the full width at half maximum (FWHM) of the farfield (in degrees) which the LSD emits when illuminated with a collimated beam. Therefore it is clear that the higher the number of the LSD, the higher the maximum angle of the excited modes.

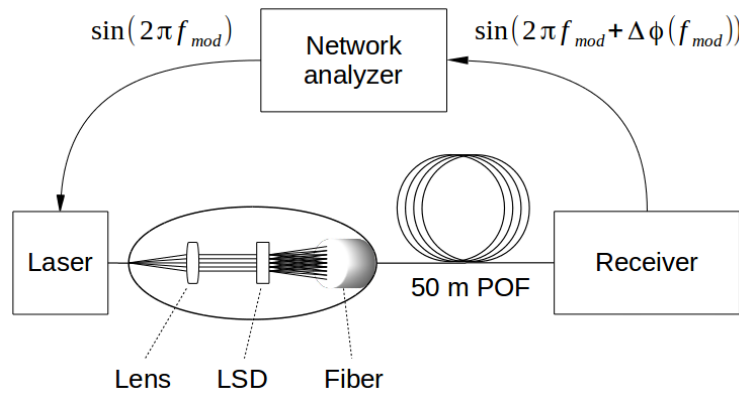


Figure 1. Phase response measurement setup

Since we use the network analyzer to record the amplitude and phase response, it is clear that these functions cannot be measured directly. The fiber cannot be used without light source, receiver and the electrical connections to the network analyzer. All these components influence the full transmission system and contribute to its frequency response. In order to remove their influences, we set the measurement up with a short piece (10 cm) of SI-POF with which we calibrate the network analyzer. For this setup the network analyzer considers $R_A(f_{mod})=1$ and $R_P(f_{mod})=0^\circ$ independent of f_{mod} . We then perform the measurements with a SI-POF with a length of 50 m. Due to the calibration, we effectively determine the frequency response for a SI-POF with the length of 49.9 m.

We set the maximum modulation frequency to $f_{mod,max}=1\text{GHz}$. With the given parameters we expect a maximum phase of:

$$R_{pi}(f_{mod,max}) = \frac{-L_{fiber} 360^\circ f_{mod,max} n_{core}}{c_0} = \frac{-49.9\text{m} \cdot 360^\circ \cdot 1\text{GHz} \cdot 1.495}{299\,792\,458\text{m/s}} = -89582.57^\circ \quad (3)$$

The ideal group delay is calculated as:

$$v_{gi} = \frac{-1}{360^\circ} \frac{\partial R_{pi}(f_{mod})}{\partial f_{mod}} = \frac{L_{fiber} n_{core}}{c_0} = \frac{49.9\text{m} \cdot 1.495}{299\,792\,458\text{m/s}} = 248.84\text{ns} \quad (4)$$



Figure 2 contains the group delays derived from the phase responses recorded for the three aforementioned LSD sheets POC 10, POC 30 and POC 80 and shows some interesting effects. First of all, all measurements show a significant offset from the ideal group delay. The maximum deviation occurs for low frequencies. The higher the scattering of the LSD sheet, the higher the deviation. For POC 80, we have a maximum group delay of approximately 257.8 ns which corresponds to an error of 3.6%. POC 30 shows a maximum group delay of 257.2 ns (3.36%) and for POC 10 we have 256.2 ns (2.96%). For higher modulation frequencies the group delay has a value of 255.45 ns (2.66%) with only weak dependencies on the used POC sheet and the modulation frequency. It is also worth mentioning that the group delay for POC 80 shows an oscillating behaviour in the first half of the frequency range.

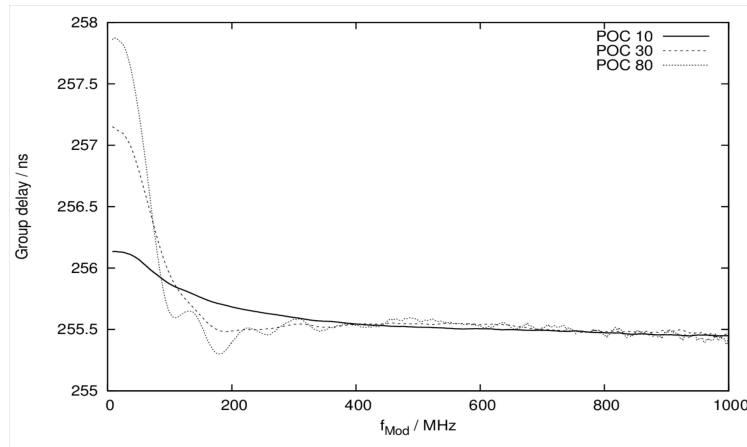


Figure 2. Measured group delay

4. Analytical model

In order to understand the measured group delays, we try to derive them from a theoretical approach. To achieve this we use an analytical model we recently presented [6]. Based on the angular and geometrical power distribution of the light source and the physical and geometrical parameters of the fiber, the modal distribution $\frac{dP}{d\theta_z}$ of the total power inside the fiber is calculated. With P being the power and θ_z being the angle relative to the fiber's axis. The next step is the transformation of the modal distribution to the impulse response of the fiber:

$$\frac{dP}{dt} = \frac{dP}{d\theta_z} \frac{d\theta_z}{dt} \quad (5)$$

Finally we can transform the impulse response to the frequency domain and obtain the frequency response, whose argument is the desired phase response. The key to obtain a realistic phase response is the proper composition of the modal distribution. Therefore we have to consider all relevant influences. In this approach we do not model the exact laser diode which would be a complex task because of its asymmetric farfield. Instead we work with a quite simple model for the light source and focus on the differences caused by the different LSD sheets. For the light source we use a single point source that is placed at the edge of the fiber and has a constant power distribution over the solid angle. The position offers the possibility to excite the full range of guided and tunneling modes¹. The choice of a point source instead of a two-dimensional source is justified because of the angular dependency of the optical receiver. It uses a Si PIN photodiode of the type S5052 by Hamamatsu which can only capture light up to the angle of $\theta_{z0,max} = 30^\circ$. That corresponds to a maximum angle inside the fiber of:

¹ Refracted modes are not considered by the model.



$$\theta_{z,max} = \arcsin\left(\frac{n_0}{n_{core}} \sin(\theta_{z0,max})\right) = \arcsin\left(\frac{1.0}{1.495} \sin(30^\circ)\right) = 19.54^\circ \quad (6)$$

Here we have set the refractive index of the surrounding medium n_0 to 1. If we compare this to the maximum angle of the guided modes inside the fiber:

$$\theta_{zg,max} = \arccos\left(\frac{n_{clad}}{n_{core}}\right) = \arccos\left(\frac{1.42}{1.495}\right) = 18.23^\circ, \quad (7)$$

with n_{clad} being the refractive index of the cladding, we see that the receiver mainly detects guided modes and only a very small part of the tunneling modes. Since the modal distribution of guided modes which are excited by a point source are independent of its position, a point source can adequately represent a two-dimensional source in this case. Since the receiver sensitivity is not constant even for angles below $\theta_{z0,max}$, we have to consider its angular sensitivity in the model. The modal distribution can then be expressed as:

$$\frac{dP}{d\theta_z} = D_P(\theta_z) S_R(\theta_z) \quad (8)$$

$D_P(\theta_z)$ is the power distribution in the fiber caused by the light source and the geometry of the fiber and $S_R(\theta_z)$ is the normalized sensitivity of the receiver. Furthermore we consider Fresnel reflections at the beginning and at the end of the fiber, which are of course also angle-dependent:

$$\frac{dP}{d\theta_z} = D_P(\theta_z) S_R(\theta_z) F_{entry}(\theta_z) F_{exit}(\theta_z) \quad (9)$$

The final influence that we have to consider is the chosen LSD sheet. Since it causes a Gaussian farfield distribution, we can model it as a Gaussian overlay with the appropriate FWHM to our modal distribution:

$$\frac{dP}{d\theta_z} = D_P(\theta_z) S_R(\theta_z) F_{entry}(\theta_z) F_{exit}(\theta_z) S_{LSD}(\theta_z) \quad (10)$$

We simulate three different LSD sheets with a FWHM angle of 18° (Low NA), 31° (Medium NA) and 72° (High NA). The corresponding group delays are shown in Figure 3 along with the theoretical value for the group delay obtained in the previous chapter. We notice that, just like in the experiment, all group delays show the largest error for low frequencies. Also, there is a strong dependency on the FWHM of the LSD sheet. The higher the angle of the excited modes, the higher the deviation at the beginning. For the high NA, we have a maximum group delay of approximately 253.3 ns which corresponds to an error of 1.79%. The medium NA shows a maximum group delay of 251.4 ns (1.03%) and for the low NA we have 249.7 ns (0.35%). For higher modulation frequencies all group delays converge to the ideal group delay. Just like the measurement with the highest NA, the corresponding simulation shows a similar oscillation with a slightly shorter period and a slowly decreasing amplitude.

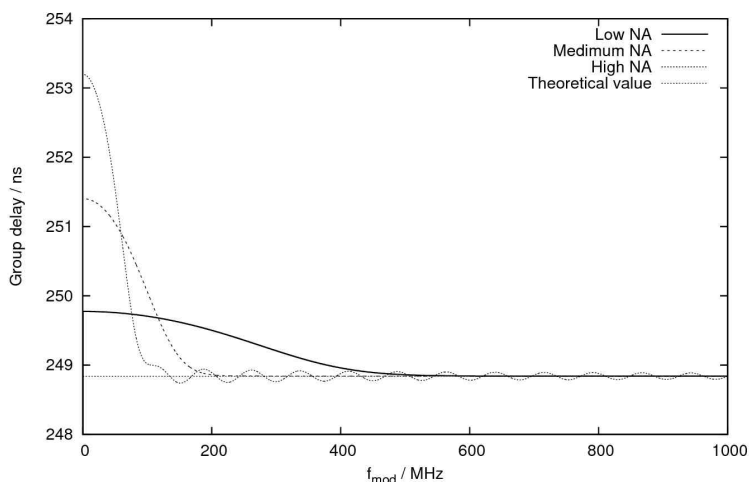


Figure 3. Group delay obtained from analytical model

5. Conclusion and outlook

We have measured the phase responses of a SI-POF under different launching conditions and compared the corresponding group delays with an analytical model that is based on the modal power distribution inside the fiber and considers several effects that influence this distribution. The model already leads to good results in some aspects. For example the general shape of the group delays are quite similar to the ones obtained in the experiment. The maximum deviation from the theoretical group delay occurs for low frequencies and shows a comparable dependency on the launching condition. For higher frequencies all group delays converge to a certain value which differs between the simulation and the measurement. In the simulation all group delays converge to the ideal group delay for a fiber free from dispersion. As a consequence, the constant offset that we observe in the experiment cannot be caused by modal dispersion. It could arise from a refractive index of the core that is higher than expected. However the difference of 2.66% seems unlikely to be caused solely by a deviation of the refractive index. Another possible explanation would be the absence of scattering in the model. Scattering in an optical waveguide leads to mode conversion. Therefore the modal distribution changes continuously along the axis of the fiber. If the fiber tends to scatter power more to higher order modes than it does to lower order modes, scattering would be an explanation for the observed increase of the mean group delay.

Another difference that we notice is the decrease of the oscillation amplitude that occurs for the high NA. In the simulation, the decrease is only small. In the experiment, the oscillation is not observable for modulation frequencies above 400 MHz. This might be caused by scattering or attenuation but could also be due to the signal-to-noise ratio (SNR) that decreases with the modulation frequency.

Also it has to be mentioned that the laser diode used in the experiment is an edge-emitter and therefore has an asymmetric farfield. The simulations were created for a light source with a symmetric farfield. Therefore the recorded group delays can be considered to be a superposition of two light sources with symmetric but different farfield distributions.

In order to further improve our understanding of the processes in a SI-POF and thus allow us to continue to increase the precision of sensing applications that are based on phase measurements, we are working on a series of scattering- and attenuation-measurements. The results will be integrated in the analytical model and should help to explain the remaining differences between the presented experiment and the current state of the model.

6. Acknowledgements

The POF-AC Nürnberg is a project of the Hightech Offensive Bavaria.



The work was supported by the Bavarian Ministry of Education, Culture, Science and Art and the European Regional Development Fund inside the Projects “Optika²” (No. F1116.NÜ/13) and “OHM-Netze” (No. EU-1607-0017).

7. References

- [1] H. Poisel, “POF Strain Sensor Using Phase Measurement Techniques”, SPIE Conference Smart Sensor Phenomena, Technology, Networks, and Systems, 6933-35, San Diego, 12.3.2008.
- [2] G. Durana, M. Kirchhof, M. Lubert, I. Sáez de Ocáriz, H. Poisel, J. Zubia, G. Aldabaldetrekú and C. Vázquez “Design and Evaluation of a Novel Fiber Optical Elongation Sensor“ in Proceedings of 17th International Conference. POF’08, Santa Clara (USA), Aug. 2008.
- [3] M. Lubert, H. Poisel, S. Loquai, C. Neuner, A. Bachmann, O. Ziemann, and E. Hartl, “POF strain sensor using phase measurement techniques,” in Proceedings of 16th International Conference on POFs and Applications, POF’07, Turin (Italy), Sep. 2007, pp. 29–32.
- [4] M. Lubert, H. Poisel, O. Ziemann, J. Diez, G. Durana M. Schukar, “Erfahrungen mit dem praktischen Einsatz eines faseroptischen Dehnungssensors“ in Proceedings of 19th International Scientific Conference Mittweida, IWKM 2008, Mittweida, 05.-06.Nov. 2008, pp. 26-30.
- [5] T. Becker, S. Loquai, H. Poisel, O. Ziemann, M. Lubert, and B. Schmauss, “Influence of modal dispersion on impulse and frequency response of step-index polymer optical fiber,” in POF Simulation beyond Data Transmission - Summary of the 3rd International POF Modelling Workshop 2015, C. A. Bunge and R. Kruglov, Eds. Norderstedt: Books on Demand, September 2015, p. 23ff.
- [6] T. Becker, B. Schmauss, M. Gehrke, E. Nkiwane and O. Ziemann, “Analytical model for the angle-dependent power distribution in optical multimode fibers” in Proceedings of 25th International Conference on POFs and Applications, POF’16, Birmingham (England), Sep. 2016.



USB to Gigabit Ethernet POF link using KDPOF technology

M. Leitmeir, J. Vinogradov, M. Bloos, O. Ziemann

POF-AC, Technische Hochschule Nürnberg Georg Simon Ohm, Wassertorstrasse 10,
90489 Nuremberg, Germany

*Corresponding author: juri.vinogradov@pofac.th-nuernberg.de

Abstract: The Polymer Optical Fiber (POF) is a real alternative for home networking in the future. It is very robust, inexpensive, can be easily cut and installed directly next to power lines in buildings. In this project the possibilities to develop an Universal Serial Bus (USB) to a POF Gigabit Ethernet link are investigated and a functional prototype was made. The solution is based on the usage of the USB 3.0 Gigabit Ethernet Controller from ASIX Electronics Corporation, connected to the Ethernet Transceiver from Marvell Semiconductor, Inc, and the Gigabit POF Transceiver from KDPOF.

1. Introduction

With the commercial available fully integrated Gigabit POF Ethernet transceiver [1] from KDPOF the POF has a real chance to be used in private and commercial buildings. With this device it's possible to transmit Gigabit Ethernet over 50 m with a step index POF (SI-POF) using different light sources [2,3]. The Gigabit POF-based application is currently in the standardization process by the Institute of Electrical and Electronics Engineers (IEEE 802.3bv) [3,4]. The goal of this work was the development of an USB 3.0 to Gigabit Ethernet POF link. Currently there is no standard interface for a Gigabit Ethernet POF connection at modern computers available. But there is the Universal Serial Bus 3.0 (USB), which supports Gigabit Ethernet speed. The backward compatibility of USB allows the usage of modern USB 3.0 and older USB 2.0 interfaces as well. The power is supplied by the USB cable which reduces the connected wires.

The physical architectures and topologies of USB and Gigabit Ethernet are working differently. USB has a master/slave architecture [5] and only the master is able to initialize a communication. In an Ethernet network every node is sending whenever it likes and collisions are resolved by a special algorithm [6]. Therefore a hardware implementation of USB to Ethernet interface requires the usage of a suitable approaches and devices.

2. Concept

The KD1001B from KDPOF offers a Gigabit transmission over 50 m SI-POF using the optical transceiver AFBR-59F3Z from Avago Technologies [3,7]. For the data transmission on the electrical side the KD1001B contains a Reduced Gigabit Media Independent Interface (RGMI) [8]. A solution for the USB to Ethernet interfaces would be an USB 3.0 to Gigabit Ethernet converter working as Ethernet Media Access Control (MAC) with an RGMI. Unfortunately such devices are currently not available on the market. But USB 3.0 to Gigabit Ethernet components with an integrated 1000Base-T Ethernet PHY are existing. For this purpose a device from ASIX Electronics Corporation [9] was chosen. It's connected to a commercial available PHY, which transmit the Ethernet signals over the RGMI to the KD1001B Gigabit POF Ethernet transceiver. This structure is shown in Fig. 1.

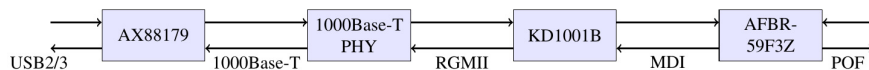


Figure 1. Structure of USB to Ethernet interface

The required power of the USB to Ethernet adapter should be supplied over the USB interface. USB 2.0 provides 2.5 W at 5V and USB 3.0 4.5 W at 5 V. The devices shown in Fig. 1 require six different supply voltages. For a sufficient efficiency switching regulators have to be used. Such regulators create noise on the supply lines, which leads to a lower margin of the data transmission system. Therefore is it necessary to implement sufficient decoupling and filtering, in order to achieve a better performance. As switching



regulators dual buck regulators from Texas Instruments Incorporated are used. They have a high switching frequency of 2.4 MHz and allow the usage of small inductivities. The higher voltages with lower currents are generated by a Linear Dropout Regulators (LDO).

For evaluating the influence of switching regulators on the link margin, a media converter board with the KD1001B and a commercial available Ethernet transceiver was developed (Fig.2). The power supply is implemented on an additional PCB, which can be plugged on top of the media converter.

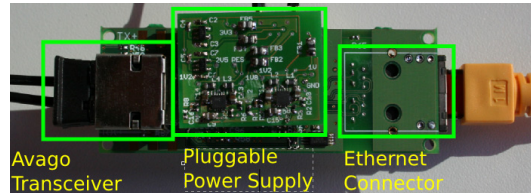


Figure 2. 1000Base-T to POF Gigabit Ethernet mediaconverter with KD1001B and changeble power supply

This supply PCB exists in a version with LDO's and a clean voltage output, which provides not sufficient efficiency. Another version with switching regulators improves this behaviour. After the evaluation of the influence of the switching regulators on the link margin, the complete USB to POF Gigabit Ethernet adapter was developed, shown in Fig. 3.

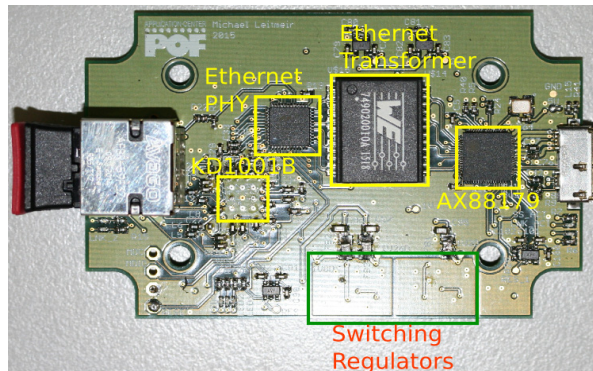


Figure 3. Complete USB 3.0 to POF Gigabit Ethernet Adapter

3. Measurement Setup

3.1 Influence of switching regulators on the Link margin

To analyse the influence of the switching regulator noise on the link margin, the 1000Base-T to POF Gigabit Ethernet Media converter (Fig. 2) was investigated. The link is utilized by an Ethernet Protocol Tester and the link margin is measured by the Media Converter Evaluation Kit (KD-EVK1001BMC) and the Software from KDPOF [3,10] (Fig 4.).

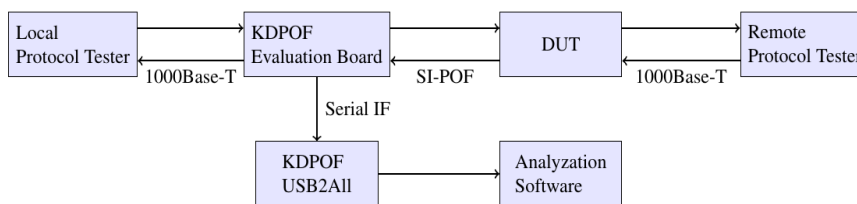


Figure 4: Measurement setup for the testing of the power supply



3.2 Connectivity of the USB 3 to POF Gigabit Ethernet Adapter

The USB connection (Fig. 3) of the USB 3 to POF Gigabit Ethernet adapter is measured with the Ethernet protocol tester. A computer with Linux was exploited for bridging it's USB and it's Ethernet Port to reach the remote station of the Ethernet protocol tester. As counterpart for the POF connection the KDPOF Media Converter Evaluation Kit (KD-EVK1001BMC) [3,10] was used.

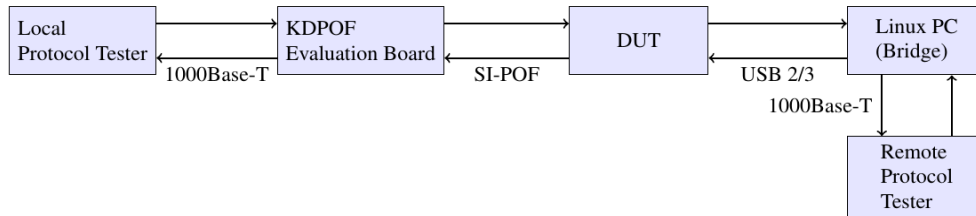


Figure 5 Measurement setup for the testing of USB connectivity

4. Measurement results

The media converter (Fig. 2) provided a link speed of 1 Gbit/s over 50 m of SI-POF with both power supply structures. The switching regulators lowered the link margin by 0.5 dB compared to the LDO supply. The performance of the USB 3 to Gigabit POF Ethernet adapter varies with the packet size of the 1000Base-T packets, which is controllable by the Ethernet protocol tester. The Fig. 6 shows the drop of maximum link speed if the packet size is reduced. Is the link utilized with mixed packets this frame loss is also measurable. The media converter application shows the maximum of raw transmitted data. A smaller packet size leads to a bigger overhead because of more packet headers. This causes also a loss of data. This could be a indication for an additional header introduced by the USB interface which leads to the packet loss.

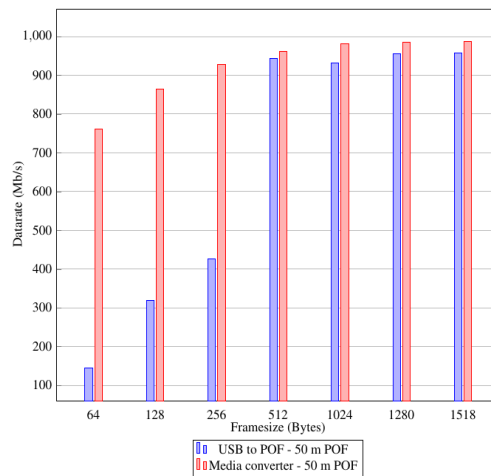


Figure 6: Achieved bit rates over the frame size



5. Conclusion

The functional adapter could be developed with three different IC's for a USB 3 to Gigabit Ethernet connection. It behaves like the available evaluation boards. The adapter works with USB 2 and 3, but the configuration of the Ethernet port must be changed to 100 Mbit/s to achieve a good connection with USB 2. The influence of switching regulators compared to linear regulators was evaluated. The discrepancy between both regulators was low, but measurable. A loss in link speed for packets with a small packet size was detected.

6. References

- [1] O. Ciordia, C. Esteban, C. Pardo, R. Pérez de Aranda, "COMMERCIAL SILICON FOR GIGABIT COMMUNICATION OVER SI-POF, POF2013, Rio de Janeiro, Brasil
- [2] J. Vinogradov, R. Kruglov, S. Loquai, J.-W. Shi, O.Ziemann, "GaN OPTICAL SOURCES WITH THE KDPOF GIGABIT POF TRANSCEIVER", POF2015, Nuernberg, Germany
- [3] V. Goetzfried, T. Lichtenegger, J. Wittl, C. Esteban, Ó. Ciordia, "Gigabit Ethernet over POF (GEPOF) –Latest Status of Technology and Standardization", POF2015, Nuernberg, Germany
- [4] IEEE P802.3bv Gigabit Ethernet Over Plastic Optical Fiber Task Force, <http://www.ieee802.org/3/bv/>
- [5] "Universal Serial Bus 3.0 Specification", Hewlett-Packard Company, Intel Corporation, Microsoft Corporation, NEC Corporation, ST-NXP Wireless, Texas Instruments, Rev.1 (2008)
- [6] Jörg Rech, "Ethernet Technologien und Protokolle für die Computervernetzung", Heise, 2014
- [7] Avago Technologies Data Sheet, "AFBR-59F3Z, Compact 650 nm Transceiver for 1 Gbps Data communication MLCC (Multilevel Coset Coded) over POF (Polymer Optical Fiber)", AV02-4655EN, December 17, 2014,
- [8] Reduced Gigabit Media Independent Interface, http://www.hp.com/rnd/pdfs/RGMIIv2_0_final_hp.pdf, Mar. 2015
- [9] "AX88179 USB 3.0 to 10/100/1000M Gigabit Ethernet Controller Data sheet", ASIX Electronics Corporation. Tech. Rep. 2014.
- [10] KD-EVK1001B-MC and KD-EVK1011B-MC Evaluation Kit, User Manual, Revision 1.3, October 2014, www.kdpof.com

The use of high power LED as photo converters and optical receivers in low speed POF sensor networks

T. Schuster¹, J. Fischer¹, O. Ziemann^{1*}

¹ POF-AC, Technische Hochschule Nürnberg Georg Simon Ohm, Wassertorstraße 10, 90489 Nuremberg, Germany

*Corresponding author: olaf.ziemann@pofac.th-nuernberg.de

Abstract: An optical powered and operated sensor link requires typically four different optical components. For the data communication a fast LED as a transmitter and a photo diode as a receiver is required. Another pair of a high power LED for seeding the power and a photonic converter at the remote sensor side is used for optical powering.

This paper will demonstrate the approach to use a single device for all purposes in the system. The same LED is used as a data source, power source, photonic power converter and optical data receiver. For sure, the usable photo current is smaller compares with optimized converters. But it is possible to save two devices, a second fibre or fiber splitters. More over the paper will demonstrate the frequency responses of the LED as a transmitter, as a photonic converter and as a receiver in reverse voltage operation. The data transmission capability will be presented.

1. Introduction

A LED can not only be used as a light source but also as a light detector. Of course a LED is optimized to emit light but in its basic construction it is a semiconductor component with p-n junction like any other photodiode which are used for receivers in optical data transmissions. Furthermore, LED's can also be used to convert light into electrical energy like solar cells. This interchangeability between light emission and detection was already researched in the 1970's by Forrest W. Mims [1].

These characteristics make it possible to develop a communication system in which only one active optical component (LED) per communication node is necessary to take over the task of the transmitter and receiver. Additionally the nodes can be supplied remotely with energy over this common optical link so that only one optical fiber per node is needed.

2. System Concept

The planed sensor network shall be realized with POF and LED's. Each sensor node will be connected via one single fiber. Therefore, the transmission of energy and data have to be done in a time division duplex (TDD) procedure.

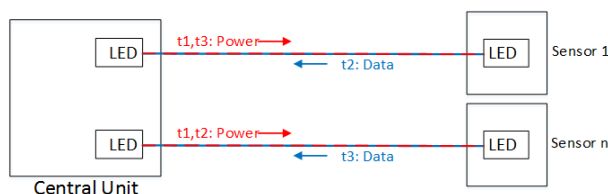


Figure 1: System concept

This TDD principle is shown in Figure 1. In timeslot t1, both sensor nodes are receiving energy to charge their energy storage. In t2, only the power transmission for sensor 1 stops, and the captured measurement data are send to the central unit. Thereby, one after another of the sensors can be polled.

3. LED as Photodetector

In the recent years, the LED technology has made enormous proceedings, especially in terms of efficiency and light output. Because of the expected moderate detector characteristics of the LED, a high optical output power is a favored basic prerequisite. In addition the POF has very high attenuation compared to optical fibers which

are made of glass whereby a non-negligible part of optical power will be lost across the transmission link. Nevertheless, to reach a usable light detection and thereby the gain of enough electrical power is achieved, the area which is absorbing light should be large to capture as much as possible light that exits the fiber and irradiated the receiving LED. The LED's [2, 3] in Table 1 fits these requirements wherefore they have been chosen for the following investigations.

Table 1: Investigated LED's

Procucer	Typ
Cree	XLamp XQ-E (High Intensity)
Lumileds	LUXEON Z (Colors)

3.1 Responsivity of LED's

An important characteristic of optical detectors is the conversion ratio of optical energy into electrical energy (generated photocurrent). This ratio is called responsivity \mathfrak{R} of the photoelectric converter.

$$\mathfrak{R} = \frac{I_{photo}[A]}{P_{optical}[W]} = \eta \cdot \frac{e}{h \cdot f} \tag{1}$$

Figure 2 shows the results of the wavelength depended responsivity (dashed lines) for three different colours of Cree XLamp XQ-E LED's. In addition the emission spectra (solid lines) of the LED's and the attenuation of the POF are plotted. Both spectra (emission and absorption) are normalized to the respective maximum.

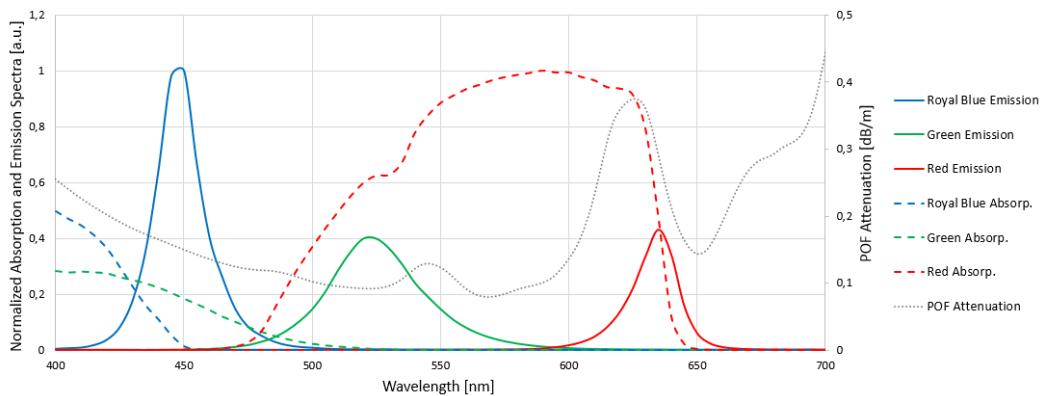


Figure 2: Normalized emission and absorption spectra [4]

These values are determined by end surface coupling of the LED's and a standard 1 mm SI-POF (Mitsubishi GH4001). The absolute ratings of the fibre-coupled responsivity measurements are shown in Figure 3.

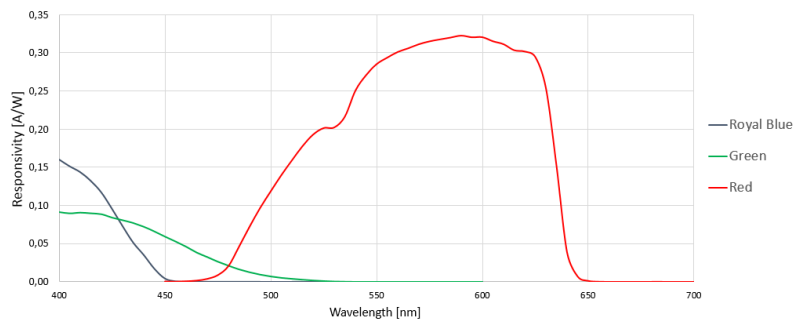


Figure 3: Absolute ratings of responsivity measurements [4]

3.2 Self-Absorption-Rate

To choose the most promising type of LED for a bidirectional communication and energy transport respectively, the responsivity of the LED should be high in the wavelength range of its own emission spectra. Therefore the overlapping of emission and absorption spectra (“Self-Absorption-Rate”) is calculated in percentage and shown in Figure 4.

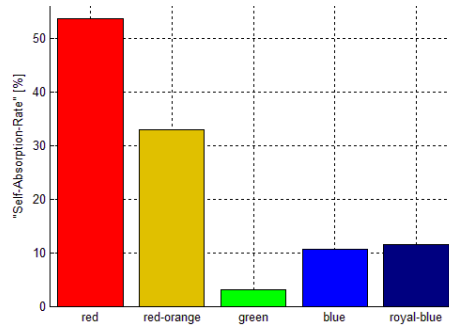


Figure 4: Self-Absorption-Rate of Cree XQ-E

For the planned sensor network, you have also take into account the wavelength depended attenuation of the POF and the different optical output powers of the LED’s.

3.3 Photoelectric Power Conversion

To determine the maximum electrical output power of the LED’s in photovoltaic operation mode, depended on the optical power which is absorbed, the transmitter and the receiver, are the very same type in the test setup. The procedure was done for different output powers of the transceiver LED. The results are shown in Figure 5.

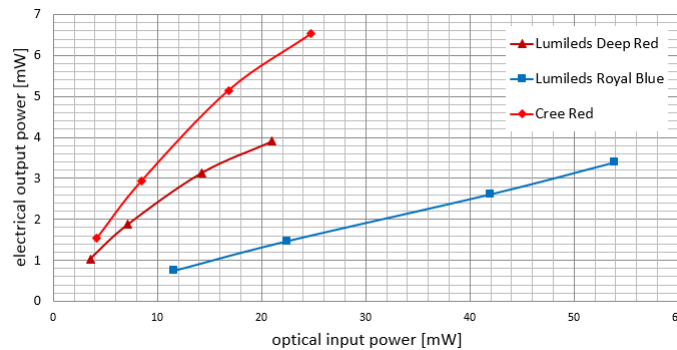


Figure 5: Results of the power conversion tests [4]

The load of the receiver LED was adjusted, so that the Maximum-Power-Point (MPP) was found. It is approx. 80% for blue LED’s and approx. 90% for the red LED’s of the open-circuit voltage.

3.4 Frequency responses

The Frequency response of the receiver is depended to the capacitance of the LED and the value of the ohmic resistance of the receiver circuit. Typically, the 3 dB cut-off frequency follows a first order low-pass filter. By adjusting the resistor value a compromise between receiving signal strength and bandwidth is set as follows:

$$u_{signal}^2 = R^2 \cdot (P_{optical} \cdot \mathfrak{R}_{LED})^2 \quad (2)$$

$$f_{3dB} = \frac{1}{2\pi \cdot R \cdot C} \quad (3)$$

In the following, the 3 dB cut-off frequencies for different modes of operation are presented in Figure 6 (left: RX cut-off, right: TX cut-off). The two different RX modes are: the photovoltaic mode (zero-bias) with 1 kΩ and 50 Ω resistor value and the photoconductive mode (reverse-bias) with 50 Ω and 5 V reverse voltage.

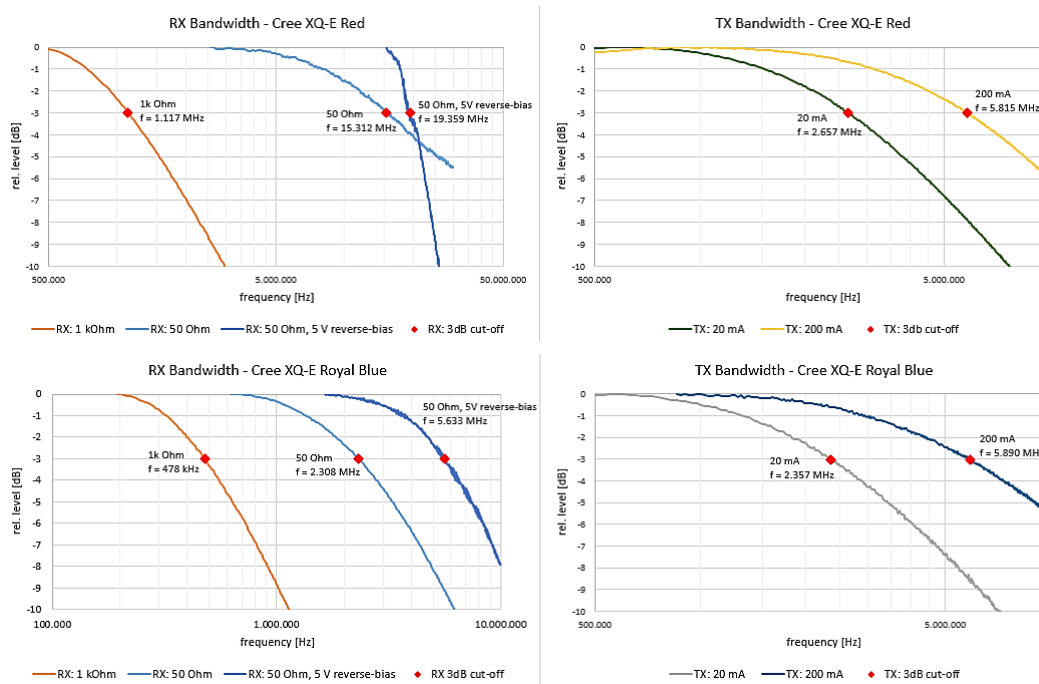


Figure 6: 3dB cut-off frequencies - Cree XQ-E

3.5 Q-Factor and BER

For an Estimation of the expected Bit-Error-Rate (BER) of the LED to LED communication, Personick’s Q-factor is used. The Q-factor is adapted from Personick’s work in 1973 [5]. This factor is the argument to the error function for the purpose of calculating the BER [6]. It is defined as:

$$Q = \frac{|\mu_1 - \mu_0|}{\sigma_1 + \sigma_0} \tag{4}$$

$$BER = \frac{1}{2} \cdot \operatorname{erfc} \left(\frac{Q}{\sqrt{2}} \right) \approx \frac{\exp(-Q^2 / 2)}{Q\sqrt{2\pi}} \tag{5}$$

In this case, μ_1 and μ_0 correspond to the levels of the transmitted data ‘1’s and ‘0’s, and σ_1 and σ_0 correspond to the standard deviation of the noise on ‘1’s and ‘0’s respectively. The needed parameters to calculate the Q-factor can be determined out of the eye pattern and is calculated by the oscilloscope respectively. The example in Figure 7 shows the eye pattern for a 1 Mbit/s transmission with an optical Power at the receiver $P_{\text{opt}} = -10.4$ dBm (horizontal 200 ns/div, vertical 1 mV/div).

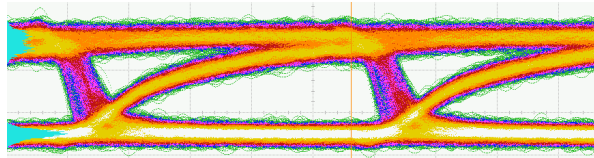


Figure 7: Eye-pattern for Cree XQ-E Red, 1Mbit/s, 50Ohm, 20mA TX drive current, Q-Factor: 6.8

Figure 8 shows a selection of the results from the BER estimation. The BER (or rather $\log(\text{BER})$) is plotted over the optical power which reaches the RX LED. So the sensitivity for a desired BER (e.g. 10^{-9}) can be estimated.

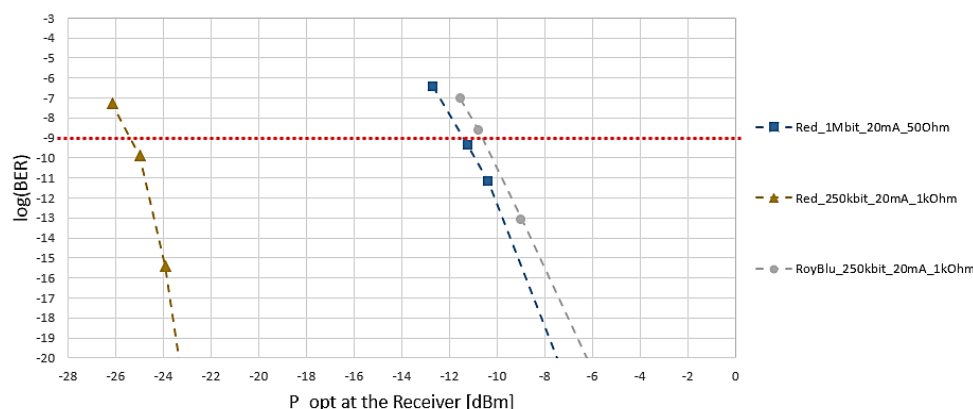


Figure 8: Estimated Bit-Error-Rates by measuring the Q-Factor (Cree XQ-E)

4. Conclusion

This paper shows the basic concept and components of a sensor network which is powered over POF. The results have shown that LED's are able to work as photodetectors and that they can be used for half duplex power and data transmission in a sensor network system. With this concept the sensor nodes can be connected with one single POF for power and data transmission. The expected electrical output power which will supply the sensor nodes is up to 5 mW using a 10 m POF transmission link (with Cree XQ-E Red, 400 mA TX drive current). For shorter links more energy will be transmit, because the attenuation of the POF is one important limiting factor. In combination with energy-harvesting on the sensor platform, this energy is sufficient to run the microcontroller based measurement capturing and sending the data to the central unit for further processing. The first system test of the data communication using the UART protocol with a baud rate of 9600 baud/s over 10 m POF was successful (with Cree XQ-E Red, 1 k Ω resistor, 20 mA TX drive current).

5. Acknowledgements

This work has been developed in the project POF-Control. The authors would like to thank the Bavarian Ministry of Education and Culture, Science and Art for funding POF-Control (reference number: VIII.2-F1116.NÜ/16/3).

6. References

- [1] P. Dietz, D. Leigh, and W. Yezazunis, "Very Low-Cost Sensing and Communication using Bidirectional LEDs," 2003. Available: http://www.forth-ev.de/filemgmt_data/files/TR2003-35.pdf.
- [2] Cree, "Cree XLamp XQ-E LED Data sheet," 2013. Available: <http://www.cree.com/~media/Files/Cree/LED-Components-and-Modules/XLamp/Data-and-Binning/ds-XQE.pdf>.
- [3] Lumileds, "LUXEON Z Colors Data sheet," 2015. Available: <http://www.lumileds.com/uploads/404/DS120-pdf>.
- [4] T. Schuster, "LED as Photodetector used for Half Duplex Power and Data Transmission," Projektbericht, TH Nürnberg - Georg Simon Ohm, POF-AC, Nürnberg, 2016.
- [5] S. D. Personick, "Reiceiver Design for Digital Fiber Optic Communication Systems, I," *The Bell System Technical Journal*, vol. 52, no. 6, pp. 843–874, <https://ia601609.us.archive.org/2/items/bstj52-6-843/bstj52-6-843.pdf>, 1973.
- [6] I. P. Kaminow and T. L. Koch, *Optical fiber telecommunications IIIA*. San Diego, CA: Academic Press, 1997.



Annealing and etching effects on strain and stress sensitivity of polymer optical fibre Bragg grating sensors

A. Pospori^{*1}, C. A. F. Marques¹, D. Sáez-Rodríguez², K. Nielsen³, O. Bang³, D. J. Webb^{1*}

1 Aston Institute of Photonic Technologies, Aston University, Aston Triangle, Birmingham, B7 4ET, United Kingdom

2 Optical and Quantum Communications Group, ITEAM Research Institute, Universitat Politècnica de Valencia, 46022 Valencia, Spain

3 DTU Fotonik, Department of Photonics Engineering, DK-2800 Kgs. Lyngby, Denmark

*Corresponding author: a.posporis@aston.ac.uk; orcid.org/0000-0003-4866-1361

Abstract: Thermal annealing and chemical etching effects on the strain and stress sensitivity of polymer optical fibre based sensors are investigated. Bragg grating sensors have been photo-inscribed in PMMA optical fibre and their strain and stress sensitivity has been characterised before and after any annealing or etching process. The annealing and etching processes have been tried in different sequence in order to investigate their impact on the sensor's performance. Results show with high confidence that fibre annealing can improve both strain and stress sensitivities. The fibre etching can also provide stress sensitivity enhancement, however the strain sensitivity changes seems to be random.

1. Introduction

Bragg grating sensors recorded in polymer optical fibre (POF) offer some interesting and potentially useful differences compared to gratings in silica fibre [1]. Amongst other things they provide an enhanced sensitivity to force and pressure [2], due to the lower elastic modulus of polymers compared to glass [3], and for certain polymeric fibre materials a sensitivity to the water activity of the environment surrounding the fibre [4]. One of the drawbacks of POF is its viscoelastic nature. The stress and strain in viscoelastic materials are not in phase, as a result hysteresis and creep effects are introduced when cyclic loading is applied to the fibre [5]. POF thermal annealing has been shown to reduce these effects [6]. Thermal annealing of POF was first used for FBG sensor multiplexing purposes, due to the ability of POF to shrink in length when is exposed above the β -transition temperature, which in turn induces a permanent negative Bragg wavelength shift [7]. Then, it was demonstrated that annealing can provide additional benefits, such as strain [8] and humidity [9] sensitivity enhancement and longer operational range in temperature monitoring [10]. Chemically etching POF to reduce the fibre diameter was also demonstrated in order to improve the force and pressure sensitivity [11] as well as the response time to humidity changes [12]. In these cases, benefit is obtained from changing the physical dimensions of the fibre in order to either decrease the cross sectional area where the force is applied or reduce the distance between the external environment and the Bragg grating's location in the fibre core. However, recently it was demonstrated that chemical etching can change not only the physical but also the mechanical properties of the material, such as its Young's modulus [13].

In the work to be reported here, the strain and stress sensitivities of POF Bragg grating sensors are investigated before and after they have been thermally annealed and chemically etched. First, a number of Bragg grating devices have been photo-inscribed in a poly(methyl methacrylate) (PMMA) based optical fibre by using the typical phase-mask technique. After the fabrication, each sensor has been characterised with respect the strain and stress sensitivity. In the next step, some sensors have been thermally annealed while some other have been chemically etched with acetone. The strain and stress sensitivity of each sensor has been characterised again at this point. Then, some annealed sensors were placed for etching and some etched sensors were placed for annealing in order to investigate the possibility for further strain and stress sensitivity enhancement.

2. Experimental details

A continuous-wave He-Cd laser (Kimmon IK3301R-G) emitting light at 325 nm with an output power of 30 mW and a phase-mask technique is used to fabricate the POFBG sensors with Bragg wavelengths located in 850 nm region. The POF that is used in these experiments is PMMA single-mode micro-structured optical fibre with the core doped with benzyl dimethyl ketal for photo-sensitivity enhancement [14]. A super-luminescent diode



(Superlum SLD-371) and an optical spectrum analyser (HP 86142A) were connected with a single-mode silica fibre coupler for POFBG spectra monitoring in reflection. Grating lengths between 1.2 mm and 10 mm were fabricated; this parameter defines only the reflectivity of the grating and it does not play any role in our experimental results. During the photo-inscription process the POF was butt-coupled with a SOF patchcord which was connected with the coupler for interrogation. After the grating fabrication, each POF was placed and glued in a demountable FC/PC connector in order to facilitate easier Bragg wavelength interrogation compared with the butt coupling method.

The strain and stress sensitivities have been calculated before and after the annealing or etching process. The strain sensitivity equals $\Delta\lambda_B/\varepsilon$, where $\Delta\lambda_B$ is the Bragg wavelength shift and ε is the applied strain in the fibre. To strain the fibre, it was attached between a fixed support and a translation stage by using magnetic fibre clamps. The translation stage can stretch the fibre along the fibre axis with accuracy of 1 μm . All POFs were strained 0.5% assuring they did not exceed the elastic limit of the polymer material. In order to stress the fibre, a mass of a known value was added at the end of the fibre which was held by a fibre clamp perpendicular to the ground thereby using gravitational force to stress the fibre. The stress can be expressed as

$$\sigma = \frac{F}{A} = \frac{mg}{\pi\left(\frac{d}{2}\right)^2}, \quad (1)$$

where F is the gravitational force which can be calculated by multiplying the added mass m and the Earth's gravity acceleration g (9.8 m/s), and A is the area where the force is applied which can be calculated by measuring the diameter d of the fibre where the POFBG sensor is located. The diameter of the fibre was measured with a microscope before and after the annealing or etching process. The stress sensitivity can be defined as $\Delta\lambda_B/\sigma$. In order to conduct thermal annealing, each POF was placed in a metallic tank filled with hot water with a constant temperature. The reason of using hot water is to control the equilibrium relative humidity during annealing (100% in this case). Two different temperatures are used for thermal annealing (55 ± 2 °C and 60 ± 2 °C), however the temperature difference does not clearly provide any impact on the annealing results. Chemical etching is performed by placing POFs in a tank filled with pure acetone for 5-7 minutes. The percentage of the fibre diameter reduction after etching is 31% - 41%.

3. Results

Table 1 depicts the strain and stress sensitivities of 6 sensors before and after the fibre annealing. Results show strain and stress sensitivity enhancement in all cases. Our explanation for this observation is as follows. During the fibre drawing, the polymer molecules align with the fibre axis due to drawing force. When these stretched polymer chains are cooled down, they have less mobility compared with the bulk material due to internal stress [15, 16]. It is believed that exposing the material above the β relaxation temperature, which is 50°C for PMMA [17], can reorganise the conformation of the polymer backbone chain and relax the stressed polymer chains [18, 19]. The molecular relaxation can increase the mobility of the molecules and the fibre therefore becomes more sensitive to mechanical stress.

Table 1: Strain and stress sensitivity before and after annealing

Sensor	Strain sensitivity before annealing (pm/ μe)	Strain sensitivity after annealing (pm/ μe)	Stress sensitivity before annealing (pm/kPa)	Stress sensitivity after annealing (pm/kPa)
1	0.708 \pm 0.007	0.902 \pm 0.016	0.180 \pm 0.027	0.260 \pm 0.030
2	0.541 \pm 0.019	0.694 \pm 0.012	0.147 \pm 0.021	0.201 \pm 0.025
3	0.681 \pm 0.009	0.739 \pm 0.019	0.141 \pm 0.021	0.217 \pm 0.026
4	0.711 \pm 0.007	0.879 \pm 0.025	0.163 \pm 0.026	0.191 \pm 0.018
5	0.726 \pm 0.007	0.875 \pm 0.025	0.176 \pm 0.009	0.208 \pm 0.015
6	0.728 \pm 0.004	0.889 \pm 0.033	0.182 \pm 0.006	0.220 \pm 0.014



Table 2 shows an additional three sensors that have been annealed and then etched. Strain and stress sensitivities have been also improved after annealing as in Table 1. Then, the same sensors have been etched in order to investigate any changes regarding the strain and stress sensitivity. The results in Table 2 show a slight reduction of strain sensitivity after etching, while the stress sensitivity has been slightly improved. Table 3 depicts additional sensors that were first etched before they were annealed. In this case, there is a strain sensitivity enhancement only for sensors 14 and 15, but due to the high measurement error, no solid conclusion can be made on this matter, even with an indication of strain sensitivity enhancement in literature [13]. On the other hand, the stress sensitivity has been enhanced in the majority of sensors after etching. It is shown that fibre etching can change the internal stress distribution [20] of the fibre and decrease the Young's modulus of PMMA [13]. After annealing, the strain and stress sensitivity of the etched POFBG sensors have been further improved, as was expected from the previous results. The fact that etching can affect the sensitivity of the device to stress and strain suggests that the fibre material is radially inhomogeneous. This may have arisen either during the preform polymerisation or during the fibre drawing process.

Table 2: Strain and stress sensitivity before and after annealing, and after etching

Sensor	Strain sensitivity before annealing (pm/ $\mu\epsilon$)	Strain sensitivity after annealing (pm/ $\mu\epsilon$)	Strain sensitivity after etching (pm/ $\mu\epsilon$)	Stress sensitivity before annealing (pm/kPa)	Stress sensitivity after annealing (pm/kPa)	Stress sensitivity after etching (pm/kPa)
7	0.690 ± 0.011	0.883 ± 0.025	0.854 ± 0.031	0.191 ± 0.016	0.221 ± 0.024	0.259 ± 0.020
8	0.727 ± 0.015	0.849 ± 0.015	0.755 ± 0.012	0.197 ± 0.013	0.258 ± 0.028	0.260 ± 0.011
9	0.771 ± 0.016	0.943 ± 0.016	0.848 ± 0.012	0.173 ± 0.028	0.202 ± 0.030	0.241 ± 0.006

Table 3: Strain and stress sensitivity before and after etching, and after annealing

Sensor	Strain sensitivity before etching (pm/ $\mu\epsilon$)	Strain sensitivity after etching (pm/ $\mu\epsilon$)	Strain sensitivity after annealing (pm/ $\mu\epsilon$)	Stress sensitivity before etching (pm/kPa)	Stress sensitivity after etching (pm/kPa)	Stress sensitivity after annealing (pm/kPa)
10	0.709 ± 0.024	-	0.834 ± 0.031	0.199 ± 0.032	0.191 ± 0.016	0.249 ± 0.019
11	0.649 ± 0.014	-	0.944 ± 0.022	0.169 ± 0.009	0.183 ± 0.015	0.200 ± 0.016
12	0.657 ± 0.014	-	0.962 ± 0.023	0.146 ± 0.020	0.211 ± 0.015	0.223 ± 0.001
13	0.720 ± 0.044	0.667 ± 0.026	-	0.194 ± 0.004	0.238 ± 0.002	-
14	0.726 ± 0.044	0.768 ± 0.034	-	0.185 ± 0.007	0.200 ± 0.010	-
15	0.728 ± 0.044	0.810 ± 0.027	-	0.189 ± 0.003	0.217 ± 0.005	-

4. Conclusion

The effects of annealing and etching on the strain and stress sensitivities of PMMA optical fibre Bragg grating sensors are investigated. The annealing and etching processes have been tried in a different sequence in order to investigate their impact on sensor's performance. Results show with high confidence that thermal annealing can enhance both strain and stress sensitivities. The fibre etching process seems to improve the stress sensitivity in the majority of sensors before or after the annealing process. If the sensors are etched after annealing, the strain sensitivity seems to be slightly reduced, however due to the magnitude of measurement errors a solid conclusion cannot be made for the etching effects on the un-annealed sensors and further investigation on this matter is needed.

5. Acknowledgements

The research leading to these results has received funding from the People Programme (Marie Curie Actions) of the European Union's Seventh Framework Programme FP7/2007-2013/ under REA grant agreement No. 608382. This work was supported by Marie Curie Intra European Fellowships included in the 7th Framework Program of the European Union (projects PIEF-GA-2013-628604 and PIEF-GA-2011-302919).



6. References

- [1] D. J. Webb, "Fibre Bragg grating sensors in polymer optical fibres," *Measurement Science and Technology*, vol. 26, p. 092004, 2015.
- [2] C. A. F. Marques, A. Pospori, S. D. x00E, R. ez, x00Ed, *et al.*, "Aviation Fuel Gauging Sensor Utilizing Multiple Diaphragm Sensors Incorporating Polymer Optical Fiber Bragg Gratings," *IEEE Sensors Journal*, vol. 16, pp. 6122-6129, 2016.
- [3] J. G. A. Griffiths, "Tables of physical and chemical constants. By G. W. C. Kaye and T. H. Laby," *The Analyst*, vol. 73, p. 704, 1948.
- [4] W. Zhang, D. J. Webb, and G. D. Peng, "Investigation Into Time Response of Polymer Fiber Bragg Grating Based Humidity Sensors," *Journal of Lightwave Technology*, vol. 30, pp. 1090-1096, 2012.
- [5] M. C. J. Large, J. Moran, and L. Ye, "The role of viscoelastic properties in strain testing using microstructured polymer optical fibres (mPOF)," *Measurement Science & Technology*, vol. 20, 2009.
- [6] A. Abang and D. J. Webb, "Effects of annealing, pre-tension and mounting on the hysteresis of polymer strain sensors," *Measurement Science and Technology*, vol. 25, 2014.
- [7] I. P. Johnson, D. J. Webb, and K. Kalli, "Utilisation of thermal annealing to record multiplexed FBG sensors in multimode microstructured polymer optical fibre," in *21st International Conference on Optical Fiber Sensors (OFS21)*, Ottawa, Canada, 2011, pp. 7327-7753.
- [8] W. Yuan, A. Stefani, M. Bache, T. Jacobsen, B. Rose, N. Herholdt-Rasmussen, *et al.*, "Improved thermal and strain performance of annealed polymer optical fiber Bragg gratings," *Optics Communications*, vol. 284, pp. 176-182, 2011.
- [9] G. Woyessa, K. Nielsen, A. Stefani, C. Markos, and O. Bang, "Temperature insensitive hysteresis free highly sensitive polymer optical fiber Bragg grating humidity sensor," *Optics Express*, vol. 24, pp. 1206-1213, 2016/01/25 2016.
- [10] K. Carroll, A. Argyros, K. Kalli, M. Large, D. J. Webb, and C. Zhang, "Extending the working temperature range of Bragg gratings in microstructured polymer optical fibre by annealing," in *International Conference on Plastic Optical Fibres*, Turin, Italy, 2007.
- [11] G. Rajan, B. Liu, Y. Luo, E. Ambikairajah, and G.-D. Peng, "High Sensitivity Force and Pressure Measurements Using Etched Singlemode Polymer Fiber Bragg Gratings," *IEEE SENSORS JOURNAL*, vol. 13, pp. 1794-1800, 2013.
- [12] G. Rajan, Y. M. Noor, B. Liu, E. Ambikairaja, D. J. Webb, and G.-D. Peng, "A fast response intrinsic humidity sensor based on an etched singlemode polymer fiber Bragg grating," *Sensors and Actuators a-Physical*, vol. 203, pp. 107-111, 2013.
- [13] K. Bhowmik, P. Gang-Ding, E. Ambikairajah, V. Lovric, W. R. Walsh, B. G. Prusty, *et al.*, "Intrinsic High-Sensitivity Sensors Based on Etched Single-Mode Polymer Optical Fibers," *Photonics Technology Letters, IEEE*, vol. 27, pp. 604-607, 2015.
- [14] D. Saez-Rodriguez, K. Nielsen, H. K. Rasmussen, O. Bang, and D. J. Webb, "Highly photosensitive polymethyl methacrylate microstructured polymer optical fiber with doped core," *Optics Letters*, vol. 38, pp. 3769-3772, 2013.
- [15] S. Fakirov, *Oriented polymer materials*: Wiley Online Library, 1996.
- [16] S. Kukureka, G. Craggs, and I. Ward, "Analysis and modelling of the die drawing of polymers," *Journal of materials science*, vol. 27, pp. 3379-3388, 1992.
- [17] K. Fukao, S. Uno, Y. Miyamoto, A. Hoshino, and H. Miyaji, "Dynamics of α and β processes in thin polymer films: Poly(vinyl acetate) and poly(methyl methacrylate)," *Physical Review E*, vol. 64, p. 051807, 10/24/ 2001.
- [18] E. Muzeau, J. Perez, and G. P. Johari, "Mechanical spectrometry of the .beta.-relaxation in poly(methyl methacrylate)," *Macromolecules*, vol. 24, pp. 4713-4723, 1991/08/01 1991.
- [19] K. Schmidt-Rohr, A. S. Kulik, H. W. Beckham, A. Ohlemacher, U. Pawelzik, C. Boeffel, *et al.*, "Molecular Nature of the .beta. Relaxation in Poly(methyl methacrylate) Investigated by Multidimensional NMR," *Macromolecules*, vol. 27, pp. 4733-4745, 1994/08/01 1994.
- [20] K.-S. Lim, H.-Z. Yang, W.-Y. Chong, Y.-K. Cheong, C.-H. Lim, N. M. Ali, *et al.*, "Axial contraction in etched optical fiber due to internal stress reduction," *Optics Express*, vol. 21, pp. 2551-2562, 2013/02/11 2013.



Study of doping non-PMMA polymer fibre canes with UV photosensitive compounds

H. U. Hassan^{1*}, A. Fasano², J. Janting¹, G. Demirci³, O. Çetinkaya⁴, G. Woyessa¹, H.K. Rasmussen², O. Bang¹

1 DTU Fotonik, Department of Photonics Engineering, Technical University of Denmark, 2800 Kgs. Lyngby, Denmark

2 DTU Mekanik, Department of Mechanical Engineering, Technical University of Denmark, 2800 Kgs. Lyngby, Denmark

3 Department of Polymer Chemistry, Maria Curie-Skłodowska-University, Gliniana St. 33, 20-031 Lublin, Poland

4 Laboratory of Optical Fiber Technology, Maria Curie-Skłodowska-University, Pl. Skłodowskiej 3, 20-031 Lublin, Poland

*Corresponding author: hafha@fotonik.dtu.dk

Abstract: We propose a solution doping method for polycarbonate (PC) and TOPAS polymer optical fibre (POF) canes using different UV photosensitive dopants aiming to reduce the fibre Bragg grating inscription time at the typical Bragg grating inscription wavelength (325nm). Three-ring solid-core PC mPOF canes and hollow-core TOPAS canes were doped with a solution of dopants in acetone/methanol and hexane/methanol, respectively. Doping time, solvent mixture concentration and doping temperature were optimised. A long and stepwise drying process was applied to the doped canes to ensure complete solvent removal. This is required to avoid the formation of any bubbles during the fibre drawing process.

Key Words: Microstructured polymer optical fibre cane, UV inscription, Polycarbonate, TOPAS.

1. Introduction

Polymer optical fibres (POFs) can be used for different sensing applications. One of the advantages of polymer fibres over conventional silica glass fibres is their small Young modulus compared to silica. For instance PMMA's Young modulus is typically 2-3 GPa, which is about 30 times smaller than that of silica (72 GPa) [1]. Lower Young modulus implies a higher sensitivity to stress. Furthermore, polymer fibres are biocompatible and potentially cheap to manufacture. These properties make them very attractive for different sensing applications such as structural health monitoring and biomedical sensing devices, e.g. glucose sensors [2]. Polymer optical fibres can be made from different materials, such as PMMA (polymethyl methacrylate), Zeonex [3], et cetera. The most commonly used is PMMA (polymethyl methacrylate). However, interest has recently developed in polycarbonate (PC) mPOFs due to the fact that PC has good mechanical properties as well as high operating temperature range due to its high glass transition temperature of 144 °C. Fibre Bragg gratings (FBGs) can be inscribed in PC fibres and can be used for sensing applications [4]. One limitation in the manufacture of POFBGs is typically represented by the FBG inscription time. One of the ways to reduce the fibre Bragg grating inscription time is to dope the polymer with the photosensitive materials before fibre drawing. E.g. Benzyl Dimethyl Ketal (BDK) is used to dope PMMA [5]. The reduced inscription time may help in the commercialization of POFBG sensors. Polycarbonate has been shown to be photosensitive at typical inscription conditions and to have shorter inscription time compared to PMMA at same inscription wavelength [4]. Doping PC with different photosensitive dopants can further increase its photosensitivity and therefore reduce the grating inscription time. Another non-PMMA material that has drawn attention in recent years is TOPAS, which is a cyclic olefin copolymer used for many applications in healthcare, optics, packaging and electronics applications. The main advantage of TOPAS over PMMA is its humidity insensitivity which is highly desirable for some sensing applications [6-7]. In this work we investigate solution doping methods for mPOF cane doping. We test several UV photosensitive dopants. The aim is to reduce the fibre Bragg grating inscription time at the typical Bragg grating inscription wavelength (325nm).

2. Doping

The doping experiments involved the use of various photosensitive compounds, such as BDK, coumarin and the recently developed monomer 2,7-NAF.DM [8], at various dopant concentrations. Two different solution-

based doping techniques were investigated. The first was applied to PC and was similar to the one adopted by Large et al. [9], as displayed in Figure 1(a). Polycarbonate mPOF canes were left in a solution containing the dopant for a time ranging from hours to days - depending on the solution concentration - until the solvent/dopant diffusion had met around the core. At this point we tried out two different routes, both of which were proposed in [9]. We either left the mPOF canes in the solution until the diffusion fronts met in the core or we applied heat to them in order to facilitate further diffusion of the dopant towards the core. Also, the drawing conditions themselves can facilitate further diffusion because of the elevated temperature involved. Note that in Figure 1(a) the inward diffusion of the solvent/dopant solution occurring through the outer wall of the cane is not shown for the sake of clarity. Figure 1(b) shows the alternative doping technique that was developed. A hollow-core polymer cane was initially doped with a solution of the desired dopant for a limited time in order to allow a mild inward diffusion to occur. This method was applied to TOPAS 5013 POF canes. The single-hole can then be collapsed by fibre drawing to obtain a doped solid core. Notice, the latter step has not been tested yet.

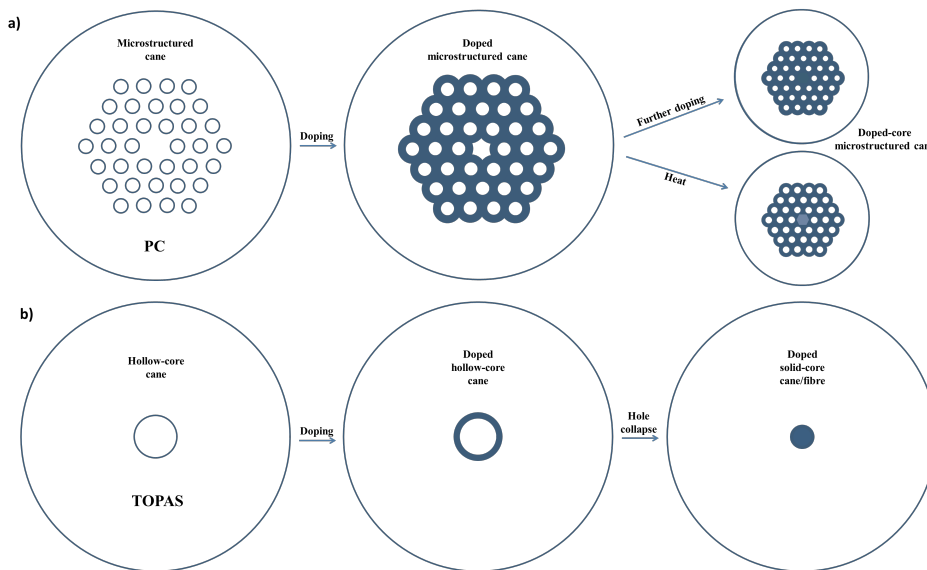


Figure 1. (a) Doping method used for PC mPOF canes. (b) Hollow-core TOPAS POF cane doping technique with further suggestion of hole collapse to obtain fibres with a doped solid core.

In both PC and TOPAS cane doping techniques, a swelling agent was required to open the structure of the polymer and allow an easier and rapid diffusion of dopant into the cane. In PC, acetone represented a good candidate for such purpose. Acetone can indeed diffuse very rapidly, but the fast swelling brings about environmental stress cracking [10]. Therefore, a proper diluent such as methanol was required. Methanol indeed diffuses much slower into PC than does acetone as the former is a relatively poor solvent for PC [10]. We conducted a series of preliminary experiments with methanol/acetone solutions aiming to optimise the swelling of polycarbonate but, at the same time, avoiding stress cracking issues. Short samples of the canes with a length of approximately 10-15mm were left in a mixture acetone/methanol ranging from 20% to 50% v/v for about 2 days at room temperature. The canes used for drawing the fibers are needed to be one order magnitude longer than the samples. Nevertheless, the results from short samples can be related to the real canes where the required doping time is expected to be longer. At concentrations of acetone around 40% v/v the PC mPOF canes lost their original transparency irreversibly, as shown in Figure 2. The best result for rather fast diffusion without losing transparency was obtained for a solution acetone/methanol 33:67% v/v. This may be seen in Figure 3, which shows the diffusion pattern for shortsamples from the same mPOF cane left at various acetone/methanol mixture concentrations for the same doping time. The percentage refers to the



volumetric concentration of acetone. For 25 %, the diffusion was too slow as confirmed by the diffusion area, i.e. the ring around the holes, being very small. At higher concentrations of acetone the diffusion speed increased with increasing acetone concentration as expected.



Figure 2. Preliminary test for solution concentration optimisation.

At 34-35% the diffusion speed was therefore relatively fast. However, the canes started to lose some transparency, while, for a concentration of 33%, no significant decrease in transparency was observed. At 33% the swelling action, mainly due to the acetone, was still adequate, and considerably higher than at lower acetone concentrations.

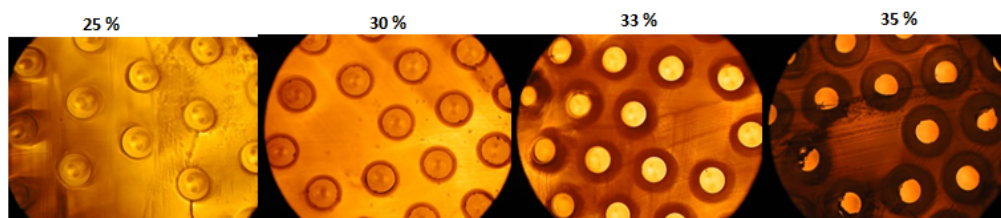


Figure 3. Diffusion pattern for a PC 3-ring mPOF cane at different acetone/methanol concentrations where the same doping time is applied.

Notice, acetone/methanol 33:67% v/v was the optimum for doping at room temperature, i.e. 25 °C. For higher temperatures the optimal condition was found to vary. In particular, the optimum shifted towards lower concentrations when the doping temperature was increased. For instance, at 40 °C the optimal acetone/methanol concentration was found to be 30:70% v/v.

A similar procedure was carried out for hollow-core TOPAS 5013 canes. We used a solution methanol/n-hexane where the latter acts as the swelling agent. Since mixtures methanol-hexane present partial miscibility at around room temperature, the maximum concentration of hexane in methanol considered in our experiments was 40% v/v, i.e. below the solubility limit of 41.34% v/v, 46.32% v/v and 53.97% v/v at 20 °C, 25 °C and 30 °C, respectively, reported in [11]. As done for PC, the doping conditions were optimized by varying the concentration of hexane in methanol in order to maintain a high clarity of the cane after doping with the best doping speed possible. The optimum concentration was found to be 70% methanol and 30% hexane v/v.

3. Drying

Drying resulted to be the most critical step before drawing the fibre from the doped canes. Evaporation of acetone/methanol solutions from PC canes was rather difficult and required the application of a long and stepwise drying process. Likewise, also drying TOPAS canes after doping with hexane/methanol solutions required a treatment similar to that of PC. All canes were dried first at room temperature for at least one day and then in an oven for several days where the temperature was gradually increased from 40 °C up to 110 °C (TOPAS) or 120 °C (PC). The canes were weighted before and after the doping to ensure complete solvent removal. Ideally, to have an easier drying process, the doping time – and therefore the absorption/swelling –



should be fairly limited. Figure 4 shows an example of what may happen during the drying process when the solvent content is too high.



Figure 4. Bubble formation in a TOPAS cane after drying above 70 °C.

4. Conclusion

Until now the main limitation has been the significantly higher loss introduced by the combination of doping-drying process. One doped PC mPOF with reasonable transmission loss was produced, but it did not show any significant increase in photosensitivity. This may be due to insufficient concentration of dopant in the core, which still requires optimisation. Moreover, a few rather transparent doped canes were obtained, but the fibre transmission loss after fibre drawing was very high, probably because of the formation of small bubbles during the drying and drawing stages. In this regard, work is in progress to optimise the drying process for complete removal of the solvent without creating bubbles in the polymer cane. This is needed to make sure that there is no bubble formation during fibre drawing. In addition, the introduction of photosensitive compounds in the core itself tends to increase transmission loss due to higher scattering loss and the transparency of the dopant being typically lower than that of the host polymer. This may represent an intrinsic limitation in doping PC and TOPAS, where the fibre losses are in general higher than those of PMMA.

5. Acknowledgements

This work was supported by the People Programme (Marie Curie Actions) of the European Union's Seventh Framework Programme FP7/2007-2013/ under REA grant agreement number 608382.

6. References

- [1] S. H. Law, M. A. van Eijkelenborg, G. W. Barton, C. Yan, R. Lwin, and J. Gan, "Cleaved end-face quality of microstructured polymer optical fibres," *Opt. Commun.* 265(2), 513–520 (2006).
- [2] H.U. Hassan, K. Nielsen, S. Aasmul, O. Bang, "Polymer optical fiber compound parabolic concentrator tip for enhanced coupling efficiency for fluorescence based glucose sensors" *Biomed. Opt. Express* 6(12), 5008–5020 (2015).
- [3] J. Anthony, R. Leonhardt, A. Argyros, M.C.J. Large, "Characterization of a microstructured Zeonex terahertz fiber," *J.Opt.Soc.Am B* 28(5), 1013–1018 (2011).
- [4] A. Fasano, G. Woyessa, P. Stajanca, C. Markos, A. Stefani, K. Nielsen, H.K. Rasmussen, K. Krebber, O. Bang, "Fabrication and characterization of polycarbonate microstructured polymer optical fibers for high-temperature-resistant fiber Bragg grating strain sensors," *Opt. Mater. Express* 6(2), 649-659 (2016).
- [5] Y. Lua, Q. Zhang, H. Liu, G-D. Peng., "Gratings fabrication in benzildimethylketal doped photosensitive polymer optical fibers using 355 nm nanosecond pulsed laser," *Opt. Letters* 35(5), 751-753 (2010).
- [6] W. Yuan, L. Khan, D.J. Webb, K. Kalli, H.K. Rasmussen, A.Stefani, O.Bang., "Humidity insensitive TOPAS polymer fiber Bragg grating sensor," *Opt. Express* 19(20), 19731-19739 (2011).
- [7] C. Markos, A. Stefani, K. Nielsen, H. K. Rasmussen, W. Yuan, O. Bang, "High-Tg TOPAS microstructured polymer optical fiber for fiber Bragg grating strain sensing at 110 degrees," *Opt. Express* 21(4), 4758-4765 (2013).



- [8] M. Gil, B. Podkościelna, L. Czyzewska, J. Pędzisz, A. Walewski, J. Kopec, W. Podkościelny, A. Gorgol, P. Mergo, "Spectral characteristics of PMMA doped with dimethacrylate derivative of naphthalene-2,7-diol use full in UV sensors," *Photonics Lett. Pol.* 8 (1), 20-22 (2016).
- [9] M.C.J. Large, S. Ponrathnam, A. Argyros, N. S. Pujari, F. Cox, "Solution doping of microstructured polymer optical fibres," *Opt. Express* 12(9), 1966-1971 (2004).
- [10] R.A. Grinsted, J.L. Koenig, "Study of multicomponent diffusion into polycarbonate rods using NMR imaging," *Macromolecules* 25(4), 1229–1234 (1992).
- [11] P. Alessi, M. Fermeglia, I. Kikic, "Liquid-liquid equilibrium of cyclohexane-n-hexane-methanol mixtures: effect of water content," *J. Chem. Eng. Data* 34(2), 236–240 (1989).



Assessing central arterial pressure with a collar POF intensity sensor

C. Leitão^{1*}, P. Antunes¹, C. Marques¹, Maria F. Domingues^{1,2}, J. Pinto¹, J. Mesquita Bastos³, P. André⁴

¹Instituto de Telecomunicações, I3N and Department of Physics, University of Aveiro, 3810-193 Aveiro, Portugal

²CSIC, ctra. Campo Real, 28500 Arganda del Rey, Madrid, Spain

³Centro Hospitalar do Baixo Vouga E.P.E., Avenida Artur Ravara, 3810-501 Aveiro, Portugal

⁴Instituto de Telecomunicações and Department of Electrical and Computer Engineering, Instituto Superior Técnico, University of Lisbon, 1049-001 Lisboa, Portugal

*Corresponding author: catia.leitao@ua.pt

The clinical relevance of the central arterial pressure, defined as the arterial pressure immediately at the heart output and following elastic arteries that irrigate the heart, kidney and brain, is increasing when compared to brachial blood pressure, which is measured in the arm. Central pressure is clinically relevant because it seems to be more closely related with cardiovascular outcomes [1] and can be differently modified by cardiovascular drugs [2]. One way of access the central pressure is calibrating the carotid arterial pulse with brachial pressure values. Pulse waveform assessment in the carotid is usually performed with electromechanical tonometers, being currently very expensive, and for that underused in primary care and hypertension control. Plastic optical fibre sensors based on intensity modulation had appeared as a reliable and low cost alternative [3, 4]. These sensors are suitable as medical devices as they are flexible, lightweight, highly sensitive, immune to electromagnetic radiation and do not conduct electric current, being intrinsically safer than electronic devices. In this work, a collar with an intensity POF sensor to assess the central systolic pressure is presented. The sensor and pulse acquisition system can be seen on Fig 1a. The probe has a flexible membrane with an interior reflective surface. A visible optical signal from an LED is applied to the reflective surface which moves with the arterial interior pressure changes, modulating the reflected signal with the arterial pulse pattern, which is then detected in a photodiode. The sensor has grooves to allow a simple fixation (similar to a button) of the device to the neck of the patient, with a textile collar using a Velcro closure, allowing a stable signal acquisition. In this work, the sensor characterization and preliminary results in human testing are presented, as can be seen on Fig. 1b.

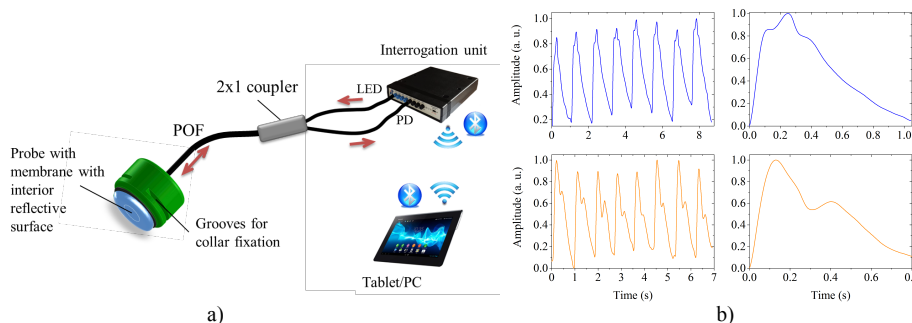


Figure 1. Pulse waveform acquisition – a) acquisition scheme and probe and b) pulse waves assessed in humans.

Acknowledgements: FEDER funds through COMPETE 2020 Program, National Funds through FCT—Portuguese Foundation for Science and Technology under the projects UID/EEA/50008/2013, UID/EMS/00481/2013 and UID/CTM/50025. C.Leitão, P. Antunes, C. Marques and M. F. Domingues acknowledge the following FCT fellowships: SFRH/BD/84076/2012, SFRH/BPD/76735/2011, SFRH/BPD/109458/2015 and SFRH/BPD/101372/2014, respectively.

References

- [1] Roman J, Devereux B, Kizer R, Okin P, Lee E, Wang W, Umans J, Calhoun D, Howard B, “High central pulse pressure is independently associated with adverse cardiovascular outcome: The Strong Heart Study”, *J Am Coll Cardiol*. 54 (18) 1730-1734, 2009.
- [2] Williams B, Lacy P, Thom S, Cruickshank K, Stanton A, Collier D, Hughes A, Thurston H, and O’Rourke M, “Differential impact of blood pressure-lowering drugs on central aortic pressure and clinical outcomes: principal results of the conduit artery function evaluation (CAFE) study”, *Circulation*, 113:1213-1225, 2006.
- [3] Leitão C, Antunes P, Bastos J, Pinto J, André P, “Plastic optical fiber sensor for noninvasive arterial pulse waveform monitoring”, *IEEE Sensors J*. 15 (1) 14-18, 2015.
- [4] Leitão C, Antunes P, Pinto J, Bastos J, André P, “Optical fiber sensors for central arterial pressure monitoring”, *Opt Quant Electron*, 48:218, 2016.

Key Words: POF, carotid pulse waveform, central pressure, intensity fibre sensor, hypertension.

Preferred presentation method: poster.



Statistical approach to copolymerization parameter forecast using PM7 calculations

D. Zaremba¹, O. Laudi, R. Evert¹, W. Kowalsky¹, R. Caspary¹, H.-H. Johannes^{1*}

¹ Institut für Hochfrequenztechnik, TU Braunschweig, Schleinitzstraße 22, 38106 Braunschweig, Germany.

*Corresponding author: h2.johannes@ihf.tu-bs.de

Abstract: Copolymers are a special kind of polymers consisting of more than one monomer. Their respective proportion represents an easy method to fulfil custom properties. For example, an increase in the glass transition temperature or specific variations in the refractive index can be achieved. These characteristics make them attractive for a variety of applications such as found in optics. However, for reproducible copolymer properties an exact knowledge of the reaction processes is inevitable, in particular when using bulk processing. Suitable indicators are the copolymerisation- or r -parameters. These can be found in extensive laboratory experiments or by simplified empirical assessments using the ALFREY-PRICE (AP) parameters. This paper presents a statistical approach towards a fully computer based simulation of r -parameter sets for various copolymers. MOPAC2016 (Version: 16.146W, James J. P. Stewart, Stewart Computational Chemistry) was used to calculate the level of distinguished orbital energies (PM7) like the HOMO, LUMO or alpha and beta SOMO. Based on these energies a response to the reaction probability is given which is applied to the current chain growth of the copolymer in a weighted random experiment. Thereby the algorithm forms copolymer compositions that match the experimental data in sufficient manner. This method could be used to determine suitable monomer combination in advance of the actual experiment in the laboratory whereby a considerable time saving is obtained. In addition the reduced use of chemicals decreases both cost and environmental load.

1. Introduction

In general there is a variety of polymers that meet certain requirements like special temperature strengths or desirable optical behaviour. Often these are so-called homopolymers that consist of only one type of monomer. Examples with relevance for POFs are MMA, Styrene or Cytop [1]. Unfortunately, the properties of various homopolymers cannot be combined by blending. Instead a strong performance loss is visible for most materials. A different approach is to use copolymers. These can be made by using a mixture of two or more selected monomers in free radical or ionic polymerisations. However, even for the simplest binary copolymer using two monomers (M1 and M2) five different copolymer types can be found. These copolymers types are related to the composition of the polymer chain and can be *statistical* (random order of M1 and M2), *alternating* (regular alternating composition of M1 and M2), *block* (long uniform sequences of the monomers), *graft* (branched block copolymers) or *stereoblock* (features distinguished ordered block structures). [2, 3]

The distinction between the copolymer types is of notable importance, since the composition of the chain, the kind and the amount of the monomers are responsible for the polymer characteristics in an equivalent manner. A theoretical basis is given with the MAYO-LEWIS equation (eq. 1). For steady state conditions one can estimate the r -parameters which define relative reactivity ratios in between the growing polymer chains and the respective added monomers (eq. 2). These characteristic parameters provide an easy access to the given copolymerization behaviour. [r : copolymerisation parameter, k : reaction rate constant, m_n : monomer ratio, M_n : monomer feed]

$$\frac{m_1}{m_2} = \frac{[M_1]}{[M_2]} \cdot \frac{r_1[M_1] + [M_2]}{[M_1] + r_2[M_2]} \quad (1)$$

$$r_1 = \frac{k_{11}}{k_{12}} \quad r_2 = \frac{k_{22}}{k_{21}} \quad (2)$$



The required r -parameter sets are usually determined experimentally in time and material consuming test series. Further an approximation for r_1 and r_2 can be achieved using the ALFREY-PRICE method (Q, e -scheme) which is based on empirical parameters [4]. On occasion those are not available or determined insufficiently. As a result the comparison with the experimental data sometimes proves as false. However, some background for those reactions as well as a number of examples is given by Y. KOIKE [5], a detailed view on copolymer effects and the interpretation of specific r -parameter sets is described by COWIE [2]. Amongst others the determination of the r -parameters for several methacrylate based materials and some applications for copolymeric POFs have been shown by our group at POF2015 [6].

Several drawbacks, which in particular concern the experimental cost and accuracy of the empirical determination of the r -parameters, lead to problems while working with copolymers. This raises the question whether it is possible to determine the r -parameter easier, faster and more accurately than today. Our approach is to carry out a simulation using calculated data for the energy levels of the monomers and growing polymer chains. The virtually generated polymers can be evaluated similar to the data found in experiments, thus providing direct connections back to the r -values. Also common evaluation routines according to FINEMAN-ROSS (FR) [7] and KELEN-TÜDÖS (KT) [8] can be used.

2. Simulation Setup

2.1 Principle

For the reaction of M1 and M2 four elementary reaction steps must be distinguished. These are shown in Figure 1. Thereby k represents the reaction rate constant. In a simplified model it can also be interpreted as reaction probability. If the k values are known one can consider the reaction as a statistical selection experiment, since the monomer availability takes fixed values for each composition in an assumed quasi-steady state. Here, only the case is considered in which a polymer chain having a specific end group reacts with a random available monomer M1 or M2. Then the subsequent chain unit is determined in a two-stage random experiment. Firstly the present monomer is chosen by its availability chance as specified in the experiment. Secondly its reaction probability is determined by means of its reactivity ratio. If the positive event occurs the chosen monomer is added to the chain. Otherwise the selection experiment will be restarted. The targeted chain length is in the scope from 1000 to 1500 repetition units which is in the order of real molecules.

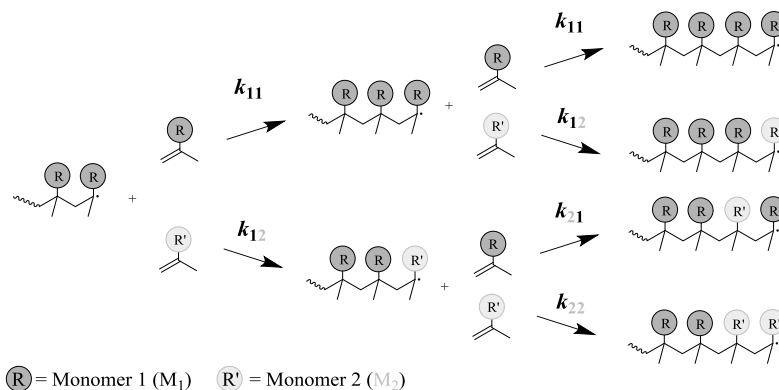


Figure 1. Schematic view on radically initiated copolymer chains growth for monomers M1 and M2, with reactivity rates k .

2.2 Reactivity Ratios

The estimation of the reactivity ratios is the key step to a successful simulation. As basis the energy levels of the monomers (HOMO/LUMO) and of the growing polymer chains (alpha and beta SOMO/LUMO) are



computed using PM7 calculations with MOPAC2016 (Version: 16.146W, James J. P. Stewart, Stewart Computational Chemistry). Thereby MM2 optimised structures serve as starting point (Chem3D Pro, V15.1, Perkin Elmer Informatics Inc.). To reduce the amount of necessary calculations, the energy level calculation is limited to fourth order polymer chains. This means that only the last four units of the polymer chain are considered which delivers 16 combinations. This practice is feasible, as the differences from the third order (8 combinations) are already in a negligible range (up to 0.3 percent deviation in the final simulation result). From the size of the overlapping orbital energy a transition probability is derived, which is interpreted from the selection algorithm as reaction probability. This is done by the copolymer simulation tool (CPTool), which was developed by our group.

The CPTool design makes it possible to simulate a specified number of repetitions for any monomer combination. The distance between the data points is in an arbitrarily accurate resolution. Depending on the parameterisation of the algorithm (energy level evaluation (ELE)) the simulation can already reproduce experimental or literature data in good approximation. The required computing time is only a few minutes per experiment.

3. Results

As test system the well-studied copolymer Styrene-*co*-MMA was chosen. For a radical copolymerisation at 60 °C r -parameter sets with $r_1 = 0.52$ and $r_2 = 0.46$ are described in the literature [3]. Very similar values are obtained using the empiric AP parameters with $Q = 0.74$ and $e = 0.40$ [5] (cf. Figure 2a). In practically performed experiments with Lauroylperoxide as the free radical initiator at 60 °C we found $r_1 = 0.784$ and $r_2 = 0.280$ according to the KELEN-TÜDÖS (KT) linear adaptive evaluation method at 2% monomer conversion. The detailed experimental setup is described elsewhere [6]. Figure 2 shows the copolymerisation diagrams for the calculated r -parameters according to AP (a), our experimental data with KT evaluation (b) and two simulation results using the statistical PM7 based forecast method with different ELE parameters (c and d). Here the r -values are obtained directly from the data using MAYO-LEWIS (ML) fit functions.

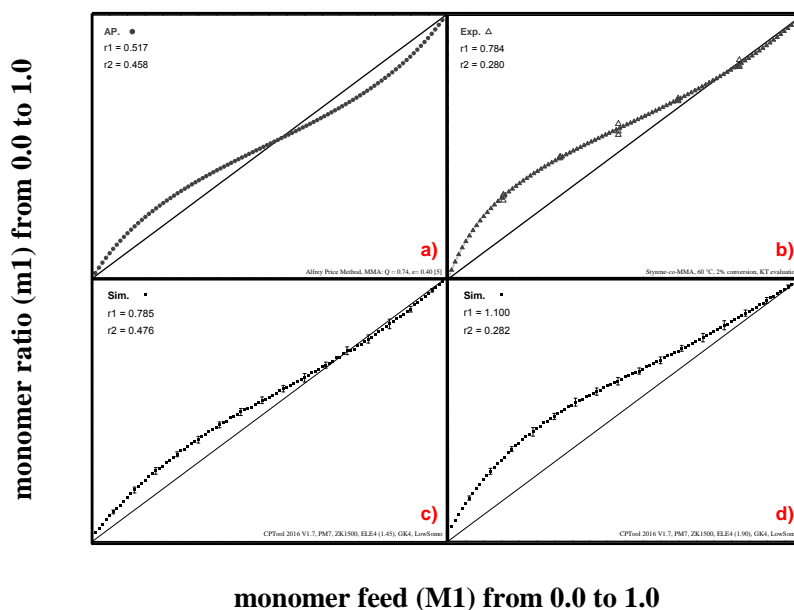


Figure 2. Copolymerisation diagrams for Styrene-*co*-MMA copolymers with bisecting guide line (truly random copolymerisation). a: Calculated values AP method; b: experimental data with KT evaluation; c: simulated data, ELE 1.45; d: simulated data, ELE 1.90.



For both shown simulations (Figure 2c and 2d) a chain length of 1500 repetition units is obtained. The SOMO with the lowest energy level has been selected for the combination of the orbitals. Moreover the resolution of the experiment is 1% at a repetition rate of 25 cycles per data point. In comparison to the 15 incorporated polymeric samples from the experiment (Figure 2b) there are 2525 measuring points available in the performed simulation. It is evident that through parameterisation of the evaluation algorithm different copolymerisation behaviours can be achieved. As result for an ELE parameter of 1.45 (simulation 2c) a copolymerisation with $r_1 = 0.785$ and $r_2 = 0.476$ occurs. ELE 1.90 leads to $r_1 = 1.100$ and $r_2 = 0.282$ (simulation 2d). The first simulation matches the expected pattern according to AP (2a). The second covers our own experiments (2b) quite well. This attempt indicates that a fine-tuning of the evaluation logic is necessary for each experiment at the moment. Further training of the algorithm must meet the real conditions in the future. This includes in particular the laboratory environment and the execution of the experiment. The ultimate goal is a safe copolymerization parameter forecast. This requires further tests on various monomers and different copolymer compositions.

4. Applications in the field of POF

The major advantage of copolymeric POFs is the possibility to adjust physical and chemical characteristics. This covers properties like the refractive index [9], the glass transition temperature (T_g) [10, 11, 12] or active functionalisations with copolymerisable dyes [13]. For solid state application like the preform production for fibre drawing only truly random or azeotropic copolymerisations can be used. For this special reaction types both r -parameter are either 1 (truly random) or less than 1 (azeotropic). The presented simulation method can help to run or exclude certain monomer combinations before the experiment.

5. Conclusion

The simulation program CPTool is able to map the copolymerization behaviour of Styrene-*co*-MMA copolymers based on distinguished energy levels of the monomers or the growing polymer chains respectively. Through parameterisation of the evaluation algorithm it is possible to achieve results that are in a good approximation to real experiments. Further training of the system and better adaptation to the conditions in the laboratory will deliver more precise results. Thus a prediction of the r -parameters relying exclusively on computer chemical calculations is available. Furthermore it is fast, cost-effective and independent on Q, e -values. Further testing with different monomer combinations has to show the practical value of this new method.

6. References

- [1] D. Zaremba, R. Evert: *Materials, Chemical Properties and Analysis in Polymer optical fibres: Fibre types, materials, fabrication, characterisation and applications*, Ed.: M. Beckers, T. Gries, C.-A. Bunge, Woodhead Publishing, **2016**.
- [2] J. M. G. Cowie, V. Arrighi, *Polymers: Chemistry and Physics of modern Materials 3rd Edition*, CRC Press, Boca Raton, 2008.
- [3] B. Tieke, *Makromolekulare Chemie*, Wiley-VCH Verlag GmbH & Co.KGaA, Weinheim, Germany **2012**.
- [4] T. Alfrey, C. C. Price, *J. Polym. Sci.* **1947**, 2, 101–106.
- [5] Y. Koike, *Fundamentals of plastic optical fibers*, Wiley-VCH Verlag GmbH & Co.KGaA, Weinheim, Germany, **2015**.
- [6] D. Zaremba, R. Evert, L. Neumann, M. Steinhoff, W. Kowalsky, R. Caspary, H.-H. Johannes: *Copolymer Optical Fibers and related Applications*, in Proc. 24th International Conference on Plastic Optical Fibers (POF2015), Nuremberg (Germany), SEP. 22-24, **2015**.
- [7] Fineman, M.; Ross, S.D. *J. Polym. Sci.* **1950**, 5, 259–262.



- [8] Kelen, T.; Tüdös, F.; Turcsányi, B. *Polymer Bulletin* **1980**, *2*, 71-76.
- [9] Gang Ding Peng, P. K. Chu, Zhengjun Xiong, T. W. Whitbread, R. P. Chaplin, *J. Lightwave Technol.* **1996**, *14*, 2215–2223.
- [10] A. Kondo, T. Araki, Y. Koike: *Binary Amorphous Copolymers Based Graded Index Polymer Optical Fiber*, in Proc. 21st International Conference on Plastic Optical Fibers (POF2012), Atlanta (USA), SEP. 10-12, **2012**.
- [11] K. Koike, F. Mikeš, Y. Okamoto, Y. Koike, *J. Polym. Sci. A Polym. Chem.* **2009**, *47*, 3352–3361.
- [12] D. Zaremba, R. Evert, A. Cichosch, R. Caspary, W. Kowalsky, H.-H. Johannes: *Novel Concepts for Copolymer Based High Temperature POFs*, in Proc. 23rd International Conference on Plastic Optical Fibers (POF2014), Yokohama (Japan), OCT. 08-10, **2014**.
- [13] S. Möhl, A. Cichosch, S. Schütz, R. Caspary, W. Kowalsky, H.-H. Johannes: *Materials for Polymer Optical Fiber Amplifiers, Fiber*, 21st International Conference on Plastic Optical Fibers (POF2012), Atlanta (USA), SEP. 10-12, **2012**.

Polymer Optical Fiber Sensor for Temperature Measurement in Liquids

R. Guijarro¹, A. Tapetado^{1*}, P. J. Pinzón¹, P. C. Lallana¹, D. S. Montero¹, J. Zubia², C. Vázquez¹

¹ Electronics Technology Dpt., Carlos III University of Madrid, Avda. Universidad 30, 28911, Leganés, Spain

² Applied Physics Dpt., University of the Basque Country, Alameda de Urquijo s/n, 48013, Bilbao, Spain

*Corresponding author: atapetad@ing.uc3m.es

Abstract: The dependence of the fiber attenuation on the water-absorption ratio in poly methyl methacrylate (PMMA)-based step-index (SI) polymer optical fibers (POF) is discussed to clarify the effect of humidity on POF-based macrobend sensors. After immersing a macrobend temperature sensor in pure water for more than 45h, the stabilization of the water-absorption ratio is reached. In this region, the sensor attenuation stability becomes 0.06dB. Thus, considering a POF macrobend sensor with a bend radius of 2mm, a temperature error of 4°C is obtained for a temperature range from 27.2 and 50.2°C.

1. Introduction

Fiber-optics sensors can be applied for measuring temperature in industrial and biomedical applications. In recent years, fiber optic sensing technology based on POF has attracted much attention from researchers. Compared with glass optical fibers (GOFs), POFs can provide low loss in the visible spectrum and are more flexible. Furthermore, POFs are cheaper with regards to both their production and experimental equipment [1]. With their special focus on light intensity modulation schemes and low-cost solutions [2], [3], they can be considered a cost-effective alternative to GOF-based sensors. In addition, the thermo-optic coefficient of the POF is one order of magnitude above its GOF counterpart and thus, the POF core and cladding refractive indices are both highly affected by temperature variations.

These POF advantages have also been exploited for temperature sensing, but PMMA-based POFs can experience the influence of the water absorption [4], [5]. Although the stability and moisture absorption of POFs were significantly improved in the last years using novelty polymer materials such as cyclic olefin copolymer (TOPAS) [6], low-cost PMMA SI POFs remain significantly affected by humidity. Almost all of the previous work reported in literature aimed to enhance the stability and moisture absorption of POFs but focusing their use in high-speed communications through doped graded-index (GI) POF [7], [8]. Nevertheless only very few studies have been reported on the effects of high temperature and humidity conditions on the performance of PMMA-based POF sensors [9], [10]. The temperature-dependent changes in the fiber's physical properties –in particular, the surface morphology and deformation trajectory– can have an effect on temperature measurement consistency and sensitivity of the PMMA POF temperature sensors in water that has not yet been analysed. This effect can influence the long term performance of different POF sensors immersed in fluids and based on intensity measurements such as [11], [12].

In this context, the purpose of this work is to investigate the attenuation stability of a PMMA-based SI POF macrobend temperature sensor [3] under high temperature and humidity environments. There is a relation between the increment of the fiber attenuation and the amount of absorbed water [5]. Thus, the maximum attenuation is reached when the water absorbed by the fiber reaches its maximum value. Thereby, this work pretends to analyse the influence of the fiber attenuation related to the water-absorption phenomenon in low-cost fiber-optic intensity sensors that can be used for measuring temperature in the presence of water.

2. Water Absorption stability in a PMMA core SI POF

The water-absorption stability for a POF sample is measured with respect to the water-immersion time. The optical fiber used in this experiment is a SI POF with a PMMA core and a fluorinated polymer cladding. The fiber core and cladding have a diameter of 980 and 1000µm, respectively. The experiment is performed immersing the dried POF sample into a hermetic tank full of pure water, see Figure 1. The length of the fiber sample is 6cm. The water temperature is fixed at 50°C using a dry block calibrator which ensures a maximum temperature stability and uncertainty of ±0.03°C and ±0.17°C, respectively. The liquid temperature is fixed at 50°C in order to maximize the weight changes, while keeping constant both the fiber diameter and the fiber length [9]. Then, the amount of water absorption is calculated by measuring the weight changes of the POF sample using a high precision scale. Its maximum capacity and readability are 65g and 0.1g, respectively. A

total set of fifteen weight measurements are taken along a total of three days of water-immersion time. Thus, the water-absorption ratio, $W_n(t)$, is calculated from the experimental values using a normalized weight change as [10]:

$$W_n(t) = \frac{W(t) - W_{dry}}{W_{dry}} \cdot 100 \tag{1}$$

where $W(t)$ is the weight of the POF sample at time t in percentage units, and W_{dry} is the equilibrated weight in a drier environment with a relative humidity and temperature of 25% and 25°C, respectively.



Figure 1. Photograph of the dry block calibrator and the POF sample.

Figure 2 shows the water-absorption ratio plotted with respect to the water-immersion time at 50°C. As expected, the water-absorption increases with the water-immersion time. It can be seen that the change is significantly pronounced along the first 20 hours of experiment and nearly levelled off at >40h. The measured saturated water-absorption ratio is around 1.35%. This value is obtained when no changes in the fiber sample weight are observed. Thus, the maximum value is reached after 45h. The water-absorption ratio is clearly limited by the resolution of the precision scale. These measures could be enhanced using a higher resolution scale.

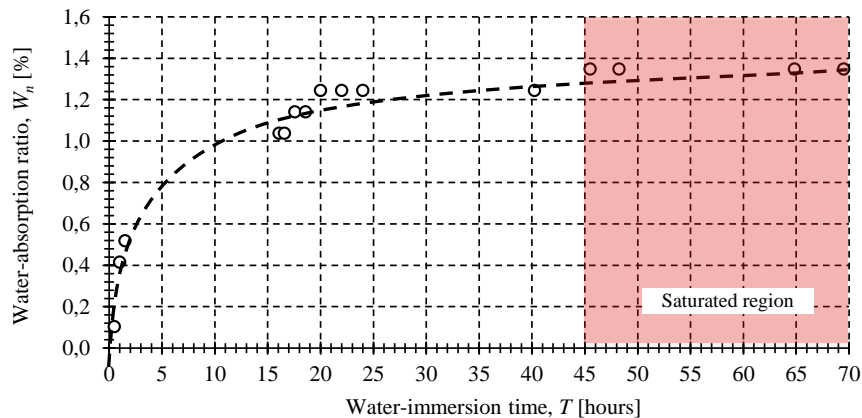


Figure 2. Amount of PMMA SI POF water absorption versus time, at a temperature of 50°C.

These results are in good agreement with other measurements reported by K. Minakawa et. al. in [10]. In this latter work, a cylindrical PMMA sample with a 1.5mm thickness was immersed in pure water at a temperature of 40°C and the water absorption change was mostly pronounced at <24h and nearly levelled off at >96h.

3. Water-absorption influence on the sensor attenuation

The water-absorption influence on the attenuation of a POF macrobend temperature sensor, similar to of the one reported in [3], is investigated. The schematic of the experimental set-up is shown in Figure 3.

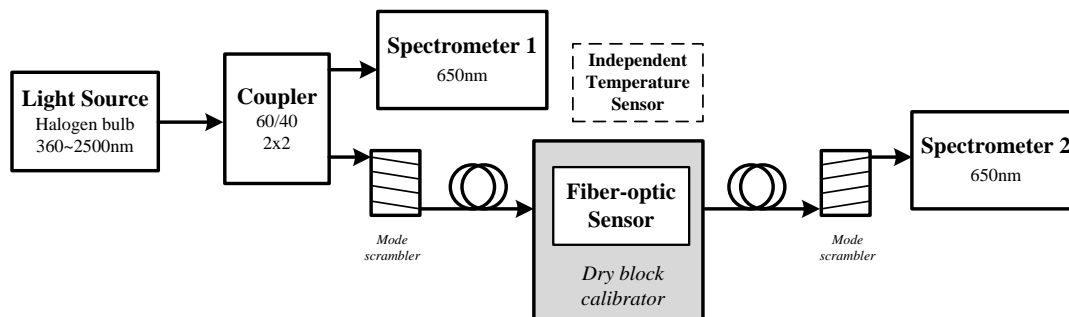


Figure 3. Schematic of the experimental set-up for characterizing the water-absorption influence on the sensor attenuation.

The light source employed is a 360-2500nm stabilized halogen bulb. To measure the input optical power, a visible (VI) spectrometer is connected to the main light source using a 60/40 POF coupler. The fiber macrobend temperature sensor used in this experiment is formed by creating a single 180° loop with a bend radius of 2mm [3]. The sensor sensitivity for a temperature range from 27.2 to 50.2°C is $1.28 \cdot 10^{-2} \text{dB}/^\circ\text{C}$. The dried macrobend sensor is connected to the 60% output port of the POF coupler and then immersed into a hermetic tank full of pure water. A thermal isolated stage is performed for supporting the macrobend sensor when it is placed inside the water tank. The water temperature is fixed at 50°C using the dry block shown in Figure 1. A second VI spectrometer is connected to the macrobend sensor to monitor the optical power launched into the sensor. Two mode scramblers are placed before and after the macrobend sensor to produce a stable mode distribution in the fiber regardless of the launching conditions.

In the experiment, the input and output optical powers at 650nm are measured for each water-immersion time. A time interval of 15min is set between each measure during a total of 3 days. The attenuation increment, $\alpha(t)$, is calculated from the experimental values using the following equation:

$$\alpha(t) = 10 \cdot \log \left(\frac{P_O(t)}{P_I(t)} \right) - 10 \cdot \log \left(\frac{P_O(t_0)}{P_I(t_0)} \right) \quad (2)$$

where $P_O(t)$ is the sensor output power, $P_I(t)$ is the sensor input power, t is time, and t_0 is the initial time.

Figure 4 shows the evolution of the fiber attenuation for the proposed macrobend sensor. The sensor attenuation increment is nearly levelled off at >45h, reaching a maximum value of 0.91dB. The saturation time is equal to the time taken by the PMMA SI POF to reach the saturated water-absorption ratio. The sensor stability during the permanent regime is 0.06dB. Using this value and the sensor sensitivity, a temperature error of around 4°C can be obtained for a temperature range from 27.2 and 50.2°C if this effect is not considered. The effect can be higher in the first moment the sensor is immersed in water.

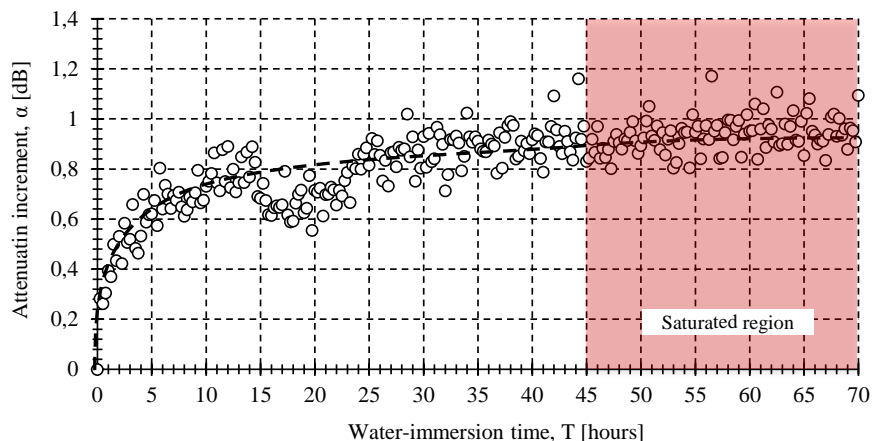


Figure 4. Relation between the fiber attenuation increment and the water-immersion time at 650nm, at 50°C.

4. Conclusions

In summary, the attenuation stability of a (PMMA)-based SI POF macrobend temperature sensors under high temperature and humidity environments is analysed. It is shown that the water absorption can greatly affect the sensor performance in the first hours of the sensor being immersed in water. The stabilization time is around 45h, after that a temperature error of around 4°C can be obtained for a temperature range from 27.2 and 50.2°C if this effect is not considered.

5. Acknowledgements

This work was partially supported by the Spanish Ministry of Economy and the European Regional Development Fund under grant TEC2015-63826-C3-2-R (MINECO/FEDER) and from Comunidad de Madrid under grant S2013/MIT-2790.

6. References

- [1] J. Zubia and J. Arrue, "Plastic Optical Fibers: An Introduction to Their Technological Processes and Applications," *Opt. Fiber Technol.*, vol. 7, no. 2, pp. 101–140, 2001.
- [2] A. Tapetado, P. J. Pinzon, J. Zubia, and C. Vazquez, "Polymer Optical Fiber Temperature Sensor With Dual-Wavelength Compensation of Power Fluctuations," *J. Light. Technol.*, vol. 33, no. 13, pp. 2716–2723, Jul. 2015.
- [3] A. Moraleda, C. García, J. Zaballa, and J. Arrue, "A Temperature Sensor Based on a Polymer Optical Fiber Macrobend," *Sensors*, vol. 13, no. 10, pp. 13076–13089, Sep. 2013.
- [4] T. Kaino, "Influence of water absorption on plastic optical fibers.," *Appl. Opt.*, vol. 24, no. 23, p. 4192, 1985.
- [5] T. Kaino, "Absorption Losses of Low Loss Plastics Optical Fibers," *Jpn. J. Appl. Phys.*, vol. 24, no. 12, p. 1661, 1985.
- [6] D. J. Webb, K. Kalli, C. Zhang, M. Komodromos, A. Argyros, M. Large, G. Emiliyanov, O. Bang, and E. Kjaer, "Temperature sensitivity of Bragg gratings in PMMA and TOPAS microstructured polymer optical fibres," in *Photonic Crystal Fibers II*, 2008, p. 69900L.
- [7] K. Makino, T. Kado, A. Inoue, and Y. Koike, "Low loss graded index polymer optical fiber with high stability under damp heat conditions," *Opt. Express*, vol. 20, no. 12, pp. 12893–12898, 2012.
- [8] T. Ishigure, M. Sato, A. Kondo, Y. Tsukimori, and Y. Koike, "Graded-index polymer optical fiber with high temperature and high humidity stability," *J. Light. Technol.*, vol. 20, no. 10, pp. 1818–1825, 2002.
- [9] N. Zhong, Q. Liao, X. Zhu, M. Zhao, Y. Huang, and R. Chen, "Temperature-independent polymer optical fiber evanescent wave sensor," *Sci. Rep.*, vol. 5, p. 11508, Jun. 2015.
- [10] K. Minakawa, K. Koike, N. Hayashi, Y. Koike, Y. Mizuno, and K. Nakamura, "Dependence of Brillouin frequency shift on water absorption ratio in polymer optical fibers," *J. Appl. Phys.*, vol. 119, no. 22, p. 223102, Jun. 2016.
- [11] D. S. Montero, P. C. Lallana, and C. Vázquez, "A Polymer Optical Fiber Fuel Level Sensor: Application to Paramotoring and Powered Paragliding," *Sensors*, vol. 12, no. 12, pp. 6186–6197, May 2012.
- [12] D. S. Montero, C. Vázquez, I. Möllers, J. Arrúe, and D. Jäger, "A self-referencing intensity based polymer optical fiber sensor for liquid detection," *Sensors*, vol. 9, no. 8, pp. 6446–6455, 2009.



Polymer Optical Fibre Bragg Grating Humidity Sensor at 100°C

G. Woyessa^{1*}, A. Fasano², C. Markos¹, H.K. Rasmussen², O. Bang¹

1 DTU Fotonik, Department of Photonics Engineering, Technical University of Denmark, DK-2800 Kgs. Lyngby, Denmark

2 DTU Mekanik, Department of Mechanical Engineering, Technical University of Denmark, DK-2800 Kgs. Lyngby, Denmark

*Corresponding author: gewoy@fotonik.dtu.dk

Abstract: We have demonstrated a polymer optical fibre Bragg grating humidity sensor that can be operated up to 100°C. The sensor has been fabricated from a polycarbonate (PC) microstructured polymer optical fibre Bragg grating (mPOFBG). PC mPOFBG gave a relative humidity (RH) sensitivity of 6.95 ± 0.83 pm/% RH in the range 10-90% RH at 100°C and a temperature sensitivity of 25.94 ± 0.47 pm/°C in the range 20 - 100 °C at 90% RH. Despite PC mPOFBGs shows smaller humidity sensitivity compared to PMMA mPOFBGs, they can be used to sense humidity beyond the operating temperature limit of PMMA mPOFBGs.

Key Words: Polymer optical fibre, Fibre Bragg grating, Fibre optic sensor, Humidity sensor, Annealing.

1. Introduction

The interest in polymer optical fibres (POFs) in sensing is steadily increasing because of their low processing temperature, high flexibility in bending, high fracture toughness, ease of handling, and non-brittle nature, which are properties that glass fibres do not have [1-2]. In addition, POFs are biocompatible and have a high elastic strain limit and low Young's modulus, which makes them advantageous for fibre Bragg grating (FBG) based strain and bio-sensing applications [3-5]. Some polymers, such as PMMA, are humidity sensitive and strongly absorb water [6], while other polymers, such as TOPAS 5013, were shown to be insensitive to humidity and high operating temperature [7]. Nevertheless, it is polycarbonate microstructured polymer optical fibre (mPOF) that has the highest operating temperature among currently existing POFs [8]. Due to the moisture absorbing capability of PMMA based POFs, which leads to a change in the refractive index and size of the fibre, both of which contribute to a change in Bragg wavelength [9], they are used for developing humidity sensors [10]. PC has also moisture absorbing capability although it is smaller than that of PMMA. The water absorption (saturation value) at 23°C of PC is 0.3% [11], and PMMA is 2.1% [12]. This means that the water absorption capability of PC is 7 times smaller than that of PMMA but about 40°C larger glass transition temperature (T_g) as compared to PMMA.

For PMMA POFBGs the temperature operational limit is strongly dependent on the surrounding relative humidity (RH) level at which they are being operated, in addition to its T_g . If they are operated at ambient or less RH level, this limit is 15-20°C below their T_g . For instance, at ambient RH PMMA POFBGs has been operated up to 90 °C [13]. But, when the surrounding RH is high, the temperature operational limit significantly decreases. For instance, at 90% RH they can be operated only up to 75 °C [14]. This is due to the fact that for such polymers the glass transition temperature decreases with increasing humidity. Similarly, when PMMA POFBGs are used as humidity sensor the RH range of operation highly dependent on the temperature of the environment in which the sensors are being operated. PMMA POFBG has been operated from 10-90% RH up to 75°C. However, beyond this temperature the grating could not handle it. If the temperature in which PMMA POFBGs humidity sensors are being operated is higher than 75°C, the maximum RH should be less than 90%. For instance, if we want to operate PMMA POFBGs at 85 °C, the range of RH operation will be limited to only 60% RH for stable operation. Likewise, at 90°C the range of possible RH becomes even narrower. Thus, it is important to develop POFBG humidity sensors which can operate at high temperature and also with wide range of RH for some applications. Here we demonstrated a stable and highly linear mPOFBGs humidity sensor that can be operated beyond 100°C and with RH range of up to 90%. This sensor is developed with PC mPOFBGs.



2. Experiment

The fibre used in this experiment is a PC mPOF. The diameter of the fiber is $130\mu\text{m}$, and the hole and the pitch size are $1.5\mu\text{m}$ and $4.2\mu\text{m}$, respectively. The hole to pitch ratio is 0.38, ensuring that the fiber is endlessly single mode [15]. First FBG was inscribed by using phase mask technique. The setup used was the same as described in ref. 16. The Bragg wavelength of the grating was 892.67nm and the full width half maximum was 0.8nm . The PC mPOFBG was first connectorized [17] and coupled with a single mode silica fibre and then placed in the CLIMACELL environmental chamber. A Supercontinuum source (NKT Photonics A/S) has been used as a light source and Compact CCD Spectrometer (THORLABS) has been used to continuously track the grating in the chamber during the experiment. The FBG has been first annealed at 100°C and 90% relative humidity (RH). The annealing process was stopped when the rate of blue shift was less than $0.1\text{nm}/\text{hour}$. This process took 26 hours. The amount of blue shift was 8nm .

After annealing the humidity response of the mPOFBG sensor has been measured at 100°C in the interval of 10-90% RH. At this temperature and RH range the environmental chamber has a precision of 0.5°C and 1% RH. The humidity measurement has been done first by increasing the RH from 10% to 90%, with step of 10% and then decreasing it from 90% to 10% with step of 10%. The stabilization period after incrementing or decrementing the RH was 60 minutes.

We have also measured the temperature sensitivity at 90% RH in the range 20 to 100°C . The temperature measurement has been done first by increasing the temperature from 20 to 100°C , with steps of 10°C and then decreasing it back to 20°C with same amount of step. The stabilization period after incrementing or decrementing the temperature was 60 minutes.

3. Results

The response of the PC mPOFBGs for both increasing and decreasing relative humidity at 100°C for the stabilized period is shown in Fig. 1.

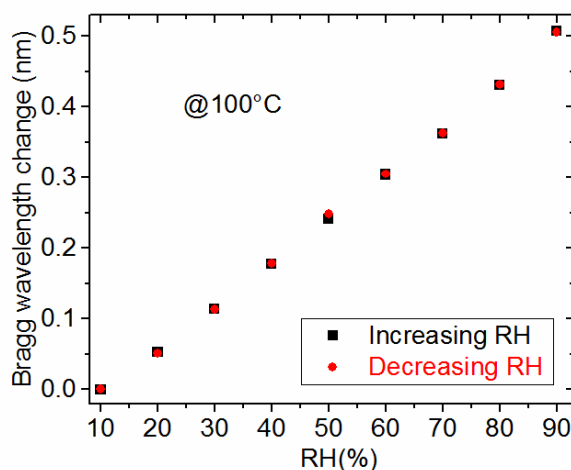


Figure 1. Measured humidity response at 100°C of the PC mPOFBG.



The humidity sensitivity at 100°C was 6.95 ± 0.83 pm/%RH for both increasing and decreasing humidity. The R-squared for this fitted regression line is 0.998. The humidity sensitivity of a PMMA mPOFBG at 75 °C, which is the maximum operating temperature at higher RH, in the 850nm region is typically around 45 pm/%RH in the range 10-90%. This shows that PC mPOFBG has wider operating temperature range but lower RH sensitivity as compared to PMMA mPOFBGs.

The response of the PC mPOFBGs for both increasing and decreasing temperature at 90% RH is shown in Fig. 2. The temperature sensitivity at 90 % RH was 25.94 ± 0.47 pm/°C for both increasing and decreasing temperature. The R-squared for this fitted regression line is 0.998. There were no hysteresis observed for both humidity and temperature measurement. This is due to the fact the FBG was annealed well enough.

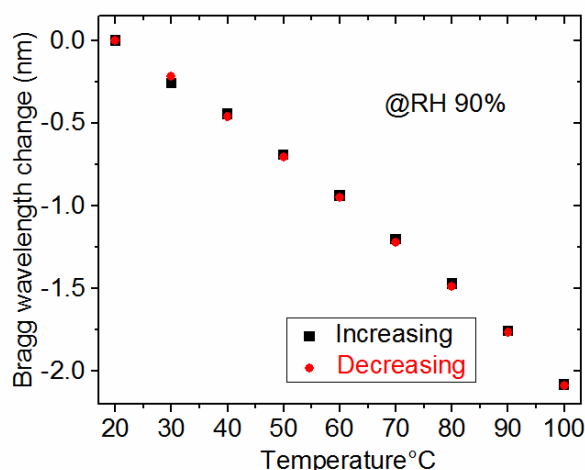


Figure 2. Measured temperature response at 90% RH of the PC mPOFBG.

4. Conclusion

We have developed a polymer optical fibre Bragg grating humidity sensor that can be operated up to 100°C. The sensor has been fabricated from a PC mPOFBG. PC mPOFBG gave a RH sensitivity of 6.95 ± 0.83 pm/%RH in the range 10-90% RH at 100°C and a temperature sensitivity of 25.94 ± 0.47 pm/°C in the range 20-100 °C at 90% RH. Thus, PC mPOFBGs humidity sensors can be used beyond the operating temperature limit of PMMA mPOFBGs.

Acknowledgments

The research leading to these results has received funding from the People Programme (Marie Curie Actions) of the European Union's Seventh Framework Programme FP7/2007-2013/ under REA grant agreement n° 608382.

References

- [1].K. Peters, "Polymer optical fiber sensors - A review," *Smart Mater. Struct.* **20**(1), 013002 (2011).
- [2].H. Dobb, D. J. Webb, K. Kalli, A. Argyros, M. C. J. Large, and M. A. van Eijkelenborg, "Continuous wave ultraviolet light-induced fiber Bragg gratings in few- and single-mode microstructured polymer optical fibers," *Opt. Lett.* **30**(24), 3296–3298 (2005).



- [3].Z. Xiong, G. D. Peng, B. Wu, and P. L. Chu, "Highly tunable Bragg gratings in single-mode polymer optical fibers," *IEEE Photon. Technol. Lett.* **11**(3), 352–354 (1999).
- [4].H.Ul Hassan, K.Nielsen, S.Aasmul, and O.Bang, "Polymer optical fiber compound parabolic concentrator tip for enhanced coupling efficiency for fluorescence based glucose sensors", *Bio.Opt. Express* **12**(2), 5008–5020 (2015).
- [5].C.Broadway, D.Gallego, G.Woyessa, A.Pospori, G.Carpintero, O.Bang, K.Sugden, and H.Lamela, "Fabry-Perot microstructured polymer optical fiber sensors for opto-acoustic endoscopy", *Proc. SPIE* **9531**, 953116 (2015).
- [6].C. Zhang, W. Zhang, D. J. Webb, and G. D. Peng, "Optical fiber temperature and humidity sensor," *Electron. Lett.* **46**(9), 643–644 (2010).
- [7].C. Markos, A. Stefani, K. Nielsen, H. K. Rasmussen, W. Yuan, and O. Bang, "High-Tg TOPAS microstructured polymer optical fiber for fiber Bragg grating strain sensing at 110 degrees, " *Opt. Express* **21**(4), 4758–4765 (2013).
- [8].A.Fasano, G.Woyessa, P.Stajanca, C. Markos, A.Stefani, K.Nielsen, H. K. Rasmussen, K. Krebber, and O. Bang, "Fabrication and characterization of polycarbonate microstructured polymer optical fibers for high-temperature-resistant fiber Bragg grating strain sensors" *Opt. Mater. Express*, **6**(2), 649-659(2016).
- [9].N. G. Harbach, "Fiber Bragg gratings in polymer optical fibers," PhD Thesis, Lausanne, EPFL (2008).
- [10].Z. F. Zhang and X. M. Tao, "Synergetic effects of humidity and temperature on PMMA based fiber Bragg gratings," *J. Lightwave Technol.* **30**(6), 841–845 (2012).
- [11].<http://www.plastics.covestro.com/en/Products/Makrolon/ProductList/201305212210/Makrolon-LED2245>
- [12].<http://www.gehrplastics.com/pmma-acrylic.html>
- [13].K. E. Carroll, C. Zhang, D. J. Webb, K. Kalli, A. Argyros, and M. C. J. Large, "Thermal response of Bragg gratings in PMMA microstructured optical fibers," *Opt. Express* **15**(14), 8844–8850 (2007).
- [14].G.Woyessa, K.Nielsen, A.Stefani, C.Markos and O.Bang, "Temperature insensitive hysteresis free highly sensitive polymer optical fiber Bragg grating humidity sensor", *Opt. Express* **24**(2), 1206-1213 (2016).
- [15].T. A. Birks, J. C. Knight, and P. St.J. Russell, "Endlessly single-mode photonic crystal fiber," *Opt. Lett.* **22**(13), 961–963 (1997).
- [16].I.-L. Bundalo, K. Nielsen, C. Markos, and O. Bang, "Bragg grating writing in PMMA microstructured polymer optical fibers in less than 7 minutes," *Opt. Express* **22**(5), 5270–5276 (2014).
- [17].A. Abang and D. J. Webb, "Demountable connection for polymer optical fiber grating sensors," *Opt. Eng.* **51**(8), 080503-1 (2012).



Intrinsic Pressure Response of a Single-Mode Cyclo Olefin Polymer Microstructured Optical Fibre Bragg Grating

J. K. M. Pedersen^{1*}, G. Woyessa¹, K. Nielsen¹, O. Bang¹

¹ Department of Photonics Engineering, Technical University of Denmark, 2800 Kgs. Lyngby, Denmark

*Corresponding author: jkmp@fotonik.dtu.dk

Abstract: The intrinsic pressure response of a Fibre Bragg Grating (FBG) inscribed in a single-mode cyclo olefin polymer (COP) microstructured polymer optical fibre (mPOF) in the range 0-200 bar is investigated for the first time. In order to efficiently suppress the effects from changes in temperature and relative humidity the pressure calibration is performed in a gas free environment with the FBG submerged in water. As a result of the incompressible nature of water no temperature effects due to rapid pressure changes are observed. We find a highly linear, hysteresis-free response with a sensitivity of 2.982 ± 0.002 pm/bar. The corresponding fractional sensitivity is found to be $34.5 \cdot 10^{-6}$ MPa⁻¹ which is of the same order of magnitude as the results obtained for a multimode PMMA mPOF-FBG at 1562 nm previously reported in the literature. The resulting pressure resolution of our sensor is estimated to be 2 bar based on a root mean square deviation of 6 pm.

1. Introduction

Polymer Optical Fibre Bragg Gratings (POFBGs) have in the recent years attracted increasing attention due to a range of advantageous properties, such as a low Young's modulus and a high temperature sensitivity compared to FBGs inscribed in conventional silica optical fibres. In addition to their small size, FBGs remain unaffected by external electromagnetic disturbance, which makes them a promising alternative to existing electrical sensors. The first reported case of a successful fabrication of a POFBG was seen in 1999 [1], where an FBG was inscribed into a PMMA step-index fibre. Since then FBGs have also been inscribed in microstructured polymer optical fibres (mPOF) made of PMMA [2] and TOPAS [3]. One of the clear advantages of mPOFs is that they can be made endlessly single-mode, which cannot be facilitated in a step-index fibre [4]. Single mode operation in FBGs is advantageous due to the very narrow bandwidth of the reflection peak, which ultimately leads to a higher sensing resolution compared to Bragg-gratings inscribed in few-mode or multimode fibres [5].

A long range of possible applications of POFBGs have been addressed in the literature, such as strain- [6], temperature- [7, 8] and humidity sensing [9, 10]. Moreover, the possibility of using POFBGs to measure hydrostatic pressure has been reported [11, 12]. Existing work on POFBG-based pressure sensing has focused solely on PMMA optical fibres, however in recent years other types of POFs have emerged that exhibit interesting properties such as humidity insensitivity and higher melting points [3, 6, 13]. In this work we present for the first time a thorough investigation of the intrinsic pressure response of an FBG inscribed in a single mode cyclo-olefin polymer (COP) optical fibre.

1.1 Principle of FBG Hydrostatic Pressure Sensing

The operation principle of an FBG can be summarized with the Bragg-formula

$$\lambda_B = 2n_{eff}\Lambda, \quad (1)$$

where λ_B is the Bragg-wavelength, n_{eff} the effective index of the fibre mode and Λ is the pitch of the grating. From this relation, the pressure response of an FBG is found to be

$$\frac{1}{\lambda_B} \frac{\partial \lambda_B}{\partial P} = \frac{1}{n_{eff}} \frac{\partial n_{eff}}{\partial P} + \frac{1}{\Lambda} \frac{\partial \Lambda}{\partial P}, \quad (2)$$

where the first term on the right hand side accounts for the strain-optic effect and the second term is due to the volumetric contraction/expansion of the FBG due to changes in the pressure. As the hydrostatic pressure acting on the FBG is increased, the strain-optic effect will add to a positive shift in Bragg wavelength as the material is compressed, whereas the grating pitch will be reduced, leading to a negative shift. The resulting



Bragg-wavelength shift is thus a competition between the two mentioned effects. A negative pressure response was previously reported for a silica FBG [14], indicating a dominating volumetric effect, whereas investigations of PMMA-based FBGs have shown a positive response [11, 12] showing that the strain-optic effect is the dominating factor in these fibres.

2. Experiment and Results

2.1 Experimental Setup

In order to investigate the pressure characteristics of the FBG, we used the setup schematized in Figure 1. A pressure calibration device with inner diameter of 5 mm was filled with water and a hand screw connected with a rubber cylinder was used to apply pressure to the water surface. The FBG was submerged into the water and the fibre sealed off with a custom rubber seal in order to avoid water from leaking out of the system. Due to the incompressible nature of water we avoided any effects from temperature variations due to rapid pressure changes as would be otherwise present in a gas-filled environment [11, 12].

By continuously turning the screw the pressure could be varied from 0 – 200 bar. The applied pressure was recorded by logging the analogue output from the pressure gauge (Druck DPI 104) using a 10-bit A/D converter and a PC resulting in a pressure resolution of 0.2 bar. The 600-900 nm part of a supercontinuum light source (SuperK Compact, NKT Photonics A/S) was launched into the mPOF through a 3 dB fibre coupler and the spectrum reflected from the FBG was recorded using a CCD-spectrometer (Thorlabs CCS175) with a FWHM-resolution of 0.6 nm.

In order to accurately measure the shift in the Bragg-wavelength we have implemented a dynamic gate peak tracking algorithm [15] and applied it to the recorded spectrum, which allows us to determine the Bragg wavelength with a sub-pixel resolution of 2 pm (taken as the standard deviation of the noise for a 30 sec recording with no load on the FBG).

During the experiment the temperature was monitored using a thermocouple device (Type K) mounted outside of the brass chamber which was in good thermal contact with the water inside. The temperature variation was found to be within 0.2 °C which was mainly due to the heat transfer from the hand when turning the screw.

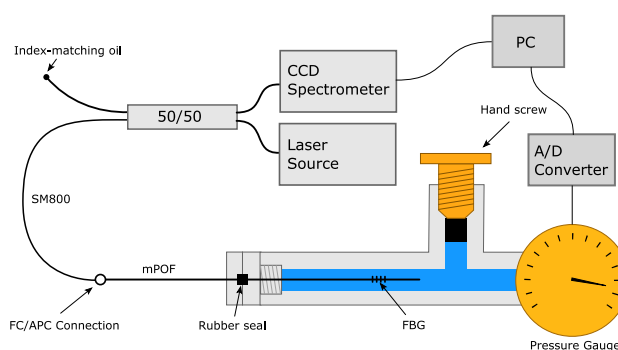


Figure 1. Schematic diagram of the experimental setup used to investigate the pressure response of the FBG.

2.2 Results

In Figure 2 the measured FBG response versus the applied pressure is shown. The pressure was repeatedly increased and decreased in order to ensure that no hysteresis was present. In Figure 3(a) an example of the reflection peak as measured by the CCD-spectrometer is shown. The FWHM of the peak is measured to be 1 nm. By plotting the Bragg-wavelength shift versus applied pressure we obtain the calibration curve shown in Figure 3(b). A very high degree of linearity is observed and the pressure sensitivity is determined to be 2.982 pm/bar with a standard error of 0.002 pm/bar.

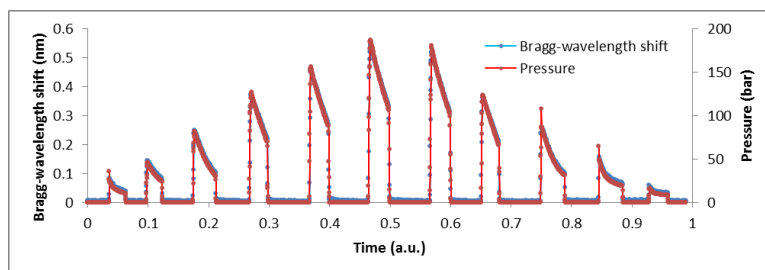


Figure 2. Pressure and corresponding Bragg-wavelength shift recorded in the experiment. The slow pressure reduction after each increase is mainly due to the holes in the fibre which were left unsealed in order to avoid a collapse of the microstructure at high pressure.

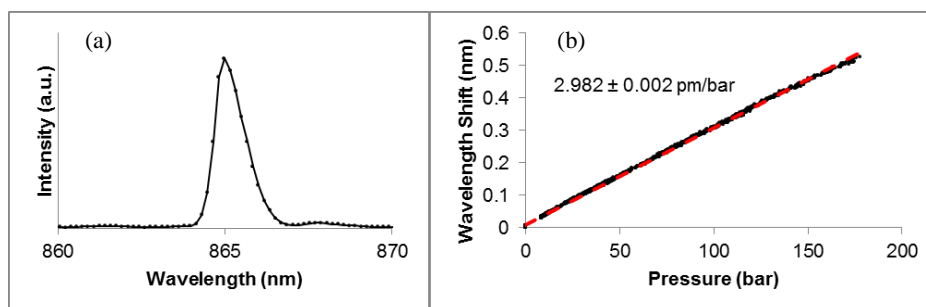


Figure 3. (a) Spectrum reflected from the FBG. (b) Hydrostatic pressure response of the FBG.

In order to estimate the resolution R of our sensor we use the relation

$$R = \frac{\sigma_{RMS}}{\alpha_p},$$

where $\sigma_{RMS} = 6$ pm is the root mean square deviation of the residuals of the linear fit and $\alpha_p = \partial\lambda_B/\partial P$ is the pressure sensitivity of the grating. From this we find a resolution of 2 bar.

In order to compare with previously obtained results for POFBGs at different wavelengths we calculate the fractional sensitivity $F = \alpha_p/\lambda_B$. The reason for calculating this is due to the wavelength scaling of the sensitivity in Eq. (2). For the FBG in question we obtain $F = 3.447 \cdot 10^{-6} \text{ bar}^{-1}$ which is of the same order of magnitude as the fractional sensitivity of $8.3 \cdot 10^{-6} \text{ bar}^{-1}$ reported in [11] for an FBG at 1562 nm inscribed in a PMMA multimode mPOF.

3. Conclusion

We have presented, to our best knowledge, the first investigation of the intrinsic pressure response of a Bragg-grating inscribed in a microstructured cyclo-olefin-polymer optical fibre in the pressure range 0-200 bar. The sensitivity was found to be 2.982 ± 0.002 pm/bar, which is of the same order of magnitude as results previously reported in the literature for an FBG inscribed in a multimode PMMA fibre. The positive value indicates that the strain-optic effect is the dominating part of the response. The response was found to have a very high degree of linearity in the sensing range of interest, and no hysteresis during the experiments was observed. Using a carefully chosen peak tracking algorithm we were able to resolve changes in the Bragg-wavelength shift down to 2 pm, which lead to a pressure resolution of our sensor of 2 bar. In conclusion, we note that this novel kind of polymer optical fibre Bragg grating shows a great potential in hydrostatic pressure sensing in terms of linearity and absence of hysteresis, however further improvements on the sensitivity may be required in order to obtain a better sensing resolution depending on the application in mind.



4. Acknowledgements

The authors acknowledge the financial support from the Danish foundation 'Innovationsfonden' as part of the innovation consortium BIOFORS, contract no. 1382-00058B. The authors also acknowledge financial support from the People Programme (Marie Curie Actions) of the European Union's Seventh Framework Programme FP7/2007-2013/ under REA grant agreement n° 608382.

5. References

- [1] G. D. Peng, Z. Xiong, and P. L. Chu, "Photosensitivity and Gratings in Dye-Doped Polymer Optical Fibers," *Opt. Fiber Technol.*, vol. 5, no. 2, pp. 242–251, 1999.
- [2] H. Dobb, D. J. Webb, K. Kalli, A. Argyros, M. C. J. Large, and M. A. van Eijkelenborg, "Continuous wave ultraviolet light-induced fiber Bragg gratings in few- and single-mode microstructured polymer optical fibers," *Opt. Lett.*, vol. 30, no. 24, p. 3296, Dec. 2005.
- [3] I. P. Johnson, W. Yuan, A. Stefani, K. Nielsen, H. K. Rasmussen, L. Khan, D. J. Webb, K. Kalli, and O. Bang, "Optical fibre Bragg grating recorded in TOPAS cyclic olefin copolymer," *Electron. Lett.*, vol. 47, no. 4, p. 271+, 2011.
- [4] T. A. Birks, J. C. Knight, and P. S. J. Russell, "Endlessly single-mode photonic crystal fiber," *Opt. Lett.*, vol. 22, no. 13, p. 961, Jul. 1997.
- [5] K. Peters, "Polymer optical fiber sensors—a review," *Smart Mater. Struct.*, vol. 20, no. 1, p. 013002, 2011.
- [6] C. Markos, A. Stefani, K. Nielsen, H. K. Rasmussen, W. Yuan, and O. Bang, "High-Tg TOPAS microstructured polymer optical fiber for fiber Bragg grating strain sensing at 110 degrees," *Opt. Express*, vol. 21, no. 4, pp. 4758–65, 2013.
- [7] Z. F. Zhang and X. M. Tao, "Intrinsic temperature sensitivity of fiber bragg gratings in PMMA-based optical fibers," *IEEE Photonics Technol. Lett.*, vol. 25, no. 3, pp. 310–312, 2013.
- [8] W. Zhang and D. J. Webb, "Factors influencing the temperature sensitivity of PMMA based optical fiber Bragg gratings," *Proc. SPIE*, vol. 9128, 2014.
- [9] W. Zhang and D. J. Webb, "Humidity responsivity of poly (methyl methacrylate) - based optical fiber Bragg grating sensors," *Opt. Lett.*, vol. 39, no. 10, pp. 3026–3029, 2014.
- [10] G. Woyessa, K. Nielsen, A. Stefani, C. Markos, and O. Bang, "Temperature insensitive hysteresis free highly sensitive polymer optical fiber Bragg grating humidity sensor," *Opt. Express*, vol. 24, no. 2, pp. 1206–13, 2016.
- [11] I. P. Johnson, D. J. Webb, and K. Kalli, "Hydrostatic pressure sensing using a polymer optical fibre Bragg gratings," *Proc. SPIE*, vol. 8351, pp. 835106–835106–7, 2012.
- [12] K. Bhowmik, S. Member, G. Peng, Y. Luo, E. Ambikairajah, V. Lovric, W. R. Walsh, and G. Rajan, "Experimental Study and Analysis of Hydrostatic Pressure Sensitivity of Polymer Fibre Bragg Gratings," *J. Light. Technol.*, vol. 33, no. 12, pp. 2456–2462, 2015.
- [13] W. Yuan, L. Khan, D. J. Webb, K. Kalli, H. K. Rasmussen, A. Stefani, and O. Bang, "Humidity insensitive TOPAS polymer fiber Bragg grating sensor," *Opt. Express*, vol. 19, no. 20, p. 19731, 2011.
- [14] M. G. Xu, L. Reekie, Y. T. Chow, and J. P. Dakin, "Optical in-fibre grating high pressure sensor," *Electron. Lett.*, vol. 29, no. 4, pp. 398–399, 1993.
- [15] D. Ganziy, O. Jespersen, G. Woyessa, B. Rose, and O. Bang, "Dynamic gate algorithm for multimode fiber Bragg grating sensor systems," *Appl. Opt.*, vol. 54, no. 18, pp. 5657–5661, 2015.

Development and characterization of a low cost sediment concentration optical sensor

N. Oliveira^{1*}, D. Duarte¹, C. Ferreira², P.A. Silva², R. Nogueira⁴, L. Bilro^{1,3}

1 Instituto de Telecomunicações, Aveiro, Portugal

2 CESAM, Department of Physics, University of Aveiro, Aveiro, Portugal

3 I3N/FSCOSD, Department of Physics, University of Aveiro, Aveiro, Portugal

4 WATGRID LDA., Aveiro Portugal

*Corresponding author: duarteoliveira@av.it.pt

Abstract: The polymer optical fiber (POF) based technology has been identified with high potential in the development of optical sensors for various applications because of its low cost (specially intensity based approaches), immunity to electromagnetic interference, flexibility and robustness.

In this paper we propose a sediment concentration POF sensor able to do real time measurements, of a wide range of sediment concentration values usually found in nature.

This sensor has four LEDs with different wavelengths that are connected independently but sequentially to the emitter fiber using a coupler. The light is guided to a measurement cell where the solution sample is present. Two receiving fibers will be used to measure both transmitted (180°) and scattered light (90°).

The calibration of the sensor was performed using sediments samples collected in Mira beach, Portugal, with a median grain size of [0.2-0.25] mm. In parallel it was also performed a calibration of *OBS Campbell Scientific* turbidity sensors.

Results showed that the POF based sensor had higher dynamic range when compared to the commercial solution OBS.

Key Words: Optical fiber sensor; POF; OBS; sediment concentration; optical sensors

1. Introduction

The interaction of light with particles in a solution is dependent on the particles form, size, composition and the light wavelength. Depending on the characteristic of the particles, the light that is transmitted and scattered will have unique signatures. For pure water mostly of the light will be transmitted, presenting a small scattering effect [1].

A model that adequately describes this behavior is the Beer-Lambert law considering that the intensity of transmitted light is also absorbed and attenuated by the particles.

$$I_t = I_0 e^{-[\alpha_a + \alpha_b]XC} \quad (1)$$

Where, I_T is transmitted light intensity, I_0 the incident radiation intensity, X is the optical cavity distance, C is solution concentration, α_a the absorption coefficient and α_b the scattering coefficient. In the case where the solution has particles with different absorption coefficients, the variable α_a is the sum of the absorption coefficients. The same principle is considered for particles with different scattering coefficients, the variable α_b will be the result of the scattering coefficients summation [2]. Therefore, the attenuation coefficient μ can be written as the sum of α_a coefficient and α_b scattering coefficient.

$$\mu = \alpha_a + \alpha_b \quad (2)$$

Turbidity is determined by the concentration of particles suspended in a provided solution and can be quantified by the intensity of light that is scattered by particles presented in the solution [3].

These particles change the characteristics of the incident light beam path which will be depended on the features of these particles, promoting the existence of dispersions, absorptions and transmissions in different physical quantities. It may therefore be an indicator of the concentration of suspended solids [4].

Turbidity is generally measured in nephelometric units (NTU) which is based on the nephelometric principle points where a beam of light is focused to a liquid sample and the intensity of light scattered at 90° relative to the beam is measured [5].

Knowing the turbidity value, it is possible to correlate it with the quantity of total suspended solids (TSS) which is frequently the parameter used to evaluate the quality of water and is given by the weight of the particulates present in a liter of pure water (mg/l) unit [2].

The correlation between TSS e NRU was established by *C. P. Holliday* [6]:

$$NTU = aa(TSS)^{bb} \quad (3)$$

Where *aa* and *bb* are regression coefficients to estimate, with *bb* practically equal to 1 for all particles. This expression is not appropriate for high concentrations because of the obtained non-linearity relationship between the turbidity and scattering of light that starts to appear [7]. It also fails when particle samples with various compositions are present [2]. The different materials can have different coefficients of dispersion and absorption. *F.J. Boogert* tested the performance of a newly developed POF sensor compared with that of a OBS-3+ sensor, using artificial samples of sediments. Nevertheless, a consistently better relationship (higher R^2 values) was found for POF than for OBS-3+ sensor [8].

Optical sensor to measurement sediments

a) Optical backscatter point sensor (OBS)

The optical backscatter point sensor (OBS) is an optical sensor capable of measuring turbidity with a simple operation method [9]. This sensor uses a light source, usually an infrared LED, so that the absorption of the beam is minimal or non-existence on colored solutions. It has an excellent response to the size shape and composition of the particles in suspension. The sensor changes its response to different particles and thus requires a different calibration for each type of particles. OBS also has a detector usually consisting of photodiodes and a filter that allows to reduce the effect of outside light. This sensor is often used for measuring the sediment concentration of sands and clays in the coastal zone of the ocean [10].

In very clear water can cover a depth of about 50 cm. The relationship between the signal provided by the OBS and sediment concentration are nearly linear [11].

Another disadvantage normally associated with OBS is the need for a high water volume which allows the emitted cone of light suffer minimal reflections in the edges of the container used to measure the solution.

b) POF sensor

One of the low cost multiparameter optical sensor capable to measure the discussed physical parameters is the POF (polymer optical fiber) based sensor. The POF based technology has been used in the development of optical sensors in many fields since it allows the design of low cost monitoring or cost managed systems while presenting advantages in terms of immunity to electromagnetic interference and flexibility [12].

Normally, a POF sensor has a source of monochromatic light like a LED and different wavelengths can be used, typically infrared and RGB.

As a matter of intensity optimization basic turbidity (based on the ISO 7027), it is used 90° and 180° as the specific angles to the incident POF [2]. The sensor used in this work is done in teflon (chemically inert) has four LEDs with different wavelengths (470 nm, 530 nm, 660 nm and 870 nm) that are connected independently but sequentially to the transmitter using a fiber coupler. The light is guided to the measurement cell that contains the solution sample and the transmitted and scattered light are measured by photodetectors which is guided by the two receiving fibers.

The data acquisition was performed by a main controller board with a micro-controller with built in analogue to digital converter and Bluetooth® module. This process is represented schematically in Figure 1.

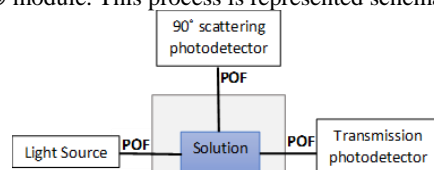


Figure 1- Schematic configuration of an example of a POF turbidimeter.

2. Experimental Setup

The calibration was performed using sand collected in Mira beach in Portugal with a median particle size $d_{50} = [0.2 - 0.25]$ mm (fine sand).

The sand was added in known amounts to a column of 3.5 l of water contained in an acrylic cuvette (Figure 2). A mechanical mixer with an adjustable rotation speed was used to homogenize the solution.

The optical sensor (POF) was placed at a constant depth to ensure the maximum possible homogeneity of the solution. Both calibrations of POF sensor and OBS sensor were performed in parallel at an approximately equal depth.

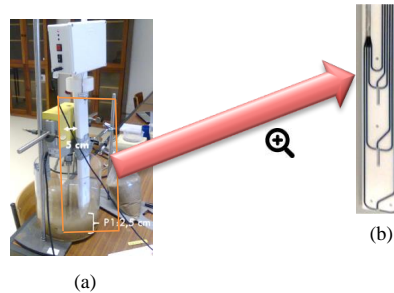


Figure 2- Experimental setup calibration with different granulometry sediments. b) Teflon sensor inside.

3. Results

The results obtained for the calibration of fine sediments using the OBS and the POF sensor are shown in Figure 3.

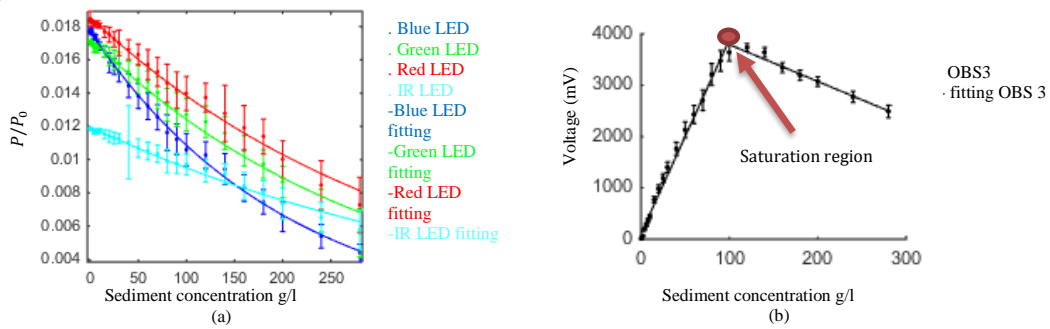


Figure 3. Response POF sensor (a) and OBS sensor (b) with the sediment concentration for the fine sands.

The regressions equations referring to graphs in Figure 3 are presented in Table 1.

Table 1- Regressions referring to graphs in Figure 14.

Sand	Range concentration g/l	Sensor	Regression equation	Regression parameters	Correlation coefficient R^2	RMSE g/l
Fine [0.2-0.25] mm	0-100	OBS3	$Voltage = a \times (C_{sed}) + b$	$a=37,77$ $b=111,3$	0,992	3,122
	100-260	OBS3	$Voltage = a \times (C_{sed}) + b$	$a= -7,177$ $b= 4510$	0,963	12,810
	0-260	Blue LED (POF) sensor	$\frac{Power}{Power_0} = a \times \exp^{(b \times (C_{sed}))}$	$a=1,771e-02$ $b= -4,889e-03$	0,998	3,977
		Green LED (POF) sensor	$\frac{Power}{Power_0} = a \times \exp^{(b \times (C_{sed}))}$	$a=1,730e-02$ $b= -3,318e-03$	0,975	14,310
		Red LED (POF) sensor	$\frac{Power}{Power_0} = a \times \exp^{(b \times (C_{sed}))}$	$a=1,857e-02$ $b= -2,946e-03$	0,985	10,650
		Infrared LED (POF) sensor	$\frac{Power}{Power_0} = a \times \exp^{(b \times (C_{sed}))}$	$a=1,197e-02$ $b= -2,307e-03$	0,985	10,730

The maximum limit value of the measured concentration of sediments (C_{sed}) (observed in Figure 3 (b)) was 260 g/l since it was not possible to ensure the homogeneity of the solution for higher values.

In the turbidity and sediment calibrations, it was found that the transmission channel is in accordance with the Beer-Lambert law (Equation 1), as expected. However, the POF sensor has a higher root mean square error (RMSE) because of their greater sensitivity, which makes it more sensitive to disturbance caused by the magnetic stirrer.

4. Conclusion

The test results show that the POF sensor has a high range compared to OBS for sediment concentration measurements. It was also noted that the saturation of the OBS sensor signal was obtained at 100 g/l which does not happen with POF sensor. The increased dynamic range obtained with the POF sensor for sediment concentration measurements and its good response at high and low concentrations are noticeable advantages compared to other commercial multiparameter sensors (for example OBS). Considering also its low cost and accuracy, which can be proven by the high value of the correlation coefficient and small RMSE value, confirm that these sensors have a great potentiality to real time fluid monitoring commercial application.

5. Acknowledgements

This work is funded by FCT/MEC through national funds and when applicable co-funded by FEDER – PT2020 partnership agreement under the project UID/EEA/50008/2013 (project sWAT and Daniel Duarte research grant in the framework of PROLAB 2015), hiPOF (PTDC/EEI-TEL/7134/2014), and investigator grant (Lúcia Bilro: IF/01664/2014; project INITIATE).

6. Reference

- [1] M. J. Sadar, "Turbidity Science," *HACH - Tech. informations Ser. Bookl. No. 11*, no. 11, 1998.
- [2] A. F. Bin Omar and M. Z. Bin MatJafri, "Turbidimeter design and analysis: A review on optical fiber sensors for the measurement of water turbidity," *Sensors*, vol. 9, no. 10, pp. 8311–8335, 2009.
- [3] W. G. Walter, "STANDARD METHODS FOR THE EXAMINATION OF WATER AND WASTEWATER (11th ed.)," *Am. J. Public Heal. Nations Heal.*, vol. 51, no. 6, pp. 146–155, 1961.
- [4] O. a. Postolache, P. M. B. S. Girão, J. M. D. Pereira, and H. M. G. Ramos, "Multibeam optical system and neural processing for turbidity measurement," *IEEE Sens. J.*, vol. 7, no. 5, pp. 677–684, 2007.
- [5] J. W. O'Del, "Determination of Turbidity By Nephelometry," *Stand. Methods Exam. Water Wastewater*, no. August, pp. 1–10, 1993.
- [6] C. P. Holliday, T. C. Rasmussen, and W. P. Miller, "Establishing the Relationship Between Turbidity and Total Suspended Sediment Concentration," *Proc. 2003 Georg. Water Resour. Conf.*, pp. 23–24 April, 2003.
- [7] C. G. Campbell, D. T. Laycak, W. Hoppes, N. T. Tran, and F. G. Shi, "High concentration suspended sediment measurements using a continuous fiber optic in-stream transmissometer," *J. Hydrol.*, vol. 311, no. 1–4, pp. 244–253, 2005.
- [8] F. J. Boogert, M. a S. Martins, L. Bilro, S. a Prats, R. N. Nogueira, and J. J. Keizer, "Assessing the potential of a newly-developed turbidity sensor for estimating sediment yields from recently burnt catchments," vol. 4, no. 3, pp. 139–141, 2013.
- [9] J. Downing, "Twenty-five years with OBS sensors: The good, the bad, and the ugly," *Cont. Shelf Res.*, vol. 26, no. 17–18, pp. 2299–2318, 2006.
- [10] T. Butt, J. Miles, P. Ganderton, and P. Russell, "A simple method for calibrating optical backscatter sensors in high concentrations of non-cohesive sediments," *Mar. Geol.*, vol. 192, no. 4, pp. 419–424, 2002.
- [11] J. C. Pernetta and J. D. Milliman, "Land-ocean interactions in the coastal zone - implementation plan," *IGBP Rep.*, vol. 33, no. 1, p. 215, 1995.
- [12] P. Polishuk, "Plastic optical fibers branch out," *IEEE Commun. Mag.*, vol. 44, no. 9, pp. 1–21, 2006.



Investigation of the in-solution relaxation of polymer optical fibre Bragg gratings

A. Fasano^{1*}, G. Woyessa², J. Janting², H.K. Rasmussen¹, O. Bang²

1 DTU Mekanik, Department of Mechanical Engineering, Technical University of Denmark, 2800 Kgs. Lyngby, Denmark

2 DTU Fotonik, Department of Photonics Engineering, Technical University of Denmark, 2800 Kgs. Lyngby, Denmark

*Corresponding author: andfas@mek.dtu.dk

Abstract: We investigate the response of PMMA microstructured polymer optical fibre Bragg gratings when immersed in methanol/water solutions. Overall we observe a permanent blue-shift in Bragg grating wavelength after solvent evaporation. The main contribution in the resonance wavelength shift probably arises from a permanent change in the size of the fibre, as already reported for high-temperature annealing of polymer optical fibres. As a consequence of the solution concentration dependence of the glass transition temperature of polymers, different methanol/water solutions lead to various degrees of frozen-in stress relaxation with an overall blue-shift of the Bragg grating wavelength.

Key Words: Polymer, Microstructured polymer optical fibre, Fibre Bragg grating, Annealing, Solution.

1. Introduction

Annealing of polymer optical fibre Bragg grating (POFBG) sensors has recently been the subject of an increasing number of studies as this process can enhance their thermal stability and widen the range of linear response of the gratings to temperature. Typical annealing conditions to obtain thermally stable hysteresis-free and wide operating range polymethyl methacrylate (PMMA) FBG sensors are 80°C and 90% RH [1]. The glass transition temperature (T_g) of a polymeric material equilibrated with a solvent differs from that of a pure polymer. Early investigations showed that the T_g of PMMA approaches room temperature when the polymer is equilibrated with methanol [2], whereas, at equilibrium with water, T_g is lowered by 20°C compared to pure PMMA [3]. This suggests that immersing a PMMA fibre in a suitable solution at room temperature may have an effect akin to annealing a solvent-free fibre at high temperature.

The aim of this work is to investigate the relaxation of PMMA mPOFBGs when immersed in methanol/water solutions. As a consequence of the solution concentration dependence of the T_g of PMMA, varying methanol/water ratio implies changing the T_g of a PMMA FBG when equilibrated with the solution, which results in a different degree of frozen-in drawing stress relaxation.

2. In-solution relaxation

The T_g of a polymer equilibrated with a solvent in general differs from the one for a solvent-free polymer. Early studies by Williams et al. [2] investigated the effect of presence of methanol on the T_g of PMMA. Depending on the weight-average molecular weight (M_w), the reported values for methanol-equilibrated PMMA systems range from 20°C ($M_w = 23500$ g/mol) to 30°C ($M_w = 550000$ g/mol), where M_w can be thought of as an average length of the polymer chain. PMMA polymers optimal for fibre drawing processes have an M_w of about 60000 g/mol [4]. This means that the T_g of a methanol-equilibrated PMMA fibre is around room temperature. Annealing is typically required for extending the temperature operating range of POFs and POFBGs as a polymer fibre tends to relax drawing stresses when it is heated up to high temperature (i.e., a temperature non far from their T_g). This can affect the dimensional stability of the fibre and therefore limit its operating temperature to values well below the theoretical ones. Heating up an un-annealed fibre to even modest temperatures may cause a permanent (blue-)shift in the Bragg reflection wavelength, and also its optical and mechanical properties may be affected. The fibre drawing process aligns the polymer chains in the draw direction to an extent mainly depending on the applied drawing forces. This leads to frozen-in stresses in the final fibre. Indeed, as a result of the fibre drawing process, polymer chains are in a non-equilibrium state and tend to move back towards the original configuration as soon as they are provided with enough energy to do so. The higher the temperature the greater the energy available for the polymer chains to rearrange themselves. This relaxation typically has the effect of changing the dimensions (i.e. length and diameter) of a



fibre. If we consider that approaching T_g is the condition required for the relaxation to occur, we can theoretically obtain an effect similar to annealing if we lower the T_g of the polymer fibre by immersing it in a methanol-based solution at room temperature. Pure methanol has been already used for the doping of PMMA POF canes with various compounds, e.g. Rhodamine 6G [5] and benzyl dimethyl ketal (BDK) [6]. Nevertheless, pure methanol cannot be directly used for stress relaxation in PMMA mPOFBGs as it corresponds to a too high annealing temperature. Hence we used water to dilute methanol. Water (Milli-Q) was chosen as it is miscible with methanol and the T_g of water-saturated PMMA was known from the literature to be approximately 20°C lower than that of the pure polymer [3]. So that we could expect that the addition of water would increase the T_g of PMMA equilibrated with a methanol/water solution, starting from a T_g being around room temperature when pure methanol is used.

3. Experiments and results

The PMMA mPOF was made by using the drill-and-draw method [4]. The average diameter of the fibre was around 150 μm . The fibre was two-ring microstructured with an 8 μm core. The hole pitch and hole diameter were 5 μm and 2 μm , respectively. The fibre was single-mode as the hole to pitch ratio was 0.40. Bragg gratings were inscribed into the fibre by using a CW HeCd laser operating at 325 nm (IK57511-G, Kimmon). For grating writing the phase mask method was used. The inscription setup was the same as in Bundalo et al. [7]. The laser power for grating writing was 20 mW. A custom-made phase mask by Ibsen Photonics A/S was used, optimised for writing at 325 nm and having a uniform period of 572.4 nm. Two FBGs were inscribed in two PMMA mPOFs from the same fibre draw and tested in solutions at two different methanol/water concentrations, 60:40% and 70:30% v/v. The initial resonance wavelengths (before immersion) were 846.2 nm and 847.3 nm, respectively. CHROMASOLV methanol (for HPLC, $\geq 99.9\%$, Sigma-Aldrich) and Milli-Q water were used in the experiments. In both cases, 10 ml solutions were prepared in 10 ml graduated cylinders sealed at the top to avoid evaporation throughout the experiments. The FBGs were removed from the solution once the rate of Bragg reflection wavelength shift (absolute value) was around 0.55 nm/hour.

Figure 1 shows the Bragg grating wavelength of a PMMA mPOFBG immersed in a solution of methanol and water 60:40% v/v for 33 hours. After the stopping criterion was met, the FBG was removed from the solution and monitored for further 9 hours in order to study the grating response during solvent evaporation. In this experiment we observed an overall blue-shift of 82.0 nm.

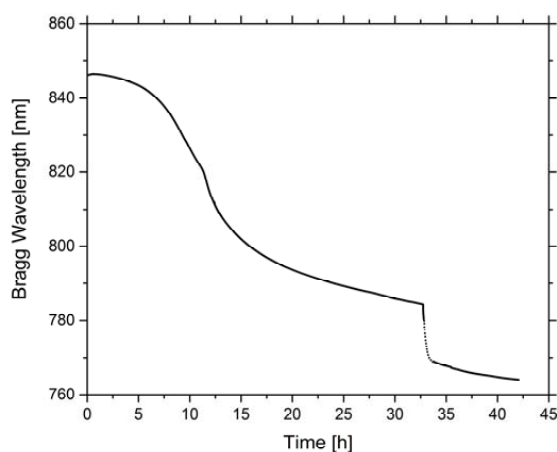


Figure 1. PMMA mPOFBG resonance wavelength monitored over 42 hours (immersion time = 33 hours). The solution is methanol/water 60:40% v/v. Two distinct regions can be observed: absorption-relaxation (0-33 hours) and desorption (33-42 hours). Note that a few experimental data were missing due to high reflection noise. Hence, in that region of the graph the curve was fitted (dotted line).



The absorption of the methanol/water solution in general changes both refractive index and fibre size. Since the shift was permanent, the relaxation probably corresponds to a permanent change in the size of the fibre, as already observed in high-temperature annealing of polymer optical fibres [8]. Some initial red-shift in Bragg wavelength was observed, with a maximum of +0.3 nm. This was the results of a temporary positive balance between red-shift due to solution-mediated swelling and blue-shift caused by chain alignment relaxation. However, after about 100 minutes the total shift referred to the initial Bragg wavelength became constantly negative. This corresponds to the tendency towards relaxation becoming stronger and stronger after an initial lag phase due to the initial diffusion of the solution into the fibre. However, the real contribution due to absorption/swelling, which would lead to a much greater red-shift than the observed one, was hidden by the incipient relaxation (blue-shift). This can easily be seen from Fig. 1, where a sudden and very sharp blue-shift of the resonance wavelength corresponding to a very fast solvent evaporation upon FBG removal from the solution is shown (time = 33 hours). The fast evaporation process was probably facilitated by the small diameter of the fibre (150 μm). The further down-shift occurred after removal of the Bragg grating from the solution was measured to be -20.2 nm (time = 42 hours). The shift was towards blue as evaporation implied de-swelling of the methanol/water solution, which caused further fibre shrinkage. The mild decrease observed after the sharp downward jump in resonance wavelength was probably due to solvent evaporation and some residual relaxation becoming less and less important as the solvent evaporation went on. An overall shift of -82.0 nm is comparable with the effect of 80 $^{\circ}\text{C}$ and 30% RH annealing conditions on PMMA mPOFBGs as reported by Woyessa et al. [1]. We further repeated the experiment applying similar conditions to a PMMA mPOF from the same draw in order to measure the total fibre shrinkage. The corresponding fibre shrinkage was measured to be about 8%.

Figure 2 shows the Bragg grating wavelength versus time for a PMMA mPOFBG immersed in a solution methanol/water 70:30% v/v. After 24 hours the FBG was removed from the solution (sharp downward jump in Fig. 2) and monitored for further 9 hours during evaporation as done for the case 60:40% v/v. As expected, the effect on the reflection wavelength was more pronounced, as a total blue-shift of 113.8 nm was recorded. Notice, the final resonance wavelength of 733.5 nm approximately corresponds to the resonance wavelength obtainable when the annealing of 850 nm PMMA mPOFBGs is performed at 80 $^{\circ}\text{C}$ and 70% RH [1].

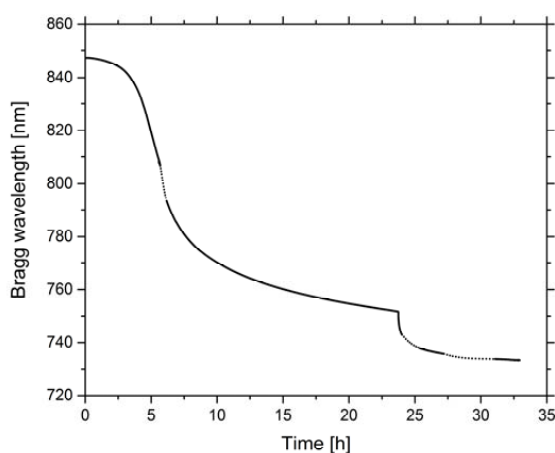


Figure 2. PMMA mPOFBG resonance wavelength monitored over 33 hours (immersion time = 24 hours). The solution is methanol/water 70:30% v/v. Two distinct regions may be seen: absorption-relaxation (0-24 hours) and desorption (24-33 hours). As happened in the case 60:40% v/v, some data were missing because of high reflection noise and were therefore obtained by non-linear fitting (dotted lines).



Unlike the previous case of methanol/water 60:40% v/v, we did not observe any significant initial red-shift when using methanol/water 70:30% v/v. Also, the relaxation process was visibly faster as methanol is a stronger swelling agent for PMMA than is water. The total blue-shift in resonance wavelength measured from FBG removal from the solution (time = 24 hours) until the end of the experiment (time = 33 hours) was 18.4 nm, comparable with the previous experiment. As done in the case 60:40% v/v, we repeated the experiment on the PMMA mPOF to evaluate the corresponding fibre shrinkage. The overall shrinkage for the same fibre after being immersed in a solution methanol/water 70:30% v/v for the same time and left dry was approximately 16%.

4. Conclusion

The possibility of relaxing stresses frozen in the fibre by using methanol/water solutions was demonstrated. A tunability up to 82.0 nm and 113.8 nm was shown for solutions methanol/water 60:40% v/v and 70:30% v/v, respectively. Both blue-shifts were permanent and obtained at room temperature by immersing two-ring PMMA mPOFBGs in a methanol-based solution at various concentrations of water. This suggests that solution stress relaxation may represent a viable process to improve the thermal stability of PMMA mPOFBGs as an alternative to conventional annealing. In addition, with an appropriate combination of solvents, the same principle could also be applied to other polymers, such as TOPAS and polycarbonate. This solution-based method could be particularly advantageous when thermally activated degradation processes associated with long exposure times at high temperature are an issue. Moreover, it may represent a cheap way of annealing as no complex and expensive climate chamber is required.

5. Acknowledgements

This work was supported by the People Programme (Marie Curie Actions) of the European Union's Seventh Framework Programme FP7/2007-2013/ under REA grant agreement number 608382.

6. References

- [1] G. Woyessa, K. Nielsen, A. Stefani, C. Markos, O. Bang, "Temperature insensitive hysteresis free highly sensitive polymer optical fiber Bragg grating humidity sensor," *Opt. Express* 24(2), 1206-1213 (2016).
- [2] D.R.G. Williams, P.E.M. Allen, V.T. Truong, "Glass transition temperature and stress relaxation of methanol equilibrated poly (methyl methacrylate)," *Eur. Polym. J.* 22(11), 911-919 (1986).
- [3] L.S.A. Smith, V. Schmitz, "The effect of water on the glass transition temperature of poly(methyl methacrylate)," *Polymer* 29(10), 1871-1878 (1988).
- [4] M.C.J. Large, G.W. Barton, L. Poladian, M.A. van Eijkelenborg, "Microstructured Polymer Optical Fibres," Springer, 2008.
- [5] M.C.J. Large, S. Ponrathnam, A. Argyros, N. S. Pujari, F. Cox, "Solution doping of microstructured polymer optical fibres," *Opt. Express* 12(9), 1966-1971 (2004).
- [6] D. Sáez-Rodríguez, K. Nielsen, H. K. Rasmussen, O. Bang, D. J. Webb, "Highly photosensitive polymethyl methacrylate microstructured polymer optical fiber with doped core," *Opt. Lett.* 38(19), 3769-3772 (2013).
- [7] I.-L. Bundalo, K. Nielsen, C. Markos, O. Bang, "Bragg grating writing in PMMA microstructured polymer optical fibers in less than 7 minutes," *Opt. Express* 22(5), 5270-5276 (2014).
- [8] P. Stajanca, O. Cetinkaya, M. Schukar, K. Krebber, "Molecular alignment relaxation in polymer optical fibers for sensing applications," *Opt. Fiber Technol.* 28, 11-17 (2016).

3D-printed PMMA Preform for Hollow-core POF Drawing

M. G. Zubel^{1*}, A. Fasano², G. Woyessa³, K. Sugden¹, H. K. Rasmussen², O. Bang³

1 Aston Institute of Photonic Technologies, Aston University, B4 7ET Birmingham, United Kingdom

2 Department of Mechanical Engineering, Technical University of Denmark, 2800 Kgs. Lyngby, Denmark

3 Department of Photonics Engineering, Technical University of Denmark, 2800 Kgs. Lyngby, Denmark

*Corresponding author: m.zubel@aston.ac.uk

Abstract: In this paper we report the first, to our knowledge, 3D-printed hollow-core poly(methyl methacrylate) (PMMA) preform for polymer optical fibre drawing. It was printed of commercial PMMA by means of fused deposition modelling technique. The preform was drawn to cane, proving good enough quality of drawing process and the PMMA molecular weight to be appropriate for drawing. This ascertains that the manufacturing process provides preforms suitable for hollow-core fibre drawing. The paper focuses on maximisation of transparency of PMMA 3D printouts by optimising printing process parameters: nozzle temperature, printing speed and infill.

1. Introduction

3D printing, or additive-layer manufacturing (ALM), is a group of techniques that have recently been revolutionising the field of manufacturing [1, 2]. They are widely considered the manufacturing technologies of the future. It is due, among other things, to ever lower price and hence wider accessibility, ease of customisability, ability to reproduce complex shapes, as well as growing number of available materials and capabilities stemming from them.

The particular ALM technique used in this paper is fused deposition modelling (FDM). It is the most popular ALM technique, and it seems especially well suited to use in manufacturing polymer optical fibre (POF) preforms. Firstly, FDM relies on printing with polymers that are thermoplastic, which is also the key material requirement for preform fabrication. Moreover, this technique can be capable of creating preforms that would be extremely difficult to make in another way, e.g. having non-circular holes. Finally, FDM offers the highest ability of all ALM techniques to mix various materials within one printout. This opens up the possibility of tuning wide range of material properties with unprecedented ease (chemical composition, refractive index, transparency, coefficient of thermal expansion, flexibility, affinity to water, biodegradability, etc.).

Hollow-core (HC) microstructured optical fibres are drawing increasing attention as they can offer better transmission at those wavelengths where material loss is high. Air-guidance is of particular interest for microstructured polymer optical fibres (mPOF), in which attenuation is generally an issue. Especially given the problem of high transmission losses reported for optical fibres drawn from a 3D-printed solid-core polymer preform [3]. Moreover, the effects of other material properties such as non-linearity can be reduced if a HC is used [4]. For example, within some regions of the infrared Argyros et al. [5] demonstrated loss much lower than the respective material loss for a HC mPOF made of poly(methyl methacrylate) (PMMA). In this work we have chosen to 3D print a HC mPOF preform with a structure similar to the one proposed by Pryamikov et al. [6] in silica fibres, where the guidance was not based the photonic band gap principle or Kagome lattice claddings, but relied on the negative curvature of the core wall and the scattering characteristics of the cladding elements. As a proof of concept, this type of structure is supposed to be relatively easier to 3D print from the viewpoint of printing resolution than typical HC mPOF preforms having several tens of tiny holes. A thick HC fibre with negative curvature has been 3D printed by Cruz et al. for terahertz applications [7]. The possibility of producing HC mPOF preforms that are drawable can make the range of possible applications much wider.

The FDM technique has already been used by Cook et al. [3] to 3D-print a solid-core preform of styrene-butadiene copolymer and polystyrene. The authors managed to draw fibre from the preform, but a high loss value excluded any practical applications. In this paper we report the first, to our knowledge, 3D printed hollow-core preform for POF drawing. The reason behind the use of a HC structure is to reduce importance of material transparency, as the highest light density corresponds to the air region of the core. The preform was printed of PMMA, which has been proven to display good transparency, and which is the best-studied material

for POF drawing. Choice of design and fabrication procedure are described, paying special attention to transparency optimisation during 3D printing stage. We show that the HC PMMA mPOF preform is drawable to a cane, an intermediate step between preform and fibre. This suggests that a HC mPOF may be obtained by using the proposed method. The results of drawing the preform to cane are presented and discussed in order to identify potential points of improvement.

2. Design and fabrication

2.1 Design

The preform was designed as an enlarged version of the structure of the silica HC microstructured optical fibre investigated by Pryamikov et al. [6]. The structure to 3D print basically consisted of eight capillary tubes inserted into an outer hollow tube, as shown in Figure 1. In the fibre manufactured in [6], the relative preform was made by capillary stacking and the capillaries were fused together by using an oxygen-hydrogen burner. The CAD design was carried out by using SolidWorks 2015. The external and internal diameters of the outer tube were 65.0 and 45.6 mm, respectively. The length of the preform was 102.5 mm. The eight tubes inside the larger tube had the same external and internal diameter, i.e. 12.6 mm and 9.6 mm, respectively. The resulting air core diameter of the preform was 20.4 mm.

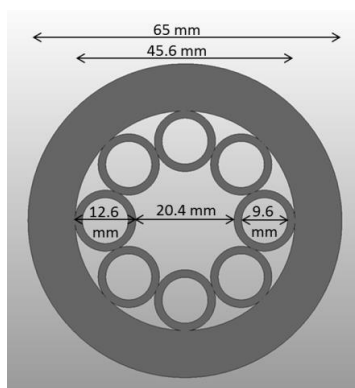


Figure 1. Cross section view of the preform to 3D print.

2.2 3D printing

The main focus of the optimisation of 3D printing parameters was transparency increase. Despite all the advantages of the FDM technique introduced above, it is intrinsically not well-suited for manufacturing transparent printouts, as opposed to some other competing AML techniques. In FDM, a printout layer is created by melting together threads of plastic filament, normally leaving air voids between them, which leads to creating sources of light scattering. Transparency optimisation of FDM-printed structures relied then on assuring that adjacent threads melt together as much as possible, leaving no air voids in the printout.

All printouts described in this paper were printed from a commercially-available PMMA filament, dried at 85 °C for drawing. The machine was an UP! 3D printer, working with the dedicated UP! slicer (software which transforms a 3D model into a series of printer commands) with the FixUp3D extension.

Transparency optimisation experiments were performed on 4 mm thick slices of the preform. After printing, the samples were polished from top, bottom and the side, which allowed for qualitative assessment of transparency.

The following parameters were varied during optimisation process:

- Nozzle temperature
- Printing speed (speed of nozzle movement)
- Infill

All these parameters are machine- and filament-dependent, so the optimised values should be treated as an indication only. Moreover, the software uses a non-standard parameter set for infill, which is not easily comparable with those of other slicers. For these reasons, qualitative discussion of optimisation process is presented below, and quantitative data are provided where possible.

Nozzle temperature values from 250 °C to 300 °C with 10 °C step were tested to find that the optimal temperature values from the viewpoint of transparency were 280-290 °C. For the temperatures below 280 °C filament threads seemed not to melt together well, whereas for 300 °C viscosity was probably too low. The nozzle temperature used for fabricating the final preform was decided to be 290 °C.

Printing speed, which is the speed at which the nozzle moves, was varied from 40 mm/s down. The general rule was found to be that the lower the speed, the better the transparency. Practical constraints are the only limiting factor keeping the speed high, as lowering the printing speed increases overall manufacturing time. Transparency improvement at low printing speed seems to be linked to heat transfer from the nozzle to the sample. If printing speed is low, the areas adjacent to the thread being deposited have more time to heat up. This results in the adjacent threads melting together better, minimising formation of air voids. The speed at which the final preform was printed was decided to be 5 mm/s.

The need for optimal infill (or filament feed rate) was identified, while too high and too low values were resulting in transparency decrease. When infill was too low, there was not enough material deposited by the nozzle to fill all required volume of printout. Too high infill values were making excessive material aggregate at printout walls, deteriorating print precision and hindering operation of the printer. In this case, air voids at thread junctions were also found bigger.

Apart from the optimised parameters described above, there were two parameters that were kept constant throughout the tests: layer thickness and printing bed temperature. The former was set to 150 µm, which was the lowest value recommended for the 3D printer, and any lower value would result in tremendous increase in preform fabrication time. On the other hand, higher layer thickness would decrease lateral (XY) resolution of printout. Regarding printing bed temperature, it was kept at around 105 °C (the highest settable value for the machine). As it has already been mentioned, the higher the temperature of the adjacent threads, the better they melt together. However, the favourable influence of the printing bed temperature was only visible until around 2 cm up from the printing bed, while at higher distances the heat coming from the printing bed was being dissipated.

The final preform was printed in 9 days, 16 hours and 43 min (232.7 h), consuming 226.8 g of the material (Figure 2). The printing time was much longer than this reported by Cook et al. [3] (6 h) to provide highest practically achievable transparency of the preform.



Figure 2. Hollow-core PMMA mPOF preform on the printing bed.

2.3 Post-print processing

The preform was dried for two days at 85 °C, after which it was machined in order to reduce surface roughness resulting from the 3D printing process. The final diameter (i.e. diameter of the outer tube) and length of the preform were 60.0 mm and 100.0 mm, respectively, giving an aspect ratio of 0.6. The preform was then dried at 80 °C for six days before drawing.

2.4 Drawing to cane

The drawing conditions were unknown for the particular PMMA grade the preform was made of. In particular, important parameters such as the molecular weight, which gives information about the average chain length of the polymer, were not available. The optimal molecular weight for drawing PMMA is around 60000 g/mol [4]. Also considering the specific HC structure, we decided to start from a low temperature (around 50 °C below the usual temperature for commercial PMMA rods, which is around 190 °C) and increase it gradually to find the minimum temperature suitable for drawing. The final drawing temperature was 10 °C below the usual drawing temperature for PMMA. We conducted the process at high tension aiming to decrease surface roughness. High tension can indeed yield lower roughness and therefore help reduce fibre loss [8]. Several canes were obtained from the HC mPOF preform, as shown in Figure 3.

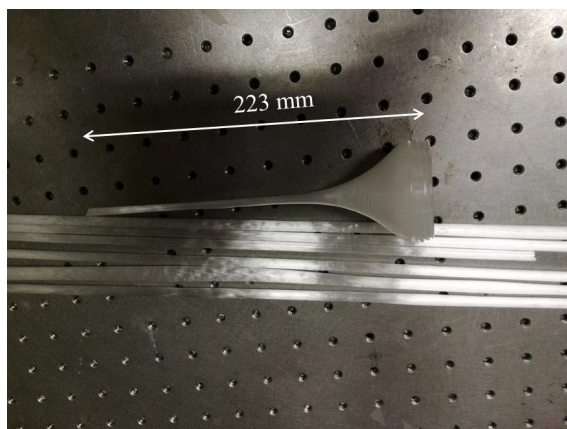


Figure 3. Hollow-core PMMA mPOF canes obtained from 3D printed preform drawing.

Figure 4 displays the cross-section of one of the HC PMMA mPOF canes, whereas the geometrical parameters are reported in Table 1. In Figure 4 it may be seen that the drawing led to two phenomena. First, some capillaries moved away from each other. This may be a consequence of the very thin layer of material keeping them joined. Furthermore, even a small inhomogeneity in heat distribution within the preform can strongly affect the fluid mechanical response of the HC structure and break its initial symmetry. The second phenomenon we observed is the holes becoming elliptical. As a result, relative to the outer diameter of the cane, the air core diameter was larger than at the preform stage ($2.2\text{ mm}/4.7\text{ mm}=47\%$ instead of $20.4\text{ mm}/60.0\text{ mm}=34\%$). Also, the walls of the capillaries were thicker than those in the preform. Such deviations from the initial design can be reduced by improving the drawing conditions for these particular types of HC structure and PMMA.

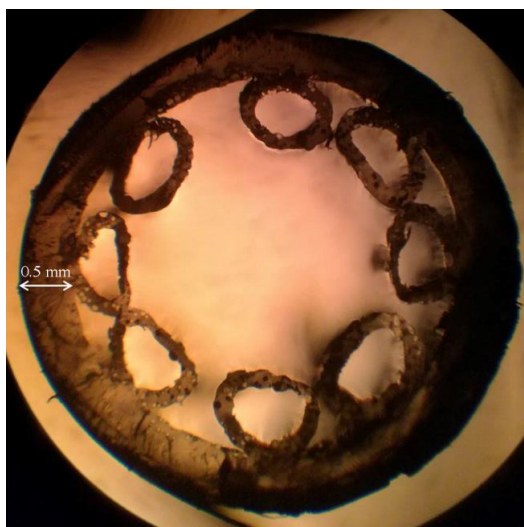


Figure 4. Cross-section of a HC PMMA mPOF cane.

Wall thickness of the capillaries	0.16 mm
Wall thickness of the outer tube	0.5 mm
Diameter of the air core	2.2 mm
Major diameter of elliptical holes	0.6 mm
Minor diameter of elliptical holes	0.4 mm
External diameter of the cane	4.7 mm

Table 1. Average geometrical parameters for a HC PMMA mPOF cane.

3. Conclusions and outlook

To the best of our knowledge, this paper presented the first 3D-printed hollow-core preform for POF drawing. It was made of PMMA, which is the most popular and hence best-studied material for preform fabrication. It is expected that, thanks to this, further drawing optimisation process should be relatively quick and straightforward, leading to favourable mechanical and optical preform properties. The preform was proven to be drawable, which implies that the optimised procedure should be suitable for producing hollow-core POF.

In the next step, the cane presented in the paper will be drawn to fibre and light guidance will be checked. Further changes to the fabrication procedure will encompass improvement of drawing conditions (to avoid separation of capillaries), as well as performing high-temperature annealing before drawing. Furthermore, a new design will be proposed, as the current one was originally developed for silica [6].

3. Acknowledgement

The research leading to these results has received funding from the People Programme (Marie Curie Actions) of the European Union's Seventh Framework Programme FP7/2007-2013/ under REA grant agreement n° 608382.

4. References

- [1] S. H. Huang, P. Liu, A. Mokasdar, and L. Hou, "Additive manufacturing and its societal impact: A literature review," *International Journal of Advanced Manufacturing Technology*, vol. 67, pp. 1191-1203, 2013.
- [2] T. J. Horn and O. L. A. Harrysson, "Overview of current additive manufacturing technologies and selected applications," *Science Progress*, vol. 95, pp. 255-282, 2012.
- [3] K. Cook, J. Canning, S. Leon-Saval, Z. Reid, M. A. Hossain, J. E. Comatti, *et al.*, "Air-structured optical fiber drawn from a 3D-printed preform," *Opt Lett*, vol. 40, pp. 3966-9, Sep 1 2015.
- [4] M. C. J. Large, L. Poladian, G. W. Barton, and M. A. Van Eijkelenborg, *Microstructured polymer optical fibres*: Springer US, 2008.
- [5] A. Argyros, M. A. van Eijkelenborg, M. C. Large, and I. M. Bassett, "Hollow-core microstructured polymer optical fiber," *Optics Letters*, vol. 31, pp. 172-174, 2006/01/15 2006.
- [6] A. D. Pryamikov, A. S. Biriukov, A. F. Kosolapov, V. G. Plotnichenko, S. L. Semjonov, and E. M. Dianov, "Demonstration of a waveguide regime for a silica hollow - core microstructured optical fiber with a negative curvature of the core boundary in the spectral region $> 3.5 \mu\text{m}$," *Optics Express*, vol. 19, pp. 1441-1448, 2011/01/17 2011.
- [7] A. L. S. Cruz, V. A. Serrão, C. L. Barbosa, M. A. R. Franco, C. M. B. Cordeiro, A. Argyros, *et al.*, "3D printed hollow core fiber with negative curvature for terahertz applications," *Journal of Microwaves, Optoelectronics and Electromagnetic Applications*, vol. 14, pp. S145-S153, 2015.
- [8] A. Argyros, R. Lwin, S. G. Leon-Saval, J. Poulin, L. Poladian, and M. C. J. Large, "Low Loss and Temperature Stable Microstructured Polymer Optical Fibers," *Journal of Lightwave Technology*, vol. 30, pp. 192-197, 2012.